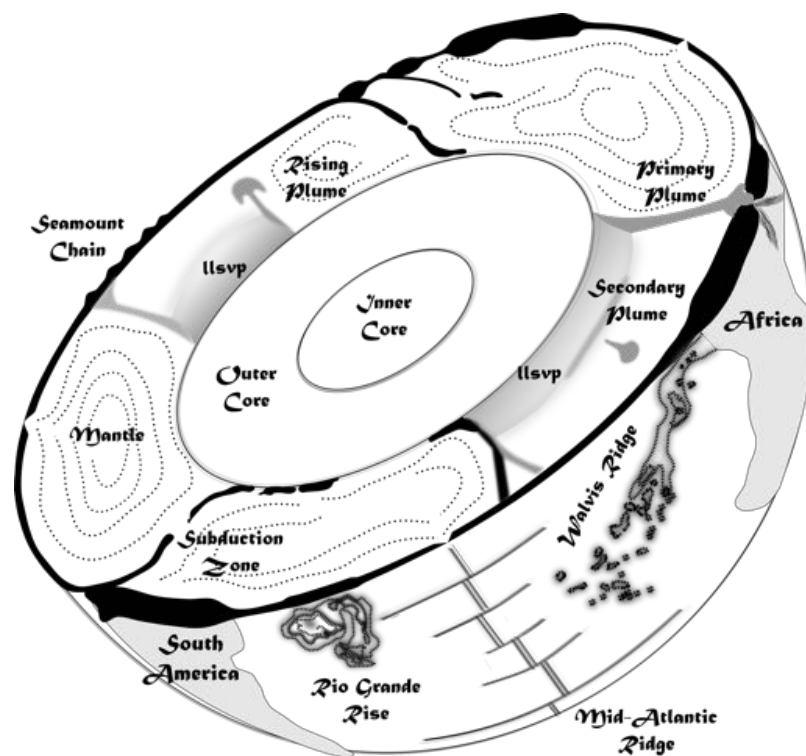


# Insights into the temporal and geochemical evolution of the Walvis Ridge

---

## A connection between HIMU and EM I end members in the South Atlantic



Dissertation

zur Erlangung des Doktorgrades

der Mathematisch-Naturwissenschaftlichen Fakultät

der Christan-Albrechts-Universität zu Kiel

vorgelegt von

**Stephan Homrighausen**

Kiel, 2018

Erster Gutachter .....Prof. Dr. Kaj Hoernle  
Zweiter Gutachter.....Prof. Dr. Colin Devey  
Tag der mündlichen Prüfung.....25.05.2018

## EIDESSTATTLICHE ERKLÄRUNG

---

Stephan Homrighausen

Parkstraße 16

24306 Plön

Hiermit versichere ich, dass

1. ich die vorliegende Doktorarbeit selbständig und ohne Zuhilfenahme unerlaubter Hilfsmittel erstellt habe.
2. diese noch eine ähnliche Arbeit an einer anderen Hochschule im Rahmen eines Prüfungsverfahrens vorgelegt, veröffentlicht oder zur Veröffentlichung vorgelegt wurde.
3. die Arbeit unter Einhaltung der Regeln guter wissenschaftlicher Praxis der Deutschen Forschungsgemeinschaft entstanden ist.

Kiel den 17.04.2018

---

Stephan Homrighausen

## **PREFACE**

The following dissertation is composed of three independent articles that are either accepted for publication or submitted to an international peer-reviewed journal. The first manuscript reviews the distribution of the HIMU mantle end member and presents a conceptual model of a widespread lowermost mantle reservoir in an Archean geodynamical setting. The second paper focuses on late-stage volcanism on the Walvis Ridge in the South Atlantic and the last article summarizes the temporal and spatial geochemical evolution of South Atlantic intraplate lavas.

My dissertation was funded by the German Ministry for Research and Education (BMBF; grants SO233 WALVIS II and SO234 Spaces; 03G0233A) and the GEOMAR Helmholtz Centre for Ocean Research Kiel.

## ABSTRACT

The Walvis Ridge, located in the South Atlantic, represents the oldest submarine expression of the Tristan-Gough seamount chain, which extends from the Namibian coast to the active volcanic islands of Tristan da Cunha and Gough. As a reference locality of the EM I end member (enriched mantle one) and a type locality of the classical mantle plume concept, the poorly sampled Walvis Ridge represents an excellent opportunity to examine fundamental geological concepts. To provide further insights into the origin and evolution of the Tristan-Gough seamount chain, my PhD thesis presents a comprehensive geochemical (major and trace elements and Sr-Nd-Pb-Hf isotopes) and geochronological data set ( $^{40}\text{Ar}/^{39}\text{Ar}$  data) of 35 new sample sites from the Walvis Ridge.

The combined results of my bathymetric, geochemical and geochronological data revealed that the Walvis Ridge experienced two magmatic pulses. During the first magmatic phase, the broad ridge crest (basement) was emplaced. These basement lavas have an EM I-type composition and show an excellent age progression of  $\sim 31$  mm/a along the entire Tristan-Gough hotspot track, indicating relatively constant plate motion over a deep-rooted mantle melt anomaly in the last  $\sim 115$  Ma. In combination with seismic data (French and Romanowicz, 2015; Schlömer et al., 2017) and high  $^3\text{He}/^4\text{He}$  ratios (Stroncik et al., 2017), the excellent age progression indicates that the Tristan-Gough mantle plume derive from the margin of the African Large Low Shear Velocity Province (LLSVP) in the lowermost mantle.

A more detailed analysis of the collected lavas revealed that the majority of the superimposed seamounts/ridges on and adjacent to the Walvis Ridge were emplaced 20 to 40 Myr after the formation of the Walvis Ridge basement (EM I), representing the second magmatic pulse. The geochemical signature of these seamounts is characterized

by St. Helena HIMU end member type composition. The long volcanic quiescence and the HIMU-like geochemical signature of the seamounts are unusual for classical hotspot related late-stage (rejuvenated/post-erosional) volcanism, indicating that these seamounts are not associated with the deep-rooted Tristan-Gough mantle plume. HIMU-like lavas along the southwestern African coast have similar emplacement ages (80-50 Ma), suggesting a larger-scale event and possibly mantle upwellings from the internal portions of the African LLSVP.

Based on the characteristic geochemical fingerprints of the South Atlantic intraplate lavas and their position relative to the 1 %  $\partial V_s$  velocity contour of the African LLSVP, I propose that the spatial and temporal geochemical heterogeneities in the South Atlantic hotspots ultimately reflects the sampling of different geochemical domains outside and inside the African LLSVP.

I also present new geochemical and geochronological data from the Richardson Seamount in the South Atlantic Ocean and the Manihiki Plateau and Eastern Chatham Rise in the southwest Pacific Ocean. The new data, combined with literature data documents a more widespread (nearly global) distribution of the HIMU end member than previously postulated. The restricted trace element and isotopic composition (St. Helena type HIMU), but the near-global distribution point to a deep-seated, widespread reservoir, which formed most likely in the Archean. In this context I re-evaluate the origin of HIMU in an Archean geodynamic setting.

## KURZFASSUNG

Der Walvisrücken ist die älteste submarine Spur der Tristan-Gough Vulkankette, die sich von der namibischen Küste bis zu den aktiven Vulkaninseln Tristan da Cunha und Gough erstreckt. Trotz seiner Wichtigkeit als südatlantische Typlokalität des geochemisch angereicherten Mantelendgliedes EM I und Teil einer klassischen Hotspotspur, ist der Walvisrücken bislang nur lückenhaft beprobt. Um weitere Einblicke in die Entstehung, sowie in die zeitliche und geochemische Entwicklung der gesamten Vulkankette zu erlangen, wurde im Rahmen der „Expedition SO233“ eine detaillierte Beprobung durchgeführt. Meine Doktorarbeit umfasst einen vollständigen geochemischen (Haupt- und Spurenelement, Sr-Nd-Pb-Hf Isotopie) und geochronologischen Datensatz von 35 neuen Beprobungsorte des Walvisrückens.

Batymetrische, geochemische und geochronologische Daten belegen, dass der Walvisrücken von zwei unterschiedlichen magmatische Phasen geprägt ist. Während der ersten magmatischen Hauptphase wurde der breite und plateauähnliche Walvisrücken gebildet, wohingegen in einer Spätphase vereinzelte Vulkane auf und neben ihm entstanden sind. Die magmatische Hauptphase ist durch eine EM I Signatur geprägt und weist eine exzellente Alterprogression von ca. 31 mm/a entlang der gesamten Hotspotspur auf, was auf eine relativ konstante Plattengeschwindigkeit und tiefe Schmelzanomalie (Mantelplume) seit 115 Ma hinweist. Diese exzellente Alterprogression in Verbindung mit seismischen Daten (French and Romanowicz, 2015; Schlömer et al., 2017) und hohen  $^3\text{He}/^4\text{He}$  Verhältnis (Etendeka; Stroncik et al., 2017) deutet an, dass der Tristan-Gough Mantelplume vom Rande der afrikanischen Large Low Shear Velocity Province (LLSVP) im unteren Erdmantel entstammt.

Eine detaillierte Analyse meines erhobenen Datensatzes zeigt, dass der überwiegende Anteil der Vulkane auf und neben dem Walvisrückens 20 bis 40 Ma jünger

sind als die EM I geprägte Hauptphase. Diese vulkanische Spätphase weist eine St. Helena HIMU Mantelendglied Signatur auf. Die ungewöhnlich späte vulkanische Reaktivierung und die HIMU geprägte Zusammensetzung der Spätphase sind untypisch für Hotspotvulkanismus, was darauf hindeutet, dass diese Vulkane nicht durch den Tristan-Gough Mantelplume entstanden sind. Laven mit HIMU Signatur entlang der südwestafrikanischen Küste sind zeitgleich mit der Spätphase des Walvisrückens eruptiert (80-50 Ma). Dies impliziert ein großräumliches Event und möglicherweise eine tiefe Schmelzanomalie von einer zentraleren Position der afrikanischen LLSVP.

Basierend auf den charakteristischen geochemischen Zusammensetzung des südatlantischen Hotspotvulkanismus und ihrer Position relativ zu der 1 %  $\partial V_s$  Kontur der afrikanischen LLSVP, kann die räumliche und zeitliche geochemische Entwicklung im Südatlantik durch unterschiedliche Reservoirs außer- und innerhalb der LLSVP erklärt werden.

Des Weiteren umfasst meine Doktorarbeit geochemische und geochronologische Daten vom „Richardson Seamount“ im Südatlantik, sowie vom „Manihiki Plateau“ und östlichem „Chatham Rise“. In Verbindung mit Literaturdaten zeige ich, dass das HIMU Mantelendglied (St. Helena Zusammensetzung) nahezu weltweit verbreitet ist und wahrscheinlich im Archaikum geformt wurde. In diesem Zusammenhang präsentiere ich ein alternatives Modell zur Entstehung eines weitverbreiteten HIMU Reservoirs in einem archaisch-tektonischem Rahmen.



## CONTENTS

<b>EIDESSTATTLICHE ERKLÄRUNG</b>	<b>II</b>
<b>PREFACE</b>	<b>III</b>
<b>ABSTRACT</b>	<b>IV</b>
<b>KURZFASSUNG</b>	<b>VI</b>
<b>1. GENERAL INTRODUCTION</b>	<b>1</b>
1.1 <i>The geochemical heterogeneity of the Earth's mantle</i>	1
1.2 <i>The mantle plume theory</i>	3
1.3 <i>The Walvis Ridge</i>	7
1.4 <i>Main objectives</i>	11
1.5 <i>References</i>	13
<b>2. CONTRIBUTION TO SCIENTIFIC JOURNALS</b>	<b>16</b>
<b>CHAPTER I</b>	<b>19</b>
<b>GLOBAL DISTRIBUTION OF THE HIMU END MEMBER: FORMATION THROUGH ARCHEAN PLUME-LID TECTONICS</b>	
Abstract	20
1. Introduction	22
2. Geological background of the sample locations	26
2.1 <i>The Walvis Ridge</i>	26
2.2 <i>Richardson Seamount (Shona hotspot track)</i>	29
2.3 <i>The Manihiki-Hikurangi plateau seamounts</i>	30
3. Analytical methods	32

3.1	<i><sup>40</sup>Ar/<sup>39</sup>Ar dating</i>	32
3.2	<i>Alteration and age correction of radiogenic isotope ratios</i>	34
4.	Results and HIMU geochemistry	36
4.1	<i>Major elements</i>	37
4.2	<i>Trace elements</i>	40
4.3	<i>Sr-Nd-Pb-Hf isotope data</i>	43
5.	Worldwide distribution of HIMU	45
5.1	<i>Distribution of end member HIMU in the oceans</i>	45
5.2	<i>Distribution of end member HIMU on the continents</i>	49
6.	Shallow or deep HIMU reservoir(s)?	52
7.	HIMU reservoir formation in an Archean geodynamical context	56
7.1	<i>Age of the HIMU reservoir formation</i>	56
7.2	<i>The style of Archean tectonics</i>	57
7.3	<i>An alternative model for the HIMU reservoir formation in the Archean tectonic system</i>	58
8.	Conclusions	65
9.	Acknowledgments	67
10.	Funding	67
11.	Declaration of interest	67
	References	68
	<b>CHAPTER II</b>	<b>77</b>
	<b>UNEXPECTED HIMU-TYPE LATE-STAGE VOLCANISM ON THE WALVIS RIDGE</b>	
	Abstract	78

1. Introduction	80
2. Geological Background	83
3. Analytical Methods	86
4. Results	86
4.1 <i><sup>40</sup>Ar/<sup>39</sup>Ar age dating</i>	86
4.2 <i>Geochemistry</i>	90
5. Discussion	98
5.1 <i>Morphology and age of seamounts from the Walvis Ridge</i>	98
5.2 <i>Compositional variation of the Walvis Ridge seamounts</i>	101
5.3 <i>Possible models for the origin of the late-stage         Walvis Seamount volcanism</i>	106
6. Conclusions	111
7. Acknowledgments	112
8. Declaration of interest	112
References	113

**CHAPTER III** **116**

**COMPARISON OF NEW AGE AND GEOCHEMICAL DATA FROM THE WALVIS RIDGE WITH OTHER**

**SOUTH ATLANTIC HOTSPOTS: MAPPING THE BASE OF THE LOWER MANTLE BENEATH**

**THE SOUTH ATLANTIC**

Abstract	117
1. Introduction	119
2. Geological Background	122
3. Analytical Methods	124

4. Results	124
4.1 <i>Alteration and age correction of radiogenic isotope ratios</i>	124
4.2 <i>Geochemical results</i>	128
4.3 <i><sup>40</sup>Ar/<sup>39</sup>Ar dating</i>	134
5. Discussion	137
5.1 <i>The age progressive Walvis Ridge</i>	137
5.2 <i>The Gough-type composition: The dominant composition in South Atlantic hotspots</i>	141
5.2.1 <i>The beginning of the geochemical zonation in the Tristan-Gough hotspot track</i>	141
5.2.2 <i>Geochemical Variations of the Gough-type lavas in the Tristan-Gough hotspot track</i>	143
5.2.3 <i>A common EM I-type in South Atlantic hotspots</i>	145
5.2.4 <i>Deep or shallow heritage of the common Gough-type composition?</i>	147
5.3 <i>Geochemical heterogeneity in the South Atlantic</i>	149
5.3.1 <i>The Tristan and Southern Discovery EM I-type flavors</i>	149
5.3.2 <i>FOZO and HIMU in the South Atlantic</i>	151
6. Towards a South Atlantic geodynamic model	153
7. Acknowledgments	156
8. Declaration of interest	156
References	157
<b>3. CONCLUSIONS AND OUTLOOK</b>	<b>161</b>
3.1 <i>Conclusions</i>	161

3.2 Outlook	166
<b>APPENDICES (CHAPTER I)</b>	<b>169</b>
<i>Appendix A: Analytical Methods</i>	169
<i>Appendix B: <sup>40</sup>Ar/<sup>39</sup>Ar age, major element, trace element                     and isotope data</i>	176
<i>Appendix C: <sup>40</sup>Ar/<sup>39</sup>Ar analytical data</i>	179
<b>APPENDICES (CHAPTER II)</b>	<b>180</b>
<i>Appendix A: Analytical Methods</i>	180
<i>Appendix B: <sup>40</sup>Ar/<sup>39</sup>Ar age, major element, trace element                     and isotope data</i>	194
<i>Appendix C: <sup>40</sup>Ar/<sup>39</sup>Ar analytical data</i>	197
<b>APPENDICES (CHAPTER III)</b>	<b>210</b>
<i>Appendix A: Analytical Methods and Supplementary Figures</i>	210
<i>Appendix B: <sup>40</sup>Ar/<sup>39</sup>Ar age, major element, trace element                     and isotope data</i>	228
<i>Appendix C: <sup>40</sup>Ar/<sup>39</sup>Ar analytical data</i>	231
<b>APPENDICES (DATA QUALITY AND LITERATURE DATA)</b>	<b>255</b>
<i>Appendix D: Accuracy of major element data</i>	255
<i>Appendix E: Accuracy of trace element data</i>	258
<i>Appendix F: Literature Data</i>	260
<b>DANKSAGUNG</b>	<b>268</b>
<b>CURRICULUM VITAE</b>	<b>270</b>

# 1. GENERAL INTRODUCTION

## 1.1 *The geochemical heterogeneity of the Earth's mantle*

For several decades, geochemists have recognized that the geochemical signature of volcanic rocks provides insights into the evolution of the Earth. The geochemical fingerprint of volcanic rocks carries information from its petrogenetic evolution and source composition. Based on the Sr-Nd-Pb-Hf isotope systematics of oceanic lavas, four distinct mantle end members were identified, which can describe the large-scale heterogeneity of the Earth's mantle (e.g., Zindler and Hart, 1986; Hofmann, 1997; Willbold and Stracke, 2006; White, 2015). These end members are as follows:

- 1) Depleted Mantle (**DM**; characterized by relatively unradiogenic Sr and Pb, but radiogenic Nd and Hf isotope ratios)
- 2) Enriched Mantle type one (**EM I**; characterized by unradiogenic Nd, Hf and  $^{206}\text{Pb}/^{204}\text{Pb}$  but relatively radiogenic Sr,  $^{207}\text{Pb}/^{204}\text{Pb}$  and  $^{208}\text{Pb}/^{204}\text{Pb}$ )
- 3) Enriched Mantle type two (**EM II**; characterized by highly radiogenic Sr,  $^{207}\text{Pb}/^{204}\text{Pb}$  and  $^{208}\text{Pb}/^{204}\text{Pb}$  but relatively unradiogenic Nd, Hf and intermediate  $^{206}\text{Pb}/^{204}\text{Pb}$ )
- 4) Mantle with high time-integrated  $\mu$  (high  $^{238}\text{U}/^{204}\text{Pb}$  = **HIMU**; characterized by very radiogenic  $^{206}\text{Pb}/^{204}\text{Pb}$  and  $^{207}\text{Pb}/^{204}\text{Pb}$ , intermediate  $^{208}\text{Pb}/^{204}\text{Pb}$  and Sr, Nd, Hf isotope ratios projecting beneath the EM-DM mantle array)

Since many MORBs (Mid-Ocean Ridge Basalts) and OIBs (Ocean Island Basalts) converge on an intermediate Sr-Nd-Pb-Hf isotopic composition, a “common” or “prevalent” mantle component (Zindler and Hart, 1986; Hart et al., 1992; Hanan and Graham, 1996), termed PREMA (PREvalent MAntle; Zindler and Hart, 1986), FOZO

(FOcal ZOne; Hart et al., 1992) or C (Common component; Hanan and Graham, 1996) has been proposed. This component is characterized by slightly more radiogenic Sr-Nd-Hf isotope ratios and less radiogenic Pb isotope ratios compared to that of HIMU and has been associated in many cases with high  $^3\text{He}/^4\text{He}$  ratios ( $>9R/R_a$ ; Zindler and Hart, 1986; Hart et al., 1992; Hanan and Graham, 1996). Therefore, it has been proposed that it may be a distinct mantle end member rather than a mix of the other end members (e.g., Zindler and Hart, 1986; Hanan and Graham, 1996).

The Sr-Nd-Pb-Hf isotope systematics show that oceanic basalts are derived from chemically and isotopically distinct reservoirs. In turn, these reservoirs reflect the long-time evolution of the Earth, which is mainly characterized by continuous upper mantle depletion and re-enrichment by recycled material (e.g., Armstrong, 1968; Zindler and Hart, 1986). It has been suggested that the different geochemical end members of OIBs (EM I, EM II, HIMU and FOZO/C/PREMA) are derived by various recycled materials (e.g., Zindler and Hart, 1986), which were introduced to the mantle at subduction zones as subducting slabs  $\pm$  sediments and continental erosion, as well as continental delamination (e.g., Bird, 1979; Stern, 2011). The long-time isolation of these recycled materials led to the characteristic isotope ratios of the respective mantle end members. The Walvis Ridge became famous in the early 1980s for representing the EM I reference location in the South Atlantic (e.g., Richardson et al., 1982; Richardson et al., 1984; Zindler and Hart, 1986). This ridge forms part of the geochemically enriched DUPAL anomaly (EM I-type) observed in the South Atlantic and western Indian Ocean MORBs and OIBs (e.g., Hart, 1984). The source of the DUPAL anomaly is often discussed (e.g., Regelous et al., 2009; Class and le Roex, 2011), and the Walvis Ridge represents a perfect observation site to evaluate the origin and heritage of the EM I mantle end member and possibly the entire DUPAL anomaly.

## **1.2     *The mantle plume theory***

The seafloor is dotted by innumerable seamounts, which are not related to plate boundaries where magma sources are easy to identify (e.g., subduction zones or mid-ocean ridges). The most striking structures on the ocean floor are linear seamount chains, which extend over several thousand kilometers. The most prominent examples are the Hawaii-Emperor chain in the Pacific Ocean, the Ninety-East Ridge in the Indian Ocean and the Walvis Ridge in the Atlantic Ocean. The origin of these seamount chains is controversial, and two fundamentally different hypotheses exist, which are expressed in “The Great Plume Debate” (mantle plume vs. plate model).

The mantle plume theory is based on the early studies by Wilson (1963) and Morgan (1971). In general, it has been proposed that linear volcanic island chains form by oceanic crust moving over a fixed thermal anomaly, where hot material rises from the deep mantle to the base of the lithosphere (Morgan, 1971). The rising material melts through the crust and forms a volcano and with successive plate motion, the melt supply of the seamount is cut off and a new volcano forms next to the older one; this process results in age progressive volcanic chains with the active volcanic island(s) close to the hotspot position (Fig. 1). In addition to the natural observation that seamount chains are often spatially and temporally associated with flood basalt provinces (Morgan, 1971; Morgan, 1981), the synthesis of laboratory experiments (e.g., Whitehead and Luther, 1975; Farnetani and Richards, 1994), numerical simulations (e.g., McKenzie et al., 1974; Ribe and Christensen, 1999) and seismic data (e.g., Zhang and Tanimoto, 1993; Bijwaard and Spakman, 1999; Montelli et al., 2006; Zhao, 2007) led to the deep-rooted head-tail mantle plume model (e.g., Richards et al., 1989; Campbell, 2007). This hypothesis states that hot material rises from a thermal boundary layer, such as the core-mantle boundary, in a mushroom-like form. When the broad plume head (~1000 km in



diameter; Campbell, 2007) arrives at the base of the lithosphere, it spreads out laterally (2000-2500 km; Campbell, 2007) and causes a massive short-lived volcanic outburst (<5 Myr). This initial stage is associated with large igneous provinces (LIPs), such as the Etendeka-Parana or Deccan flood basalt provinces. After the initial plume head stage, the narrow (100-300 km; Campbell, 2007) but long-lived mantle plume tail remains more or less stationary beneath the moving plate causing the age progressive seamount chains (Fig. 1).

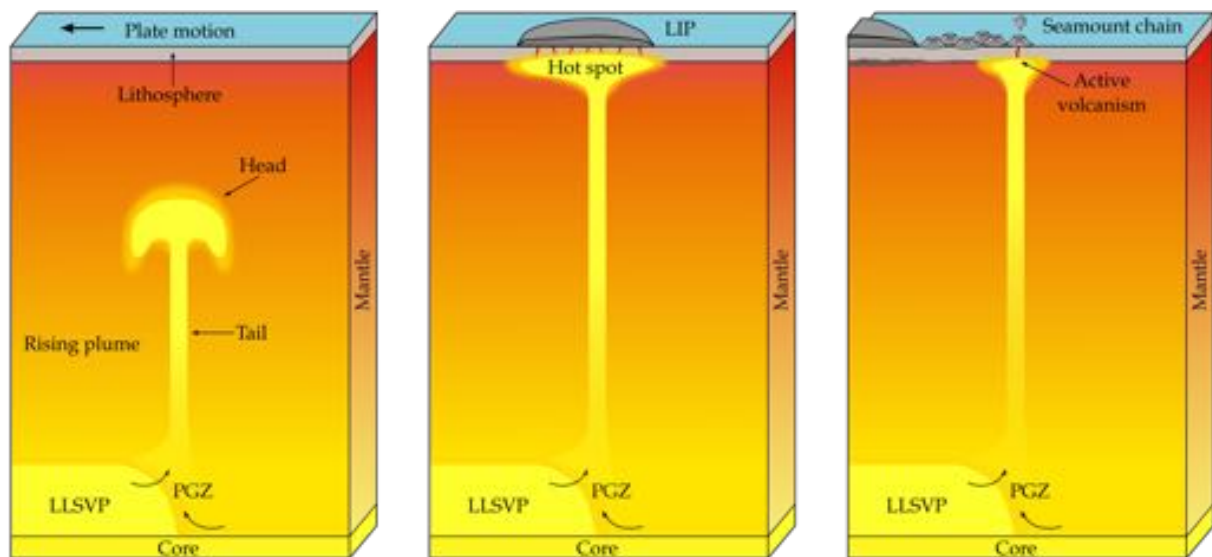


**Figure 1: Cartoon of a mantle plume ascending from the lowermost mantle at the boundary of the Large Low Shear Velocity Province (LLSVP), the so-called Plume Generation Zone (PGZ; Burke et al., 2008). A) The mantle plume rises in a mushroom-like shape. B) As the mantle plume head arrives at the lithospheric base it spreads out and cause massive volcanism. C) The plume tail produces a seamount chain as the plate overrides the plume position.**

The observations that several seamount chains are neither long-lived (e.g., Ascension, Cape Verde; Courtillot et al., 2003), nor associated with LIPs (e.g., Canary, Cape Verde; Courtillot et al., 2003), whereas some LIPs lack any obvious plume tail trace (e.g., Manihiki plateau; Taylor, 2006) challenged the mantle plume theory. Alternative models, such as the plate model were introduced and are based on tectonic related

processes (e.g., Anderson, 2000; Foulger, 2002; Anderson, 2005; Foulger, 2017). The plate model comprises localized processes, such as cracking of the lithosphere or extensional sectors (Gans et al., 2003; Sandwell and Fialko, 2004; Geldmacher et al., 2006), small-scale sublithospheric convection (King and Ritsema, 2000; Geldmacher et al., 2005; Ballmer et al., 2007), lithospheric detachment (e.g., Hoernle et al., 2006; Elkins-Tanton, 2007) and/or heterogeneous upper mantle fertilities (Fig. 2; e.g. Anderson, 2005). For example, Sheth (1999) proposed that age progressive volcanic island chains could be developed by propagating cracks associated with long-lasting stress fields. The formation of LIPs, on the other hand, are attributed to small-scale convection cells in the shallow mantle, which are produced at the base of the lithosphere at steep gradients in lithospheric thickness (e.g. King and Ritsema, 2000).

However, “The Great Plume Debate” does not indicate that all seamounts were formed by deep-rooted mantle plumes or shallow plate-related processes. As noted by Hofmann and Hart (2007), finding an intraplate volcano that is not a product of a mantle plume does not disprove the plume theory. In fact, there are many examples of intraplate volcanoes and even volcanic provinces that are clearly not related to a mantle plume (e.g., Hanan et al., 2004; Hoernle et al., 2011; Kipf et al., 2014). On the other hand, there are also examples, such as Hawaii, that can be more easily explained by the mantle plume model than any alternative. In the context of the two proposed models (plate vs. plume), the geochemical signatures of intraplate lavas are either derived from a shallow- or deep-seated reservoir. Since the enriched mantle end members (EM I, EM II, HIMU and FOZO) are related to various recycled materials, the proposed models have direct implications on the structure and evolution of the Earth.

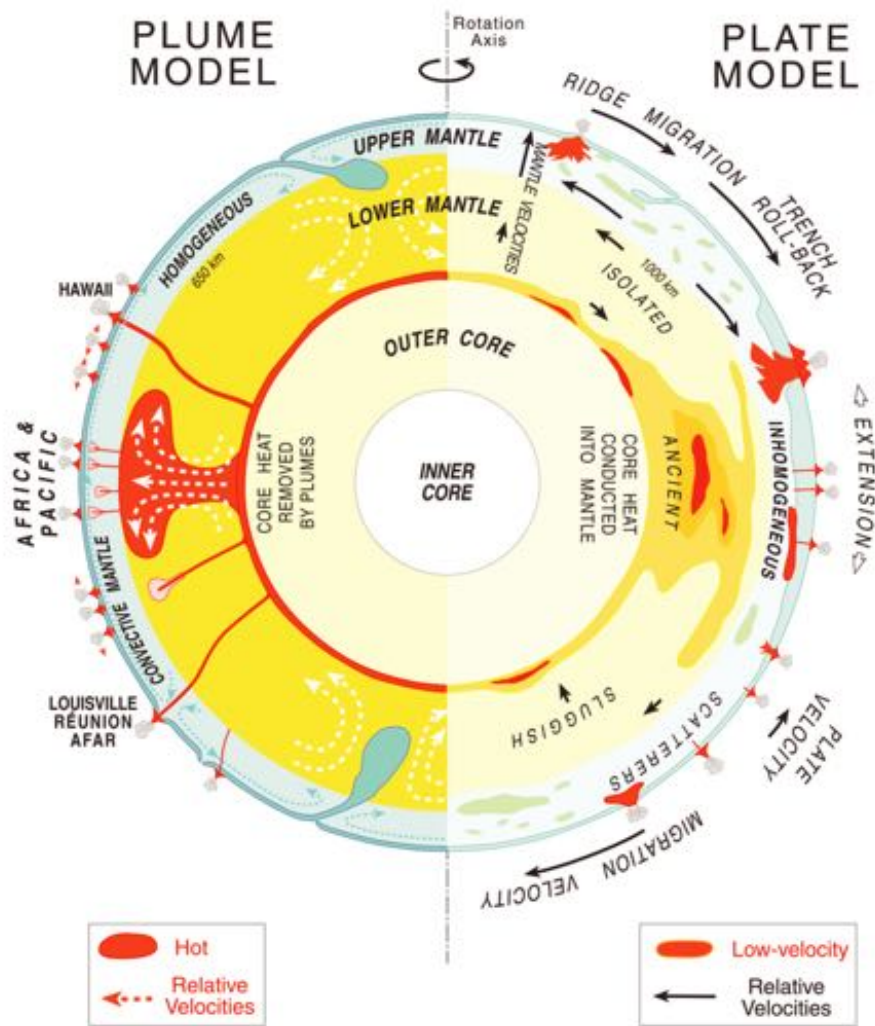
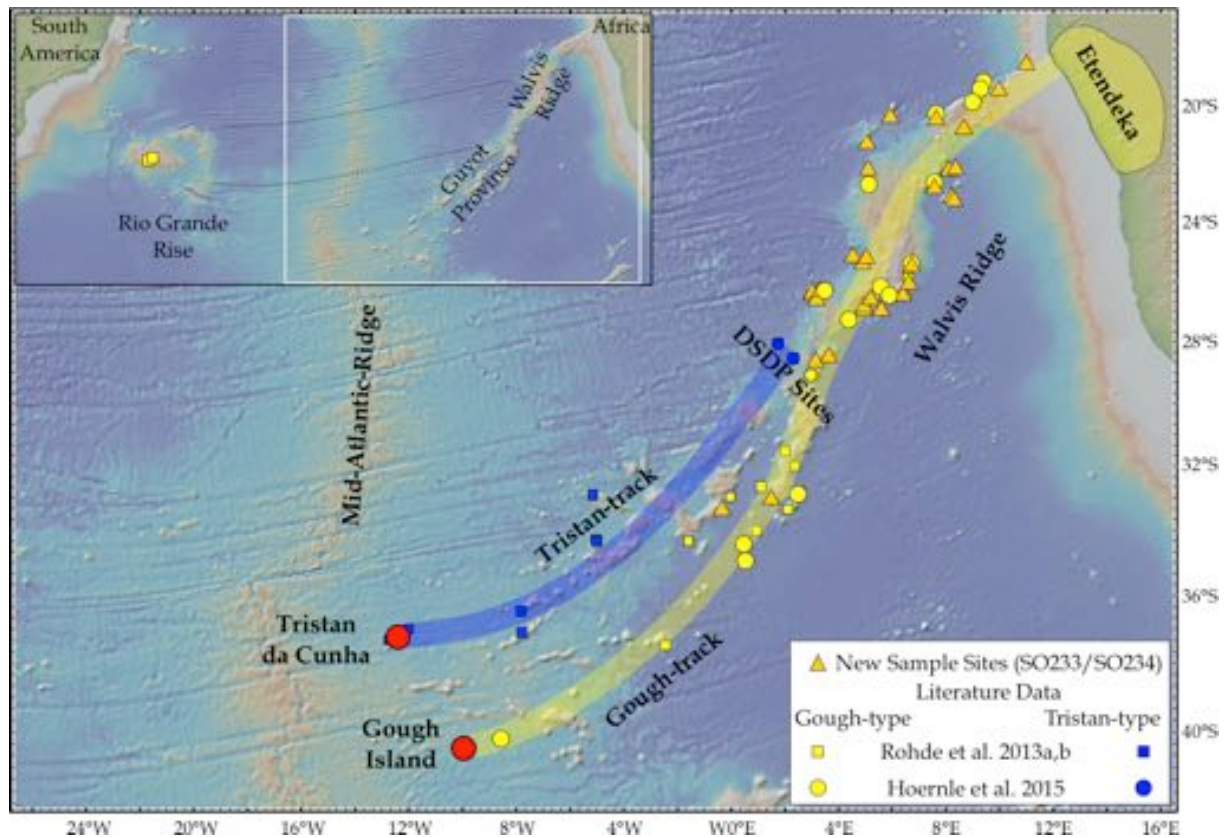


Figure 2: Cartoon of the mantle plume and plate model (Anderson, 2005). The mantle plume model assumes a relatively homogeneous upper mantle, whereas distinct and heterogeneous material is accumulated in the lower mantle, which rises as hot material with deep-rooted mantle upwellings. In contrast, the plate model predicts an extreme heterogeneous upper mantle and melt anomalies are correlated to localized stress and pre-existing fabric of plates.

### **1.3     *The Walvis Ridge***

The Walvis Ridge is the most striking bathymetric anomaly in the South Atlantic and forms the oldest part of the ~3000 km long Tristan-Gough seamount chain. This northeast-southwest trending volcanic chain can be divided as follows: (1) the aseismic Walvis Ridge, which extends from the African coast to the DSDP Site transect and then splits into three ~450 km long ridge-like arms, and (2) the Guyot Province characterized by diffuse and discontinuous chains of seamounts and ridges, which leads to the active volcanic islands of Tristan da Cunha and Gough (Fig. 3). The Tristan-Gough seamount chain can be spatially and temporally extended to Etendeka, which was emplaced at ~132 Ma (Renne et al., 1996; Renne, 2015). The volcanic counterparts on the South American plate are the Rio Grande Rise, an ~800 x 800 km submarine plateau, and the Parana LIP. The Rio Grande Rise can be traced across the South Atlantic along oceanic fracture zones to the central portion of the Walvis Ridge, suggesting a co-genetic origin (e.g., O'Connor and Duncan, 1990).



**Figure 3: Map of the Tristan-Gough seamount chain with main geological structures and sample sites from SO233 and SO234 (WALVIS II; new sample sites) and from WALVIS I (Rohde et al., 2013a; Rohde et al., 2013b; Hoernle et al., 2015). The blue and yellow lines show the spatial geochemical zonation.**

The Tristan-Gough seamount chain is one of the rare structures, that exhibits a spatial and temporal connection between an LIP (Etendeka-Parana) and an active volcanic island (Tristan-Gough). It is considered one of the seven primary hotspots, after Courtillot et al. (2003), which originated from and samples the lowermost mantle. After the classical head-tail mantle plume model (e.g., Wilson, 1963; Morgan, 1971; Wilson, 1973; Richards et al., 1989), the deep-rooted Tristan-Gough hotspot system was initiated by an upwelling mantle plume head that caused a massive volcanic outburst, which formed the continental flood basalt province Parana-Etendeka (135-132 Ma, Renne et al., 1996; Renne, 2015). Due to the opening of the South Atlantic, the LIPs were separated and then the mantle plume interacted with the newly evolved Mid-Atlantic Ridge (MAR), forming the Walvis Ridge and Rio Grande Rise (e.g., Humphris and

Thompson, 1983; O'Connor and Duncan, 1990; O'Connor and Jokat, 2015b). The Walvis Ridge and Rio Grande Rise split apart between 80 and 60 Ma by several ridge jumps (e.g., Humphris and Thompson, 1983; O'Connor and Duncan, 1990; O'Connor and Jokat, 2015b). After ~60 Ma, the plume conduit migrated beneath the African plate and formed the scattered Guyot Province.

The preceding project WALVIS I, which focused on the Guyot Province, yielded two fundamental results. First, the Tristan-Gough volcanic chain shows a linear age progression from the active volcanic islands to the southern Walvis Ridge (DSDP Sites) and can be extrapolated to the African coast and the Etendeka LIP (Rohde et al., 2013b). If the Rio Grande Rise is rotated back along the oceanic fracture zones, the  $^{40}\text{Ar}/^{39}\text{Ar}$  age data fit the calculated age progression of the Tristan-Gough track (Rohde et al., 2013b). Therefore, the age progressive trend with high precision  $^{40}\text{Ar}/^{39}\text{Ar}$  age data supports the deep-rooted mantle plume theory and the simultaneous evolution of the Walvis Ridge and Rio Grande Rise.

Secondly, Rohde et al. (2013a) showed that the proposed Tristan-Gough hotspot track exhibited spatial geochemical zonation over the last 70 Ma, which can be divided into the Tristan and Gough tracks (Fig. 3). The Gough-type composition has higher  $^{207}\text{Pb}/^{204}\text{Pb}$  ratios, but similar  $^{208}\text{Pb}/^{204}\text{Pb}$  ratios at a given  $^{206}\text{Pb}/^{204}\text{Pb}$  isotope ratio and extending to lower  $^{143}\text{Nd}/^{144}\text{Nd}$  and  $^{176}\text{Hf}/^{177}\text{Hf}$  ratios and higher  $^{87}\text{Sr}/^{86}\text{Sr}$  values in relation to the chain leading to Tristan da Cunha (Rohde et al., 2013a; Hoernle et al., 2015). Northward of the DSDP sites (>70 Ma), the Walvis Ridge seems to be entirely composed of the EM I Gough-type composition (Rohde et al., 2013a; Hoernle et al., 2015).

Although the Tristan-Gough volcanic chain shows many characteristic features of a classical mantle plume, there are several critical observations. Compared to other

mantle plume reference locations (e.g., Hawaii, Ninetyeast Ridge) the structure of the Tristan-Gough track is characterized by a broad region with scattered seamounts at the younger end. The active volcanic islands of Gough and Tristan da Cunha lie 400 km apart from each other, and thus, it seems implausible that a 200 km wide mantle plume conduit, as predicted by the plume model, forms the two volcanic islands. On the other hand, only five ages are available for the Walvis Ridge between the Deep Sea Drilling Project Sites and the northeastern end of the Walvis Ridge (Fig. 2) (Rohde et al., 2013b; O'Connor and Jokat, 2015a), which cover ~1500 km of the entire track. Of these five ages, only two were close to what was expected for a linear age progression. In fact, three samples are ~30 Ma younger than the predicted age progressive trend (Rohde et al., 2013b; O'Connor and Jokat, 2015a). Such an exceptionally long volcanic quiescence is unusual for hotspot tracks or ridges (e.g., Clague and Dalrymple, 1987; Hoernle and Schmincke, 1993; Geldmacher et al., 2005; Garcia et al., 2010). Finally, Hoernle et al. (2015) argued that the Tristan- and Gough-type components represent distinct mantle sources, implicating that the DUPAL anomaly inherited various EM I-types.

In conclusion, the origin of the Tristan-Gough volcanic chain and especially the temporal and geochemical evolution of the Walvis Ridge remain controversial (e.g., Rohde et al., 2013b; Foulger, 2017; O'Connor et al., 2018). Therefore, systematic sampling of the Walvis Ridge combined with geochemical and geochronological analyses provide not only further insights into the formation of the Tristan-Gough seamount chain but also the origin of the EM I mantle end member(s) and the possibly the origin of the entire South Atlantic DUPAL anomaly.

## **1.4 Main objectives**

The aim of my thesis is to evaluate the origin and the temporal and geochemical evolution of the Walvis Ridge and to identify potential associations to other proposed hotspots in the South Atlantic. The main objectives are as follows:

1. Is the Tristan-Gough volcanic chain formed by a classical mantle plume?
2. What is the geochemical signature of the Walvis Ridge and when does the geochemical zonation of the Tristan-Gough track start?
3. Do the distinct Tristan- and Gough-type compositions contain temporal or spatial variations? What are the potential source components?
4. Is the geochemical signature of the Walvis Ridge associated with other intraplate lavas in the South Atlantic?
5. What is the geochemical fingerprint of the lavas with anomalously young ages?
6. How old are the seamounts on and next to the Walvis Ridge? Are they related to the emplacement of the Walvis Ridge basement?
7. Does the temporal and spatial evolution of the Tristan-Gough track yields further insights into the origin of the geochemical heterogeneity of the South Atlantic intraplate lavas?

To answer these research questions, I processed and evaluated major and trace element data, Sr-Nd-Pb-Hf isotope ratios and  $^{40}\text{Ar}/^{39}\text{Ar}$  age data from 35 new sample sites, which were recovered through dredging at the following areas: 1) steep scarps on the margins of the ridge, 2) walls of cross-cutting graben systems, and 3) seamounts on and nearby the Walvis Ridge. A detailed description of the sample sites is presented by Hoernle et al. (2014) and Werner and Wagner (2014). Together with Walvis I, which



focused on the volcanic province south of the Walvis Ridge, the recovered lavas represent one of the best sample collections worldwide of an oceanic seamount chain and provide unique insights into its origin and temporal evolution. The next chapter contains the three independent articles accepted for publication or submitted to international scientific journals. The last chapter summarizes the conclusions and gives an outlook for further research.

## 1.5 References

- Anderson, D. L., 2000, The thermal state of the upper mantle; No role for mantle plumes: *Geophysical Research Letters*, v. 27, no. 22, p. 3623-3626.
- , 2005, Scoring hotspots: The plume and plate paradigms, *in* Foulger, G. R., Natland, J. H., Presnall, D. C., and Anderson, D. L., eds., *Plates, plumes and paradigms*, Geological Society of America.
- Armstrong, R. L., 1968, A model for the evolution of strontium and lead isotopes in a dynamic Earth: *Reviews of Geophysics*, v. 6, no. 2, p. 175-199.
- Ballmer, M. D., van Hunen, J., Ito, G., Tackley, P. J., and Bianco, T. A., 2007, Non-hotspot volcano chains originating from small-scale sublithospheric convection: *Geophysical Research Letters*, v. 34, no. 23, p. n/a-n/a.
- Bijwaard, H., and Spakman, W., 1999, Tomographic evidence for a narrow whole mantle plume below Iceland: *Earth and Planetary Science Letters*, v. 166, no. 3-4, p. 121-126.
- Bird, P., 1979, Continental delamination and the Colorado Plateau: *Journal of Geophysical Research: Solid Earth*, v. 84, no. B13, p. 7561-7571.
- Burke, K., Steinberger, B., Torsvik, T. H., and Smethurst, M. A., 2008, Plume Generation Zones at the margins of Large Low Shear Velocity Provinces on the core-mantle boundary: *Earth and Planetary Science Letters*, v. 265, no. 1-2, p. 49-60.
- Campbell, I. H., 2007, Testing the plume theory: *Chemical Geology*, v. 241, no. 3, p. 153-176.
- Clague, D. A., and Dalrymple, G. B., 1987, The Hawaiian-Emperor volcanic chain. part I. Geologic evolution: *Volcanism in Hawaii*, v. 1, p. 5-54.
- Class, C., and le Roex, A., 2011, South Atlantic DUPAL anomaly — Dynamic and compositional evidence against a recent shallow origin: *Earth and Planetary Science Letters*, v. 305, no. 1-2, p. 92-102.
- Courtillot, V., Davaille, A., Besse, J., and Stock, J., 2003, Three distinct types of hotspots in the Earth's mantle: *Earth and Planetary Science Letters*, v. 205, no. 3-4, p. 295-308.
- Elkins-Tanton, L. T., 2007, Continental magmatism, volatile recycling, and a heterogeneous mantle caused by lithospheric gravitational instabilities: *Journal of Geophysical Research: Solid Earth*, v. 112, no. B3, p. n/a-n/a.
- Farnetani, C. G., and Richards, M. A., 1994, Numerical investigations of the mantle plume initiation model for flood basalt events: *Journal of Geophysical Research: Solid Earth*, v. 99, no. B7, p. 13813-13833.
- Foulger, G. R., 2002, Plumes, or plate tectonic processes?: *Astronomy & Geophysics*, v. 43, no. 6, p. 6.19-16.23.
- Foulger, G. R., 2017, Origin of the South Atlantic igneous province: *Journal of Volcanology and Geothermal Research*, v. In Press.
- Gans, K. D., Wilson, D. S., and Macdonald, K. C., 2003, Pacific Plate gravity lineaments: Diffuse extension or thermal contraction?: *Geochemistry, Geophysics, Geosystems*, v. 4, no. 9, p. 1074.
- Garcia, M. O., Swinnard, L., Weis, D., Greene, A. R., Tagami, T., Sano, H., and Gandy, C. E., 2010, Petrology, Geochemistry and Geochronology of Kaua'i Lavas over 4-5 Myr: Implications for the Origin of Rejuvenated Volcanism and the Evolution of the Hawaiian Plume: *Journal of Petrology*, v. 51, no. 7, p. 1507-1540.
- Geldmacher, J., Hoernle, K., Bogaard, P. v. d., Duggen, S., and Werner, R., 2005, New <sup>40</sup>Ar / <sup>39</sup>Ar age and geochemical data from seamounts in the Canary and Madeira volcanic provinces: Support for the mantle plume hypothesis: *Earth and Planetary Science Letters*, v. 237, no. 1-2, p. 85-101.
- Geldmacher, J., Hoernle, K., Klügel, A., Bogaard, P. v. d., Wombacher, F., and Berning, B., 2006, Origin and geochemical evolution of the Madeira-Tore Rise (eastern North Atlantic): *Journal of Geophysical Research: Solid Earth*, v. 111, no. B9, p. B09206.
- Hanan, B. B., Blichert-Toft, J., Pyle, D. G., and Christie, D. M., 2004, Contrasting origins of the upper mantle revealed by hafnium and lead isotopes from the Southeast Indian Ridge: *Nature*, v. 432, no. 7013, p. 91-94.
- Hanan, B. B., and Graham, D. W., 1996, Lead and Helium Isotope Evidence from Oceanic Basalts for a Common Deep Source of Mantle Plumes: *Science*, v. 272, no. 5264, p. 991-995.
- Hart, S. R., 1984, A large-scale isotope anomaly in the Southern Hemisphere mantle: *Nature*, v. 309, no. 5971, p. 753-757.
- Hart, S. R., Hauri, E. H., Oschmann, L. A., and Whitehead, J. A., 1992, Mantle Plumes and Entrainment: *Isotopic Evidence*: *Science*, v. 256, no. 5056, p. 517-520.
- Hoernle, K., Hauff, F., Werner, R., van den Bogaard, P., Gibbons, A. D., Conrad, S., and Muller, R. D., 2011, Origin of Indian Ocean Seamount Province by shallow recycling of continental lithosphere: *Nature Geosci*, v. 4, no. 12, p. 883-887.

- Hoernle, K., Rohde, J., Hauff, F., Garbe-Schonberg, D., Homrighausen, S., Werner, R., and Morgan, J. P., 2015, How and when plume zonation appeared during the 132 Myr evolution of the Tristan Hotspot: *Nature Communication*, v. 6, p. 10.1038/ncomms8799.
- Hoernle, K., and Schmincke, H.-U., 1993, The Role of Partial Melting in the 15 Ma Geochemical Evolution of Gran Canaria: A Blob Model for the Canary Hotspot: *Journal of Petrology*, v. 34, no. 3, p. 599-626.
- Hoernle, K., Werner, R., and Lüter, C., 2014, RV SONNE Fahrtbericht/Cruise Report SO233 WALVIS II, 14.05-21.06. 2014, Cape Town, South Africa-Walvis Bay, Namibia: GEOMAR Report v. no. 23 (N. Ser.), p. 53 pp + Appendices.
- Hoernle, K., White, J. D. L., van den Bogaard, P., Hauff, F., Coombs, D. S., Werner, R., Timm, C., Garbe-Schönberg, D., Reay, A., and Cooper, A. F., 2006, Cenozoic intraplate volcanism on New Zealand: Upwelling induced by lithospheric removal: *Earth and Planetary Science Letters*, v. 248, no. 1-2, p. 350-367.
- Hofmann, A. W., 1997, Mantle geochemistry: the message from oceanic volcanism: *Nature*, v. 385, no. 6613, p. 219-229.
- Hofmann, A. W., and Hart, S. R., 2007, Another Nail in Which Coffin?: *Science*, v. 315, no. 5808, p. 39-40.
- Humphris, S. E., and Thompson, G., 1983, Geochemistry of rare earth elements in basalts from the Walvis Ridge: implications for its origin and evolution: *Earth and Planetary Science Letters*, v. 66, no. Supplement C, p. 223-242.
- King, S. D., and Ritsema, J., 2000, African Hot Spot Volcanism: Small-Scale Convection in the Upper Mantle Beneath Cratons: *Science*, v. 290, no. 5494, p. 1137-1140.
- Kipf, A., Hauff, F., Werner, R., Gohl, K., van den Bogaard, P., Hoernle, K., Maicher, D., and Klügel, A., 2014, Seamounts off the West Antarctic margin: A case for non-hotspot driven intraplate volcanism: *Gondwana Research*, v. 25, no. 4, p. 1660-1679.
- McKenzie, D. P., Roberts, J. M., and Weiss, N. O., 1974, Convection in the Earth's mantle: towards a numerical simulation: *Journal of Fluid Mechanics*, v. 62, no. 3, p. 465-538.
- Montelli, R., Nolet, G., Dahlen, F. A., and Masters, G., 2006, A catalogue of deep mantle plumes: New results from finite-frequency tomography: *Geochemistry, Geophysics, Geosystems*, v. 7, no. 11, p. Q11007.
- Morgan, W. J., 1971, Convection Plumes in the Lower Mantle: *Nature*, v. 230, no. 5288, p. 42-43.
- Morgan, W. J., 1981, 13. Hotspot tracks and the opening of the Atlantic and Indian Oceans: The oceanic lithosphere, v. 7, p. 443.
- O'Connor, J., Jokat, W., Wijbrans, J., and Colli, L., 2018, Hotspot tracks in the South Atlantic located above bands of fast flowing asthenosphere driven by waning pulsations from the African LLSVP: *Gondwana Research*, v. 53, no. Supplement C, p. 197-208.
- O'Connor, J. M., and Duncan, R. A., 1990, Evolution of the Walvis Ridge-Rio Grande Rise Hot Spot System: Implications for African and South American Plate motions over plumes: *Journal of Geophysical Research: Solid Earth*, v. 95, no. B11, p. 17475-17502.
- O'Connor, J. M., and Jokat, W., 2015a, Tracking the Tristan-Gough mantle plume using discrete chains of intraplate volcanic centers buried in the Walvis Ridge: *Geology*, v. 43, no. 8, p. 715-718.
- , 2015b, Age distribution of Ocean Drill sites across the Central Walvis Ridge indicates plate boundary control of plume volcanism in the South Atlantic: *Earth and Planetary Science Letters*, v. 424, p. 179-190.
- Regelous, M., Niu, Y., Abouchami, W., and Castillo, P. R., 2009, Shallow origin for South Atlantic Dupal Anomaly from lower continental crust: Geochemical evidence from the Mid-Atlantic Ridge at 26°S: *Lithos*, v. 112, no. 1-2, p. 57-72.
- Renne, P., Age and Duration of the Paraná-Etendeka Flood Basalts and Related Plumbing System, *in* Proceedings AGU Fall Meeting Abstracts 2015.
- Renne, P. R., Glen, J. M., Milner, S. C., and Duncan, A. R., 1996, Age of Etendeka flood volcanism and associated intrusions in southwestern Africa: *Geology*, v. 24, no. 7, p. 659-662.
- Ribe, N. M., and Christensen, U. R., 1999, The dynamical origin of Hawaiian volcanism: *Earth and Planetary Science Letters*, v. 171, no. 4, p. 517-531.
- Richards, M. A., Duncan, R. A., and Courtillot, V. E., 1989, Flood basalts and hot-spot tracks: plume heads and tails: *Science*, v. 246, no. 4926, p. 103-107.
- Richardson, S. H., Erlank, A. J., Duncan, A. R., and Reid, D. L., 1982, Correlated Nd, Sr and Pb Isotope Variation in Walvis Ridge Basalts and Implications for the Evolution of their Mantle Source: *Earth and Planetary Science Letters*, v. 59, no. 2, p. 327-342.
- Richardson, S. H., Erlank, A. J., Reid, D. L., and Duncan, A. R., 1984, Major and Trace-Elements and Nd and Sr Isotope Geochemistry of Basalts from the Deep-Sea Drilling Project Leg-74 Walvis Ridge Transect: Initial Reports of the Deep Sea Drilling Project, v. 74, no. Mar, p. 739-754.
- Rohde, J., Hoernle, K., Hauff, F., Werner, R., O'Connor, J., Class, C., Garbe-Schönberg, D., and Jokat, W., 2013a, 70 Ma chemical zonation of the Tristan-Gough hotspot track: *Geology*, v. 43, no. 3, p. 335-338.

- Rohde, J. K., van den Bogaard, P., Hoernle, K., Hauff, F., and Werner, R., 2013b, Evidence for an age progression along the Tristan-Gough volcanic track from new  $^{40}\text{Ar}/^{39}\text{Ar}$  ages on phenocryst phases: *Tectonophysics*, v. 604, p. 60-71.
- Sandwell, D., and Fialko, Y., 2004, Warping and cracking of the Pacific plate by thermal contraction: *Journal of Geophysical Research: Solid Earth*, v. 109, no. B10, p. B10411.
- Sheth, H. C., 1999, Flood basalts and large igneous provinces from deep mantle plumes: fact, fiction, and fallacy: *Tectonophysics*, v. 311, no. 1, p. 1-29.
- Stern, C. R., 2011, Subduction erosion: rates, mechanisms, and its role in arc magmatism and the evolution of the continental crust and mantle: *Gondwana Research*, v. 20, no. 2, p. 284-308.
- Taylor, B., 2006, The single largest oceanic plateau: Ontong Java–Manihiki–Hikurangi: *Earth and Planetary Science Letters*, v. 241, no. 3–4, p. 372-380.
- Werner, R., and Wagner, H.-J., 2014, RV SONNE Fahrtbericht/Cruise Report SO234/1 “SPACES”: Science or the Assessment of Complex Earth System Processes, 22.06.–06.07. 2014, Walvis Bay/Namibia-Durban/South Africa: GEOMAR Report v. no. 17 (N. Ser.), p. 29 pp + Appendices.
- White, W. M., 2015, Isotopes, DUPAL, LLSVPs, and Anekantavada: *Chemical Geology*, v. 419, p. 10-28.
- Whitehead, J. A., and Luther, D. S., 1975, Dynamics of laboratory diapir and plume models: *Journal of Geophysical Research*, v. 80, no. 5, p. 705-717.
- Willbold, M., and Stracke, A., 2006, Trace element composition of mantle end-members: Implications for recycling of oceanic and upper and lower continental crust: *Geochemistry, Geophysics, Geosystems*, v. 7, no. 4, p. Q04004.
- Wilson, J. T., 1963, Evidence from Islands on the Spreading of Ocean Floors: *Nature*, v. 197, no. 4867, p. 536-538.
- , 1973, Mantle plumes and plate motions: *Tectonophysics*, v. 19, no. 2, p. 149-164.
- Zhang, Y.-S., and Tanimoto, T., 1993, High-resolution global upper mantle structure and plate tectonics: *Journal of Geophysical Research: Solid Earth*, v. 98, no. B6, p. 9793-9823.
- Zhao, D., 2007, Seismic images under 60 hotspots: Search for mantle plumes: *Gondwana Research*, v. 12, no. 4, p. 335-355.
- Zindler, A., and Hart, S. R., 1986, Chemical Geodynamics: *Annual Review of Earth and Planetary Sciences*, v. 14, no. 1, p. 493-571.

## 2. CONTRIBUTION TO SCIENTIFIC JOURNALS

### **GLOBAL DISTRIBUTION OF THE HIMU END MEMBER: FORMATION THROUGH ARCHEAN PLUME-LID TECTONICS**

Stephan Homrighausen, Kaj Hoernle, Folkmar Hauff, Jörg Geldmacher, Jo-Anne Wartho, Paul van den Bogaard, Dieter Garbe-Schönberg

*accepted for publication in Earth Science Reviews*

We present new major and trace element, Sr-Nd-Pb-Hf isotope and geochronological data from the Walvis Ridge and Richardson Seamount in the South Atlantic Ocean and the Manihiki Plateau and Eastern Chatham Rise in the southwest Pacific Ocean. Our new data, combined with literature data documents a more widespread (nearly global) distribution of the HIMU end member than previously postulated. The restricted trace element and isotopic composition (St. Helena type HIMU), but the near-global distribution point to a deep-seated, widespread reservoir, which formed most likely in the Archean. In this context we re-evaluate the origin of HIMU in an Archean geodynamic setting.

I wrote the manuscript with contributions from all of the co-authors. Kaj Hoernle supervised the work and was Chief Scientist during Cruise SO233. I prepared the samples for the geochemical analyses. Folkmar Hauff and I performed the isotope measurements. Paul van Bogaard and Jo-Anne Wartho performed the Ar-Ar and Dieter Garbe-Schönberg the trace element determinations. Kaj Hoernle, Folkmar Hauff and Reinhard Werner conceived the project.

## UNEXPECTED HIMU-TYPE LATE-STAGE VOLCANISM ON THE WALVIS RIDGE

Stephan Homrighausen, Kaj Hoernle, Jörg Geldmacher, Jo-Anne Wartho, Folkmar Hauff,  
Maxim Potnyagin, Reinhard Werner, Paul van den Bogaard, Dieter Garbe-Schönberg  
*accepted for publication in Earth and Planetary Science Letters*

We present the first comprehensive data set of  $^{40}\text{Ar}/^{39}\text{Ar}$  ages, trace element and Sr-Nd-Pb-Hf isotopic data from seamounts on and next to the Walvis Ridge. Based on an average age offset of 20-40 Myr from the local Walvis Ridge basement and a distinct composition compared to the EM I-type basement, we conclude that the seamounts are not related to the Tristan-Gough mantle plume. The HIMU-like signature was most likely derived from the lowermost mantle. We propose that the EM I signature was derived from the margin of the African Large Low Shear Velocity Province, whereas HIMU rose from a more central portion.

I wrote the manuscript with contributions from all of the co-authors. Kaj Hoernle supervised the work and was Chief Scientist during Cruise SO233. Reinhard Werner was Chief Scientist during Cruise SO234. I prepared the samples for the geochemical and geochronological data and performed the isotope measurements. Paul van Bogaard and Jo-Anne Wartho performed the Ar-Ar and Dieter Garbe-Schönberg the trace element determinations. Kaj Hoernle, Folkmar Hauff and Reinhard Werner proposed the project.

**COMPARISON OF NEW AGE AND GEOCHEMICAL DATA FROM THE WALVIS RIDGE WITH OTHER SOUTH ATLANTIC HOTSPOTS: MAPPING THE BASE OF THE LOWER MANTLE BENEATH THE SOUTH ATLANTIC**

Stephan Homrighausen, Kaj Hoernle, Folkmar Hauff, Jo-Anne Wartho, Paul van den Bogaard, Dieter Garbe-Schönberg

*submitted to Geochimica et Cosmochimica Acta*

We report Ar-Ar age data combined with geochemical data from the Walvis Ridge, which shows an excellent age progression supporting the deep-rooted mantle plume model. The geochemical data confirm that the Gough-type composition is the long-lived component of the Walvis Ridge, which is also identified at the Discovery and Shona hotspot tracks. Mixing of Gough-type material with continental crust and a FOZO-like component can reproduce the geochemical heterogeneity in the South Atlantic DUPAL region. We present a model where the geochemical compositions of the South Atlantic Ocean island basalts reflect sampling from different portions of the African LLSVP and the surrounding ambient lower mantle.

I wrote the manuscript with contributions from Kaj Hoernle, Folkmar Hauff and Jo-Anne Wartho. Kaj Hoernle supervised the work and was Chief Scientist during Cruise SO233. I prepared the samples for the geochemical and geochronological data. Folkmar Hauff and I performed the isotope measurements. Paul van Bogaard and Jo-Anne Wartho performed the Ar-Ar and Dieter Garbe-Schönberg the trace element determinations. Kaj Hoernle, Folkmar Hauff and Reinhard Werner proposed the project.

## **CHAPTER I**

# **GLOBAL DISTRIBUTION OF THE HIMU END MEMBER: FORMATION THROUGH ARCHEAN PLUME-LID TECTONICS**

Stephan Homrighausen<sup>1\*</sup>, Kaj Hoernle<sup>1,2</sup>, Folkmar Hauff<sup>1</sup>, Jörg Geldmacher<sup>1</sup>, Jo-Anne Wartho<sup>1</sup>, Paul van den Bogaard<sup>1</sup>, Dieter Garbe-Schönberg<sup>2</sup>

<sup>1</sup> GEOMAR Helmholtz Centre for Ocean Research Kiel, Wischhofstr. 1-3, 24118 Kiel, Germany

<sup>2</sup> Christian-Albrechts-University of Kiel, Ludewig-Meyn-Str. 10, 24118 Kiel, Germany

\* Corresponding author (shomrighausen@geomar.de)

**Keywords: HIMU; FOZO; Walvis Ridge; Chatham Rise; Manihiki Plateau; Shona  
hotspot**



## Abstract

Oceanic basalts reflect the heterogeneities in the earth's mantle, which can be explained by five mantle end members. The HIMU end member, characterized by high time-integrated  $\mu$  ( $^{238}\text{U}/^{204}\text{Pb}$ ), is defined by the composition of lavas from the ocean islands of St. Helena, South Atlantic Ocean and Mangaia and Tubuai (Cook-Austral Islands), South Pacific Ocean. It is widely considered to be derived from a mantle reservoir that is rarely sampled and not generally involved in mixing with the other mantle components. On the other hand, the FOZO end member, located at the FOcal ZOne of oceanic volcanic rock arrays on isotope diagrams, is considered to be a widespread common component with slightly less radiogenic  $^{206}\text{Pb}/^{204}\text{Pb}$  and intermediate Sr-Nd-Hf isotopic compositions. Here we present new major and trace element, Sr-Nd-Pb-Hf isotope and geochronological data from the Walvis Ridge and Richardson Seamount in the South Atlantic Ocean and the Manihiki Plateau and Eastern Chatham Rise in the southwest Pacific Ocean. Our new data, combined with literature data, document a more widespread (nearly global) distribution of the HIMU end member than previously postulated. Our survey shows that HIMU is generally associated with low-volume alkaline, carbonatitic and/or kimberlitic intraplate volcanism, consistent with derivation from low degrees of melting of  $\text{CO}_2$ -rich sources. The majority of end member HIMU locations can be directly related to hotspot settings. The restricted trace element and isotopic composition (St. Helena type HIMU), but near-global distribution, point to a deep-seated, widespread reservoir, which most likely formed in the Archean. In this context we re-evaluate the origin of a widespread HIMU reservoir in an Archean geodynamic setting. We point out that the classic ocean crust recycling model cannot be applied in a plume-lid dominated tectonic setting, and instead

propose that delamination of carbonatite- metasomatized subcontinental lithospheric mantle could be a suitable HIMU source.

## 1. Introduction

Incompatible elements and Sr-Nd-Pb-Hf isotope compositions of mafic oceanic basalts have been used to identify at least four mantle end members that can explain the large-scale geochemical heterogeneity of the Earth's mantle. These are 1) Depleted Mantle (DM), 2) mantle with high time-integrated  $\mu$  ( $^{238}\text{U}/^{204}\text{Pb}$ ; HIMU), 3) Enriched Mantle One (EMI), and 4) Enriched Mantle Two (EM II) (Zindler and Hart, 1986; Hofmann, 1997; White, 2015). Since Mid-Ocean Ridge Basalts (MORBs) and many ocean island basalts (OIBs) converge on an intermediate Sr-Nd-Pb isotopic composition, the concept of a "common" (C, Hanan and Graham, 1996) or "prevalent" (PREMA, Zindler and Hart, 1986; Stracke, 2012) mantle component has been proposed. This "omnipresent" mantle component, which we refer to as FOZO (FOcal ZOne; Hart et al., 1992) henceforth after Stracke et al. (2005), lies within the isotopic space of DM, HIMU, EM. In some cases FOZO has been associated with high  $^3\text{He}/^4\text{He}$  ( $> 9 \text{ R/Ra}$ ), leading some to propose that it may be a distinct mantle end member rather than a mix of the other end members (e.g. Zindler and Hart, 1986; Hart et al., 1992; Hanan and Graham, 1996).

The HIMU mantle end member is defined by the composition of lavas from the ocean islands of St. Helena in the South Atlantic Ocean, and of Mangaia and Tubuaii (hereafter termed Cook-Austral) in the Southwest Pacific Ocean (Zindler and Hart, 1986; Chaffey et al., 1989; Woodhead, 1996). This end member is characterized by radiogenic  $^{206}\text{Pb}/^{204}\text{Pb}$  ( $> 20.5$ ) and  $^{207}\text{Pb}/^{204}\text{Pb}$  ( $> 15.7$ ), but  $^{208}\text{Pb}/^{204}\text{Pb}$  ratios well below the Northern hemisphere reference line (Hart, 1984) and Sr-Nd-Hf isotope ratios projecting beneath the EM-DM mantle array (e.g., Zindler and Hart, 1986; Woodhead, 1996; Stracke et al., 2005; Kawabata et al., 2011; Hanyu et al., 2014; White, 2015). Its isotopic composition must reflect long-term, time-integrated enrichment of U and Th relative to

Pb (~1.0–3.2 Ga; e.g., Tatsumoto, 1978; Hofmann, 1997; Stracke et al., 2005; Hanyu et al., 2011; Cabral et al., 2013; Nebel et al., 2013; Castillo, 2015), coupled with time-integrated low Th/U and Rb/Sr ratios, but moderate Sm/Nd and Lu/Hf ratios. It should be noted that we use the term end member HIMU in this manuscript to refer to the composition of the reference HIMU localities of St. Helena and Cook-Austral Islands as is common in the literature, while recognizing that the “real end member” could have more extreme compositions than the reference localities.

It is widely accepted that HIMU represents a rare mantle end member, whereas the prevalent FOZO (C or PREMA) end member is a common mixing component present in MORBs and OIBs (e.g., Hart et al., 1992; Hanan and Graham, 1996; Stracke et al., 2005; Stracke, 2012). In the last few decades numerous models were proposed to explain the restricted and unique composition of HIMU (e.g., Zindler and Hart, 1986; Chauvel et al., 1992; Stracke et al., 2003; Pilet et al., 2005; Willbold and Stracke, 2006; Hanyu et al., 2011; Castillo, 2015), whereas FOZO (also termed “Young HIMU”; Thirlwall, 1997) is usually explained by a similar reservoir formation mechanism, but with overall younger formation ages compared to HIMU (e.g., Thirlwall, 1997; Stracke et al., 2005; Castillo, 2015).

In the classic ocean crust-recycling model, the combination of hydrothermal alteration and subduction modification/slab dehydration are proposed to produce these unique trace element ratios in the subducting oceanic slab, followed by long-term storage in the lower mantle and eventual ascent to the surface in mantle plumes (e.g., Hofmann and White, 1982; Zindler and Hart, 1986; Chauvel et al., 1992; Stracke et al., 2003; Cabral et al., 2013; Hanyu et al., 2014; Kimura et al., 2016). Several observations, however, challenge this model. First, recycled oceanic crust transforms under mantle conditions to eclogite/pyroxenite, but these source lithologies alone cannot generate

partial melts with the characteristic HIMU major element composition (e.g., Jackson and Dasgupta, 2008; Dasgupta et al., 2010; Mallik and Dasgupta, 2012). Instead, low Ni concentrations and high Mn/Fe and Ca/Al ratios in olivine phenocrysts from HIMU lavas indicate that peridotite is the dominant source lithology (Herzberg et al., 2014; Weiss et al., 2016). Another problem with the ocean-crust-recycling model is that MORB does not trend towards the HIMU reference localities on Pb isotope diagrams (e.g.  $^{206}\text{Pb}/^{204}\text{Pb}$  versus  $^{208}\text{Pb}/^{204}\text{Pb}$  and  $^{87}\text{Sr}/^{86}\text{Sr}$ ), precluding a simple relation between HIMU and MORB (Stracke et al., 2005; Castillo, 2015; Weiss et al., 2016). In addition, Hanyu et al. (2011) stated that recycled oceanic crust has extremely high Re/Os ratios and after billions of years the  $^{187}\text{Os}/^{188}\text{Os}$  should be highly evolved ( $> 1$ ) relative to chondrites and the average earth's mantle ( $\sim 0.127$ ). In their model, mixing of pure recycled and long-term isolated oceanic crust with the depleted mantle cannot reproduce the observed Os-Pb-Hf systematics of HIMU lavas ( $^{187}\text{Os}/^{188}\text{Os}$  ratios of 0.14-0.15).

In response to these critical observations, several alternative explanations for the origin of the HIMU source were introduced (e.g., Pilet et al., 2005; Collerson et al., 2010; Hanyu et al., 2011; Castillo, 2015; Weiss et al., 2016). For example, Pilet et al. (2005) proposed that metasomatized recycled oceanic lithosphere could represent the HIMU source. Castillo (2015) argued that small amounts of recycled Archean marine carbonates are the main source of HIMU. Alternatively, it has been proposed that HIMU could develop within the (peridotitic) subcontinental lithospheric mantle (SCLM) by infiltration of (carbonatitic) fluids and/or melts (e.g., Hart et al., 1986; Stein et al., 1997; Lucassen et al., 2008; Rooney et al., 2014; McCoy-West et al., 2016; Weiss et al., 2016). However, all these various HIMU reservoir formation models have one thing in common - that the formation of HIMU is associated to modern-style tectonics. Recently, Cabral et al. (2013) showed that the negative  $\Delta^{33}\text{S}$  ratios in olivines from Cook-Austral HIMU lavas

require their source to be  $\geq 2.45$  Ga with ages of up to 3.2 Ga being proposed by Nebel et al. (2013). The style of Archean plate tectonics, however, remains highly controversial (Foley et al., 2003; Bédard, 2006; Van Kranendonk, 2010; Gerya, 2014; Harris and Bédard, 2014; Moyen and Laurent, 2018) and it is questionable if modern-style plate tectonics can be used as an analog.

In this study we report new geochemical and geochronological data from selected submarine lavas, recovered during five cruises with German research vessels (R/V Maria S. Merian and R/V Sonne), and show that these samples have a St. Helena HIMU end member composition. Combined with literature data, we demonstrate that end member HIMU is an almost globally distributed mantle end member reflecting a widespread reservoir(s) in the lowermost mantle. Based on proposed reservoir formation ages of  $>2.45$  Ga (Cabral et al., 2013; Nebel et al., 2013; Castillo, 2015), we re-evaluate the formation of a globally distributed HIMU end member in the context of the Archean geodynamic setting.

## 2. Geological background of the sample locations

We recovered submarine lavas from five cruises with German research vessels: Cruises S084 and S0233 to the Walvis Ridge, South Atlantic, cruise MSM19/3 with the R/V Maria S. Merian to Richardson seamount, South Atlantic, cruise S0193 to the Manihiki plateau, SW Pacific, and cruise S0168 with the R/V Sonne to the Eastern Chatham Rise, SW Pacific. In the following we present a brief geological background of the respective sample locations.

### *2.1 The Walvis Ridge*

The continuous aseismic Walvis Ridge represents the oldest submarine expression of the age progressive Tristan-Gough hotspot track (Rohde et al., 2013a; Rohde et al., 2013b; Hoernle et al., 2015; O'Connor and Jokat, 2015a), which extends from the Parana and Etendeka flood basalt provinces to the Walvis Ridge and then to the Guyot Province, ending at the active volcanic islands of Tristan da Cunha and Gough. The age progression is the strongest evidence that the track was formed by a mantle plume, which is supported by recent seismic tomographic data that images a low-velocity conduit-like structure with a radius of 100 km down to a depth of 250km, just to the southwest of Tristan da Cunha (Schlömer et al., 2017). This shallow velocity anomaly lies above a broader vertically continuous conduit-like structure with  $\partial V_s$  ratios of  $< -0.5\%$  in the depth range of 1000-2800 km (French and Romanowicz, 2015). High  $^3\text{He}/^4\text{He}$  ratios ( $> 10 R_A$ ) from olivines in Etendeka flood basalts provide further support for a lower mantle origin (Stroncik et al., 2017).

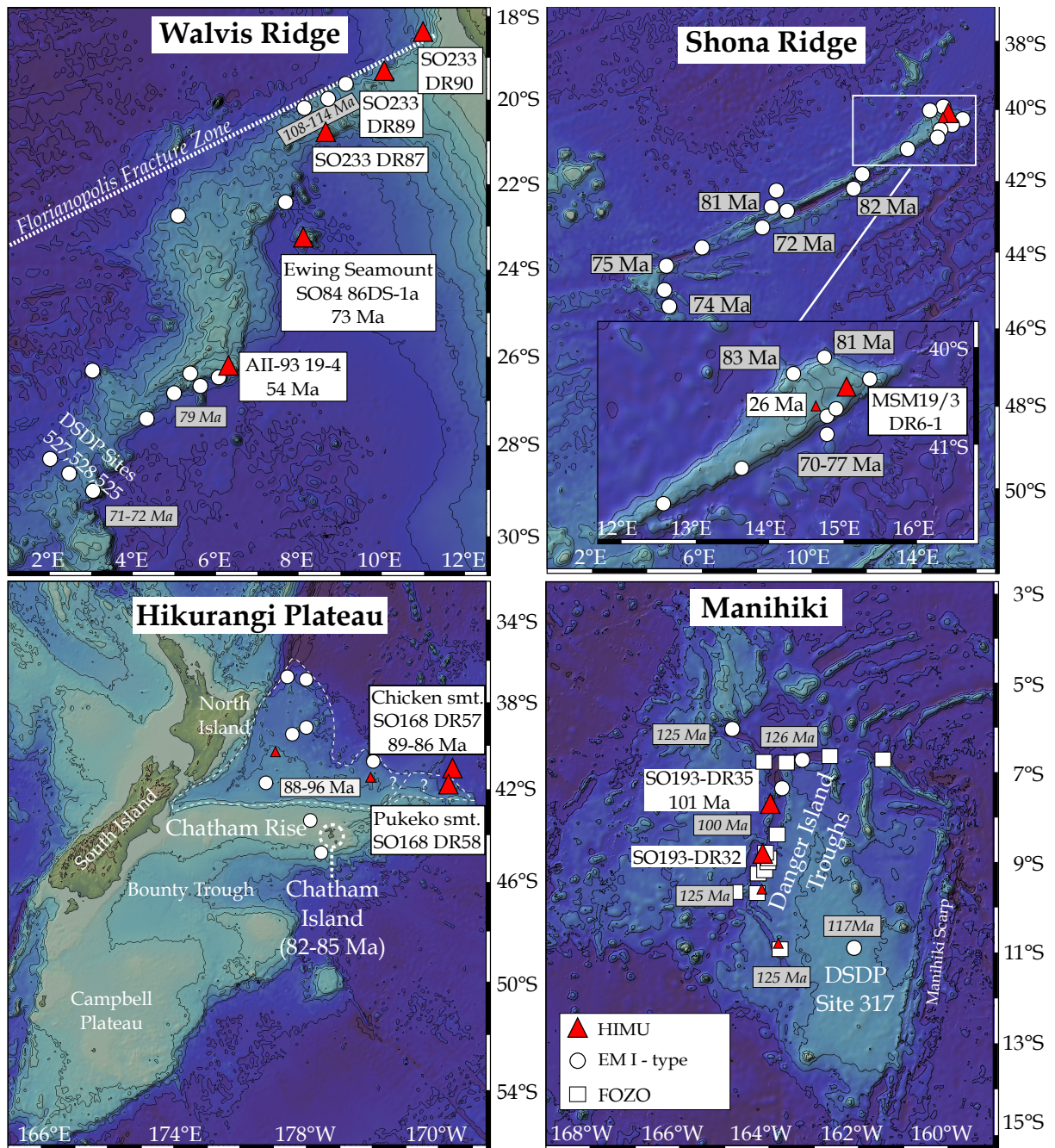


**Fig. 1: Maps of the Walvis Ridge, Manihiki Plateau, Hikurangi Plateau and Shona Ridge/Richardson seamount with sample sites from the respective cruises (red triangles). Sample sites from the literature with 1) EM I-type compositions are shown as white circles, 2) HIMU with small red triangles and 3) FOZO compositions with squares. Source of bathymetric map: <http://www.geomapapp-org>. Sample sites and age data: Walvis Ridge (Richardson et al., 1984; Thompson and Humphris, 1984; Salters and Sachi-Kocher, 2010; Rohde et al., 2013a; Rohde et al., 2013b; Hoernle et al., 2015; O'Connor and Jokat, 2015a, b), Manihiki plateau (Ingle et al., 2007; Hoernle et al., 2010; Timm et al., 2011; Golowin et al., 2017), Zealandia and Hikurangi Plateau (Panter et al., 2006; Hoernle et al., 2010; Timm et al., 2010) and Shona Ridge/Richardson seamount (Le Roex et al., 2010; O'Connor et al., 2012; Hoernle et al., 2016).**



Consistent with the mantle plume model (e.g., Wilson, 1963; Morgan, 1971; Richards et al., 1989), the Tristan-Gough hotspot track initiated with the Etendeka and Parana flood basalt provinces at ~135 Ma (Renne et al., 1996) and were subsequently split apart by seafloor spreading related to the opening of the South Atlantic Ocean. Thereafter, the mantle plume interacted with the Mid-Atlantic ridge, forming the Walvis Ridge and Rio Grande Rise (120-60 Ma, Humphris and Thompson, 1983; O'Connor and Duncan, 1990; Rohde et al., 2013a; Hoernle et al., 2015; O'Connor and Jokat, 2015a, b) and since ~60 Ma became intraplate forming the Guyot Province, which connects the Walvis Ridge with the active volcanic islands of Tristan da Cunha and Gough.

The last 70 Ma of the Tristan-Gough hotspot track shows geochemical zonation primarily in Pb isotopic composition (Rohde et al., 2013a; Hoernle et al., 2015) with the zonation beginning at the DSDP Site transect at the SW end of the Walvis Ridge (Fig. 1). Both compositional types (Tristan and Gough) lie within the compositional range of EM I. In the >70 Ma portion of the Walvis Ridge hotspot track (there are few available samples from the Rio Grande Rise), only Gough-type compositions have been documented thus far (e.g., Hoernle et al., 2015). DSDP Site 525 (Gough-type) on the southern Walvis Ridge is considered to be the Atlantic type locality for the EM I end member (e.g., Zindler and Hart, 1986; White, 2015).

The top of the central portion of the Walvis Ridge, Valdivia Bank, and the northeastern end of the Walvis Ridge are flat (Hoernle et al., 2014), suggesting that these parts of the Walvis Ridge were once subaerially exposed and eroded to sea level. Seamounts on the Walvis Ridge postdate this erosional stage and thus must be significantly younger in age than the Walvis Ridge basement.  $^{40}\text{Ar}/^{39}\text{Ar}$  dating shows that late-stage (post-erosional) volcanism on (sample AII-93-19-4; Rohde et al., 2013b) and adjacent to the Walvis Ridge (sample S084 86DS-1a; O'Connor and Jokat, 2015a) is

~30 Ma younger than the corresponding ridge basement (geochemical data for both samples in Appendix B). During R/V Sonne cruise SO233, three late-stage seamounts were sampled by dredging (Fig.1): Two seamounts (SO233 dredge locations DR87 and DR89) are located on the flat northeastern part of the Walvis Ridge. A third seamount (SO233 dredge station DR90) is located on the seafloor northwest of the Florianopolis Fracture Zone (FFZ). As a result of several ridge jumps, the oceanic crust northwest of this fracture zone became part of the South American plate. The ocean crust beneath the seamount dredged at SO233 DR90 is estimated to be ~93 Ma (O'Connor and Jokat, 2015b), providing a maximum age for this seamount and sample (Fig.1).

## *2.2 Richardson Seamount (Shona hotspot track)*

Richardson seamount (69-84 Ma) is located ~2000 km south of the Walvis Ridge and belongs to the Shona hotspot track (Fig. 1; O'Connor et al., 2012; Hoernle et al., 2016). Samples from the older part of the Shona hotspot track have an EM I-type geochemical signature, similar to the Gough subtrack and most of the Walvis Ridge basement (Hoernle et al., 2016). Several small late-stage cones are located on the flat (erosional) top of this elongated guyot, post-dating erosion to sea level and subsequent subsidence. An  $^{40}\text{Ar}/^{39}\text{Ar}$  age of  $26 \pm 0.3$  Ma ( $2\sigma$ ) was obtained from one of these post-erosional cones (O'Connor et al., 2012), which is  $\geq 40$  Ma younger than the guyot basement (Hoernle et al., 2016). We assume a similar age for our sample MSM19/3 DR6-1 from a nearby post-erosional cone, since it has the same tectonic setting and similar major and trace element characteristics to the dated sample (D35-1; Le Roex et al., 2010).

### *2.3 The Manihiki-Hikurangi plateau seamounts*

Seafloor fabric data, similar formation ages (~123-116 Ma), plate tectonic reconstructions and geochemical data suggest that the Ontong-Java, Hikurangi and Manihiki oceanic plateaus were once part of a giant plateau, which may have been emplaced by a massive mantle upwelling (Fig. 1; e.g. Taylor, 2006; Davy et al., 2008; Hoernle et al., 2010; Timm et al., 2011; Chandler et al., 2015; Hochmuth et al., 2015; Golowin et al., 2017). The basements of these three oceanic plateaus are characterized by EM I-type affinities, with various sub-groups (e.g., Kwaimbaita-, Kroenke-, Singalloy-type; see Tejada et al., 1996; Tejada et al., 2002; Hoernle et al., 2010; Timm et al., 2011; Jackson et al., 2015; Golowin et al., 2017 for a detailed description). The Manihiki basement rocks show evidence of a HIMU-type component (Timm et al., 2011; Golowin et al., 2017). After the combined Ontong Java – Manihiki – Hikurangi Plateau broke into the three respective plateaus (Taylor, 2006; Davy et al., 2008; Chandler et al., 2015; Hochmuth et al., 2015), the Hikurangi plateau drifted southward until it collided with the Eastern Gondwana margin and clogged this subduction system at ~105 Ma (Bradshaw, 1989; Davy et al., 2008; Hoernle et al., 2010).

In contrast to the tholeiitic basement lavas, alkalic volcanism is present in the form of seamounts on Manihiki and Hikurangi Plateaus and dikes in the Ontong Java Plateau, largely emplaced between 110-65 Ma (Beiersdorf et al., 1995; Tejada et al., 1996; Tejada et al., 2002; Ingle et al., 2007; Hoernle et al., 2010; Pietsch and Uenzelmann-Neben, 2015). On the Hikurangi plateau, the seamounts formed primarily between 99-87 Ma (Hoernle et al., 2010) followed by rifting and seafloor spreading that separated the blocked portion of the Gondwana subduction zone (Zealandia) from West Antarctica beginning at  $\geq 85$  Ma (Davy et al., 2008; Hoernle et al., 2010). Gondwana breakup was accompanied by volcanism on the Chatham Islands taking place between

85-82 Ma (Panter et al., 2006). Several models argue that breakup between Zealandia and Antarctica was triggered by a mantle plume with a HIMU signature beneath the Gondwana margin during the Late Cretaceous (Weaver et al., 1994; Hart et al., 1997; Storey et al., 1999; Panter et al., 2006; Hoernle et al., 2010; Kipf et al., 2014).

During the R/V Sonne SO193 cruise, samples from late-stage volcanic centers on the western flank of the prominent Danger Island Troughs graben system of the Manihiki plateau were recovered (Werner and Hauff, 2007). Since both seamounts are located at the edge of the en echelon Danger Island Troughs, we assume a causal relationship to the rift zone dissecting the Manihiki plateau between 118 – 100 Ma (Taylor, 2006; Ingle et al., 2007; Timm et al., 2011; Hochmuth et al., 2015), suggesting that the seamounts formed within this time interval.

During R/V Sonne SO168 cruise, one seamount was sampled by dredging on the easternmost portion of the Chatham Rise (Pukeko Seamount; SO168 DR58) and one just north of the Eastern Chatham Rise (Chicken/Hühnchen Seamount; SO168 DR57; Hoernle et al., 2003; Fig.1). Both seamounts are assumed to sit on the stretched and thinned continental crust of the Eastern Chatham Rise (part of Zealandia), which was affected by the sudden change from the collision with the Hikurangi plateau and following break up from Antarctica (e.g. Bradshaw, 1989; Weaver et al., 1994; Davy et al., 2008). The Chicken Seamount is a guyot with a flat top (2000 m below sea level) most likely formed by wave base abrasion, whereas the smaller Pukeko Seamount has a ridge-type structure and is 300 m lower than Chicken and possibly never reached sea level (Hoernle et al., 2003).

### 3. Analytical methods

Details about sample preparation;  $^{40}\text{Ar}/^{39}\text{Ar}$  age dating and geochemical (major and trace element and radiogenic isotope) methods are reported in Appendices A-E. In the following section, we present the  $^{40}\text{Ar}/^{39}\text{Ar}$  age data derived from the submarine samples from the Eastern Chatham Rise and Manihiki plateau seamount(s). Afterwards, we evaluate the potential effects of seawater alteration and describe the method we used to compare HIMU localities over an age range of  $\sim 130$  Ma.

#### 3.1. $^{40}\text{Ar}/^{39}\text{Ar}$ dating

We report the results of two new  $^{40}\text{Ar}/^{39}\text{Ar}$  ages from Eastern Chatham Rise and Manihiki plateau using acid-leached plagioclase separates. We monitored the Ca/K ratios and calculated  $^{36}\text{Ar}/^{37}\text{Ar}$  plagioclase alteration index (AI) values (Baksi, 2007; van den Bogaard, 2013). We used the calculated  $^{36}\text{Ar}/^{37}\text{Ar}$  plagioclase Alteration Index (AI) cut-off value of 0.00006 (Baksi, 2007; van den Bogaard, 2013), and the percent of atmospheric  $^{40}\text{Ar}$  ( $^{40}\text{Ar}_{\text{atm}}$ ) values to determine the degree of alteration of the laser step-heating or total fusion analyses. Inverse isochron ages were calculated to confirm both the plateau and total fusion ages and identify if the samples preserved initial atmospheric  $^{40}\text{Ar}/^{36}\text{Ar}$  ratios, without the presence of extraneous  $^{40}\text{Ar}$  components (i.e., an atmospheric  $^{40}\text{Ar}/^{36}\text{Ar}$  ratio of 295.5; Steiger and Jäger, 1977).

We consider  $^{40}\text{Ar}/^{39}\text{Ar}$  step-heating analyses as statistically valid if the following widely accepted criteria are fulfilled (e.g., Lanphere and Dalrymple, 1978; Pringle et al., 1993; O'Connor and Jokat, 2015b): (1) a well-defined age spectrum plateau created by three or more continuous and concordant steps (at the  $2\sigma$  confidence level) with  $> 50\%$  of the cumulative  $^{39}\text{Ar}$ , (2) the mean square of weighted deviations (MSWD) is  $\leq 2$ , and

the probability (P) of fit is  $> 0.05$ , and (3) the calculated plateau and isochron ages are concordant at 95 % confidence levels (Table 1; Appendix C).

Plagioclase step-heating of sample SO193 DR35-1 (Manihiki plateau) yields a statistically valid plateau age of  $100.70 \pm 0.93$  Ma ( $2\sigma$ ; MSWD = 1.60; P = 0.18; 61.9 %  $^{39}\text{Ar}$ ). All plateau steps yield high  $^{36}\text{Ar}/^{37}\text{Ar}$  AI values, above the plagioclase  $^{36}\text{Ar}/^{37}\text{Ar}$  cut-off value of 0.00006 (Baksi, 2007), and elevated  $^{40}\text{Ar}$  atmospheric ( $^{40}\text{Ar}_{\text{atm}}$ ) values, indicating the degassing of Ar from altered material. The statistically invalid inverse isochron age of  $100.3 \pm 3.3$  Ma (95% conf.; MSWD = 7.9; P = 0.00; initial  $^{40}\text{Ar}/^{36}\text{Ar} = 298 \pm 16$ ; Spreading Factor (SF) = 43.0%), however, confirms the plateau age. Due to the alteration of this sample, the  $^{40}\text{Ar}/^{39}\text{Ar}$  plateau age of sample SO193 DR35-1 of  $100.70 \pm 0.93$  Ma ( $2\sigma$ ) should be treated with some caution, but this plateau age lies within the age range of the formation of the Danger Island Troughs (118-100 Ma).

Laser total fusion  $^{40}\text{Ar}/^{39}\text{Ar}$  dating of 5 plagioclase analyses (weighing between 0.18-0.42 mg) from the Chicken seamount (SO168-DR57-1) yield a statistically valid weighted mean age of  $85.5 \pm 3.3$  Ma ( $2\sigma$ , MSWD = 0.63, P = 0.64). The statistically valid inverse isochron age of  $83.6 \pm 2.6$  Ma (95% conf.; MSWD = 1.9; P = 0.13; initial  $^{40}\text{Ar}/^{36}\text{Ar} = 297.7 \pm 2.1$ ; but with a spreading factor value of only 22.0%, below the cut-off of  $> 40\%$  suggested by Jourdan et al. (2009)) shows that these analyses preserved initial atmospheric  $^{40}\text{Ar}/^{36}\text{Ar}$  ratios. The inverse isochron age, however, is within error of the weighted mean age. Nevertheless, the 5 analyses yield  $^{36}\text{Ar}/^{37}\text{Ar}$  AI values above the plagioclase cut-off value of Baksi (2007) and elevated %  $^{40}\text{Ar}_{\text{atm}}$  values indicate the degassing of Ar from altered material. Therefore the weighted mean age should be treated with caution. However, it should be noted that the SO168 DR57-1 plagioclase age of  $85.5 \pm 3.3$  Ma ( $2\sigma$ ) from East Chatham Rise lies within the age range of the

seamounts from the nearby Hikurangi plateau (99-87 Ma; Hoernle et al., 2010), and the first magmatic phase of Chatham Island (85-82 Ma; Panter et al., 2006).

**Table 1:  $^{40}\text{Ar}/^{39}\text{Ar}$  results and calculated ages from Eastern Chatham Rise and Manihiki plateau.**

<b>Laser total fusion results</b>								
<b>Sample</b>	<b>Location</b>	<b>Rock Type</b>	<b>Phase</b>	<b>Age (Ma)</b>	<b><math>2\sigma</math></b>	<b>MSWD</b>	<b>P</b>	<b>No. of analyses</b>
S0168 DR 57-1	Chicken	Trachyte	Plag.	85.5	$\pm 3.3$	0.63	0.64	5 out of 16
<b>Laser step-heating results</b>								
<b>Sample</b>	<b>Location</b>	<b>Rock Type</b>	<b>Phase</b>	<b>Age (Ma)</b>	<b><math>2\sigma</math></b>	<b>MSWD</b>	<b>P</b>	<b>Cum. % <math>^{39}\text{Ar}</math></b>
S0193 DR 35-1	Smt. -DIT	Mugearite	Plag.	100.7	$\pm 0.93$	1.6	0.18	61.9 %

Abbreviations: Plag. = plagioclase; Cum. = cumulative; MSWD = Mean Squares Weighted Deviation; P = probability; conf. = confidence; WMA = weighted mean age

### *3.2 Alteration and age correction of radiogenic isotope ratios*

The evaluation of geochemical data from aged oceanic rocks needs to take into account the effect of seawater alteration. To minimize the effects of alteration, we sampled the freshest parts of the lavas by careful handpicking under a binocular microscope (size fraction 0.5-1mm). The loss on ignition (LOI), a common indicator for the degree of alteration, is relatively low (LOI < 3.3 wt. %) for these oceanic rocks (excluding 2 out of 19 samples with LOI values of 5.7 and 7.6 wt. %). In general, the HFSE, such as Zr, Nb, Ta and Hf, as well as the REE, are considered to be relatively immobile during low temperature seawater alteration, whereas the alkali elements, LILE and U are prone to low-temperature alteration and Pb to hydrothermal alteration (e.g. Hart, 1969; Hart et al., 1974; Thompson, 1983; Bienvenu et al., 1990; Verma, 1992; Jochum and Verma, 1996). Since our samples (with LOI < 3.3 wt.% and MgO > 2wt. %) have comparable correlation coefficients for immobile vs. immobile elements (e.g. Zr vs Nb, Th, Ba with the best fit line ( $R^2$ ) values of 0.74-0.80; not shown) and immobile vs

mobile elements (Zr vs Rb, K, Pb;  $R^2=0.73-0.86$ ; not shown), we believe that our sample collection is relatively fresh. Accordingly, the major and incompatible multi-element diagrams show no evidence of seawater alteration through anomalous enrichment or depletion of the mobile elements irrespective of the LOI values (Figs. 2-4).

In order to compare the isotopic composition of rocks with different ages, we first calculate initial isotope ratios of samples based on their measured parent/daughter ratios (P/D) and then project these values to a common age of 60 Ma using source P/D values. Here, we use the proposed end member source compositions for HIMU (and EM I values for the basement lavas are shown in brackets) after Stracke et al. (2003) and Willbold and Stracke (2006) with the following concentrations in ppm: Sr = 80.27 for HIMU (21.75 for EM I basement), Rb = 0.57 (0.44), Sm = 2.68 (0.48), Nd = 7.45 (1.42), U = 0.028 (0.012), Th = 0.088 (0.0592), Pb = 0.092 (0.088), Lu = 0.449 (0.095) and Hf = 1.78 (0.35).



#### 4. Results and HIMU geochemistry

In this section, we discuss the major and trace elements and isotopic variability of the HIMU reference locations and compare the geochemical compositions of our analyzed submarine samples to the compositions of the respective basement lavas and HIMU reference locations.

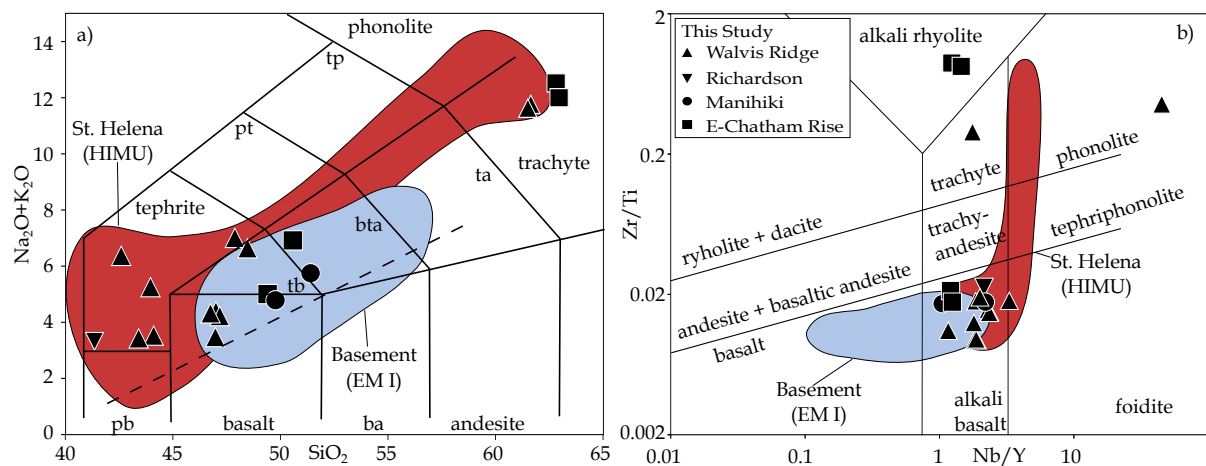


**Fig. 2:** Classification diagrams with a)  $\text{SiO}_2$  vs total alkalis ( $\text{Na}_2\text{O}+\text{K}_2\text{O}$ ) normalized to 100% on a volatile-free basis, after Le Maitre et al. (2005) and b)  $\text{Nb}/\text{Y}$  vs.  $\text{Zr}/\text{Ti}$  after Pearce (1996). The dashed line in a) divides the alkaline and sub-alkaline series, after MacDonald (1968). Basement (EM I) comprises the Richardson seamount, Manihiki Plateau and Walvis Ridge EM I-type basement lavas. Note, only EM I Gough-type composition is shown for the Walvis Ridge. The source of basement data is reported in Fig.1. St. Helena literature data: Baker, 1969; Grant et al., 1976; Weaver et al., 1987; Chaffey et al., 1989; Willbold and Stracke, 2006, 2010; Kawabata et al., 2011; Salters et al., 2011; Hanyu et al., 2014. Abbreviations: pb = microbasalt, pt = phonotephrite, tp = tephriphonolite, tb = trachybasalt, bta = basaltic trachyandesite, ta = trachyandesite, ba = basaltic andesite.

#### 4.1 Major elements

Mafic lavas ( $\text{MgO} > 5\text{wt.}\%$ ) from the HIMU reference localities are alkalic and silica-undersaturated, characterized by low  $\text{SiO}_2$  and  $\text{Al}_2\text{O}_3$ , but high CaO and total FeO ( $\text{FeO}^T$ ) contents, and high  $\text{CaO}/\text{Al}_2\text{O}_3$  ratios compared to other OIBs (Figs. 2-3; e.g. Kogiso et al., 1998; Jackson and Dasgupta, 2008). While volatile-free peridotite or pure eclogite/pyroxenite (high pressure modification of MORB) cannot reproduce the major element characteristics of the HIMU end member lavas (e.g., Pertermann and Hirschmann, 2003; Kogiso and Hirschmann, 2006; Spandler et al., 2008; Dasgupta et al., 2010), experimental studies indicate that  $\text{CO}_2$  is required in the mantle source to generate HIMU lavas (e.g., Dasgupta et al., 2007; Gerbode and Dasgupta, 2010; Mallik and Dasgupta, 2012, 2013). The involvement of  $\text{CO}_2$  in the formation of silica-poor ocean island HIMU-type basalts is supported by phenocrysts with  $\text{CO}_2$ -rich inclusions (Cook-Austral: Saal et al., 1998; Weiss et al., 2011; Weiss et al., 2016). The characteristic major element composition of HIMU end member lavas is associated with the interaction (infiltration or metasomatism) of MORB-eclogite/pyroxenite derived melts and carbonated peridotite or a hybrid source, e.g. carbonated MORB-eclogite/pyroxenite derived melts added to peridotite (e.g., Dasgupta et al., 2007; Jackson and Dasgupta, 2008; Dasgupta et al., 2010; Gerbode and Dasgupta, 2010; Mallik and Dasgupta, 2012, 2013; Herzberg et al., 2014; Mallik and Dasgupta, 2014). Olivine phenocrysts with low Ni and high Ca contents, and low Fe/Mn ratios from HIMU lavas are consistent with peridotite as the dominate source lithology (Herzberg et al., 2014; Weiss et al., 2016), which became infiltrated/metasomatized by MORB-eclogite/pyroxenite derived melts (Herzberg et al., 2014) and/or carbonatitic fluids/melts (Weiss et al., 2016).

The volcanic rocks from the Walvis Ridge, Richardson, Eastern Chatham Rise/Hikurangi Plateau and Manihiki Plateau seamounts are also silica undersaturated, ranging from alkali basalts through trachytes to basanites through tephrites (Fig 2; Pearce, 1996; Le Maitre et al., 2005). On binary diagrams with MgO, the submarine samples (with LOI < 3.3 wt. %) form negative correlations with SiO<sub>2</sub>, Al<sub>2</sub>O<sub>3</sub>, K<sub>2</sub>O, Na<sub>2</sub>O and positive correlations with CaO, FeO<sup>T</sup> and TiO<sub>2</sub> (Fig. 3), consistent with fractional crystallization of the observed phenocryst phases (olivine, clinopyroxene, feldspar and Fe-Ti oxides). The change in slope of the positive MgO versus CaO, SiO<sub>2</sub>, FeO<sup>T</sup> and TiO<sub>2</sub> trends at MgO values of ~ 5 wt. % indicates that clinopyroxene and Fe-Ti oxides become major fractionating phases at this stage of differentiation. P<sub>2</sub>O<sub>5</sub> forms a similar trend as TiO<sub>2</sub> (not shown), indicating apatite fractionation at more evolved stages of differentiation (MgO < 4 wt. %). At a given MgO content (> 5 wt. %), the analyzed late-stage samples have distinct major element compositions trending to lower SiO<sub>2</sub> and higher FeO<sup>T</sup> and TiO<sub>2</sub>, compared to their respective EM I-type basement rocks (Fig. 3). The major element data for our samples lie within the compositional range of HIMU lavas from St. Helena and Cook-Austral islands (Fig. 3).

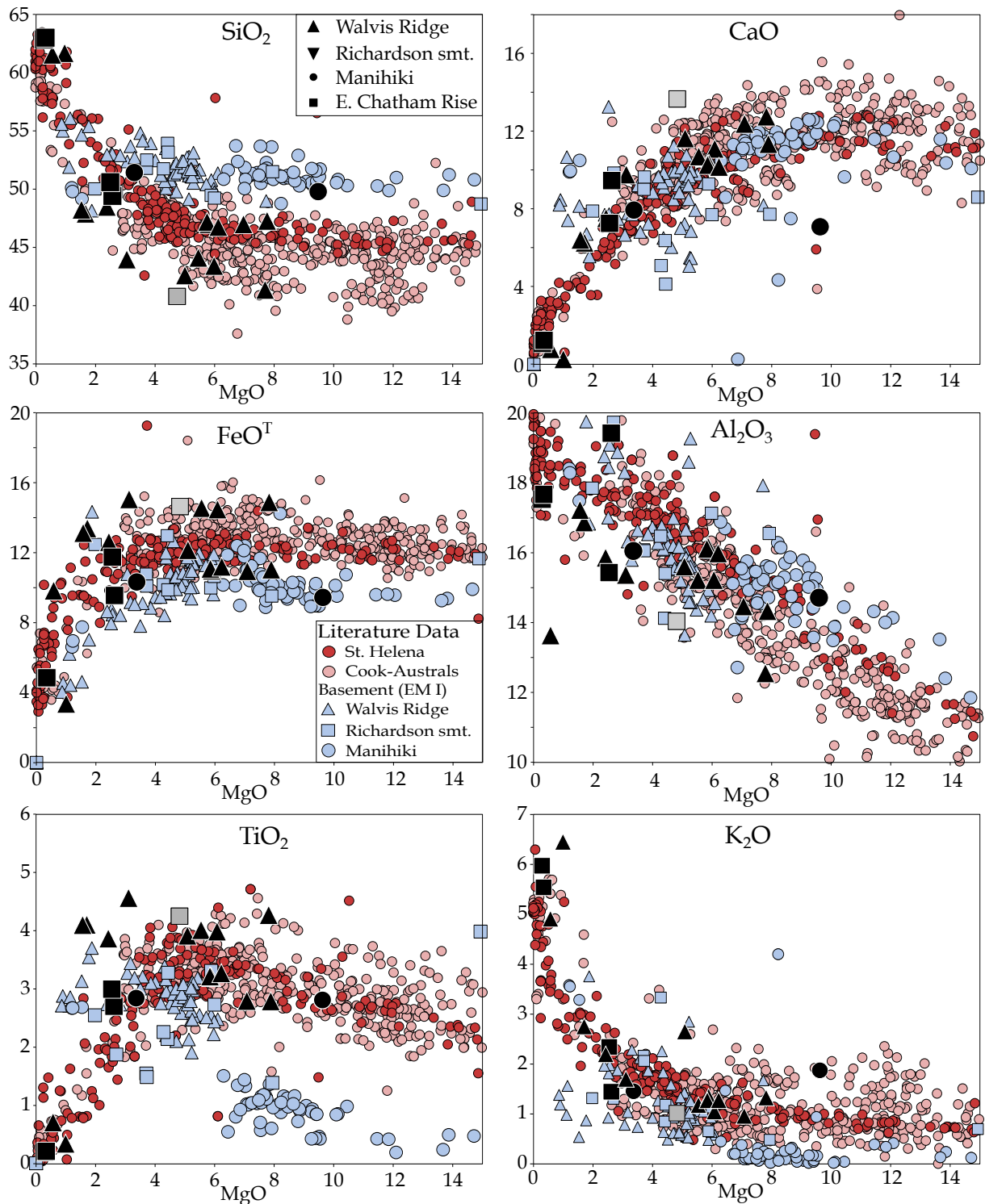


Fig. 3: Bivariate diagrams of MgO versus major elements with references from the EM-type basement lavas from the Manihiki plateau, Walvis Ridge and Richardson seamount, and St. Helena lavas and Cook-Austral island rocks for HIMU (Dupuy et al., 1989; Chauvel et al., 1992; Woodhead, 1996; Kogiso et al., 1997b; Lassiter et al., 2003; Hanyu et al., 2011; Salters et al., 2011; Hanyu et al., 2013; Maury et al., 2013). The gray rectangle (D35-1; Le Roex et al., 2010), which is also from a late-stage cone on Richardson Seamount, has a similar major element composition to our basanite sample from another late-stage cone on Richardson seamount. Major element oxides were normalized to 100% on a volatile-free basis. Literature data as in Fig.2.

#### 4.2 Trace elements

The HIMU reference localities have remarkably similar trace element compositions characterized by high primitive-mantle-normalized Nb and Ta concentrations relative to Ba, Th and Rb with decreasing normalized concentrations from Nb to Cs, and overall low Pb, Rb, and Ba concentrations relative to EM basalts (Fig. 4; Willbold and Stracke, 2006; Stracke, 2012). Willbold and Stracke (2006) pointed out that all HIMU basalts have low Ba/La, Rb/La, Rb/Sr and high U/Pb ratios compared to EM-type basalts, which is consistent with a source with lower (Rb, Ba, Th, U)/REE and Rb/Sr ratios and higher (U, Th)/Pb, Sm/Nd and Nb/La ratios compared to bulk Earth. The characteristic relative depletion of highly incompatible trace elements (e.g., Cs, Rb and Ba) and high (Nb, Ta)/(U, La) and Nd/Pb ratios could indicate a source, which is 1) depleted in highly incompatible elements and 2) additionally modified by loss of fluid-mobile elements (e.g., Chauvel et al., 1992; Woodhead, 1996; Stracke et al., 2003; Willbold and Stracke, 2006; Kawabata et al., 2011; Stracke, 2012). Stracke et al., 2003) showed that melting (~1%) of subduction-modified oceanic crust produces melts that broadly resemble those of HIMU basalts, even if the calculated melts have more pronounced positive Nb-Ta anomalies and higher Cs/Rb ratios (their Fig. 3). A critical aspect of the classic ocean-crust-recycling model remains that the overlying sediments are effectively removed from the subducting slab, since even small quantities would lead to radiogenic isotope ratios distinct from HIMU (e.g., Chauvel et al., 1992; Stracke et al., 2003). Alternatively, the HIMU multi-element pattern could reflect incompatible-element enrichment and depletion processes (e.g., Pilet et al., 2005; Castillo, 2015; Weiss et al., 2016). For example, Weiss et al. (2016) showed that depleted SCLM metasomatized by carbonatitic melts can reproduce the incompatible-element pattern of Archean metasomatized mantle xenoliths (Grégoire et al., 2003) and average post-

Archean SCLM (McDonough, 1990), which at low degrees of melting can produce HIMU-like multi-element patterns (their Fig. 2).

Our submarine samples also have distinct incompatible element abundances compared to the EM-type compositions of their basement lavas. As with reference HIMU, our seamount samples have greater enrichments in Nb and Ta relative to Rb, Ba, Th and LREEs, greater depletion in Pb relative to Ce and Nd, and depletion in Ti relative to Zr, Hf and Eu (Fig. 4). The seamount lavas have also higher incompatible element abundances (e.g., Ba, Th, U, Nb, Ta, and LREE; Fig. 4) and higher more to less incompatible element ratios, e.g. Nb/Yb ( $> 10$ ), La/Yb ( $> 13$ ),  $\text{TiO}_2/\text{Yb}$  ( $> 1$ ) and Ti/V ( $> 150$ ), indicating low degrees and/or deep melting of an enriched source. In contrast, the EM I-type basement lavas have lower Ti/Yb and (Th, Nb)/Yb ratios, pointing to shallower melting at higher degrees and/or a more depleted source composition. Finally, the late-stage seamount samples show the characteristic HIMU-pattern with overall increasing normalized concentrations from Lu to Nb-Ta, excluding relative Pb and K depletions, and then decreasing concentrations to Cs.

In summary, the late-stage seamount lavas have incompatible element patterns distinct from their EM I basement lavas, but similar to the St. Helena HIMU end member (Fig.4). The trace element characteristics of the HIMU-type late-stage magmas are consistent with being derived from (deep) low-degree melting of silica-undersaturated, carbonated pyroxenitic/eclogitic/peridotite source material (e.g., Weiss et al., 2011; Weiss et al., 2016).

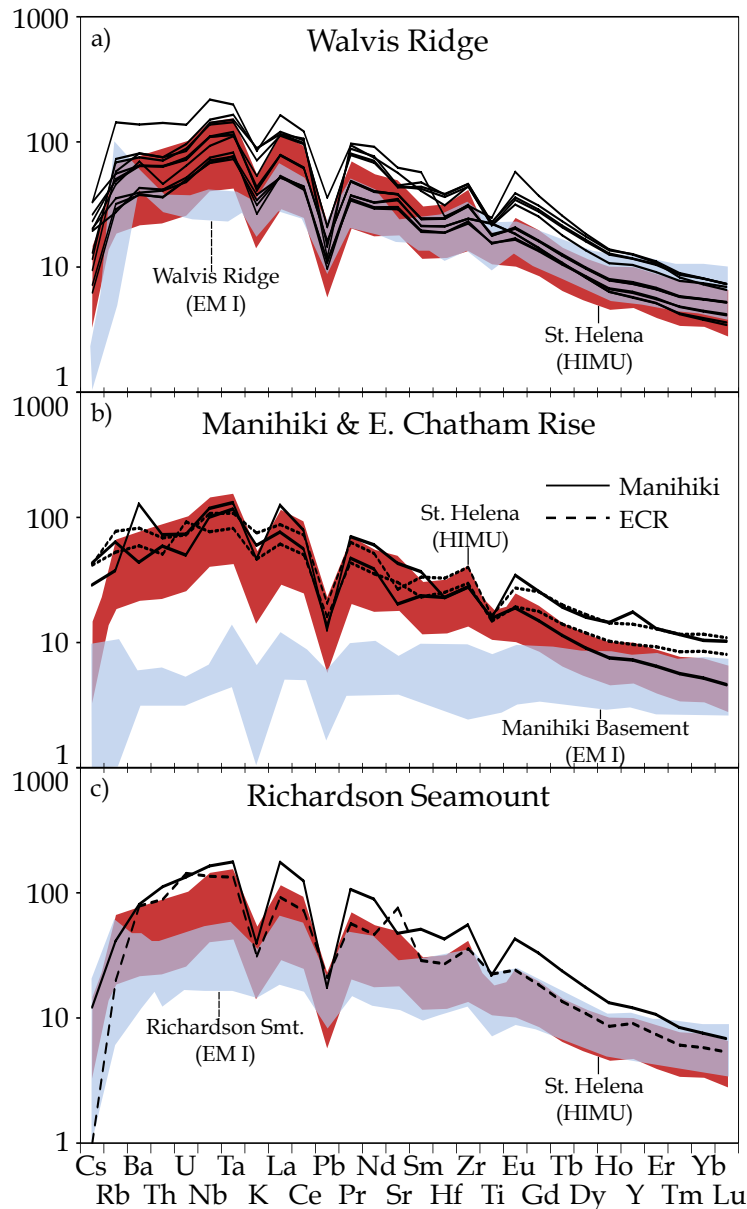


**Fig. 4:** Normalized incompatible element diagrams of a) late-stage volcanism on Walvis Ridge, b) late-stage volcanism on the Manihiki Plateau and volcanism on and adjacent to the Eastern Chatham Rise, and c) late-stage volcanism from the Richardson seamount in relation to the respective basement (blue) and St. Helena lavas (red). The element concentrations are normalized to primitive mantle after Hofmann (1988). Samples with  $MgO < 2\text{wt.}\%$  are not shown due to enhanced fractionation of accessory minerals that cause disturbance of element patterns. Note, the late-stage basanite sample (D35-1, dashed line in c) from the Richardson seamount, dated by O'Connor et al. (2012), also has a HIMU-like trace element composition (Le Roex et al., 2010), supporting a genetic and temporal association to the sample from the cone we studied (MSM19/3 DR6-1).

### 4.3 Sr-Nd-Pb-Hf isotope data

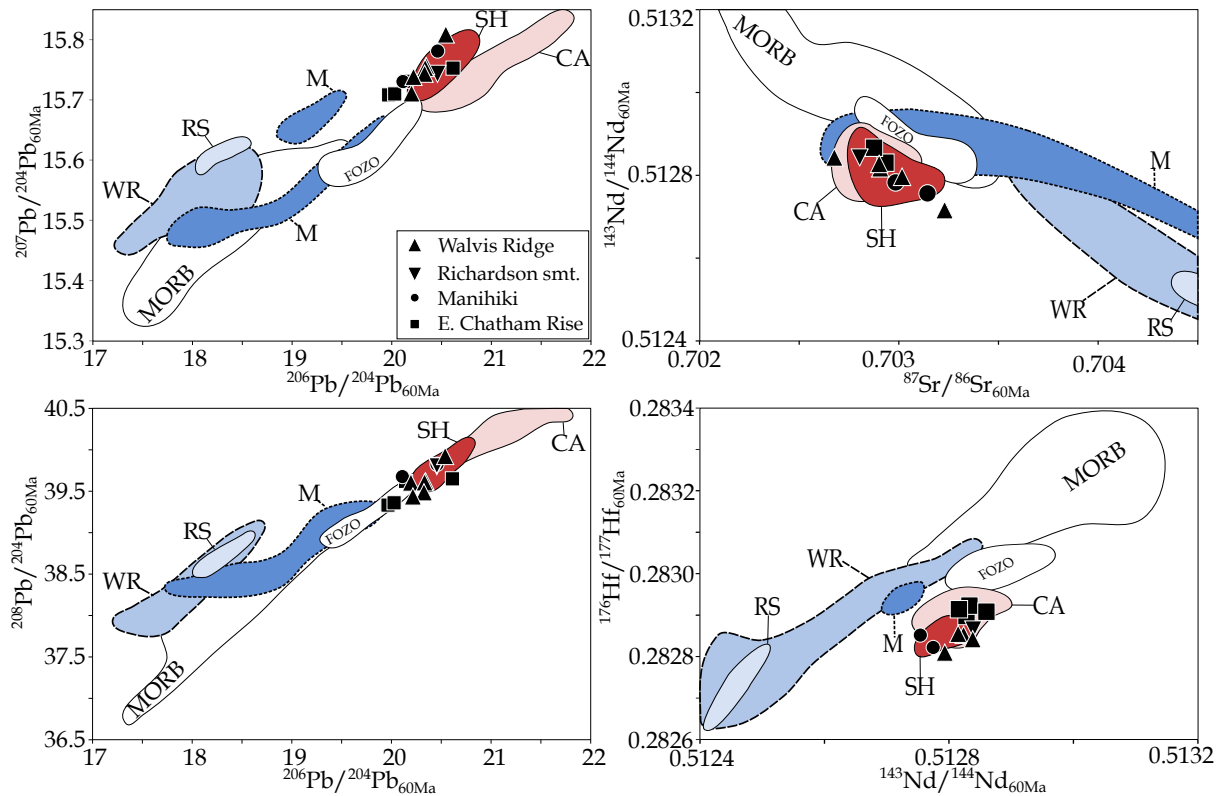


**Fig. 5:** Initial isotope ratios projected to 60 Ma using proposed source parent/daughter ratios for HIMU for the late-stage volcanism on and near the Walvis Ridge, Eastern Chatham Rise, Richardson Seamount, and the Manihiki Plateau. For comparison, fields for the respective basements are also shown, as well as Mid-Ocean Ridge Basalts (MORB), FOZO (Chauvel et al., 1992; Lassiter et al., 2003) as defined by Stracke et al. (2005), and end member HIMU reference locations, i.e. St. Helena and the Cook-Austral archipelago. Abbreviations: SH = St Helena, CA = Cook-Austral, M = Manihiki plateau, WR = Walvis Ridge, RS = Richardson seamount, MORB taken from the data compilation of Class, C. and Lehnert, K. (2012): PetDB Expert MORB (Mid-Ocean Ridge Basalt) Compilation. EarthChem Library. <http://dx.doi.org/10.1594/IEDA/100060>). The sources of other literature data are reported in Fig. 3. MORB values are corrected to 60Ma, assuming a depleted composition after Workman and Hart (2005).

The HIMU reference locations of St. Helena and Cook-Austral Islands have unique isotope ratios with  $^{87}\text{Sr}/^{86}\text{Sr}_{60\text{Ma}} = 0.7023\text{-}0.7034$ ,  $^{143}\text{Nd}/^{144}\text{Nd}_{60\text{Ma}} = 0.5127\text{-}0.5129$ ,  $^{206}\text{Pb}/^{204}\text{Pb}_{60\text{Ma}} = 20.02\text{-}21.71$ ,  $^{207}\text{Pb}/^{204}\text{Pb}_{60\text{Ma}} = 15.65\text{-}15.84$ ,  $^{208}\text{Pb}/^{204}\text{Pb}_{60\text{Ma}} = 39.48\text{-}40.50$  and  $^{176}\text{Hf}/^{177}\text{Hf}_{60\text{Ma}} = 0.2828\text{-}0.2830$  (Fig. 5). St. Helena and Cook-Austral lavas overlap in  $^{206}\text{Pb}/^{204}\text{Pb}_{60\text{Ma}}$  vs.  $^{208}\text{Pb}/^{204}\text{Pb}_{60\text{Ma}}$  and  $^{87}\text{Sr}/^{86}\text{Sr}_{60\text{Ma}}$  vs.  $^{143}\text{Nd}/^{144}\text{Nd}_{60\text{Ma}}$



isotope space, but the Cook-Austral Island lavas trend towards higher  $^{206}\text{Pb}/^{204}\text{Pb}_{60\text{Ma}}$  and  $^{208}\text{Pb}/^{204}\text{Pb}_{60\text{Ma}}$  ratios compared to St. Helena (Fig. 5). On the other hand, the St. Helena lavas are characterized by higher  $^{207}\text{Pb}/^{204}\text{Pb}_{60\text{Ma}}$  at a given  $^{206}\text{Pb}/^{204}\text{Pb}_{60\text{Ma}}$  value and slightly lower  $^{176}\text{Hf}/^{177}\text{Hf}_{60\text{Ma}}$  at a given  $^{143}\text{Nd}/^{144}\text{Nd}_{60\text{Ma}}$  value (Fig. 5). The variable  $^{207}\text{Pb}/^{206}\text{Pb}$  ratios could reflect different formation ages, whereas the slightly lower  $^{176}\text{Hf}/^{177}\text{Hf}_{60\text{Ma}}$  at a given  $^{143}\text{Nd}/^{144}\text{Nd}_{60\text{Ma}}$  value could be generated by slightly lower Lu/Hf ratios (0.006 for 2 Ga radiogenic in-growth; Hanyu et al., 2014).

The analyzed samples have the following range in isotope ratios at 60 Ma:  $^{87}\text{Sr}/^{86}\text{Sr}_{60\text{Ma}} = 0.7027\text{-}0.7032$  (except S0168 DR58 with a  $^{87}\text{Sr}/^{86}\text{Sr}_{60\text{Ma}}$  of 0.7053, most likely increased by seawater alteration),  $^{143}\text{Nd}/^{144}\text{Nd}_{60\text{Ma}} = 0.5127\text{-}0.5129$ ,  $^{206}\text{Pb}/^{204}\text{Pb}_{60\text{Ma}} = 19.96\text{-}20.61$ ,  $^{207}\text{Pb}/^{204}\text{Pb}_{60\text{Ma}} = 15.71\text{-}15.82$ ,  $^{208}\text{Pb}/^{204}\text{Pb}_{60\text{Ma}} = 39.33\text{-}39.92$  and  $^{176}\text{Hf}/^{177}\text{Hf}_{60\text{Ma}} = 0.2827\text{-}0.2829$ , which overlap with the St. Helena HIMU composition in multi-isotope space (Fig. 5). In conclusion, the late-stage seamount samples have major and trace element and Sr-Nd-Pb-Hf isotopic compositions that overlap almost completely with the St. Helena HIMU end member composition (Fig. 5).

## 5. Worldwide distribution of HIMU

Late-stage volcanism on the Walvis Ridge (Tristan-Gough hotspot track), Richardson seamount (Shona hotspot track), Manihiki Plateau and Eastern Chatham Rise/Hikurangi Plateau have distinct major and trace element and Sr-Nd-Pb-Hf isotopic compositions compared to their EM I-type basement rocks, but have similar compositions to lavas from the end member HIMU island of St. Helena (Figs. 3-5). Our selected samples from the southern South Atlantic and the SW Pacific Ocean demonstrate that end member HIMU is not limited to St. Helena and Cook-Austral islands and may have an even wider distribution. Based on a broad literature survey, other samples with HIMU-type Sr-Nd-Pb isotopic and trace element compositions occur in oceanic and continental settings (Fig. 6).

### *5.1 Distribution of end member HIMU in the oceans*

In addition to the localities for which we provide new data in this study, the oceanic settings where HIMU material was found comprise: the Cretaceous Marshall and Wake seamount group (140-80 Ma; e.g. Konter et al., 2008), late-stage volcanism on the Hikurangi plateau (99-88 Ma; Hoernle et al., 2010), alkalic lavas near the Tonga-Kermadec Trench in the western Pacific (100 Ma; Castillo et al., 2009), Paleocene Marie Byrd seamounts offshore Marie Byrd Land Antarctica (65-56 Ma; Kipf et al., 2014), Alphonse Bank in the South Atlantic (~58 Ma, which represents an extension of the Western Cape Province in South Africa; Janney et al., 2002), and the two well-known reference localities, St. Helena (14-7 Ma; e.g. Chaffey et al., 1989; Hanyu et al., 2014) and Cook-Austral Islands (Fig. 6; 20-6 Ma; e.g. Woodhead, 1996; Chauvel et al., 1997; Hanyu et al., 2011).

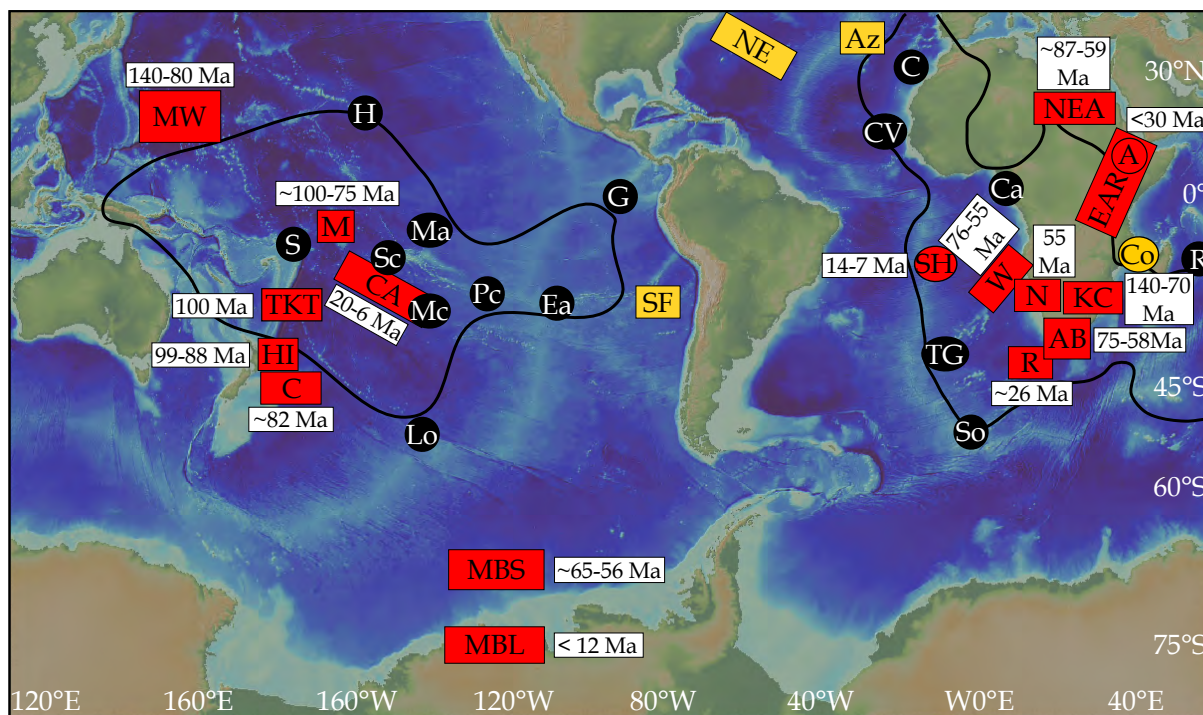


**Fig. 6: Bathymetric map showing 1) the location of primary mantle plumes after French and Romanowicz (2015), 2) the 1%  $\partial V_s$  contour (black line) defining the Pacific and African large low shear velocity provinces (LLSVPs; Torsvik et al., 2010), 3) volcanic features with HIMU compositions (red rectangles) and their age ranges, and 4) locations with low Nd isotope ratios (LoNd) falling on the LoNd Array of Hart et al. (1986) (yellow). Abbreviations: Mantle plumes: H = Hawaii, S = Samoa, Sc = Society, Ma = Marqueses, Mc = Mcdonald, Pc = Pitcairn, Lo = Louisville, Ea = Easter, G = Galapagos, So = Shona, TG = Tristan and Gough, SH = St. Helena, Ca = Cameroon, CV = Cape Verde, C = Canary, A = Afar, Co = Comoros and R = Reunion; HIMU locations with age data: MW = Marshall and Wake seamount Group (Smith et al., 1989; Staudigel et al., 1991; Koppers et al., 1995; Koppers et al., 2003; Konter et al., 2008), CA = Cook-Austral islands (includes Mangaia, Tubuai and Old Rurutu volcanism), HI = Hikurangi Plateau, TKT = alkaline field near the Tonga-Kermadec Trench (Castillo et al., 2009), C = Chatham Island and Eastern Chatham Rise (this study), MBL= Marie Byrd Land (Hart et al., 1997; Panter et al., 2000), MBS = Marie Byrd Seamounts (Kipf et al., 2014), NEA = Northeast Africa (Sudan, Egypt; Lucassen et al., 2008), AB = Alphard Bank (Janney et al., 2002), EAR = East African Rift volcanics (carbonatites: Nelson et al., 1988; Kalt et al., 1997; Bell and Tilton, 2001 and silicates: Vollmer and Norry, 1983; Paslick et al., 1995; Simonetti and Bell, 1995; Stewart and Rogers, 1996; Rogers et al., 2000; Roex et al., 2001; Furman et al., 2006; Keller et al., 2006; Mana et al., 2012), KC = Kaapvaal Craton kimberlites (Kramers, 1977; Collerson et al., 2010), N = Namibian carbonatites (Cooper and Reid, 1998; Cooper and Reid, 2000), W = Walvis Ridge (this study; Rohde et al., 2013b; O'Connor and Jokat, 2015a), R = Richardson Seamount of the Shona hotspot track (this study; O'Connor et al., 2012), M = Manihiki Plateau seamounts (this study); LoNd array (Hart et al., 1986): SF = San Felix and San Ambrosio, NE = New England Seamounts, AZ = Azores and Co = Comores. Source of map: <http://www.geomapapp-org>.**

In the oceanic intraplate settings, the most radiogenic samples (e.g.  $^{206}\text{Pb}/^{204}\text{Pb}_{60\text{Ma}}$  ratios > 20.5) of the respective locations lie within the St. Helena HIMU composition on Sr-Nd-Pb isotope plots with the exception of the Marshall-Wake seamount group, which also overlap the Cook-Austral HIMU field on the  $^{206}\text{Pb}/^{204}\text{Pb}_{60\text{Ma}}$  and  $^{207}\text{Pb}/^{204}\text{Pb}_{60\text{Ma}}$  diagram (Fig. 7). In general, the lavas from the Marshall-Wake seamount group (140-80 Ma) are the oldest submarine lavas on the seafloor with end member HIMU isotopic signature, and are therefore particularly prone to seawater alteration (e.g., elevated  $^{87}\text{Sr}/^{86}\text{Sr}_{60\text{Ma}}$  ratios of several samples; Koppers et al., 2003; Konter et al., 2008). In addition, for the majority of samples, no comprehensive parent-daughter (e.g., U-Th-Pb) elemental concentration data sets are available; therefore, we had to estimate parent/daughter ratios. Since the Marshall-Wake seamounts are believed to represent the oldest submarine expression of the Cook-Austral hotspot system (Konter et al., 2008), we use the average trace element ratios of fresh Cook-Austral HIMU island basalts to calculate the initial isotope ratios. U and/or Pb depletion/enrichment could result in an over-/under-correction of the initial isotope ratios and in part explain the scatter of  $^{208}\text{Pb}/^{204}\text{Pb}_{60\text{Ma}}$  at a given  $^{206}\text{Pb}/^{204}\text{Pb}_{60\text{Ma}}$ . However, even if the Marshall-Wake seamount group data spreads over a broader isotopic range at high  $^{206}\text{Pb}/^{204}\text{Pb}_{60\text{Ma}}$  values, the compositional domain overlaps the HIMU end member composition in isotopic composition.

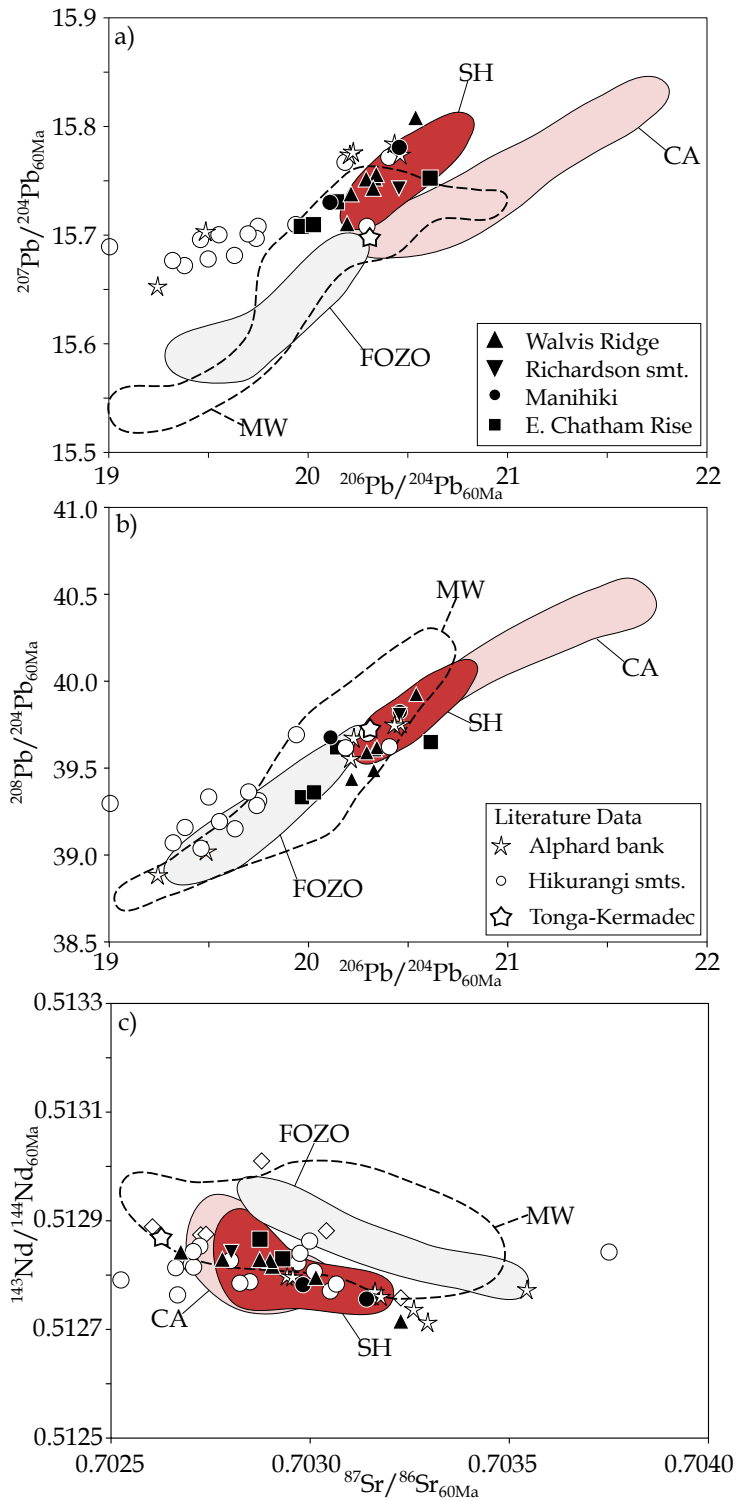


**Fig. 7: HIMU locations in oceanic settings in multi-isotope space corrected to a common age of 60 Ma, which is the medium age of all reported HIMU localities. The isotope ratios of the respective locations overlap with HIMU from St. Helena. Abbreviations: SH = St. Helena, CA = Cook-Austral islands (includes Mangaia, Tubuai and Old Rurutu volcanism) and MW = Marshall-Wake seamount group. References for the respective sites are reported in Figs 5-6.**

## *5.2 Distribution of end member HIMU on the continents*

The continental localities of the HIMU end member include fragments of the Eastern Gondwana margin, including Cenozoic rift volcanics from Marie Byrd Land in the West Antarctic (<12 Ma; Hart et al., 1997) and Late Cretaceous volcanism on the Chatham Islands, New Zealand (85-82 Ma Panter et al., 2006), Cenozoic rift-related volcanism from the East African Rift (<30 Ma; e.g. Furman et al., 2006), intraplate volcanic rocks from North Africa (Sudan and Egypt; 87-59 Ma; Lucassen et al., 2008), Group I kimberlites from the Kaapvaal Craton, South Africa (140-70 Ma; e.g. Collerson et al., 2010) and carbonatites from the Namaqua Natal Belt (Namibia; ~50 Ma; Cooper and Reid, 2000) and East African Rift (<130 Ma; e.g. Bell and Tilton, 2001; Fig. 6).

In contrast to most oceanic settings, the intraplate and rift-related continental volcanism spreads over a larger compositional range for the most radiogenic samples (e.g.  $^{206}\text{Pb}/^{204}\text{Pb}_{60\text{Ma}} > 20.5$ ), but always include the HIMU composition (Fig. 8). The greater isotopic variation could reflect continental lithospheric interaction. The lavas with the most radiogenic Pb isotopic compositions (e.g.  $^{206}\text{Pb}/^{204}\text{Pb}_{60\text{Ma}} > 20.5$ ) from Chatham Island and Marie Byrd Land lie completely within the St. Helena compositional range in multi-isotope space (Fig. 8), demonstrating that the HIMU end member composition exists in continental settings (Hart et al., 1997; Panter et al., 2000; Panter et al., 2006).

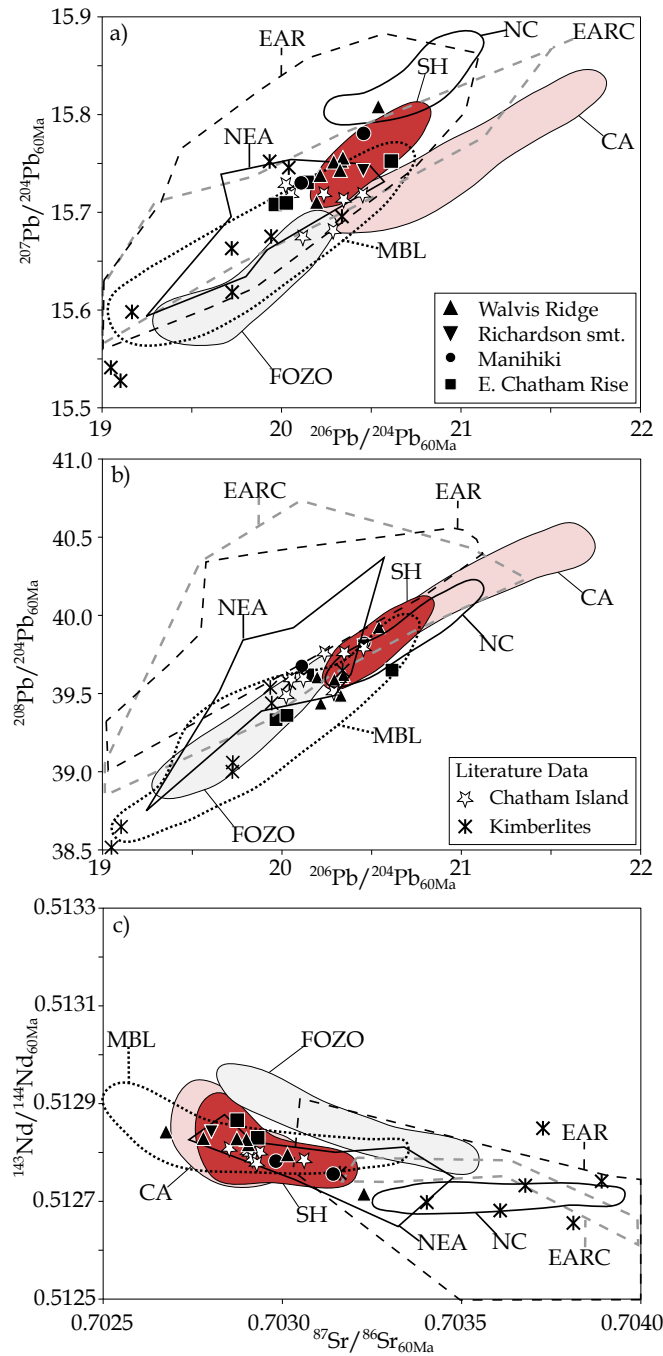


**Fig. 8: Continental HIMU locations on different isotope correlation diagrams. Note, some of the continental settings (e.g., EAR) have lower Nd and Sr isotope ratios than HIMU, possibly reflecting crustal assimilation/contamination. Due to incomplete Sr-Nd-Pb isotope data from the Namibian carbonatites, averaged Sr and Nd isotope ratios from samples from the same volcanic complex were used to estimate the range of the Pb-Nd and Pb-Sr isotope fields. Note, the Hf isotope plots are not shown in Figs. 7-8, since the data have only been published from Marie Byrd, Alphonse bank and the Group I Kimberlites. However, the Hf isotope data for these sample sites plot within the same range of St. Helena HIMU. Abbreviations: SH = St. Helena, CA = Cook-Austral islands (includes Mangaia, Tubuai and Old Rurutu volcanism), NC = Namibian carbonatites, EARC = East African Rift Carbonatites, MBL = Marie Byrd Land and seamounts, NEA = Northeast Africa and EAR = East African Rift silicates. The references for the respective sites are reported in Figs. 5-6.**

The East African Rift lavas (silicates and carbonatites) extend to more radiogenic  $^{207}\text{Pb}/^{204}\text{Pb}_{60\text{Ma}}$  and  $^{208}\text{Pb}/^{204}\text{Pb}_{60\text{Ma}}$  values, coupled with higher  $^{87}\text{Sr}/^{86}\text{Sr}_{60\text{Ma}}$  and lower  $^{143}\text{Nd}/^{144}\text{Nd}_{60\text{Ma}}$  ratios for a given  $^{206}\text{Pb}/^{204}\text{Pb}_{60\text{Ma}}$  value in relation to St. Helena (Fig. 8). Although, it has been proposed that the silicate lavas and carbonatites are derived from the same source (Nelson et al., 1988; Bell, 2001; Bell and Tilton, 2001), the silicate lavas, compared to the carbonatites, show a considerably larger range in isotopic composition (higher  $^{87}\text{Sr}/^{86}\text{Sr}_{60\text{Ma}}$ ,  $^{207}\text{Pb}/^{204}\text{Pb}_{60\text{Ma}}$  and  $^{208}\text{Pb}/^{204}\text{Pb}_{60\text{Ma}}$ , but lower  $^{143}\text{Nd}/^{144}\text{Nd}_{60\text{Ma}}$  ratios). This is consistent with greater amounts of crustal contamination affecting the silicate melts, which are generally hotter and have lower Sr, Nd and Pb concentrations than the carbonatitic lavas ( $\sim 1000$  ppm Sr on average in the silicate rocks compared to  $>5000$  ppm in carbonatites,  $\sim 80$  ppm Nd in silicates and up to 8000 ppm Nd in carbonatites, and  $\sim 8$  ppm Pb on average in silicates compared to 40 ppm in carbonatites) and thus are more susceptible to crustal contamination, whereas the high incompatible element concentrations in the carbonatites shield them from the effects of lithospheric interaction. Crustal contamination of the silicate melts is further supported by the inverse correlations of silica content with  $^{143}\text{Nd}/^{144}\text{Nd}$  and  $^{206}\text{Pb}/^{204}\text{Pb}$  and positive correlation with  $^{87}\text{Sr}/^{86}\text{Sr}$  isotope ratios for many of the silicate rocks suites (Fig. 8). The samples with the lowest silica contents have HIMU-like compositions ( $^{143}\text{Nd}/^{144}\text{Nd} \sim 0.5127$ ,  $^{206}\text{Pb}/^{204}\text{Pb} \sim 21$  and  $^{87}\text{Sr}/^{86}\text{Sr} \sim 0.7035$ ), overlapping with the field for St. Helena HIMU (Mana et al., 2012). Alternatively, some of the trends formed by the data from the different locations may reflect mixing trends with EM I, as proposed for the isotopic array of East African carbonatites (Bell and Tilton, 2001).



In summary, volcanism with HIMU incompatible-element and isotopic characteristics has been identified between  $\sim 40^{\circ}\text{N}$  and  $80^{\circ}\text{S}$  around the Earth, proving a near global distribution of HIMU (Fig. 6). Therefore, HIMU does not represent a rare, exotic composition, as previously proposed. Hart et al. (1986) proposed that intraplate volcanism in the Atlantic (St. Helena, New England Seamounts, Azores Islands and Walvis Ridge), Indian (Comoros Islands) and Pacific (Tubuaii, San Felix and San Ambrosio Islands) Oceans constitute a HIMU-EM I (or LoNd) mixing array and even Hawaiian and Samoan shield lavas show a trend towards a HIMU end member composition (e.g., Ren et al., 2009; Jackson et al., 2010; Jackson et al., 2014), which suggests that HIMU could be even more widespread in the sources of oceanic intraplate volcanism than just the end member localities noted above (Fig. 6).

## **6. Shallow or deep HIMU reservoir(s)?**

A fundamental question that needs to be addressed is the location of the HIMU reservoir(s) within the Earth. Considering the restricted incompatible-element composition and isotopic characteristics of HIMU lavas, they are likely to be genetically related and have evolved from sources with a reasonably uniform composition under similar conditions, over similar time periods (Stracke et al., 2003; Stracke et al., 2005; Hanyu et al., 2014; Kimura et al., 2016). The radiogenic Pb isotope ratios of HIMU require long-time isolation of 1-3.2 Ga (e.g. Tatsumoto, 1978; Zindler and Hart, 1986; Kawabata et al., 2011; Nebel et al., 2013; Hanyu et al., 2014; Castillo, 2015; Kimura et al., 2016). Fluid dynamic experiments and mantle convection models indicate that substantial mantle heterogeneities should be homogenized within less than 1 Ga in the convective mantle (e.g. Hoffman and McKenzie, 1985; Kellogg and Turcotte, 1990; Allègre et al., 1995; van Keken et al., 2002; Coltice and Schmalzl, 2006). Therefore, the

convective upper mantle and even most of the lower convective mantle, where mixing could be more sluggish and hampered by phase changes, cannot preserve large-scale heterogeneities over the age of the Earth (van Keken et al., 2002).

Two potential regions exist within Earth where end member HIMU could be isolated from the convecting mantle since the Archean to Early Proterozoic: 1) shallow subcontinental lithospheric mantle (SCLM) reservoir (e.g., Stein et al., 1997; Lucassen et al., 2008; Rooney et al., 2014), or 2) deep reservoir at the base of the lower mantle (e.g., Hofmann and White, 1982; Chauvel et al., 1992; Stracke et al., 2005; Hanyu et al., 2014; Weiss et al., 2016). Several lines of evidence favor derivation from a deep reservoir, as described below. To begin with, the two end member HIMU-type localities are part of age-progressive volcanic chains consistent with derivation from deep mantle plumes (e.g., Chaffey et al., 1989; Chauvel et al., 1992; O'Connor et al., 2012; Hanyu et al., 2014). A deep origin for these plumes is further supported by seismic tomography, which has imaged low seismic velocity anomalies beneath these hotspot tracks down to the lowermost mantle (e.g. Montelli et al., 2006; French and Romanowicz, 2015). Using geochemical and geophysical constraints, Jackson et al. (2018) argue that there is a strong association of the extreme HIMU signature ( $^{206}\text{Pb}/^{204}\text{Pb} > 20$ ) with deep-rooted mantle plumes.

The other oceanic HIMU settings can also be related to hotspot volcanism, e.g., the Walvis Ridge is related to the Tristan-Gough hotspot track (e.g., Richardson et al., 1982; Rohde et al., 2013b; Hoernle et al., 2015; O'Connor and Jokat, 2015a), the Richardson seamount to the Shona hotspot track (O'Connor et al., 2012; Hoernle et al., 2016) and the Marshall-Wake seamount group to the Austral-Cook hotspot system (Konter et al., 2008). The Ontong Java, Hikurangi and Manihiki plateaus are believed to have formed from a single massive upwelling from the lower mantle at  $\sim 120\text{-}125$  Ma (e.g., Taylor,

2006; Hoernle et al., 2010; Timm et al., 2011; Hochmuth et al., 2015; Golowin et al., 2017). Note that our selected samples from the Walvis Ridge, Richardson Seamount, Hikurangi Plateau and Manihiki Plateau all represent late-stage volcanism, and apart from the Manihiki Plateau (Timm et al., 2011; Golowin et al., 2017), the respective EM I-type basalments show no evidence of a HIMU signature. Therefore, it is unlikely that the late-stage Walvis, Shona and Hikurangi lavas are directly related to the mantle plumes forming the major morphological seafloor anomaly.

Carbonatites are commonly associated with mantle plumes (Nelson et al., 1988; Bell, 2001; Hoernle et al., 2002), e.g., East African Rift carbonatites and low-silica igneous rocks are related to the Afar mantle plume (Nelson et al., 1988; Bell, 2001; Bell and Tilton, 2001), whereas Canary and Cape Verde carbonatites are related to the mantle plumes forming the archipelagoes (Hoernle et al., 1991; Hoernle et al., 2002). In general, high pressure mineral phases in diamonds (e.g., Kaminsky, 2012) and primitive noble gas signatures (Sumino et al., 2006) point to a lower mantle origin for Group I kimberlites. Torsvik et al. (2010) calculated that the eruptive sites of ~80% (1112 out of 1395) of the kimberlite eruptions over the past 320 Ma lay close to the “plume generation zones” at the margins of the large low shear velocity provinces (LLSVPs) at the base of the lower mantle, and thus assume a similar source region for kimberlite magmas as postulated for mantle plumes. Experimental studies show that a continuous series from carbonatite to kimberlite and silica-undersaturated melts can be generated by increasing degrees of melting of carbonated peridotite (e.g., Dalton and Presnall, 1998; Moore and Wood, 1998; Gudfinnsson and Presnall, 2005; Dasgupta et al., 2007), indicating that they are also genetically related and may ultimately be derived from a common source (Nelson et al., 1988; Bell, 2001; Nowell et al., 2004).

It has been proposed that the HIMU signature at the Eastern Gondwana margin (EGM; including West Antarctica and Zealandia) was derived from continental lithosphere previously metasomatized by a plume with a HIMU composition that may have triggered the break-away of Zealandia from Antarctica (e.g. Weaver et al., 1994; Storey et al., 1999; Hoernle et al., 2010; Kipf et al., 2014).  $^{238}\text{U}/^{206}\text{Pb}$  and  $^{232}\text{Th}/^{208}\text{Pb}$  error chron ages for mantle xenoliths from various localities within Zealandia consistently indicate that this metasomatic event is young and occurred within the last ~120 Ma from melts that already carried a HIMU signature (McCoy-West et al., 2016). Tectonic reconstructions at 100 Ma show an elongate belt of volcanic rocks with HIMU-like Pb isotopic compositions at the boundary between parts of Zealandia and Marie Byrd Land (Finn et al., 2005), consistent with a HIMU plume initiating the break-up of Zealandia from West-Antarctica (Weaver et al., 1994; Hart et al., 1997; Storey et al., 1999; Panter et al., 2000; Panter et al., 2006; Hoernle et al., 2010; Kipf et al., 2014; McCoy-West et al., 2016). Likewise, Kipf et al. (2014) and Hart et al. (1997) proposed that the HIMU source beneath the Marie Byrd Seamounts and Marie Byrd Land represent fossilized HIMU mantle plume material preserved at the base of the western Antarctic lithosphere, which was melted by decompression caused by continental edge convection and extension related to the initiation of the West Antarctic rift system respectively.

In summary, most HIMU locations appear to be related to mantle plumes derived from the Pacific and African LLSVP's or their margins (e.g., Torsvik et al., 2006; Burke et al., 2008; Steinberger and Torsvik, 2012; French and Romanowicz, 2015). Therefore, the HIMU source material is also likely to derived from the LLSVP's or be stored as a layer on the LLSVPs.

## 7. HIMU reservoir formation in an Archean geodynamical context

### 7.1 Age of the HIMU reservoir formation

Now we will discuss the timing and mechanism of HIMU reservoir formation in the context to the geodynamic setting under which HIMU may have originated. Based on Pb model ages, the proposed HIMU reservoir formation ages range between 1 and 3.2 Ga (Tatsumoto, 1978; Hofmann, 1997; Stracke et al., 2005; Hanyu et al., 2011; Nebel et al., 2013; Castillo, 2015). Recently, Kimura et al. (2016) proposed a *minimum* reservoir formation age range for HIMU of 2.0-2.5 Ga by numerical simulation of the source evolution and mixing relationships of EM I and HIMU. Based on negative  $\Delta^{33}\text{S}$  ratios preserved in olivines from Cook-Austral HIMU lavas, Cabral et al. (2013) proposed that their source must be  $\geq 2.45$  Ga. As shown earlier (section 4.3; Fig. 5), the Atlantic HIMU end member has higher  $^{207}\text{Pb}/^{204}\text{Pb}$  ratios at a given  $^{206}\text{Pb}/^{204}\text{Pb}$  ratio compared to the Cook-Austral HIMU signature, which can be explained by an  $\sim 0.3$  Ga older age of the St. Helena HIMU source (Hanyu et al., 2014). Since our new data and almost all other HIMU localities from the literature overlap with St. Helena (excluding Marshall and Wake seamount groups, which overlap with Cook-Austral HIMU) in Pb isotope space (Fig. 8), most HIMU is likely to have formed at  $\geq 2.75$  Ga (Neoproterozoic) and possibly even in the Meso- to Paleoproterozoic (e.g., Nebel et al., 2013). Finally, Archean HIMU-like lavas have been found in western Australia and India, indicating that the HIMU source has existed at least since 2.7 Ga (Said and Kerrich (2010) Manikyamba and Kerrich (2011)).

In general, the composition of HIMU is directly related to mantle reservoirs that underwent temporal variations (e.g., isotopic composition of MORB or DM; Salters and Stracke, 2004; Stracke et al., 2005), and it has been proposed that the restricted geochemical signature of HIMU (compared to other end members) could reflect a short time interval for reservoir formation (Stracke et al., 2005; Willbold and Stracke, 2006;

Kimura et al., 2016). Interestingly, the assumed minimum age of St. Helena HIMU coincides with the peak of episodic continental crust growth at  $\sim 2.7$  Ga (e.g. McCulloch and Bennett, 1994; Stein and Hofmann, 1994; Condie, 2000; Rino et al., 2004; O'Neill et al., 2007). High continental crustal growth rates are associated with massive crustal production, as well as with increased recycling rates (Condie, 2000). During such an event a widespread HIMU reservoir(s) could have formed within a discrete age interval. Alternatively, the proposed HIMU reservoir formation ages could reflect the average age of accumulated packages of recycled material (Hanyu et al., 2014). This implies that the mechanism (recycling style) of the formation of the HIMU reservoir must have been stable over a certain time interval in the Neo- to Paleoproterozoic.

## *7.2 The style of Archean tectonics*

Now we will discuss the geodynamic setting for an Archean HIMU reservoir formation age. In general, the tectonic style of the Archean earth and thus the recycling mechanism remains a matter of considerable controversy (Foley et al., 2003; Bédard, 2006; Van Kranendonk, 2010; Gerya, 2014; Harris and Bédard, 2014; Moyen and Laurent, 2018), but it has been suggested that the Early Archean Earth and its tectonic style were comparable to present-day plume-lid tectonics on Venus. Plume-lid tectonics is mainly driven by mantle up- and down-wellings (e.g., Van Kranendonk, 2010; Gerya, 2014; Harris and Bédard, 2014; Gerya et al., 2015).

How modern-style plate tectonics (defined by self-induced plate movement with passive mantle up-wellings beneath mid-ocean ridges and “stable” subduction zones, where the slabs sink deep into the mantle) initiated is still a matter of debate, but the global geodynamic regime most likely evolved gradually from plume-lid tectonics into modern-style subduction between 3.2 - 2.5 Ga (e.g., Condie and Kröner, 2008; Shirey and

Richardson, 2011; Gerya, 2014; Moyen and Laurent, 2018). The driving recycling mechanism in the overall hotter mantle with Venus-like active-stagnant-lid regime was dominated by drip tectonics (lithospheric delamination), whereas subduction was a subordinate process (Bédard, 2006; Condie and Kröner, 2008; Gerya, 2014; Herzberg, 2014; Johnson et al., 2014). During the transition from plume-lid to modern-style tectonics, subduction was most likely flat and unstable (subducting crust was hotter and subduction angles were flatter; e.g., Karsten et al., 1996), with slab break-off being more frequent compared to present day subduction (e.g., Gerya, 2014; Bédard, 2018; Moyen and Laurent, 2018).

In summary, based on the age constraints described above (section 7.1), the minimum St. Helena HIMU reservoir formation age is likely to be  $\sim 2.75$  Ga, but Meso- to Paleoarchean reservoir formation ages are also possible (Nebel et al., 2013). Therefore, it seems unlikely that the classic end member HIMU reservoir formed as a result of modern-style tectonics. Below we discuss the possibility of classic HIMU forming in an Archean geodynamic context.

### *7.3 An alternative model for the HIMU reservoir formation in the Archean tectonic system*

In the following section, we describe a concept for the generation of a widespread HIMU reservoir(s) in an Archean geodynamic setting before modern-style tectonics became established and formed the dominant recycling mechanism. Several observations are inconsistent with the formation of reference HIMU through recycling of ocean crust: 1) major element and melt inclusion evidence that peridotite rather than eclogite/pyroxenite represents the dominant source lithology, 2) the isotopic composition of HIMU does not lie on the extension of the MORB array, precluding a simple link between MORB and reference HIMU, and 3) in the Archean (at  $>2.45$  Ga) drip tectonics

(lithospheric delamination) rather than modern-day tectonics (with the deep subduction of oceanic lithosphere) was the dominant tectonic style. Therefore, oceanic lithosphere recycled through the lower mantle is unlikely to have generated a widespread Archean HIMU reservoir(s). Therefore, we favor an alternative model, which invokes shallow subduction and carbonatitic metasomatism of SCLM followed by delamination of the metasomatized SCLM into the lower mantle, similar to the model of Weiss et al. (2016).

**Table 2: Estimates of the dehydration of subducted oceanic crust and metasomatized SCLM**

<b>Bulk ocean crust (ppm)</b>	<b>Rb</b>	<b>Sr</b>	<b>Sm</b>	<b>Nd</b>	<b>Lu</b>	<b>Hf</b>	<b>U</b>	<b>Pb</b>
	2.99	136	3.11	9.55	0.45	2.28	0.115	0.48
<b>Mobility (%)</b>	0.630	0.410	0.140	0.310	0.010	0.220	0.290	0.850
<b>Ca-rich sediment (ppm)</b>	14.45	955	3.30	14.37	0.326	1.25	1.45	11.68
<b>Mobility Melt-Sed. (%)</b>	0.340	0.460	0.200	0.210	0.200	0.450	0.310	0.130
<b>Total release (ppm)</b>	6.80	495	1.10	5.98	0.070	1.07	0.483	1.93
<b>DM (ppm)</b>	0.088	9.800	0.270	0.713	0.063	0.199	0.005	0.023
	<b>Rb/Sr</b>		<b>Sm/Nd</b>		<b>Lu/Hf</b>		<b>U/Pb</b>	
<b>% of metasomatism</b>	1%	5%	1%	5%	1%	5%	1%	5%
<b>Metasomatized SCLM (ppm)</b>	0.011	0.012	0.363	0.319	0.304	0.261	0.225	0.242
	<b>Rb/Sr</b>		<b>Sm/Nd</b>		<b>Lu/Hf</b>		<b>U/Pb</b>	
<b>HIMU reservoir formation Age</b>	min.	max.	min.	max.	min.	max.	min.	max.
<b>2.5 - 3.5 Ga (ppm)</b>	0.009	0.020	0.339	0.364	0.237	0.265	0.168	0.256

Composition of bulk oceanic crust taken from Stracke et al. (2003); mobility estimates of ocean crust dehydration are taken from Kogiso et al. (1997a); Ca-rich sediment composition is the average composition of Ca-rich sediments from Plank and Langmuir (1998); mobility estimates for melt sediment exchange at 900°C are derived according to the parameters given by Johnson and Plank (2000); DM composition after Salters and Stracke (2004), the required Rb/Sr, Sm/Nd, Lu/Hf and U/Pb ratios to produce HIMU within 2.5-3.5 Ga were calculated using the model of Stracke et al. (2003) with a HIMU compositional range of:  $^{87}\text{Sr}/^{86}\text{Sr} = 0.7027\text{-}0.7033$ ,  $^{143}\text{Nd}/^{144}\text{Nd} = 0.5128\text{-}0.5130$ ,  $^{176}\text{Hf}/^{177}\text{Hf} = 0.2828\text{-}0.2830$ ,  $^{206}\text{Pb}/^{204}\text{Pb} = 20 - 22$



The marine carbonate recycling hypothesis of Castillo (2015) invokes the recycling of Archean marine carbonates (a few %) and mixing with a depleted mantle component (oceanic lithospheric mantle) involving recycling of ocean lithosphere in the context of modern-style tectonics. Based on high U/Pb ratios (and thus high  $\mu$  values of > 30 values), relatively low  $K$  ( $^{232}\text{Th}/^{238}\text{U}$ ) and low Rb/Sr ratios ( $\sim 0.005$ ) in marine carbonates, Castillo (2015) showed that a mixture of Archean marine carbonates and depleted (oceanic lithospheric) mantle could evolve the characteristic  $^{206}\text{Pb}/^{204}\text{Pb}$ ,  $^{207}\text{Pb}/^{204}\text{Pb}$ ,  $^{208}\text{Pb}/^{204}\text{Pb}$  and  $^{87}\text{Sr}/^{86}\text{Sr}$  ratios of HIMU in  $\geq 2.5$  Ga, whereas the ancient depleted component controls the radiogenic  $^{143}\text{Nd}/^{144}\text{Nd}$  and  $^{177}\text{Hf}/^{176}\text{Hf}$  isotope ratios.

Finding low Ni contents and high Mn/Fe and Ca/Al ratios in olivines from HIMU lavas, Weiss et al. (2016) argued that Early Proterozoic/Archean subducting slabs released fluids/melts with carbonatitic affinity that metasomatized the overlying melt-depleted peridotitic SCLM. A role for carbonatitic metasomatism is also supported by high CaO contents and carbonate-rich inclusions in HIMU olivine phenocrysts (Saal et al., 1998; Weiss et al., 2011; Weiss et al., 2016). Under this scenario, the incompatible-element signature of Archean marine carbonates (high U/Pb and low Th/U and Rb/Sr ratios) is imprinted on the depleted SCLM. As mentioned above (section 4.2), such a source can produce HIMU-like incompatible-element patterns at low degrees of melting (Weiss et al., 2016). In order to calculate the composition of fluids generated through the dehydration of subducting oceanic crust and carbonate-rich marine sediments (with a composition after Plank and Langmuir, 1998), we used the model of Stracke et al. (2003). Mixing this metasomatic agent with 95-99% DM (Salters and Stracke, 2004) forms parent-daughter ratios that can generate HIMU isotopic compositions within 2.5-3.5 Ga (Table 2).

As mentioned above, a carbonated peridotite or hybrid (peridotite + eclogite/pyroxenite) source lithology is required to account for the major element systematics observed in HIMU lavas. Hanyu et al. (2011) proposed that the Re-Os systematics of HIMU lavas provide a timing of the peridotite + carbonated eclogite/pyroxenite connection. Radiogenic  $^{187}\text{Os}/^{188}\text{Os}$  ratios are derived from a source with high time-integrated Re/Os ratios, reflecting an ancient crustal source. HIMU lavas have radiogenic  $^{187}\text{Os}/^{188}\text{Os}$  ratios (0.14-15), irrespective of the Pb and Hf isotope ratios (e.g., Schiano et al., 2001; Hanyu et al., 2011). These ratios show that mixing of pure recycled and long-term isolated oceanic crust within the mantle cannot reproduce the observed Os-Pb-Hf systematics. An early (before formation of the HIMU reservoir) and significant elevation of the Os concentration is required to lower the HIMU reservoir  $^{187}\text{Os}/^{188}\text{Os}$  ratios to the presently observed values. Hanyu et al. (2011) propose that partial melts from recycled oceanic crust react with mantle material (with high Os concentrations) before the HIMU source was isolated, which is in agreement with the proposed carbonatitic metasomatism model of Weiss et al. (2016).

This model is also in accordance with the Archean geodynamic regime, i.e. plume-lid tectonics, where only small amounts of oceanic crust would be subducted to shallow mantle depths before subduction ceased and shifted to another location (Jacob and Foley, 1999; Foley et al., 2003). Accordingly, this would result in the formation of more widespread metasomatized SCLM, in contrast to modern-style tectonics where subduction zones are more stable and thus stationary over long periods of time (up to several hundred million years), and are also steeper and thus more locally focused. It has been suggested that metasomatism contributes to the destabilization, i.e. detachment/delamination of SCLM, into the mantle compared to unmetasomatized SCLM (e.g., Foley et al., 2003; Lee, 2006; Krystopowicz and Currie, 2013). Finally,

carbonate supersaturation of Archean seawater and precipitation of Ca-rich phases on the seafloor, as well as accompanying reactions with the oceanic crust (Sumner and Grotzinger, 1996; Higgins et al., 2009), could account for enhanced carbonation of the “oceanic crust”. Enhanced carbonation of the seafloor could result in predominantly carbonatitic metasomatism of the overlying lithosphere during relatively flat subduction.

Destabilization resulting in detachment/delamination of carbonatite-metasomatized SCLM in the Archean before or during the transition from plume-lid to modern-style tectonics could be a suitable process for transferring geochemically enriched SCLM to the base of the lower mantle (Fig 9). Detachment/delamination is also likely to have increased during major intervals of crustal growth, such as at ~2.75 Ga (e.g., Hofmann et al., 1986; Condie, 2000). Storage for  $\geq 2.5$  Ga before recycling to the surface by mantle plumes could allow such metasomatized material to develop a HIMU composition. One major advantage of this hypothesis, in contrast to the ocean-crust recycling model, is that the HIMU reservoir is not strictly limited to the lowermost mantle (Fig. 9). Smaller batches of carbonate-metasomatized SCLM could continue to reside beneath Archean Cratons where they can contribute to shallow, rift-related melting or be delaminated during younger continental breakup events and recycled through the shallow (e.g., Hanan et al., 2004; Kipf et al., 2014; Hoernle et al., 2016), and/or deep mantle. Therefore not all HIMU has to be associated with deep mantle plumes, although much of it appears to be.

Most OIBs and MORBs with HIMU-like characteristics require a mixing end member with radiogenic Pb isotopic composition that is distinct from the classic HIMU end member (Stracke et al., 2005), characterized by more radiogenic  $^{87}\text{Sr}/^{86}\text{Sr}$  and  $^{208}\text{Pb}/^{204}\text{Pb}$  at a given  $^{206}\text{Pb}/^{204}\text{Pb}$  isotope ratio (FOZO end member). The formation of

FOZO (also termed “Young HIMU”; Thirlwall, 1997) is usually explained by a similar mechanism, but with overall younger formation ages compared to HIMU (e.g., Thirlwall, 1997; Stracke et al., 2005; Castillo, 2015). In contrast to HIMU, FOZO lies at the enriched end on the MORB array in multi-isotope space (Fig. 5; Stracke et al., 2005; Castillo, 2015), which suggests a close genetic relationship between FOZO and MORB. Since modern-style tectonics is likely to have been established since the Archean to Proterozoic transition, recycling of oceanic crust/lithosphere could be a potential source of FOZO (e.g., Hanan and Graham, 1996; Stracke et al., 2003; Stracke et al., 2005; Kimura et al., 2016).

In contrast to HIMU, which always has low  $^3\text{He}/^4\text{He}$  ratios (lower than MORB; e.g., Kurz et al., 1982; Graham et al., 1992), some lavas with FOZO type (HIMU-like) composition have high  $^3\text{He}/^4\text{He}$  ratios. Since the  $^3\text{He}/^4\text{He}$  ratio of the depleted mantle may have decreased over time (Class and Goldstein, 2005; Jackson et al., 2008), high  $^3\text{He}/^4\text{He}$  ratios ( $> 9 R/R_a$ ) in some FOZO-like lavas could reflect ancient oceanic lithosphere, which became a closed system due to phase transformation (cf., Jackson et al., 2008; Castillo, 2015). In contrast, FOZO-like lavas with lower  $^3\text{He}/^4\text{He}$  ratios could be derived from younger recycled oceanic lithosphere and/or sources with higher U and Th concentrations that would produce greater amounts of radiogenic  $^4\text{He}$ . Therefore, the HIMU and FOZO (HIMU-like) end members are likely to be derived from different sources over different lengths of time. The change from Archean style drip tectonics, associated with carbonatitic metasomatism of SCLM, to modern style tectonics, in which ocean lithosphere is recycled through subduction and mantle plumes, is a possible mechanism that can explain the distinct isotope ratios of HIMU and FOZO.

In summary, we propose that the classic HIMU end member is derived from carbonate metasomatized SCLM that is recycled through the lower mantle via detachment/delamination and returned to the surface via mantle plumes during plume-lid tectonics taking place in the Archean. During modern-style subduction in the Proterozoic, HIMU-like (or FOZO type) ocean island basalts are formed through the recycling of ocean crust through the lower mantle.

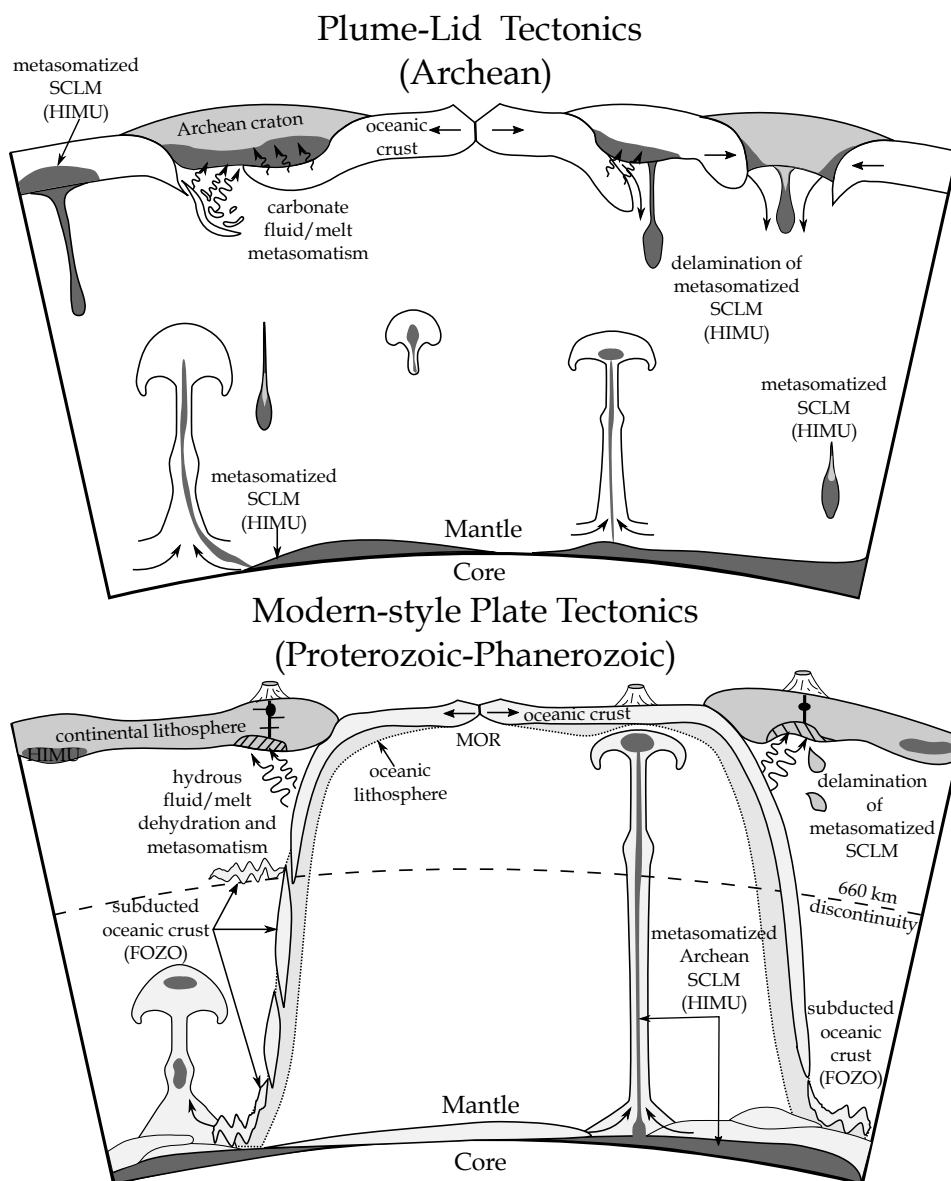


**Fig. 9: Schematic models for the formation of the HIMU and FOZO end member reservoirs in the mantle. A) In the Archean, flat subduction was an integral part of plume-lid tectonics. Decarbonation of the shallowly subducting oceanic lithosphere caused metasomatism of the subcontinental lithospheric mantle (SCLM) by carbonate-rich fluids/melts, which also destabilized the SCLM. Drip tectonics and subduction suction resulted in detachment/delamination of the SCLM to the base of the mantle. The carbonate-metasomatized SCLM had high U/Pb and low Th/U and Rb/Sr ratios that over time generated end member HIMU isotopic composition. B) Beginning roughly at the Archean-Proterozoic boundary, modern-style tectonics led to the subduction of oceanic lithosphere to the base of the lower mantle. The hydrothermally altered (shortly after formation at a mid-ocean ridge) and subsequently dehydrated (during shallow subduction) ocean crust had high U/Pb and slightly higher Th/U and Rb/Sr than the carbonate-metasomatized SCLM that generated HIMU. Over time the subducted crust stored at a thermal boundary layer such as the core-boundary and possibly upper-lower mantle boundary generated HIMU-like (FOZO) type compositions. Mantle plumes sample the delaminated Archean HIMU and the subducted ocean crust (FOZO) stored at the base of the lower mantle.**

## **8. Conclusions**

This study evaluates the distribution and origin of the HIMU end member. Our new data from late-stage volcanic edifices on the Walvis Ridge and Richardson Seamount in the South Atlantic Ocean and from the Eastern Chatham Rise and Manihiki Plateau in the Western Pacific Ocean, combined with a literature data survey, show that the HIMU end member is likely to be globally distributed and present in oceanic and continental intraplate and rift-type settings. Rock types with HIMU compositions include carbonatites, Group I kimberlites and silica-undersaturated lavas (e.g., melilitites, nephelinites and basanites and related differentiated rocks), which generally represent low-volume melts. Most HIMU end member volcanism is apparently related to deep-seated mantle plumes, as indicated by seismic tomography at HIMU-type localities. The HIMU reservoir primarily formed in the Archean ( $\geq 2.5$  Ga), which was dominated by drip tectonics (lithospheric detachment/delamination). Subduction of oceanic lithosphere was a subordinate process and only occurred to shallow depths. Drip tectonics provides a mechanism for transferring carbonate-metasomatized SCLM (Weiss

et al. (2016) into the lower mantle. During the Proterozoic-Phanerozoic, modern-style plate tectonics dominated, characterized by dehydration of subducted crust at shallow depths and subsequent recycling of oceanic lithosphere through the lower mantle. Hydrothermal alteration of the ocean crust shortly after formation and dehydration during shallow subduction gives the ocean crust the appropriate composition to evolve HIMU-like (FOZO-type) compositions, which lie on an extension of the MORB array. Therefore our model invokes a different origin for the HIMU (through carbonate metasomatism and detachment/delamination of SCLM during Archean plume-lid tectonics) and FOZO (Proterozoic and later recycling of ocean crust during modern-style tectonics) mantle end members. Small portions of HIMU material could still be stored in the SCLM and thus melting of Archean lithospheric mantle remaining in the lithosphere could also contribute to forming HIMU, i.e. it does not have to be derived from lower mantle plumes.

## **9. Acknowledgments**

We thank the captains and crews of 1) the R/V SONNE for their support during cruises SO168-Zealandia, SO193-Manihiki and SO233-Walvis II, and 2) the R/V Maria S. Merian for their support during MSM19/3. S. Hauff, K. Junge, A. Schwindrofska, J. Sticklus, J. Rohde and U. Westernströer are gratefully acknowledged for analytical support; M. Anders for help with sample preparation; and C. Devey for providing sample SO84 86DS-1a from cruise SO84. We further thank J. D. Greenough and an anonymous reviewer for constructive comments that helped improve this manuscript. This study and SH's doctoral position were funded by the German Ministry for Research and Education (BMBF; grants SO233-Walvis II to KH and FH).

## **10. Funding**

This work was funded by German Ministry for Research and Education (BMBF, grants SO168-Zealandia, SO193-Manihiki and SO233-Walvis II), German Research Association (DFG, grant MSM19/3); and the GEOMAR Helmholtz Center for Ocean Research Kiel.

## **11. Declaration of interest**

Conflict of interest: None



## References

- Allègre, C. J., Moreira, M., and Staudacher, T., 1995,  $4\text{He}/^3\text{He}$  dispersion and mantle convection: *Geophysical Research Letters*, v. 22, no. 17, p. 2325-2328.
- Baksi, A. K., 2007, A quantitative tool for detecting alteration in undisturbed rocks and minerals—I: Water, chemical weathering, and atmospheric argon: *Geological Society of America Special Papers*, v. 430, p. 285-303.
- Bédard, J. H., 2006, A catalytic delamination-driven model for coupled genesis of Archaean crust and sub-continental lithospheric mantle: *Geochimica et Cosmochimica Acta*, v. 70, no. 5, p. 1188-1214.
- , 2018, Stagnant lids and mantle overturns: Implications for Archaean tectonics, magmagenesis, crustal growth, mantle evolution, and the start of plate tectonics: *Geoscience Frontiers*, v. 9, no. 1, p. 19-49.
- Beiersdorf, H., Bach, W., Duncan, R., Erzinger, J., and Weiss, W., 1995, New evidence for the production of EM-type ocean island basalts and large volumes of volcanoclastites during the early history of the Manihiki Plateau: *Marine Geology*, v. 122, no. 3, p. 181-205.
- Bell, K., 2001, Carbonatites: relationships to mantle-plume activity: *SPECIAL PAPERS-GEOLOGICAL SOCIETY OF AMERICA*, p. 267-290.
- Bell, K., and Tilton, G. R., 2001, Nd, Pb and Sr Isotopic Compositions of East African Carbonatites: Evidence for Mantle Mixing and Plume Inhomogeneity: *Journal of Petrology*, v. 42, no. 10, p. 1927-1945.
- Bradshaw, J. D., 1989, Cretaceous geotectonic patterns in the New Zealand Region: *Tectonics*, v. 8, no. 4, p. 803-820.
- Burke, K., Steinberger, B., Torsvik, T. H., and Smethurst, M. A., 2008, Plume Generation Zones at the margins of Large Low Shear Velocity Provinces on the core-mantle boundary: *Earth and Planetary Science Letters*, v. 265, no. 1-2, p. 49-60.
- Cabral, R. A., Jackson, M. G., Rose-Koga, E. F., Koga, K. T., Whitehouse, M. J., Antonelli, M. A., Farquhar, J., Day, J. M. D., and Hauri, E. H., 2013, Anomalous sulphur isotopes in plume lavas reveal deep mantle storage of Archaean crust: *Nature*, v. 496, no. 7446, p. 490-493.
- Castillo, P. R., 2015, The recycling of marine carbonates and sources of HIMU and FOZO ocean island basalts: *Lithos*, v. 216-217, p. 254-263.
- Castillo, P. R., Lonsdale, P. F., Moran, C. L., and Hawkins, J. W., 2009, Geochemistry of mid-Cretaceous Pacific crust being subducted along the Tonga-Kermadec Trench: Implications for the generation of arc lavas: *Lithos*, v. 112, no. 1-2, p. 87-102.
- Chaffey, D. J., Cliff, R. A., and Wilson, B. M., 1989, Characterization of the St. Helena magma source: *Magmatism in the Ocean Basins*, v. 42, p. 19.
- Chandler, M. T., Wessel, P., and Taylor, B., 2015, Tectonic reconstructions in magnetic quiet zones: Insights from the Greater Ontong Java Plateau: *Geological Society of America Special Papers*, v. 511, p. 185-193.
- Chauvel, C., Hofmann, A. W., and Vidal, P., 1992, HIMU-EM : The French-Polynesian Connection: *Earth and Planetary Science Letters*, v. 110, no. 1-4, p. 99-119.
- Chauvel, C., McDonough, W., Guille, G., Maury, R., and Duncan, R., 1997, Contrasting old and young volcanism in Rurutu Island, Austral chain: *Chemical Geology*, v. 139, no. 1-4, p. 125-143.
- Class, C., and Goldstein, S. L., 2005, Evolution of helium isotopes in the Earth's mantle: *Nature*, v. 436, p. 1107.
- Collerson, K. D., Williams, Q., Ewart, A. E., and Murphy, D. T., 2010, Origin of HIMU and EM-1 domains sampled by ocean island basalts, kimberlites and carbonatites: The role of CO<sub>2</sub>-fluxed lower mantle melting in thermochemical upwellings: *Physics of the Earth and Planetary Interiors*, v. 181, no. 3-4, p. 112-131.
- Coltice, N., and Schmalzl, J., 2006, Mixing times in the mantle of the early Earth derived from 2-D and 3-D numerical simulations of convection: *Geophysical Research Letters*, v. 33, no. 23, p. n/a-n/a.
- Condie, K. C., 2000, Episodic continental growth models: afterthoughts and extensions: *Tectonophysics*, v. 322, no. 1-2, p. 153-162.
- Condie, K. C., and Kröner, A., 2008, When did plate tectonics begin? Evidence from the geologic record: *Geological Society of America Special Papers*, v. 440, p. 281-294.
- Cooper, A. F., and Reid, D. L., 1998, Nepheline Sövites as Parental Magmas in Carbonatite Complexes: Evidence from Dicker Willem, Southwest Namibia: *Journal of Petrology*, v. 39, no. 11-12, p. 2123-2136.
- Cooper, A. F., and Reid, D. L., 2000, The association of potassic trachytes and carbonatites at the Dicker Willem Complex, southwest Namibia: coexisting, immiscible, but not cogenetic magmas: *Contributions to Mineralogy and Petrology*, v. 139, no. 5, p. 570-583.

- Dalton, J. A., and Presnall, D. C., 1998, The Continuum of Primary Carbonatitic–Kimberlitic Melt Compositions in Equilibrium with Lherzolite: Data from the System CaO–MgO–Al<sub>2</sub>O<sub>3</sub>–SiO<sub>2</sub>–CO<sub>2</sub> at 6 GPa: *Journal of Petrology*, v. 39, no. 11-12, p. 1953-1964.
- Dasgupta, R., Hirschmann, M. M., and Smith, N. D., 2007, Partial Melting Experiments of Peridotite + CO<sub>2</sub> at 3 GPa and Genesis of Alkalic Ocean Island Basalts: *Journal of Petrology*, v. 48, no. 11, p. 2093-2124.
- Dasgupta, R., Jackson, M. G., and Lee, C.-T. A., 2010, Major element chemistry of ocean island basalts — Conditions of mantle melting and heterogeneity of mantle source: *Earth and Planetary Science Letters*, v. 289, no. 3–4, p. 377-392.
- Davy, B., Hoernle, K., and Werner, R., 2008, Hikurangi Plateau: Crustal structure, rifted formation, and Gondwana subduction history: *Geochemistry, Geophysics, Geosystems*, v. 9, no. 7, p. Q07004.
- Dupuy, C., Barszczus, H. G., Dostal, J., Vidal, P., and Liotard, J. M., 1989, Subducted and recycled lithosphere as the mantle source of ocean island basalts from southern Polynesia, central Pacific: *Chemical Geology*, v. 77, no. 1, p. 1-18.
- Finn, C. A., Müller, R. D., and Panter, K. S., 2005, A Cenozoic diffuse alkaline magmatic province (DAMP) in the southwest Pacific without rift or plume origin: *Geochemistry, Geophysics, Geosystems*, v. 6, no. 2, p. Q02005.
- Foley, S. F., Buhre, S., and Jacob, D. E., 2003, Evolution of the Archaean crust by delamination and shallow subduction: *Nature*, v. 421, no. 6920, p. 249-252.
- French, S. W., and Romanowicz, B., 2015, Broad plumes rooted at the base of the Earth's mantle beneath major hotspots: *Nature*, v. 525, no. 7567, p. 95-99.
- Furman, T., Kaleta, K. M., Bryce, J. G., and Hanan, B. B., 2006, Tertiary Mafic Lavas of Turkana, Kenya: Constraints on East African Plume Structure and the Occurrence of High- $\mu$  Volcanism in Africa: *Journal of Petrology*, v. 47, no. 6, p. 1221-1244.
- Gerbode, C., and Dasgupta, R., 2010, Carbonate-fluxed Melting of MORB-like Pyroxenite at 2.9 GPa and Genesis of HIMU Ocean Island Basalts: *Journal of Petrology*, v. 51, no. 10, p. 2067-2088.
- Gerya, T., 2014, Precambrian geodynamics: Concepts and models: *Gondwana Research*, v. 25, no. 2, p. 442-463.
- Gerya, T. V., Stern, R. J., Baes, M., Sobolev, S. V., and Whattam, S. A., 2015, Plate tectonics on the Earth triggered by plume-induced subduction initiation: *Nature*, v. 527, no. 7577, p. 221-225.
- Golowin, R., Portnyagin, M., Hoernle, K., Hauff, F., Gurenko, A., Garbe-Schönberg, D., Werner, R., and Turner, S., 2017, Boninite-like intraplate magmas from Manihiki Plateau require ultra-depleted and enriched source components: *Nature Communications*, v. 8, p. 14322.
- Graham, D. W., Humphris, S. E., Jenkins, W. J., and Kurz, M. D., 1992, Helium isotope geochemistry of some volcanic rocks from Saint Helena: *Earth and Planetary Science Letters*, v. 110, no. 1, p. 121-131.
- Grégoire, M., Bell, D. R., and Le Roex, A. P., 2003, Garnet Lherzolites from the Kaapvaal Craton (South Africa): Trace Element Evidence for a Metasomatic History: *Journal of Petrology*, v. 44, no. 4, p. 629-657.
- Gudfinnsson, G. H., and Presnall, D. C., 2005, Continuous gradations among primary carbonatitic, kimberlitic, melilititic, basaltic, picritic, and komatiitic melts in equilibrium with garnet lherzolite at 3–8 GPa: *Journal of Petrology*, v. 46, no. 8, p. 1645-1660.
- Hanan, B. B., Blichert-Toft, J., Pyle, D. G., and Christie, D. M., 2004, Contrasting origins of the upper mantle revealed by hafnium and lead isotopes from the Southeast Indian Ridge: *Nature*, v. 432, no. 7013, p. 91-94.
- Hanan, B. B., and Graham, D. W., 1996, Lead and Helium Isotope Evidence from Oceanic Basalts for a Common Deep Source of Mantle Plumes: *Science*, v. 272, no. 5264, p. 991-995.
- Hanyu, T., Dosso, L., Ishizuka, O., Tani, K., Hanan, B. B., Adam, C., Nakai, S. i., Senda, R., Chang, Q., and Tatsumi, Y., 2013, Geochemical diversity in submarine HIMU basalts from Austral Islands, French Polynesia: *Contributions to Mineralogy and Petrology*, v. 166, no. 5, p. 1285-1304.
- Hanyu, T., Kawabata, H., Tatsumi, Y., Kimura, J.-I., Hyodo, H., Sato, K., Miyazaki, T., Chang, Q., Hirahara, Y., Takahashi, T., Senda, R., and Nakai, S. i., 2014, Isotope evolution in the HIMU reservoir beneath St. Helena: Implications for the mantle recycling of U and Th: *Geochimica et Cosmochimica Acta*, v. 143, p. 232-252.
- Hanyu, T., Tatsumi, Y., Senda, R., Miyazaki, T., Chang, Q., Hirahara, Y., Takahashi, T., Kawabata, H., Suzuki, K., Kimura, J. I., and Nakai, S., 2011, Geochemical characteristics and origin of the HIMU reservoir: A possible mantle plume source in the lower mantle: *Geochemistry Geophysics Geosystems*, v. 12.
- Harris, L. B., and Bédard, J. H., 2014, Crustal Evolution and Deformation in a Non-Plate-Tectonic Archaean Earth: Comparisons with Venus, *in* Dilek, Y., and Furnes, H., eds., *Evolution of Archean Crust and Early Life*: Dordrecht, Springer Netherlands, p. 215-291.

- Hart, S. R., 1984, A large-scale isotope anomaly in the Southern Hemisphere mantle: *Nature*, v. 309, no. 5971, p. 753-757.
- Hart, S. R., Blusztajn, J., LeMasurier, W. E., and Rex, D. C., 1997, Hobbs Coast Cenozoic volcanism: Implications for the West Antarctic rift system: *Chemical Geology*, v. 139, no. 1-4, p. 223-248.
- Hart, S. R., Gerlach, D. C., and White, W. M., 1986, A Possible New Sr-Nd-Pb Mantle Array and Consequences for Mantle Mixing: *Geochimica Et Cosmochimica Acta*, v. 50, no. 7, p. 1551-1557.
- Hart, S. R., Hauri, E. H., Oschmann, L. A., and Whitehead, J. A., 1992, Mantle Plumes and Entrainment: Isotopic Evidence: *Science*, v. 256, no. 5056, p. 517-520.
- Herzberg, C., 2014, Early Earth: Archaean drips: *Nature Geosci*, v. 7, no. 1, p. 7-8.
- Herzberg, C., Cabral, R. A., Jackson, M. G., Vidito, C., Day, J. M. D., and Hauri, E. H., 2014, Phantom Archean crust in Mangaia hotspot lavas and the meaning of heterogeneous mantle: *Earth and Planetary Science Letters*, v. 396, p. 97-106.
- Higgins, J. A., Fischer, W. W., and Schrag, D. P., 2009, Oxygenation of the ocean and sediments: Consequences for the seafloor carbonate factory: *Earth and Planetary Science Letters*, v. 284, no. 1-2, p. 25-33.
- Hochmuth, K., Gohl, K., and Uenzelmann-Neben, G., 2015, Playing jigsaw with Large Igneous Provinces—A plate tectonic reconstruction of Ontong Java Nui, West Pacific: *Geochemistry, Geophysics, Geosystems*, v. 16, no. 11, p. 3789-3807.
- Hoernle, K., Hauff, F., van den Bogaard, P., Werner, R., Mortimer, N., Geldmacher, J., Garbe-Schönberg, D., and Davy, B., 2010, Age and geochemistry of volcanic rocks from the Hikurangi and Manihiki oceanic Plateaus: *Geochimica et Cosmochimica Acta*, v. 74, no. 24, p. 7196-7219.
- Hoernle, K., Mortimer, N., Werner, R., and Hauff, F., 2003, FS/RV SONNE Fahrtbericht SO 168= Cruise report SO168, ZEALANDIA: Causes and Effects of Plume and Rift-Related Cretaceous and Cenozoic Volcanism on Zealandia; Wellington-Sydney-Lyttleton/Christchurch; December 03, 2002-January 16, 2003;[BMBF contract No. 03G0168A].
- Hoernle, K., Rohde, J., Hauff, F., Garbe-Schonberg, D., Homrighausen, S., Werner, R., and Morgan, J. P., 2015, How and when plume zonation appeared during the 132 Myr evolution of the Tristan Hotspot: *Nature Communication*, v. 6, p. 10.1038/ncomms8799.
- Hoernle, K., Schwindrofska, A., Werner, R., van den Bogaard, P., Hauff, F., Uenzelmann-Neben, G., and Garbe-Schönberg, D., 2016, Tectonic dissection and displacement of parts of Shona hotspot volcano 3500 km along the Agulhas-Falkland Fracture Zone: *Geology*, v. 44, no. 4, p. 263-266.
- Hoernle, K., Tilton, G., Le Bas, M. J., Duggen, S., and Garbe-Schönberg, D., 2002, Geochemistry of oceanic carbonatites compared with continental carbonatites: mantle recycling of oceanic crustal carbonate: *Contributions to Mineralogy and Petrology*, v. 142, no. 5, p. 520-542.
- Hoernle, K., Tilton, G., and Schmincke, H.-U., 1991, Sr-Nd-Pb isotopic evolution of Gran Canaria: Evidence for shallow enriched mantle beneath the Canary Islands: *Earth and Planetary Science Letters*, v. 106, no. 1, p. 44-63.
- Hoernle, K., Werner, R., and Lüter, C., 2014, RV SONNE Fahrtbericht/Cruise Report SO233 WALVIS II, 14.05-21.06. 2014, Cape Town, South Africa-Walvis Bay, Namibia: GEOMAR Report v. no. 23 (N. Ser.), p. 53 pp + Appendices.
- Hoffman, N. R. A., and McKenzie, D. P., 1985, The destruction of geochemical heterogeneities by differential fluid motions during mantle convection: *Geophysical Journal of the Royal Astronomical Society*, v. 82, no. 2, p. 163-206.
- Hofmann, A. W., 1988, Chemical Differentiation of the Earth - The Relationship between Mantle, Continental Crust, and Oceanic Crust: *Earth and Planetary Science Letters*, v. 90, no. 3, p. 297-314.
- , 1997, Mantle geochemistry: the message from oceanic volcanism: *Nature*, v. 385, no. 6613, p. 219-229.
- Hofmann, A. W., Jochum, K. P., Seufert, M., and White, W. M., 1986, Nb and Pb in oceanic basalts: new constraints on mantle evolution: *Earth and Planetary Science Letters*, v. 79, no. 1, p. 33-45.
- Hofmann, A. W., and White, W. M., 1982, Mantle plumes from ancient oceanic crust: *Earth and Planetary Science Letters*, v. 57, no. 2, p. 421-436.
- Humphris, S. E., and Thompson, G., 1983, Geochemistry of rare earth elements in basalts from the Walvis Ridge: implications for its origin and evolution: *Earth and Planetary Science Letters*, v. 66, no. Supplement C, p. 223-242.
- Ingle, S., Mahoney, J. J., Sato, H., Coffin, M. F., Kimura, J.-I., Hirano, N., and Nakanishi, M., 2007, Depleted mantle wedge and sediment fingerprint in unusual basalts from the Manihiki Plateau, central Pacific Ocean: *Geology*, v. 35, no. 7, p. 595-598.
- Jackson, M., Cabral, R., Rose-Koga, E., Koga, K., Price, A., Hauri, E., and Michael, P., 2015, Ultra-depleted melts in olivine-hosted melt inclusions from the Ontong Java Plateau: *Chemical Geology*, v. 414, p. 124-137.

- Jackson, M. G., Becker, T. W., and Konter, J. G., 2018, Evidence for a deep mantle source for EM and HIMU domains from integrated geochemical and geophysical constraints: *Earth and Planetary Science Letters*, v. 484, p. 154-167.
- Jackson, M. G., and Dasgupta, R., 2008, Compositions of HIMU, EM1, and EM2 from global trends between radiogenic isotopes and major elements in ocean island basalts: *Earth and Planetary Science Letters*, v. 276, no. 1-2, p. 175-186.
- Jackson, M. G., Hart, S. R., Konter, J. G., Koppers, A. A. P., Staudigel, H., Kurz, M. D., Blusztajn, J., and Sinton, J. M., 2010, Samoan hot spot track on a "hot spot highway": Implications for mantle plumes and a deep Samoan mantle source: *Geochemistry, Geophysics, Geosystems*, v. 11, no. 12, p. Q12009.
- Jackson, M. G., Hart, S. R., Konter, J. G., Kurz, M. D., Blusztajn, J., and Farley, K. A., 2014, Helium and lead isotopes reveal the geochemical geometry of the Samoan plume: *Nature*, v. 514, no. 7522, p. 355-358.
- Jackson, M. G., Hart, S. R., Saal, A. E., Shimizu, N., Kurz, M. D., Blusztajn, J. S., and Skovgaard, A. C., 2008, Globally elevated titanium, tantalum, and niobium (TITAN) in ocean island basalts with high  $3\text{He}/4\text{He}$ : *Geochemistry, Geophysics, Geosystems*, v. 9, no. 4, p. n/a-n/a.
- Jacob, D. E., and Foley, S. F., 1999, Evidence for Archean ocean crust with low high field strength element signature from diamondiferous eclogite xenoliths: *Lithos*, v. 48, no. 1-4, p. 317-336.
- Janney, P. E., Le Roex, A. P., Carlson, R. W., and Viljoen, K. S., 2002, A Chemical and Multi-Isotope Study of the Western Cape Olivine Melilitite Province, South Africa: Implications for the Sources of Kimberlites and the Origin of the HIMU Signature in Africa: *Journal of Petrology*, v. 43, no. 12, p. 2339-2370.
- Johnson, M. C., and Plank, T., 2000, Dehydration and melting experiments constrain the fate of subducted sediments: *Geochemistry, Geophysics, Geosystems*, v. 1, no. 12, p. n/a-n/a.
- Johnson, T. E., Brown, M., Kaus, B. J. P., and VanTongeren, J. A., 2014, Delamination and recycling of Archean crust caused by gravitational instabilities: *Nature Geosci*, v. 7, no. 1, p. 47-52.
- Jourdan, F., Renne, P. R., and Reimold, W. U., 2009, An appraisal of the ages of terrestrial impact structures: *Earth and Planetary Science Letters*, v. 286, no. 1, p. 1-13.
- Kalt, A., Hegner, E., and Satir, M., 1997, Nd, Sr, and Pb isotopic evidence for diverse lithospheric mantle sources of East African Rift carbonatites: *Tectonophysics*, v. 278, no. 1, p. 31-45.
- Kaminsky, F., 2012, Mineralogy of the lower mantle: A review of 'super-deep' mineral inclusions in diamond: *Earth-Science Reviews*, v. 110, no. 1-4, p. 127-147.
- Karsten, J. L., Klein, E. M., and Sherman, S. B., 1996, Subduction zone geochemical characteristics in ocean ridge basalts from the southern Chile Ridge: Implications of modern ridge subduction systems for the Archean: *Lithos*, v. 37, no. 2, p. 143-161.
- Kawabata, H., Hanyu, T., Chang, Q., Kimura, J.-I., Nichols, A. R. L., and Tatsumi, Y., 2011, The Petrology and Geochemistry of St. Helena Alkali Basalts: Evaluation of the Oceanic Crust-recycling Model for HIMU OIB: *Journal of Petrology*, v. 52, no. 4, p. 791-838.
- Keller, J., Zaitsev, A. N., and Wiedenmann, D., 2006, Primary magmas at Oldoinyo Lengai: The role of olivine melilitites: *Lithos*, v. 91, no. 1-4, p. 150-172.
- Kellogg, L. H., and Turcotte, D. L., 1990, Mixing and the distribution of heterogeneities in a chaotically convecting mantle: *Journal of Geophysical Research: Solid Earth*, v. 95, no. B1, p. 421-432.
- Kimura, J.-I., Gill, J. B., Skora, S., van Keken, P. E., and Kawabata, H., 2016, Origin of geochemical mantle components: Role of subduction filter: *Geochemistry, Geophysics, Geosystems*, v. 17, no. 8, p. 3289-3325.
- Kipf, A., Hauff, F., Werner, R., Gohl, K., van den Bogaard, P., Hoernle, K., Maicher, D., and Klügel, A., 2014, Seamounts off the West Antarctic margin: A case for non-hotspot driven intraplate volcanism: *Gondwana Research*, v. 25, no. 4, p. 1660-1679.
- Kogiso, T., Hirose, K., and Takahashi, E., 1998, Melting experiments on homogeneous mixtures of peridotite and basalt: application to the genesis of ocean island basalts: *Earth and Planetary Science Letters*, v. 162, no. 1-4, p. 45-61.
- Kogiso, T., and Hirschmann, M. M., 2006, Partial melting experiments of biminerally eclogite and the role of recycled mafic oceanic crust in the genesis of ocean island basalts: *Earth and Planetary Science Letters*, v. 249, no. 3-4, p. 188-199.
- Kogiso, T., Tatsumi, Y., and Nakano, S., 1997a, Trace element transport during dehydration processes in the subducted oceanic crust: 1. Experiments and implications for the origin of ocean island basalts: *Earth and Planetary Science Letters*, v. 148, no. 1, p. 193-205.
- Kogiso, T., Tatsumi, Y., Shimoda, G., and Barszczus, H. G., 1997b, High  $\mu$  (HIMU) ocean island basalts in southern Polynesia: New evidence for whole mantle scale recycling of subducted oceanic crust: *Journal of Geophysical Research: Solid Earth*, v. 102, no. B4, p. 8085-8103.

- Konter, J. G., Hanan, B. B., Blichert-Toft, J., Koppers, A. A. P., Plank, T., and Staudigel, H., 2008, One hundred million years of mantle geochemical history suggest the retiring of mantle plumes is premature: *Earth and Planetary Science Letters*, v. 275, no. 3–4, p. 285-295.
- Koppers, A. A. P., Staudigel, H., Christie, D. M., Dieu, J. J., and Pringle, M. S., 1995, Sr-Nd-Pb isotope geochemistry of Leg 144 West Pacific guyots; implications for the geochemical evolution of the "SOPITA" mantle anomaly: *Proceedings of the Ocean Drilling Program, scientific results, Northwest Pacific atolls and guyots; covering Leg 144 of the cruises of the drilling vessel JOIDES Resolution, Majuro Atoll to Yokohama, Japan, sites 871-880 and Site 801, 19 May-20 July 1992*, v. 144, p. 535.
- Koppers, A. A. P., Staudigel, H., Pringle, M. S., and Wijbrans, J. R., 2003, Short-lived and discontinuous intraplate volcanism in the South Pacific: Hot spots or extensional volcanism?: *Geochemistry, Geophysics, Geosystems*, v. 4, no. 10, p. n/a-n/a.
- Kramers, J. D., 1977, Lead and strontium isotopes in Cretaceous kimberlites and mantle-derived xenoliths from Southern Africa: *Earth and Planetary Science Letters*, v. 34, no. 3, p. 419-431.
- Krystopowicz, N. J., and Currie, C. A., 2013, Crustal eclogitization and lithosphere delamination in orogens: *Earth and Planetary Science Letters*, v. 361, p. 195-207.
- Kurz, M. D., Jenkins, W. J., and Hart, S. R., 1982, Helium isotopic systematics of oceanic islands and mantle heterogeneity: *Nature*, v. 297, no. 5861, p. 43-47.
- Lanphere, M. A., and Dalrymple, G. B., 1978, The use of  $^{40}\text{Ar}/^{39}\text{Ar}$  data in evaluation of disturbed K-Ar systems: *Geological Survey Open-File Report 78-701*, p. 141-148.
- Lassiter, J. C., Blichert-Toft, J., Hauri, E. H., and Barszczus, H. G., 2003, Isotope and trace element variations in lavas from Raivavae and Rapa, Cook-Austral islands: constraints on the nature of HIMU- and EM-mantle and the origin of mid-plate volcanism in French Polynesia: *Chemical Geology*, v. 202, no. 1–2, p. 115-138.
- Le Maitre, R. W., Streckeisen, A., Zanettin, B., Le Bas, M., Bonin, B., and Bateman, P., 2005, *Igneous rocks: a classification and glossary of terms: recommendations of the International Union of Geological Sciences Subcommittee on the Systematics of Igneous Rocks*, Cambridge University Press.
- Le Roex, A., Class, C., O'Connor, J., and Jokat, W., 2010, Shona and Discovery Aseismic Ridge Systems, South Atlantic: Trace Element Evidence for Enriched Mantle Sources: *Journal of Petrology*, v. 51, no. 10, p. 2089-2120.
- Lee, C. T. A., 2006, Geochemical/petrologic constraints on the origin of cratonic mantle: Archean geodynamics and environments, p. 89-114.
- Lucassen, F., Franz, G., Romer, R. L., Pudlo, D., and Dulski, P., 2008, Nd, Pb, and Sr isotope composition of Late Mesozoic to Quaternary intra-plate magmatism in NE-Africa (Sudan, Egypt): high- $\mu$  signatures from the mantle lithosphere: *Contributions to Mineralogy and Petrology*, v. 156, no. 6, p. 765-784.
- MacDonald, G. A., 1968, *Composition and Origin of Hawaiian Lavas*: Geological Society of America Memoirs, v. 116, p. 477-522.
- Mallik, A., and Dasgupta, R., 2012, Reaction between MORB-eclogite derived melts and fertile peridotite and generation of ocean island basalts: *Earth and Planetary Science Letters*, v. 329–330, p. 97-108.
- , 2013, Reactive Infiltration of MORB-Eclogite-Derived Carbonated Silicate Melt into Fertile Peridotite at 3 GPa and Genesis of Alkalic Magmas: *Journal of Petrology*, v. 54, no. 11, p. 2267-2300.
- , 2014, Effect of variable CO<sub>2</sub> on eclogite-derived andesite and lherzolite reaction at 3 GPa—Implications for mantle source characteristics of alkalic ocean island basalts: *Geochemistry, Geophysics, Geosystems*, v. 15, no. 4, p. 1533-1557.
- Mana, S., Furman, T., Carr, M. J., Mollel, G. F., Mortlock, R. A., Feigenson, M. D., Turrin, B. D., and Swisher Iii, C. C., 2012, Geochronology and geochemistry of the Essimigor volcano: Melting of metasomatized lithospheric mantle beneath the North Tanzanian Divergence zone (East African Rift): *Lithos*, v. 155, p. 310-325.
- Manikyamba, C., and Kerrich, R., 2011, Geochemistry of alkaline basalts and associated high-Mg basalts from the 2.7Ga Penakacherla Terrane, Dharwar craton, India: An Archean depleted mantle-OIB array: *Precambrian Research*, v. 188, no. 1, p. 104-122.
- Maury, R. C., Guille, G., Guillou, H., Chauvel, C., Rossi, P., Pallares, C., and Legendre, C., 2013, Temporal evolution of a Polynesian hotspot: New evidence from Raivavae (Austral islands, South Pacific ocean): *Bulletin de la Societe Geologique de France*, v. 184, p. 557-567.
- McCoy-West, A. J., Bennett, V. C., and Amelin, Y., 2016, Rapid Cenozoic ingrowth of isotopic signatures simulating "HIMU" in ancient lithospheric mantle: Distinguishing source from process: *Geochimica et Cosmochimica Acta*, v. 187, p. 79-101.

- McCulloch, M. T., and Bennett, V. C., 1994, Progressive growth of the Earth's continental crust and depleted mantle: Geochemical constraints: *Geochimica et Cosmochimica Acta*, v. 58, no. 21, p. 4717-4738.
- McDonough, W. F., 1990, Constraints on the composition of the continental lithospheric mantle: *Earth and Planetary Science Letters*, v. 101, no. 1, p. 1-18.
- Montelli, R., Nolet, G., Dahlen, F. A., and Masters, G., 2006, A catalogue of deep mantle plumes: New results from finite-frequency tomography: *Geochemistry, Geophysics, Geosystems*, v. 7, no. 11, p. Q11007.
- Moore, K. R., and Wood, B. J., 1998, The Transition from Carbonate to Silicate Melts in the CaO—MgO—SiO<sub>2</sub>—CO<sub>2</sub> System: *Journal of Petrology*, v. 39, no. 11-12, p. 1943-1951.
- Morgan, W. J., 1971, Convection Plumes in the Lower Mantle: *Nature*, v. 230, no. 5288, p. 42-43.
- Moyen, J.-F., and Laurent, O., 2018, Archaean tectonic systems: A view from igneous rocks: *Lithos*, v. 302-303, p. 99-125.
- Nebel, O., Arculus, R. J., van Westrenen, W., Woodhead, J. D., Jenner, F. E., Nebel-Jacobsen, Y. J., Wille, M., and Eggins, S. M., 2013, Coupled Hf–Nd–Pb isotope co-variations of HIMU oceanic island basalts from Mangaia, Cook-Austral islands, suggest an Archean source component in the mantle transition zone: *Geochimica et Cosmochimica Acta*, v. 112, p. 87-101.
- Nelson, D. R., Chivas, A. R., Chappell, B. W., and McCulloch, M. T., 1988, Geochemical and isotopic systematics in carbonatites and implications for the evolution of ocean-island sources: *Geochimica et Cosmochimica Acta*, v. 52, no. 1, p. 1-17.
- Nowell, G. M., Pearson, D. G., Bell, D. R., Carlson, R. W., Smith, C. B., Kempton, P. D., and Noble, S. R., 2004, Hf Isotope Systematics of Kimberlites and their Megacrysts: New Constraints on their Source Regions: *Journal of Petrology*, v. 45, no. 8, p. 1583-1612.
- O'Connor, J. M., and Duncan, R. A., 1990, Evolution of the Walvis Ridge-Rio Grande Rise Hot Spot System: Implications for African and South American Plate motions over plumes: *Journal of Geophysical Research: Solid Earth*, v. 95, no. B11, p. 17475-17502.
- O'Connor, J. M., and Jokat, W., 2015a, Tracking the Tristan-Gough mantle plume using discrete chains of intraplate volcanic centers buried in the Walvis Ridge: *Geology*, v. 43, no. 8, p. 715-718.
- , 2015b, Age distribution of Ocean Drill sites across the Central Walvis Ridge indicates plate boundary control of plume volcanism in the South Atlantic: *Earth and Planetary Science Letters*, v. 424, p. 179-190.
- O'Connor, J. M., Jokat, W., le Roex, A. P., Class, C., Wijbrans, J. R., Keszling, S., Kuiper, K. F., and Nebel, O., 2012, Hotspot trails in the South Atlantic controlled by plume and plate tectonic processes: *Nature Geoscience*, v. 5, no. 10, p. 735-738.
- O'Neill, C., Lenardic, A., Moresi, L., Torsvik, T. H., and Lee, C. T. A., 2007, Episodic Precambrian subduction: *Earth and Planetary Science Letters*, v. 262, no. 3-4, p. 552-562.
- Panter, K. S., Blusztajn, J., Hart, S. R., Kyle, P. R., Esser, R., and McIntosh, W. C., 2006, The origin of HIMU in the SW Pacific: Evidence from intraplate volcanism in southern New Zealand and subantarctic islands: *Journal of Petrology*, v. 47, no. 9, p. 1673-1704.
- Panter, K. S., Hart, S. R., Kyle, P., Blusztajn, J., and Wilch, T., 2000, Geochemistry of Late Cenozoic basalts from the Crary Mountains: characterization of mantle sources in Marie Byrd Land, Antarctica: *Chemical Geology*, v. 165, no. 3-4, p. 215-241.
- Paslick, C., Halliday, A., James, D., and Dawson, J. B., 1995, Enrichment of the continental lithosphere by OIB melts: Isotopic evidence from the volcanic province of northern Tanzania: *Earth and Planetary Science Letters*, v. 130, no. 1, p. 109-126.
- Pearce, J. A., 1996, A user's guide to basalt discrimination diagrams: Trace element geochemistry of volcanic rocks: applications for massive sulphide exploration. Geological Association of Canada, Short Course Notes, v. 12, no. 79, p. 113.
- Pertermann, M., and Hirschmann, M. M., 2003, Partial melting experiments on a MORB-like pyroxenite between 2 and 3 GPa: Constraints on the presence of pyroxenite in basalt source regions from solidus location and melting rate: *Journal of Geophysical Research: Solid Earth*, v. 108, no. B2.
- Pietsch, R., and Uenzelmann-Neben, G., 2015, The Manihiki Plateau—A multistage volcanic emplacement history: *Geochemistry, Geophysics, Geosystems*, v. 16, no. 8, p. 2480-2498.
- Pilet, S., Hernandez, J., Sylvester, P., and Poujol, M., 2005, The metasomatic alternative for ocean island basalt chemical heterogeneity: *Earth and Planetary Science Letters*, v. 236, no. 1, p. 148-166.
- Plank, T., and Langmuir, C. H., 1998, The chemical composition of subducting sediment and its consequences for the crust and mantle: *Chemical Geology*, v. 145, no. 3-4, p. 325-394.
- Pringle, M. S., Sager, W. W., Sliter, W. V., and Stein, S., 1993, The Mesozoic Pacific: Geology, Tectonics, and Volcanism: A Volume in Memory of Sy Schlanger: Washington DC American Geophysical Union Geophysical Monograph Series, v. 77.

- Ren, Z.-Y., Hanyu, T., Miyazaki, T., Chang, Q., Kawabata, H., Takahashi, T., Hirahara, Y., Nichols, A. R. L., and Tatsumi, Y., 2009, Geochemical Differences of the Hawaiian Shield Lavas: Implications for Melting Process in the Heterogeneous Hawaiian Plume: *Journal of Petrology*, v. 50, no. 8, p. 1553-1573.
- Renne, P. R., Glen, J. M., Milner, S. C., and Duncan, A. R., 1996, Age of Etendeka flood volcanism and associated intrusions in southwestern Africa: *Geology*, v. 24, no. 7, p. 659-662.
- Richards, M. A., Duncan, R. A., and Courtillot, V. E., 1989, Flood basalts and hot-spot tracks: plume heads and tails: *Science*, v. 246, no. 4926, p. 103-107.
- Richardson, S. H., Erlank, A. J., Duncan, A. R., and Reid, D. L., 1982, Correlated Nd, Sr and Pb Isotope Variation in Walvis Ridge Basalts and Implications for the Evolution of their Mantle Source: *Earth and Planetary Science Letters*, v. 59, no. 2, p. 327-342.
- Richardson, S. H., Erlank, A. J., Reid, D. L., and Duncan, A. R., 1984, Major and Trace-Elements and Nd and Sr Isotope Geochemistry of Basalts from the Deep-Sea Drilling Project Leg-74 Walvis Ridge Transect: Initial Reports of the Deep Sea Drilling Project, v. 74, no. Mar, p. 739-754.
- Rino, S., Komiya, T., Windley, B. F., Katayama, I., Motoki, A., and Hirata, T., 2004, Major episodic increases of continental crustal growth determined from zircon ages of river sands; implications for mantle overturns in the Early Precambrian: *Physics of the Earth and Planetary Interiors*, v. 146, no. 1-2, p. 369-394.
- Roex, A. P., Späth, A., and Zartman, R. E., 2001, Lithospheric thickness beneath the southern Kenya Rift: implications from basalt geochemistry: *Contributions to Mineralogy and Petrology*, v. 142, no. 1, p. 89-106.
- Rogers, N., Macdonald, R., Fitton, J. G., George, R., Smith, M., and Barreiro, B., 2000, Two mantle plumes beneath the East African rift system: Sr, Nd and Pb isotope evidence from Kenya Rift basalts: *Earth and Planetary Science Letters*, v. 176, no. 3-4, p. 387-400.
- Rohde, J., Hoernle, K., Hauff, F., Werner, R., O'Connor, J., Class, C., Garbe-Schönberg, D., and Jokat, W., 2013a, 70 Ma chemical zonation of the Tristan-Gough hotspot track: *Geology*, v. 43, no. 3, p. 335-338.
- Rohde, J. K., van den Bogaard, P., Hoernle, K., Hauff, F., and Werner, R., 2013b, Evidence for an age progression along the Tristan-Gough volcanic track from new  $^{40}\text{Ar}/^{39}\text{Ar}$  ages on phenocryst phases: *Tectonophysics*, v. 604, p. 60-71.
- Rooney, T. O., Nelson, W. R., Dosso, L., Furman, T., and Hanan, B., 2014, The role of continental lithosphere metasomes in the production of HIMU-like magmatism on the northeast African and Arabian plates: *Geology*, v. 42(5), p. 419-422.
- Saal, A. E., Hart, S. R., Shimizu, N., Hauri, E. H., and Layne, G. D., 1998, Pb Isotopic Variability in Melt Inclusions from Oceanic Island Basalts, Polynesia: *Science*, v. 282, p. 1481-1484.
- Said, N., and Kerrich, R., 2010, Magnesian dyke suites of the 2.7Ga Kambalda Sequence, Western Australia: Evidence for coeval melting of plume asthenosphere and metasomatised lithospheric mantle: *Precambrian Research*, v. 180, no. 3, p. 183-203.
- Salters, V. J. M., Mallick, S., Hart, S. R., Langmuir, C. E., and Stracke, A., 2011, Domains of depleted mantle: New evidence from hafnium and neodymium isotopes: *Geochemistry, Geophysics, Geosystems*, v. 12, no. 8, p. n/a-n/a.
- Salters, V. J. M., and Sachi-Kocher, A., 2010, An ancient metasomatic source for the Walvis Ridge basalts: *Chemical Geology*, v. 273, no. 3-4, p. 151-167.
- Salters, V. J. M., and Stracke, A., 2004, Composition of the depleted mantle: *Geochemistry, Geophysics, Geosystems*, v. 5, no. 5, p. Q05B07.
- Schiano, P., Burton, K. W., Dupré, B., Birck, J. L., Guille, G., and Allègre, C. J., 2001, Correlated Os-Pb-Nd-Sr isotopes in the Austral-Cook chain basalts: the nature of mantle components in plume sources: *Earth and Planetary Science Letters*, v. 186, no. 3-4, p. 527-537.
- Schlömer, A., Geissler, W. H., Jokat, W., and Jegen, M., 2017, Hunting for the Tristan mantle plume – An upper mantle tomography around the volcanic island of Tristan da Cunha: *Earth and Planetary Science Letters*, v. 462, p. 122-131.
- Shirey, S. B., and Richardson, S. H., 2011, Start of the Wilson Cycle at 3 Ga Shown by Diamonds from Subcontinental Mantle: *Science*, v. 333, no. 6041, p. 434-436.
- Simonetti, A., and Bell, K., 1995, Nd, Pb and Sr Isotopic Data from the Mount-Elgon Volcano, Eastern Uganda Western Kenya - Implications for the Origin and Evolution of Nephelinite Lavas: *Lithos*, v. 36, no. 2, p. 141-153.
- Smith, W. H. F., Staudigel, H., Watts, A. B., and Pringle, M. S., 1989, The Magellan seamounts: Early Cretaceous record of the South Pacific isotopic and thermal anomaly: *Journal of Geophysical Research: Solid Earth*, v. 94, no. B8, p. 10501-10523.
- Spandler, C., Yaxley, G., Green, D. H., and Rosenthal, A., 2008, Phase Relations and Melting of Anhydrous K-bearing Eclogite from 1200 to 1600°C and 3 to 5 GPa: *Journal of Petrology*, v. 49, no. 4, p. 771-795.

- Staudigel, H., Park, K. H., Pringle, M., Rubenstone, J. L., Smith, W. H. F., and Zindler, A., 1991, The longevity of the South Pacific isotopic and thermal anomaly: *Earth and Planetary Science Letters*, v. 102, no. 1, p. 24-44.
- Steiger, R. H., and Jäger, E., 1977, Subcommittee on geochronology: Convention on the use of decay constants in geo- and cosmochronology: *Earth and Planetary Science Letters*, v. 36, no. 3, p. 359-362.
- Stein, M., and Hofmann, A. W., 1994, Mantle plumes and episodic crustal growth: *Nature*, v. 372, no. 6501, p. 63-68.
- Stein, M., Navon, O., and Kessel, R., 1997, Chromatographic metasomatism of the Arabian—Nubian lithosphere: *Earth and Planetary Science Letters*, v. 152, no. 1-4, p. 75-91.
- Steinberger, B., and Torsvik, T. H., 2012, A geodynamic model of plumes from the margins of Large Low Shear Velocity Provinces: *Geochemistry, Geophysics, Geosystems*, v. 13, no. 1, p. Q01W09.
- Stewart, K., and Rogers, N., 1996, Mantle plume and lithosphere contributions to basalts from southern Ethiopia: *Earth and Planetary Science Letters*, v. 139, no. 1-2, p. 195-211.
- Storey, B. C., Leat, P. T., Weaver, S. D., Pankhurst, R. J., Bradshaw, J. D., and Kelley, S., 1999, Mantle plumes and Antarctica-New Zealand rifting: evidence from mid-Cretaceous mafic dykes: *Journal of the Geological Society*, v. 156, no. 4, p. 659-671.
- Stracke, A., 2012, Earth's heterogeneous mantle: A product of convection-driven interaction between crust and mantle: *Chemical Geology*, v. 330-331, p. 274-299.
- Stracke, A., Bizimis, M., and Salters, V. J. M., 2003, Recycling oceanic crust: Quantitative constraints: *Geochemistry, Geophysics, Geosystems*, v. 4, no. 3, p. 8003.
- Stracke, A., Hofmann, A. W., and Hart, S. R., 2005, FOZO, HIMU, and the rest of the mantle zoo: *Geochemistry, Geophysics, Geosystems*, v. 6, no. 5, p. Q05007.
- Stroncik, N. A., Trumbull, R. B., Krienitz, M.-S., Niedermann, S., Romer, R. L., Harris, C., and Day, J., 2017, Helium isotope evidence for a deep-seated mantle plume involved in South Atlantic breakup: *Geology*, v. 45, no. 9, p. 827-830.
- Sumino, H., Kaneoka, I., Matsufuji, K., and Sobolev, A. V., 2006, Deep mantle origin of kimberlite magmas revealed by neon isotopes: *Geophysical Research Letters*, v. 33, no. 16, p. n/a-n/a.
- Sumner, D. Y., and Grotzinger, J. P., 1996, Were kinetics of Archean calcium carbonate precipitation related to oxygen concentration?: *Geology*, v. 24, no. 2, p. 119-122.
- Tatsumoto, M., 1978, Isotopic composition of lead in oceanic basalt and its implication to mantle evolution: *Earth and Planetary Science Letters*, v. 38, no. 1, p. 63-87.
- Taylor, B., 2006, The single largest oceanic plateau: Ontong Java—Manihiki—Hikurangi: *Earth and Planetary Science Letters*, v. 241, no. 3-4, p. 372-380.
- Tejada, M. L. G., Mahoney, J. J., Duncan, R. A., and Hawkins, M. P., 1996, Age and Geochemistry of Basement and Alkalic Rocks of Malaita and Santa Isabel, Solomon Islands, Southern Margin of Ontong Java Plateau: *Journal of Petrology*, v. 37, no. 2, p. 361-394.
- Tejada, M. L. G., Mahoney, J. J., Neal, C. R., Duncan, R. A., and Petterson, M. G., 2002, Basement Geochemistry and Geochronology of Central Malaita, Solomon Islands, with Implications for the Origin and Evolution of the Ontong Java Plateau: *Journal of Petrology*, v. 43, no. 3, p. 449-484.
- Thirlwall, M. F., 1997, Pb isotopic and elemental evidence for OIB derivation from young HIMU mantle: *Chemical Geology*, v. 139, no. 1, p. 51-74.
- Thompson, G., and Humphris, S., 1984, Petrology and Geochemistry of rocks from the Walvis Ridge-Deep-Sea Drilling Project Leg-74, Site525, Site527 and Site528 Initial Reports of the Deep Sea Drilling Project, v. 74, no. MAR, p. 755-764.
- Timm, C., Hoernle, K., Werner, R., Hauff, F., den Bogaard, P. v., Michael, P., Coffin, M. F., and Koppers, A., 2011, Age and geochemistry of the oceanic Manihiki Plateau, SW Pacific: New evidence for a plume origin: *Earth and Planetary Science Letters*, v. 304, no. 1-2, p. 135-146.
- Timm, C., Hoernle, K., Werner, R., Hauff, F., den Bogaard, P. v., White, J., Mortimer, N., and Garbe-Schönberg, D., 2010, Temporal and geochemical evolution of the Cenozoic intraplate volcanism of Zealandia: *Earth-Science Reviews*, v. 98, no. 1-2, p. 38-64.
- Torsvik, T. H., Burke, K., Steinberger, B., Webb, S. J., and Ashwal, L. D., 2010, Diamonds sampled by plumes from the core-mantle boundary: *Nature*, v. 466, no. 7304, p. 352-355.
- Torsvik, T. H., Smethurst, M. A., Burke, K., and Steinberger, B., 2006, Large igneous provinces generated from the margins of the large low-velocity provinces in the deep mantle: *Geophysical Journal International*, v. 167, no. 3, p. 1447-1460.
- van den Bogaard, P., 2013, The origin of the Canary Island Seamount Province - New ages of old seamounts: *Scientific Reports*, v. 3, p. 2107.



- van Keken, P. E., Hauri, E. H., and Ballentine, C. J., 2002, Mantle Mixing: The Generation, Preservation, and Destruction of Chemical Heterogeneity: *Annual Review of Earth and Planetary Sciences*, v. 30, no. 1, p. 493-525.
- Van Kranendonk, M. J., 2010, Two types of Archean continental crust: Plume and plate tectonics on early Earth: *American Journal of Science*, v. 310, no. 10, p. 1187-1209.
- Vollmer, R., and Norry, M. J., 1983, Unusual isotopic variations in Nyiragongo nephelinites: *Nature*, v. 301, no. 5896, p. 141-143.
- Weaver, S. D., Storey, B. C., Pankhurst, R. J., Mukasa, S. B., DiVenere, V. J., and Bradshaw, J. D., 1994, Antarctica-New Zealand rifting and Marie Byrd Land lithospheric magmatism linked to ridge subduction and mantle plume activity: *Geology*, v. 22, no. 9, p. 811-814.
- Weiss, Y., Class, C., Goldstein, S. L., and Hanyu, T., 2016, Key new pieces of the HIMU puzzle from olivines and diamond inclusions: *Nature*, v. 537, p. 666-670.
- Weiss, Y., Griffin, W. L., Bell, D. R., and Navon, O., 2011, High-Mg carbonatitic melts in diamonds, kimberlites and the sub-continental lithosphere: *Earth and Planetary Science Letters*, v. 309, no. 3-4, p. 337-347.
- Werner, R., and Hauff, F., 2007, FS Sonne/Fahrtbericht/Cruise Report SO 193: MANIHIKI Temporal, Spatial, and Tectonic Evolution of Oceanic Plateaus: IFMGEOMAR Report, v. 13.
- White, W. M., 2015, Isotopes, DUPAL, LLSVPs, and Anekantavada: *Chemical Geology*, v. 419, p. 10-28.
- Willbold, M., and Stracke, A., 2006, Trace element composition of mantle end-members: Implications for recycling of oceanic and upper and lower continental crust: *Geochemistry, Geophysics, Geosystems*, v. 7, no. 4, p. Q04004.
- Wilson, J. T., 1963, Evidence from Islands on the Spreading of Ocean Floors: *Nature*, v. 197, no. 4867, p. 536-538.
- Woodhead, J. D., 1996, Extreme HIMU in an oceanic setting: the geochemistry of Mangaia Island (Polynesia), and temporal evolution of the Cook—Austral hotspot: *Journal of Volcanology and Geothermal Research*, v. 72, no. 1, p. 1-19.
- Workman, R. K., and Hart, S. R., 2005, Major and trace element composition of the depleted MORB mantle (DMM): *Earth and Planetary Science Letters*, v. 231, no. 1-2, p. 53-72.
- Zindler, A., and Hart, S. R., 1986, Chemical Geodynamics: *Annual Review of Earth and Planetary Sciences*, v. 14, no. 1, p. 493-571.

## CHAPTER II

### UNEXPECTED HIMU-TYPE LATE-STAGE VOLCANISM ON THE WALVIS RIDGE

S. Homrighausen<sup>1\*</sup>, K. Hoernle<sup>1,2</sup>, J. Geldmacher<sup>1</sup>, F. Hauff<sup>1</sup>, M. Portnyagin<sup>1,3</sup>, R. Werner<sup>1</sup>, J.-A. Wartho<sup>1</sup>, P. van den Bogaard<sup>1</sup>, D. Garbe-Schönberg<sup>2</sup>

<sup>1</sup> GEOMAR Helmholtz-Zentrum für Ozeanforschung Kiel, Wischhofstr. 1-3, 24148 Kiel, Germany

<sup>2</sup> Institut für Geowissenschaften, Christian-Albrechts Universität zu Kiel, Ludewig-Meyn-Str. 10, 24118 Kiel, Germany

<sup>3</sup> V.I. Vernadsky Institute of Geochemistry and Analytical Chemistry, Kosygin St. 19, 119991 Moscow, Russia

\* Corresponding author (shomrighausen@geomar.de)

**Keywords: Walvis Ridge, late-stage volcanism, trace elements and isotope geochemistry,  $^{40}\text{Ar}/^{39}\text{Ar}$  dating, high  $^{238}\text{U}/^{204}\text{Pb}$  (HIMU) mantle end member, Large Low Shear Velocity Province (LLSVP)**

## Abstract

Volcanic activity on many oceanic volcanoes, ridges and plateaus reawakens after hiatuses of up to several million years. Compared to the earlier magmatic phases, this late-stage (rejuvenated/post-erosional) volcanism is commonly characterized by a distinct geochemical composition. Late-stage volcanism raises two hitherto unanswered questions: Why does volcanism restart after an extended hiatus and what is the origin of this volcanism? Here we present the first  $^{40}\text{Ar}/^{39}\text{Ar}$  age and comprehensive trace element and Sr-Nd-Pb-Hf isotopic data from seamounts located on and adjacent to the Walvis Ridge in the South Atlantic ocean basin. The Walvis Ridge is the oldest submarine part of the Tristan-Gough hotspot track and is famous as the original type locality for the enriched mantle one (EM I) end member. Consistent with the bathymetric data, the age data indicates that most of these seamounts are 20-40 Myr younger than the underlying or nearby Walvis Ridge basement. The trace element and isotope data reveal a distinct compositional range from the EM I-type basement. The composition of the seamounts extend from the St. Helena HIMU (high time-integrated  $^{238}\text{U}/^{204}\text{Pb}$  mantle with radiogenic Pb isotope ratios) end member to an enriched (E) mid-ocean-ridge basalt (MORB) type composition, reflecting a two-component mixing trend on all isotope diagrams. The EMORB end member could have been generated through mixing of Walvis Ridge EM I with normal (N) MORB source mantle, reflecting interaction of Tristan-Gough (EM I-type) plume melts with the upper mantle. The long volcanic quiescence and the HIMU-like geochemical signature of the seamounts are unusual for classical hotspot related late-stage volcanism, indicating that these seamounts are not related to the Tristan-Gough hotspot volcanism. Two volcanic arrays in southwestern Africa (Gibeon-Dicker Willem and Western Cape province) display similar ages to the late-stage Walvis seamounts and also have HIMU-like compositions, suggesting a larger-

scale event at ~77-49 Ma. We propose that the EM I-like mantle plumes rise from the edges of the African Large Low Shear Velocity Province (LLSVP; Tristan-Gough, Discovery and Shona hotspot), whereas the HIMU-dominated intraplate lavas (St. Helena, Gibeon-Dicker Willem and Western Cape province) and the late-stage Walvis seamounts tap material from internal portions of the African LLSVP, suggesting possible lateral and/or vertical chemical zonation of the African LLSVP.

## 1. Introduction

The geochemical signatures of oceanic lavas reflect the large-scale heterogeneity of the earth's mantle. At least four mantle end members are required to describe the variation in radiogenic Sr-Nd-Pb-Hf isotope ratios: Depleted Mantle (DM), High time-integrated  $\mu=^{238}\text{U}/^{204}\text{Pb}$  Mantle (HIMU), Enriched Mantle One (EM I), and Enriched Mantle Two (EM II) (Zindler and Hart, 1986). The South Atlantic hosts two classic end member type locations: St. Helena represents HIMU and the Walvis Ridge, the oldest part of the Tristan-Gough hotspot track, represents EM I (e.g., Zindler and Hart, 1986). It is widely accepted that these structures are the surface expression of long-lived mantle plumes, which sample the lowermost mantle (e.g., Morgan, 1971; Wilson, 1973; Richardson et al., 1982; O'Connor et al., 2012; Rohde et al., 2013b; Hoernle et al., 2015; O'Connor and Jokat, 2015a).

Over the last decade, it has been increasingly recognized that some of these geochemical reference locations are compositionally more complex than previously believed. For example, the Tristan-Gough hotspot track displays long-lived spatial geochemical zonation ( $\sim 70$  Ma), implying a similar spatially distinct source heterogeneity in the lowermost mantle (Rohde et al., 2013a; Hoernle et al., 2015). Additionally, many seamounts, oceanic islands and aseismic ridges show a second magmatic pulse after a volcanic quiescence of several million years (e.g., Clague and Dalrymple, 1987; White and Duncan, 1996; Geldmacher et al., 2005; Geldmacher et al., 2006; Garcia et al., 2010; Krishna et al., 2014). This volcanism is commonly termed late-stage, post-erosional or rejuvenated volcanism, and it usually displays a different geochemical composition compared to the earlier shield-building stage or basement volcanism. In general, this late-stage volcanism is characterized by small volume alkaline lavas with incompatible-element enrichment, but has overall more depleted

isotopic compositions compared to the shield stage; e.g., Hawaii (e.g., Clague and Dalrymple, 1987; Garcia et al., 2010), Society (White and Duncan, 1996), Madeira (Geldmacher et al., 2006) or Canary Islands (e.g., Hoernle et al., 1991; Geldmacher et al., 2005).

Late-stage volcanism on hotspot tracks usually takes place within a few million years after formation of the main volcanic edifices or shield stage volcanism (hereafter referred to as "basement"). Models for the origin of late-stage volcanism range from weak, secondary melting zones 300-500 km downstream of the upwelling plume stem (e.g., Ribe and Christensen, 1999) to lithospheric flexure-induced decompression melting (e.g., Bianco et al., 2005). However, in certain locations, such volcanism has been documented after far longer periods of volcanic quiescence. At Dacia Seamount in the North Atlantic (NE of the Canary Islands), for example, volcanism occurred 38 Myr after formation of the main seamount edifice (Geldmacher et al., 2005) and at Christmas Island in the NE Indian Ocean (probably formed between 80-85 Ma) volcanism was reactivated at 44-37 Ma and again at 4.5-4.3 Ma (Hoernle et al., 2011). This much younger late-stage volcanism is considered to have formed independently of the formation of the older seamount edifices. Nevertheless, late-stage volcanism remains an enigmatic process, which can provide unique insights into the compositional heterogeneities of the mantle.

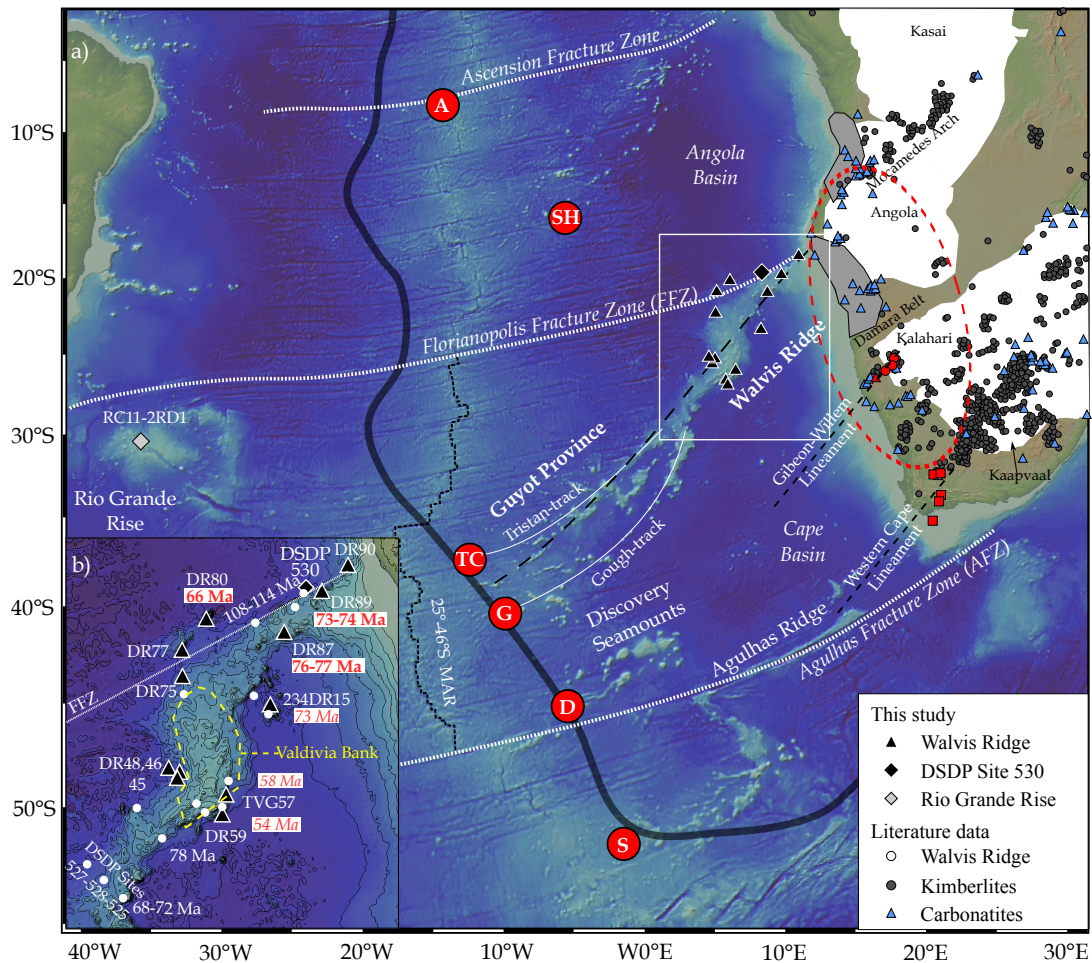


**Figure 1: Map of the South Atlantic and Southwest Africa showing the main geological structures and the 1 %  $\Delta V_s$  contour defining the African Large Low Shear Velocity Province (LLSVP, black line; Torsvik et al., 2006). Ocean island and proposed hotspot locations (red circles: A=Ascension, SH=St. Helena, TC=Tristan da Cunha, G=Gough, D=Discovery and S=Shona), and major fracture zones (dashed white lines) are shown. The Mid-Atlantic Ridge (MAR) between the Florianopolis-Fracture-Zone (FFZ) and Agulhas Fracture Zone (AFZ) is highlighted and referred to as 25°-46°S MAR. The following are shown in Southwest Africa: (1) major African cratons (light-colored regions), (2) Etendeka continental flood basalt province (grey fields), (3) location of kimberlites and carbonatites, (4) magmatic lineaments including the Gibeon-Willem Lineament (red triangles=carbonatites and red circles=kimberlites), and Western Cape olivine-melilitite province (red squares), and (5) the approximate extent of the low-velocity zone beneath southwest Africa (red dashed circle) based on the tomography model of French and Romanowicz (2015). Dashed black line indicates the proposed hotspot track of the Tristan-Gough mantle plume (O'Connor et al., 2012). Inset (b) shows the Walvis Ridge and  $^{40}\text{Ar}/^{39}\text{Ar}$  age data from the literature (in white). The new  $^{40}\text{Ar}/^{39}\text{Ar}$  ages (bold) and  $^{40}\text{Ar}/^{39}\text{Ar}$  age data from the literature (italic), anomalously young volcanism on the Walvis Ridge, are shown in red. The yellow dashed line marks the Valdivia Bank and Ewing Seamount is located at dredge station S0234DR15. Literature data: GEOROC Database (<http://georoc.mpch-mainz.gwdg.de/georoc/>); reported in detail in Appendix F. Source of the bathymetric map: <http://www.geomapapp.org>.**

In this study, we present the first data set of  $^{40}\text{Ar}/^{39}\text{Ar}$  ages and comprehensive trace elements and Sr-Nd-Pb-Hf isotopic data from seamounts on and close to the Walvis Ridge in the South Atlantic Ocean. We evaluate for the first time late-stage volcanism on an aseismic ridge with a volcanic hiatus of 20-40 Ma after the basement formation and provide unique insights into the evolution of a classic hotspot track. The late-stage seamounts have isotopic compositions ranging from St. Helena HIMU to EMORB, which makes the Walvis Ridge the first location worldwide where EM I and St. Helena HIMU end member compositions have been documented. Finally, we propose that the temporal evolution of the Walvis Ridge reflects spatial heterogeneities within the African Large Low Shear Velocity Province (LLSVP).

## **2. Geological Background**

The Walvis Ridge is the most striking bathymetric high in the eastern South Atlantic, rising up to 4000 m above the surrounding seafloor. The continuous aseismic ridge represents the oldest submarine part of the northeast-southwest trending Tristan-Gough hotspot track (Fig. 1). Recent tomographic data suggests that the mantle plume feeding the Tristan-Gough hotspot can be traced to the margin of the African Large Low Shear Velocity Province (LLSVP) in the lowermost mantle (e.g., Torsvik et al., 2006; French and Romanowicz, 2015).

Consistent with the mantle plume model (e.g., Morgan, 1971; Wilson, 1973), the Tristan-Gough hotspot volcanism started with the emplacement of the Parana-Etendeka continental flood basalt province at ~132 Ma (Renne et al., 1996). Although it is controversially debated whether or not the flood basalt event triggered the opening of the South Atlantic, spreading along the South Atlantic Mid-Ocean Ridge split the originally continuous flood basalt province. At this stage, the presumed tail of the mantle



plume interacted with the newly formed Mid-Atlantic Ridge (MAR) creating the aseismic Walvis Ridge and Rio Grande Rise (~120-60 Ma; e.g., Humphris and Thompson, 1983; O'Connor and Duncan, 1990; O'Connor and Jokat, 2015b) (Fig. 1). The Sao Paulo plateau, now located offshore Brazil, and a portion of oceanic crust that was initially formed at the northeastern margin of the Walvis Ridge were transferred by major ridge jumps to the South American Plate between 95-85 Ma along the Florianopolis Fracture Zone (FFZ; Pérez-Díaz and Eagles, 2014). The oldest sediments cored above the oceanic crust at the DSDP (Deep Sea Drilling Program) Site 530, next to the northern end of Walvis Ridge, are late Albian clays (~102.5 Ma; Hay et al., 1984), consistent with magnetic data indicating that the oceanic crust north of the FFZ is ~10 Ma younger than the adjacent ~114 Ma Walvis Ridge basement (Rohde et al., 2013b; O'Connor and Jokat, 2015a). Between 80-60 Ma, the Walvis Ridge and Rio Grande Rise were separated by several major ridge jumps (Humphris and Thompson, 1983; O'Connor and Duncan, 1990; Rohde et al., 2013b; O'Connor and Jokat, 2015b). Thereafter, the hotspot became intraplate, being located beneath the African plate, and formed two separate sub-tracks ending at the active volcanic islands of Tristan da Cunha and Gough Island (Fig. 1). In contrast to the massive Walvis Ridge that formed at the MAR, the intraplate part of the hotspot track consists of discrete guyot- and ridge-shaped seamounts and is referred to as the Guyot Province.

The Tristan and Gough subtracks have distinct isotopic compositions, but both lie within the EM I range (Rohde et al., 2013a; Hoernle et al., 2015). Rocks from the Tristan volcanic sub-track (comprising the DSDP Site 527-528, Tristan-track lavas and lavas from the Tristan Islands) have lower  $^{207}\text{Pb}/^{204}\text{Pb}$  values at a given  $^{206}\text{Pb}/^{204}\text{Pb}$  isotope ratio compared to the volcanic sub-track leading to Gough Island. The geochemical zoning has been traced from the active islands to the DSDP Sites 525, 527 and 528, at the

southern end of the Walvis Ridge (Fig. 1). Northward of these drill sites, the Walvis Ridge appears to have primarily Gough-type composition (Rohde et al., 2013a; Hoernle et al., 2015). Based on the isotopic characteristics, the Gough-type composition comprises lavas from the entire Walvis Ridge north of the DSDP Sites, DSDP Site 525, the Gough-track and Gough Island (Fig. 1).

$^{40}\text{Ar}/^{39}\text{Ar}$  age data show that the Tristan-Gough hotspot track is age progressive with ages systematically decreasing from the ~132 Ma Etendeka flood basalts to the active volcanic islands of Tristan and Gough (Rohde et al., 2013b; O'Connor and Jokat, 2015a). However, much younger ages than expected for the Walvis Ridge basement were reported from two volcanic edifices at the eastern margin of the Walvis Ridge (58 and 54 Ma, derived from two sample sites on the Valdivia bank) and from the Ewing seamount, an isolated seamount east of the Walvis Ridge (73 Ma; Rohde et al., 2013b; O'Connor and Jokat, 2015a) (Fig. 1). Samples from the three sites yielded ages ~30 Myr younger than the extrapolated ages of the adjacent or underlying Walvis Ridge basement (Rohde et al., 2013b; O'Connor and Jokat, 2015a). One late-stage sample from the Rio Grande Rise, for which geochemical data is reported here (RC11-2RD1; Appendix B), is also 30 Myr younger than the basement (Rohde et al., 2013b).

Numerous small seamounts (most being flat-topped guyots) and small ridges are mounted on or lie next to the relatively flat Walvis Ridge crest (Fig. 1). On R/V Sonne cruises S0233 and S0234, three guyot-like seamounts (samples DR87, DR89 & DR90; Fig. 1) on the Walvis Ridge near the Namibian coast, one small plateau on the Valdivia Bank (TVG57) and one elongated guyot at the footwall south of the FFZ (DR75) were sampled by dredging (DR) or with the television (camera) grab (TVG; Fig. 1). In addition, six isolated volcanic structures (small cones, ridges and seamounts) on the adjacent oceanic crust (but near the Walvis Ridge) were also sampled by dredging (Fig. 1). Finally,

we report the composition of three oceanic crust samples, cored at DSDP Site 530 close to the northeastern Walvis Ridge (Fig. 1).

### **3. Analytical Methods**

The analytical procedures for the  $^{40}\text{Ar}/^{39}\text{Ar}$  dating and determination of the major elements, trace element concentration and radiogenic isotope ratios are described in Appendix A and all data are reported in Appendices B to E.

### **4. Results**

The dredge hauls during the S0233 and S0234 cruises (samples from S0233 are labeled without S0233 and from S0234 with “234” before the sample name in the following text) were conducted between ~1600 and 4100 m depths and mainly recovered (pillow) lava fragments, but also some volcanoclastic rocks. The aphyric to porphyritic (altered olivine  $\pm$  feldspar  $\pm$  pyroxene) lava fragments contain vesicles ranging between 0-30 vol. %, which are partly filled with calcite and/or chalcedony. The matrix consists of olivine  $\pm$  feldspar  $\pm$  pyroxene  $\pm$  apatite and Fe-Ti oxide phases.

#### **4.1 $^{40}\text{Ar}/^{39}\text{Ar}$ age dating**

Four  $^{40}\text{Ar}/^{39}\text{Ar}$  step-heating analyses were conducted on hydrofluoric acid-leached mineral separates (2-7 mg of plagioclase or K-feldspar) and hot hydrochloric/nitric acid-treated groundmass separates (3-3.5 mg) from 3 sample sites (DR80, DR87 and DR89; Figs. 2-3). Old submarine lavas can be affected by variable degrees of alteration. Therefore to ensure the best quality and geological meaningful ages, we monitored the Ca/K ratios to avoid mixed phase analyses, and the  $^{36}\text{Ar}/^{39}\text{Ar}$  or  $^{36}\text{Ar}/^{37}\text{Ar}$  alteration index values (AI, after Baksi, 2007) and % of atmospheric  $^{40}\text{Ar}$

( $^{40}\text{Ar}_{\text{atm}}$ ) values to determine the degree of alteration of the heating steps. In general, the  $^{40}\text{Ar}/^{39}\text{Ar}$  age spectra of the 6 samples were disturbed, with low-temperature steps yielding high AI values indicating the presence of alteration phases, higher %  $^{40}\text{Ar}_{\text{atm}}$  values and variable Ca/K ratios relative to the medium- to high-temperature steps. In addition to determining step-heating  $^{40}\text{Ar}/^{39}\text{Ar}$  plateau ages, inverse isochron ages were also calculated to confirm the plateau ages and to determine if the samples preserved atmospheric  $^{40}\text{Ar}/^{36}\text{Ar}$  ratios, without the presence of extraneous  $^{40}\text{Ar}$  components (Figs. 2-3). In all cases, the inverse isochron ages lie within  $2\sigma$  errors of the calculated plateau ages, and also yield initial  $^{40}\text{Ar}/^{36}\text{Ar}$  ratios that are within  $2\sigma$  errors of the atmospheric  $^{40}\text{Ar}/^{36}\text{Ar}$  ratio of 295.5. A detailed description of the  $^{40}\text{Ar}/^{39}\text{Ar}$  release spectra and inverse isochrons (Figs. 2-3) are reported in Appendix A. Note that all  $^{40}\text{Ar}/^{39}\text{Ar}$  ages are quoted with  $2\sigma$  errors, unless otherwise stated.

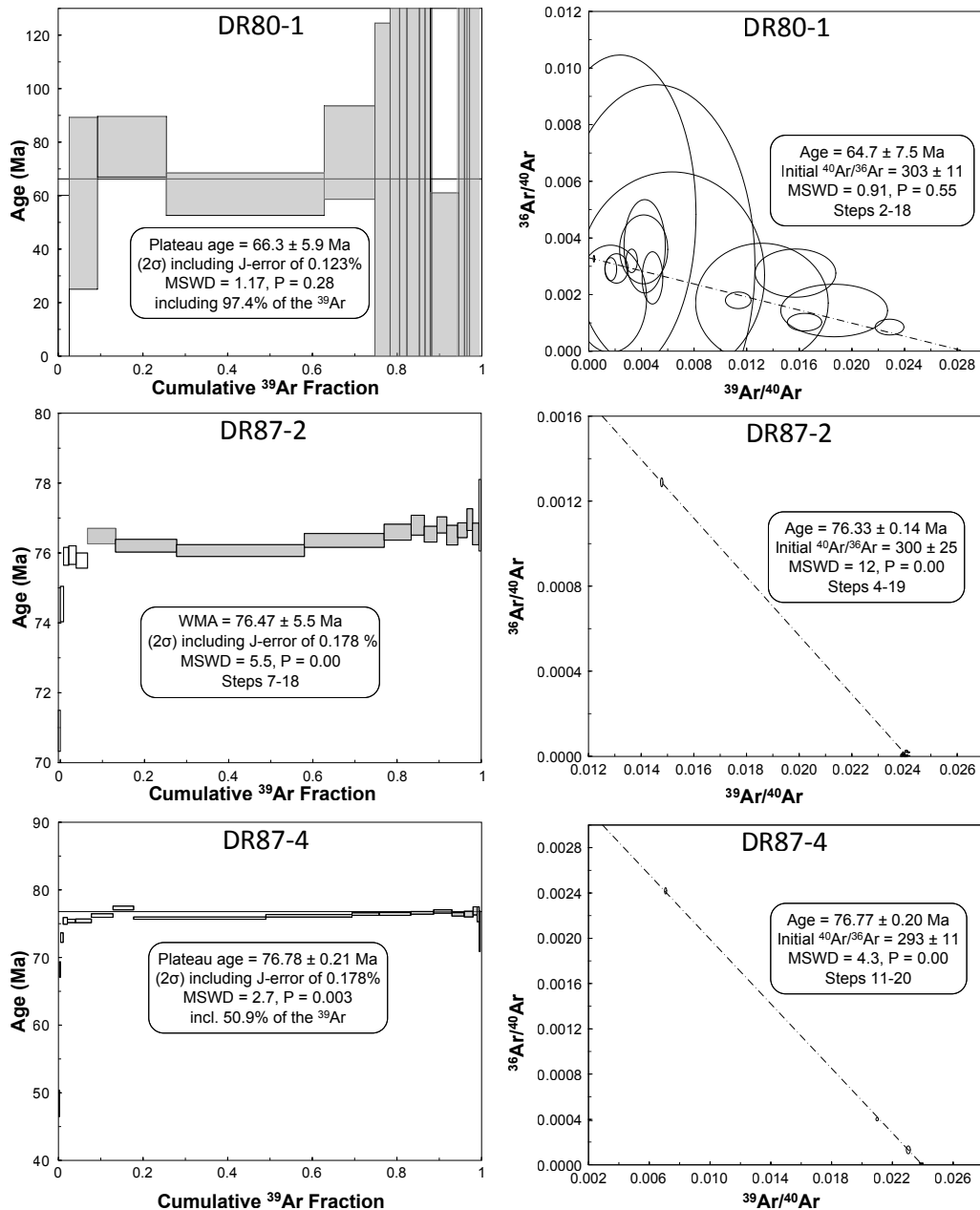


**Figure 2: Feldspar  $^{40}\text{Ar}/^{39}\text{Ar}$  step-heating age spectra and inverse isochrons of the studied late-stage samples from the Walvis Ridge. Sample DR80-1 was recovered from a seamount north of the Florianopolis Fracture Zone and dredge sites DR87 from a guyot on the northeastern Walvis Ridge. Plateau steps are shown in gray and rejected steps in white, with heights of the step age boxes reflecting  $2\sigma$  errors. The elliptical errors on the inverse isochron points are shown at 63.3% ( $1\sigma$ ) confidence level. Abbreviations: MSWD = Mean Square Weighted Deviation, WMA = Weighted Mean Age and P = Probability. Note, DR80-1 (with an extremely low weight %  $\text{K}_2\text{O}$  value of 0.02) yielded a disturbed age spectrum resulting in large analytical uncertainties and should therefore only be treated as an estimate. DR87-2 does not yield a plateau age and has a statistically poor inverse isochron age of  $76.47 \pm 5.5$  Ma (95% confidence,  $2\sigma$ ) due to clustering of analyses near the radiogenic  $^{40}\text{Ar}$  x-axis. Low %  $^{40}\text{Ar}_{\text{atm}}$  and  $^{36}\text{Ar}/^{39}\text{Ar}$  AI values in DR87-2 indicate the presence of fresh or very fresh K-feldspar (Appendix C), which yielded a statistically invalid weighted mean age of  $76.47 \pm 0.17$  Ma (steps 7-18, MSWD = 5.5, P = 0.00).**

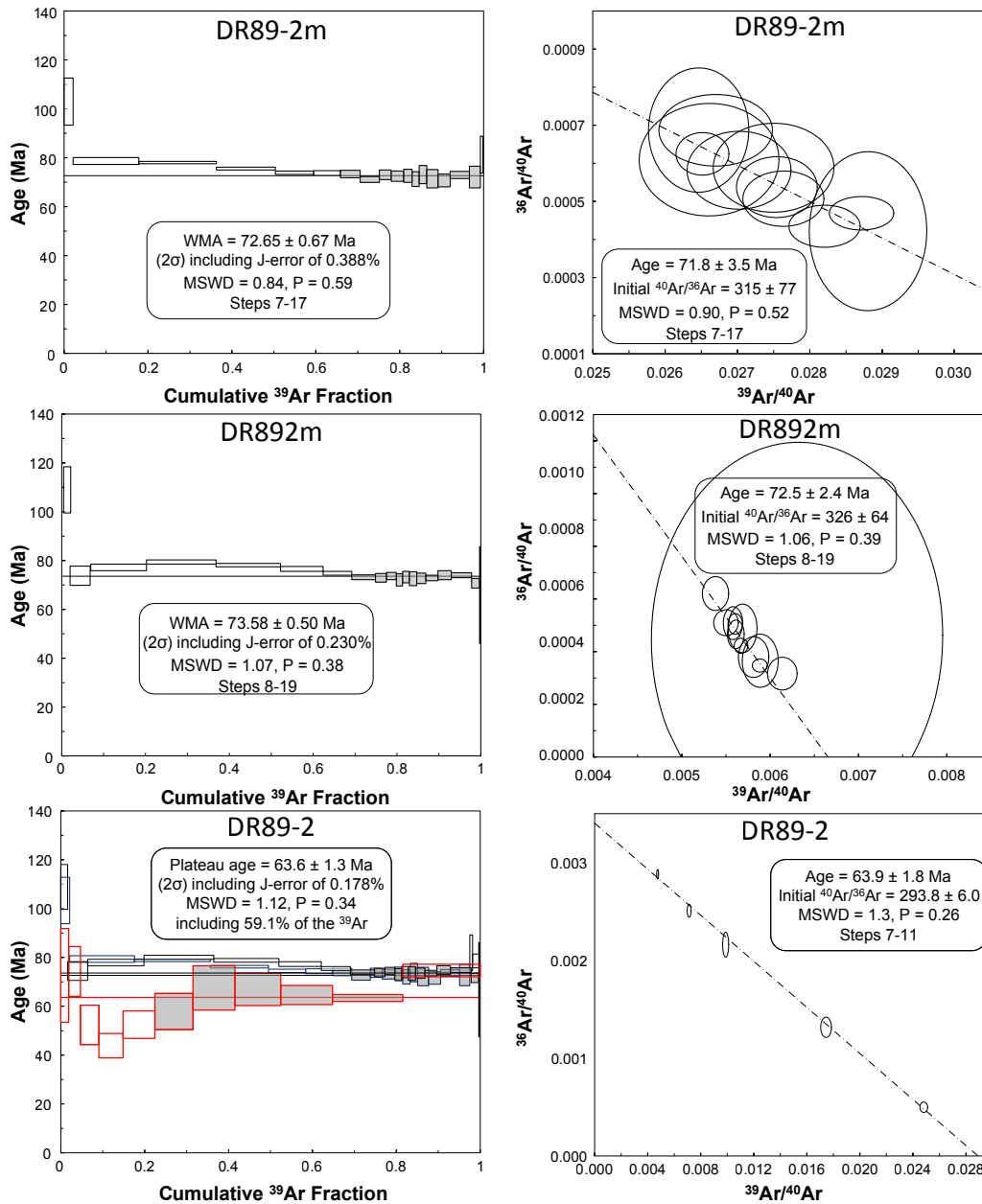


**Figure 3:**  $^{40}\text{Ar}/^{39}\text{Ar}$  step-heating age spectra and inverse isochrons from two groundmass (top 2 sets of figures, DR89-2m and DR892m) and one plagioclase (bottom set of figures; DR89-2) analysis. All 3 step-heating analyses were derived from one sample (DR89-2) collected from dredge site DR89, which is located on the northeastern Walvis Ridge, close to site DR87 (Fig. 1). The plagioclase age spectra (DR89-2, red boxes and solid red line indicating the plateau age) also shows the two groundmass age spectra (DR89-2m and DR892m). The last and freshest heating step of plagioclase sample DR89-2 yielded an age of  $74.71 \pm 2.7$  Ma, which agrees within  $2\sigma$  errors with the weighted mean age and inverse isochron ages of the two DR89-2 groundmass separate splits. Abbreviations are reported in Fig. 2.

## 4.2 Geochemistry

Despite sampling the freshest parts of the samples by careful handpicking under a binocular microscope (size fraction 0.5-1 mm), variable amounts of secondary overprint are inevitable in many of the submarine rocks, with 20 out of the 29 samples showing loss on ignition (LOI's) between 5-12 wt.%. Therefore, we focus on immobile elements, such as Ti, Zr, Y, Nb, Hf, Th and REE, and radiogenic isotope data, which are considered to be relatively resistant to alteration processes. In order to minimize contamination of the chips during crushing and picking, we leached 150-200 mg whole-rock chips in 2N HCl at 70°C for one hour to remove surface contaminants. The Nd-Hf-Pb isotope systems are relatively resistant to low temperature seawater alteration, whereas the Sr isotope ratios in older seafloor rocks are commonly elevated by addition of, or exchange with, seawater Sr. Additional Sr isotope analyses were carried out on sample powders leached with 6N HCl at 150 °C for 3 days in an attempt to remove possible seawater alteration effects more thoroughly than the mild acid treatment of chips. As a result, 21 out of 24 samples produced lower  $^{87}\text{Sr}/^{86}\text{Sr}$  ratios for the leached powders compared to the chips, while three powder samples yielded slightly higher ratios (Appendix B). Therefore, the lowest  $^{87}\text{Sr}/^{86}\text{Sr}$  values obtained from both the powder and chip samples are presumed to be closest to the primary magmatic values, and are thus used for petrogenetic interpretations. Uptake of U (from seawater) is also common in seafloor samples, which can affect the correction for radiogenic ingrowth of lead isotopes, particularly  $^{206}\text{Pb}$ . On the other hand, thorium (i.e.,  $^{232}\text{Th}$  is the parent of  $^{208}\text{Pb}$ ) is relatively immobile during seafloor alteration. If Pb has not been affected by hydrothermal alteration and the U/Pb isotope systems have not been reopened by tectonic or magmatic processes, the age correction using the measured U/Pb ratios on unleached powders will yield initial  $^{206}\text{Pb}/^{204}\text{Pb}$  and  $^{207}\text{Pb}/^{204}\text{Pb}$  ratios close to those of

the unaltered lavas. The reasonably good correlations of initial  $^{208}\text{Pb}/^{204}\text{Pb}$  vs. initial  $^{206}\text{Pb}/^{204}\text{Pb}$  ( $R^2=0.84$ ) and initial  $^{207}\text{Pb}/^{204}\text{Pb}$  ( $R^2=0.87$ , both not shown) calculated with measured U concentrations from unleached powder are better than those from the measured isotope ratios, suggesting that the age corrections produce reasonable initial values.



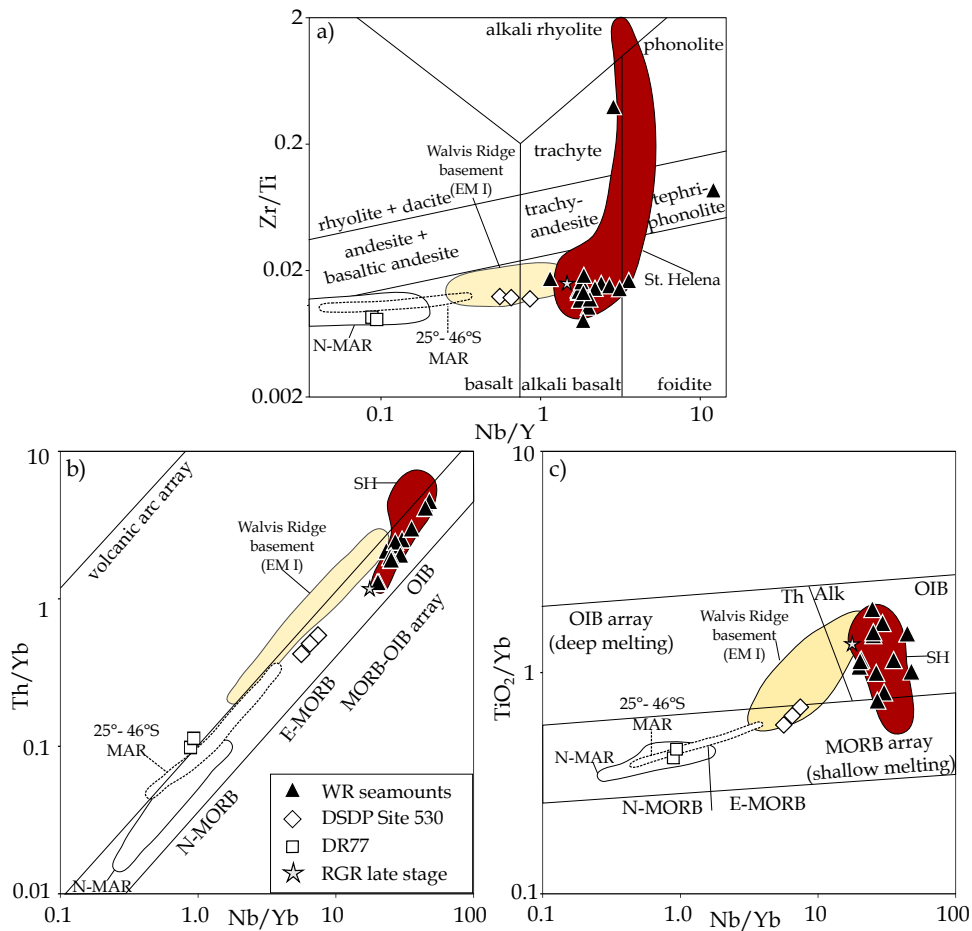


**Figure 4: Rock classification using immobile incompatible element ratios (a) Nb/Y vs. Zr/Ti (Pearce, 1996) b) Nb/Y vs. Th/Yb and c) Nb/Y vs. TiO<sub>2</sub>/Yb (both from Pearce, 2008) of the studied Walvis Ridge rocks. Note, only samples with MgO values >2wt.% are shown. For comparison, the fields for normal mid-Atlantic Ridge (N-MAR) basalts (with La/Yb<1 and La/Sm<1.5), mid-Atlantic Ridge between 25° and 46°S latitudes (25°-46°S MAR), Walvis Ridge EM I-type basement with Gough-type composition and St. Helena HIMU lavas (Chaffey et al., 1989; Willbold and Stracke, 2006; Kawabata et al., 2011) are shown. The Gough-type composition of the Walvis Ridge comprises all dredged samples from Rohde et al. (2013a) and Hoernle et al. (2015) and lavas from DSDP Site 525 (Salters and Sachi-Kocher, 2010; Rohde et al., 2013a). Abbreviations: Alk=alkaline, Th=tholeiitic. Literature data are taken from GEOROC Database (<http://georoc.mpch-mainz.gwdg.de/georoc/>). MAR basalts are taken from the compilation of Class, C. and Lehnert, K. (2012): PetDB Expert MORB (Mid-Ocean Ridge Basalt) Compilation. EarthChem Library. <http://dx.doi.org/10.1594/IEDA/100060>).**

According to discrimination schemes that only use highly alteration-immobile elements such as Nb/Y vs. Zr/Ti (Pearce, 1996), the majority of rocks are alkali basalts, but rare tholeiitic basalts (DR77 and DSDP-Site 530), a tephriphonolite (DR45-1) and a trachyte (DR87-4) were also recovered (Fig. 4a). In plots of immobile incompatible elements, such as Nb/Yb against  $(\text{Th}, \text{TiO}_2)/\text{Yb}$  (Fig. 4b-c), the studied samples fall within the MORB – OIB (ocean island basalt) array, defined by Pearce (2008), with the samples from the seamounts of the Walvis Ridge and Rio Grande Rise showing the highest OIB affinities (similar to St. Helena), whereas DSDP Site 530 basalts show EMORB- and DR77 basalts NMORB-like compositions (Fig. 4b-c). The elevated  $\text{TiO}_2/\text{Yb}$  ratios, combined with steep inverse trends for heavy rare earth elements (HREE) in incompatible multi-element diagrams (Fig. 5a), indicate that the seamount melts were derived from deep melting within the garnet stability field. In contrast, samples from dredge site DR77 are characterized by tholeiitic NMORB-type compositions (Fig. 4) and flat HREE patterns (Fig. 5a), consistent with derivation at shallower depths (within the spinel stability field) compared to the other Walvis seamounts. Lavas from DSDP Site 530 show slightly fractionated HREE ratios (Fig. 5b).

The alkaline Walvis seamount lavas have relatively uniform incompatible-element patterns, displaying greater enrichment in highly incompatible elements compared to less compatible elements and HREE fractionation, as noted above (Fig. 5a). Compared to the Walvis Ridge EM I-type basement, the seamount lavas have a positive Nb-Ta anomaly relative to Th and La and a more pronounced negative Pb anomaly, similar to HIMU lavas from St. Helena Island. Lavas from the tholeiitic oceanic crust at DSDP Site 530 and the late-stage sample from the Rio Grande Rise have similar incompatible-element patterns (e.g. positive Nb-Ta anomaly and negative Pb anomaly), but have less incompatible element enrichment (Fig. 5). The tholeiitic basalts from

sample site DR77 (seamount north of the Florianopolis-Fracture-Zone; Fig. 1) display relatively depleted incompatible-element patterns similar to NMORB. In summary, Site 530, Walvis seamount and Rio Grande Rise late-stage lavas have distinct geochemical compositions compared to the basement of the Walvis Ridge, but their multi-element patterns are similar to those of St. Helena HIMU-type lavas, displaying high (>1) primitive-mantle normalized (Nb, Ta)/(Th, La) ratios.

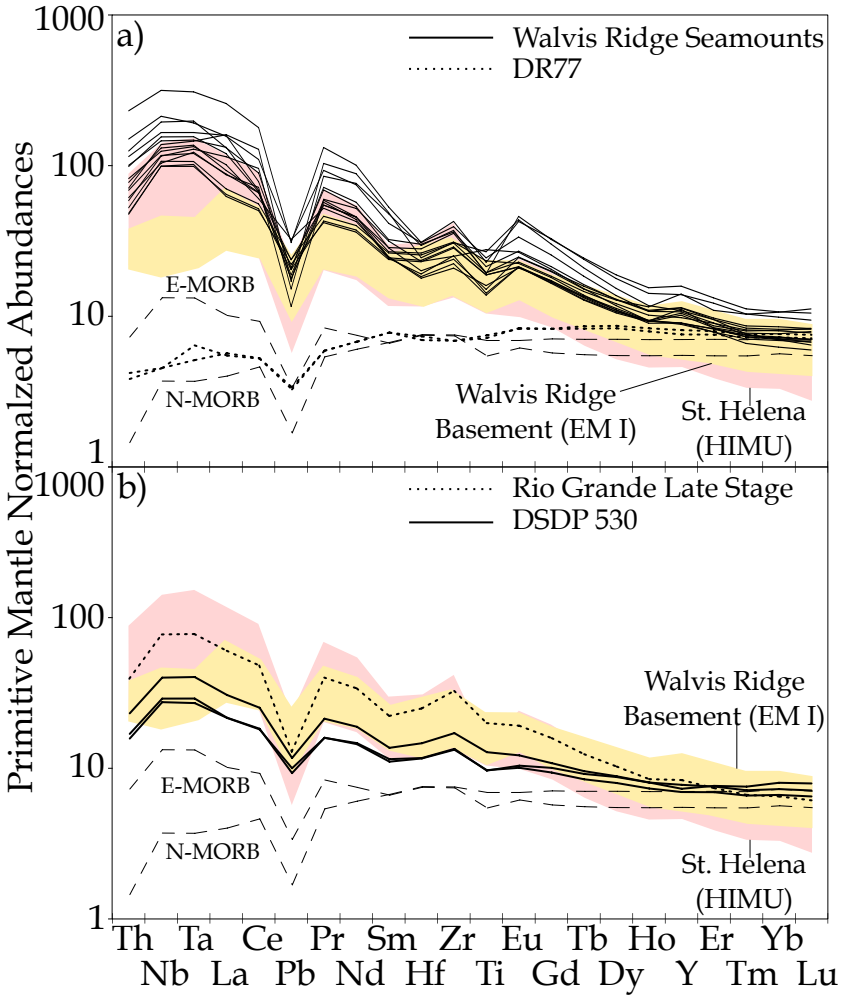


**Figure 5: Normalized incompatible element diagrams of a) late-stage lavas from the Walvis Ridge seamounts, which have incompatible-element patterns distinct from Walvis Ridge basement lavas, but are similar to St. Helena lavas (e.g., enrichment in Nb and Ta relative to Th and LREEs), and b) DSDP Site 530 (oceanic crust north of the Florianopolis Fracture Zone (FFZ; Fig. 1), and late-stage volcanism from the Rio Grande Rise compared to the Walvis Ridge basement (described in detail in Figure 4), St. Helena lavas, and NMORB and EMORB from Sun and McDonough (1989). Concentrations of the elements are normalized to primitive-mantle after Hofmann (1988). Samples with MgO concentrations of < 2 wt. % are not shown. Literature data are reported in Figure 4.**

In order to evaluate the isotope data for the samples with large differences in age, we calculated initial isotope ratios and projected them to a common age of 60 Ma. Since we compare our data to end member type localities (DM - EM I - HIMU), which derive from distinct sources with characteristic trace element concentrations, we projected the initial isotope ratios to 60 Ma with proposed source parent/daughter ratios (Stracke et al., 2003; Workman and Hart, 2005; Willbold and Stracke, 2006). Based on the initial isotope ratios, we assume the HIMU source composition for samples with  $^{206}\text{Pb}/^{204}\text{Pb}_i > 19$ , the EM I source composition for lavas with  $\Delta 7/4_i > 10$ ,  $\Delta 8/4_i > 50$ ,  $^{87}\text{Sr}/^{86}\text{Sr}_i > 0.704$  and  $^{143}\text{Nd}/^{144}\text{Nd}_i < 0.5126$ , and the DM source for lavas that do not fulfill these criteria. The calculated initial isotope ratios were projected to a common age of 60 Ma using the following source concentrations (all in ppm) to determine parent-daughter ratios: (1) for HIMU, Sr=80.270, Rb=0.568, Sm=2.677, Nd=7.4549, U=0.028, Th=0.088, Pb=0.092, Lu=0.449 and Hf=1.781, (2) for EM I, Sr=21.751, Rb=0.443, Sm=0.480, Nd=1.421, U=0.012, Th=0.0592, Pb=0.0876, Lu=0.095 and Hf=0.347 (Stracke et al., 2003; Willbold and Stracke, 2006), and (3) for DM, Rb=0.050, Sr=7.664, Sm=0.239, Nd=0.581, U=0.003, Th=0.008, Pb=0.018, Lu=0.058 and Hf=0.157 (Workman and Hart, 2005).

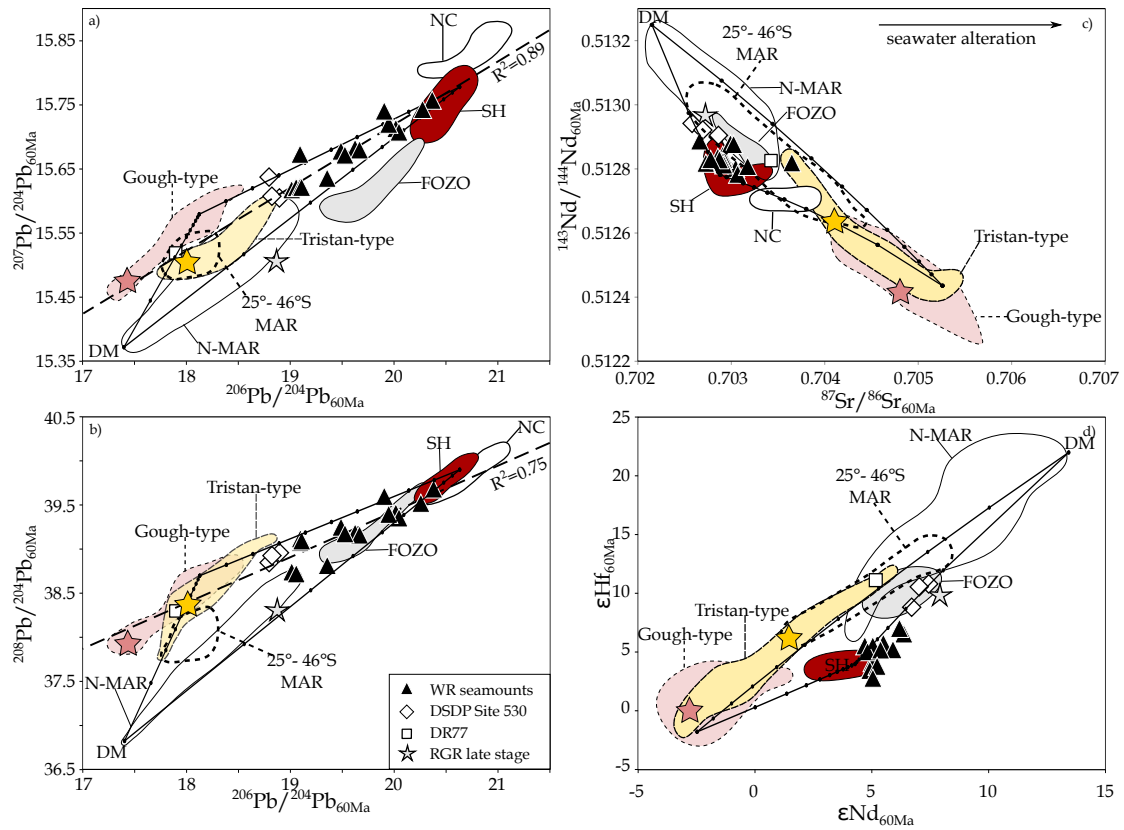


**Figure 6: Initial isotope ratios for the (a) uraniumogenic and (b) thorogenic Pb isotope correlation diagrams, (c)  $^{87}\text{Sr}/^{86}\text{Sr}_{60\text{Ma}}$  vs.  $^{143}\text{Nd}/^{144}\text{Nd}_{60\text{Ma}}$ , and (d)  $\epsilon\text{Nd}_{60\text{Ma}}$  vs.  $\epsilon\text{Hf}_{60\text{Ma}}$  plots projected to 60 Ma using proposed source parent/daughter ratios for the studied samples (see chapter Results section). Note that seawater alteration of lavas can raise their  $^{87}\text{Sr}/^{86}\text{Sr}$  ratios. Lavas from the Tristan-Gough hotspot system are divided into Tristan-type, including DSDP Site 527 & 528 (Salters and Sachi-Kocher, 2010; Rohde et al., 2013a), the Tristan-subtrack (Rohde et al., 2013a; Hoernle et al., 2015) and Tristan Islands (Le Roex et al., 1990; Cliff et al., 1991), and Gough-type compositions, comprising the Gough-type Walvis Ridge basement (defined in Figure 4; Salters and Sachi-Kocher, 2010; Rohde et al., 2013a; Hoernle et al., 2015), Gough-subtrack (Rohde et al., 2013a; Hoernle et al., 2015) and Gough Island (Le Maitre, 1962; Class and le Roex, 2008). Note, the seamounts on the Walvis Ridge overlie basement with Gough-type composition (Rohde et al., 2013a; Hoernle et al., 2015). The average composition of DSDP Sites are: reddish star = DSDP Site 525 and yellow star = DSDP Site 527 & 528. For comparison, fields from the Normal-Mid-Atlantic Ridge with  $\text{La}/\text{Yb} < 1$  and  $\text{La}/\text{Sm} < 1.5$  (N-MAR), 25°-46°S MAR, St. Helena (Chaffey et al., 1989; Reisberg et al., 1993; Willbold and Stracke, 2006; Kawabata et al., 2011) and FOZO after Stracke et al. (2005) are shown. The dashed black line on the Pb-isotope plots is the calculated regression line for the Walvis Ridge seamount samples excluding site DR77 and DSDP Site 530 lavas. The solid black lines are calculated mixing lines with average St. Helena HIMU, EM I (SO233 DR3-1; Hoernle et al., 2015) and the most depleted sample from the MAR (CHRR188-016-101, from the MORB data compilation). Note that the Sr and Nd isotope data are estimated for Dicker Willem carbonatites (Nambia Carbonatites=NC) based on rocks associated with this carbonatite complex. Abbreviations: WR=Walvis Ridge, RGR=Rio Grande Rise, SH=St. Helena.**

The lavas from the Walvis Ridge seamounts have relatively restricted  $^{143}\text{Nd}/^{144}\text{Nd}_{60\text{Ma}}$  (0.5128-0.5129),  $^{87}\text{Sr}/^{86}\text{Sr}_{60\text{Ma}}$  (0.7027-0.7031; excluding two seawater altered samples with  $^{87}\text{Sr}/^{86}\text{Sr}_{60\text{Ma}}$  isotope ratios of 0.7036 and 0.7048) and  $^{176}\text{Hf}/^{177}\text{Hf}_{60\text{Ma}}$  ratios (0.2828-0.2829), but show relatively large variations in  $^{206}\text{Pb}/^{204}\text{Pb}_{60\text{Ma}}$  (19.01-20.37),  $^{207}\text{Pb}/^{204}\text{Pb}_{60\text{Ma}}$  (15.62-15.76) and  $^{208}\text{Pb}/^{204}\text{Pb}_{60\text{Ma}}$  ratios (38.72-39.67; Fig. 6). Samples from dredge site DR77 have more radiogenic  $^{87}\text{Sr}/^{86}\text{Sr}_{60\text{Ma}}$  (0.7034) and  $^{176}\text{Hf}/^{177}\text{Hf}_{60\text{Ma}}$  (0.2830) ratios, similar  $^{143}\text{Nd}/^{144}\text{Nd}_{60\text{Ma}}$  (0.5128) ratios, but less radiogenic  $^{206}\text{Pb}/^{204}\text{Pb}_{60\text{Ma}}$  (18.87),  $^{207}\text{Pb}/^{204}\text{Pb}_{60\text{Ma}}$  (15.52) and  $^{208}\text{Pb}/^{204}\text{Pb}_{60\text{Ma}}$  ratios (38.31; Fig. 6). DSDP Site 530 samples plot close to the enriched end of the Normal Mid-Atlantic Ridge (N-MAR) array for latitudes north of 25°S with  $\text{La}/\text{Yb} < 1$  and  $\text{La}/\text{Sm} < 1.5$  (Fig. 6). The DR77 samples with NMORB-type incompatible element compositions plot consistently within or adjacent to the 25°-46°S MAR field between the N-MAR and Walvis Ridge basement (Gough-type) compositions (Fig. 6).

The Walvis Ridge seamount lavas form a trend in Pb-isotope space between St. Helena HIMU and the DSDP Site 530 and DR77 samples (Fig. 6). The Rio Grande Rise late-stage sample lies near the enriched end of the N-MAR field and seems totally unrelated to the samples from the east side of the Mid-Atlantic Ridge (Fig. 6). This sample is characterized by lower  $^{207}\text{Pb}/^{204}\text{Pb}$  and  $^{208}\text{Pb}/^{204}\text{Pb}$  ratios for a given  $^{206}\text{Pb}/^{204}\text{Pb}$  isotope ratio compared to the Walvis seamounts (Fig. 6), indicating derivation from a different source than the Walvis samples, i.e., from the upper mantle MORB source.

## 5. Discussion

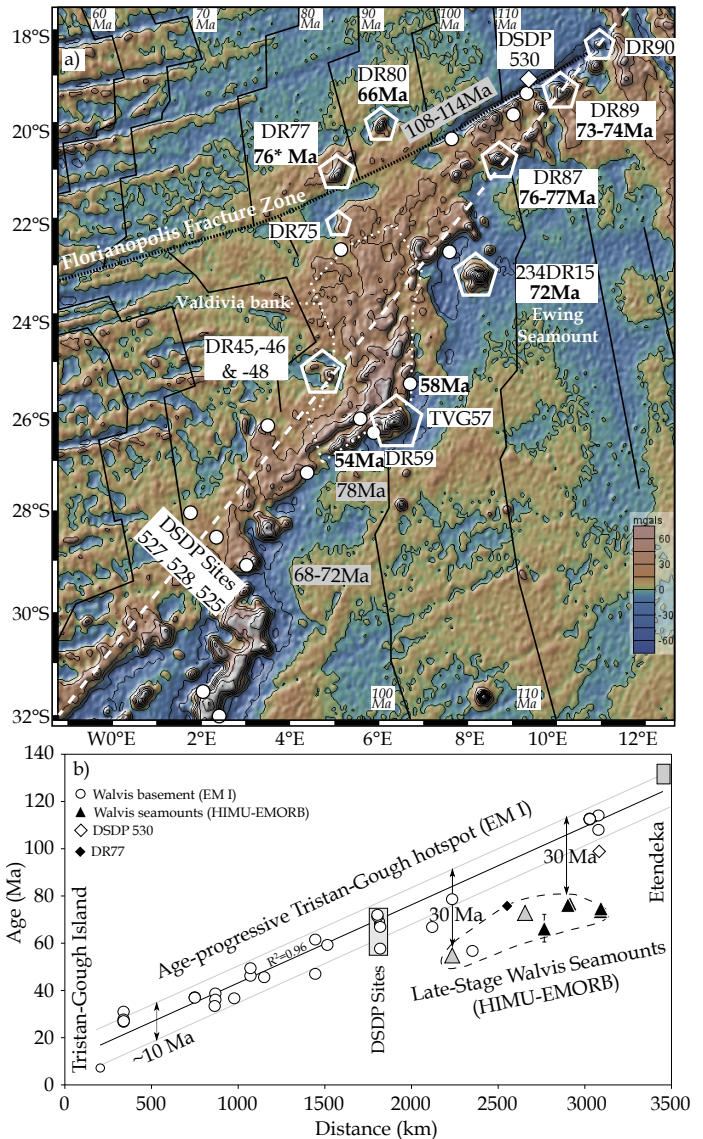
### 5.1 Morphology and age of seamounts from the Walvis Ridge

The broad Walvis Ridge crest is covered and flanked by numerous seamounts and ridge-like structures, which were proposed to form the major trace of the Tristan-Gough hotspot track (Fig. 7a; O'Connor and Jokat, 2015a). However, several lines of evidence suggest that the majority of these seamounts are considerably younger than the underlying or adjacent Walvis Ridge basement and thus post-date the Tristan-Gough hotspot volcanism. Bathymetric data collected during the S0233 cruise reveal that the Walvis Ridge crest, including Valdivia Bank, is generally flat, most likely reflecting erosion of the former subaerially-exposed ridge to sea level, followed by subsidence related to lithospheric cooling (Hoernle et al., 2014). Seamounts from the Walvis Ridge dated with the  $^{40}\text{Ar}/^{39}\text{Ar}$  method range in age from  $76.78 \pm 0.2$  Ma near the Namibian coast to  $54.80 \pm 0.1$  Ma at the southern end of the Valdivia Bank (this study and Rohde et al., 2013b) and thus formed 20 to 40 Myr after the formation of the underlying or nearby Walvis Ridge basement (Fig. 7), confirming that they are considerably younger than the age-progressive Walvis Ridge.

The original oceanic crust north of the Florianopolis-Fracture-Zone (FFZ), a former transform fault cutting the northeastern end of the Walvis Ridge, has been transferred to the South American Plate and is now located offshore South America (e.g., Pérez-Díaz and Eagles, 2014). Magnetic data (Müller et al., 1997) and the oldest sediments at DSDP Site 530 (Hay et al., 1984), both north of the FFZ, indicate that the oceanic crust presently adjacent to the NE Walvis Ridge is at least 5 Ma younger than the extrapolated age of the adjacent Walvis Ridge basement (i.e., 114-93 Ma; Fig. 7a;  $^{40}\text{Ar}/^{39}\text{Ar}$  age data from Rohde et al., 2013b). Seamount sample DR80-1 (with a  $^{40}\text{Ar}/^{39}\text{Ar}$  age estimate of  $\sim 66$  Ma) suggests an  $\sim 30$  Ma younger age for this seamount

(at least for the sampled lava) than the neighboring Walvis Ridge basement. Another guyot sampled at site DR77 located north of the FFZ, lies ~200 km further ESE from DR80 (Fig. 7a), has an estimated age of ~76 Ma based on the height of its erosional platform.

**Figure 7: a) Free-air gravity field map of the Walvis Ridge (Sandwell and Smith, 2009). Pentagons show the sample sites of cruises S0233 and S0234, white diamond displays DSDP Site 530 and white circles indicate EM I-type basement sample sites from the literature (Richardson et al., 1982; Salters and Sachi-Kocher, 2010; Rohde et al., 2013a; Rohde et al., 2013b; Hoernle et al., 2015; O'Connor and Jokat, 2015a, b). The  $^{40}\text{Ar}/^{39}\text{Ar}$  ages with white backgrounds indicate HIMU-EMORB-type volcanism on or near the Walvis Ridge, and the ages with grey backgrounds indicate EM I-type basement samples. The white dashed line represents the proposed hotspot track. Isochrons (black lines) determined from magnetic data for the oceanic crust are taken from Müller et al. (1997). (b) Distance to the active volcanic islands (Tristan and Gough) versus  $^{40}\text{Ar}/^{39}\text{Ar}$  ages for the Tristan-Gough hotspot track and Rio Grande Rise. Sample sites were projected orthogonally to the proposed hotspot track. Black triangles represent new  $^{40}\text{Ar}/^{39}\text{Ar}$  age data, grey triangles represent HIMU-EMORB compositions (literature data), and white circles EM I-type compositions from literature data (Rohde et al., 2013b; O'Connor and Jokat, 2015a). The black diamond represents site DR77. Its age estimate is based on the subsidence history and depth of the erosion platform compared to the  $^{40}\text{Ar}/^{39}\text{Ar}$  of site DR80. Since the flat-top of seamount DR77 is ~600 m deeper than the flat-top of the nearby seamount sampled at site DR80 (Hoernle et al., 2014), the DR77 seamount has to be older than the seamount sampled at DR80. We estimate that the age for DR77 is ~10 Ma older than the age for DR80 (~66 Ma) to account for the deeper depth of this seamount's erosional plateau, yielding a DR77 age estimate of ~76 Ma.**





Three en-echelon ridge-like seamounts westward of the Valdivia Bank (DR45, -46 and -48) are located on oceanic crust, which was formed after the separation and westward migration of the Rio Grande Rise between 60-80 Ma (O'Connor and Jokat, 2015b). Using the age progression for the Walvis Ridge basement formation (Fig. 7b), the southwestern part of the ridge (at the same latitude as the DR45, -46 and -48 seamounts) should yield ages between 85-90 Ma (Rohde et al., 2013b; O'Connor and Jokat, 2015a) and therefore the ridge-like seamounts must be at least 5-30 Myr younger than the neighboring Walvis Ridge basement. Moreover, a  $^{40}\text{Ar}/^{39}\text{Ar}$  age of  $72.80 \pm 1.62$  Ma has been reported from the Ewing Seamount (sample S084-86DS-3; O'Connor and Jokat, 2015a), which is located 100 km east of the central Walvis Ridge (Fig. 7a). We therefore assume a similar age for our dredge site S0234 DR15 from the Ewing Seamount, which is  $\sim 30$  Myr younger than the estimated age of 100 Ma for the adjacent portion of the Walvis Ridge. Therefore, our new and published data indicate that all these isolated volcanic structures are at least 5-30 Myr younger than the underlying or nearby EM I-type Walvis Ridge basement.

In summary, the available morphological and age data indicate that the seamounts on or near the NE-end of the Walvis Ridge (Fig. 7) are considerably younger than the underlying Walvis Ridge basement. Since late-stage volcanism generally occurs within a few million years after the main volcanic phase at other hotspot tracks (e.g., Clague and Dalrymple, 1987; White and Duncan, 1996; Geldmacher et al., 2006; Garcia et al., 2010), the long  $\sim 20$ -40 Myr volcanic hiatus at the Walvis Ridge (based on all age dated structures; Fig. 7) indicates that these post-erosional seamounts are unlikely to be related to the Tristan-Gough mantle plume. Notably, such late-stage volcanism has only been found on and to both sides of the Walvis Ridge, but not in the Guyot Province thus far.

## 5.2 Compositional variation of the Walvis Ridge seamounts

We will now evaluate which source components are involved in the late-stage volcanism on or near the Walvis Ridge. The observed crude linear correlations of the seamount data on the radiogenic isotope diagrams can be explained by two-component mixing of a high- $\mu$  (high  $^{206}\text{Pb}/^{204}\text{Pb}_{60\text{Ma}}$ ) with a low- $\mu$  component (low  $^{206}\text{Pb}/^{204}\text{Pb}_{60\text{Ma}}$ ). The seamount lavas from the Walvis Ridge with high  $^{206}\text{Pb}/^{204}\text{Pb}_{60\text{Ma}}$  ratios (Fig. 6) are characterized by (1) alkaline compositions (high (Nb, Th, Ti)/(Yb, Y) ratios; Figs. 4 & 5), (2) enriched incompatible trace element concentrations relative to less incompatible-elements with positive Nb-Ta anomaly in normalized multi-element patterns (high (Nb, Ta)/(Th, La) ratios; Fig. 5), (3) very radiogenic  $^{207}\text{Pb}/^{204}\text{Pb}_{60\text{Ma}}$  ratios (Fig. 6), and (4) Sr-Nd-Hf isotope ratios plotting below the Tristan-Gough-MORB array (Fig. 6). Based on these characteristics, potential high- $\mu$  mixing end members could be the proposed “common” or “prevalent” mantle component (e.g., FOZO or PREMA; Zindler and Hart, 1986; Hart et al., 1992; Stracke et al., 2005) or St. Helena HIMU, which represents the type locality for the Atlantic HIMU end member (e.g., Zindler and Hart, 1986). FOZO, as defined according to Stracke et al. (2005), differs from HIMU in having overall lower Pb isotope ratios and higher projected  $^{208}\text{Pb}/^{204}\text{Pb}$ ,  $^{87}\text{Sr}/^{86}\text{Sr}$  and  $^{176}\text{Hf}/^{177}\text{Hf}$  ratios, but similar  $^{143}\text{Nd}/^{144}\text{Nd}$  ratios with  $^{206}\text{Pb}/^{204}\text{Pb} > 19$  (Figs. 6 & 8). The late-stage lavas from the Walvis Ridge clearly have higher  $^{207}\text{Pb}/^{204}\text{Pb}_{60\text{Ma}}$  ratios, and lower  $^{143}\text{Nd}/^{144}\text{Nd}_{60\text{Ma}}$ ,  $^{176}\text{Hf}/^{177}\text{Hf}_{60\text{Ma}}$  ratios, plus trend to lower  $^{87}\text{Sr}/^{86}\text{Sr}_{60\text{Ma}}$  at a given  $^{206}\text{Pb}/^{204}\text{Pb}_{60\text{Ma}}$  ratio, compared to FOZO. In addition, the samples with the most radiogenic  $^{206}\text{Pb}/^{204}\text{Pb}_{60\text{Ma}}$  isotopic ratios overlap the St. Helena HIMU end member composition in Sr-Nd-Hf and Pb isotopic ratios, suggesting that St. Helena HIMU and not FOZO (regardless of which definition is used, see summary in Stracke et al., 2005) serves as the high- $\mu$  mixing component (Figs. 6 & 8).

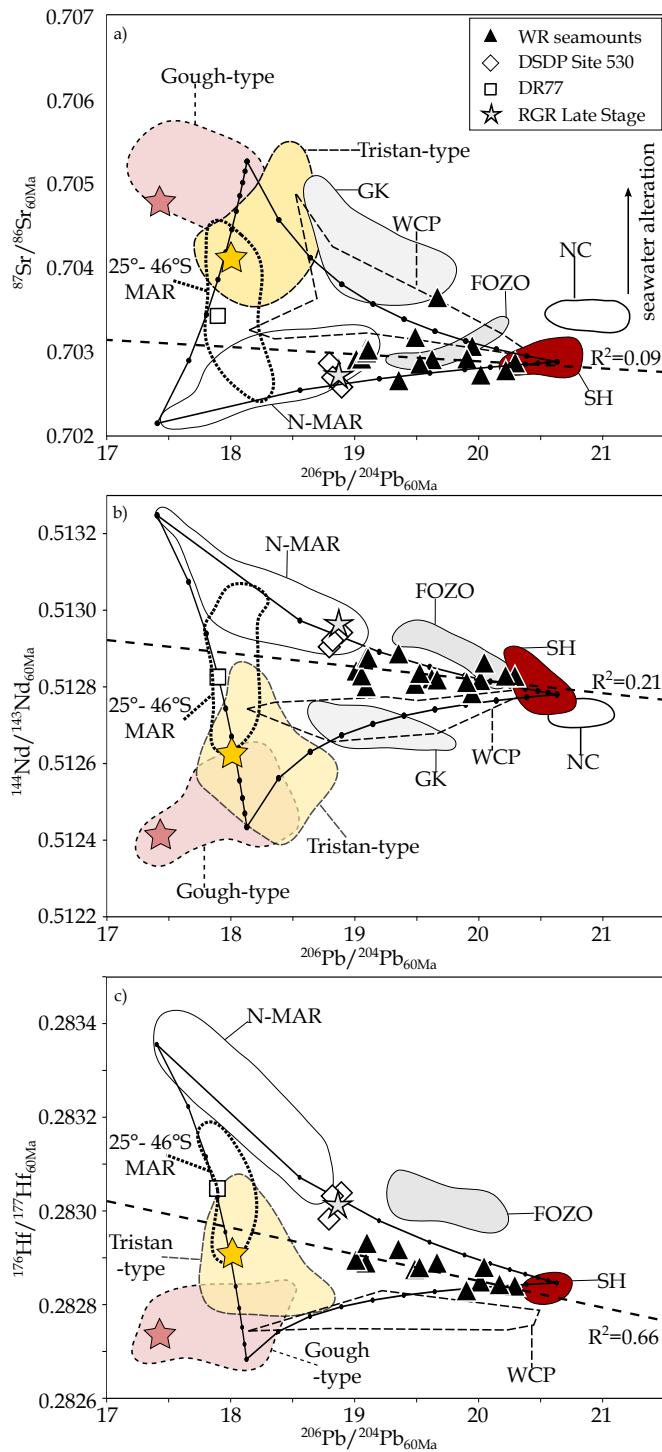


**Figure 8: Source-corrected to 60 Ma initial isotope ratios for the studied samples on  $^{206}\text{Pb}/^{204}\text{Pb}_{60\text{Ma}}$  vs (a)  $^{87}\text{Sr}/^{86}\text{Sr}_{60\text{Ma}}$ , (b)  $^{143}\text{Nd}/^{144}\text{Nd}_{60\text{Ma}}$  and (c)  $^{176}\text{Hf}/^{177}\text{Hf}_{60\text{Ma}}$  isotope diagrams. See Figure 6 caption for mixing line calculation, abbreviations and data sources. Dashed black line shows the linear regression line of the late-stage lavas from the Walvis Ridge (excluding lavas from DR77 and DSDP Site 530). Gough-type and Tristan-type lavas are defined as in Figure 6. The average composition of DSDP Site compositions are: reddish star = DSDP Site 525 and yellow star = DSDP Site 527 & 528. Note that seawater alteration of lavas can raise their  $^{87}\text{Sr}/^{86}\text{Sr}$  ratios and thus  $^{87}\text{Sr}/^{86}\text{Sr}$  ratios should be considered to be maximum values. Data for the age progressive lineaments in southeast Africa includes: GK=Gibeon Kimberlites (Davies et al., 2001; Luchs et al., 2013) and associated Dicker Willem carbonatites (NC; Cooper and Reid, 1998; Cooper and Reid, 2000) and WCP= Western Cape province (Rogers et al., 1992; Janney et al., 2002). Literature data is taken from GEOROC Database (<http://georoc.mpch-mainz.gwdg.de/georoc/>) and are reported in detail in Figure 6.**

Compared to the high- $\mu$  end member, the low- $\mu$  end member of the late-stage Walvis seamount samples is characterized by low (Nb, Th, Ti)/Yb ratios (Figs. 4 & 5), and less radiogenic Pb isotope compositions, but more radiogenic Nd and Hf isotope ratios (Fig. 6). Although the late-stage samples trend towards the DSDP Site 527 & 528 (Tristan-type EM I) composition on the  $^{206}\text{Pb}/^{204}\text{Pb}_{60\text{Ma}}$  vs. a)  $^{207}\text{Pb}/^{204}\text{Pb}_{60\text{Ma}}$ , b)  $^{208}\text{Pb}/^{204}\text{Pb}_{60\text{Ma}}$  and c)  $^{176}\text{Hf}/^{177}\text{Hf}_{60\text{Ma}}$  isotope diagrams (Figs. 6 & 8), they do not trend

towards either Gough- or Tristan-type EM I (Tristan-Gough hotspot track compositions, including DSDP Sites 527 and 528 samples) on the  $^{87}\text{Sr}/^{86}\text{Sr}_{60\text{Ma}}$  vs.  $^{143}\text{Nd}/^{144}\text{Nd}_{60\text{Ma}}$ ,  $\epsilon\text{Nd}_{60\text{Ma}}$  vs.  $\epsilon\text{Hf}_{60\text{Ma}}$  and  $^{206}\text{Pb}/^{204}\text{Pb}_{60\text{Ma}}$  vs.  $^{87}\text{Sr}/^{86}\text{Sr}_{60\text{Ma}}$  isotope diagrams, but instead trend towards MAR or depleted mantle (DM; Figs. 6 & 8). On the other hand, mixing between HIMU and the MAR source (DM) is not consistent with  $^{206}\text{Pb}/^{204}\text{Pb}_{60\text{Ma}}$  vs. a)  $^{207}\text{Pb}/^{204}\text{Pb}_{60\text{Ma}}$ , b)  $^{208}\text{Pb}/^{204}\text{Pb}_{60\text{Ma}}$ , c)  $^{176}\text{Hf}/^{177}\text{Hf}_{60\text{Ma}}$  and d)  $^{143}\text{Nd}/^{144}\text{Nd}_{60\text{Ma}}$  isotope diagrams (Fig. 8). DSDP Site 530 ocean crust lavas, which formed through interaction of the Tristan-Gough plume and the upper mantle beneath the MAR, consistently plot near the end of the Walvis seamount array, but have higher Nd and Hf isotopic compositions than the possible mixing end member (Figs. 6 & 8). The tholeiitic basalts from site DR77 are the most depleted samples (in terms of both incompatible elements and isotope ratios) reported so far from the Walvis Ridge or nearby seamounts (Figs. 4, 6 & 8). The Sr-Nd-Pb-Hf isotopic composition of DR77 lavas lie within the compositional range of the Mid-Atlantic Ridge basalts (or very close to it on the thorogenic Pb isotope diagram) adjacent to the Walvis Ridge (25°-46°S MAR) between the Florianopolis Fracture Zone (FFZ; ~26°S) and Agulhas Fracture Zone (AFZ; ~46°S) (Figs. 6 & 8). These enriched MAR segments project from N-MAR basalts towards an EM I-type isotopic composition and most likely reflect interaction of depleted mantle beneath the MAR with the Gough-flavored plume material (mixing of DM and EM I; e.g., Class and le Roex, 2011 and references therein). On most isotope correlation diagrams, the late-stage Walvis seamount array extends towards a composition similar to DR77, except on the Sr vs. Nd and Nd vs. Hf isotope diagrams (Fig. 6). Calculated regression lines for the late-stage Walvis seamount lavas (e.g., uraniumogenic Pb isotope diagram:  $R^2=0.74$  and thorogenic Pb isotope diagram:  $R^2=0.89$ , excluding site DR77 and DSDP Site 530; Fig. 6) extend from the St. Helena field to the field for lavas from the MAR between 25°-46°S latitudes on all

isotope correlation diagrams, indicating that upper mantle (lithosphere or uppermost asthenosphere) contaminated with Gough-type plume material can serve as the low- $\mu$  mixing end member.

In general, the isotopic composition of the 25°-46°S MAR (including site DR77) can be modeled by mixing ~65% DM with ~35% Gough-type mantle forming an EMORB-type composition (Fig. 6 & 8). Note, the Tristan-type component (including DSDP Site 527 & 528) seems to be an inappropriate EM I type mixing end member, since the 25°-46°S MAR on the uranogenic Pb isotope diagram lies early completely within the Tristan-type compositional domain, but lies between Tristan and MAR in the thorogenic Pb isotope diagram (Fig. 6). Additionally, the first documented occurrence of the Tristan-type composition (DSDP Site 527 & 528) lies ~400km south from the southernmost HIMU-type late-stage seamount and does not represent most of the Walvis Ridge basement composition. Interestingly, the 25°-46°S MAR basalts have relatively restricted  $^{206}\text{Pb}/^{204}\text{Pb}_{60\text{Ma}}$ ,  $^{207}\text{Pb}/^{204}\text{Pb}_{60\text{Ma}}$  and  $^{208}\text{Pb}/^{204}\text{Pb}_{60\text{Ma}}$  ratios, but highly variable  $^{87}\text{Sr}/^{86}\text{Sr}_{60\text{Ma}}$ ,  $^{143}\text{Nd}/^{144}\text{Nd}_{60\text{Ma}}$  and  $^{176}\text{Hf}/^{177}\text{Hf}_{60\text{Ma}}$  compositions (Figs. 6 & 8). Although seawater alteration could in part explain the Sr isotope variations, heterogeneous EM I - DM mixing proportions are required to explain the variability of Nd and Hf isotope ratios.

The low- $\mu$  EMORB-like component could reside in the uppermost asthenosphere. Alternatively it could be acquired through contamination/assimilation of lithospheric mantle or oceanic crust formed through plume-ridge interaction. In this case, we would expect a higher imprint of this EMORB-type composition in late-stage seamounts located on the up to 35 km thick Walvis Ridge crest compared to the seamounts on the adjacent oceanic crust with average thickness of 5-6 km (Fromm et al., 2015). In fact, the late-stage Walvis lavas with the strongest HIMU signature (e.g., DR89) lie on the Walvis

Ridge with the thickest oceanic crust, whereas DR77, which could serve as the low- $\mu$  end member, lies on the adjacent oceanic crust. Therefore, it seems unlikely that the Walvis Ridge crust is the source for the low- $\mu$  component, or that extensive crustal assimilation affected the geochemical signature of the late-stage Walvis lavas.

With the exception of one late-stage sample (AII-93-21-1 with a Gough-type composition; Rohde et al., 2013a; O'Connor and Jokat, 2015a), the observed trend of the late-stage Walvis seamount samples can be explained through mixing of the St. Helena HIMU and an EMORB-type end member. The EMORB end member could have been formed by mixing depleted mantle (DM = MORB source upper mantle) with Gough EM I-type mantle from the early Tristan-Gough plume (Figs. 6 and 8).

### **5.3 Possible models for the origin of the late-stage Walvis Seamount volcanism**

As opposed to the Walvis Ridge seamounts, the late-stage lavas from the Rio Grande Rise have a depleted Atlantic MORB-type composition (Figs. 6 & 8), most likely formed by similar processes as normal rejuvenated/post-erosional volcanism. In contrast, the late-stage volcanism on the Walvis Ridge is not only distinct by the long duration of the volcanic hiatus, but also in its peculiar geochemical composition (HIMU to EMORB-type) compared to most late-stage lavas on ocean islands and seamount volcanoes, which are characterized by more depleted isotopic composition in relation to the main volcanic phase forming the volcanic edifice (e.g., Clague and Dalrymple, 1987; Garcia et al., 2010; Hoernle et al., 1991; Geldmacher et al., 2005). The entire Tristan-Gough hotspot track basement (Fig. 6; Salters and Sachi-Kocher, 2010; Rohde et al., 2013a; Hoernle et al., 2015), as well as lavas from the Discovery and Shona hotspot track basement, which appear to come from a similar source as the Walvis Ridge basement lavas, show no evidence of any involvement of a HIMU component (e.g., Hoernle et al., 2016; Schwindrofska et al., 2016). Therefore, we conclude that neither the HIMU-signature nor the emplacement of the late-stage Walvis Ridge lavas is related to the Tristan-Gough mantle plume.

Several factors link the late-stage Walvis volcanism to Africa. To begin with, the HIMU-type late-stage volcanism is only located on the oldest part of the hotspot track near the African continental margin (Fig. 1) and the HIMU signature increases systematically towards Africa (Fig. 9). On the southwest African continental margin, the Western Cape province and the Gibeon-Dicker Willem magmatic lineaments were emplaced simultaneously (between 77 to 49 Ma; Janney et al., 2002 and references therein) with the late-stage Walvis seamounts. Whereas the Namibian Dicker Willem carbonatite complex has Nd-Pb isotopic compositions overlapping with that of St.

Helena (Sr isotopes show small amount of crustal contamination compared to St. Helena; Cooper and Reid, 2000), the Western Cape melilitite lavas trend from a HIMU-like composition towards an EM I-type composition, interpreted to reflect continental lithospheric interaction (Janney et al., 2002) (Figs. 6 & 8). Based on the contemporaneous emplacement and the shared St. Helena HIMU end member composition, we suggest a link between the HIMU-type volcanism in the eastern South Atlantic and southwestern Africa.

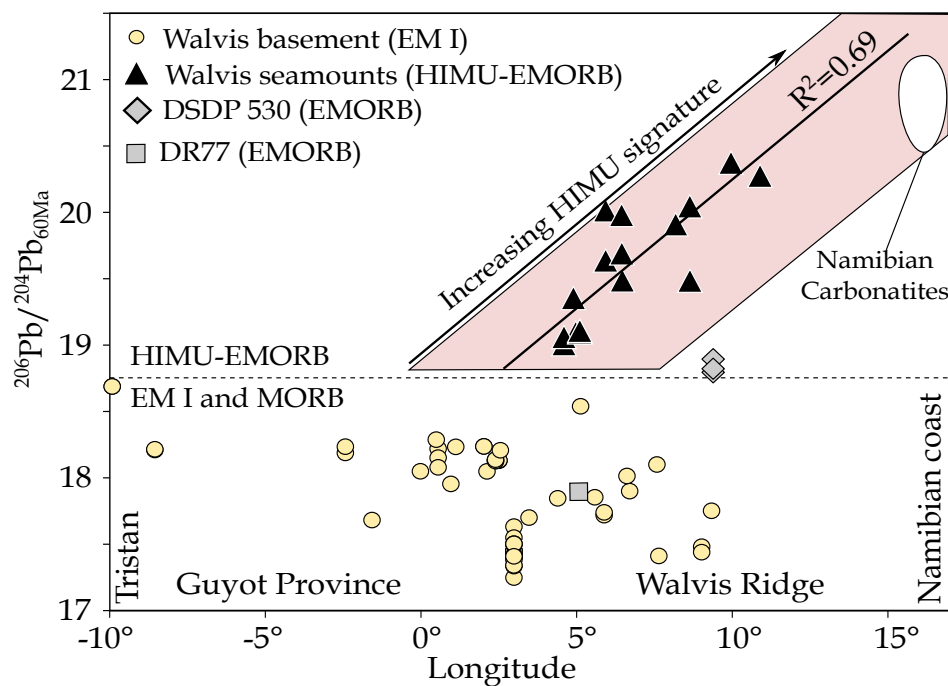


**Figure 9: Longitude versus  $^{206}\text{Pb}/^{204}\text{Pb}_{60\text{Ma}}$  of the late-stage Walvis seamount lavas (black triangles), the EM-I type basement lavas from the Walvis Ridge (white circles) and the Namibian carbonatites from Dicker Willem. The Pb-isotope ratios of the late-stage Walvis seamount lavas become more radiogenic (HIMU-like) with increasing proximity to the Namibian coast. The black line is the calculated regression line of the late-stage Walvis seamount lavas without the DR77 and DSDP Site 530 samples. The Dicker Willem volcanism has  $^{206}\text{Pb}/^{204}\text{Pb}_{60\text{Ma}}$  of  $> 20$  near the African coast. Sources of literature data are reported in Figure 6.**

Although a possible source for the HIMU component could be the subcontinental lithospheric mantle (SCLM), there are several arguments against derivation from the southwest African SCLM. The source for HIMU is believed to have formed prior to 2.45 Ga (Cabral et al., 2013), but the age of the lithosphere along the entire Namibian and



South African west coast (including the Kaoko-Damara-Namaqua-Natal mobile belts) is younger than 2.2 Ga (e.g., Becker et al., 2006; Eglinton, 2006). The lithospheric terranes in southwest Africa were subject to several intense deformation phases, coupled with extensive melt extraction (e.g., Becker et al., 2006; Eglinton, 2006). Such events are likely to erase any pre-existing mantle enrichments (Janney et al., 2002). The oldest HIMU-type volcanism found to date in southwest Africa is ~77 Ma (Janney et al., 2002) and believed to be derived from the melting of small enriched HIMU-type pods of material brought up from the deep, rather than from the lithospheric mantle (Janney et al., 2002).

Since seismic tomography has imaged a mantle plume extending into to the lower mantle beneath St. Helena (e.g., Montelli et al., 2006; French and Romanowicz, 2015), it is most likely that St. Helena HIMU material is brought to the surface from the lowermost mantle. St. Helena Island is located 2000 km northwestward of the Tristan-Gough hotspot track. Since the upper mantle is predicted to flow westwards beneath the South Atlantic Ocean (e.g., Colli et al., 2014), it is implausible that HIMU material from the St. Helena hotspot could travel 2000 km through the upper mantle to the southeast. Therefore, we propose that St. Helena HIMU material may also be upwelling beneath southwestern Africa (Janney et al., 2002). This assumption is supported by a diffuse vertical low velocity anomaly, which extends from the African LLSVP to the transitional zone beneath southwest Africa (red dashed circle in Fig. 1; French and Romanowicz, 2015; their Extended Data Figure 3 (a-e)).

The African volcanic lineaments (Gibeon – Dicker Willem and Western Cape province) are aligned sub-parallel to and in the direction of plate motion, suggesting that the broad low-velocity anomaly could represent multiple smaller mantle upwellings (weak plumes or upwelling strings of blobs) rather than a large-scale upwelling.

Beneath the thick African lithosphere, only very small degree kimberlitic, carbonatitic, melilitic and nephelinitic melts could form, which preferentially rose to the surface along zones of lithospheric weakness (Fig. 10). The westward flow of the upper mantle in this region (e.g., Colli et al., 2014) could entrain upwelling HIMU material carrying it westwards along the base of the African lithosphere. As the HIMU material moves westwards and upwards as the lithosphere thins towards the west, it could continue to melt by decompression (Fig. 10a). Alternatively, swarms of small blobs of HIMU material could upwell beneath southwestern Africa and the southeast South Atlantic Ocean and also melt by decompression, with the degree of melting being controlled by lithospheric thickness (Fig. 10b).

It has been proposed that the southern South Atlantic mantle plumes (EM I-type) originate from the edge of the African LLSVP (e.g., Torsvik et al., 2006; Burke et al., 2008). Recent numerical simulations imply that short-lived mantle upwellings could also initiate and detach from the top of the LLSVP (Ballmer et al., 2016). Seismic observations favor a thermo-chemical nature of the LLSVP with internal heterogeneities (Ballmer et al., 2016 and references therein). Upwellings from a more central portion of the LLSVP could possibly tap a different reservoir within the LLSVP with a distinct geochemical signature compared to the long-lived mantle plumes rising from its margins. The presently active locations of the Tristan-Gough, Discovery and Shona hotspots overlie the margin of the African LLSVP, and all have EM I-type compositions (Fig. 1; Richardson et al., 1982; Salters and Sachi-Kocher, 2010; Class and le Roex, 2011; Rohde et al., 2013a; Hoernle et al., 2015; Hoernle et al., 2016; Schwindrofska et al., 2016), suggesting that the EM I-type composition is derived from the margin of the LLSVP. In contrast, the St. Helena HIMU-type hotspot is located above a more central portion of the LLSVP (Fig. 1).

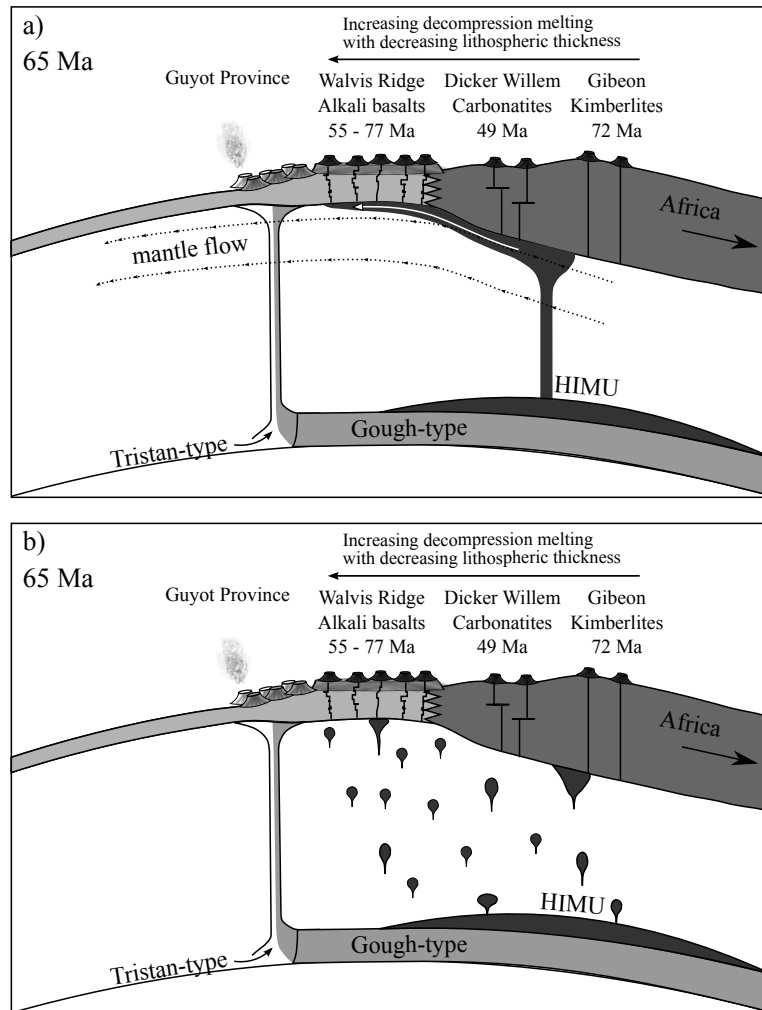


**Figure 10: Schematic model showing the origin of EM I-type hotspot tracks and HIMU-type volcanism in southwestern Africa and the southeastern South Atlantic Ocean. The Tristan-Gough, Discovery and Shona hotspots are formed by long-lived EM I-type mantle plumes, ascending from the margins of the African LLSVP. The late-stage HIMU-like Walvis Seamounts and the HIMU-type volcanism in southwest Africa (e.g., Gibeon - Dicker Willem, Western Cape province) may represent (a) upwelling plumes or (b) blobs from internal portions of the African LLSVP. The different compositional domains in the African LLSVP could possibly reflect a layer of HIMU material over- or underlying an EM I layer of material in the inner portions of the LLSVP or alternatively a lateral change in composition from EM I to HIMU towards the interior of the LLSVP (not shown). Upwelling HIMU-type plume material could be deflected westwards as it flows along the base of the thinning lithosphere from the African continent beneath the South Atlantic Ocean and the Walvis Ridge. Alternatively, blobs of HIMU-type material may be upwelling from different locations on or within the inner part of the African LLSVP.**

## 6. Conclusions

The combination of geochemical, geochronological and morphological analyses of both the Walvis Ridge and associated late-stage seamounts shows that the evolution of the Walvis Ridge is more complex than previously thought. The Walvis Ridge represents the first location worldwide, where EM I and St. Helena HIMU end member compositions have been found together. Seamounts on and adjacent to the Walvis Ridge with HIMU to EMORB type compositions originated 20-40 Myr after formation of the main body of the Walvis Ridge with EM I type composition. The distinct geochemistry of the late-stage Walvis seamounts can be explained by mixing of St. Helena end member HIMU with EMORB, with the latter representing a mixture of Gough-type plume material (EM I) with depleted upper mantle (DM). Comparable emplacement ages and a HIMU component shared with African carbonatitic and kimberlitic volcanism near the African continental margin point to a common origin for the eastern South Atlantic and southwestern African HIMU-type volcanism, most likely through (1) a large-scale, westward-deflected mantle upwelling (plume) or (2) a swarm of discrete smaller upwelling blobs having HIMU composition. We propose that the EM I Walvis Ridge basement and HIMU-type late-stage volcanism are both ultimately derived from different parts of the LLSVP. Whereas EM I-flavored mantle plumes apparently rise from the edges of the LLSVP (Tristan-Gough, Discovery and Shona mantle plumes), HIMU-dominated intraplate lavas (St. Helena, Gibeon-Dicker Willem and Western Cape lineaments), including the late-stage Walvis seamounts, are derived from more internal portions of the LLSVP. As already proposed by Hart et al. (1986) and Chauvel et al. (1992), there appears to be a close relationship between the EM I and the HIMU end members.

## **7. Acknowledgments**

We thank Captain Meyer and the crew of the R/V SONNE for their support on board during cruises S0233-Walvis II and S0234/1-Spaces; S. Hauff, K. Junge, J. Rohde, J. Sticklus and U. Westernströer for analytical support; and M. Anders for help with sample preparation. We further thank V. J. M. Salters and B. White for constructive reviews that helped improve this manuscript, as well as T.A. Mather for editorial handling. This research used samples provided by the Integrated Ocean Drilling Program. This study and SH's doctoral position were funded by the German Ministry for Research and Education (BMBF; grants S0233-Walvis II to KH and FH and S0234/1-Spaces to RW) and the GEOMAR Helmholtz Centre for Ocean Research Kiel.

## **8. Declaration of interest**

Conflicts of interest: None

## References

- Baksi, A. K., 2007, A quantitative tool for detecting alteration in undisturbed rocks and minerals—I: Water, chemical weathering, and atmospheric argon: *Geological Society of America Special Papers*, v. 430, p. 285-303.
- Ballmer, M. D., Schumacher, L., Lekic, V., Thomas, C., and Ito, G., 2016, Compositional layering within the large low shear-wave velocity provinces in the lower mantle: *Geochemistry, Geophysics, Geosystems*, v. 17, no. 12, p. 5056-5077.
- Becker, T., Schreiber, U., Kampunzu, A. B., and Armstrong, R., 2006, Mesoproterozoic rocks of Namibia and their plate tectonic setting: *Journal of African Earth Sciences*, v. 46, no. 1–2, p. 112-140.
- Bianco, T. A., Ito, G., Becker, J. M., and Garcia, M. O., 2005, Secondary Hawaiian volcanism formed by flexural arch decompression: *Geochemistry, Geophysics, Geosystems*, v. 6, no. 8, p. Q08009.
- Burke, K., Steinberger, B., Torsvik, T. H., and Smethurst, M. A., 2008, Plume Generation Zones at the margins of Large Low Shear Velocity Provinces on the core–mantle boundary: *Earth and Planetary Science Letters*, v. 265, no. 1–2, p. 49-60.
- Cabral, R. A., Jackson, M. G., Rose-Koga, E. F., Koga, K. T., Whitehouse, M. J., Antonelli, M. A., Farquhar, J., Day, J. M. D., and Hauri, E. H., 2013, Anomalous sulphur isotopes in plume lavas reveal deep mantle storage of Archaean crust: *Nature*, v. 496, no. 7446, p. 490-493.
- Chaffey, D. J., Cliff, R. A., and Wilson, B. M., 1989, Characterization of the St. Helena magma source: *Magmatism in the Ocean Basins*, v. 42, p. 19.
- Chauvel, C., Hofmann, A. W., and Vidal, P., 1992, HIMU-EM : The French-Polynesian Connection: *Earth and Planetary Science Letters*, v. 110, no. 1-4, p. 99-119.
- Clague, D. A., and Dalrymple, G. B., 1987, The Hawaiian-Emperor volcanic chain. part I. Geologic evolution: *Volcanism in Hawaii*, v. 1, p. 5-54.
- Class, C., and le Roex, A., 2011, South Atlantic DUPAL anomaly — Dynamic and compositional evidence against a recent shallow origin: *Earth and Planetary Science Letters*, v. 305, no. 1–2, p. 92-102.
- Class, C., and le Roex, A. P., 2008, Ce anomalies in Gough Island lavas — Trace element characteristics of a recycled sediment component: *Earth and Planetary Science Letters*, v. 265, no. 3–4, p. 475-486.
- Cliff, R. A., Baker, P. E., and Mateer, N. J., 1991, Geochemistry of inaccessible island volcanics: *Chemical Geology*, v. 92, no. 4, p. 251-260.
- Colli, L., Stotz, I., Bunge, H. P., Smethurst, M., Clark, S., Iaffaldano, G., Tassara, A., Guillocheau, F., and Bianchi, M. C., 2014, Rapid South Atlantic spreading changes and coeval vertical motion in surrounding continents: Evidence for temporal changes of pressure-driven upper mantle flow: *Tectonics*, v. 33, no. 7, p. 1304-1321.
- Cooper, A. F., and Reid, D. L., 1998, Nepheline Sövites as Parental Magmas in Carbonatite Complexes: Evidence from Dicker Willem, Southwest Namibia: *Journal of Petrology*, v. 39, no. 11-12, p. 2123-2136.
- Cooper, A. F., and Reid, D. L., 2000, The association of potassic trachytes and carbonatites at the Dicker Willem Complex, southwest Namibia: coexisting, immiscible, but not cogenetic magmas: *Contributions to Mineralogy and Petrology*, v. 139, no. 5, p. 570-583.
- Davies, G. R., Spriggs, A. J., and Nixon, P. H., 2001, A Non-cognate Origin for the Gibeon Kimberlite Megacryst Suite, Namibia: Implications for the Origin of Namibian Kimberlites: *Journal of Petrology*, v. 42, no. 1, p. 159-172.
- Eglington, B. M., 2006, Evolution of the Namaqua-Natal Belt, southern Africa – A geochronological and isotope geochemical review: *Journal of African Earth Sciences*, v. 46, no. 1–2, p. 93-111.
- French, S. W., and Romanowicz, B., 2015, Broad plumes rooted at the base of the Earth's mantle beneath major hotspots: *Nature*, v. 525, no. 7567, p. 95-99.
- Fromm, T., Planert, L., Jokat, W., Ryberg, T., Behrmann, J. H., Weber, M. H., and Haberland, C., 2015, South Atlantic opening: A plume-induced breakup?: *Geology*, v. 43, no. 10, p. 911-934.
- Garcia, M. O., Swinnard, L., Weis, D., Greene, A. R., Tagami, T., Sano, H., and Gandy, C. E., 2010, Petrology, Geochemistry and Geochronology of Kaua'i Lavas over 4-5 Myr: Implications for the Origin of Rejuvenated Volcanism and the Evolution of the Hawaiian Plume: *Journal of Petrology*, v. 51, no. 7, p. 1507-1540.
- Geldmacher, J., Hoernle, K., Bogaard, P. v. d., Duggen, S., and Werner, R., 2005, New  $^{40}\text{Ar} / ^{39}\text{Ar}$  age and geochemical data from seamounts in the Canary and Madeira volcanic provinces: Support for the mantle plume hypothesis: *Earth and Planetary Science Letters*, v. 237, no. 1–2, p. 85-101.
- Geldmacher, J., Hoernle, K., Klügel, A., Bogaard, P. v. d., Wombacher, F., and Berning, B., 2006, Origin and geochemical evolution of the Madeira-Tore Rise (eastern North Atlantic): *Journal of Geophysical Research: Solid Earth*, v. 111, no. B9, p. B09206.

- Hart, S. R., Gerlach, D. C., and White, W. M., 1986, A Possible New Sr-Nd-Pb Mantle Array and Consequences for Mantle Mixing: *Geochimica Et Cosmochimica Acta*, v. 50, no. 7, p. 1551-1557.
- Hart, S. R., Hauri, E. H., Oschmann, L. A., and Whitehead, J. A., 1992, Mantle Plumes and Entrainment: Isotopic Evidence: *Science*, v. 256, no. 5056, p. 517-520.
- Hay, W., Sibuet, J., and Party, t. S. S., 1984, Site 530: southeastern corner of the Angola Basin: *Init. Rep., Deep Sea Drilling Project*, v. 75, p. 20-285.
- Hoernle, K., Hauff, F., Werner, R., van den Bogaard, P., Gibbons, A. D., Conrad, S., and Muller, R. D., 2011, Origin of Indian Ocean Seamount Province by shallow recycling of continental lithosphere: *Nature Geosci*, v. 4, no. 12, p. 883-887.
- Hoernle, K., Rohde, J., Hauff, F., Garbe-Schonberg, D., Homrighausen, S., Werner, R., and Morgan, J. P., 2015, How and when plume zonation appeared during the 132 Myr evolution of the Tristan Hotspot: *Nature Communication*, v. 6, p. 10.1038/ncomms8799.
- Hoernle, K., Schwindrofska, A., Werner, R., van den Bogaard, P., Hauff, F., Uenzelmann-Neben, G., and Garbe-Schönberg, D., 2016, Tectonic dissection and displacement of parts of Shona hotspot volcano 3500 km along the Agulhas-Falkland Fracture Zone: *Geology*, v. 44, no. 4, p. 263-266.
- Hoernle, K., Tilton, G., and Schmincke, H.-U., 1991, Sr-Nd-Pb isotopic evolution of Gran Canaria: Evidence for shallow enriched mantle beneath the Canary Islands: *Earth and Planetary Science Letters*, v. 106, no. 1, p. 44-63.
- Hoernle, K., Werner, R., and Lüter, C., 2014, RV SONNE Fahrtbericht/Cruise Report SO233 WALVIS II, 14.05-21.06. 2014, Cape Town, South Africa-Walvis Bay, Namibia: *GEOMAR Report v. no. 23 (N. Ser.)*, p. 53 pp + Appendices.
- Hofmann, A. W., 1988, Chemical Differentiation of the Earth - The Relationship between Mantle, Continental Crust, and Oceanic Crust: *Earth and Planetary Science Letters*, v. 90, no. 3, p. 297-314.
- Humphris, S. E., and Thompson, G., 1983, Geochemistry of rare earth elements in basalts from the Walvis Ridge: implications for its origin and evolution: *Earth and Planetary Science Letters*, v. 66, no. Supplement C, p. 223-242.
- Janney, P. E., Le Roex, A. P., Carlson, R. W., and Viljoen, K. S., 2002, A Chemical and Multi-Isotope Study of the Western Cape Olivine Melilitite Province, South Africa: Implications for the Sources of Kimberlites and the Origin of the HIMU Signature in Africa: *Journal of Petrology*, v. 43, no. 12, p. 2339-2370.
- Kawabata, H., Hanyu, T., Chang, Q., Kimura, J.-I., Nichols, A. R. L., and Tatsumi, Y., 2011, The Petrology and Geochemistry of St. Helena Alkali Basalts: Evaluation of the Oceanic Crust-recycling Model for HIMU OIB: *Journal of Petrology*, v. 52, no. 4, p. 791-838.
- Krishna, K., Bull, J., Ishizuka, O., Scrutton, R., Jaishankar, S., and Banakar, V., 2014, Growth of the Afanasy Nikitin seamount and its relationship with the 85 E Ridge, northeastern Indian Ocean: *Journal of earth system science*, v. 123, no. 1, p. 33-47.
- Le Maitre, R. W., 1962, Petrology of Volcanic Rocks, Gough Island, South Atlantic: *Geological Society of America Bulletin*, v. 73, no. 11, p. 1309-1340.
- Le Roex, A. P., Cliff, R. A., and Adair, B. J. I., 1990, Tristan da Cunha, South Atlantic: Geochemistry and Petrogenesis of a Basanite-Phonolite Lava Series: *Journal of Petrology*, v. 31, no. 4, p. 779-812.
- Luchs, T., Brey, G. P., Gerdes, A., and Höfer, H. E., 2013, The lithospheric mantle underneath the Gibeon Kimberlite field (Namibia): A mix of old and young components—Evidence from Lu-Hf and Sm-Nd isotope systematics: *Precambrian Research*, v. 231, p. 263-276.
- Montelli, R., Nolet, G., Dahlen, F. A., and Masters, G., 2006, A catalogue of deep mantle plumes: New results from finite-frequency tomography: *Geochemistry, Geophysics, Geosystems*, v. 7, no. 11, p. Q11007.
- Morgan, W. J., 1971, Convection Plumes in the Lower Mantle: *Nature*, v. 230, no. 5288, p. 42-43.
- Müller, R. D., Roest, W. R., Royer, J.-Y., Gahagan, L. M., and Sclater, J. G., 1997, Digital isochrons of the world's ocean floor: *Journal of Geophysical Research: Solid Earth*, v. 102, no. B2, p. 3211-3214.
- O'Connor, J. M., and Duncan, R. A., 1990, Evolution of the Walvis Ridge-Rio Grande Rise Hot Spot System: Implications for African and South American Plate motions over plumes: *Journal of Geophysical Research: Solid Earth*, v. 95, no. B11, p. 17475-17502.
- O'Connor, J. M., and Jokat, W., 2015a, Tracking the Tristan-Gough mantle plume using discrete chains of intraplate volcanic centers buried in the Walvis Ridge: *Geology*, v. 43, no. 8, p. 715-718.
- , 2015b, Age distribution of Ocean Drill sites across the Central Walvis Ridge indicates plate boundary control of plume volcanism in the South Atlantic: *Earth and Planetary Science Letters*, v. 424, p. 179-190.
- O'Connor, J. M., Jokat, W., le Roex, A. P., Class, C., Wijbrans, J. R., Keszling, S., Kuiper, K. F., and Nebel, O., 2012, Hotspot trails in the South Atlantic controlled by plume and plate tectonic processes: *Nature Geoscience*, v. 5, no. 10, p. 735-738.

- Pearce, J. A., 1996, A user's guide to basalt discrimination diagrams: Trace element geochemistry of volcanic rocks: applications for massive sulphide exploration. Geological Association of Canada, Short Course Notes, v. 12, no. 79, p. 113.
- Pearce, J. A., 2008, Geochemical fingerprinting of oceanic basalts with applications to ophiolite classification and the search for Archean oceanic crust: *Lithos*, v. 100, no. 1-4, p. 14-48.
- Pérez-Díaz, L., and Eagles, G., 2014, Constraining South Atlantic growth with seafloor spreading data: *Tectonics*, v. 33, no. 9, p. 2014TC003644.
- Reisberg, L., Zindler, A., Marcantonio, F., White, W., Wyman, D., and Weaver, B., 1993, Os isotope systematics in ocean island basalts: *Earth and Planetary Science Letters*, v. 120, no. 3, p. 149-167.
- Renne, P. R., Glen, J. M., Milner, S. C., and Duncan, A. R., 1996, Age of Etendeka flood volcanism and associated intrusions in southwestern Africa: *Geology*, v. 24, no. 7, p. 659-662.
- Ribe, N. M., and Christensen, U. R., 1999, The dynamical origin of Hawaiian volcanism: *Earth and Planetary Science Letters*, v. 171, no. 4, p. 517-531.
- Richardson, S. H., Erlank, A. J., Duncan, A. R., and Reid, D. L., 1982, Correlated Nd, Sr and Pb Isotope Variation in Walvis Ridge Basalts and Implications for the Evolution of their Mantle Source: *Earth and Planetary Science Letters*, v. 59, no. 2, p. 327-342.
- Rogers, N. W., Hawkesworth, C. J., and Palacz, Z. A., 1992, Phlogopite in the generation of olivine-melilitites from Namaqualand, South Africa and implications for element fractionation processes in the upper mantle: *Lithos*, v. 28, no. 3, p. 347-365.
- Rohde, J., Hoernle, K., Hauff, F., Werner, R., O'Connor, J., Class, C., Garbe-Schönberg, D., and Jokat, W., 2013a, 70 Ma chemical zonation of the Tristan-Gough hotspot track: *Geology*, v. 43, no. 3, p. 335-338.
- Rohde, J. K., van den Bogaard, P., Hoernle, K., Hauff, F., and Werner, R., 2013b, Evidence for an age progression along the Tristan-Gough volcanic track from new  $^{40}\text{Ar}/^{39}\text{Ar}$  ages on phenocryst phases: *Tectonophysics*, v. 604, p. 60-71.
- Salters, V. J. M., and Sachi-Kocher, A., 2010, An ancient metasomatic source for the Walvis Ridge basalts: *Chemical Geology*, v. 273, no. 3-4, p. 151-167.
- Sandwell, D. T., and Smith, W. H., 2009, Global marine gravity from retracked Geosat and ERS - 1 altimetry: Ridge segmentation versus spreading rate: *Journal of Geophysical Research: Solid Earth*, v. 114, no. B1, p. B01411.
- Schwindrofska, A., Hoernle, K., Hauff, F., van den Bogaard, P., Werner, R., and Garbe-Schönberg, D., 2016, Origin of enriched components in the South Atlantic: Evidence from 40 Ma geochemical zonation of the Discovery Seamounts: *Earth and Planetary Science Letters*, v. 441, p. 167-177.
- Stracke, A., Bizimis, M., and Salters, V. J. M., 2003, Recycling oceanic crust: Quantitative constraints: *Geochemistry, Geophysics, Geosystems*, v. 4, no. 3, p. 8003.
- Stracke, A., Hofmann, A. W., and Hart, S. R., 2005, FOZO, HIMU, and the rest of the mantle zoo: *Geochemistry, Geophysics, Geosystems*, v. 6, no. 5, p. Q05007.
- Sun, S.-s., and McDonough, W. F., 1989, Chemical and isotopic systematics of oceanic basalts: implications for mantle composition and processes: Geological Society, London, Special Publications, v. 42, no. 1, p. 313-345.
- Torsvik, T. H., Smethurst, M. A., Burke, K., and Steinberger, B., 2006, Large igneous provinces generated from the margins of the large low-velocity provinces in the deep mantle: *Geophysical Journal International*, v. 167, no. 3, p. 1447-1460.
- White, W. M., and Duncan, R. A., 1996, Geochemistry and Geochronology of the Society Islands: New Evidence for Deep Mantle Recycling, in Basu, A., and Hart, S. R., eds., *Earth Processes: Reading the Isotopic Code*: Washington D. C., American Geophysical Union, p. 183-206.
- Willbold, M., and Stracke, A., 2006, Trace element composition of mantle end-members: Implications for recycling of oceanic and upper and lower continental crust: *Geochemistry, Geophysics, Geosystems*, v. 7, no. 4, p. Q04004.
- Wilson, J. T., 1973, Mantle plumes and plate motions: *Tectonophysics*, v. 19, no. 2, p. 149-164.
- Workman, R. K., and Hart, S. R., 2005, Major and trace element composition of the depleted MORB mantle (DMM): *Earth and Planetary Science Letters*, v. 231, no. 1-2, p. 53-72.
- Zindler, A., and Hart, S. R., 1986, Chemical Geodynamics: *Annual Review of Earth and Planetary Sciences*, v. 14, no. 1, p. 493-571.



## **CHAPTER III**

# **COMPARISON OF NEW AGE AND GEOCHEMICAL DATA FROM THE WALVIS RIDGE WITH OTHER SOUTH ATLANTIC HOTSPOTS: MAPPING THE BASE OF THE LOWER MANTLE BENEATH THE SOUTH ATLANTIC**

S. Homrighausen<sup>1\*</sup>, K. Hoernle<sup>1,2</sup>, F. Hauff<sup>1</sup>, J.-A. Wartho<sup>1</sup>, P. van den Bogaard<sup>1</sup>, D. Garbe-Schönberg<sup>2</sup>

<sup>1</sup> GEOMAR Helmholtz-Zentrum für Ozeanforschung Kiel, Wischhofstr. 1-3, 24148 Kiel

<sup>2</sup> Institut für Geowissenschaften, Christian-Albrechts Universität zu Kiel, Ludewig-Meyn-Str. 10, 24118 Kiel

Corresponding author (shomrighausen@geomar.de)

**Keywords: Walvis Ridge, isotope geochemistry,  $^{40}\text{Ar}/^{39}\text{Ar}$  dating, DUPAL-anomaly, EM I mantle end member, Large Low Shear Velocity Province (LLSVP)**

## Abstract

The six proposed South Atlantic hotspots (Ascension, St. Helena, Tristan-Gough, Discovery, Shona and Bouvet) show considerable geochemical variation ranging from end member EM I-type (Enriched Mantle One) at the Tristan-Gough, Discovery and Shona hotspots, to end member HIMU (high time-integrated  $\mu=^{238}\text{U}/^{204}\text{Pb}$ ) at St. Helena, to HIMU-like (Ascension) and FOZO (FOcal ZOne of oceanic hotspot arrays)-like composition at Bouvet island. Long-lived spatial geochemical zonation of the Tristan-Gough and Discovery hotspot tracks and temporal variations from EM I-type basement formation to HIMU-type late-stage volcanism at the Walvis Ridge and Shona hotspot tracks point to a complex evolution of the South Atlantic mantle. Here we report major and trace element data, Sr-Nd-Pb-Hf isotope ratios and  $^{40}\text{Ar}/^{39}\text{Ar}$  age data for samples from 16 new sites on the Walvis Ridge, which is the oldest submarine expression of the Tristan-Gough mantle plume and represents the initial reference locality of the EM I end member in the South Atlantic Ocean. The lavas from the basement display an excellent age progressive trend of  $\sim 31$  mm/a along the entire Tristan-Gough hotspot track, indicating relatively constant plate motion over a deep-rooted mantle plume in the last  $\sim 115$  Ma. The Gough-type EM I composition of the Tristan-Gough (Walvis Ridge and subtrack extending through the Guyot Province to Gough Island) can also be identified in the northern Discovery and Shona hotspot tracks, suggesting that these hotspots tap a common source reservoir in the lower mantle. The Tristan and Southern Discovery EM I-type flavors can be reproduced by mixing of the Gough-type component with (1) FOZO to produce Tristan-type lavas, and (2) continental crust to yield a Southern Discovery-type composition. Based on the characteristic geochemical fingerprints of the South Atlantic hotspots and their position relative to the 1 %  $\partial V_s$  velocity contour of the African Large Low Shear Velocity Province (LLSVP), we propose that the spatial and

temporal geochemical heterogeneities in the South Atlantic hotspots ultimately reflects sampling of different geochemical domains outside and within the African LLSVP. We propose that the Gough-type EM I of the Tristan-Gough, Southern Discovery and Shona hotspots samples the outer margins of the LLSVP, whereas St. Helena and Ascension hotspots and Late-stage Walvis and Shona volcanism sample HIMU from inner portions of the LLSVP. The ambient lowermost mantle outside of the LLSVP consists of subducted ocean crust (FOZO), as sampled by the Bouvet Hotspot, and subducted marine sediment or continental crust, as sampled by the Southern Discovery Hotspot.

## 1. Introduction

The Tristan-Gough, Discovery and Shona (also referred to as Meteor) volcanic tracks form the most prominent bathymetric features on the South Atlantic seafloor (Fig. 1). These age-progressive volcanic chains (Fig. 1) have an enriched mantle one (EM I) type composition, characterized by high  $^{87}\text{Sr}/^{86}\text{Sr}$ ,  $^{207}\text{Pb}/^{204}\text{Pb}$  and  $^{208}\text{Pb}/^{204}\text{Pb}$  ratios at a given  $^{206}\text{Pb}/^{204}\text{Pb}$  value (or high  $\Delta 7/4\text{Pb}$  and  $\Delta 8/4\text{Pb}$  respectively; Hart, 1984), and low  $^{206}\text{Pb}/^{204}\text{Pb}$ ,  $^{143}\text{Nd}/^{144}\text{Nd}$  and  $^{176}\text{Hf}/^{177}\text{Hf}$  isotope ratios (Zindler and Hart, 1986). These oceanic basalts form part of a geochemically-enriched anomaly (DUPAL anomaly; Hart, 1984) observed in the southern South Atlantic and western Indian Ocean mid-ocean-ridge basalts (MORBs) and intraplate ocean island basalts (OIBs) (e.g., Hart, 1984). The DUPAL-anomaly in the South Atlantic is surrounded by intra-plate lavas with radiogenic Pb and intermediate Sr-Nd-Hf isotope ratios. St. Helena represents the type locality of HIMU (high time-integrated  $\mu=^{238}\text{U}/^{204}\text{Pb}$ ) end member (Zindler and Hart, 1986), whereas Ascension can be described as HIMU-like (HIMU+DM), and Bouvet islands as a FOZO-like composition (FOcal ZOne of ocean island basalt arrays on Sr-Nd-Pb isotope diagrams; Hart et al., 1992; Stracke et al., 2005) with lower Pb isotope ratios, but slightly higher Sr and Hf isotope ratios compared to HIMU (Stracke et al., 2005).

The NE-SW-oriented submarine volcanic chains associated with the islands of St. Helena/Ascension, Tristan-Gough, Discovery and Shona are consistent with having formed by the NE movement of the African plate over relatively stationary (or synchronously shifted) hotspots or mantle plumes (Fig. 1) (O'Connor and le Roex, 1992; O'Connor et al., 2012). Seismic data (e.g., Montelli et al., 2006; Zhao, 2007; French and Romanowicz, 2015) and high  $^3\text{He}/^4\text{He}$  ratios ( $>10$  the atmospheric He ratio  $R_A$ ) from the Tristan-Gough, Discovery and Shona hotspot tracks (Kurz et al., 1998; Sarda et al., 2000; Stroncik et al., 2017) support an origin from the base of the lower mantle.

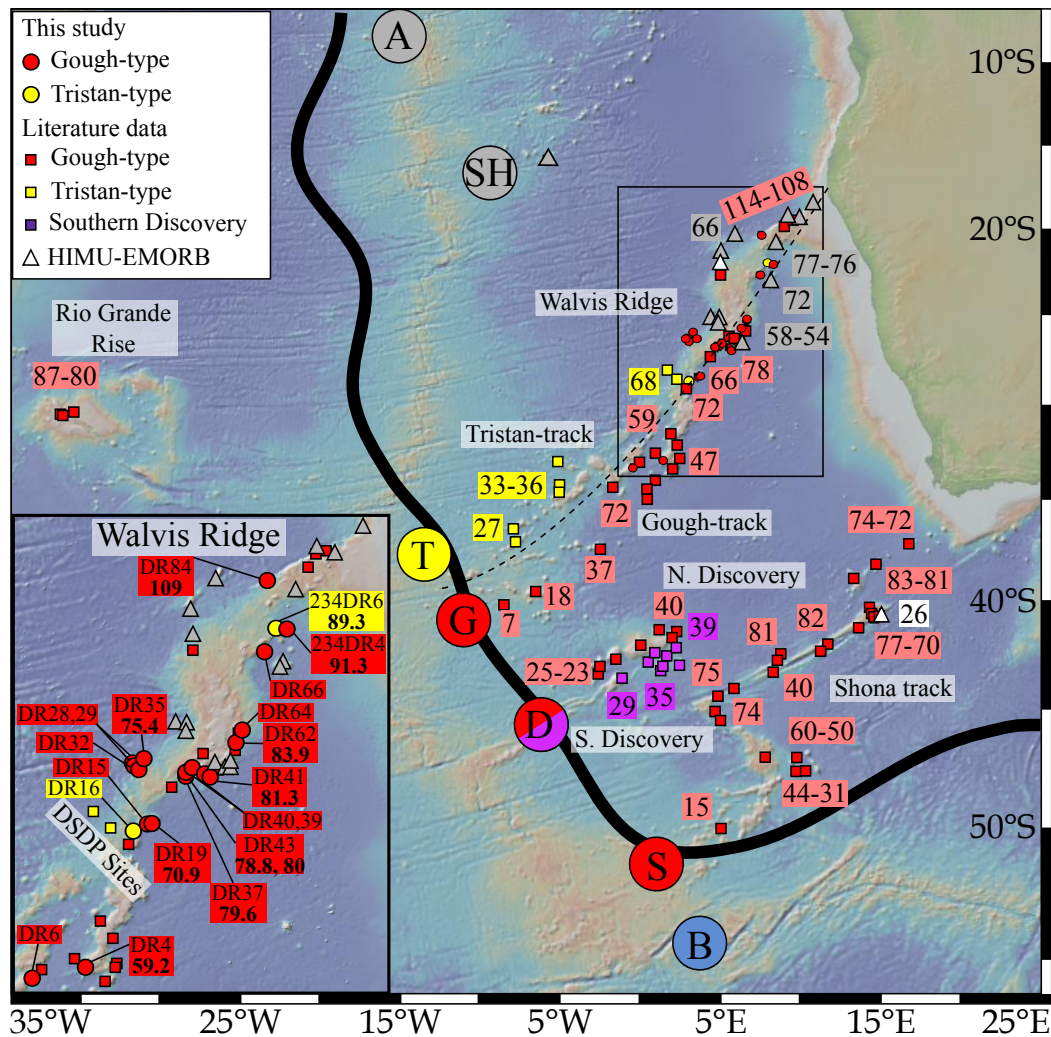


**Figure 1: Map of the South Atlantic showing:** 1) the proposed hotspot locations (large circles with A = Ascension, SH = St. Helena, T = Tristan, G = Gough, D = Discovery, S = Shona and B = Bouvet), 2) new sample sites from Walvis Ridge S0233 and S0234 cruises (red circles), 3)  $^{40}\text{Ar}/^{39}\text{Ar}$  ages (Ma; Rohde et al., 2013b; O'Connor and Jokat, 2015a, b; Homrighausen et al., in review-b), 4) the proposed Tristan-Gough hotspot track (dashed line; O'Connor and Duncan, 1990), and 5) the 1 %  $\partial V_s$  contour (black thick line) defining the western limit of the African Large Low Shear Velocity Province (LLSVP; Torsvik et al., 2006). Note that the background color of the ages is related to the different geochemical signatures (yellow = Tristan-type, red = Gough-type, purple = Southern Discovery-type, grey = HIMU-like). The location of the Tristan hotspot (or plume conduit), positioned at the yellow "T", shows the current location of a low velocity anomaly in the upper mantle (Schlömer et al., 2017). For comparison, sample sites from the literature (rectangles for EM I types and triangles for HIMU-EMORB lavas) are included. Inset shows the Walvis Ridge with new samples and new age data. Literature data is taken from the GEOROC Database (<http://georoc.mpch-mainz.gwdg.de/georoc/>) and are reported in detail in Appendix F. Source of bathymetric map: <http://www.geomapapp.org>.

Spatial geochemical zonation has been identified in the Tristan-Gough (since ~70 Ma) and the Discovery (since ~40 Ma) seamount chains (Fig. 1). Based on variable  $^{207}\text{Pb}/^{204}\text{Pb}$  ratios, but almost uniform  $^{208}\text{Pb}/^{204}\text{Pb}$  ratios at a given  $^{206}\text{Pb}/^{204}\text{Pb}$  value, three distinct EM I-type compositional domains have been identified in the South Atlantic DUPAL-anomaly (Rohde et al., 2013a; Hoernle et al., 2015; Schwindrofska et al., 2016). It has been proposed that geochemical zonation in mantle plumes reflects sampling of the boundaries of the Large Low Shear Velocity Province (LLSVP), entraining geochemically distinct materials from the LLSVP and the surrounding ambient lower mantle (e.g., Huang et al., 2011; Weis et al., 2011; Rohde et al., 2013a; Hoernle et al., 2015; Harrison et al., 2017). If all the different geochemical flavors (EM I-types, HIMU and FOZO) in the South Atlantic are derived from the lowermost mantle, the LLSVP and/or the lowermost ambient mantle must be highly heterogeneous.

Although the respective seamount chains show many characteristic features of a classical mantle plume (Wilson, 1963; Morgan, 1971; Wilson, 1973; Richards et al., 1989), there are several contradictory observations (e.g., Fairhead and Wilson, 2005; Regelous et al., 2009; Foulger, 2017; O'Connor et al., 2018). For example, the Walvis Ridge represents nearly half of the entire Tristan-Gough seamount chain and some of the available age data is non-age progressive with several ages up to 40 Ma younger than the expected linear age progression (O'Connor and Duncan, 1990; Rohde et al., 2013b; O'Connor and Jokat, 2015a). The Late-Stage Walvis and Shona (Richardson) seamount lavas, with ages >20 Ma younger than the basement, have distinct St Helena HIMU-type incompatible-element and isotope compositions (Homrighausen et al., in review-b; Homrighausen et al., in review-a). No HIMU lavas have been found in the basement of the Gough EM I type hotspot tracks. It remains a mystery how the various EM I-types (Gough, Tristan, Southern Discovery) in the South Atlantic DUPAL-anomaly

are related. Do they derive from a common source, and how can the complex spatial and temporal geochemical variability in the South Atlantic be explained?

To contribute to this discussion, we report new major and extensive trace element, Sr-Nd-Pb-Hf isotope and  $^{40}\text{Ar}/^{39}\text{Ar}$  age data from the Walvis Ridge. The Walvis Ridge is the oldest submarine expression of the proposed Tristan-Gough hotspot track and represents the EM I-type locality (DSDP Site 525A) in the South Atlantic (Zindler and Hart, 1986). Due to the sparse sampling (only 5 sample sites yielded  $^{40}\text{Ar}/^{39}\text{Ar}$  age data spread over 1500 km), the age progression and the history of a possible geochemical zonation of the Walvis Ridge remains poorly constrained. In this study we re-evaluate the origin of not only the Walvis Ridge, but also the geochemical variability of intra-plate volcanism in the South Atlantic Ocean.

## **2. Geological Background**

Consistent with the mantle plume model (e.g., Wilson, 1963; Morgan, 1971; Richards et al., 1989), the Tristan-Gough hotspot track initiated with the emplacement of the Parana-Etendeka continental flood basalt province (135-132 Ma, Renne et al., 1996; Renne, 2015), which was split by the opening of the South Atlantic. Thereafter, the Walvis Ridge and Rio Grande Rise were formed by the interaction of the plume tail with the newly formed Mid-Atlantic Ridge (MAR; e.g., Humphris and Thompson, 1983; O'Connor and Duncan, 1990; Rohde et al., 2013a; O'Connor and Jokat, 2015b). Between 80-60 Ma, several major ridge jumps divided the Rio Grande Rise from the Walvis Ridge (Humphris and Thompson, 1983; O'Connor and Duncan, 1990). After ~60 Ma, the Tristan-Gough plume was located beneath the African plate. At the southern Walvis Ridge the Tristan-Gough track bifurcates, forming two separated volcanic tracks leading to the active volcanic islands of Tristan da Cunha and Gough, termed the Tristan and

Gough subtracks (Fig. 1). The two subtracks show distinct EM I-type geochemical compositions, displaying a bilateral geochemical zonation (Rohde et al., 2013a; Hoernle et al., 2015). The Gough subtrack has higher  $^{207}\text{Pb}/^{204}\text{Pb}$  ratios, but similar  $^{208}\text{Pb}/^{204}\text{Pb}$  ratios at a given  $^{206}\text{Pb}/^{204}\text{Pb}$  value, and extends to lower  $^{143}\text{Nd}/^{144}\text{Nd}$  and  $^{176}\text{Hf}/^{177}\text{Hf}$  ratios and higher  $^{87}\text{Sr}/^{86}\text{Sr}$  ratios compared to the Tristan subtrack. Thus far, only the Gough-type EM I composition has been documented northward of the DSDP sites (Site 525A, 527 and 528), which form a transect across the southern Walvis Ridge. Therefore, it seems that the geochemical zonation initiated at  $\sim 70$  Ma (Rohde et al., 2013a; Hoernle et al., 2015).

Although the Tristan-Gough volcanic chains show many characteristic features of a classical mantle plume (e.g., Courtillot et al., 2003), the bifurcation of the Walvis Ridge southwest of DSDP Sites and the reported age data for the Walvis Ridge (Fig. 1) (O'Connor and Duncan, 1990; Rohde et al., 2013b; O'Connor and Jokat, 2015a) challenge the classical mantle plume model. For example, Fairhead and Wilson (2005) suggest that the Walvis Ridge developed as a result of periodic release of intraplate stress along deformation zones that penetrate short distances into the plate from the MAR at that time. Recently, O'Connor et al. (2018) interpreted bands of seismically slow material in the upper asthenosphere as fast flowing channels, which are fed by a large-scale plume upwelling from the African LLSVP located near the Southwest African coast and propose that the southern South Atlantic hotspot tracks developed above these fast flowing channels.



### **3. Analytical Methods**

The analytical procedures for the  $^{40}\text{Ar}/^{39}\text{Ar}$  age dating and determination of the major and trace element contents and radiogenic isotope ratios are described in detail in Appendix A and all data are reported in Appendices B and C.

### **4. Results**

New samples were obtained from the Walvis Ridge during the S0233 and S0234 cruises of R/V Sonne at depths of 1900-4000 m through dredging 1) the steep scarps on the margins of the ridge and the walls of cross-cutting Graben systems on the top of the plateau, 2) three neighboring seamounts along the eastern margin of the ridge, and 3) two seamounts in the Guyot Province (Fig.1). A detailed description of the sample localities is given in Hoernle et al. (2014) and Werner and Wagner (2014).

#### **4.1 Alteration and age correction of radiogenic isotope ratios**

The recovered submarine rocks from the Walvis Ridge have experienced variable degrees of seawater alteration. Even though we selected the freshest parts of the lavas, crushed them and then carefully handpicked the freshest pieces under a binocular microscope (0.5-1 mm size fraction), not all altered material could be removed from the analyzed sample material. Overall, the weight % (wt. %) loss on ignition (LOI) values, a common indicator for the degree of alteration, are relatively low for such old submarine rocks (LOI < 4.0 wt. % for 28 of the 38 samples). During low temperature seawater alteration, the HFSEs (e.g., Zr, Nb) and REEs are considered to be relatively immobile, whereas the alkali elements, LILE (e.g., Rb, Sr), U and Pb are prone to mobilization during alteration (e.g., Jochum and Verma, 1996). If we exclude the samples with LOI values of > 4.0 wt. %, we obtain a reasonably good correlation coefficient for immobile

vs. immobile element concentrations (e.g., Nb vs Zr, Ba, La and Th with the best fit line ( $R^2$ ) value of 0.86-0.92, not shown) and immobile vs. mobile element concentrations (e.g., Nb vs Rb, Sr, U and Pb with  $R^2 = 0.70-0.78$ , not shown). The correlations indicate that secondary processes have not completely altered the chemistry of the samples. Nevertheless, to minimize the effects of seawater alteration, we focus on immobile elements and radiogenic isotope ratios in this study.

Since radiogenic isotope ratios increase progressively with time through radiogenic in-growth of the parent to the daughter isotopes, age correction followed by projection to a common age is necessary to compare radiogenic isotope ratios of samples with varying emplacement ages, especially when dealing with volcanic rocks formed over an age range of 130 Myr (see Fig. A1 in Appendix A). After calculating the initial isotope ratios, they are projected to a common age of 60 Ma, using the proposed EM I source ratios of Willbold and Stracke (2006). Seawater alteration could change the parent/daughter element concentrations and ratios and thus age correction can result in an under- or over-estimation of initial isotope ratios.

We analyzed 150-200 mg whole-rock chips leached with 2N HCl at 70°C for one hour, to remove potential surface contamination. In general, the Sm-Nd and Lu-Hf isotope systems are considered to be resistant to low temperature alteration and thus the initial isotope ratios are assumed to be close to those of the magmatic sources. In contrast, the Sr isotope ratios can be significantly elevated by addition of or exchange with seawater Sr ( $^{87}\text{Sr}/^{86}\text{Sr}$  ratios of  $\sim 0.707-0.709$  over the last 130 Ma; Jones and Jenkyns, 2001 and references therein). Therefore, rock powders, leached in 6N HCl at 150 °C for 3 days and then triple rinsed in 18.2 M $\Omega$  deionized water, were additionally analyzed for all samples. Twenty-three out of 32 samples produced slightly to significantly lower  $^{87}\text{Sr}/^{86}\text{Sr}$  ratios for the strongly leached powders than the mildly

leached chips, whereas 8 leached powders yielded slightly higher Sr isotope ratios compared to the chips. We assume that the lowest  $^{87}\text{Sr}/^{86}\text{Sr}$  values from pairs of powder and chips are closest to the prime magmatic values and we thus use them for the petrogenetic interpretation. The relatively good correlation of  $^{87}\text{Sr}/^{86}\text{Sr}_{\text{initial}}$  vs.  $^{143}\text{Nd}/^{144}\text{Nd}_{\text{initial}}$  ( $R^2 = 0.71$ , not shown) and  $^{176}\text{Hf}/^{177}\text{Hf}_{\text{initial}}$  ( $R^2 = 0.65$ , not shown) compared to initial Nd vs. Hf ( $R^2 = 0.60$ , not shown), suggests that the initial  $^{87}\text{Sr}/^{86}\text{Sr}$  ratios are representative of the primary magmatic ratios.

The Pb isotope ratios are essential to discriminate between the Tristan- and Gough-type components (Rohde et al., 2013a; Hoernle et al., 2015). Although Th is highly immobile, U is mobile even during low-temperature seafloor alteration and Pb can be mobilized by hydrothermal fluids. Fresh lavas (LOI < 2 wt. %) from the entire Tristan-Gough hotspot track have Nd/Pb ratios of  $12 \pm 3$  ( $n = 121$ ; 1 standard deviation (SD)), which is similar to the Nd/Pb ratios ( $12 \pm 3$ ; 1 SD; Fig. A2 in Appendix A) of our samples. Since Nd is relatively immobile during seafloor alteration, we assume that the Pb concentrations in our samples are also close to the primary magmatic values (Fig. A2 in Appendix A). In contrast, the average Th/U and Nb/U ratios of fresh Tristan-Gough hotspot seamount lavas (Th/U =  $4.7 \pm 0.7$ ; Nb/U =  $43 \pm 7$ ;  $n = 121$ ; LOI < 2 wt. %) compared to our samples (Th/U =  $4.2 \pm 1.7$ ; Nb/U =  $35 \pm 16$ ; Fig. A2 in Appendix A) suggest U uptake in some of our samples. If the U uptake took place shortly after the emplacement of the volcanic rocks and the rock became a closed system thereafter, the calculated initial  $^{206}\text{Pb}/^{204}\text{Pb}$  and  $^{207}\text{Pb}/^{204}\text{Pb}$  isotope ratios using the measured U-Pb concentrations should reflect those of the source (Hauff et al., 2000). However, uranium mobilization occurring long after emplacement of the volcanic rocks will result in over- or under-correction of initial uraniumogenic Pb isotope ratios. If the lavas were affected relatively recently, the U concentration for each sample can be estimated from the Th/U

ratios of the freshest lavas of the Tristan-Gough track ( $4.7 \pm 0.7$ ). The estimated U concentrations can then be used to calculate the initial uranogenic Pb isotope ratios (e.g., Nobre Silva et al., 2013; Harrison et al., 2017). Since we are unaware of the exact process of U mobilization (e.g., timing, single event and/or progressive process), we use the calculated  $^{206}\text{Pb}/^{204}\text{Pb}_{60\text{Ma}}$  ratios of the measured and normalized U concentration to delimit the maximum over- or undercorrection (Appendix A\_Fig. 1). The Pb isotope data derived from the two approaches show similar trends for the Tristan-Gough hotspot track and thus we believe that our initial Pb isotope data can be used to make inferences about the isotopic source compositions of the lavas (Fig. A1 in Appendix A). In this study, we use the initial Pb isotope data calculated using the U concentrations estimated from the average Th/U ratio of fresh samples ( $4.7 \pm 0.7$ ).

## 4.2 Geochemical results

The freshest samples (LOI < 4.0 wt. %) have MgO values between 2.1 and 6.3 wt. %, except one sample (S0233 DR43-3) with 11.2 wt. %, and SiO<sub>2</sub> contents from 47.6 to 51.6 wt. %. Based on the limited spread of MgO and SiO<sub>2</sub> contents in our samples, they show no clear trends on plots using these differentiation indicators versus other major elements (Fig. A3 in Appendix A). Irrespective of the LOI values, all samples lie within the compositional range of previously published lavas from the Tristan-Gough hotspot system (Fig. A3 in Appendix A).

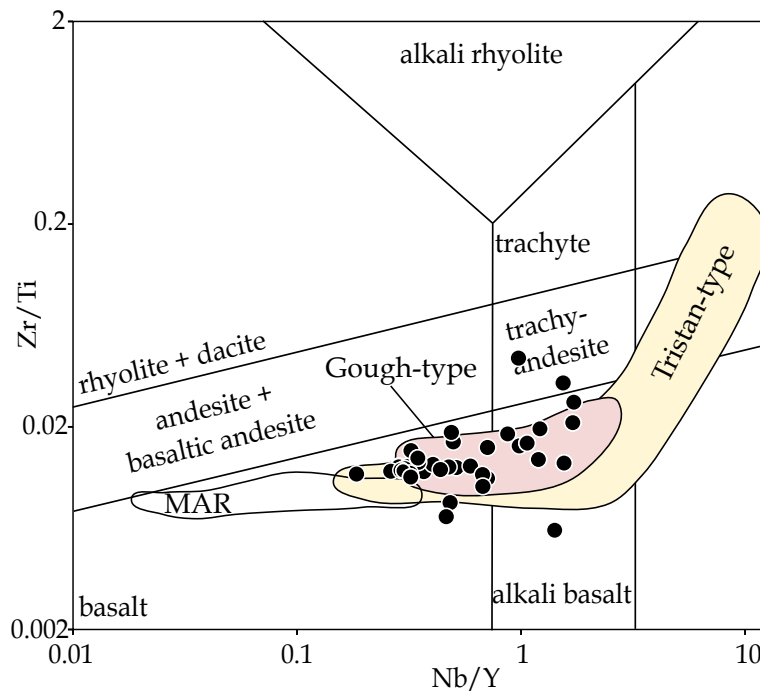


**Figure 2: Rock classification (Nb/Y vs. Zr/Ti plot) using immobile trace element ratios after Pearce (1996) of the studied Walvis Ridge rocks compared to lavas from the Tristan-Gough hotspot track. The Tristan-type lavas come from the Tristan-track (including Tristan Islands) and DSDP Sites 527 & 528, whereas the Gough-type lavas include those from the Walvis Ridge and the Gough-track (including Gough Island). Also shown is the field for normal Mid-Atlantic Ridge (MAR) basalts defined as having La/Yb ratios of < 1 and La/Sm ratios of < 1.5, taken from the compilation of Class and Lehnert (2012). Note that only samples with MgO contents of > 2 wt.% are included. The literature is taken from the GEOROC Database and are reported in detail in Appendix F.**

Using the Nb/Y vs. Zr/Ti immobile element discrimination diagram (Pearce, 1996), the recovered lavas are primarily basaltic, with nine being alkali basalts and two trachyandesite samples (S0233 DR40-1 and DR19-1A; Fig. 2). On a Nb/Yb vs. Th/Yb diagram (Fig. 3a), the new data extend from OIB type compositions to compositions above the EMORB field (Enriched Mid-Ocean Ridge Basalts) or in the field for subduction zone volcanic rocks (Pearce, 2008). The Th/Nb ratio is a proxy for crustally derived components (Pearce, 2008). On a Nb/Yb vs.  $TiO_2/Yb$  plot (Fig. 3b), our samples show a crude positive slope extending from tholeiitic EMORBs to enriched tholeiitic ocean island basalt (OIB) type compositions to alkaline OIB field, which is typical for lavas formed by a mantle plume interacting with a mid-ocean ridge (Pearce, 2008).

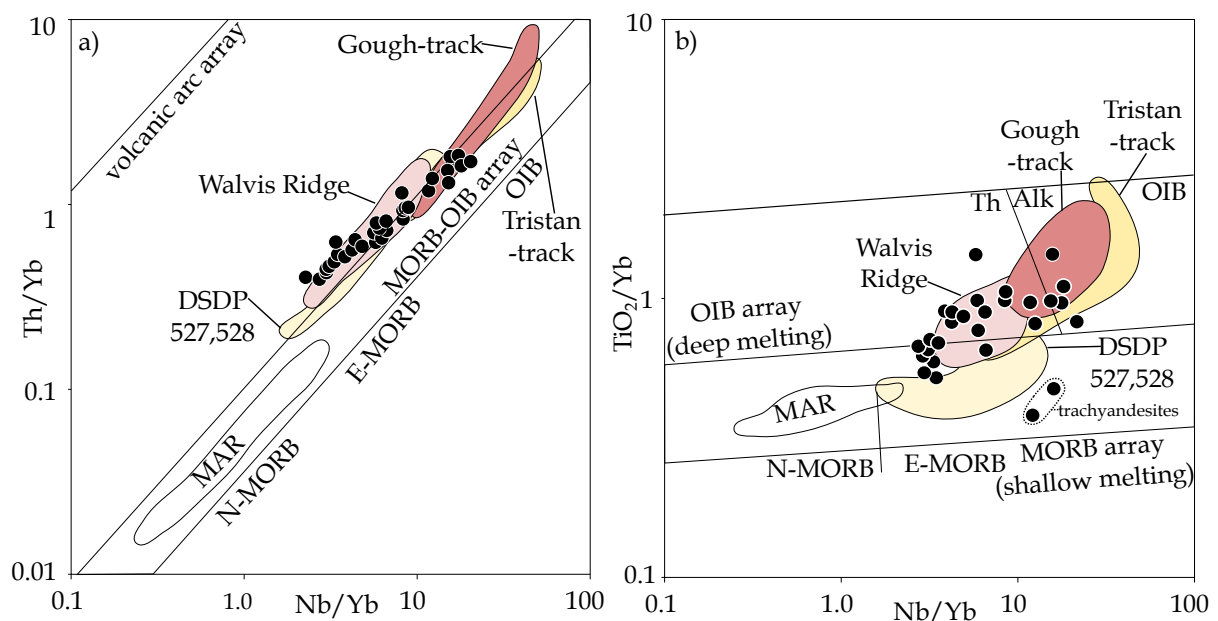


**Figure 3: Nb/Yb vs. a) Th/Yb and b)  $TiO_2/Yb$  after Pearce (2008) of the studied rocks compared to lavas from the Tristan-Gough hotspot. Abbreviations: Th = tholeiites and Alk = alkaline. The Tristan-type lavas are subdivided into Tristan subtrack and DSDP Sites 527 & 528, and the Gough-type lavas are divided into those from the Walvis Ridge and the Gough subtrack. Also shown is the field for normal Mid-Atlantic Ridge (MAR) basalts. Note that only samples with MgO > 2 wt. % are included. Literature data is reported in Appendix F.**

On incompatible multi-element diagrams (Fig. 4), the lavas show variable degrees of Nb-Ta enrichment/depletion in relation to Th and La, with Nb/Th ratios normalized to primitive mantle (0.73 - 1.38) and Nb/La ratios normalized to primitive mantle (0.62 - 1.03, using samples with MgO contents of > 3 wt.% and LOI values of < 4 wt. %). The tholeiitic rocks (Ti/V < 40; Nb/Y < 0.7) generally have flat to negative Nb-Ta anomalies ( $Nb_N/Th_N < 1$ ; excluding sample S0233 DR62-2; Fig., 4a), whereas the alkaline rocks (Ti/V > 50; Nb/Y > 0.7) show positive Nb-Ta anomalies ( $Nb_N/Th_N > 1$ ; Fig. 4b). All patterns are characterized by a pronounced negative Pb anomaly relative to the neighboring REEs (Ce and Pr, Nd), which is typical of OIBs (Fig. 4). All samples also show a positive Zr anomaly relative to Hf with  $Zr_N/Hf_N$  ratios = 1.07-1.31 and a negative Ti anomaly relative to Eu (Fig. 4). Overall the most incompatible elements are enriched relative to the less incompatible elements (Fig. 4). In general, the tholeiitic samples have similar trace element patterns to previously published lavas from the Walvis Ridge (Fig. 4a), whereas the alkali basalts have comparable trace element patterns to lavas from the Guyot Province with overall higher concentrations of the most incompatible elements (Fig. 4b).

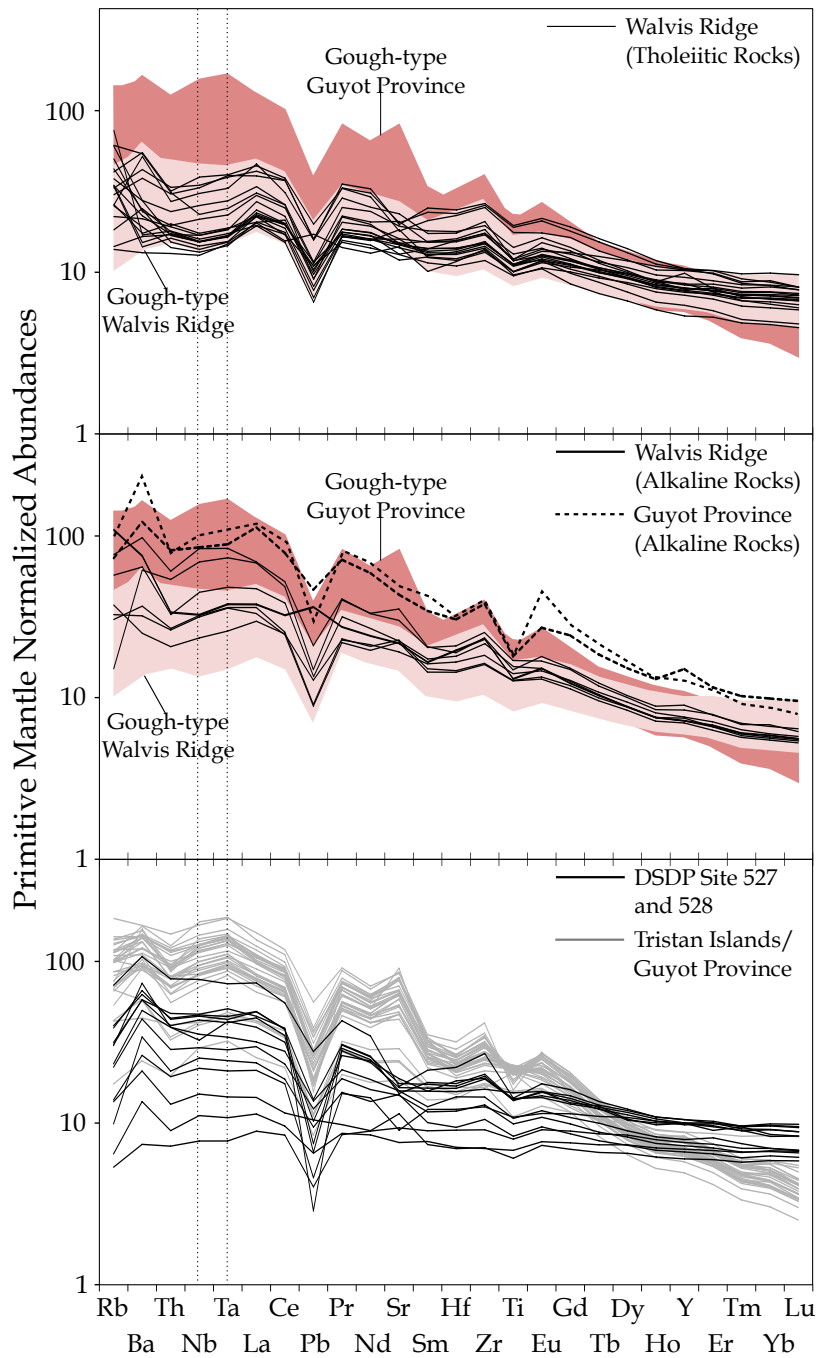


**Figure 4: Normalized incompatible element diagrams of a) tholeiitic basement lavas from the Walvis Ridge, b) alkaline lavas from the Walvis Ridge basement, and the Guyot Province with Gough-type compositions compared to the Gough-type Guyot Province lavas and Walvis Ridge. c) shows tholeiitic and alkaline lavas from DSDP Sites 527 & 528, Tristan sub-track Guyot Province and Tristan Islands (i.e., Tristan da Cunha, Nightingale and Inaccessible) from the literature. It should be noted that the Gough-type tholeiitic rocks are characterized by Nb-Ta troughs (Fig. 4a) and the Gough-type alkaline rocks have Nb-Ta peaks relative to neighboring La and Th, whereas the Tristan-type rocks show exclusively flat to positive Nb-Ta anomalies relative to neighboring elements (Fig. 4c). The element concentrations are normalized to primitive mantle after Hofmann (1988). Only samples with MgO contents of > 3 wt. % and LOI < 4 wt. % are shown. Literature data is taken from the GEOROC Database and are reported in detail in Appendix F.**



Isotope data of our new samples have the following isotopic ratios: radiogenic  $^{87}\text{Sr}/^{86}\text{Sr}_{60\text{Ma}}$  (0.704 - 0.706), unradiogenic  $^{143}\text{Nd}/^{144}\text{Nd}_{60\text{Ma}}$  (0.5123 - 0.5126) and  $^{176}\text{Hf}/^{177}\text{Hf}_{60\text{Ma}}$  (0.2826 - 0.2828), elevated  $^{207}\text{Pb}/^{204}\text{Pb}_{60\text{Ma}}$  (15.46 - 15.63) and  $^{208}\text{Pb}/^{204}\text{Pb}_{60\text{Ma}}$  (38.01 - 38.93) for their given  $^{206}\text{Pb}/^{204}\text{Pb}_{60\text{Ma}}$  values (17.42 - 18.52), and thus high  $\Delta 7/4\text{Pb}$  and  $\Delta 8/4\text{Pb}$  values characterize the EM I-type lavas (Fig. 4; Hart, 1984). In summary, the geochemical data lie largely within the range of previously published lavas from the Gough-type compositional group from the Tristan-Gough hotspot system, but a few samples either expand the Gough-type field in multi-isotope space or have Tristan-type compositions (Fig. 5).

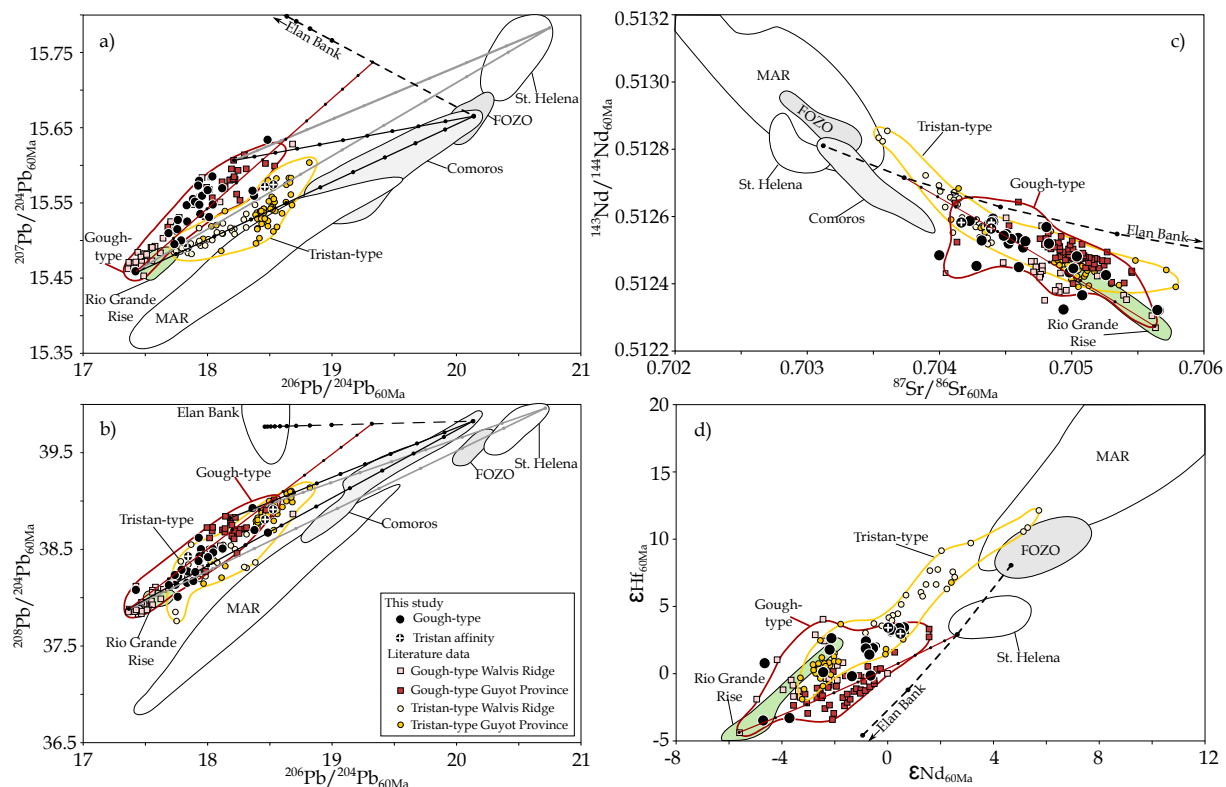


**Figure 5: Initial isotope ratios projected to 60 Ma using source parent/daughter ratios for the: (a) uraniumogenic ( $^{206}\text{Pb}/^{204}\text{Pb}_{60\text{Ma}}$  vs.  $^{207}\text{Pb}/^{204}\text{Pb}_{60\text{Ma}}$ ) and (b) thorogenic ( $^{206}\text{Pb}/^{204}\text{Pb}_{60\text{Ma}}$  vs.  $^{208}\text{Pb}/^{204}\text{Pb}_{60\text{Ma}}$ ) Pb isotope correlation diagrams, and (c)  $^{87}\text{Sr}/^{86}\text{Sr}_{60\text{Ma}}$  vs.  $^{143}\text{Nd}/^{144}\text{Nd}_{60\text{Ma}}$  and (d)  $\epsilon\text{Nd}_{60\text{Ma}}$  vs.  $\epsilon\text{Hf}_{60\text{Ma}}$  plots. The lavas from the Tristan-Gough hotspot track are divided into: 1) Gough-type composition, comprising lavas from the Walvis Ridge, Gough sub-track and Gough Island, and 2) Tristan-type composition, consisting of lavas from DSDP Site 527 & 528 on the Walvis Ridge, Tristan sub-track and Tristan da Cunha Island. On the Pb isotope diagrams (Figs. 5a-b), mixing lines are shown for Gough-type lavas with the most radiogenic samples from the Comoros (gray line), representing a FOZO-type composition, and St. Helena HIMU (black line). In all the plots the mixing lines of the EM II-like component (Elan Bank; Ingle et al., 2002; Nobre Silva et al., 2013) with Comoros (black dashed line) and Gough-type lavas with a mixture of 10% EM II and 90% FOZO (red line) are shown. The compositions of the mixing components are reported in Appendix A. For comparison, fields from the Mid-Atlantic Ridge (MAR; with  $\text{La}/\text{Yb} < 1$  and  $\text{La}/\text{Sm} < 1.5$ ), the Rio Grande Rise, St. Helena, Comoros and FOZO (after Stracke et al., 2005) are shown. Literature data is taken from the GEOROC Database and are reported in detail in Appendix F.**

### 4.3 $^{40}\text{Ar}/^{39}\text{Ar}$ dating

We report the results of 12 new  $^{40}\text{Ar}/^{39}\text{Ar}$  step-heated ages from 10 different sample sites using hydrofluoric acid-leached mineral separates (4-8 mg of plagioclase and/or K-feldspar) and one glass sample (dredge sample S0234 DR6-1). As mentioned previously, submarine lavas are affected by variable degrees of alteration, therefore we monitored the Ca/K ratios and calculated  $^{36}\text{Ar}/^{39}\text{Ar}$  K-feldspar and basalt or  $^{36}\text{Ar}/^{37}\text{Ar}$  plagioclase alteration index (AI) values (Baksi, 2007; van den Bogaard, 2013). We used the calculated AI and % of atmospheric  $^{40}\text{Ar}$  ( $^{40}\text{Ar}_{\text{atm}}$ ) values to determine the degree of alteration of the step-heating analyses. The  $^{40}\text{Ar}/^{39}\text{Ar}$  step-heating age spectra of our samples preserve good to disturbed age spectra with low-temperature steps yielding higher AI values (i.e., above the  $^{36}\text{Ar}/^{37}\text{Ar}$  plagioclase and  $^{36}\text{Ar}/^{39}\text{Ar}$  K-feldspar AI cut-off values of 0.00006, and the  $^{36}\text{Ar}/^{39}\text{Ar}$  basalt AI cut-off value of 0.0006; Baksi, 2007; van den Bogaard, 2013), higher %  $^{40}\text{Ar}_{\text{atm}}$  values, and variable Ca/K ratios relative to the medium- to high-temperature steps. This indicates that the low-temperature steps are affected by degassing of altered material compared to the fresh medium- and high-temperature steps. Inverse isochron ages were calculated to confirm both the plateau ages and identify if the samples preserved initial atmospheric  $^{40}\text{Ar}/^{36}\text{Ar}$  ratios, without the presence of extraneous  $^{40}\text{Ar}$  components. In the majority of samples, the inverse isochron ages of the plateau steps overlap within 95% confidence (95% conf.) errors of the calculated plateau ages, and yield initial  $^{40}\text{Ar}/^{36}\text{Ar}$  ratios within 95% conf. errors of the atmospheric  $^{40}\text{Ar}/^{36}\text{Ar}$  ratio of 295.5 (Steiger and Jäger, 1977).

**Table 1:  $^{40}\text{Ar}/^{39}\text{Ar}$  step-heating results and calculated ages from the Walvis Ridge**

Cruise	Sample	Phase	Plateau age (Ma)	$\pm 2\sigma$ (Ma)	Cum. % $^{39}\text{Ar}$	MSWD	P	Steps	Inverse isochron age (Ma $\pm$ 95% conf.)
S0233	DR 4-1	K-feld	59.17	$\pm 0.20$	91.8	0.51	0.90	2-13	Plateau steps = $59.14 \pm 0.23$
S0233	DR 19-1A	Plag	70.84*	$\pm 0.28$	41.9	0.83	0.48	9-12	Plateau steps = $71.20 \pm 0.47$
S0233	DR 35-12	Plag	75.40	$\pm 1.2$	55.4	1.6	0.15	6-11	Plateau steps = $76.3 \pm 2.6$
S0233	DR 41-2	Plag	81.31	$\pm 0.21$	94.7	0.82	0.62	5-16	Plateau steps = $81.27 \pm 0.27$
S0233	DR 43-3	Plag	78.84	$\pm 0.50$	51.9	2.0	0.06	9-15	No isochron
S0233	DR 43-6	Plag	80.00	$\pm 0.52$	89.5	0.96	0.49	5-18	Plateau steps = $79.86 \pm 0.71$
S0233	DR 62-1	Plag	83.85	$\pm 0.48$	52.1	1.4	0.21	8-16	Plateau steps = $87.4 \pm 1.0$
S0233	DR 62-2	Plag	84.20	$\pm 1.2$	57.1	1.3	0.24	2.9	Plateau steps = $84.2 \pm 2.0$
WMA	DR62-1/-2		83.90	$\pm 0.45$		0.29	0.59		
S0233	DR 84-2	P/K	109.00*	$\pm 1.0^{\wedge}$	48	3.8	0.00	7-16	Plateau steps = $109.1 \pm 2.5$
S0234	DR 4-1	Plag	91.34	$\pm 0.34$	66.6	2.2	0.03	4-11	Plateau steps = $91.24 \pm 0.57$
S0234	DR 6-1	Glass	89.33	$\pm 0.20$	87.4	0.79	0.69	4-19	Plateau steps = $89.01 \pm 0.27$
Cruise	Sample	Phase	WMA (Ma)	$\pm 2\sigma$ (Ma)		MSWD	P	Steps	Inverse isochron age (Ma $\pm$ 95% conf.)
S0233	DR37-1A	Plag	79.59	$\pm 0.72$	0.48	2.0	0.07	8-10 & 12-14	WMA steps = $80.4 \pm 2.1$

Abbreviations: Plag. = plagioclase; K-feld. = K-feldspar; P/K = plagioclase/K-feldspar mixture; Cum. = cumulative; MSWD = Mean Squares Weighted Deviation; P = probability; conf. = confidence; WMA = weighted mean age; \* = pseudo-plateau age (40-50%  $^{39}\text{Ar}$ ); and  $\wedge$  = 95% conf. error..

We consider  $^{40}\text{Ar}/^{39}\text{Ar}$  step-heating analysis as statistically valid if the following widely accepted criteria are fulfilled (e.g., Lanphere and Dalrymple, 1978; Pringle et al., 1993; O'Connor and Jokat, 2015b): (1) a well-defined age spectrum plateau created by three or more continuous and concordant steps (at the  $2\sigma$  confidence level) with  $> 50\%$  of the cumulative  $^{39}\text{Ar}$ , (2) the mean square of weighted deviations (MSWD) is  $\leq 2$ , and the probability of fit is  $> 0.05$ , and (3) calculated plateau and isochron ages are concordant at 95 %confidence levels (Table 1; Appendix C).

The step-heating analyses mostly yielded medium-to high-temperature plateau ages with a general younging trend from northeast to southwest (ages in Ma are all errors quoted at  $\pm 2\sigma$ , unless otherwise noted) of  $109.0 \pm 1.0$  (95% conf.; S0233 DR84-2),  $91.34 \pm 0.34$  (S0234 DR4-1),  $89.33 \pm 0.20$  (S0234 DR6-1),  $83.85 \pm 0.48$  (S0233 DR62-1),  $84.2 \pm 1.2$  (S0233 DR62-2),  $81.31 \pm 0.21$  (S0233 DR41-2),  $78.84 \pm 0.50$  (S0233 DR43-3),  $80.00 \pm 0.52$  (S0233 DR43-6),  $79.90 \pm 1.2$  Ma (S0233 DR37-1A),  $75.4 \pm 1.2$  (S0233 DR35-12),  $70.84 \pm 0.28$  (S0233 DR19-1A) and  $59.17 \pm 0.20$  (S0233 DR4-1). A detailed description of the  $^{40}\text{Ar}/^{39}\text{Ar}$  age spectra and inverse isochrons (Table 1) are reported in Appendix A.

## 5. Discussion

### 5.1 The age progressive Walvis Ridge

With our new sample set, we fill a major gap in the temporal and geochemical evolution of the Tristan-Gough hotspot track. Previously ages from only five sample sites were available for the Walvis Ridge between the DSDP Sites and the northeastern end of the Walvis Ridge (Rohde et al., 2013b; O'Connor and Jokat, 2015a), which covers ~1500 km (nearly half) of the entire hotspot track. Of these obtained five  $^{40}\text{Ar}/^{39}\text{Ar}$  ages, only two were close to what was expected for a linear age progression, placing considerable doubt as to whether the Walvis Ridge fit a simple age-progressive hotspot model (Figs. 1 and 6). In an attempt to explain the lack of a good correlation in age versus distance for the Walvis Ridge, O'Connor and Jokat (2015a) invoked tectonic complexities related to plume-ridge interactions. Other explanations, proposed to explain the younger ages of some of the samples, include east-west orientated fast flowing channels in the uppermost mantle or shallow tectonic processes (Fairhead and Wilson, 2005; Foulger, 2017; O'Connor et al., 2018). However, it should be noted that the anomalously young lavas have distinct HIMU-type compositions (excluding one sample with EM I-type composition) (Figs. 1 and 4), indicating that the younger volcanism is not related to the Tristan-Gough hotspot (Homrighausen et al., in review-b).

Our new  $^{40}\text{Ar}/^{39}\text{Ar}$  data, together with previously published  $^{40}\text{Ar}/^{39}\text{Ar}$  ages (Rohde et al., 2013b; O'Connor and Jokat, 2015a, b), show a continuous age progression along the entire Walvis Ridge beginning at  $114.1 \pm 0.4$  Ma at the northeastern end, close to the Namibian coast (Rohde et al., 2013b) to  $68.2 \pm 0.7$  Ma at DSDP Site 527 near the southeastern end (Fig. 6; O'Connor and Jokat, 2015b), excluding the HIMU-type Late-Stage volcanism samples (Homrighausen et al., in review-b; Homrighausen et al., in review-a). The  $^{40}\text{Ar}/^{39}\text{Ar}$  age data from basement samples with EM I-type compositions

from the submarine Tristan-Gough hotspot track show an age progression of 31.05 mm/a ( $R^2 = 0.97$ ). The Etendeka flood basalts (135-132 Ma; Renne et al., 1996; Renne, 2015) and the Tristan da Cunha and Gough Islands (0.12 -2.6 Ma; Maund et al., 1988; Hicks et al., 2012) plot close to this array, providing further support for the age progression (Fig. 6). Our calculated migration rate is significantly higher than the 26 mm/a proposed by O'Connor and Jokat (2015a), but is similar to the 30 mm/a rate proposed by Rohde et al. (2013b).

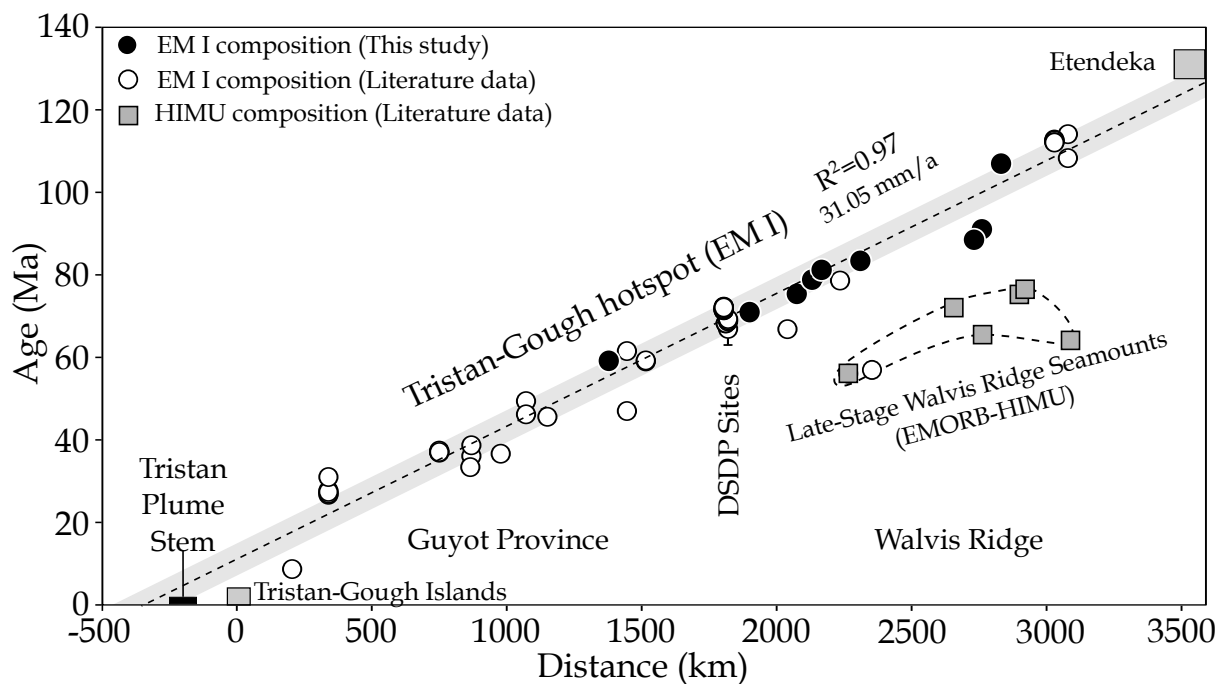


**Figure 6: Distance from the active volcanic islands (Tristan-Gough) versus  $^{40}\text{Ar}/^{39}\text{Ar}$  ages for the Tristan-Gough hotspot track with EM I-type compositions (literature data = Rohde et al., 2013b; O'Connor and Jokat, 2015a, b). Sample sites were projected orthogonally to the proposed hotspot track (dashed line in Fig. 1). The dashed line in this figure shows the calculated age progression for the entire data set (31.05 mm/a;  $R^2$  line fit = 0.96) of the submarine lavas from the Tristan-Gough hotspot track. The grey field around the age progression line represents the duration of the main volcanic stage with an average age range of 8 Ma at a given location (i.e., distance from the islands), but this duration can be twice as long in some locations. The late-stage (post-erosional) volcanism, which has a distinct composition from the basement lavas (HIMU-EMORB versus EM I type chemical composition), is generally 20-40 Ma younger than the underlying basement at that location (Homrighausen et al., in review-b). The black bar marks the low velocity anomaly of the Tristan plume stem after Schlömer et al. (2017). Note, that the age from Etendeka (135-132 Ma; Renne et al., 1996; Renne, 2015) and Tristan / Gough islands (0.12 -2.6 Ma; Maund et al., 1988; Hicks et al., 2012) are shown for comparison (large grey boxes).**

O'Connor et al. (1999) proposed that the age progression may have slowed down at or after ~45 Ma. The  $^{40}\text{Ar}/^{39}\text{Ar}$  age data for the 40 Ma old Discovery hotspot track, located ~600 km to the south but with a sub-parallel trend to the Tristan-Gough hotspot has a well-constrained age progression of 27 mm/a (Schwindrofska et al., 2016). A change in plate motion at or after 45 Ma could explain why the youngest dated seamounts and the Tristan-Gough Islands fall below the trend for the >45 Ma portion of the hotspot track (Fig. 6). Alternatively, the plate velocity has remained unchanged since ~115 Ma and both Tristan da Cunha and Gough Island may have begun forming ~10 Ma ago. This implies that the present position of the proposed hotspot(s) lie(s) ~310 km closer to the MAR (Fig. 1), whereas the observed low-velocity seismic anomaly in the upper mantle is ~200 km to the west of Tristan da Cunha (Schlömer et al., 2017).

Most lavas along the entire Tristan-Gough hotspot track lie within  $\pm 4$  Ma ( $2\sigma$ ) of our calculated age progression line, whereas most alkaline lavas at the Walvis Ridge (e.g., sites SO233 DR41, SO234 DR4 & 6) show overall younger ages compared to the average age progression (Appendix C). Late-stage (also referred to as rejuvenated or post-erosional) volcanism, occurring up to 15 Ma after the formation of the main volcanic edifice, is a characteristic of many intraplate volcanic systems, e.g., the Canary (15 Ma) and Hawaiian Islands (5 Ma) (Hoernle and Schmincke, 1993; Garcia et al., 2010). Some lavas from the Walvis Ridge are up to 20-40 Ma younger than the underlying or nearby basement (Rohde et al., 2013b; O'Connor and Jokat, 2015b; Homrighausen et al., in review-b), which is unusual for aseismic ridges and hotspot tracks. These rocks were recovered from superimposed seamounts on the Walvis Ridge or nearby seamounts and ridges (Fig. 1). Homrighausen et al. (in review-b) shows that these lavas have a St. Helena HIMU end member to EMORB composition, and conclude that these rocks were



derived from a younger magmatic event unrelated to the Tristan-Gough mantle plume (Fig. 1).

In conclusion, the Tristan-Gough hotspot track (EM I-type), excluding late-stage volcanism with a different composition (HIMU-EMORB), displays an excellent linear age progression (Fig. 6), characteristic of a deep-rooted mantle plume (e.g., Morgan, 1971; Wilson, 1973; Morgan, 1981; Campbell, 2007).

## **5.2 The Gough-type composition: The dominant composition in South Atlantic hotspots**

### *5.2.1 The beginning of the geochemical zonation in the Tristan-Gough hotspot track*

The Tristan-Gough hotspot track comprises two EM I-type compositional fields that can be best distinguished using an uranogenic Pb isotope diagram with Gough-type compositions having higher  $^{207}\text{Pb}/^{204}\text{Pb}_{60\text{Ma}}$  at a given  $^{206}\text{Pb}/^{204}\text{Pb}_{60\text{Ma}}$  ratio (Figs. 5 and 7). The two EM I-types also show differences in Nb/Zr ratios (Fig. 7). In a Nb/Y vs. Zr/Y plot, the Tristan subtrack lavas have higher Nb/Y ratios at a given Zr/Y ratio than the Gough-type lavas (MgO > 3 wt. % and LOI < 5 % wt. %; Fig. 7).

Most of our new samples lie within the Gough compositional domain, confirming that the Walvis Ridge is primarily composed of this EM I-type composition (Figs. 5 and 7). Nevertheless, a few samples either expand the Gough-field towards the Tristan compositional field, or the first appearance of the Tristan-type can be extended to about 90 Ma (Figs. 1, 5 and 7). Since these lavas are from the eastern side of the Walvis Ridge, they suggest the local presence of Tristan-type material before the hotspot track became zoned (Fig. 1). Although no clear evidence has been found thus far for the presence of Tristan-type material during the formation of the Etendeka and Parana flood basalts (Hoernle et al., 2015), there is not enough data (samples from only two sites have been reported thus far; Rohde et al., 2013a) to evaluate whether Tristan-type compositions are present on the Rio Grande Rise. The Rio Grande Rise was located westward of the Walvis Ridge during its formation, and thus could extend the history of geochemical zonation further back in time.

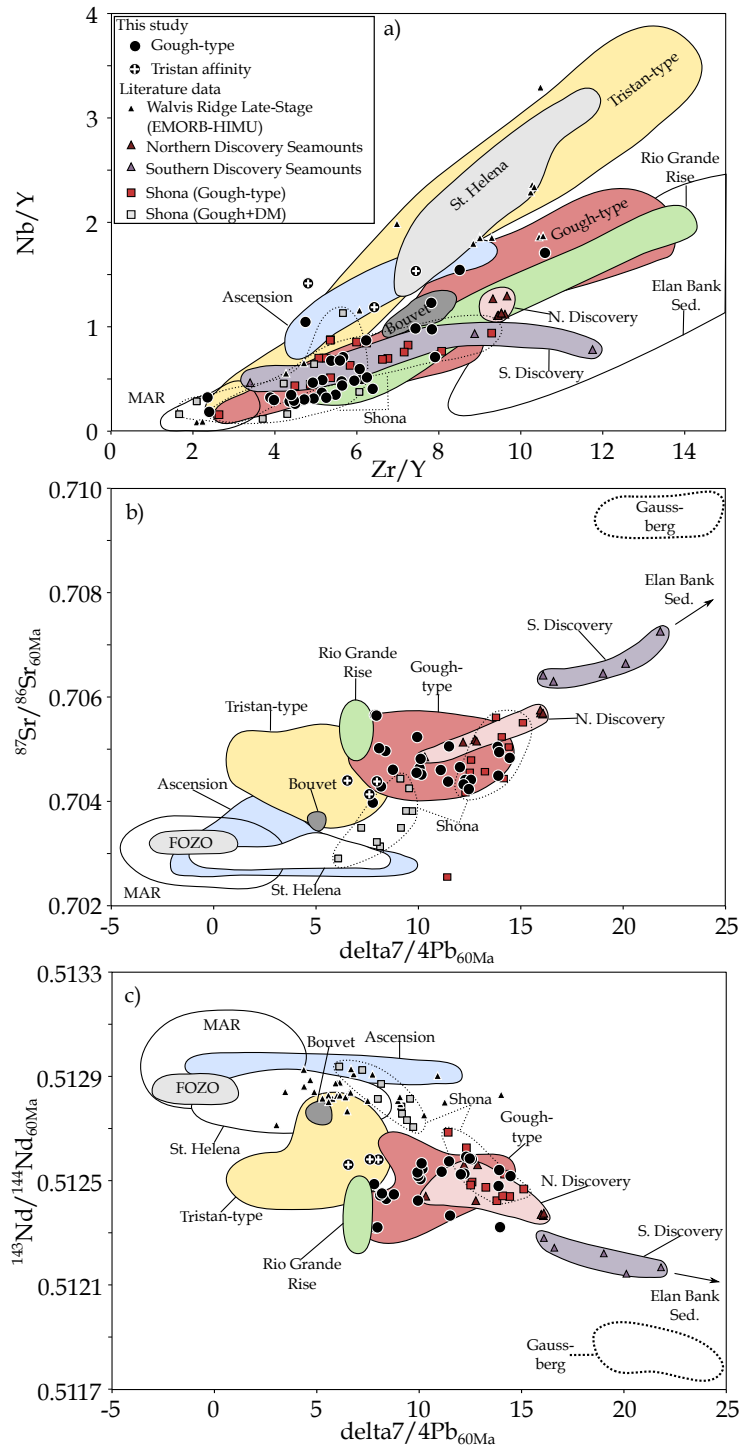


**Figure 7: South Atlantic intraplate lavas from St. Helena, Ascension, Tristan-Gough basement lavas (subdivided into Tristan- and Gough-types), Late-Stage Walvis Seamounts, Discovery, Shona and Bouvet lavas shown on: a) Nb/Y vs. Zr/Y (MgO > 3 wt. % and LOI < 5 wt. %), and  $\delta 7/4\text{Pb}_{60\text{Ma}}$  vs. b)  $^{87}\text{Sr}/^{86}\text{Sr}_{60\text{Ma}}$  and c)  $^{143}\text{Nd}/^{144}\text{Nd}_{60\text{Ma}}$  ratios. Possible mixing end members are also shown: Gaussberg lamproites, Elan Bank sediments (Sed.) from the Kerguelen plateau, and FOZO (after Stracke et al. (2005)). Literature data is taken from the GEOROC Database and are reported in detail in Appendix F.**

### 5.2.2 Geochemical Variations of the Gough-type lavas in the Tristan-Gough hotspot track

Since the Gough-type composition is present throughout the entire history of the Tristan-Gough mantle plume, we now focus on the geochemical diversity of this compositional type. The vast majority of the Walvis Ridge lavas are characterized by tholeiitic compositions ( $\text{Nb}/\text{Y} < 0.7$ ;  $\text{Nb}/\text{Yb} < 10$ ,  $\text{TiO}_2/\text{Yb} < 1$ ,  $\text{Ti}/\text{V} < 40$ ; Fig. 3) with a flat to negative Nb-Ta anomaly (e.g.,  $\text{Nb}_\text{N}/\text{Th}_\text{N} < 1$ ; Fig. 4) and relatively depleted incompatible trace element concentrations. In contrast the alkaline Gough-type lavas ( $\text{Nb}/\text{Y} > 0.7$ ;  $\text{Nb}/\text{Yb} > 10$ ,  $\text{TiO}_2/\text{Yb} > 1$ ,  $\text{Ti}/\text{V} > 50$ ) from the Guyot Province overall display flat to positive Nb-Ta anomalies (e.g.,  $\text{Nb}_\text{N}/\text{Th}_\text{N} > 1$ ) and relatively enriched incompatible trace elements (Figs. 3 and 4). As mentioned above, the alkaline Gough-type lavas from the Walvis Ridge have similar geochemical characteristics to lavas from the Guyot Province (Fig. 4). In general, the lower incompatible element abundances of the tholeiitic Walvis Ridge lavas relative to the alkaline lavas from the Guyot Province are consistent with the change from plume-ridge interaction during the Walvis Ridge formation (e.g., Humphris and Thompson, 1983; O'Connor and Duncan, 1990), with low pressure and high melting degrees of 15-24 % (Gibson et al., 2005; Salters and Sachi-Kocher, 2010), to intraplate volcanism, with an increase in lithospheric thickness resulting in higher pressure and lower melting degrees of 5-8% in the Guyot Province (Gibson et al., 2005; Weit et al., 2017).

However, the Nb-Ta systematics cannot be explained by variable degrees of melting or depth of melting alone (Jackson et al., 2008; Peters and Day, 2014). In general, EM I-type OIBs are characterized by flat to positive Nb-Ta anomalies (e.g., Willbold and Stracke, 2006; Jackson et al., 2008). Negative Nb-Ta anomalies in intra-plate lavas are either associated with the retention of Nb and Ta in residual Ti-oxides (e.g., rutile or titanite; Bromiley and Redfern, 2008) or are derived from the source. The negative Nb-

Ta anomalies in the majority of the tholeiitic Walvis Ridge lavas and positive Nb-Ta anomalies in the alkaline Guyot Province lavas is the opposite of what we would expect from partial melting with a residual phase retaining Nb and Ta from the source. The source TiO<sub>2</sub> phases would be expected to be exhausted at higher melting degrees (> 5-10 %; e.g., Pertermann and Hirschmann, 2003; Bromiley and Redfern, 2008), indicating that the negative Nb-Ta anomalies of the Walvis Ridge lavas with melting degrees of 15-24% must be source characteristics (Gibson et al., 2005; Salters and Sachi-Kocher, 2010). The Walvis Ridge tholeiites, similar to continental crust and pelagic sediments (e.g., GLOSS), are depleted in Nb-Ta relative to the neighboring Th and La trace elements (Plank and Langmuir, 1998; Rudnick and Gao, 2003; Plank, 2014) and also have Th/Yb above the mantle array at a given Nb/Yb ratio (Figs. 3 and 4; Pearce, 2008). In contrast, the alkaline Walvis Ridge and the Guyot Province lavas have flat to positive Nb-Ta anomalies and Th/Yb within the mantle array (Figs. 3 and 4), suggesting that the low degrees melts sample different source materials compared to tholeiitic high degree melts. The distinct Nb-Ta systematics of the Gough-type lavas supports the interpretation of Salters and Sachi-Kocher (2010) that the variation of DSDP Site 525 Gough-type lavas reflects mixing of two distinct components, where the component containing the unradiogenic Pb is EM I with a negative Nb-Ta anomaly.

The slope of the Gough-type array (Fig. 5;  $R^2 = 0.90$ ) on the uraniumogenic Pb isotope diagram (Fig. 5) is equivalent to an age of 2.4 Ga (Rohde et al., 2013a). Alternatively, this linear trend could be interpreted as mixing of low- $\mu$  (containing unradiogenic Pb isotope ratios) and high- $\mu$  (containing radiogenic Pb isotope ratios) components. The DSDP Site 525 and Rio Grande Rise lavas could serve as the low- $\mu$  mixing component (Zindler and Hart, 1986; Salters and Sachi-Kocher, 2010), characterized by negative Nb-Ta anomalies and elevated Th/Yb ratios above the mantle array. In multi-isotope space, the Gough

domain trends neither towards the proposed FOZO (e.g., Hart et al., 1992; Stracke et al., 2005) nor the EM II end member compositions (Fig. 5; Zindler and Hart, 1986). However, FOZO mixed with small proportion of EM II-like material (~10%), such as found in the Kerguelenen plateau (Ingle et al., 2002), could form a suitable high- $\mu$  component containing flat to positive Nb-Ta anomalies and lying on the MORB-OIB mantle array (Figs. 3 and 4). It should be noted that there is a weak correlation of the Nb-Ta anomaly (e.g.,  $Nb_N/Th_N$ ) versus  $^{206}Pb/^{204}Pb_{60Ma}$  (plot not shown), suggesting mixing of recycled lower continental crust (EM I, e.g., DSDP Site 525) with recycled oceanic crust (FOZO, similar to Comoros), plus sediments (EM II, similar to the Elan Bank sediments; Fig. 5). One possible explanation could be that at higher degrees of melting the resulting tholeiitic lavas at Walvis Ridge sample preferentially the lower continental crustal component (low- $\mu$ ), whereas at lower degrees of melting the alkaline lavas, such as primarily occur in the Guyot Province and Gough Islands sample mainly recycled ocean crust  $\pm$  sediments (high- $\mu$ ), possibly in the form of eclogite/garnet pyroxenite.

### 5.2.3 A common EM I-type in South Atlantic hotspots

The Discovery seamount chain represents the second long-lived spatially zoned hotspot track in the South Atlantic (Fig. 1; Schwindrofska et al., 2016). The Northern Discovery seamounts lie strictly within the Gough-type domain on Sr-Nd-Pb-Hf isotope plots, suggesting a common Gough source (Figs. 7 and 8; Schwindrofska et al., 2016). In contrast, the Southern Discovery seamounts have higher  $^{207}Pb/^{204}Pb_{60Ma}$  and  $^{87}Sr/^{86}Sr_{60Ma}$  ratios, and lower  $^{143}Nd/^{144}Nd_{60Ma}$  and  $^{176}Hf/^{177}Hf_{60Ma}$  ratios, but similar  $^{208}Pb/^{204}Pb_{60Ma}$  ratios at a given  $^{206}Pb/^{204}Pb_{60Ma}$  value (Figs. 7 and 8). This composition represents the third distinct and most enriched EM I-type composition in the South Atlantic.

The isotopic composition of the lavas from the Shona mantle plume largely overlap with the Gough-type lavas in multi-isotope space, but many samples trend to lower  $^{207}\text{Pb}/^{204}\text{Pb}_{60\text{Ma}}$ ,  $^{208}\text{Pb}/^{204}\text{Pb}_{60\text{Ma}}$  and  $^{87}\text{Sr}/^{86}\text{Sr}_{60\text{Ma}}$  ratios, and higher  $^{143}\text{Nd}/^{144}\text{Nd}_{60\text{Ma}}$  and  $^{176}\text{Hf}/^{177}\text{Hf}_{60\text{Ma}}$  ratios at given  $^{206}\text{Pb}/^{204}\text{Pb}_{60\text{Ma}}$  value (Figs. 7 and 8). In contrast to the Tristan-type composition, the range of Shona isotopic compositions is consistent with mixing of the Gough-type and a depleted MORB-like component (Hoernle et al., 2015; Hoernle et al., 2016). In conclusion, the Gough-type composition is also the dominant component in the Shona and Northern Discovery Seamounts (Figs. 7 and 8).

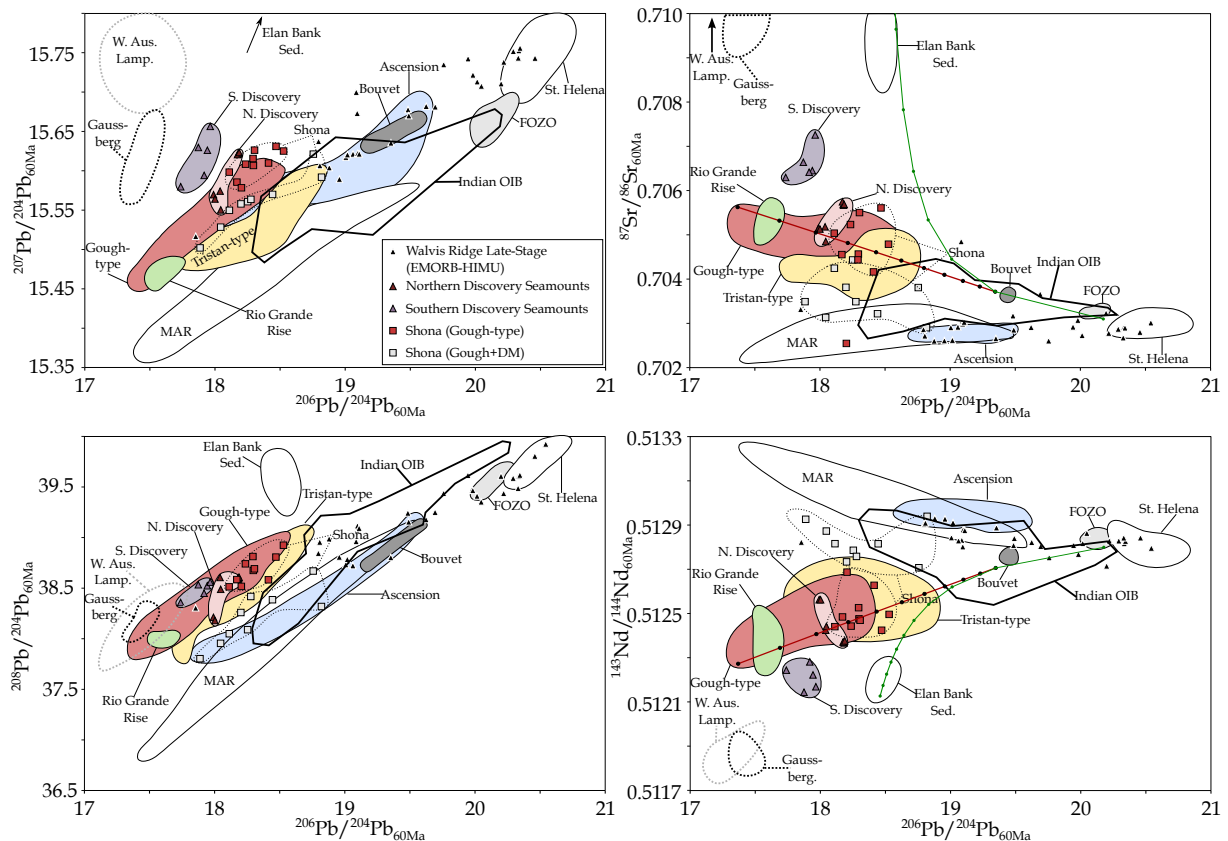


**Figure 8: Initial isotope ratios projected to 60 Ma for South Atlantic intraplate lavas on  $^{206}\text{Pb}/^{204}\text{Pb}_{60\text{Ma}}$  ratios vs. a)  $^{207}\text{Pb}/^{204}\text{Pb}_{60\text{Ma}}$ , b)  $^{208}\text{Pb}/^{204}\text{Pb}_{60\text{Ma}}$ , c)  $^{87}\text{Sr}/^{86}\text{Sr}_{60\text{Ma}}$ , and d)  $^{143}\text{Nd}/^{144}\text{Nd}_{60\text{Ma}}$  ratios. The diagrams show that the Shona and Northern Discovery lavas lie within the Gough-type compositional array. Mixing lines between FOZO and Elan bank sediments (EM II; green line) and Gough-type lavas with a mixture of 10% EM II and 90% FOZO (red line) are show in the Pb vs. Sr and Nd isotope diagrams (Figs. 8b and d). Indian OIB comprises lavas from Comoros, Crozet, Reunion and Prince Edward. Literature data is taken from the GEOROC Database and are reported in detail in Appendix F. Abbreviations: W. Aus. Lamp. = Western Australien Lamproites.**

#### *5.2.4 Deep or shallow heritage of the common Gough-type composition?*

As shown above, the Gough-type composition can be identified in the Tristan-Gough, Discovery and Shona intraplate lavas, which seems to be the common EM I-type in the South Atlantic DUPAL anomaly. A common geochemical signature suggests that the proposed EM I-type mantle plumes are derived from a common reservoir, located in the lowermost mantle (e.g., Richardson et al., 1982; Hanan et al., 1986; Weaver et al., 1987; O'Connor and Duncan, 1990; Fontignie and Schilling, 1996; Le Roex et al., 2010; Class and le Roex, 2011; O'Connor et al., 2012; Rohde et al., 2013a; Rohde et al., 2013b; Hoernle et al., 2015; Schwindrofska et al., 2016; Hoernle et al., 2016).

Overall, the excellent age progressions along the entire Tristan-Gough and Discovery (Schwindrofska et al., 2016) hotspot tracks indicate stable and deep-rooted melt anomalies (Fig. 6). Seismic tomographic data image a low-velocity conduit-like structure with a radius of 100 km down to a depth of 250 km located southwest of Tristan da Cunha (Schlömer et al., 2017). This shallow velocity anomaly overlies a broader (800-1000 km) vertically continuous conduit-like structure with  $\partial V_s$  ratios of  $< -0.5\%$  in the depth range of 1000-2800 km (French and Romanowicz, 2015). High  $^3\text{He}/^4\text{He}$  ratios ( $> 10 R_A$ ) in Gough-type dikes from the Etendeka flood basalt province indicates that the Tristan-Gough mantle plume tapped a primitive-undegassed reservoir (Stroncik et al., 2017), suggesting that the deeper and shallower seismic velocity anomalies are connected, but that the 250 to 1000 km portion of the mantle upwelling cannot be sufficiently imaged by seismic tomography.

The Discovery hotspot, located south of the Tristan-Gough track, has been zoned for the last 40 Ma, with both types of plume material (Northern and Southern) flowing into the Southern MAR, where they create enriched geochemical anomalies (Douglass et al., 1999; Sarda et al., 2000; Schwindrofska et al., 2016). Lavas with Northern Discovery



Sr-Nd-Pb (Gough-type) isotopic compositions also have high  $^3\text{He}/^4\text{He}$  isotope ratios (up to 15  $R_A$ ; Sarda et al., 2000), providing further evidence that the Gough-type composition is derived from the lower mantle. The Shona and Discovery hotspot tracks were believed to lie above separate mantle plumes, extending from the uppermost mantle to the margin of the LLSVP (e.g., Le Roex et al., 2010; Class and le Roex, 2011; Schwindrofska et al., 2016; Hoernle et al., 2016). Based on recent tomographic cross-sections (extended data Figs. 2f-j in French and Romanowicz, 2015), the Discovery and Shona hotspots seem to overlie the same large-scale velocity anomaly as the Tristan-Gough mantle plume located in the lowermost mantle (at depths of 1000-2800 km), consistent with all three hotspot being derived from a common lower mantle upwelling and ultimately a common source at the base of the lower mantle.

## 5.3 Geochemical heterogeneity in the South Atlantic

### 5.3.1 The Tristan and Southern Discovery EM I-type flavors

In general, the distinct compositional fields in the southern South Atlantic Ocean form a crude array in  $^{206}\text{Pb}/^{204}\text{Pb}_{60\text{Ma}}$  versus  $^{208}\text{Pb}/^{204}\text{Pb}_{60\text{Ma}}$  and, Sr, Nd and Hf isotope diagrams (Fig. 8). Schwindrofska et al. (2016) proposed that the compositional range could have formed by mixing of two main components: a) a low- $\mu$  component represented by a range of lamproites and Group II kimberlites (sub-continental lithospheric mantle (SCLM)  $\pm$  lower continental crust) with b) a high- $\mu$  component that is either FOZO (Hart et al., 1992; Stracke et al., 2005), C (Hanan and Graham, 1996), and/or HIMU  $\pm$  DM (e.g., Zindler and Hart, 1986). The proposed low- $\mu$  end member, in particular the Gaussberg and Western Australien lamproites, can explain the complex Pb-isotope compositions of the Tristan-Gough, Shona and Discovery hotspots, consisting of variable  $^{207}\text{Pb}/^{204}\text{Pb}$  ratios, but a constant  $^{208}\text{Pb}/^{204}\text{Pb}$  ratio at a given  $^{206}\text{Pb}/^{204}\text{Pb}$  value. However, significantly lower  $^{206}\text{Pb}/^{204}\text{Pb}$  isotope ratios of the proposed low- $\mu$  end member are required to reproduce the Walvis Ridge lavas (e.g., DSDP Site 525; Fig. 8). Otherwise, the low- $\mu$  end member needs the addition of DM, which is inconsistent with the thorogenic isotope diagram (Fig. 8).

Compared to the Gough compositional domain, the Tristan compositional array is shifted to more radiogenic  $^{206}\text{Pb}/^{204}\text{Pb}_{60\text{Ma}}$ ,  $^{143}\text{Nd}/^{144}\text{Nd}_{60\text{Ma}}$  and  $^{176}\text{Hf}/^{177}\text{Hf}_{60\text{Ma}}$  ratios, but less radiogenic  $^{86}\text{Sr}/^{87}\text{Sr}_{60\text{Ma}}$  and  $^{207}\text{Pb}/^{204}\text{Pb}_{60\text{Ma}}$  ratios (for a given  $^{206}\text{Pb}/^{204}\text{Pb}_{60\text{Ma}}$  value; Fig. 5). In addition to forming distinct fields on the uranium isotope diagrams, the Tristan-type samples are characterized by higher Nb/Y ratios and overall flat to positive Nb-Ta anomalies (Figs. 4, 5 and 7). These compositional variations could be explained by interaction with a HIMU-like component (Salters and Sachi-Kocher, 2010). The FOZO component proposed by Stracke et al. (2005) differs from the St. Helena HIMU

end member by having overall lower  $^{206}\text{Pb}/^{204}\text{Pb}$  and  $^{207}\text{Pb}/^{204}\text{Pb}$  isotope ratios and higher projected  $^{208}\text{Pb}/^{204}\text{Pb}$ ,  $^{87}\text{Sr}/^{86}\text{Sr}$  and  $^{176}\text{Hf}/^{177}\text{Hf}$  ratios, but similar  $^{143}\text{Nd}/^{144}\text{Nd}$  ratios at  $^{206}\text{Pb}/^{204}\text{Pb}$  values of  $> 19$ . Note that both components are characterized by a pronounced positive Nb-Ta anomaly (Stracke et al., 2005; Willbold and Stracke, 2006). The addition of a FOZO-like component (such as Comoros) into the Gough compositional array would shift the resulting mixture within the Gough domain in a thorogenic diagram (e.g., Fig. 5), but would displace it to distinctly lower  $^{207}\text{Pb}/^{206}\text{Pb}$  ratios (Fig. 5). In contrast, mixing of St. Helena HIMU and Gough-type EM I components requires additional DM to reproduce the Tristan-type EM I in the uranogenic diagram (Fig. 5). However, the addition of DM would cause a considerable change in the  $^{208}\text{Pb}/^{206}\text{Pb}$  ratios. Therefore, we propose the prevalent FOZO-like composition as a potential mixing component, which was also proposed by Salters and Sachi-Kocher (2010) for the DSDP Site 527 and 528 lavas.

The higher  $^{87}\text{Sr}/^{86}\text{Sr}_{60\text{Ma}}$  values, and lower  $^{143}\text{Nd}/^{144}\text{Nd}_{60\text{Ma}}$  and  $^{176}\text{Hf}/^{177}\text{Hf}_{60\text{Ma}}$  ratios, as well as pronounced negative Nb-Ta anomalies in samples from the Southern Discovery seamounts could also be explained by the addition of continental crust (Figs. 7 and 8). Mixing of small proportions of upper continental crust (EM II-like) as reported from the Kerguelen plateau (Ingle et al., 2002) with the Gough-type signature (low- $\mu$  DSDP Site 525-type) could reproduce the Southern Discovery signature in multi-isotope space (Figs. 7 and 8). In this case, the geochemical heterogeneity in the South Atlantic DUPAL anomaly region can be explained by a common Gough-type composition, which became flavored with FOZO- and EM II-like contaminants, which could represent recycled oceanic lithosphere (FOZO; Stracke et al., 2005) and subducted sediments and/or upper continental crust (EM II).

### 5.3.2 FOZO and HIMU in the South Atlantic

Apart from the DUPAL-anomaly, a distinct type of intra-plate lavas (with radiogenic Pb and intermediate Sr-Nd-Hf isotope ratios) characterizes the northern- and southernmost South Atlantic. St. Helena represents the South Atlantic type locality of HIMU, which is traditionally explained by the combination of hydrothermal overprint and subduction modification/slab dehydration of ancient oceanic crust (e.g., Hofmann and White, 1982; Zindler and Hart, 1986; Chauvel et al., 1992; Stracke et al., 2003; Cabral et al., 2013; Hanyu et al., 2014; Kimura et al., 2016). Alternatively, it has been proposed that HIMU could develop within the peridotitic SCLM by infiltration of fluids and/or melts (e.g., Hart et al., 1986; Stein et al., 1997; Lucassen et al., 2008; Rooney et al., 2014; McCoy-West et al., 2016; Weiss et al., 2016). In both cases, radiogenic Pb isotope ratios of HIMU require long-term isolation (e.g., Zindler and Hart, 1986; Kawabata et al., 2011; Hanyu et al., 2014) and the source formation of HIMU is constrained to be  $\geq 2.45$  Ga (Cabral et al., 2013).

In general, two potential regions exist on Earth where end member HIMU could be isolated from the convecting mantle since the Archean to Early Proterozoic: 1) in the shallow SCLM (e.g., Stein et al., 1997; Lucassen et al., 2008; Rooney et al., 2014), or 2) at the base of the lower mantle (e.g., Hofmann and White, 1982; Chauvel et al., 1992; Stracke et al., 2005; Hanyu et al., 2014; Weiss et al., 2016). Since seismic tomography has imaged a low seismic velocity anomaly beneath St. Helena extending to the base of the lower mantle (e.g., Montelli et al., 2006; French and Romanowicz, 2015), it seems most likely that St. Helena is derived from a deep reservoir. Furthermore, Jackson et al. (2018) shows that hotspots with extreme HIMU signatures are usually associated with deep-rooted mantle plumes.

The neighboring Ascension Island is characterized by a HIMU-like composition (Figs. 7 and 8). Seismic tomographic models suggest that both islands overlie the same velocity anomaly in the lowermost mantle, which splits at a depth of ~650-350 km into two distinct conduit-like structures (Montelli et al., 2006). Therefore, a common source region seems straightforward and in this case the geochemical composition of Ascension could be explained by mixing St. Helena HIMU and DM  $\pm$  EM I.

Bouvet Island represents the southernmost proposed mantle plume in the South Atlantic (Le Roex et al., 1985; Kurz et al., 1998; Douglass et al., 1999; Montelli et al., 2006) and is characterized by similar Pb isotope ratios, but more radiogenic  $^{87}\text{Sr}/^{86}\text{Sr}_{60\text{Ma}}$  and lower  $^{143}\text{Nd}/^{144}\text{Nd}_{60\text{Ma}}$  ratios at a given  $^{206}\text{Pb}/^{204}\text{Pb}_{60\text{Ma}}$  value relative to Ascension, suggesting that it is derived from a FOZO type component as defined by Stracke et al. (2005) (Fig. 8). Mid-ocean ridge (MOR) lavas next to Bouvet Island have high  $^3\text{He}/^4\text{He}$  ratios of up to 14  $R_A$ , which indicates a deep-seated reservoir (Kurz et al., 1998).

Late-stage lavas with St. Helena HIMU end member compositions have been reported from the Walvis Ridge and Shona (Richardson seamount) hotspot tracks (Fig. 1; Homrighausen et al., in review-a). Since St. Helena HIMU is not documented thus far in the EM I-type Walvis Ridge basement, and considering the exceptionally long volcanic hiatus of 20-40 Ma after EM I type basement formation, the HIMU signature is believed to be unrelated to the Tristan-Gough mantle plume, and is instead derived from separate upwellings from the base of the lower mantle (Homrighausen et al., in review-b).

## 6. Towards a South Atlantic geodynamic model

We will now summarize the constraints for the geochemical heterogeneities and will also present our suggested explanation. As discussed above, the Gough-type composition is present in the Tristan-Gough, Discovery and Shona mantle plumes and reflects the dominant EM I-type composition in the South Atlantic. A suitable source for the Gough-type composition is a subduction package of oceanic lithosphere (FOZO; Stracke et al., 2005), lower continental crust (EM I; Zindler and Hart, 1986) and upper continental crust/marine sediments  $\pm$  SCLM (EM II; Zindler and Hart, 1986). Geochemical, geochronological and geophysical studies all support a lower mantle origin for this composition.

We have shown that the geochemical zonation of the Tristan-Gough hotspot track (Tristan-type composition) and Discovery seamounts (Southern Discovery composition) can be produced by the addition of FOZO (recycled oceanic lithosphere; Stracke et al., 2005) and/or EM II (upper continental crust or pelagic sediments) to the Gough-type composition (Figs. 4 and 7). It has been proposed that geochemically zoned hotspot tracks (such as Hawaii and Tristan-Gough) reflect sampling along the LLSVP boundaries, entraining geochemically distinct materials from the LLSVP and ambient lower mantle outside of the LLSVP (e.g., Huang et al., 2011; Weis et al., 2011; Rohde et al., 2013a; Hoernle et al., 2015; Harrison et al., 2017). Bouvet island, which lies  $\sim$ 400 km outside the LLSVP margin (Fig. 1), shows no evidence of the involvement of the Gough-type composition (Figs. 6 and 7), but instead it trends towards a FOZO type composition (Fig. 8). Its high  $^3\text{He}/^4\text{He}$  ratio of  $\sim 14 R_A$  (Kurz et al., 1998) points to a lower mantle origin for this FOZO-type material. In the Indian Ocean, the ocean islands with FOZO-type compositions (Comoros, Crozet, Prince Edward and Reunion) also overlie the ambient lowermost mantle outside the African LLSVP (Fig. 1 in French and Romanowicz, 2015).

Therefore, we speculate that FOZO (recycled ocean crust; Stracke et al., 2005) represents the ambient mantle outside of the African LLSVP, whereas the Gough-type composition makes up the SW African LLSVP. As proposed by Burke et al. (2008), subducting oceanic lithosphere could push mantle against the margins of the LLSVPs triggering mantle upwellings (or plumes). In this scenario, the zoned Tristan-Gough plume could represent sampling of Gough-type African LLSVP with part of the plume entraining and mixing with subducted oceanic lithosphere (FOZO) outside of the African LLSVP, whereas the zoned Discovery seamounts also taps the Gough-type composition of the LLSVP (Northern Discovery Seamounts), but mixes with subducted oceanic sediments (EM II)  $\pm$  subducted oceanic crust (FOZO) outside of the LLSVP.

A link between HIMU and EM I components has long been postulated in ocean island basalts and carbonatites. HIMU and EM I components seem to form mixing arrays in hotspots (LoNd array), and Hart et al. (1986) proposed that both components are derived from the core-mantle boundary. Bell and Tilton (2001) showed that East African carbonatites also form a mixing array between HIMU and EM I and pointed out that the presence of a low-seismic velocity anomaly also placed the source of these end members in the lower mantle. Recently Jackson et al. (2018) presented further evidence in the form of geochemical and geophysical constraints for a deep origin for extreme HIMU and EM I. In contrast to the EM I-like mantle plumes in the South Atlantic that overlie the edges of the African LLSVP (Tristan-Gough, Discovery and Shona hotspot), the HIMU-dominated intraplate lavas (St. Helena and Ascension) and the Late-Stage Walvis Ridge and Shona (Richardson seamount) volcanism formed over a more internal portions of the African LLSVP (Fig. 1; Homrighausen et al. 2018a in review).

In summary, we propose that the FOZO-like composition is primarily derived from the ambient lowermost mantle outside the LLSVP, which could represent recycled

oceanic crust, whereas the EM I-type component (s) are derived from the margins of the LLSVP. Finally, HIMU is derived from more internal parts of the LLSVP (Fig. 9).

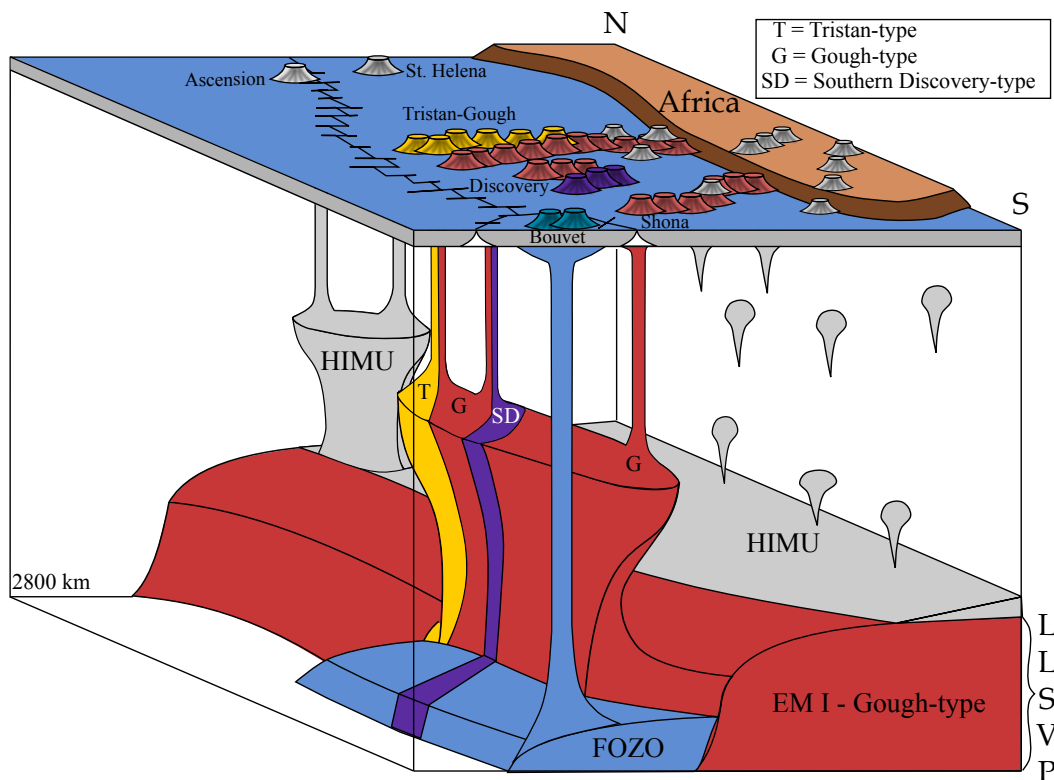


**Figure 9: A potential model to explain the observed geochemical heterogeneities in the South Atlantic. The long-lived spatial geochemical zonation of the Tristan-Gough and Discovery hotspots indicates that these plumes tap the boundaries of distinct compositional reservoirs at their source. Following the seismic tomographic model of French and Romanowicz, 2015) the Tristan-Gough, Discovery and Shona mantle plumes rise from the same broad velocity anomaly extending from 1000-2800 km depth in the lower mantle, which ultimately rises from the margin of the African LLSVP. Based on the geographic position of the South Atlantic mantle plumes relative to the 1%  $\partial V_s$  contour of the African LLSVP, we assume that a FOZO-like component forms the ambient mantle outside of the African LLSVP. We propose that the Gough-type composition (G; red) forms the margin of the African LLSVP and the HIMU-type composition (grey) lies in a more internal portion of the African LLSVP. Subducting oceanic lithosphere (light blue, FOZO; Stracke et al., 2005) could push mantle material up against the margins of the LLSVP triggering mantle upwellings (Burke et al., 2008). Therefore, the Tristan-type composition (T; yellow) could represent entrainment and mixing of Gough EM I- and FOZO-type materials at the boundary of the African LLSVP, whereas the Southern Discovery-type composition (SD; purple) could be generated by entrainment and mixing of Gough-type mantle (EM I) with EM II-like mantle (i.e., subducted marine sediments/continental crust) from the boundary of the LLSVP, south of the Tristan-Gough plume. The St. Helena and Ascension hotspots overlie the same velocity anomaly in the lower mantle, which splits in the upper mantle into two distinct conduit-like structures (Montelli et al., 2006). The addition of DM to HIMU could explain the composition of the Ascension Island hotspot lavas.**



The spatial relationship between HIMU and Gough-type EM I is not clear. Is HIMU located within the African LLSVP, beneath the LLSVP, or on the LLSVP? Could these two compositional end members be intimately related, i.e., formed contemporaneously, together or through similar types of processes? For example, it has been recently proposed that HIMU was derived in the Archean through metasomatism of SCLM (Weis et al. 2016) by volatiles from shallow subduction, related to drip tectonics (Homrighausen et al., in review-a). Delamination of HIMU-type SCLM and lower continental crust could conceivably transfer HIMU and Gough-type EM I to the base of the lower mantle.

## **7. Acknowledgments**

We thank Captain Meyer and the crew of the R/V SONNE for their support during cruises SO233-Walvis II and SO234/1-Spaces; S. Hauff, K. Junge, J. Sticklus and U. Westernströer for analytical support; and M. Anders for help with sample preparation. This study and Ph.D. position of S.H. was funded by the German Ministry for Research and Education (BMBF; grants SO233-Walvis II to KH and FH and SO234/1-Spaces to RW) and the GEOMAR Helmholtz Center for Ocean Research Kiel.

## **8. Declaration of interest**

Conflicts of interest: None

## References

- Baksi, A.K. (2007) A quantitative tool for detecting alteration in undisturbed rocks and minerals—I: Water, chemical weathering, and atmospheric argon. *Geological Society of America Special Papers* **430**, 285-303.
- Bell, K. and Tilton, G.R. (2001) Nd, Pb and Sr Isotopic Compositions of East African Carbonatites: Evidence for Mantle Mixing and Plume Inhomogeneity. *J Petrol* **42**, 1927-1945.
- Bromiley, G.D. and Redfern, S.A.T. (2008) The role of TiO<sub>2</sub> phases during melting of subduction-modified crust: Implications for deep mantle melting. *Earth Planet Sc Lett* **267**, 301-308.
- Burke, K., Steinberger, B., Torsvik, T.H. and Smethurst, M.A. (2008) Plume Generation Zones at the margins of Large Low Shear Velocity Provinces on the core–mantle boundary. *Earth Planet Sc Lett* **265**, 49-60.
- Cabral, R.A., Jackson, M.G., Rose-Koga, E.F., Koga, K.T., Whitehouse, M.J., Antonelli, M.A., Farquhar, J., Day, J.M.D. and Hauri, E.H. (2013) Anomalous sulphur isotopes in plume lavas reveal deep mantle storage of Archaean crust. *Nature* **496**, 490-493.
- Campbell, I.H. (2007) Testing the plume theory. *Chem Geol* **241**, 153-176.
- Chauvel, C., Hofmann, A.W. and Vidal, P. (1992) HIMU-EM : The French-Polynesian Connection. *Earth Planet Sc Lett* **110**, 99-119.
- Class, C. and le Roex, A. (2011) South Atlantic DUPAL anomaly — Dynamic and compositional evidence against a recent shallow origin. *Earth Planet Sc Lett* **305**, 92-102.
- Courtillot, V., Davaille, A., Besse, J. and Stock, J. (2003) Three distinct types of hotspots in the Earth's mantle. *Earth Planet Sc Lett* **205**, 295-308.
- Douglass, J., Schilling, J.-G. and Fontignie, D. (1999) Plume-ridge interactions of the Discovery and Shona mantle plumes with the southern Mid-Atlantic Ridge (40°-55°S). *Journal of Geophysical Research: Solid Earth* **104**, 2941-2962.
- Fairhead, J.D. and Wilson, M. (2005) Plate tectonic processes in the South Atlantic Ocean: Do we need deep mantle plumes?, in: Foulger, G.R., Natland, J.H., Presnall, D.C., Anderson, D.L. (Eds.), *Plates, plumes and paradigms*. Geological Society of America.
- Fontignie, D. and Schilling, J.G. (1996) Mantle heterogeneities beneath the South Atlantic: A Nd-Sr-Pb isotope study along the Mid-Atlantic Ridge (3°S-46°S). *Earth Planet Sc Lett* **142**, 209-221.
- Foulger, G.R. (2017) Origin of the South Atlantic igneous province. *Journal of Volcanology and Geothermal Research* **In Press**.
- French, S.W. and Romanowicz, B. (2015) Broad plumes rooted at the base of the Earth's mantle beneath major hotspots. *Nature* **525**, 95-99.
- Garcia, M.O., Swinnard, L., Weis, D., Greene, A.R., Tagami, T., Sano, H. and Gandy, C.E. (2010) Petrology, Geochemistry and Geochronology of Kaua'i Lavas over 4-5 Myr: Implications for the Origin of Rejuvenated Volcanism and the Evolution of the Hawaiian Plume. *J Petrol* **51**, 1507-1540.
- Gibson, S.A., Thompson, R.N., Day, J.A., Humphris, S.E. and Dickin, A.P. (2005) Melt-generation processes associated with the Tristan mantle plume: Constraints on the origin of EM-1. *Earth Planet Sc Lett* **237**, 744-767.
- Hanan, B.B., Kingsley, R.H. and Schilling, J.G. (1986) Pb isotope evidence in the South Atlantic for migrating ridge-hotspot interactions. *Nature* **322**, 137-144.
- Hanan, B.B. and Graham, D.W. (1996) Lead and Helium Isotope Evidence from Oceanic Basalts for a Common Deep Source of Mantle Plumes. *Science* **272**, 991-995.
- Hanyu, T., Kawabata, H., Tatsumi, Y., Kimura, J.-I., Hyodo, H., Sato, K., Miyazaki, T., Chang, Q., Hirahara, Y., Takahashi, T., Senda, R. and Nakai, S.i. (2014) Isotope evolution in the HIMU reservoir beneath St. Helena: Implications for the mantle recycling of U and Th. *Geochimica et Cosmochimica Acta* **143**, 232-252.
- Harrison, L.N., Weis, D. and Garcia, M.O. (2017) The link between Hawaiian mantle plume composition, magmatic flux, and deep mantle geodynamics. *Earth Planet Sc Lett* **463**, 298-309.
- Hart, S.R. (1984) A large-scale isotope anomaly in the Southern Hemisphere mantle. *Nature* **309**, 753-757.
- Hart, S.R., Gerlach, D.C. and White, W.M. (1986) A Possible New Sr-Nd-Pb Mantle Array and Consequences for Mantle Mixing. *Geochimica Et Cosmochimica Acta* **50**, 1551-1557.
- Hart, S.R., Hauri, E.H., Oschmann, L.A. and Whitehead, J.A. (1992) Mantle Plumes and Entrainment: Isotopic Evidence. *Science* **256**, 517-520.
- Hauff, F., Hoernle, K., Tilton, G., Graham, D.W. and Kerr, A.C. (2000) Large volume recycling of oceanic lithosphere over short time scales: geochemical constraints from the Caribbean Large Igneous Province. *Earth Planet Sc Lett* **174**, 247-263.
- Hicks, A., Barclay, J., Mark, D.F. and Loughlin, S. (2012) Tristan da Cunha: Constraining eruptive behavior using the <sup>40</sup>Ar/<sup>39</sup>Ar dating technique. *Geology* **40**, 723-726.

- Hoernle, K. and Schmincke, H.-U. (1993) The Role of Partial Melting in the 15 Ma Geochemical Evolution of Gran Canaria: A Blob Model for the Canary Hotspot. *J Petrol* **34**, 599-626.
- Hoernle, K., Werner, R. and Lüter, C. (2014) RV SONNE Fahrtbericht/Cruise Report SO233 WALVIS II, 14.05-21.06. 2014, Cape Town, South Africa-Walvis Bay, Namibia. *GEOMAR Report no. 23 (N. Ser.)*, 53 pp + Appendices.
- Hoernle, K., Rohde, J., Hauff, F., Garbe-Schonberg, D., Homrighausen, S., Werner, R. and Morgan, J.P. (2015) How and when plume zonation appeared during the 132 Myr evolution of the Tristan Hotspot. *Nature Communication* **6**, 10.1038/ncomms8799.
- Hoernle, K., Schwindrofska, A., Werner, R., van den Bogaard, P., Hauff, F., Uenzelmann-Neben, G. and Garbe-Schönberg, D. (2016) Tectonic dissection and displacement of parts of Shona hotspot volcano 3500 km along the Agulhas-Falkland Fracture Zone. *Geology* **44**, 263-266.
- Hofmann, A.W. and White, W.M. (1982) Mantle plumes from ancient oceanic crust. *Earth Planet Sc Lett* **57**, 421-436.
- Hofmann, A.W. (1988) Chemical Differentiation of the Earth - The Relationship between Mantle, Continental Crust, and Oceanic Crust. *Earth Planet Sc Lett* **90**, 297-314.
- Homrighausen, S., Hoernle, K., Hauff, F., Geldmacher, J., van den Bogaard, P. and Garbe-Schönberg, C.D. (in review-a) Global distribution of the HIMU end member: A change in Plate Tectonic Regime in the Late Archean. *Earth Science Reviews*.
- Homrighausen, S., Hoernle, K., Geldmacher, J., Hauff, F., Potnyagin, M., Werner, R., Wartho, J.-A., van den Bogaard, P. and Garbe-Schönberg, C.D. (in review-b) Unexpected HIMU-type Late-Stage Volcanism on the Walvis Ridge. *Earth Planet Sc Lett*.
- Huang, S., Hall, P.S. and Jackson, M.G. (2011) Geochemical zoning of volcanic chains associated with Pacific hotspots. *Nature Geosci* **4**, 874-878.
- Humphris, S.E. and Thompson, G. (1983) Geochemistry of rare earth elements in basalts from the Walvis Ridge: implications for its origin and evolution. *Earth Planet Sc Lett* **66**, 223-242.
- Ingle, S., Weis, D. and Frey, F.A. (2002) Indian Continental Crust Recovered from Elan Bank, Kerguelen Plateau (ODP Leg 183, Site 1137). *J Petrol* **43**, 1241-1257.
- Jackson, M.G., Hart, S.R., Saal, A.E., Shimizu, N., Kurz, M.D., Blusztajn, J.S. and Skovgaard, A.C. (2008) Globally elevated titanium, tantalum, and niobium (TITAN) in ocean island basalts with high  $3\text{He}/4\text{He}$ . *Geochemistry, Geophysics, Geosystems* **9**, n/a-n/a.
- Jackson, M.G., Becker, T.W. and Konter, J.G. (2018) Evidence for a deep mantle source for EM and HIMU domains from integrated geochemical and geophysical constraints. *Earth Planet Sc Lett* **484**, 154-167.
- Jochum, K.P. and Verma, S.P. (1996) Extreme enrichment of Sb, Tl and other trace elements in altered MORB. *Chem Geol* **130**, 289-299.
- Jones, C.E. and Jenkyns, H.C. (2001) Seawater strontium isotopes, oceanic anoxic events, and seafloor hydrothermal activity in the Jurassic and Cretaceous. *American Journal of Science* **301**, 112-149.
- Kawabata, H., Hanyu, T., Chang, Q., Kimura, J.-I., Nichols, A.R.L. and Tatsumi, Y. (2011) The Petrology and Geochemistry of St. Helena Alkali Basalts: Evaluation of the Oceanic Crust-recycling Model for HIMU OIB. *J Petrol* **52**, 791-838.
- Kimura, J.-I., Gill, J.B., Skora, S., van Keken, P.E. and Kawabata, H. (2016) Origin of geochemical mantle components: Role of subduction filter. *Geochemistry, Geophysics, Geosystems* **17**, 3289-3325.
- Kurz, M.D., le Roex, A.P. and Dick, H.J.B. (1998) Isotope Geochemistry of the Oceanic Mantle Near the Bouvet Triple Junction. *Geochimica et Cosmochimica Acta* **62**, 841-852.
- Lanphere, M.A. and Dalrymple, G.B. (1978) The use of  $40\text{Ar}/39\text{Ar}$  data in evaluation of disturbed K-Ar systems. *Geological Survey Open-File Report 78-701*, 141-148.
- Le Roex, A., Class, C., O'Connor, J. and Jokat, W. (2010) Shona and Discovery Aseismic Ridge Systems, South Atlantic: Trace Element Evidence for Enriched Mantle Sources. *J Petrol* **51**, 2089-2120.
- Le Roex, A.P., Dick, H.J.B., Reid, A.M., Frey, F.A., Erlank, A.J. and Hart, S.R. (1985) Petrology and geochemistry of basalts from the American-Antarctic Ridge, Southern Ocean: implications for the westward influence of the Bouvet mantle plume. *Contrib Mineral Petr* **90**, 367-380.
- Lucassen, F., Franz, G., Romer, R.L., Pudlo, D. and Dulski, P. (2008) Nd, Pb, and Sr isotope composition of Late Mesozoic to Quaternary intra-plate magmatism in NE-Africa (Sudan, Egypt): high- $\mu$  signatures from the mantle lithosphere. *Contrib Mineral Petr* **156**, 765-784.
- Maund, J.G., Rex, D.C., Le Roex, A.P. and Reid, D.L. (1988) Volcanism on Gough Island: a revised stratigraphy. *Geological Magazine* **125**, 175-181.
- McCoy-West, A.J., Bennett, V.C. and Amelin, Y. (2016) Rapid Cenozoic ingrowth of isotopic signatures simulating "HIMU" in ancient lithospheric mantle: Distinguishing source from process. *Geochimica et Cosmochimica Acta* **187**, 79-101.

- Montelli, R., Nolet, G., Dahlen, F.A. and Masters, G. (2006) A catalogue of deep mantle plumes: New results from finite-frequency tomography. *Geochemistry, Geophysics, Geosystems* **7**, Q11007.
- Morgan, W.J. (1971) Convection Plumes in the Lower Mantle. *Nature* **230**, 42-43.
- Morgan, W.J. (1981) 13. Hotspot tracks and the opening of the Atlantic and Indian Oceans. *The oceanic lithosphere* **7**, 443.
- Nobre Silva, I.G., Weis, D., Scoates, J.S. and Barling, J. (2013) The Ninetyeast Ridge and its Relation to the Kerguelen, Amsterdam and St. Paul Hotspots in the Indian Ocean. *J Petrol* **54**, 1177-1210.
- O'Connor, J., Jokat, W., Wijbrans, J. and Colli, L. (2018) Hotspot tracks in the South Atlantic located above bands of fast flowing asthenosphere driven by waning pulsations from the African LLSVP. *Gondwana Research* **53**, 197-208.
- O'Connor, J.M. and Duncan, R.A. (1990) Evolution of the Walvis Ridge-Rio Grande Rise Hot Spot System: Implications for African and South American Plate motions over plumes. *Journal of Geophysical Research: Solid Earth* **95**, 17475-17502.
- O'Connor, J.M. and le Roex, A.P. (1992) South Atlantic hot spot-plume systems: 1. Distribution of volcanism in time and space. *Earth Planet Sc Lett* **113**, 343-364.
- O'Connor, J.M., Stoffers, P., van den Bogaard, P. and McWilliams, M. (1999) First seamount age evidence for significantly slower African plate motion since 19 to 30 Ma. *Earth Planet Sc Lett* **171**, 575-589.
- O'Connor, J.M., Jokat, W., le Roex, A.P., Class, C., Wijbrans, J.R., Keszling, S., Kuiper, K.F. and Nebel, O. (2012) Hotspot trails in the South Atlantic controlled by plume and plate tectonic processes. *Nat Geosci* **5**, 735-738.
- O'Connor, J.M. and Jokat, W. (2015a) Tracking the Tristan-Gough mantle plume using discrete chains of intraplate volcanic centers buried in the Walvis Ridge. *Geology* **43**, 715-718.
- O'Connor, J.M. and Jokat, W. (2015b) Age distribution of Ocean Drill sites across the Central Walvis Ridge indicates plate boundary control of plume volcanism in the South Atlantic. *Earth Planet Sc Lett* **424**, 179-190.
- Pearce, J.A. (1996) A user's guide to basalt discrimination diagrams. *Trace element geochemistry of volcanic rocks: applications for massive sulphide exploration. Geological Association of Canada, Short Course Notes* **12**, 113.
- Pearce, J.A. (2008) Geochemical fingerprinting of oceanic basalts with applications to ophiolite classification and the search for Archean oceanic crust. *Lithos* **100**, 14-48.
- Pertermann, M. and Hirschmann, M.M. (2003) Partial melting experiments on a MORB-like pyroxenite between 2 and 3 GPa: Constraints on the presence of pyroxenite in basalt source regions from solidus location and melting rate. *Journal of Geophysical Research: Solid Earth* **108**.
- Peters, B.J. and Day, J.M.D. (2014) Assessment of relative Ti, Ta, and Nb (TITAN) enrichments in ocean island basalts. *Geochemistry, Geophysics, Geosystems* **15**, 4424-4444.
- Plank, T. and Langmuir, C.H. (1998) The chemical composition of subducting sediment and its consequences for the crust and mantle. *Chem Geol* **145**, 325-394.
- Plank, T. (2014) 4.17 - The Chemical Composition of Subducting Sediments in: Turekian, K.K. (Ed.), *Treatise on Geochemistry (Second Edition)*. Elsevier, Oxford, pp. 607-629.
- Pringle, M.S., Sager, W.W., Sliter, W.V. and Stein, S. (1993) The Mesozoic Pacific: Geology, Tectonics, and Volcanism: A Volume in Memory of Sy Schlanger. *Washington DC American Geophysical Union Geophysical Monograph Series* **77**.
- Regelous, M., Niu, Y., Abouchami, W. and Castillo, P.R. (2009) Shallow origin for South Atlantic Dupal Anomaly from lower continental crust: Geochemical evidence from the Mid-Atlantic Ridge at 26°S. *Lithos* **112**, 57-72.
- Renne, P. (2015) Age and Duration of the Paraná-Etendeka Flood Basalts and Related Plumbing System, AGU Fall Meeting Abstracts.
- Renne, P.R., Glen, J.M., Milner, S.C. and Duncan, A.R. (1996) Age of Etendeka flood volcanism and associated intrusions in southwestern Africa. *Geology* **24**, 659-662.
- Richards, M.A., Duncan, R.A. and Courtillot, V.E. (1989) Flood basalts and hot-spot tracks: plume heads and tails. *Science* **246**, 103-107.
- Richardson, S.H., Erlank, A.J., Duncan, A.R. and Reid, D.L. (1982) Correlated Nd, Sr and Pb Isotope Variation in Walvis Ridge Basalts and Implications for the Evolution of their Mantle Source. *Earth Planet Sc Lett* **59**, 327-342.
- Rohde, J., Hoernle, K., Hauff, F., Werner, R., O'Connor, J., Class, C., Garbe-Schönberg, D. and Jokat, W. (2013a) 70 Ma chemical zonation of the Tristan-Gough hotspot track. *Geology* **43**, 335-338.
- Rohde, J.K., van den Bogaard, P., Hoernle, K., Hauff, F. and Werner, R. (2013b) Evidence for an age progression along the Tristan-Gough volcanic track from new <sup>40</sup>Ar/<sup>39</sup>Ar ages on phenocryst phases. *Tectonophysics* **604**, 60-71.

- Rooney, T.O., Nelson, W.R., Dosso, L., Furman, T. and Hanan, B. (2014) The role of continental lithosphere metasomes in the production of HIMU-like magmatism on the northeast African and Arabian plates. *Geology* **42**(5), 419-422.
- Rudnick, R.L. and Gao, S. (2003) 3.01 - Composition of the Continental Crust in: Turekian, K.K. (Ed.), *Treatise on Geochemistry*. Pergamon, Oxford, pp. 1-64.
- Salters, V.J.M. and Sachi-Kocher, A. (2010) An ancient metasomatic source for the Walvis Ridge basalts. *Chem Geol* **273**, 151-167.
- Sarda, P., Moreira, M., Staudacher, T., Schilling, J.-G. and Allègre, C.J. (2000) Rare gas systematics on the southernmost Mid-Atlantic Ridge: Constraints on the lower mantle and the Dupal source. *Journal of Geophysical Research: Solid Earth* **105**, 5973-5996.
- Schlömer, A., Geissler, W.H., Jokat, W. and Jegen, M. (2017) Hunting for the Tristan mantle plume – An upper mantle tomography around the volcanic island of Tristan da Cunha. *Earth Planet Sc Lett* **462**, 122-131.
- Schwindrofska, A., Hoernle, K., Hauff, F., van den Bogaard, P., Werner, R. and Garbe-Schönberg, D. (2016) Origin of enriched components in the South Atlantic: Evidence from 40 Ma geochemical zonation of the Discovery Seamounts. *Earth Planet Sc Lett* **441**, 167-177.
- Steiger, R.H. and Jäger, E. (1977) Subcommittee on geochronology: Convention on the use of decay constants in geo- and cosmochronology. *Earth Planet Sc Lett* **36**, 359-362.
- Stein, M., Navon, O. and Kessel, R. (1997) Chromatographic metasomatism of the Arabian—Nubian lithosphere. *Earth Planet Sc Lett* **152**, 75-91.
- Stracke, A., Bizimis, M. and Salters, V.J.M. (2003) Recycling oceanic crust: Quantitative constraints. *Geochemistry, Geophysics, Geosystems* **4**, 8003.
- Stracke, A., Hofmann, A.W. and Hart, S.R. (2005) FOZO, HIMU, and the rest of the mantle zoo. *Geochemistry, Geophysics, Geosystems* **6**, Q05007.
- Stroncik, N.A., Trumbull, R.B., Krienitz, M.-S., Niedermann, S., Romer, R.L., Harris, C. and Day, J. (2017) Helium isotope evidence for a deep-seated mantle plume involved in South Atlantic breakup. *Geology* **45**, 827-830.
- Torsvik, T.H., Smethurst, M.A., Burke, K. and Steinberger, B. (2006) Large igneous provinces generated from the margins of the large low-velocity provinces in the deep mantle. *Geophysical Journal International* **167**, 1447-1460.
- van den Bogaard, P. (2013) The origin of the Canary Island Seamount Province - New ages of old seamounts. *Scientific Reports* **3**, 2107.
- Weaver, B.L., Wood, D.A., Tarney, J. and Joron, J.L. (1987) Geochemistry of ocean island basalts from the South Atlantic: Ascension, Bouvet, St. Helena, Gough and Tristan da Cunha. *Geological Society, London, Special Publications* **30**, 253-267.
- Weis, D., Garcia, M.O., Rhodes, J.M., Jellinek, M. and Scoates, J.S. (2011) Role of the deep mantle in generating the compositional asymmetry of the Hawaiian mantle plume. *Nature Geosci* **4**, 831-838.
- Weiss, Y., Class, C., Goldstein, S.L. and Hanyu, T. (2016) Key new pieces of the HIMU puzzle from olivines and diamond inclusions. *Nature* **537**, 666-670.
- Weit, A., Trumbull, R.B., Keiding, J.K., Geissler, W.H., Gibson, S.A. and Veksler, I.V. (2017) The magmatic system beneath the Tristan da Cunha Island: Insights from thermobarometry, melting models and geophysics. *Tectonophysics* **716**, 64-76.
- Werner, R. and Wagner, H.-J. (2014) RV SONNE Fahrtbericht/Cruise Report SO234/1 "SPACES": Science or the Assessment of Complex Earth System Processes, 22.06.–06.07. 2014, Walvis Bay/Namibia-Durban/South Africa. *GEOMAR Report no. 17 (N. Ser.)*, 29 pp + Appendices.
- Willbold, M. and Stracke, A. (2006) Trace element composition of mantle end-members: Implications for recycling of oceanic and upper and lower continental crust. *Geochemistry, Geophysics, Geosystems* **7**, Q04004.
- Wilson, J.T. (1963) Evidence from Islands on the Spreading of Ocean Floors. *Nature* **197**, 536-538.
- Wilson, J.T. (1973) Mantle plumes and plate motions. *Tectonophysics* **19**, 149-164.
- Zhao, D. (2007) Seismic images under 60 hotspots: Search for mantle plumes. *Gondwana Research* **12**, 335-355.
- Zindler, A. and Hart, S.R. (1986) Chemical Geodynamics. *Annual Review of Earth and Planetary Sciences* **14**, 493-571.

### **3. CONCLUSIONS AND OUTLOOK**

#### **3.1 Conclusions**

The aim of my PhD thesis was to provide further insights into the origin and the temporal and geochemical evolution of the Walvis Ridge. By collecting new bathymetric data and combining them with geochemical and geochronological analyses from 35 new sample sites on and next to the Walvis Ridge I could address all my objectives (see section 1.4. and below).

#### **Is the Tristan-Gough volcanic chain formed by a classical mantle plume?**

Based on bathymetric and geochemical data, I could identify at least two magmatic events, that were confirmed by the  $^{40}\text{Ar}/^{39}\text{Ar}$  age data. Together with the literature data (Rohde et al., 2013; O'Connor and Jokat, 2015a, b), the basement samples with EM I-type compositions of the entire Tristan-Gough seamount chain display an excellent linear age progression (Fig. 6 in section 3.3). This array can be extrapolated to the Etendeka flood basalts (135-132 Ma; Renne et al., 1996; Renne, 2015) and the active volcanic islands of Tristan da Cunha and Gough (0.12 -2.6 Ma; Maund et al., 1988; Hicks et al., 2012), providing further support for the age progression. The age progression is the strongest evidence that a deep-rooted mantle plume formed the track. Recent seismic tomographic data supports this conclusion, which images a low-velocity conduit-like structure with a radius of 100 km down to a depth of 250 km just to the southwest of Tristan da Cunha (Schlömer et al., 2017). This shallow velocity anomaly lies above a broader vertically continuous conduit-like structure with  $\partial V_s$  ratios of  $< -0.5\%$  at a depth range of 1000-2800 km (French and Romanowicz, 2015). Furthermore, Stroncik et al. (2017) report high  $^3\text{He}/^4\text{He}$  ratios ( $> 10 R_A$ ) from the Etendeka flood basalt province, which additionally support a lower mantle origin. The fan-out

mechanism of the Guyot Province towards the active volcanic islands remains enigmatic but could be related to a weakening mantle plume (Rohde et al., 2013).

**What is the geochemical signature of the Walvis Ridge and when does the geochemical zonation of the Tristan-Gough track start?**

The majority of the new basement samples from the Walvis Ridge lie within the Gough compositional domain, confirming that the Walvis Ridge is primarily composed of this EM I-type composition (Fig. 5 in section 3.3). Nevertheless, a few samples either expand the Gough-field towards the Tristan compositional field, or the first appearance of the Tristan-type material can be extended to approximately 90 Ma. Interestingly, these lavas are from the eastern side of the Walvis Ridge and suggest the local presence of Tristan-type material before the hotspot track became zoned. Finally, there is not enough data (samples from only two sites have been reported thus far; Rohde et al., 2013a) to evaluate whether Tristan-type compositions are present on the Rio Grande Rise or Sao Paulo plateau.

**Do the distinct Tristan- and Gough-types compositions contain temporal or spatial variations? What are the potential source components?**

Since the Gough-type composition represents the long-lived mantle plume component, I focused on this compositional type. The vast majority of the Walvis Ridge is characterized by tholeiitic compositions and relatively depleted incompatible trace element concentrations, whereas the Gough-type Guyot Province lavas are overall alkalic and relatively enriched in trace elements (Figs. 3-4 in section 3.3). The geochemical variations along the track are consistent with the change from plume-ridge interaction during the Walvis Ridge formation to intraplate volcanism, with an increase

in lithospheric thickness resulting in higher pressure and lower melting degrees. The Nb-Ta systematics (e.g., Nb/Th) indicate that the Gough-type composition reflects the mixing of two distinct components. In accordance, mixing of a lower continental crust component with a mixture of recycled oceanic crust (FOZO) ± sediments (EM II) can reproduce the Gough domain in multi-isotope space (Figs 5, 7-8 in section 3.3). The Guyot Province lavas seem to have an overall higher imprint of the FOZO-EM II component (e.g., higher  $^{206}\text{Pb}/^{204}\text{Pb}_{60\text{Ma}}$ ), compared to the Walvis Ridge lavas, which could be coupled to the melting degree. One possible explanation could be that the Walvis Ridge lavas preferentially sample the lower continental crustal component, whereas at lower degrees of melting (alkaline lavas, which primarily occur in the Guyot Province and Gough Islands) sample mainly recycled ocean crust ± sediments, possibly in the form of eclogite/garnet pyroxenite.

### **Is the geochemical signature of the Walvis Ridge associated with other intraplate lavas in the South Atlantic?**

The Gough-type component can also be identified in the Discovery and Shona mantle plumes, indicating that these hotspots sample the same reservoir (Figs. 7-8 in section 3.3). The various EM I-type flavors in the South Atlantic can be reproduced by the mixing of Gough-type composition with the following: 1) FOZO to produce the Tristan-type composition, 2) upper continental crust to yield the Southern Discovery-type composition and 3) depleted mantle to cover the compositional domain of the Shona lavas (Figs. 5,7-8 in section 3.3). Therefore, it seems that the Gough-type composition represents the common and widespread EM I-type in the South Atlantic DUPAL anomaly.



**What is the geochemical fingerprint of the lavas with anomalously young ages? Are they related to the Tristan-Gough seamount chain? What is the origin of the seamounts next to the Walvis Ridge? Do they belong to a later stage of volcanism?**

The combined analyses of bathymetric, geochemical and geochronological data demonstrate that the majority of seamounts on and close to the Walvis Ridge belong to a later volcanic activity. The sampled seamounts are 20-40 Ma younger than the age progressive Walvis Ridge basement, and the isotopic compositions of the seamounts extend from the St. Helena HIMU end member to E-MORB (Figs. 5-7 in section 3.2). Based on the unusually long volcanic quiescence and HIMU-like composition, I concluded that these seamounts were derived from a distinct source and are not related to the Tristan-Gough mantle plume.

**Does the temporal and spatial evolution of the Tristan-Gough track yield further insights into the origin of the geochemical heterogeneity of the South Atlantic intraplate lavas?**

Based on the temporal and spatial evolution of the Tristan-Gough hotspot track and the characteristic geochemical fingerprints of the South Atlantic hotspots relative to their position to the 1 %  $\partial V_s$  velocity contour of the African Large Low Shear Velocity Province (LLSVP), I propose that the spatial and temporal geochemical heterogeneities in the South Atlantic hotspots ultimately reflect sampling from different geochemical domains outside and within the African LLSVP. The model shows that the Gough-type composition of the Tristan-Gough, Southern Discovery and Shona hotspots was derived from the outer margins of the LLSVP, whereas St. Helena and Ascension hotspots and late-stage Walvis and Shona volcanism sample HIMU from inner portions of the LLSVP (Fig. 9 in section 3.3). The ambient lowermost mantle outside of the LLSVP consists of

subducted ocean crust (FOZO), as sampled by the Bouvet hotspot, and subducted marine sediment or continental crust, as sampled by the Southern Discovery hotspot.

### **HIMU-type volcanism**

Finally, I used selected submarine samples from the Walvis Ridge, Shona track, Eastern Chatham Rise and Manihiki plateau combined with a literature data survey to demonstrate a more widespread (nearly global) distribution of the HIMU end member than previously postulated (Fig. 6 in section 3.1). This survey shows that HIMU is generally associated with low-volume alkaline, carbonatitic and/or kimberlitic intraplate volcanism, consistent with the derivation through low degrees of melting of CO<sub>2</sub>-rich sources. The majority of end member HIMU locations can be directly related to hotspot settings. The restricted trace element and isotopic compositions (St. Helena-type HIMU) but near-global distribution, point to a deep-seated, widespread reservoir, which most likely formed in the Archean. In this context, I re-evaluated the origin of a widespread HIMU reservoir in an Archean geodynamic setting. In my PhD thesis, I note that the classical oceanic crust recycling model cannot be applied in a plume-lid dominated tectonic setting and propose that delamination of carbonatite-metasomatized subcontinental lithospheric mantle could be a suitable HIMU source (Fig. 10 in section 3.1). In contrast, hydrothermal alteration of the ocean crust and dehydration during subduction gives the ocean crust the appropriate composition to evolve HIMU-like (FOZO-type) compositions. Therefore our model invokes a different origin for the HIMU (through carbonate metasomatism and detachment/delamination of SCLM during Archean plume-lid tectonics) and FOZO (Proterozoic and later recycling of ocean crust during modern-style tectonics) mantle end members.

### **3.2 Outlook**

The recovered lavas during WALVIS I and II represent one of the best worldwide sample collections from a submarine volcanic chain. My PhD thesis demonstrates a more complex volcanic history, as previously thought, and raises further questions. The majority of seamounts and ridges on and close to the Walvis Ridge have a HIMU-type composition and were emplaced 20 to 40 Ma after the underlying or nearby EM I-type basement. Based on two magmatic lineaments with similar ages and isotopic compositions, I proposed a genetic relationship and a widespread volcanism between 80 and 50 Ma. However, the geochemical and geochronological data of this area are sparse, and a detailed sampling of the Mocamedes Arch and volcanic edifices along the East African coast could clarify the situation. Rock samples from potential late-stage volcanism from the Etendeka LIP have already been collected to test this hypothesis (Hoernle pers. comm.).

In the last few decades, the Tristan-Gough seamount chain (Etendeka-Walvis Ridge-Guyot Province) was always related to Tristan da Cunha. My thesis shows that the Gough-type composition represents the long-lived mantle plume component, and further seismic observations should focus on Gough Island. Overall, increased seismic tomographic resolution would help to understand the recent structure of the Tristan-Gough mantle plume. Does the mantle plume split into two arms? Where? Or does the mantle plume consist of numerous rising “blobs”?

The geochemical heterogeneity of the South Atlantic DUPAL anomaly can be explained by Gough-type composition flavored with FOZO and continental material. Note, that the majority of our lavas are differentiated ( $MgO < 5\text{wt.}\%$ ) and were affected by varying degrees of alteration, which could decouple the trace element signature from the isotopic fingerprint. To test the mixing hypothesis, more fresh and primitive

materials are required. Additionally, Stroncik et al. (2017) showed that some Gough-type lavas from Etendeka have high  $^3\text{He}/^4\text{He}$  ratios ( $> 10 R_A$ ). Until now, only lavas with extremely low  $^3\text{He}/^4\text{He}$  ratios ( $< 6 R_A$ ; Kurz et al., 1982) are reported from Tristan and Gough, and further work could provide new insights. Based on the presented model (Tristan = Gough-type + FOZO), I would expect even higher  $^3\text{He}/^4\text{He}$  ratios at Tristan compared to Gough (if FOZO is characterized by high helium ratios). Furthermore, new samples from Rio Grande Rise and especially the Sao Paulo plateau could provide further insights into the evolution of the Tristan-Gough mantle plume. Where does the geochemical zonation start? Is there also widespread late-stage volcanism, and what is the geochemical signature? If HIMU-type late-stage lavas can be recovered from the Rio Grande Rise, HIMU could be part of the Tristan-Gough mantle plume. In this case, the mechanism of late-stage volcanism remains enigmatic but could indicate an even closer association between HIMU and EM I.

Finally, the spatial and temporal geochemical evolution of the South Atlantic mantle plumes could be used to map the lowermost mantle. A comparison of the DUPAL anomaly from the South Atlantic and Indian Oceans could provide further insights into the spatial geochemical heterogeneity of the African LLSVP and ambient lowermost mantle. For example, the geochemical composition of some Kerguelen lavas overlaps with the Gough-type composition and could indicate that the Gough-type composition is also present in Indic mantle plumes. In this case, the Gough-type composition is not limited to the westernmost margin of the African LLSVP.

## REFERENCES

- French, S. W., and Romanowicz, B., 2015, Broad plumes rooted at the base of the Earth's mantle beneath major hotspots: *Nature*, v. 525, no. 7567, p. 95-99.
- Hicks, A., Barclay, J., Mark, D. F., and Loughlin, S., 2012, Tristan da Cunha: Constraining eruptive behavior using the  $^{40}\text{Ar}/^{39}\text{Ar}$  dating technique: *Geology*, v. 40, no. 8, p. 723-726.
- Kurz, M. D., Jenkins, W. J., and Hart, S. R., 1982, Helium isotopic systematics of oceanic islands and mantle heterogeneity: *Nature*, v. 297, no. 5861, p. 43-47.
- Maund, J. G., Rex, D. C., Le Roex, A. P., and Reid, D. L., 1988, Volcanism on Gough Island: a revised stratigraphy: *Geological Magazine*, v. 125, no. 2, p. 175-181.
- O'Connor, J. M., and Jokat, W., 2015a, Tracking the Tristan-Gough mantle plume using discrete chains of intraplate volcanic centers buried in the Walvis Ridge: *Geology*, v. 43, no. 8, p. 715-718.
- , 2015b, Age distribution of Ocean Drill sites across the Central Walvis Ridge indicates plate boundary control of plume volcanism in the South Atlantic: *Earth and Planetary Science Letters*, v. 424, p. 179-190.
- Renne, P., Age and Duration of the Paraná-Etendeka Flood Basalts and Related Plumbing System, *in* Proceedings AGU Fall Meeting Abstracts 2015.
- Renne, P. R., Glen, J. M., Milner, S. C., and Duncan, A. R., 1996, Age of Etendeka flood volcanism and associated intrusions in southwestern Africa: *Geology*, v. 24, no. 7, p. 659-662.
- Rohde, J. K., van den Bogaard, P., Hoernle, K., Hauff, F., and Werner, R., 2013, Evidence for an age progression along the Tristan-Gough volcanic track from new  $^{40}\text{Ar}/^{39}\text{Ar}$  ages on phenocryst phases: *Tectonophysics*, v. 604, p. 60-71.
- Schlömer, A., Geissler, W. H., Jokat, W., and Jegen, M., 2017, Hunting for the Tristan mantle plume – An upper mantle tomography around the volcanic island of Tristan da Cunha: *Earth and Planetary Science Letters*, v. 462, p. 122-131.
- Stroncik, N. A., Trumbull, R. B., Krienitz, M.-S., Niedermann, S., Romer, R. L., Harris, C., and Day, J., 2017, Helium isotope evidence for a deep-seated mantle plume involved in South Atlantic breakup: *Geology*, v. 45, no. 9, p. 827-830.

## **Appendices A-C: Global distribution of the HIMU end member: Formation through Archean Plume-lid Tectonics**

---

### **Appendix A: Analytical Methods**

#### *1.1 Age determination*

##### *<sup>40</sup>Ar/<sup>39</sup>Ar age determinations*

The <sup>40</sup>Ar/<sup>39</sup>Ar analyses was carried out at the GEOMAR Argon Geochronology in Oceanography (ARGO) Laboratory. First, the plagioclase separates were handpicked under a binocular microscope from crushed, sieved and washed sample fractions of 250-500 µm. Following this, the plagioclase separates were treated with 5% hydrofluoric acid for 10 minutes, rinsed with distilled water, cleaned with distilled water for 4 minutes using an ultrasonic stick, and dried overnight in a 50°C oven. Approximately 20 mg of each unknown mineral separate was loaded into small 99.999% aluminium disks, which were stacked and bolted together, and then placed in a 99.9% Al canister to make up the irradiation package. Grains of Taylor Creek sanidine (TCR-2) age standard (27.87 ± 0.04 Ma; 1σ error; M.A. Lanphere, pers. comm., calibrated to SB-3 biotite; Lanphere and Dalrymple, 2000) were regularly interspersed in the aluminium disks with the unknown samples to monitor the fast neutron gradient. The separates were irradiated in two separate irradiations, both for 7 days in the C6 position, at the 5 MW GKSS Reactor Centre in Geesthacht, Germany.

Upon return of the irradiation canisters, single age standard grains and unknown sample separates were loaded into variously sized holes aluminium laser palettes. A laser palette and glass coverslips were loaded into an ultra-high vacuum 4.5" laser chamber fitted with a Kovar viewport that was baked at 230°C, and the whole extraction

line was baked in an oven at 195°C for 8 hours, and then pumped for 2 days to remove adsorbed atmospheric argon from the samples and chamber walls.

A 25 W Spectra Physics argon ion laser, with a computer-controlled isel X-Y stage, was used to incrementally heat the unknown samples or totally fuse the age standard single grains for 45 seconds. The laser system was fitted with a binocular microscope and light source for sample illumination and X-Y stage calibration, and a camera for video recording of the laser heating of each sample.

The gases released by laser heating were cleaned for 3 minutes using an automatically-refilling liquid nitrogen Dewar attached to a glass finger, and two SAES AP10 getter pumps (one at 400°C and one at room temperature) to remove all active gases. The remaining noble gases were equilibrated into a high sensitivity MAP 216 mass spectrometer, containing a Bauer-Signer-type source, operated at a 240 uA emission current, with a Becton Dickinson MM-1 Mesh electron multiplier, and a mass spectrometer sensitivity of  $2.70 \times 10^{-10} \text{ cm}^3/\text{V}$  ( $1.203\text{E-}14 \text{ moles}/\text{V}$ ) using the normal operating gain value.

The five Ar isotopes ( $^{36}\text{Ar}$  to  $^{40}\text{Ar}$ ) and baselines (masses 35.5 to 40.5) for the system blanks, age standards and unknown samples were measured via peak-hopping using a single electron multiplier with two variable gain settings. The fully automated laser heating, X-Y stage movement, automated valves operation, and data acquisition were computer controlled using a Turbo Pascal program.

Unknown analyses were corrected for (1) peak tails from adjoining Ar peaks, (2) baselines, (3) blanks (see Appendix C), (4) mass spectrometer discrimination using a linear law mass discrimination factor of 1.00980 per atomic mass unit measured from air pipette shots and modern glasses, and (5) the following nuclear interference reaction correction factors:  $^{39}\text{Ar}/^{37}\text{Ar}_{\text{Ca}} = 9.94 \times 10^{-4}$ ,  $^{36}\text{Ar}/^{37}\text{Ar}_{\text{Ca}} = 4.42 \times 10^{-4}$ , and  $^{40}\text{Ar}/^{39}\text{Ar}_{\text{K}} =$

$6.00 \times 10^{-3}$ . Errors are quoted at  $1\sigma$  and  $2\sigma$  levels, and the  $^{40}\text{Ar}/^{39}\text{Ar}$  ages were calculated using the  $^{40}\text{K}$  decay constants ( $^{40}\text{K}_{\beta^-} = 4.962 \times 10^{-10}$  years,  $^{40}\text{K}_e + ^{40}\text{K}_{e'} = 5.810 \times 10^{-11}$  years, and a total  $^{40}\text{K} \lambda = 5.543 \times 10^{-10}$  years)  $^{40}\text{K}/\text{K}$  ratio (0.01167) and  $^{40}\text{Ar}/^{36}\text{Ar}$  atmospheric ratio (295.5) of Steiger and Jäger (1977). The J values and errors for each unknown sample are noted in the sample  $^{40}\text{Ar}/^{39}\text{Ar}$  data tables (Appendix C). All the plots and plateau and inverse isochron age determinations were made using the Excel Isoplot macro v. 4.15 (Ludwig, 2011). Inverse isochron % spreading factor (SF) values were calculated using the equation of Jourdan et al. (2009), who suggested a SF value of  $> \sim 40\%$  to indicate a statistically valid spread of inverse isochron data between the atmospheric and radiogenic  $^{40}\text{Ar}$  reservoirs within the sample.

## *1.2 Geochemistry*

Dredged rock samples were cut on-board to obtain the least altered parts for on shore preparation of rock chips and powders. After drying the rock slabs at  $50^\circ\text{C}$ , they were crushed in a steel jaw crusher, sieved, washed with deionized water to remove dust and then dried again. The size fraction 0.5-1 mm was carefully handpicked under a binocular microscope to obtain the freshest possible material. Then, several grams of the picked rock chips were milled to fine powder with an agate mortar grinder and a planetary ball mill. This powder was used for major and trace element analysis, Hf isotopes and Sr isotopes on hot-acid leached powders. The remaining half of the rock chips was used for Sr-Nd-Pb isotopic analysis.

Major element compositions were obtained on fused pellets at the Institute of Mineralogy and Petrography at the University of Hamburg by X-ray Fluorescence Analysis (XRF, Magix Pro PW 2540). Reference materials JGB-1, JB-3, JB-2, JA-3, JG3 and JG-2 were determined along with the samples and the accuracy of the standards lies



within 3% of the reference values from Govindaraju (1994) for most elements. At element concentrations significantly below 1 wt.% larger deviations from the suggested values are observed (see Appendix D).

Trace element concentrations were measured by inductively coupled plasma mass spectrometry (ICP-MS) at the Institute of Geosciences, Christian-Albrechts-University of Kiel, using an AGILENT 7500cs ICP-MS. For each sample, 100 mg of powder was dissolved by pressure digestion and analyzed following the method of Garbe-Schönberg (1993). International rock standards BHVO-2 and BIR-1 were run along with the samples and for most elements agree within 5% of the GeoReM reference values (<http://georem.mpch-mainz.gwdg.de/>). Reproducibility of replicates by means of separate digests are typically better than 2% for standards and samples (Appendix E).

Radiogenic isotope analyses were carried out at GEOMAR Helmholtz Centre for Ocean Research Kiel using a Thermo Scientific TRITON+ thermal ionization mass spectrometer (TIMS) for Sr-Nd-Pb and a Nu-Plasma MC-ICPMS for Hf with both instruments operating in static multi-collektion mode. Sr, Nd and Pb chemistry was conducted on 100-250 mg whole-rock chips and followed established standard procedures (Hoernle et al., 2008). Prior to dissolution in a 5:1 mixture of concentrated HF and HNO<sub>3</sub> they were leached in 2N HCl at 70°C for one hour and thereafter triple rinsed in 18.2 MΩ water. Additional Sr isotope analyses were carried out on 100 mg of leached powders (6N HCl at 150 °C for 3 days) for each sample to eventually remove possible seawater alteration effects more thoroughly than the mild leaching of chips. In fact five out of nine samples produced slightly to significantly lower <sup>87</sup>Sr/<sup>86</sup>Sr (0.000074-0.000254) for the leached powders than the chips while three gave slightly higher (0.000035-0.000046) and one identical <sup>87</sup>Sr/<sup>86</sup>Sr in comparison to the chips. These observations suggest that effects of seawater alteration on <sup>87</sup>Sr/<sup>86</sup>Sr are relatively

minor and that leaching of powders in hot 6N HCl does not always remove the seawater derived imprint. Therefore the lowest  $^{87}\text{Sr}/^{86}\text{Sr}$  obtained in pairs of powder and chips is presumably closest to the prime magmatic value and thus used for petrogenetic interpretations. The total chemistry blanks for Sr were smaller than 100pg and lower than 50pg for Nd. Nd and Sr ratios were normalized within run to  $^{146}\text{Nd}/^{144}\text{Nd}=0.7219$  and  $^{86}\text{Sr}/^{88}\text{Sr}=0.1194$ , respectively. NBS987 and La Jolla reference materials were measured 4-6 times for each sample turret. The numerical average obtained for the standards is subtracted from the preferred standard values and the off-set value applied to the sample data. This measure compensates for long-term machine drift and thereby ensures maximum comparability and quality of data generated at different times. Sample data are reported relative to  $^{87}\text{Sr}/^{86}\text{Sr}=0.710250\pm 0.000007$  (n=37; 2SD external reproducibility) for NBS987 and  $^{143}\text{Nd}/^{144}\text{Nd}=0.511850\pm 0.000005$  (n=23; 2SD external reproducibility) for La Jolla. Sr-Nd total chemistry were below 100pb and 50pg respectively. The Pb double spike (DS) technique of Hoernle et al. (2011) was used to mass bias correct Pb isotope ratios. DS corrected NBS981 values are  $^{206}\text{Pb}/^{204}\text{Pb} = 16.9413\pm 0.0020$ ,  $^{207}\text{Pb}/^{204}\text{Pb} = 15.4984 \pm 0.0027$ ,  $^{208}\text{Pb}/^{204}\text{Pb} = 36.7220 \pm 0.0068$ ,  $^{207}\text{Pb}/^{206}\text{Pb} = 0.91483 \pm 0.00006$  and  $^{208}\text{Pb}/^{206}\text{Pb} = 2.16760 \pm 0.00015$ (n=7; 2SD). The total Pb chemistry blanks were below 20 pg and thus considered negligible.

Hf chemistry used 200-300mg of unleached rock powder and chemical separation followed the procedure of Blichert-Toft et al. (1997). Total chemistry blanks for Hf were smaller than 50pg. The in-house standard SPEX Hf ICP solution (lot#9) has been calibrated with  $^{176}\text{Hf}/^{177}\text{Hf}=0.282170$  to JMC457 with  $^{176}\text{Hf}/^{177}\text{Hf}=0.282163$  (Blichert-Toft et al., 1997) and was measured every 4<sup>th</sup> sample. The resulting standard bracketing normalized 2SD external reproducibility of Hf SPEX is  $^{176}\text{Hf}/^{177}\text{Hf}=0.282170 \pm 0.000006$  (n=386; 2SD, 2011-2016) on the NU MC-ICPMS at GEOMAR. Two samples

replicates were analyzed for Sr-Nd-Pb and lie within 2SD of the standards except Pb ratios involving  $^{206}\text{Pb}$ , which reflects variable U uptake by seawater interaction. The variable  $^{206}\text{Pb}$  abundance, however does not affect the overall scientific interpretation and conclusion.

## References

- Blichert-Toft, J., Chauvel, C., and Albarède, F., 1997, Separation of Hf and Lu for high-precision isotope analysis of rock samples by magnetic sector-multiple collector ICP-MS: *Contributions to Mineralogy and Petrology*, v. 127, no. 3, p. 248-260.
- Garbe-Schönberg, C.-D., 1993, Simultaneous Determination of 37 Trace-Elements in 28 International Rock Standards by ICP-MS: *Geostandards Newsletter*, v. 17, no. 1, p. 81-97.
- Govindaraju, K., 1994, Compilation of Working Values and Sample Description for 383 Geostandards: *Geostandards Newsletter*, v. 18, no. 2, p. 331-331.
- Hoernle, K., Abt, D. L., Fischer, K. M., Nichols, H., Hauff, F., Abers, G. A., van den Bogaard, P., Heydolph, K., Alvarado, G., Protti, M., and Strauch, W., 2008, Arc-parallel flow in the mantle wedge beneath Costa Rica and Nicaragua: *Nature*, v. 451, no. 7182, p. 1094-1097.
- Jourdan, F., Renne, P. R., and Reimold, W. U., 2009, An appraisal of the ages of terrestrial impact structures: *Earth and Planetary Science Letters*, v. 286, no. 1, p. 1-13.
- Lanphere, M. A., and Dalrymple, G. B., 2000, First-principles calibration of  $^{38}\text{Ar}$  tracers: Implications for the ages of  $^{40}\text{Ar}/^{38}\text{Ar}$  fluence monitors: US Geological Survey Professional Paper, no. 1621, p. 1-10.
- Ludwig, K. R., 2011, Users manual for Isoplot 4.15: A geochronological toolkit for Microsoft Excel: Special Publication 4, Berkeley, p. 77.
- Steiger, R. H., and Jäger, E., 1977, Subcommittee on geochronology: Convention on the use of decay constants in geo- and cosmochronology: *Earth and Planetary Science Letters*, v. 36, no. 3, p. 359-362.

Appendix B: <sup>40</sup>Ar/<sup>39</sup>Ar age, major element, trace element and isotope data

Sample	Location/Structure	Ar/Ar Age (Ma)	Lat (°)	Long. (°)	Rock type (TAS)	Method	SiO <sub>2</sub> (wt %)	TiO <sub>2</sub> (wt %)	Al <sub>2</sub> O <sub>3</sub> (wt %)	Fe <sub>2</sub> O <sub>3</sub> (wt %)	MnO (wt %)	MgO (wt %)	CaO (wt %)	Na <sub>2</sub> O (wt %)	K <sub>2</sub> O (wt %)	P <sub>2</sub> O <sub>5</sub> (wt %)	SO <sub>3</sub> (wt %)	L.O.I. (wt %)	Sum (wt %)	SiO <sub>2</sub> <sup>a</sup> (wt %)	TiO <sub>2</sub> <sup>a</sup> (wt %)	Al <sub>2</sub> O <sub>3</sub> <sup>a</sup> (wt %)	Fe <sub>2</sub> O <sub>3</sub> <sup>a</sup> (wt %)	MnO <sup>a</sup> (wt %)	MgO <sup>a</sup> (wt %)	CaO <sup>a</sup> (wt %)	Na <sub>2</sub> O <sup>a</sup> (wt %)	K <sub>2</sub> O <sup>a</sup> (wt %)		
<b>Evling Seamant</b>																														
SO1465C-1a	Evling Seamant	72.86	-23.11	8.17		Tephrite	41.0	3.77	15.0	13.0	0.25	4.89	11.2	3.57	2.55	1.45	n.a.	2.9	99.5	42.6	3.92	15.6	13.5	0.26	5.09	11.6	3.71	2.65		
<b>Mor's Ridge</b>																														
MO151	Mor's Ridge	54.9h	-26.48	-6.25		Tephrite	57.7	0.370	19.7	3.48	0.14	0.92	0.24	4.07	6.04	0.04	0	2.59	101.2	61.6	0.35	21.1	3.72	0.15	0.99	0.26	5.31	6.45		
SO233-DRS7-6	Govot	831	-19.29	8.64		Tephrite	50.1	0.650	13.1	1.05	0.14	0.55	0.75	6.45	4.2	0.01	0	2.11	98.22	61.5	0.72	13.6	10.9	0.13	0.57	0.75	5.21	4.91		
SO233-DRS9-1	Govot	821	-19.29	9.96		Tephrite	45.0	3.92	14.9	1.58	0.18	5.41	10.4	2.29	1.13	0.32	0	2.9	100.48	44.1	4.02	15.2	16.2	0.18	5.54	10.7	2.85	1.18		
SO233-DRS9-2	Govot	821	-19.29	9.96		Tephrite	42.2	3.88	14.8	1.56	0.15	5.91	10.8	2.31	1.02	0.53	0	3.07	100.26	43.4	3.99	15.2	16.1	0.15	6.08	11.1	2.89	1.05		
SO233-DRS9-5	Govot	821	-19.29	9.96		Tephrite	41.9	4.35	14.6	1.52	0.19	2.96	9.30	3.38	1.62	2.8	0	2.72	99.74	44.0	4.57	15.4	16.7	0.20	3.11	0.77	3.53	1.70		
SO233-DRS9-6	Govot	821	-19.29	9.96		Tephrite	46.6	4.00	16.4	1.45	0.26	6.66	9.09	4.14	2.68	1.36	0	1.78	99.48	47.9	4.11	16.9	14.9	0.27	1.71	6.26	4.23	2.73		
SO233-DRS9-9	Govot	821	-19.29	9.96		Phenocryst trachybasalt	47.7	3.81	15.6	1.38	0.19	2.39	7.40	4.37	2.16	1.31	0.03	0	1.3	100.03	45.3	3.97	15.9	14.9	0.19	2.83	7.52	4.44	2.20	
SO233-DRS9-10	Govot	871	-18.44	10.89		Basalt	46.0	3.14	15.8	1.19	0.17	5.76	10.1	2.97	1.52	0.66	0	2.05	99.90	47.0	3.21	16.2	12.2	0.17	5.89	10.3	3.04	1.35		
SO233-DRS9-2	Govot	871	-18.44	10.89		Basalt	46.3	3.16	15.8	1.21	0.18	5.73	10.1	2.89	1.53	0.66	0.01	2.83	100.41	47.2	3.22	16.1	12.3	0.18	5.84	10.3	2.95	1.27		
SO233-DRS9-10	Govot	871	-18.44	10.89		Basalt	45.4	2.71	14.0	1.18	0.17	6.85	12.0	2.43	0.93	0.48	0	3.28	100.01	47.0	2.80	14.5	12.2	0.18	7.08	12.4	2.51	0.96		
SO233-DRS9-11	Govot	871	-18.44	10.89		Basalt	43.9	3.08	15.0	1.17	0.18	5.85	9.55	2.86	1.20	0.62	0	1.93	95.92	46.7	3.28	16.0	12.4	0.19	6.22	10.2	3.04	1.28		
<b>Richardson Seamant</b>																														
MSM1913	Richardson Seamant	268	-40.47	15.09		Tephrite	38.3	3.96	11.6	15.3	0.29	7.24	11.8	1.85	1.23	2.07	0.14	5.74	99.58	41.4	4.28	12.5	16.5	0.31	7.82	12.7	2.00	1.33		
<b>Nainika Plateau</b>																														
SO193-DR32-1	Seamant	100.7m	-8.75	-164.24		Phenocryst trachybasalt	48.1	2.72	14.2	10.1	0.12	9.29	6.83	2.81	1.81	0.59	n.a.	3.12	99.66	49.4	2.82	14.7	10.5	0.12	9.62	7.07	2.91	1.87		
SO193-DR35-1	Ridge-like structure of a seamant	100.7m	-7.68	-163.92		Mugearite	49.8	2.76	15.6	11.1	0.15	3.26	7.69	4.16	1.41	1.66	n.a.	1.76	99.32	51.4	2.85	16.0	11.5	0.15	3.36	7.94	4.29	1.46		
<b>Eastern Chatham Rise</b>																														
SO168-DRS7-1	Chicken	88.6m	41.06	169.09		Hawaiite	48.9	2.68	19.2	10.5	0.15	2.59	9.35	3.52	1.43	0.62	n.a.	1.85	100.75	49.4	2.71	19.4	10.6	0.15	2.62	9.45	3.56	1.45		
SO168-DRS7-5b	Chicken	88.6m	41.06	169.09		Mugearite	49.9	2.96	15.2	12.9	0.21	2.51	7.15	4.51	2.31	1.06	n.a.	1.3	99.94	50.6	3.00	15.4	13.0	0.21	2.55	7.25	4.57	2.34		
SO168-DRS8-1	Potato	88.6m	41.73	169.28		Tephrite	62.8	0.21	17.5	5.35	0.14	0.29	1.07	6.55	5.97	0.06	n.a.	0.52	100.46	62.8	0.21	17.5	5.35	0.14	0.29	1.07	6.55	5.97		
SO168-DRS8-4	Potato	88.6m	41.73	169.28		Tephrite	62.5	0.22	17.5	5.33	0.16	0.34	1.22	6.41	5.5	0.05	n.a.	0.77	100.03	63.0	0.22	17.7	5.37	0.16	0.34	1.23	6.46	5.97		

<sup>a</sup> calculated to 100% on a volatile free basis; P<sub>2</sub>O<sub>5</sub> set to 1.0 wt% for normalization if > 1 wt%.

<sup>b</sup> Major element data by ICP-ES from Acmé Analytical Laboratories Ltd.

<sup>c</sup> Mineralogisch-Petrographisches Institut, Universität Hamburg.

<sup>d</sup> Trace element data by ICP-MS from the Institute of Geosciences at the Christian-Albrechts University of Kiel.

<sup>e</sup> least radiogenic 87Sr/86Sr from either leached powder or chips analysis

<sup>f</sup> leached chips; 6N HCl at 150°C for 72 hours and thereafter triple rinsed in 18MΩ H<sub>2</sub>O

<sup>g</sup> leached chips; 2N at 70°C for 1 hour and thereafter triple rinsed in 18MΩ H<sub>2</sub>O.

<sup>h</sup> Ages from Rohde et al. (2013).

<sup>i</sup> Ages from O'Connor, J.M. & lokeat (2015)

<sup>j</sup> Ages calculated after age progression - 30Ma after Rohde et al. (2013).

<sup>k</sup> Age from O'Connor et al. (2012)

<sup>l</sup> Assumed age

<sup>m</sup> measured age (this study)

<sup>n</sup> GEOMAR

n.a. not analyzed

<sup>1</sup> Ze within run errors shown for the last significant digit(s).

<sup>2</sup> Hfr ratios measure on a VG Axium MC-CPMS

BDL = Below detection limit

XXX-Rep= isotopic ratio measurement of replica

Sample	Method	Li	Sc	V	Cr	Co	Ni	Cu	Zn	Ga	Rb	Sr	Y	Zr	Nb	Cs	Ba	La	Ce	Pr	Nd	Sm	Eu	Gd	Tb	Dy	Ho	Er	Tm	Yb	Lu	Hf	Ta	Pb	Th	U		
Twining Scarnount																																						
SO193 DR35-1a	ICP-MSd	11.0	10.9	284.3	1.7	31.1	67.6	38.2	133	22.5	77.1	1035	41.0	430	135	0.886	836	101	195	22.8	89.1	157.7	4.62	13.0	1.69	8.71	1.53	3.81	0.500	3.08	0.443	8.36	7.01	6.28	20.0	2.80		
Metals Ridge																																						
SO233 DR37-6	ICP-MSd	47.2	1.97	34.1	BDL	BDL	23.2	20.8	77.3	21.1	183	247	7.23	1004	34.4	0.968	173	17.0	37.8	3.77	12.1	1.07	0.54	1.58	0.240	1.36	0.266	0.800	0.133	0.633	0.151	16.8	10.2	7.45	46.9	2.76		
SO233 DR39-1	ICP-MSd	1.68	2.41	27.0	7.15	3.84	6.03	8.95	212	53.4	37.6	36.1	4.52	1312	262	0.288	193	21.6	30.1	50.2	192	36.4	8.77	30.5	4.76	26.3	5.72	17.0	2.70	20.1	3.21	32.3	1.65	14.3	23.4	0.307		
SO233 DR39-1 Rep	ICP-MSd	8.56	2.93	330	209	35.6	115	86.2	130	23.5	136	663	22.7	237	42.2	0.168	232	31.8	70.9	9.08	39.0	82.6	2.70	7.25	1.02	5.82	0.994	2.16	0.271	1.58	0.220	5.67	2.71	1.94	2.94	1.01		
SO233 DR39-2	ICP-MSd	12.8	35.0	395	255	52.3	123	136	137	24.4	171	640	22.5	237	42.1	0.193	292	32.4	70.4	9.04	39.1	83.4	2.60	7.34	1.01	5.88	0.905	2.15	0.274	1.63	0.230	5.68	2.57	1.69	2.96	1.02		
SO233 DR39-5	ICP-MSd	17.2	16.3	198	51.5	19.8	62.9	62.3	151	25.1	246	1137	49.8	302	57.2	0.336	423	71.0	17.1	23.5	109	22.4	8.95	19.1	2.43	11.8	1.98	4.53	0.532	3.02	0.419	6.78	3.92	2.09	3.72	1.32		
SO233 DR39-6	ICP-MSd	8.15	16.2	221	31.2	26.9	62.3	10.4	151	29.3	393	791	46.2	449	88.3	0.311	472	71.0	15.8	19.6	84.2	1.70	5.27	14.8	2.02	10.6	1.83	4.41	0.567	3.36	0.467	10.3	5.31	3.65	6.15	1.73		
SO233 DR39-6	ICP-MSd	6.27	15.3	199	31.7	21.6	64.0	10.8	135	29.4	369	804	46.0	428	85.3	0.349	432	69.2	15.1	19.1	81.3	1.64	5.03	14.3	1.96	10.3	1.80	4.35	0.560	3.36	0.470	9.73	5.07	3.72	5.78	1.80		
SO233 DR39-1	ICP-MSd	28.6	23.8	235	160	38.9	86.5	68.5	112	24.3	300	700	29.0	298	66.4	0.887	393	48.5	99.7	11.7	47.5	93.4	2.96	8.26	1.16	6.22	1.11	2.72	0.372	2.29	0.332	6.33	4.01	2.79	5.18	1.42		
SO233 DR39-2 Rep	ICP-MSd	35.6	21.8	237	151	38.3	84.2	65.4	113	24.1	263	694	30.0	307	66.4	0.706	389	48.0	96.9	11.9	48.3	93.0	3.03	8.37	1.20	6.35	1.14	2.65	0.377	2.31	0.333	6.53	4.24	2.76	5.19	1.53		
SO233 DR39-2 Rep	ICP-MSd	24.1	28.8	280	44.6	48.6	179	88.7	116	22.2	190	529	24.5	217	44.1	0.547	239	32.4	66.7	8.26	35.0	74.0	2.41	6.89	0.986	5.37	0.95	2.31	0.312	1.86	0.268	5.05	2.69	1.99	3.33	0.974		
SO233 DR39-11	ICP-MSd	27.9	24.4	262	165	40.0	90.1	70.4	114	24.4	271	698	29.0	300	67.9	0.624	393	48.6	100	11.8	47.8	93.8	2.97	8.31	1.17	6.27	1.12	2.79	0.374	2.30	0.336	6.59	4.03	2.85	5.24	1.48		
Richardson Steamvent																																						
MSM193 DR3-1	ICP-MSd	36.8	25.2	284	241	59.4	160	94.7	217	24.3	221	867	47.6	542	102	0.326	491	109	201	25.9	107	199	6.26	17.0	2.25	11.3	1.89	4.46	0.540	3.14	0.436	11.5	6.24	3.07	9.14	2.73		
Waimiki Plateau																																						
SO193 DR32-1	ICP-MSd	117.6	33.2	n.a.	n.a.	37.0	325.7	102	358	19.3	343	372	28.7	273	62.6	1.16	266	47.3	90.7	11.5	46.4	91.9	2.77	7.71	1.08	5.80	1.08	2.71	0.365	2.17	0.295	6.18	4.13	2.42	4.83	1.02		
SO193 DR35-1	ICP-MSd	60.8	21.7	n.a.	n.a.	11.4	30.8	16.5	141	25.7	202	788	69.6	271	73.5	0.78	782	77.6	128	17.1	72.4	143	5.07	13.3	1.82	10.2	2.07	5.41	0.750	4.34	0.656	6.15	4.65	2.22	5.96	1.50		
Eastern Chatham Rise																																						
SO168 DR57-1	ICP-MSd	6.48	16.2	185	1.90	20.0	11.4	26.0	148	24.2	283	552	38.0	290	47.6	1.11	360	37.7	80.8	10.5	42.2	8.95	2.81	9.12	1.32	7.62	1.46	3.85	0.533	3.53	0.512	6.75	2.88	2.82	4.14	1.88		
SO168 DR57-3b	ICP-MSd	5.50	16.2	164	1.17	15.2	7.62	10.0	298	25.7	41.6	486	55.3	390	66.7	1.14	499	54.0	11.6	15.3	61.4	12.9	3.98	13.1	1.88	10.7	2.04	5.32	0.748	4.84	0.696	8.77	3.80	3.62	5.59	1.48		
SO168 DR58-1	ICP-MSd	10.0	0.1	385	0.3	0.2	2.3	5.59	94.4	36.9	112.1	34.0	97.3	1148	124.0	0.487	689	106	21.5	24.8	87.8	163	2.44	15.4	24.6	15.6	3.31	10.2	1.64	11.5	1.76	24.3	5.72	6.15	15.4	2.13		
SO168 DR58-4	ICP-MSd	4.96	0.2	21.6	0.8	0.3	4.4	6.30	84.6	36.1	111.5	32.8	70.9	1130	105	0.645	731	94.1	20.8	22.7	80.2	146	2.36	13.5	20.5	12.6	2.69	8.36	1.30	1.59	24.6	5.38	5.45	14.9	1.80			

Sample	$^{87}\text{Sr}/^{86}\text{Sr}$	$^{42}\text{Ar}$	$^{87}\text{Sr}/^{86}\text{Sr}$	$^{42}\text{Ar}$	$^{87}\text{Rb}/^{86}\text{Sr}$	$^{87}\text{Sr}/^{86}\text{Sr}$	$^{87}\text{Sr}/^{86}\text{Sr}$	$^{42}\text{Ar}$	$^{147}\text{Sm}/^{144}\text{Nd}$	$^{143}\text{Nd}/^{144}\text{Nd}$	$^{42}\text{Ar}$	$^{147}\text{Sm}/^{144}\text{Nd}$	$^{229}\text{Th}/^{232}\text{Th}$	$^{232}\text{Th}/^{238}\text{U}$	$^{232}\text{Th}/^{235}\text{U}$	$^{230}\text{Th}/^{232}\text{Th}$	$^{230}\text{Th}/^{238}\text{U}$	$^{230}\text{Th}/^{232}\text{Th}$	$^{230}\text{Th}/^{238}\text{U}$	$^{230}\text{Th}/^{232}\text{Th}$	$^{230}\text{Th}/^{238}\text{U}$	$^{230}\text{Th}/^{238}\text{U}$	$^{230}\text{Th}/^{238}\text{U}$	$^{230}\text{Th}/^{238}\text{U}$	$^{230}\text{Th}/^{238}\text{U}$			
least rad.																												
<b>Evans Seamount</b>																												
SO168 DRS5-1a	0.702233	4	0.702233	4	0.215	0.70301	0.702233	3	0.106	0.512278	0.512238	3	40.6878	124	30.2	0.22	129.1	4.38	20.50	15.81	39.92	0.282805	5	0.0076	0.282729			
Melville Ridge																												
SO233 DR57-6	0.704903	6	0.704903	6	2.143	0.70223	0.512758	3	0.098	0.512272	0.512758	3	40.8126	38	24.9	0.18	437.4	17.53	20.21	15.71	39.62	0.282872	4	0.0013	0.282827			
SO233 DR59-1	0.702983	5	0.703819	5	0.702983	0.70290	0.512854	5	0.127	0.51279	0.512854	5	39.9607	38	34.6	0.25	104.6	3.02	20.27	15.75	39.54	0.282845	5	0.0056	0.282824			
SO233 DR59-2	0.703003	5	0.703022	5	0.703003	0.703003	0.512861	5					40.0016	39														
SO233 DR59-2	0.702983	6	0.703030	5	0.702983	0.70289	0.512864	4	0.127	0.51280	0.512864	4	40.0413	20	40.3	0.29	121.3	3.01	20.27	15.75	39.54	0.282847	5					
SO233 DR59-5																												
SO233 DR59-6																												
SO233 DR 50-1	0.702803	4	0.702803	4	0.702944	0.70287	0.512872	4	0.118	0.51280	0.512872	4	39.9622	37	37.1	0.27	130.4	3.52	20.24	15.74	39.40	0.282831	5	0.0073	0.28282			
SO233 DR 50-2	0.702936	5	0.702936	5	0.702936	0.702936	0.512878	6					39.9687	37														
SO233 DR 50-10																												
SO233 DR 50-11																												
<b>Richardson Seamount</b>																												
MSM19-3 DR6-1	0.702839	6	0.702874	4	0.702839	0.70281	0.512910	4	0.112	0.51289	0.512910	4	40.1833	36	59.7	0.43	206.5	3.46	20.56	15.75	39.92	0.282899	6	0.0054	0.28290			
<b>Nainika Plateau</b>																												
SO193 DR32-1	0.703509	6	0.703509	6	0.267	0.70313	0.512777	3	0.119	0.51270	0.512777	3	40.2328	50	28.3	0.21	138.2	4.89	19.99	15.72	39.55	0.282838	5	0.0068	0.28283			
SO193 DR35-1	0.703076	6	0.703076	6	0.074	0.70297	0.512804	3	0.119	0.51273	0.512804	3	40.6272	20	46.0	0.33	188.3	4.10	20.33	15.78	39.69	0.282822	4	0.0153	0.28279			
<b>Eastern Chatham Rise</b>																												
SO168 DR57-1	0.703098	4	0.703098	4	0.148	0.70291	0.512867	3	0.128	0.51279	0.512867	3	39.9943	51	44.9	0.33	102.3	2.28	20.50	15.75	39.54	0.282905	5	0.0109	0.28289			
SO168 DR57-5b	0.703156	4	0.703156	4	0.248	0.70284	0.512903	2	0.127	0.51283	0.512903	2	39.9807	16	27.2	0.20	106.4	3.91	20.05	15.73	39.54	0.282913	5	0.0114	0.28289			
SO168 DR58-1	0.716311	5	0.716311	5	9.549	0.70229	0.512864	2	0.111	0.51280	0.512864	2	39.9588	18	23.0	0.17	171.5	7.45	19.90	15.71	39.26	0.282919	4	0.0104	0.28290			
SO168 DR58-4	0.716631	5	0.716631	5	9.851	0.70227	0.512860	2	0.109	0.51279	0.512860	2	40.0489	15	21.9	0.16	188.0	8.57	19.96	15.71	39.29	0.282906	4	0.0093	0.28289			

### Appendix C: $^{40}\text{Ar}/^{39}\text{Ar}$ analytical data

Sample: S0193 DR35-1  
 Mass = 2.075 mg  
 J = 0.003726 0.20

Step #	Laser Power (W)	$^{40}\text{Ar}/^{39}\text{Ar}$	$^{37}\text{Ar}/^{39}\text{Ar}$	$^{36}\text{Ar}/^{39}\text{Ar}$	$^{39}\text{Ar}/\text{Ar}$ (moles)	$\text{Ca}/\text{K}$	% $^{40}\text{Ar}_{\text{atm}}$	% $^{39}\text{Ar}_{\text{atm}}$	Cumulative $^{39}\text{Ar}$ fraction	Age (Ma)	$\pm 2\sigma$ (Ma)	$^{36}\text{Ar}/^{37}\text{Ar}$ AI
1	0.3	244.0	7.44	0.7654	4.923E-16	14.69	92.3	0.1	123.0	10.2	0.03815	
2	0.4	36.5	7.07	0.0749	9.895E-16	13.94	58.1	0.2	100.5	2.5	0.00379	
3	0.5	23.2	7.61	0.0295	1.26E-15	15.03	33.3	0.4	102.0	1.7	0.00128	
4	0.6	19.0	8.32	0.0167	1.451E-15	16.44	20.2	0.5	100.0	1.6	0.00058	
5	0.7	18.2	8.73	0.0142	8.515E-16	17.25	16.8	0.6	99.5	2.0	0.00044	
6	0.8	21.4	9.23	0.0236	5.667E-16	18.24	26.9	0.7	103.3	3.8	0.00079	
7	1.0	37.4	9.70	0.0750	4.218E-16	19.20	55.9	0.7	108.4	4.1	0.00272	
8	1.2	44.7	10.07	0.1014	2.564E-16	19.92	64.1	0.8	105.6	5.9	0.00359	
9	1.4	22.8	10.53	0.0304	1.275E-16	20.85	33.4	0.8	100.2	12.6	0.00091	
10	1.5	34.6	10.69	0.0599	1.032E-16	21.18	47.1	0.8	120.3	17.5	0.00192	
11	2.0	26.4	10.91	0.0378	1.02E-16	21.62	36.9	0.8	109.7	15.5	0.00113	
12	3.0	26.4	11.01	0.0426	1.66E-16	21.81	42.2	0.8	100.9	9.8	0.00128	
13	4.0	23.4	12.41	0.0283	4.213E-16	24.62	28.8	0.9	109.6	4.2	0.00068	
14	6.0	22.6	12.13	0.0287	4.144E-16	24.05	30.5	0.9	103.7	3.7	0.00072	
15	8.0	20.2	11.57	0.0185	2.128E-16	22.94	19.6	1.0	107.2	8.6	0.00043	
16	10.0	18.1	11.39	0.0148	1.293E-16	22.58	16.0	1.0	100.3	14.1	0.00032	
17	12.0	18.3	8.72	0.0210	4.941E-17	17.23	27.8	1.0	87.2	29.9	0.00073	
18	15.0	19.2	11.25	0.0130	6.495E-17	22.29	12.4	1.0	110.7	23.2	0.00027	

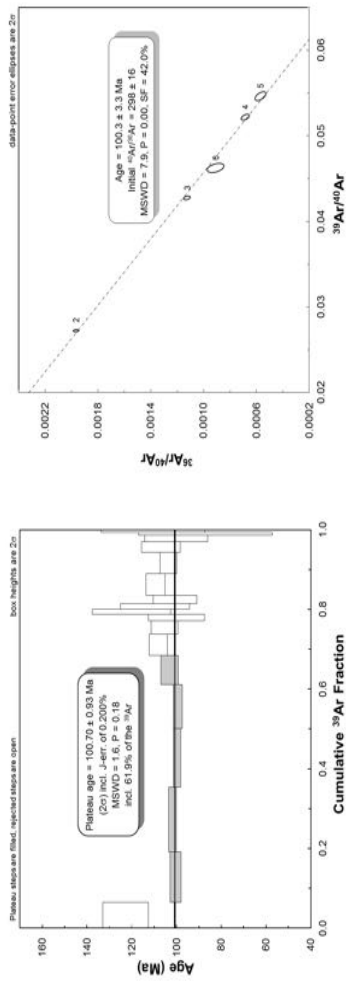


Figure 1: Laser step-heating results S0193 DR35-1

$^{40}\text{Ar}/^{39}\text{Ar}$  laser total fusion data  
 Sample: S0168 DR57-1  
 J = 0.004030 0.38

Analysis #	Mass (mg)	$^{40}\text{Ar}/^{39}\text{Ar}$	$^{37}\text{Ar}/^{39}\text{Ar}$	$^{36}\text{Ar}/^{39}\text{Ar}$	$^{39}\text{Ar}/\text{Ar}$ (moles)	$\text{Ca}/\text{K}$	% $^{40}\text{Ar}_{\text{atm}}$	Age (Ma)	$\pm 2\sigma$ (Ma)	$^{36}\text{Ar}/^{37}\text{Ar}$ AI
1	0.422	37.3	31.24	0.1011	2.40E-15	63.09	69.2	83.9	4.8	0.00113
2	0.343	35.3	39.16	0.0979	1.61E-15	79.71	67.4	84.9	6.5	0.00083
3	0.218	88.0	36.64	0.2703	1.11E-15	74.38	85.3	94.8	15.1	0.00279
4	0.368	37.7	43.28	0.1068	1.64E-15	88.44	68.8	86.9	7.6	0.00082
5	0.172	114.1	22.21	0.3549	1.52E-15	44.46	89.4	87.8	7.4	0.00626

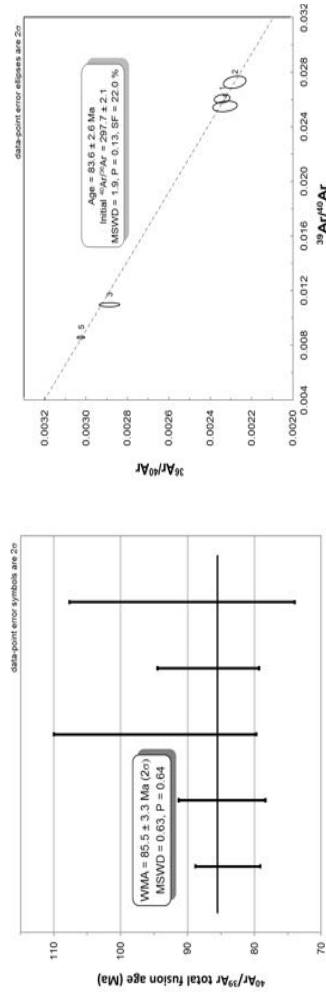


Figure 2: Laser step-heating results S0168 DR57-1

$^{36}\text{Ar}/^{37}\text{Ar}$  alteration index (AI) values shown in bold indicate fresh material, other values indicate altered material. The grey shaded analyses in the tables indicate the plateau steps.

$^{40}\text{Ar}_{\text{atm}}$  = atmospheric  $^{40}\text{Ar}$ , WMA = weighted mean age, MSWD = mean square weighted deviation, and P = probability.



### Appendix A: Analytical Methods

---

#### *Sample preparation*

The dredged rock samples were cut on-board to prepare rock chips, powders and mineral separates for further on-shore analytical methods. To ensure the best possible analytical quality, only the freshest parts of the rocks were used and altered parts and encrustation were cut-off. After drying the rock slabs at 50°C, they were crushed in a steel jaw crusher, dry sieved and cleaned with deionized water in an ultrasonic bath to remove dust. The 0.5-1 mm size fractions were carefully handpicked under a binocular microscope to obtain the freshest whole rock material for geochemical analyses. For the geochemical methods, several grams of the picked rock chips were milled to a fine powder using an agate mortar grinder and an agate planetary ball mill. This powder was used for major and trace element analysis, Hf isotopes and Sr isotopes on hot-acid leached samples. The remaining half of the rock chips were used for Sr-Nd-Pb isotopic analysis.

Feldspars for  $^{40}\text{Ar}/^{39}\text{Ar}$  dating were hand-picked under a binocular microscope from the 0.25-0.5 mm size fraction. Following this, the feldspar separates were treated with 5% hydrofluoric acid for 10 minutes, rinsed with distilled water, cleaned with distilled water for 4 minutes using an ultrasonic stick, and dried overnight in a 50°C oven.

Groundmass separates for  $^{40}\text{Ar}/^{39}\text{Ar}$  dating were magnetically separated using a Frantz magnet separator to enrich the feldspar-rich portion of the 0.25 -0.5 mm size fraction. Similar to the groundmass hot-acid leaching technique of Koppers et al. (2000)

this feldspar-enriched portion was then hot-acid treated with 3.5 N HCl acid for 1 hour, followed by 1 N HNO<sub>3</sub> acid for 1 hour, and finally with distilled water for 1 hour at 65°C in an ultrasonic bath. Between each step of the acid treatments and after the last ultrasonic bath treatment in water, the groundmass was rinsed five times with distilled water.

### ***<sup>40</sup>Ar/<sup>39</sup>Ar dating methods***

Approximately 20 mg of each unknown mineral separate was loaded into small 99.999% aluminium disks, which were stacked and bolted together, and then placed in a 99.9% Al canister to make up the irradiation package. Grains of Taylor Creek sanidine (TCR-2) age standard ( $27.87 \pm 0.04$  Ma;  $1\sigma$  error; M.A. Lanphere, pers. comm., calibrated to SB-3 biotite; Lanphere and Dalrymple, 2000) were regularly interspersed in the aluminium disks with the unknown samples to monitor the fast neutron gradient. The feldspar irradiation package (including samples DR80-1, DR87-2, DR87-4 and DR89-2; irradiation can #41) was irradiated with fast neutrons in the Cadmium-Lined In-Core Irradiation Tube (CLICIT) reactor core position for 4 hours at the Oregon State University (OSU) nuclear reactor, Corvallis, USA. The two DR89-2 groundmass samples were irradiated in 1-2 irradiation canisters, with sample DR89-2m being doubly-irradiated for 4 hours (Can #43) followed by 1 hour (Can #45), both in the OSU CLICIT position. Double irradiation of the DR89-2m sample was necessary due to a series of laser and mass spectrometer breakdowns plus reconstruction work in the GEOMAR laboratory during 2017, which resulted in >6 months elapsing since the irradiation of the Can #43 Ca-bearing samples, thus allowing the majority the <sup>37</sup>Ar<sub>Ca</sub> to decay away. Groundmass sample DR892m was only irradiated for 1 hour (Can #45) in the OSU CLICIT position.

The sample separates were loaded into variously sized aluminium laser palettes, which were loaded into an ultra-high vacuum 4.5" laser chamber with a Kovar viewport that was baked at 230°C, and the whole extraction line was baked in an oven at 195°C for 8 hours, and then pumped for 2 days to remove adsorbed atmospheric argon from the samples and chamber walls. The <sup>40</sup>Ar/<sup>39</sup>Ar analyses was carried out at the GEOMAR Argon Geochronology in Oceanography (ARGO) Laboratory using an 25 W Coherent

Sabre 25TSM argon ion laser ( $\lambda = 455\text{-}515$  nm), with a computer-controlled isel X-Y stage and a Mass Analyser Products (MAP) 216 noble gas mass spectrometer. Each incremental laser heating step was performed with a 0.25-1.0 mm diameter laser beam for 45 seconds. The laser system was fitted with a binocular microscope and light source for sample illumination and X-Y stage calibration, and a camera for video recording of the laser heating of each sample.

The gases released by laser heating were cleaned for 3 minutes using an automatically-refilling liquid nitrogen Dewar attached to a glass finger, and two SAES AP10 getter pumps (one at 400°C and one at room temperature) to remove all active gases. The remaining noble gases were equilibrated into a high sensitivity MAP 216 mass spectrometer, containing a Bauer-Signer-type source, operated at a 240 uA emission current, with a Becton Dickinson MM-1 Mesh electron multiplier, and a mass spectrometer sensitivity of  $2.70 \times 10^{-10}$  cm<sup>3</sup>/V (1.203E-14 moles/V, for the 2013-2017 mass spectrometer filament; Can #41 samples) and  $2.718 \times 10^{-10}$  cm<sup>3</sup>/V ( $1.211 \times 10^{-14}$  moles/V; for the 2017-present filament; Can #43 and #45 samples), using the normal operating gain value.

The five Ar isotopes (<sup>36</sup>Ar to <sup>40</sup>Ar) and baselines (masses 35.5 to 40.5) for the system blanks, age standards and unknown samples were measured via peak-hopping using a single electron multiplier with two variable gain settings. The fully automated laser heating, X-Y stage movement, automated valves operation, and data acquisition were computer controlled using a Turbo Pascal program.

The extraction system blank Ar isotope measurements obtained before and after every 5 unknown sample analyses are listed in Appendix C. Unknown analyses were corrected for 1) peak tails from adjoining Ar peaks (using a Turbo Pascal program written by Jan Sticklus), 2) baselines, 3) blanks, 4) mass spectrometer discrimination

using a linear law mass discrimination factor of 1.0084 per atomic mass unit (Can #41 samples), and a power law mass discrimination factor of  $1.0098 \pm 0.21\%$  ( $1\sigma$ ) per atomic mass unit (Can #43 and #45 samples) and 4) nuclear interference reaction correction factors of  $^{40}\text{Ar}/^{39}\text{Ar}_K = 7.30 \times 10^{-4}$ ,  $^{36}\text{Ar}/^{37}\text{Ar}_{Ca} = 2.65 \times 10^{-4}$ , and  $^{39}\text{Ar}/^{37}\text{Ar}_{Ca} = 7.02 \times 10^{-4}$  for the Can #41 samples (Renne et al., 2013; Renne et al., 2015). The  $^{39}\text{Ar}/^{37}\text{Ar}_{Ca}$ ,  $^{38}\text{Ar}/^{37}\text{Ar}_{Ca}$ ,  $^{36}\text{Ar}/^{37}\text{Ar}_{Ca}$ ,  $^{40}\text{Ar}/^{39}\text{Ar}_K$ ,  $^{38}\text{Ar}/^{39}\text{Ar}_K$ , and  $^{37}\text{Ar}/^{39}\text{Ar}_K$  nuclear interference reaction correction factors and errors used for the Cans #43 and #45 samples are listed in the DR89-2m and DR892m samples ArArCALC spreadsheets in Appendix C (Renne et al., 2013; Renne et al., 2015). The corrections and age determinations for the Can #41 samples were made using a Turbo Pascal program (Paul van den Bogaard, pers. comm.), and the age spectra and inverse isochron plots were made using the Excel Isoplot macro v. 4.15 (Ludwig, 2011). The Can #43 and #45 corrections, age determinations, and plateau and isochron plots were made using the Excel ArArCALC macro v. 2.5.2, developed by Anthony Koppers (Koppers, 2002). Selected plateau ages, shown in the ArArCALC spreadsheets, were determined using Isoplot v. 4.15 (Ludwig, 2011). Errors are quoted at  $1\sigma$  and  $2\sigma$  levels, and the  $^{40}\text{Ar}/^{39}\text{Ar}$  ages were calculated using the the  $^{40}\text{K}$  decay constants ( $^{40}\text{K}_{\beta^-} = 4.962 \times 10^{-10}$  years,  $^{40}\text{K}_e + ^{40}\text{K}_{e'} = 5.810 \times 10^{-11}$  years, and a total  $^{40}\text{K} \lambda = 5.543 \times 10^{-10}$  years)  $^{40}\text{K}/\text{K}$  ratio (0.01167) and  $^{40}\text{Ar}/^{36}\text{Ar}$  atmospheric ratio (295.5) of Steiger and Jäger (1977). Other decay constants used in the ArArCALC program include  $^{39}\text{Ar} = 2.941 \times 10^{-7}$  hours ( $\pm 0.558\%$   $1\sigma$ ; Stoenner et al., 1965),  $^{37}\text{Ar} = 8.262 \times 10^{-4}$  hours ( $\pm 0.229\%$   $1\sigma$ ; Renne and Norman, 2001), and  $^{36}\text{Cl} = 2.257 \times 10^{-6}$  years ( $\pm 0.65\%$   $1\sigma$ ; Renne et al., 2008). The ingrowth of  $^{36}\text{Ar}$  from the decay of  $^{36}\text{Cl}$  was corrected using the  $^{36}\text{Cl}/^{38}\text{Cl}$  production ratio of  $262.8 \pm 1.7$  ( $1\sigma$ ; Renne et al., 2008). The J values and errors are noted in the sample  $^{40}\text{Ar}/^{39}\text{Ar}$  data tables (Appendix C).

The  $^{40}\text{Ar}/^{39}\text{Ar}$  ages reported here were determined by the following criteria (e.g., Lanphere and Dalrymple, 1978): 1) a valid  $^{40}\text{Ar}/^{39}\text{Ar}$  plateau age contains least three consecutive laser heating steps, comprising >50% of the  $^{39}\text{Ar}$  released, with ages overlapping within  $2\sigma$  errors, 2) the plateau and inverse isochron ages should be concordant at the 95% confidence level. The statistical validity of plateau, weighted mean and inverse isochron  $^{40}\text{Ar}/^{39}\text{Ar}$  ages was tested by calculating Mean Squared Weighted Deviation values (MSWD) and probability values ( $P > 0.05$  at  $2\sigma/95\%$  confidence levels). Alteration index (AI) values were determined and used as a guide to gauge the alteration/freshness of a sample, and were calculated for basalts, plagioclases and K-feldspars using the criteria of Baksi (2007), Hames et al. (2000) and van den Bogaard (2013), using cut-off values of  $^{36}\text{Ar}/^{39}\text{Ar}$  AI < 0.0006 for basalt,  $^{36}\text{Ar}/^{37}\text{Ar}$  AI < 0.00006 (< 0.00004 for very fresh material) for plagioclase, and  $^{36}\text{Ar}/^{39}\text{Ar}$  < 0.00006 for K-feldspar.. In addition, the % atmospheric  $^{40}\text{Ar}$  ( $^{40}\text{Ar}_{\text{atm}}$ ) and Ca/K ratios (obtained from measured  $^{37}\text{Ar}_{\text{Ca}}/^{39}\text{Ar}_{\text{K}}$  ratios) were used to check for the presence of alteration or mixed phases in the samples, respectively.

The notations used in the ArArCALC spreadsheets (Appendix C) are as follows: The blue dots in the Relative Abundances tables denote the analyses used to calculate the plateau/weighted mean ages listed in “Age plateau” the underlying results section, and for the normal and inverse isochron plots. Red numbers in the tables denote negative values, and the MDF abbreviation in the Sample Parameters tables = Mass Discrimination Factor (per atomic mass unit). The green and blue squares in the normal and inverse isochron plots show the selected analyses (i.e., the blue dot analyses in the Relative Abundances table) and unselected analyses, respectively. The pink and black lines isochron lines show the fit through the selected data, and the fit through an

atmospheric  $^{40}\text{Ar}/^{36}\text{Ar}$  ratio of 295.5, respectively. The error ellipses in the inverse isochron plots are  $2\sigma$  errors.

## Ar-Ar step-heating results and sample description

Table 1:  $^{40}\text{Ar}/^{39}\text{Ar}$  step-heating results from the Walvis Ridge seamounts.

Plateau ages									
Sample	Mineral	Rock type	$K_2O^*$	Age (Ma)	$\pm 2\sigma$	Cum. % $^{39}\text{Ar}$	MSWD	P	Steps
DR80-1	Plag.	Alkali Basalt	0.02	66.3	5.9	97.4	1.2	0.28	2-18
DR87-4	K-feld.	Trachyte	4.32	76.8	0.2	50.9	2.7	0.00	11-20
DR89-2	Plag.	Alkali Basalt	0.13	63.6	1.3	59.1	1.1	0.34	7-11
Inverse isochron ages									
Sample	Mineral	Rock type	$K_2O^*$	Age (Ma)	$\pm 95\%$ conf.	Initial $^{40}\text{Ar}/^{36}\text{Ar}$	MSWD	P	Steps
DR80-1	Plag.	Alkali Basalt	0.02	64.7	7.5	303 $\pm$ 11	0.9	0.55	2-18
DR87-2	K-feld.	n.a.	5.87	76.3	0.1	300 $\pm$ 25	12	0.00	4-19
DR87-4	K-feld.	Trachyte	4.32	76.8	0.2	293 $\pm$ 11	4.3	0.00	11-20
DR89-2	Plag.	Alkali Basalt	0.13	63.9	1.8	293.8 $\pm$ 6.0	1.3	0.26	7-11
DR89-2m	Matrix	Alkali Basalt	0.6	71.8	3.5	315 $\pm$ 77	0.9	0.52	7-17
DR892m	Matrix	Alkali Basalt	0.7	72.5	2.4	326 $\pm$ 64	1.1	0.39	8-19
Weighted mean ages									
Sample	Mineral	Rock type	$K_2O^*$	Age (Ma)	$\pm 2\sigma$		MSWD	P	Steps
DR87-2	K-feld.	n.a.	5.87	76.47	5.5		5.5	0.000	7-18
DR89-2m	Matrix	Alkali Basalt	0.6	72.65	0.67		0.8	0.59	7-17
DR892m	Matrix	Alkali Basalt	0.7	73.58	0.50		1.1	0.38	8-19

Plag. = plagioclase; K-feld. = K-feldspar; \* Weight %  $K_2O$  calculated from total  $^{39}\text{Ar}$  concentrations and sample weight; n.a.= not analyzed; Cum = cumulative; MSWD = Mean Squares Weighted Deviation; P = probability.

K-feldspar sample DR87-2 has a slightly disturbed age spectrum that does not yield a plateau age, and has a statistically poor inverse isochron age of  $76.47 \pm 5.5$  Ma (95% conf., MSWD=12, P=0.00, initial  $^{40}\text{Ar}/^{36}\text{Ar}$ =300  $\pm$  25), due to the majority of analyses clustering near the radiogenic  $^{40}\text{Ar}$  x-axis (Fig. 2; Appendix C). However, the majority of the  $^{36}\text{Ar}/^{39}\text{Ar}$  AI values are low (i.e., steps 5-17), and together with the low %  $^{40}\text{Ar}_{\text{atm}}$  values this indicates the presence of fresh or very fresh K-feldspar (Appendix C).

$^{40}\text{Ar}/^{39}\text{Ar}$  step-heating analysis on K-feldspar sample DR87-4, from dredge location S0233DR-87, yields a plateau age of  $76.78 \pm 0.21$  Ma (50.9%  $^{39}\text{Ar}$  released, MSWD=2.7, P=0.003; Appendix C). The plateau age was mostly sourced from steps



degassed from very fresh material (steps 11-17 with  $^{36}\text{Ar}/^{39}\text{Ar}$  AI values of  $<0.00004$ ; Hames et al., 2000), with only steps 18-20 showing evidence of alteration. The inverse isochron age of the DR87-4 K-feldspar plateau steps is  $76.77 \pm 0.20$  Ma (95% conf., MSWD=4.3,  $P=0.00$ , initial  $^{40}\text{Ar}/^{36}\text{Ar}=293 \pm 11$ ; Appendix C). The MSWD and probability values of these DR87-4 plateau and isochron ages are not statistically robust, however, the additional K-feldspar sample (DR87-2) from the same dredge site yields a nearly identical weighted mean  $^{40}\text{Ar}/^{39}\text{Ar}$  age of  $76.47 \pm 0.17$  Ma (95% conf., MSWD=5.5,  $P=0.00$ ), which agrees within  $2\sigma$  errors and backs up the  $76.77 \pm 0.20$  Ma DR87-4  $^{40}\text{Ar}/^{39}\text{Ar}$  plateau age.

Plagioclase sample S0233 DR89-2 yields a disturbed age spectrum, but has a statistically valid plateau age of  $63.6 \pm 1.3$  Ma (59.1%  $^{39}\text{Ar}$  released, MSWD = 1.12,  $P = 0.34$ ; Fig. 3). The low wt. %  $\text{K}_2\text{O}$  value (0.13 wt. %) and limited sample material resulted in low  $^{39}\text{Ar}$  concentrations, yielding larger than normal errors in the  $^{40}\text{Ar}/^{39}\text{Ar}$  ages (Appendix C). The  $^{36}\text{Ar}/^{37}\text{Ar}$  AI values are elevated in the low- and medium-temperature steps indicating the presence of alteration in the sample, with only the last 3 steps showing Ar degassing from fresh plagioclase (i.e., below the AI cut-off value of  $<0.00006$ ) with the last step showing the lowest AI of 0.000032 and the lowest %  $^{40}\text{Ar}_{\text{atm}}$  value of 8.76%). The last heating step (step #12) yielded an age of  $74.7 \pm 2.6$  Ma, which may suggest an older age for this sample, compared to the younger plateau age of  $63.6 \pm 1.3$  Ma obtained from this plagioclase separate (Fig. 3; Appendix C).

Two basaltic groundmass separates from the same DR89-2 sample as the plagioclase separate mentioned above, yielded disturbed L-shaped age spectra, but have relatively concordant and statistically valid high-temperature weighted mean ages of  $72.65 \pm 0.67$  Ma (S0233 DR89-2m; steps 7-17) and  $73.58 \pm 0.50$  Ma (S0233 DR892m; steps 8-18; Fig. 3; Appendix C), with both overlap within their  $2\sigma$  errors. These two

weighted mean ages agree with the statistically valid inverse isochron ages of  $71.8 \pm 3.5$  Ma (SO233 DR89-2m) and  $72.5 \pm 2.4$  Ma (SO233 DR892m; steps 8-18; Fig. 3). The initial  $^{40}\text{Ar}/^{36}\text{Ar}$  ratios from the DR89-2m and DR892m groundmass inverse isochrons yield atmospheric  $^{40}\text{Ar}/^{36}\text{Ar}$  ratio values (i.e.,  $315 \pm 77$  and  $326 \pm 64$ , respectively), although they have very large errors due to clustering of the analyses, with low spreading factor (SF) values of 7.1 and 13.3%, respectively, whereas Jourdan et al. (2009) recommend SF values of >40% (Fig. 3). The majority of the DR89-2 groundmass analyses have elevated  $^{36}\text{Ar}/^{39}\text{Ar}$  AI values indicating the presence of alteration, although the % of radiogenic  $^{40}\text{Ar}$  ( $^{40}\text{Ar}^*$ ) in the WMA steps is high at 80-87 and 85-91%, respectively. However, as the freshest DR89-2 plagioclase step age of  $74.7 \pm 2.6$  Ma is within  $2\sigma$  agreement with the weighted mean and inverse isochron ages from the two DR89-2 groundmass separates (Fig. 3), the two high-temperature groundmass weighted mean ages are taken to be the most meaningful ages for this sample (Appendix C).

## ***Geochemistry***

Major element compositions were carried out on fused pellets at the Institute of Mineralogy and Petrography, University of Hamburg, by X-ray Fluorescence analysis (XRF) using a Magix Pro PW 2540. Reference materials JGB-1, JB-3, JB-2, JA-3, JG3 and JG-2 were analysed along with the samples, and the accuracy of the standards is within 3% of the reference values of Govindaraju (1994) for most elements. At element concentrations significantly < 1 wt. %, larger deviations from the suggested values are observed (see Appendix D).

Trace element concentrations were measured by inductively coupled plasma mass spectrometry (ICP-MS) at the Institute of Geosciences, Christian-Albrechts-University of Kiel, using an AGILENT 7500cs Inductively Coupled Plasma – Mass Spectrometer (ICP-MS). 100 mg of powdered sample was dissolved by pressure digestion and analyzed following the methods of Garbe-Schönberg (1993). International rock standards BHVO-2 and BIR-1 were analysed together with the samples and most elements agree within 5% of the GeoReM reference values (<http://georem.mpch-mainz.gwdg.de/>). Reproducibility of separately replicated samples are typically better than 2% for standards and samples (Appendix E.).

Radiogenic isotope analyses were carried out at GEOMAR Helmholtz Centre for Ocean Research Kiel using a Thermo Scientific TRITON+ thermal ionization mass spectrometer (TIMS) for Sr-Nd-Pb analyses and a Nu-Plasma Multi-Collector-ICPMS (MC-ICPMS) for Hf analyses, with both instruments operating in static multi-collection mode. Sr, Nd and Pb chemistry was conducted on 100-250 mg whole-rock chips. Prior to dissolution in a 5:1 mixture of concentrated HF and HNO<sub>3</sub> acids they were leached in 2N HCl at 70°C for one hour and then triple rinsed in 18.2 MΩ deionized water. Additional Sr isotope analyses were carried out on 100 mg of leached powders (6N HCl at 150 °C

for 3 days) on each sample to aid in better removal of possible seawater alteration effects, compared to the initial mild leaching of the rock chips. As a result, 20 out of 23 prolonged-leached samples produced lower  $^{87}\text{Sr}/^{86}\text{Sr}_{\text{Measured}}$  ratios (between 0.00006 and 0.00457 lower ratios) for the leached powders, compared to the mildly-leached rock chips, while the three remaining samples gave higher  $^{87}\text{Sr}/^{86}\text{Sr}_{\text{Measured}}$  ratio values (between 0.00005 and 0.00184 higher ratios). These observations suggest that the effects of seawater alteration on  $^{87}\text{Sr}/^{86}\text{Sr}$  ratios are relatively minor for the majority of samples (4 samples have significantly higher  $^{87}\text{Sr}/^{86}\text{Sr}_{\text{Measured}}$  in the rock chips with 0.0015-0.0045 higher ratios compared to the prolonged leached powders) and that prolonged acid leaching of the sample powders in hot 6N HCl does not always remove the seawater-derived Sr imprint. Therefore, the lowest  $^{87}\text{Sr}/^{86}\text{Sr}$  ratios obtained from pairs of powder and rock chips are presumed to be closest to the primary magmatic values and thus are used for petrogenetic interpretations.

Ion chromatography methods followed established standard procedures of Hoernle et al. (2008). Nd and Sr ratios were normalized within the analytical run to values of  $^{146}\text{Nd}/^{144}\text{Nd} = 0.7219$  and  $^{86}\text{Sr}/^{88}\text{Sr} = 0.1194$ , respectively. NBS 987 and LaJolla reference materials were measured 4-6 times in each sample turret. The numerical average obtained for the standards is subtracted from the preferred standard values and the off-set value is applied to the sample data. This measure compensates for long-term machine drift and thereby ensures maximum comparability and quality of data generated at different times. Sample data are reported relative to  $^{87}\text{Sr}/^{86}\text{Sr} = 0.710250 \pm 0.000007$  ( $n = 37$ ; 2 standard deviation (SD) external reproducibility) for NBS987 and  $^{143}\text{Nd}/^{144}\text{Nd} = 0.511850 \pm 0.000005$  ( $n = 23$ ; 2SD external reproducibility) for La Jolla. The Pb double spike (DS) technique of Hoernle et al. (2011) was used to mass bias correct the Pb isotope ratios. DS corrected NBS981 values are  $^{206}\text{Pb}/^{204}\text{Pb} = 16.9413 \pm$

0.0020,  $^{207}\text{Pb}/^{204}\text{Pb} = 15.4984 \pm 0.0027$ ,  $^{208}\text{Pb}/^{204}\text{Pb} = 36.7220 \pm 0.0068$ ,  $^{207}\text{Pb}/^{206}\text{Pb} = 0.91483 \pm 0.00006$ , and  $^{208}\text{Pb}/^{206}\text{Pb} = 2.16760 \pm 0.00015$  ( $n = 7$ ; 2SD). The total Pb chemistry blanks were below 20 pg and are thus considered negligible.

Hf chemistry methods used 200-300mg of unleached rock powder and chemical separation followed the procedure of Blichert-Toft et al. (1997). The in-house standard SPEX Hf ICP solution (lot#9) has been calibrated with a  $^{176}\text{Hf}/^{177}\text{Hf}$  ratio of 0.282170 to JMC457 with a  $^{176}\text{Hf}/^{177}\text{Hf}$  ratio of 0.282163 (Blichert-Toft et al., 1997). SPEX Hf was measured before and after every 4<sup>th</sup> sample analysis and resulted in a standard bracketing normalized 2SD external reproducibility of  $^{176}\text{Hf}/^{177}\text{Hf} = 0.282170 \pm 0.000006$  ( $n = 386$ ; 2SD, analyzed during 2011-2016) on a NU MC-ICP-MS at GEOMAR. Two samples were replicated for Sr-Nd-Pb and a single sample replicated for Hf. They have  $^{143}\text{Nd}/^{144}\text{Nd}_{\text{Measured}}$ ,  $^{208}\text{Pb}/^{204}\text{Pb}_{\text{Measured}}$ ,  $^{207}\text{Pb}/^{204}\text{Pb}_{\text{Measured}}$  and  $^{176}\text{Hf}/^{177}\text{Hf}_{\text{Measured}}$  within 2SD errors of the standards. Expectedly  $^{87}\text{Sr}/^{86}\text{Sr}$  displays slightly higher deviations from standard reproducibility in both replicates and the applied leaching techniques. Finally  $^{206}\text{Pb}/^{204}\text{Pb}$  was reproduced slightly outside 2SD of NBS981 in a single sample. Both observations reflect inhomogeneous distribution of seawater alteration, namely exchange with seawater derived Sr and uptake of seawater derived U but they do not affect the overall scientific interpretations. (see Appendix B for details).

## References

- Baksi, A. K., 2007, A quantitative tool for detecting alteration in undisturbed rocks and minerals—I: Water, chemical weathering, and atmospheric argon: Geological Society of America Special Papers, v. 430, p. 285-303.
- Blichert-Toft, J., Chauvel, C., and Albarède, F., 1997, Separation of Hf and Lu for high-precision isotope analysis of rock samples by magnetic sector-multiple collector ICP-MS: Contributions to Mineralogy and Petrology, v. 127, no. 3, p. 248-260.
- Garbe-Schönberg, C.-D., 1993, Simultaneous Determination of 37 Trace-Elements in 28 International Rock Standards by ICP-MS: Geostandards Newsletter, v. 17, no. 1, p. 81-97.
- Govindaraju, K., 1994, Compilation of Working Values and Sample Description for 383 Geostandards: Geostandards Newsletter, v. 18, no. 2, p. 331-331.
- Hames, W. E., Renne, P. R., and Ruppel, C., 2000, New evidence for geologically instantaneous emplacement of earliest Jurassic Central Atlantic magmatic province basalts on the North American margin: Geology, v. 28, no. 9, p. 859-862.
- Hoernle, K., Abt, D. L., Fischer, K. M., Nichols, H., Hauff, F., Abers, G. A., van den Bogaard, P., Heydolph, K., Alvarado, G., Protti, M., and Strauch, W., 2008, Arc-parallel flow in the mantle wedge beneath Costa Rica and Nicaragua: Nature, v. 451, no. 7182, p. 1094-1097.
- Jourdan, F., Renne, P. R., and Reimold, W. U., 2009, An appraisal of the ages of terrestrial impact structures: Earth and Planetary Science Letters, v. 286, no. 1, p. 1-13.
- Koppers, A. A. P., 2002, ArArCALC—software for  $^{40}\text{Ar}/^{39}\text{Ar}$  age calculations: Computers & Geosciences, v. 28, no. 5, p. 605-619.
- Koppers, A. A. P., Staudigel, H., and Wijbrans, J. R., 2000, Dating crystalline groundmass separates of altered Cretaceous seamount basalts by the  $^{40}\text{Ar}/^{39}\text{Ar}$  incremental heating technique: Chemical Geology, v. 166, no. 1, p. 139-158.
- Lanphere, M. A., and Dalrymple, G. B., 1978, The use of  $^{40}\text{Ar}/^{39}\text{Ar}$  data in evaluation of disturbed K-Ar systems: Geological Survey Open-File Report 78-701, p. 141-148.
- Lanphere, M. A., and Dalrymple, G. B., 2000, First-principles calibration of  $^{38}\text{Ar}$  tracers: Implications for the ages of  $^{40}\text{Ar}/^{38}\text{Ar}$  fluence monitors: US Geological Survey Professional Paper, no. 1621, p. 1-10.
- Ludwig, K. R., 2011, Users manual for Isoplot 4.15: A geochronological toolkit for Microsoft Excel: Special Publication 4, Berkeley, p. 77.
- Renne, P. R., Deino, A. L., Hilgen, F. J., Kuiper, K. F., Mark, D. F., Mitchell, W. S., Morgan, L. E., Mundil, R., and Smit, J., 2013, Time Scales of Critical Events Around the Cretaceous-Paleogene Boundary: Science, v. 339, no. 6120, p. 684-687.
- Renne, P. R., and Norman, E. B., 2001, Determination of the half-life of  $^{37}\text{Ar}$  by mass spectrometry: Physical Review C, v. 63, no. 4, p. 047302.
- Renne, P. R., Sharp, Z. D., and Heizler, M. T., 2008, Cl-derived argon isotope production in the CLICIT facility of OSTR reactor and the effects of the Cl-correction in  $^{40}\text{Ar}/^{39}\text{Ar}$  geochronology: Chemical Geology, v. 255, no. 3, p. 463-466.
- Renne, P. R., Sprain, C. J., Richards, M. A., Self, S., Vanderkluysen, L. ø., and Pande, K., 2015, State shift in Deccan volcanism at the Cretaceous-Paleogene boundary, possibly induced by impact: Science, v. 350, no. 6256, p. 76-78.
- Steiger, R. H., and Jäger, E., 1977, Subcommittee on geochronology: Convention on the use of decay constants in geo- and cosmochronology: Earth and Planetary Science Letters, v. 36, no. 3, p. 359-362.
- van den Bogaard, P., 2013, The origin of the Canary Island Seamount Province - New ages of old seamounts: Scientific Reports, v. 3, p. 2107.

Appendix B: <sup>40</sup>Ar/<sup>39</sup>Ar age, major element, trace element and isotopic data

Sample	Ar/ <sup>39</sup> Ar Age (Ma)	Lat. (°)	Long. (°)	Location	Rock type	Method	SiO <sub>2</sub> (wt.%)	TiO <sub>2</sub> (wt.%)	Al <sub>2</sub> O <sub>3</sub> (wt.%)	Fe <sub>2</sub> O <sub>3</sub> (wt.%)	MnO (wt.%)	MgO (wt.%)	CaO (wt.%)	Na <sub>2</sub> O (wt.%)	K <sub>2</sub> O (wt.%)	P <sub>2</sub> O <sub>5</sub> (wt.%)	SO <sub>3</sub> (wt.%)	L.O.I. (wt.%)	Sum (wt.%)	SiO <sub>2</sub> (wt.%)	TiO <sub>2</sub> (wt.%)	Al <sub>2</sub> O <sub>3</sub> (wt.%)	Fe <sub>2</sub> O <sub>3</sub> (wt.%)	MnO (wt.%)	MgO (wt.%)	CaO (wt.%)	Na <sub>2</sub> O (wt.%)	K <sub>2</sub> O (wt.%)	P <sub>2</sub> O <sub>5</sub> (wt.%)	SO <sub>3</sub> (wt.%)	
<b>Rita Grande Rise</b>																															
RC11-28D1	46	-30.42	-35.97		Alkali Basalt	ICP-MS <sup>a</sup>	43.2	3.66	17.45	12.97	0.2	4.02	9.62	3.01	0.87	1.1		3.7	99.6	45.05	3.61	18.20	13.52	0.21	4.19	10.03	3.14	0.91	1.15		
RC11-28D5	46	-30.42	-35.97		Alkali Basalt	ICP-MS <sup>a</sup>	43.77	0.79	14.97	6.04	0.2	5.23	7.62	3.5	5.28	0.33		11.9	99.63	49.89	0.90	17.06	6.88	0.23	5.96	8.69	3.99	6.02	0.38		
RC11-28D9	46	-30.42	-35.97		Alkali Basalt	ICP-MS <sup>a</sup>	43.08	3.01	16.65	8.46	0.08	4.54	5.06	2.99	5.87	0.93		8.9	99.57	47.51	3.32	18.36	9.33	0.09	5.01	5.58	3.30	6.47	1.03		
<b>DSDP Site 530</b>																															
DSDP Leg 75 Site 530 A	100 <sup>ns</sup>	19.19	9.39	DSDP Site 530	Alkali Basalt	XRF <sup>b</sup>	39.41	2.58	15	10.87	0.13	2.83	12.17	2.85	0.73	0.29		13.4	99.76	46.31	2.32	19.77	12.70	0.58	7.66	8.01	3.05	0.76	0.35		
DSDP Leg 75 Site 530 A	100 <sup>ns</sup>	19.19	9.39	DSDP Site 530	Basalt	XRF <sup>b</sup>	43.53	2.46	14.48	11.96	0.09	4.33	8.44	2.95	0.28	0.28		10.8	99.7	50.03	1.75	15.67	11.73	0.27	6.73	9.92	2.92	0.67	0.28		
DSDP Leg 75 Site 530 A	100 <sup>ns</sup>	19.19	9.39	DSDP Site 530	Basalt	XRF <sup>b</sup>	46.41	2.2	13.24	12.72	0.17	5.53	9.85	2.64	0.32	0.25		4.4	99.73	49.07	1.76	15.93	10.42	0.21	7.43	11.23	3.14	0.55	0.25		
<b>Isolated seamounts and ridges on the oceanic crust next to the Walvis Ridge</b>																															
SO233-DR7-1	76 <sup>a</sup>	-21.23	5.07	Elongated Gwot	Basalt	XRF <sup>b</sup>	47.75	1.24	15.46	10.9	0.12	5.1	11.28	2.65	0.82	0.13	0.01	4.22	99.68	50.03	1.30	16.20	11.42	0.13	5.34	11.82	2.78	0.86	0.14	0.01	
SO233-DR7-2	76 <sup>a</sup>	-21.23	5.07	Elongated Gwot	Basalt	XRF <sup>b</sup>	47.74	1.28	15.71	11.49	0.11	5.25	10.37	2.79	0.95	0.14	0	3.95	99.78	49.89	1.34	16.42	11.86	0.11	5.49	10.84	2.92	0.99	0.15	0.00	
SO233-DR45-1	53	-25.33	4.90	Ridge-like seamount	Tephriphonolite	XRF <sup>b</sup>	36.29	3.78	12.31	14.69	0.21	6.93	13.33	0.81	1.17	2.02	0	8.39	99.93	39.64	4.13	13.45	16.05	0.23	7.57	14.56	0.88	1.28	2.21	0.00	
SO233-DR45-2	53	-25.33	4.90	Ridge-like seamount	Alkali Basalt	XRF <sup>b</sup>	30.14	3.83	9.91	15.84	0.21	5.14	14.55	1.13	1.62	7.09	0.19	8.91	98.56	33.69	4.28	11.08	17.71	0.23	5.75	16.26	1.26	1.81	7.93	0.21	
SO233-DR46-1	54	-25.15	4.97	Ridge-like seamount	Alkali Basalt	XRF <sup>b</sup>	42.09	2.63	14.91	11.63	0.07	5.57	10.3	1.29	1.27	1.15	0.05	8.79	99.71	46.30	2.89	16.40	12.79	0.08	6.13	11.33	1.42	1.40	1.26	0.01	
SO233-DR48-1	53	-25.09	4.59	Ridge-like seamount	Alkali Basalt	XRF <sup>b</sup>	38.29	2.81	17.74	12.15	0.08	2.46	10.24	1.91	1.36	3.16	0.05	10.09	99.84	42.69	2.58	19.78	13.55	0.09	2.74	11.42	2.13	1.52	3.52	0.06	
SO233-DR48-2	53	-25.09	4.59	Ridge-like seamount	Alkali Basalt	XRF <sup>b</sup>	37.4	2.43	17.01	12.58	0.07	1.7	10.83	2.03	1.48	4.61	0.18	8.5	98.82	41.49	2.70	18.87	13.96	0.08	1.89	12.01	2.23	1.64	5.11	0.20	
SO233-DR59-1	53	-26.48	6.47	Small seamount	Alkali Basalt	XRF <sup>b</sup>	34.96	4.63	13.68	16.25	0.17	6.36	13.27	0.74	0.99	1.4	0.02	8.06	100.53	37.82	5.01	14.80	17.58	0.18	6.88	14.35	0.80	1.07	1.51	0.02	
SO233-DR80-1	66.3	-20.22	5.93	Gwot-like seamount	Alkali Basalt	XRF <sup>b</sup>	46.1	1.15	21.83	8.1	0.13	1.47	4.19	3.33	1.81	0.26	0	10.69	99.06	52.17	1.30	24.70	9.17	0.15	1.66	4.74	3.77	2.05	0.29	0.00	
SO233-DR80-3	66.3	-20.22	5.93	Gwot-like seamount	Alkali Basalt	XRF <sup>b</sup>	38.24	3.43	18.11	10.27	0.09	3.03	7.82	2.1	1.7	3.78	0.19	10.63	99.39	43.17	3.87	20.45	11.60	0.10	3.42	8.83	2.37	1.92	4.27	0.21	
<b>Ewing Seamount</b>																															
SO234-DR15-1	72.8 <sup>a</sup>	-23.04	8.18	Ewing Seamount	Alkali Basalt	XRF <sup>b</sup>	40.04	3.71	13.6	15.75	0.09	3.35	5.87	2.1	2.1	2.79	0.13	10	99.53	44.79	4.15	15.21	17.62	0.10	3.75	6.57	2.35	2.35	3.12	0.15	
<b>Superimposed edifices on the Walvis Ridge</b>																															
SO233-FVG57-1	76	-26.31	6.45	Gwot	Alkali Basalt	XRF <sup>b</sup>	34.37	3.97	13.26	14.58	0.16	7.69	12.33	0.83	0.91	1.66	0.07	10.31	100.14	38.29	4.42	14.77	16.24	0.18	8.57	13.74	0.92	1.01	1.85	0.08	
SO233-FVG57-7	76	-26.30	6.44	Gwot	Alkali Basalt	XRF <sup>b</sup>	41.1	4.6	15.33	13.33	0.19	4.99	11.13	2.4	1.25	1.85	0	3	99.17	42.74	4.78	15.94	13.86	0.20	5.19	11.57	2.50	1.30	1.92	0.00	
SO233-DR75-1	63	-22.08	5.10	Ridge-like seamount	Alkali Basalt	XRF <sup>b</sup>	42.05	3.11	18.34	13.16	0.15	2.45	7	2.35	1.95	0.77	0.01	8.66	100	46.04	3.41	20.08	14.41	0.16	2.68	7.66	2.57	2.14	0.84	0.01	
<b>SO233-DR75-1Rcp</b>																															
SO233-DR75-3	63	-22.08	5.10	Ridge-like seamount	Alkali Basalt	XRF <sup>b</sup>	43.94	3.25	18.57	13.32	0.15	2.46	5.25	2.66	2.86	1.15	0.03	6.98	99.92	46.94	3.47	19.84	14.23	0.16	2.63	5.61	2.84	3.06	1.23	0.03	
SO233-DR75-5	63	-22.08	5.10	Ridge-like seamount	Alkali Basalt	XRF <sup>b</sup>	45	3.13	18.03	12.72	0.1	2.99	4.82	2.51	3.16	0.84	0	6.45	99.75	48.23	3.35	19.21	13.63	0.11	3.20	5.17	2.69	2.39	0.90	0.00	
SO233-DR75-6	63	-22.08	5.10	Ridge-like seamount	Alkali Basalt	XRF <sup>b</sup>	42.2	3.25	19.09	13.44	0.13	1.25	6.02	4.4	2.73	1.66	0.04	7.48	99.69	45.78	3.53	20.21	14.58	0.14	3.30	6.53	2.60	2.46	1.80	0.04	
SO233-DR77-1	76.6	-2.05	1.64	Gwot	Alkali Basalt	XRF <sup>b</sup>	40.35	3.26	16.28	14.99	0.13	0.99	9.13	3.36	1.31	3.87	0.11	5.66	99.64	42.98	3.47	17.84	15.97	0.14	1.05	9.73	3.58	1.61	4.12	0.12	
SO233-DR77-2	76.33	-2.05	1.64	Gwot	Trachyte	XRF <sup>b</sup>	39.11	0.69	12.99	9.91	0.19	0.13	1.34	6.68	5.32	0.36	0	0.95	98.07	61.32	0.67	13.38	10.20	0.20	0.13	1.38	6.88	5.48	0.37	0.00	
SO233-DR92-1	73	-19.29	9.96	Gwot	Alkali Basalt	XRF <sup>b</sup>	42.19	3.88	14.79	15.63	0.15	5.91	10.78	2.31	1.02	0.53	0	3.07	100.26	43.41	3.99	15.22	16.08	0.15	6.08	11.09	2.38	1.05	0.55	0.00	
SO233-DR89-2	73	-19.29	9.96	Gwot	Potassic trachyte	XRF <sup>b</sup>	47.12	4.01	16.83	14.25	0.17	1.53	6.26	3.84	2.7	1.46	0	1.74	99.91	48.01	4.09	17.15	14.52	0.17	1.56	6.38	3.91	2.75	1.45	0.00	
SO233-DR90-6	87	-18.44	10.89	Gwot	Basalt	XRF <sup>b</sup>	46.16	2.73	13.99	11.97	0.25	7.7	11.07	2.5	0.81	0.47	0.01	2.68	100.24	47.27	2.80	14.33	12.26	0.26	7.89	11.34	2.56	0.83	0.48	0.01	

<sup>a</sup>Recalculated to 100% on a volatile free basis.

<sup>b</sup>Trace element data by ICPMS from Acme Analytical Laboratories Ltd.

<sup>c</sup>Microradiograph-Petrographisches Institut, Universität Hamburg.

<sup>d</sup>Trace element data by ICPMS from the Institute of Geosciences at the Christian-Albrechts University of Kiel

<sup>e</sup>leached powder; 6N HCl at 150°C for 72 hours and thereafter triple rinsed in 18MD H<sub>2</sub>O

<sup>f</sup>leached chips; 2N HCl at 70°C for 1 hour and thereafter triple rinsed in 18MD H<sub>2</sub>O

<sup>g</sup>major trace and Sr-Nd-Pb-Hf data published in Homrighausen et al. Submitted

<sup>h</sup>4- $\sigma$  within run errors shown for the last significant digit(s).

<sup>i</sup>Age from Rolde, J. K. et al. (2013). doi:10.1300/G36767.1

<sup>j</sup>Minimum age from Humphries S.E. and Thompson G. (1994) doi:10.2373/48dp.proc.75.1.40

<sup>k</sup>Age from O'Connor, J.M. & Jokat, W. (2015) doi:10.1300/G36767.1

<sup>l</sup>Minimum age based on the erosion platform, see discussion

<sup>m</sup>Age in bold from analogue samples

<sup>n</sup>Age in normal font calculated after age progression - 30Ma after Rolde, J. K. et al. (2013). doi:10.1016/j.tecto.2012.08.026

<sup>ns</sup> - Below detection limit

Sample	Method	Li	Sc	V	Cr	Co	Ni	Cu	Zn	Ga	Rb	Sr	Y	Zr	Nb	Cs	Ba	La	Ce	Pr	Nd	Sm	Eu	Gd	Tb	Dy	Ho	Er	Tm	Yb	Lu	Hf	Ta	Pb	Th	U	
		ppm	ppm	ppm	ppm	ppm	ppm	ppm	ppm	ppm	ppm	ppm	ppm	ppm	ppm	ppm	ppm	ppm	ppm	ppm	ppm	ppm	ppm	ppm	ppm	ppm	ppm	ppm	ppm	ppm	ppm	ppm	ppm	ppm	ppm	ppm	
Rio Grande Rise	ICP-MS <sup>c</sup>	292	25.0	303	125	33.3	46.7	41.9	145	22.7	9.0	803	32.9	317	47.7	0.155	301	37.0	77	9.7	40.3	8.6	2.79	8.13	1.17	6.55	1.20	3.08	0.428	2.69	0.390	6.67	2.73	2.26	3.19	1.438	
IC11-2RD1	ICP-MS <sup>c</sup>	206	2.0	63	1	10.4	25.1	6.7	66	18.2	133.3	596	19.7	445	71.3	0.786	1092	75.4	135	13.1	42.8	6.0	1.69	4.77	0.64	3.52	0.67	1.83	0.267	1.77	0.269	85.6	4.17	10.64	13.56	2.248	
IC11-2RD P5	ICP-MS <sup>c</sup>	BDL	BDL	BDL	BDL	30.4	53.1	5.5	71	23.3	142.7	746	28.3	376	69.3	1.900	1289	78.0	167	17.7	67.3	10.7	2.99	9.22	1.19	5.99	1.07	2.82	0.390	2.36	0.330	88.0	3.80	4.10	10.10	2.100	
DSDP Site 530	ICP-MS <sup>c</sup>	48.6	38.2	330	110	47.2	80.5	68.6	117	19.4	1.9	282	28.8	166	24.7	0.072	177	18.8	40	5.2	22.4	5.3	1.77	5.55	0.90	5.64	1.15	3.18	0.486	3.32	0.505	3.93	1.42	2.05	1.88	0.622	
DSDP Leg 75 530-A 106.1W 4.10	ICP-MS <sup>c</sup>	112	37.4	209	112	34.5	52.9	53.6	104	19.1	17.6	239	30.6	131	17.0	0.449	121	13.3	29	39	17.5	4.4	1.52	5.16	0.96	5.53	1.14	3.15	0.459	3.01	0.454	3.13	0.95	1.75	1.29	0.325	
DSDP Leg 75 530-A 106.3W 78-84	ICP-MS <sup>c</sup>	128	37.0	292	111	28.9	87.6	75.7	85	18.1	11.7	263	27.4	129	17.9	0.334	142	13.3	29	39	17.2	4.3	1.47	4.80	0.79	5.09	1.04	2.89	0.424	2.76	0.414	3.11	1.02	1.62	1.38	0.443	
Isolated seamounts and ridges on the oceanic crust next to the Waivai Ridge																																					
SO233-DR7-1	ICP-MS <sup>c</sup>	4091	5051	268	282	40.0	65.8	140.7	144	17.2	19.0	127	31.9	67	28	1.176	42	3.4	8	1.4	8.1	3.0	1.22	4.24	0.81	5.51	1.18	3.32	0.487	3.16	0.480	1.86	0.23	0.57	0.31	0.203	
SO233-DR7-2	ICP-MS <sup>c</sup>	447	54.0	283	303	37.2	75.0	160.4	155	17.6	22.4	126	29.9	67	28	1.264	44	3.5	8	1.4	8.1	3.0	1.20	4.22	0.78	5.31	1.13	3.15	0.466	3.00	0.455	1.97	0.18	0.59	0.34	0.234	
SO233-DR45-1	ICP-MS <sup>c</sup>	52.6	31.5	304	127	35.5	56.4	104.6	186	19.5	47.9	887	54.8	414	195.4	1.59	998	159.0	287	32.0	119.9	20.6	6.20	16.81	2.25	11.36	2.02	5.09	0.665	4.09	0.600	8.29	10.86	5.40	18.82	2.992	
SO233-DR45-2	ICP-MS <sup>c</sup>	65.1	34.9	306	138	33.3	92.5	142.5	296	14.4	61.3	1215	278.1	392	200.6	1.547	942	346.6	306	50.7	197.7	32.8	9.29	35.01	4.69	28.27	6.17	17.22	2.373	14.92	3.369	84.4	10.84	34.31	21.23	4.973	
SO233-DR46-1	ICP-MS <sup>c</sup>	49.1	47.3	258	97.7	20.2	113.7	172.4	144	14.7	33.4	842	43.9	203	77.0	1.206	594	62.3	97	12.6	50.7	9.6	3.04	8.85	1.25	6.85	1.32	3.48	0.469	2.90	0.442	4.78	4.70	5.66	6.67	2.172	
SO233-DR48-1	ICP-MS <sup>c</sup>	788	26.7	262	177	10.8	70.6	69.2	152	17.0	28.5	836	40.0	245	95.9	0.981	627	73.8	107	13.8	52.2	9.4	3.09	8.48	1.20	6.71	1.31	3.50	0.496	3.17	0.504	5.10	5.47	3.10	8.02	2.638	
SO233-DR48-2	ICP-MS <sup>c</sup>	508	27.3	318	77	8.8	52.6	74.4	148	15.0	27.6	1985	55.3	232	102.5	0.850	766	97.6	125	16.7	63.6	11.0	3.57	10.14	1.43	8.17	1.64	4.56	0.664	4.40	0.712	5.36	5.83	3.68	9.35	3.099	
SO233-DR48-4	ICP-MS <sup>c</sup>	680	27.5	281	188	11.5	69.3	72.3	149	15.3	29.2	857	41.2	217	90.3	0.866	620	81.4	110	14.3	54.4	9.6	3.09	8.69	1.22	6.84	1.33	3.60	0.513	3.34	0.529	4.90	5.19	3.29	8.18	2.578	
SO233-DR59-1	ICP-MS <sup>c</sup>	45.0	40.4	371	566	42.2	150.6	86.0	123	19.9	22.9	394	34.8	243	64.2	0.555	482	53.4	115	14.5	61.9	12.2	3.88	10.52	1.44	7.50	1.33	3.27	0.424	2.58	0.380	6.18	4.31	2.03	4.99	1.495	
SO233-DR80-1	ICP-MS <sup>c</sup>	93.9	1.6	20	4	5.5	24.1	34.6	169	23.3	388	1320	17.4	680	209.6	0.675	1978	60.9	141	12.7	44.6	7.2	3.38	5.45	0.79	4.09	0.74	1.95	0.281	1.89	0.293	12.87	12.89	9.05	21.22	0.789	
SO233-DR80-3	ICP-MS <sup>c</sup>	60.3	24.1	183	57	16.1	55.4	74.0	125	17.2	31.3	630	44.7	352	120.5	0.785	841	80.7	143	17.4	68.0	12.5	3.94	10.96	1.53	8.22	1.54	3.96	0.536	3.39	0.522	8.04	6.95	3.57	10.18	2.198	
Ewing Seamount	ICP-MS <sup>c</sup>	33.4	41.9	229	434	27.3	75.8	152.6	178	20.2	64.1	6234	35.5	302	72.2	2.734	373	54.0	106	13.2	54.3	10.4	3.26	9.27	1.30	7.01	1.28	3.27	0.454	2.86	0.430	7.03	4.23	3.11	5.58	2.822	
SO234-DR15-1 Rep	ICP-MS <sup>c</sup>	85.2	37.0	317	601	38.7	182.7	76.7	182	18.7	19.3	789	42.1	382	131.5	0.434	446	96.3	176	22.5	88.8	16.0	4.89	13.09	1.74	8.75	1.53	3.76	0.482	2.94	0.428	8.25	6.75	5.54	12.22	2.270	
SO233-FVG57-1	ICP-MS <sup>c</sup>	40.3	17.4	291	15	27.5	9.9	13.7	121	22.4	25.0	2012	42.9	300	85.3	1.203	2103	98.6	206	25.0	105.2	18.9	6.36	15.47	1.97	9.77	1.67	3.96	0.490	2.89	0.410	6.54	5.11	2.98	5.77	1.337	
SO233-DR75-1	ICP-MS <sup>c</sup>	42.5	16.7	240	32	22.8	24.1	27.2	99	21.0	49.6	727	35.6	275	61.4	2.992	740	384	80	10.1	43.1	9.2	3.09	8.56	1.26	7.03	1.32	3.42	0.470	2.98	0.416	6.15	3.58	3.87	3.86	0.987	
SO233-DR75-3	ICP-MS <sup>c</sup>	32.7	18.9	259	29	20.3	29.1	37.1	106	21.9	60.0	691	38.5	298	66.1	1.430	850	43.1	89	11.2	47.6	10.2	3.32	9.46	1.37	7.73	1.45	3.74	0.521	3.31	0.494	6.83	3.74	4.16	4.37	1.333	
SO233-DR75-5	ICP-MS <sup>c</sup>	55.1	18.1	214	29	22.0	31.3	34.9	146	20.4	82.0	692	35.3	200	61.1	0.565	781	39.6	83	10.4	44.4	9.5	3.11	8.20	1.28	7.19	1.34	3.45	0.490	3.02	0.445	6.29	3.47	3.57	3.93	0.960	
SO233-DR75-6	ICP-MS <sup>c</sup>	35.4	25.1	240	156	16.0	57.3	37.0	148	21.8	51.9	726	44.9	345	31.0	0.862	766	37.1	103	13.2	54.4	11.1	3.60	10.23	1.49	8.27	1.56	4.05	0.554	3.53	0.527	7.50	3.80	4.15	6.30	2.127	
SO233-DR87-1	ICP-MS <sup>c</sup>	22.2	19.2	225	3	7.7	20.9	24.2	390	27.7	17.9	959	62.4	361	71.6	0.445	453	70.4	154	20.6	90.7	18.5	6.70	16.60	2.29	12.01	2.20	5.82	0.720	4.43	0.668	7.90	4.52	2.65	4.77	2.279	
SO233-DR87-2	ICP-MS <sup>c</sup>	19.9	3.2	86	6	0.2	7.3	20.1	163	52.9	123.0	41	85.8	16.1	245.0	0.267	211	160.7	385	42.3	163.4	31.4	7.56	25.29	3.93	21.73	3.90	10.21	1.523	10.34	1.565	36.82	18.36	7.66	22.84	0.644	
SO233-DR89-2	ICP-MS <sup>c</sup>	128	35.0	395	255	52.3	123.3	136.5	137	24.4	17.1	640	22.5	237	42.1	0.93	229	32.4	70	9.0	39.1	5.2	2.69	7.34	1.01	5.28	0.91	2.15	0.274	1.62	0.230	5.68	2.57	1.69	2.96	10.17	
SO233-DR89-7	ICP-MS <sup>c</sup>	36	13.2	202	5	22.1	6.5	5.2	77	30.6	31.2	819	50.1	451	93.4	0.25	492	74.3	165	21.4	91.4	18.4	5.69	15.93	2.19	11.25	1.94	4.64	0.58	3.38	0.47	10.18	5.82	2.54	6.15	1.916	
SO233-DR90-6	ICP-MS <sup>c</sup>	28.2	24.8	249	379	47.4	184.8	85.8	112	21.9	14.7	552	25.1	226	46.4	0.52	260	33.0	69	8.5	35.8	7.6	2.48	6.98	1.01	5.41	0.96	2.36	0.331	1.84	0.26	5.06	2.90	1.88	3.39	1.016	





### Appendix C: $^{40}\text{Ar}/^{39}\text{Ar}$ analytical data

Sample SO233 DR80-1  
Material Plagioclase

J value 0,001042  
 $2\sigma$  % error 0,123  
Mass (mg) 1,964

Step #	$^{40}\text{Ar}/^{39}\text{Ar}$	$^{37}\text{Ar}/^{39}\text{Ar}$	$^{36}\text{Ar}/^{39}\text{Ar}$	$^{39}\text{Ar}/\text{K}$ (moles)	Ca/K	% $^{40}\text{Ar}_{\text{rim}}$	Cumulative fraction of $^{39}\text{Ar}$	Age (Ma)	$\pm 2\sigma$ (Ma)	$^{36}\text{Ar}/^{37}\text{Ar}$ AI
1	95,89	0,19	0,42	3,12E-18	0,37	129,16	0,026	-53,35	113,44	434,2
2	53,61	-0,05	0,08	7,95E-18	-0,10	42,39	0,093	57,14	32,12	-
3	61,03	-0,88	0,06	1,94E-17	-1,72	30,22	0,255	78,28	11,31	-
4	43,73	0,11	0,04	4,45E-17	0,22	25,12	0,628	60,54	7,94	65,1
5	88,08	-0,23	0,16	1,43E-17	-0,45	53,06	0,748	76,09	17,44	-
6	306,48	2,93	0,98	4,29E-18	5,75	94,27	0,783	32,78	91,70	65,6
7	2534,99	6,63	8,28	2,68E-18	13,05	96,44	0,806	162,65	169,53	245,1
8	598,23	1,21	1,73	2,06E-18	2,37	85,54	0,823	155,80	171,47	281,3
9	205,90	5,51	0,53	3,52E-18	10,84	76,49	0,853	89,11	132,93	19,0
10	233,39	13,02	0,87	1,58E-18	25,76	109,44	0,866	-42,29	291,61	13,0
11	239,41	1,70	0,86	1,49E-18	3,34	106,22	0,878	-28,26	217,43	99,2
12	610,16	-11,01	1,13	3,77E-19	-21,41	54,67	0,881	453,78	1056,43	-
13	63,64	0,25	0,18	7,65E-18	0,48	81,43	0,945	22,08	38,94	139,5
14	477,33	-6,49	1,39	1,62E-18	-12,67	86,32	0,959	118,25	179,09	-
15	157,49	6,88	0,42	6,99E-19	13,56	79,15	0,965	60,99	409,60	12,0
16	196,95	-12,84	0,60	5,00E-19	-24,95	89,89	0,969	36,72	893,70	-
17	413,09	26,55	2,00	2,31E-19	53,02	142,70	0,971	-374,14	2419,29	14,8
18	75,87	1,70	0,13	3,47E-18	3,33	50,32	1,000	69,58	110,05	14,9

Plateau age	Rock type	Wt. % $\text{K}_2\text{O}^*$	Age (Ma)	$\pm 2\sigma$	% plateau $^{39}\text{Ar}$	MSWD	Prob.	Steps
DR 80-1	Alkali Basalt	0,02	66,3	5,9	97,4	1,17	0,28	2-18
Inverse isochron age	Rock type	Wt. % $\text{K}_2\text{O}^*$	Age (Ma)	$\pm 95\%$ conf.	Initial $^{40}\text{Ar}/^{39}\text{Ar}$	MSWD	Prob.	Steps
DR 80-1	Alkali Basalt	0,02	64,7	7,5	303 $\pm$ 11	0,91	0,55	2-18

Sample Material SO233 DR87-2 K-feldspar

J value 0,001042  
 2σ % error 0,178  
 Mass (mg) 6,207

Step #	$^{40}\text{Ar}/^{39}\text{Ar}$	$^{37}\text{Ar}/^{39}\text{Ar}$	$^{36}\text{Ar}/^{39}\text{Ar}$	$^{39}\text{Ar}/\text{K}$ (moles)	Ca/K	% $^{40}\text{Ar}_{\text{atm}}$	Cumulative fraction of $^{39}\text{Ar}$	Age (Ma)	$\pm 2\sigma$ (Ma)	$^{36}\text{Ar}/^{39}\text{Ar}$	Ar Ar
1	147,36	0,36	0,41	1,46E-16	0,70	81,98	0,001	49,25	3,43	0,020737	
2	48,00	0,09	0,03	4,92E-16	0,18	19,88	0,18	70,90	0,59	0,001638	
3	41,93	0,05	0,00	8,02E-16	0,11	3,47	0,014	74,53	0,51	0,000250	
4	41,54	0,03	0,00	1,29E-15	0,07	0,74	0,026	75,90	0,26	0,000053	
5	41,55	0,03	0,00	1,84E-15	0,05	0,71	0,043	75,94	0,27	0,000051	
6	41,40	0,03	0,00	2,83E-15	0,05	0,57	0,070	75,78	0,22	0,000041	
7	41,72	0,01	0,00	6,97E-15	0,02	0,40	0,137	76,48	0,22	0,000029	
8	41,49	0,01	0,00	1,52E-14	0,01	0,21	0,281	76,21	0,18	0,000015	
9	41,36	0,01	0,00	3,18E-14	0,01	0,09	0,583	76,07	0,17	0,000007	
10	41,51	0,01	0,00	1,98E-14	0,01	0,05	0,772	76,36	0,20	0,000004	
11	41,64	0,00	0,00	6,71E-15	0,01	0,05	0,835	76,59	0,23	0,000004	
12	41,81	0,01	0,00	3,26E-15	0,01	0,19	0,866	76,79	0,28	0,000014	
13	41,63	0,01	0,00	3,15E-15	0,02	0,11	0,896	76,54	0,22	0,000008	
14	41,79	0,01	0,00	2,43E-15	0,02	0,14	0,919	76,80	0,23	0,000010	
15	41,61	0,01	0,00	2,72E-15	0,02	0,09	0,945	76,51	0,28	0,000007	
16	41,66	0,01	0,00	2,33E-15	0,02	0,02	0,967	76,65	0,21	0,000002	
17	41,86	0,01	0,00	1,38E-15	0,02	0,12	0,981	76,95	0,31	0,000008	
18	41,75	0,01	0,00	1,57E-15	0,02	0,39	0,995	76,54	0,31	0,000028	
19	67,66	0,01	0,09	4,73E-16	0,01	38,09	1,000	77,08	1,03	0,004424	

Inverse isochron age	Rock type	Wt. % K <sub>2</sub> O*	Age (Ma)	$\pm 95\%$ conf.	Initial $^{40}\text{Ar}/^{39}\text{Ar}$	MSWD	Prob.	Steps
Sample DR 87-2	Trachyte	5,87	76,33	0,14	300 ± 25	12	0,000	4-19
Weighted Mean								
Sample DR 87-2	Trachyte	5,87	76,47	5,5		5,5	0,000	7-18

Sample Material SO233 DR87-4 K-feldspar

Step #	$^{40}\text{Ar}/^{39}\text{Ar}$	$2\sigma$ % error	Mass (mg)	$^{37}\text{Ar}/^{39}\text{Ar}$	$^{36}\text{Ar}/^{39}\text{Ar}$	$^{39}\text{Ar}_K$ (moles)	Ca/K	% $^{40}\text{Ar}_{\text{atm}}$	Cumulative fraction of $^{39}\text{Ar}$	Age (Ma)	$\pm 2\sigma$ (Ma)	$^{36}\text{Ar}/^{39}\text{Ar}$	Ar Ar
	J value	0,001042	7,1										
1	58,46	0,13	0,14	2,80E-17	0,25	0,00	72,06	0,00	30,45	10,99	0,00532		
2	69,23	0,10	0,14	9,38E-17	0,20	0,01	61,45	0,00	49,49	1,90	0,00538		
3	40,03	0,02	0,01	2,37E-16	0,05	0,00	6,87	0,04	68,77	1,10	0,00035		
4	40,39	0,02	0,00	5,02E-16	0,03	0,00	1,39	0,01	73,36	0,68	0,00007		
5	41,47	0,01	0,00	8,33E-16	0,02	0,00	0,75	0,20	75,77	0,48	0,00004		
6	41,33	0,01	0,00	1,60E-15	0,02	0,00	0,42	0,04	75,76	0,24	0,00002		
7	41,50	0,01	0,00	3,13E-15	0,01	0,00	0,81	0,77	75,78	0,27	0,00004		
8	42,01	0,01	0,00	4,26E-15	0,01	0,00	1,00	0,129	76,55	0,25	0,00005		
9	42,34	0,01	0,00	4,06E-15	0,01	0,00	0,36	0,178	77,63	0,27	0,00002		
10	41,47	0,00	0,00	2,60E-14	0,01	0,00	0,21	0,491	76,17	0,16	0,00001		
11	41,68	0,00	0,00	1,70E-14	0,01	0,00	0,29	0,696	76,50	0,19	0,00002		
12	41,75	0,00	0,00	5,37E-15	0,01	0,00	0,11	0,761	76,75	0,19	0,00001		
13	41,77	0,00	0,00	6,21E-15	0,01	0,00	0,15	0,835	76,76	0,21	0,00001		
14	42,02	0,01	0,00	4,51E-15	0,01	0,00	0,52	0,890	76,93	0,20	0,00003		
15	41,97	0,00	0,00	3,59E-15	0,01	0,00	0,13	0,933	77,13	0,24	0,00001		
16	41,78	0,01	0,00	2,42E-15	0,02	0,00	0,24	0,962	76,71	0,24	0,00001		
17	41,82	0,01	0,00	1,75E-15	0,02	0,00	0,28	0,983	76,75	0,41	0,00001		
18	47,63	0,01	0,02	8,03E-16	0,03	0,00	11,90	0,993	77,21	0,59	0,00072		
19	43,38	0,01	0,01	4,07E-16	0,02	0,00	3,91	0,998	76,72	1,07	0,00021		
20	141,37	0,05	0,34	1,79E-16	0,11	0,00	71,48	1,000	74,27	2,90	0,01277		

Plateau age	Rock type	Wt. % $\text{K}_2\text{O}^*$	$\pm 2\sigma$	% plateau $^{39}\text{Ar}$	MSWD	Prob.	Steps
DR 87-4	Trachyte	4,32	0,21	50,9	2,7	0,003	11-20
Inverse isochron age	Rock type	Wt. % $\text{K}_2\text{O}^*$	$\pm 95\%$ conf.	Initial $^{40}\text{Ar}/^{39}\text{Ar}$	MSWD	Prob.	Steps
DR 87-4	Trachyte	4,32	0,20	293 $\pm$ 11	4,3	0,000	11-20

**Sample Material** SO233 DR89-2  
**Plagioclase**

J value 2σ % error Mass (mg)  
0,001042 0,178 3,831

Step #	<sup>40</sup> Ar/ <sup>39</sup> Ar	<sup>37</sup> Ar/ <sup>39</sup> Ar	<sup>36</sup> Ar/ <sup>39</sup> Ar	<sup>39</sup> Ar/ <sup>K</sup>	Ca/K	% <sup>40</sup> Ar <sub>inn</sub>	Cumulative fraction of <sup>39</sup> Ar	Age (Ma)	± 2σ (Ma)	<sup>36</sup> Ar/ <sup>37</sup> Ar AI
1	43106,80	368,18	144,39	1,02E-17	973,14	98,92	0,008	910,65	235,35	0,040844
2	1328,09	90,43	4,39	1,15E-16	189,25	97,22	0,091	72,75	19,19	0,005035
3	719,98	92,66	2,33	8,30E-17	194,25	94,76	0,151	74,32	10,21	0,002596
4	287,64	66,24	0,90	1,18E-16	136,15	90,62	0,236	52,44	8,08	0,001387
5	80,40	77,64	0,22	1,01E-16	160,95	72,20	0,309	43,91	5,00	0,000263
6	227,32	72,69	0,70	1,38E-16	150,14	88,16	0,409	52,55	5,64	0,000972
7	167,81	289,19	0,56	1,11E-16	711,20	85,13	0,489	57,94	7,40	0,000174
8	90,34	153,11	0,24	6,84E-17	336,23	63,82	0,538	67,57	9,08	0,000132
9	110,09	306,75	0,36	6,85E-17	766,22	74,11	0,587	67,02	6,65	0,000093
10	51,41	146,98	0,11	1,06E-16	321,23	38,90	0,664	64,67	3,92	0,000047
11	38,90	49,09	0,03	3,30E-16	99,64	14,73	0,901	63,46	1,42	0,000041
12	43,21	40,42	0,02	1,33E-16	81,53	8,76	1,000	74,71	2,57	0,000032

Plateau age	Rock type	Wt. % K <sub>2</sub> O*	Age (Ma)	± 2σ	% plateau <sup>39</sup> Ar	MSWD	Prob.	Steps
DR 89-2	Alkali Basalt	0,13	63,6	1,3	59,1	1,12	0,34	7-11
Inverse isochron age	Rock type	Wt. % K <sub>2</sub> O*	Age (Ma)	± 95% conf.	Initial <sup>40</sup> Ar/ <sup>39</sup> Ar	MSWD	Prob.	Steps
DR 89-2	Alkali Basalt	0,13	63,9	1,8	293,8 ± 6,0	1,3	0,26	7-11

Abbreviations: Wt. % = weight percent, AI = Alteration Index, MSWD = Mean Squares Weighted Deviation, conf. = confidence, and Prob. = Probability.  
The grey shaded analyses in the table indicate the age spectrum plateau steps.  
AI values shown in italics indicate fresh material, other values indicate altered material.

Omitted AI values indicate that the AI criteria were not met to allow calculation of these values.

Sample blanks	<sup>36</sup> Ar (cm <sup>3</sup> STP) ± 1σ	<sup>37</sup> Ar (cm <sup>3</sup> STP) ± 1σ	<sup>38</sup> Ar (cm <sup>3</sup> STP) ± 1σ	<sup>39</sup> Ar (cm <sup>3</sup> STP) ± 1σ	<sup>40</sup> Ar (cm <sup>3</sup> STP) ± 1σ
SO233 DR80-1	1,4E-13	3,7E-15	5,2E-15	2,9E-15	1,1E-13
SO233 DR80-1	1,4E-13	5,9E-15	3,4E-15	4,6E-15	3,1E-15
SO233 DR80-1	1,5E-13	3,8E-15	3,8E-15	4,4E-15	3,6E-15
SO233 DR80-1	1,4E-13	6,4E-15	4,0E-15	6,0E-15	6,5E-15
SO233 DR87-2	1,1E-13	1,1E-15	5,2E-15	3,5E-15	6,4E-15
SO233 DR87-2	1,0E-13	2,5E-15	5,7E-14	3,1E-15	1,4E-12
SO233 DR87-2	1,0E-13	2,8E-15	6,2E-14	3,1E-15	1,5E-12
SO233 DR87-2	1,0E-13	5,0E-15	5,6E-14	2,2E-13	4,3E-12
SO233 DR87-4	1,0E-13	2,2E-15	4,7E-15	1,7E-15	2,1E-12
SO233 DR87-4	1,1E-13	1,5E-15	4,6E-15	2,7E-15	2,1E-12
SO233 DR87-4	1,0E-13	2,9E-15	6,6E-14	2,9E-15	1,5E-12
SO233 DR87-4	1,0E-13	2,9E-15	6,1E-14	5,5E-15	1,4E-12
SO233 DR87-4	1,0E-13	5,6E-15	5,0E-14	2,0E-13	3,1E-12
SO233 DR89-2	3,7E-13	5,7E-15	1,0E-13	3,5E-15	1,8E-12
SO233 DR89-2	1,3E-13	3,9E-15	6,5E-14	5,8E-15	6,6E-11
SO233 DR89-2	1,5E-13	5,4E-15	7,9E-14	3,6E-15	2,8E-12
SO233 DR89-2	1,5E-13	5,8E-15	7,6E-14	4,8E-15	4,7E-12
Average	1,37E-13	2,02E-13	6,62E-14	1,28E-13	6,31E-12

STP = Standard Temperature and Pressure

Relative Abundances	<sup>36</sup> Ar [V]	%1σ	<sup>37</sup> Ar [V]	%1σ	<sup>38</sup> Ar [V]	%1σ	<sup>39</sup> Ar [V]	%1σ	40Ar [V]	%1σ	40(r)/39(k) ± 2σ	Age ± 2σ (Ma)	40A(r) 39A(r)(k) (%)	K/Ca ± 2σ	<sup>36</sup> Ar/ <sup>39</sup> Ar Alt. Index	Step #	
C45BA171	0.13 W	1.827	0.0060977	7.441	0.0015432	8.379	0.0158470	1.655	2.304067	0.382	43.60744 ± 4.16053	103.12 ± 9.56	29.98	2.14	1.33 ± 0.20	0.04320	1
C45BA173	0.30 W	13.821	0.0471427	4.627	0.0018538	6.580	0.1143958	0.283	4.003870	0.309	33.19133 ± 0.58656	79.02 ± 1.37	94.80	15.47	1.24 ± 0.11	0.00077	2
C45BA174	0.40 W	0.0006046	0.0611457	0.901	0.0018499	2.486	0.1339921	0.281	4.587572	0.051	32.95048 ± 0.21456	78.46 ± 0.50	96.21	16.12	1.12 ± 0.02	0.00055	3
C45BA175	0.50 W	0.0008447	0.0601051	0.789	0.0015313	2.440	0.1027366	0.263	3.513746	0.042	31.83088 ± 0.22976	75.85 ± 0.54	93.03	13.89	0.87 ± 0.01	0.00101	4
C45BA176	0.60 W	0.0005928	0.0490132	1.031	0.0010133	4.318	0.0657445	0.371	2.250395	0.067	31.09685 ± 0.29960	74.14 ± 0.70	90.80	8.89	0.73 ± 0.02	0.00134	5
C45BA177	0.70 W	0.0005928	0.0386011	0.926	0.0007204	4.655	0.0476101	0.503	1.648561	0.127	31.03148 ± 0.42471	73.98 ± 0.99	89.57	6.44	0.61 ± 0.01	0.00153	6
C45BA178	0.80 W	0.0005275	0.0325363	1.059	0.0005543	6.019	0.0326847	0.704	1.193140	0.125	30.89024 ± 0.64846	73.65 ± 1.52	87.15	4.55	0.53 ± 0.01	0.00193	7
C45BA179	0.90 W	0.0005455	0.0282860	0.938	0.0005222	6.557	0.0286650	0.624	1.143236	0.119	29.98856 ± 0.53245	71.55 ± 1.25	86.14	4.44	0.47 ± 0.01	0.00205	8
C45BA180	1.00 W	0.0003924	0.0248222	1.131	0.0003542	9.408	0.0210388	0.812	0.760478	0.172	30.75399 ± 0.81671	73.34 ± 1.91	85.01	2.84	0.43 ± 0.01	0.00230	9
C45BA181	1.10 W	0.0004337	0.0275310	1.154	0.0003755	8.557	0.0218688	0.815	0.793041	0.154	30.52967 ± 0.86670	72.81 ± 2.03	84.11	2.96	0.40 ± 0.01	0.00244	10
C45BA182	1.20 W	0.0003190	0.0226752	1.133	0.0002190	14.576	0.0143647	1.059	0.530895	0.245	30.63769 ± 1.13532	73.06 ± 2.65	82.81	1.94	0.32 ± 0.01	0.00270	11
C45BA183	1.35 W	0.0002871	0.0200519	1.328	0.0002019	15.695	0.0131777	1.215	0.478559	0.252	30.03377 ± 1.27186	71.65 ± 2.97	82.61	1.78	0.33 ± 0.01	0.00288	12
C45BA184	1.50 W	0.0003047	0.0200363	1.949	0.0001982	18.461	0.0130471	1.458	0.489657	0.287	30.80705 ± 1.62735	73.46 ± 3.80	81.98	1.76	0.29 ± 0.01	0.00327	13
C45BA185	2.00 W	0.0005152	0.0323161	1.073	0.0004118	9.504	0.0195287	1.043	0.736992	0.244	30.10915 ± 1.62599	71.83 ± 3.80	79.69	2.64	0.31 ± 0.01	0.00328	14
C45BA186	3.00 W	0.0005535	0.0364666	0.929	0.0004128	9.006	0.0211661	1.191	0.791676	0.163	29.84800 ± 1.11481	71.22 ± 2.61	79.70	2.86	0.30 ± 0.01	0.00322	15
C45BA187	5.00 W	0.0008046	0.0562968	0.817	0.0006060	5.953	0.0355471	0.555	1.263458	0.100	30.4382 ± 0.61689	73.31 ± 1.44	81.53	4.53	0.30 ± 0.01	0.00295	16
C45BA188	8.00 W	0.0002710	0.0232945	2.676	0.0002802	16.936	0.0180951	1.095	0.627399	0.363	30.37708 ± 1.88770	72.45 ± 4.41	87.53	2.45	0.40 ± 0.02	0.00183	17
C45BA189	10.00 W	0.0000605	0.0021760	7.759	0.0000390	82.894	0.0048704	3.059	0.166890	0.679	34.27682 ± 3.17852	81.55 ± 7.39	100.01	0.66	1.14 ± 0.19	0.00020	18
C45BA190	15.00 W	0.0001951	0.0114595	1.835	0.0001823	18.543	0.0119804	1.315	0.450037	0.257	32.84865 ± 1.21847	78.22 ± 2.84	87.39	1.62	0.53 ± 0.02	0.00201	19
Σ		0.0140782	0.6087310	0.450	0.0128696	1.816	0.7395611	0.134	27.73668	0.059							

### Information on Analysis and Constants Used in Calculations

Sample = SO233 DR88-2 (89-2M)  
Material = Groundmass  
Location = Walvis Ridge  
Analyst = Jan Stickler  
Project = EXAMPLES  
Mass Discrimination Law = POW  
Irradiation = can45  
J = 0.00134900 ± 0.00000262  
TCS2 = 27.870 ± 0.039 Ma  
IGSN = Undefined  
Preferred Age = Undefined  
Classification = Undefined  
Experiment Type = SAMPLE  
Extraction Method = Undefined  
Heating = 45 sec  
Isolation = 15.00 min  
Instrument = MAP216  
Lithology = Undefined  
La/Lon = Undefined - Undefined  
Feature = Undefined  
Weight = 3.510 mg

### Results

40(a)/36(a) ± 2σ	40(r)/39(k) ± 2σ	Age ± 2σ (Ma)	39Ar(k) (%)	K/Ca ± 2σ
317.25 ± 76.65 ± 24.16%	30.45977 ± 0.26173 ± 0.86%	72.65 ± 0.67 Minimal External Error ± 0.92% Analytical Error ± 0.61	0.84 59% 1.89 1.0000	0.35 ± 0.04 2σ Confidence Limit Error Magnification
	31.56859 ± 0.555%	76.15 ± 0.50 Minimal External Error ± 0.56% Analytical Error ± 0.41	19	0.62 ± 0.01
	29.99662 ± 1.51135 ± 5.04%	71.56 ± 3.55 Minimal External Error ± 3.55% Analytical Error ± 3.54	0.91 52% 1.94 1.0000	0.0004476485 Convergence 2σ Confidence Limit Error Magnification Number of Iterations
	315.09 ± 76.65 ± 24.33%	71.77 ± 3.48 Minimal External Error ± 3.49% Analytical Error ± 3.47	0.90 52% 1.94 1.0000	0.90 32.76 11 2σ Confidence Limit Error Magnification Number of Iterations Convergence Spreading Factor

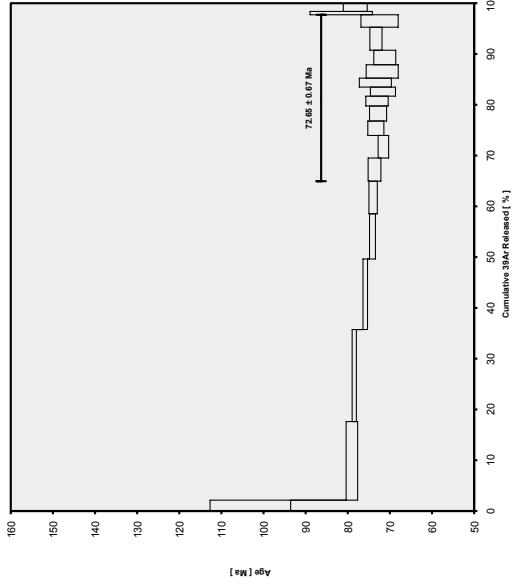
\* Alteration Index values in italics indicate analyses from fresh material, normal font is from altered material (Baker, 2007)

Procedure Blanks		36Ar [V]	1 $\sigma$	37Ar [V]	1 $\sigma$	38Ar [V]	1 $\sigma$	39Ar [V]	1 $\sigma$	40Ar [V]	1 $\sigma$
C45BA171	0,13 W	0,0001856	0,0000167	0,0003037	0,0000373	0,0000929	0,0000310	0,0002258	0,0001462	0,0028871	0,0010988
C45BA173	0,30 W	0,0002050	0,0000167	0,0003199	0,0000373	0,0001123	0,0000310	0,0002838	0,0001462	0,0033354	0,0010988
C45BA174	0,40 W	0,0002135	0,0000167	0,0003269	0,0000373	0,0001205	0,0000310	0,0003081	0,0001462	0,0035221	0,0010988
C45BA175	0,50 W	0,0002213	0,0000167	0,0003329	0,0000373	0,0001278	0,0000310	0,0003290	0,0001462	0,0036808	0,0010988
C45BA176	0,60 W	0,0002321	0,0000167	0,0003410	0,0000373	0,0001374	0,0000310	0,0003558	0,0001462	0,0038820	0,0010988
C45BA177	0,70 W	0,0002376	0,0000167	0,0003447	0,0000373	0,0001418	0,0000310	0,0003673	0,0001462	0,0039664	0,0010988
C45BA178	0,80 W	0,0002421	0,0000167	0,0003475	0,0000373	0,0001452	0,0000310	0,0003754	0,0001462	0,0040229	0,0010988
C45BA179	0,90 W	0,0002458	0,0000167	0,0003495	0,0000373	0,0001475	0,0000310	0,0003799	0,0001462	0,0040515	0,0010988
C45BA180	1,00 W	0,0002487	0,0000167	0,0003505	0,0000373	0,0001488	0,0000310	0,0003809	0,0001462	0,0040520	0,0010988
C45BA181	1,10 W	0,0002515	0,0000167	0,0003503	0,0000373	0,0001486	0,0000310	0,0003749	0,0001462	0,0039916	0,0010988
C45BA182	1,20 W	0,0002520	0,0000167	0,0003491	0,0000373	0,0001471	0,0000310	0,0003670	0,0001462	0,0039209	0,0010988
C45BA183	1,35 W	0,0002517	0,0000167	0,0003469	0,0000373	0,0001445	0,0000310	0,0003553	0,0001462	0,0038203	0,0010988
C45BA184	1,50 W	0,0002506	0,0000167	0,0003439	0,0000373	0,0001409	0,0000310	0,0003402	0,0001462	0,0036917	0,0010988
C45BA185	2,00 W	0,0002486	0,0000167	0,0003400	0,0000373	0,0001363	0,0000310	0,0003215	0,0001462	0,0035352	0,0010988
C45BA186	3,00 W	0,0002434	0,0000167	0,0003315	0,0000373	0,0001263	0,0000310	0,0002830	0,0001462	0,0032146	0,0010988
C45BA187	5,00 W	0,0002391	0,0000167	0,0003252	0,0000373	0,0001188	0,0000310	0,0002550	0,0001462	0,0029838	0,0010988
C45BA188	8,00 W	0,0002339	0,0000167	0,0003181	0,0000373	0,0001103	0,0000310	0,0002235	0,0001462	0,0027251	0,0010988
C45BA189	10,00 W	0,0002279	0,0000167	0,0003100	0,0000373	0,0001007	0,0000310	0,0001886	0,0001462	0,0024384	0,0010988
C45BA190	15,00 W	0,0002210	0,0000167	0,0003011	0,0000373	0,0000901	0,0000310	0,0001501	0,0001462	0,0021238	0,0010988



Sample Parameters	Sample	Material	Location	Analyst	Temp	Standard (in Me)	%Iσ	J	%Iσ	MDF	%Iσ	Volume Ratio	Sensitivity (molvolt)	Day	Month	Year	Hour	Min	Resist	%Iσ	K/Ca	%Iσ	K/Cl	%Iσ	Standard Name	
Irradiation Constants																										
40/36(e)																										
38/36(e)																										
38/37(ca)																										
39/37(ca)																										
38/37(ca)																										
36/37(ca)																										
40/39(k)																										
38/39(k)																										
36/38(c)																										
39/38(c)																										
36/38(c)																										
C45BA171	0.13W	SO233 DR89-2 (89-2m)	Groundmass	Walvis Ridge	Jan Stekulus	0.13	27.87	0.14	0.001349	0.194	1.0098	0.21	1,211E-14	11	FEB	2018	7	57	1	can45	0.65	0.51	0	0	0	TCS2
C45BA173	0.30W	SO233 DR89-2 (89-2m)	Groundmass	Walvis Ridge	Jan Stekulus	0.3	27.87	0.14	0.001349	0.194	1.0098	0.21	1,211E-14	11	FEB	2018	8	54	1	can45	0.65	0.51	0	0	0	TCS2
C45BA174	0.40W	SO233 DR89-2 (89-2m)	Groundmass	Walvis Ridge	Jan Stekulus	0.4	27.87	0.14	0.001349	0.194	1.0098	0.21	1,211E-14	11	FEB	2018	9	23	1	can45	0.65	0.51	0	0	0	TCS2
C45BA175	0.50W	SO233 DR89-2 (89-2m)	Groundmass	Walvis Ridge	Jan Stekulus	0.5	27.87	0.14	0.001349	0.194	1.0098	0.21	1,211E-14	11	FEB	2018	9	52	1	can45	0.65	0.51	0	0	0	TCS2
C45BA176	0.60W	SO233 DR89-2 (89-2m)	Groundmass	Walvis Ridge	Jan Stekulus	0.6	27.87	0.14	0.001349	0.194	1.0098	0.21	1,211E-14	11	FEB	2018	10	40	1	can45	0.65	0.51	0	0	0	TCS2
C45BA177	0.70W	SO233 DR89-2 (89-2m)	Groundmass	Walvis Ridge	Jan Stekulus	0.7	27.87	0.14	0.001349	0.194	1.0098	0.21	1,211E-14	11	FEB	2018	11	9	1	can45	0.65	0.51	0	0	0	TCS2
C45BA178	0.80W	SO233 DR89-2 (89-2m)	Groundmass	Walvis Ridge	Jan Stekulus	0.8	27.87	0.14	0.001349	0.194	1.0098	0.21	1,211E-14	11	FEB	2018	11	38	1	can45	0.65	0.51	0	0	0	TCS2
C45BA179	0.90W	SO233 DR89-2 (89-2m)	Groundmass	Walvis Ridge	Jan Stekulus	0.9	27.87	0.14	0.001349	0.194	1.0098	0.21	1,211E-14	11	FEB	2018	12	7	1	can45	0.65	0.51	0	0	0	TCS2
C45BA180	1.00W	SO233 DR89-2 (89-2m)	Groundmass	Walvis Ridge	Jan Stekulus	1	27.87	0.14	0.001349	0.194	1.0098	0.21	1,211E-14	11	FEB	2018	12	36	1	can45	0.65	0.51	0	0	0	TCS2
C45BA181	1.10W	SO233 DR89-2 (89-2m)	Groundmass	Walvis Ridge	Jan Stekulus	1.1	27.87	0.14	0.001349	0.194	1.0098	0.21	1,211E-14	11	FEB	2018	13	24	1	can45	0.65	0.51	0	0	0	TCS2
C45BA182	1.20W	SO233 DR89-2 (89-2m)	Groundmass	Walvis Ridge	Jan Stekulus	1.2	27.87	0.14	0.001349	0.194	1.0098	0.21	1,211E-14	11	FEB	2018	13	52	1	can45	0.65	0.51	0	0	0	TCS2
C45BA183	1.35W	SO233 DR89-2 (89-2m)	Groundmass	Walvis Ridge	Jan Stekulus	1.35	27.87	0.14	0.001349	0.194	1.0098	0.21	1,211E-14	11	FEB	2018	14	21	1	can45	0.65	0.51	0	0	0	TCS2
C45BA184	1.50W	SO233 DR89-2 (89-2m)	Groundmass	Walvis Ridge	Jan Stekulus	1.5	27.87	0.14	0.001349	0.194	1.0098	0.21	1,211E-14	11	FEB	2018	14	50	1	can45	0.65	0.51	0	0	0	TCS2
C45BA185	2.00W	SO233 DR89-2 (89-2m)	Groundmass	Walvis Ridge	Jan Stekulus	2	27.87	0.14	0.001349	0.194	1.0098	0.21	1,211E-14	11	FEB	2018	15	19	1	can45	0.65	0.51	0	0	0	TCS2
C45BA186	3.00W	SO233 DR89-2 (89-2m)	Groundmass	Walvis Ridge	Jan Stekulus	3	27.87	0.14	0.001349	0.194	1.0098	0.21	1,211E-14	11	FEB	2018	16	7	1	can45	0.65	0.51	0	0	0	TCS2
C45BA187	5.00W	SO233 DR89-2 (89-2m)	Groundmass	Walvis Ridge	Jan Stekulus	5	27.87	0.14	0.001349	0.194	1.0098	0.21	1,211E-14	11	FEB	2018	16	36	1	can45	0.65	0.51	0	0	0	TCS2
C45BA188	8.00W	SO233 DR89-2 (89-2m)	Groundmass	Walvis Ridge	Jan Stekulus	8	27.87	0.14	0.001349	0.194	1.0098	0.21	1,211E-14	11	FEB	2018	17	5	1	can45	0.65	0.51	0	0	0	TCS2
C45BA189	10.00W	SO233 DR89-2 (89-2m)	Groundmass	Walvis Ridge	Jan Stekulus	10	27.87	0.14	0.001349	0.194	1.0098	0.21	1,211E-14	11	FEB	2018	17	34	1	can45	0.65	0.51	0	0	0	TCS2
C45BA190	15.00W	SO233 DR89-2 (89-2m)	Groundmass	Walvis Ridge	Jan Stekulus	15	27.87	0.14	0.001349	0.194	1.0098	0.21	1,211E-14	11	FEB	2018	18	3	1	can45	0.65	0.51	0	0	0	TCS2

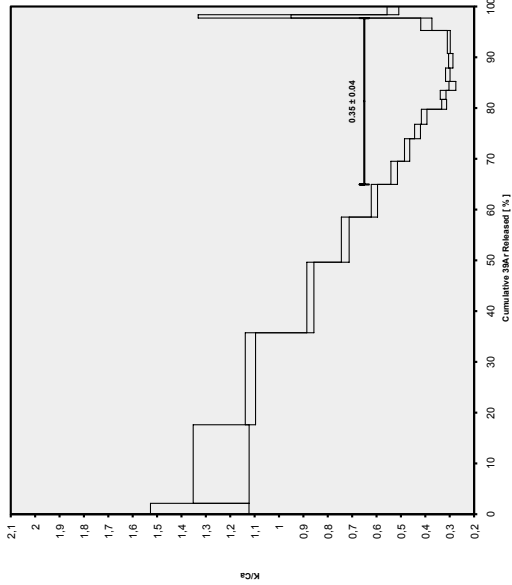
C45IT10IP3\_89-2M.AGE >>> SO233 DR89-2 (89-2M) >>> EXAMPLES PROJECT



**Ar-Ages in Ma**  
 WEIGHTED PLATEAU  
 72.66 ± 0.67  
 TOTAL FUSION  
 76.15 ± 0.50  
 NORMAL ISOCHRON  
 71.56 ± 3.55  
 INVERSE ISOCHRON  
 71.77 ± 3.48  
 MSWD  
 (PROBABILITY)  
 0.84 (59%)

**Sample Info**  
 Groundmass  
 Walvis Ridge  
 Jan Sticklius  
 IRR = can45  
 J = 0.00134900 ±  
 0.00000262

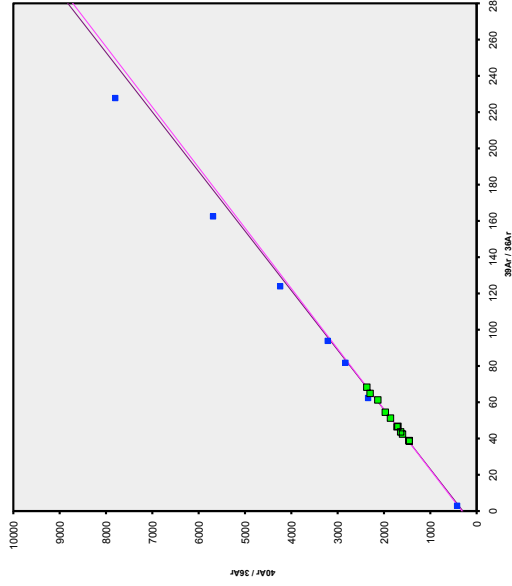
C45IT10IP3\_89-2M.AGE >>> SO233 DR89-2 (89-2M) >>> EXAMPLES PROJECT



**Ar-Ages in Ma**  
 WEIGHTED PLATEAU  
 72.66 ± 0.67  
 TOTAL FUSION  
 76.15 ± 0.50  
 NORMAL ISOCHRON  
 71.56 ± 3.55  
 INVERSE ISOCHRON  
 71.77 ± 3.48

**Sample Info**  
 Groundmass  
 Walvis Ridge  
 Jan Sticklius  
 IRR = can45  
 J = 0.00134900 ±  
 0.00000262

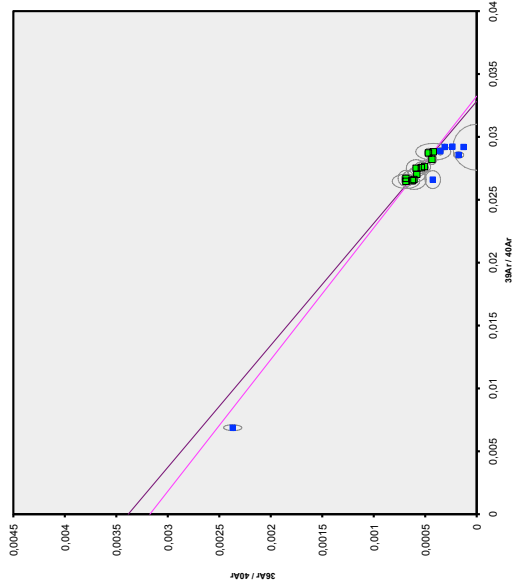
C45IT10IP3\_89-2M.AGE >>> SO233 DR89-2 (89-2M) >>> EXAMPLES PROJECT



**Ar-Ages in Ma**  
 WEIGHTED PLATEAU  
 72.66 ± 0.67  
 TOTAL FUSION  
 76.15 ± 0.50  
 NORMAL ISOCHRON  
 71.56 ± 3.55  
 INVERSE ISOCHRON  
 71.77 ± 3.48  
 MSWD  
 (PROBABILITY)  
 0.91 (52%)  
 40AR/36AR  
 INTERCEPT  
 317.2 ± 76.7

**Sample Info**  
 Groundmass  
 Walvis Ridge  
 Jan Sticklius  
 IRR = can45  
 J = 0.00134900 ±  
 0.00000262

C45IT10IP3\_89-2M.AGE >>> SO233 DR89-2 (89-2M) >>> EXAMPLES PROJECT



**Ar-Ages in Ma**  
 WEIGHTED PLATEAU  
 72.66 ± 0.67  
 TOTAL FUSION  
 76.15 ± 0.50  
 NORMAL ISOCHRON  
 71.56 ± 3.55  
 INVERSE ISOCHRON  
 71.77 ± 3.48  
 MSWD  
 (PROBABILITY)  
 0.90 (52%)  
 SPREADING FACTOR  
 7.1%  
 40AR/36AR  
 INTERCEPT  
 315.1 ± 76.7

**Sample Info**  
 Groundmass  
 Walvis Ridge  
 Jan Sticklius  
 IRR = can45  
 J = 0.00134900 ±  
 0.00000262

Relative Abundances	36Ar [V]	%1σ	37Ar [V]	%1σ	38Ar [V]	%1σ	39Ar [V]	%1σ	40Ar [V]	%1σ	40(p)/39(k) ± 2σ	Age ± 2σ (Ma)	40Ar(k) 39Ar(k) (%)	K/Ca ± 2σ	<sup>36</sup> Ar/ <sup>39</sup> Ar Alt. Index	Step #
C45BA111	0.13 W	0.0032498	1.496	0.0046496	2.715	0.0007300	3.459	0.0024088	1.507151	0.132	227.67890 ± 19.94397	108.71 ± 9.24	36.31	1.05	0.264 ± 0.023	0.03936
C45BA112	0.20 W	0.0027995	1.693	0.0181319	1.672	0.0006498	6.525	0.0069862	1.897436	0.165	153.62764 ± 8.18268	74.07 ± 3.87	56.48	4.79	0.196 ± 0.011	0.01166
C45BA113	0.30 W	0.0009993	2.951	0.0423389	1.258	0.0004284	5.585	0.0196252	3.446755	0.122	160.99788 ± 2.87515	71.54 ± 1.36	91.53	13.45	0.236 ± 0.007	0.00147
C45BA114	0.40 W	0.0002188	4.561	0.0429213	0.799	0.0003510	3.257	0.0243424	4.087338	0.082	165.59914 ± 1.75884	79.71 ± 0.83	98.50	16.68	0.289 ± 0.006	0.00025
C45BA115	0.50 W	0.0003846	3.744	0.0519904	0.867	0.0003380	5.400	0.026795	3.799334	0.042	162.95634 ± 1.62153	78.47 ± 0.76	95.51	15.54	0.222 ± 0.004	0.00048
C45BA116	0.60 W	0.0003868	3.564	0.0430495	0.880	0.0002608	4.836	0.0148131	2.471835	0.050	159.70874 ± 2.06699	76.94 ± 0.97	95.51	10.14	0.175 ± 0.004	0.00074
C45BA117	0.70 W	0.0004268	3.447	0.0379228	0.937	0.0002048	6.930	0.0101521	1.701062	0.059	155.84066 ± 1.70620	75.11 ± 0.81	92.76	6.95	0.136 ± 0.003	0.00120
C45BA118	0.80 W	0.0005074	2.861	0.0403330	0.727	0.0001983	6.980	0.0084386	1.429040	0.069	152.82485 ± 2.06631	73.55 ± 0.98	89.73	5.77	0.106 ± 0.002	0.00172
C45BA119	0.90 W	0.0003304	4.929	0.0208142	0.825	0.0001074	11.470	0.0035793	0.638825	0.153	153.29023 ± 3.65966	73.43 ± 1.73	84.98	2.45	0.087 ± 0.002	0.00265
C45BA120	1.00 W	0.0002876	4.657	0.0225060	1.027	0.0001006	16.286	0.0035295	0.626157	0.159	150.44164 ± 5.29198	74.10 ± 1.49	86.24	2.41	0.080 ± 0.002	0.00241
C45BA121	1.10 W	0.0002105	7.561	0.0147549	1.253	0.0000581	16.033	0.0024163	0.422991	0.228	150.44164 ± 5.29198	72.56 ± 2.50	85.57	1.65	0.083 ± 0.003	0.00249
C45BA122	1.20 W	0.0001506	8.120	0.0124200	1.000	0.0000500	18.018	0.0022647	0.388080	0.246	152.73839 ± 4.90459	73.65 ± 2.32	88.79	1.55	0.093 ± 0.003	0.00190
C45BA123	1.35 W	0.0001600	11.011	0.0137794	1.207	0.0000697	12.909	0.0025273	0.427575	0.233	151.48745 ± 5.95976	73.06 ± 2.82	89.20	1.73	0.093 ± 0.003	0.00180
C45BA124	1.50 W	0.0003828	4.158	0.0228616	1.075	0.0001061	11.652	0.0032824	0.606987	0.162	151.73572 ± 4.48917	73.17 ± 2.12	81.66	2.24	0.074 ± 0.002	0.00335
C45BA125	2.00 W	0.0003854	3.100	0.0331534	0.813	0.0001148	12.187	0.0041993	0.745067	0.138	151.77722 ± 2.48085	73.19 ± 1.17	85.07	2.87	0.064 ± 0.001	0.00261
C45BA126	3.00 W	0.0004493	3.836	0.0420472	1.120	0.0001531	11.676	0.0047548	0.859088	0.124	154.41704 ± 3.86101	74.44 ± 1.82	84.93	3.24	0.057 ± 0.002	0.00269
C45BA127	5.00 W	0.0005536	2.708	0.0577157	0.755	0.0002063	8.210	0.0072669	1.274405	0.080	154.35612 ± 2.11209	74.41 ± 1.00	87.53	4.96	0.064 ± 0.001	0.00216
C45BA128	8.00 W	0.0001402	7.711	0.0195710	0.974	0.0000457	26.389	0.0026290	0.426108	0.221	147.88879 ± 4.11774	71.26 ± 1.95	90.65	1.79	0.068 ± 0.002	0.00150
C45BA129	10.00 W	0.0000156	65.012	0.0016376	3.560	0.0000017	639.312	0.0002116	0.033379	2.811	137.39442 ± 4.108303	66.38 ± 19.49	86.62	0.14	0.066 ± 0.014	0.00208
Σ		0.0120489	0.775	0.5423985	0.248	0.0041683	1.843	0.1461040	26.788583	0.229						

### Information on Analysis and Constants Used in Calculations

Sample = SO233 DR89-2 (892M)  
Material = Groundmass  
Location = Walvis Ridge  
Analyst = Jan Sticklus  
Project = EXAMPLES  
Mass Discrimination Law = POW  
Irradiation = can45  
J = 0.00027280 ± 0.00000031  
TC52 = 27.870 ± 0.039 Ma  
IGSN = Undefined  
Preferred Age = Undefined  
Classification = Undefined  
Experiment Type = SAMPLE  
Extraction Method = Undefined  
Heating = 45 sec  
Isolation = 15.00 min  
Instrument = MAP216  
Lithology = Undefined  
Lab-Log = Undefined - Undefined  
Feature = Undefined  
Weight = 2.976 mg

Age Equations = Conventional  
Negative Intensities = Allowed  
Decay Constant 40K = 5.543 ± 0.009 E-10 1/a  
Decay Constant 39Ar = 2.940 ± 0.016 E-07 1/h  
Decay Constant 37Ar = 8.230 ± 0.012 E-04 1/h  
Decay Constant 36Cl = 2.257 ± 0.015 E-06 1/a  
Atmospheric Ratio 40Ar/36(a) = 295.50 ± 0.53  
Atmospheric Ratio 38Ar/36(a) = 0.1869 ± 0.0002  
Production Ratio 39Ar/37(ca) = 0.000702 ± 0.000012  
Production Ratio 38Ar/36(ca) = 0.000196 ± 0.000008  
Production Ratio 36Ar/36(ca) = 0.000270 ± 0.000008  
Production Ratio 40Ar/39(k) = 0.000730 ± 0.000090  
Production Ratio 38Ar/36(c) = 0.012150 ± 0.000033  
Production Ratio 36Ar/36(c) = 262.80  
Scaling Ratio K/Ca = 0.510

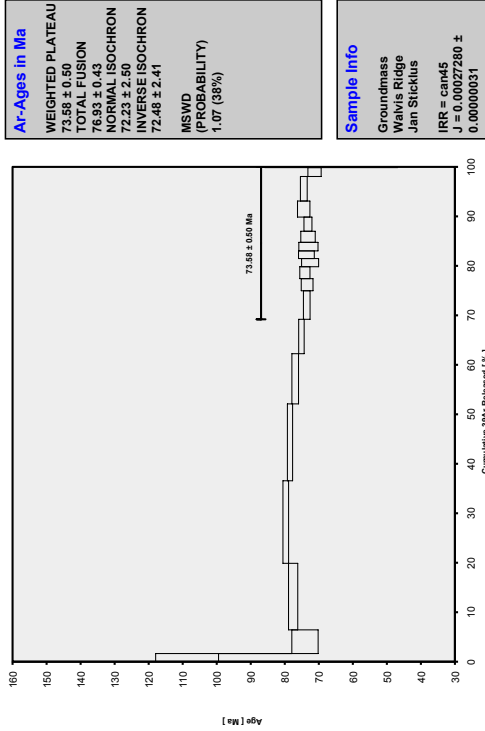
Results	40(a)/36(a) ± 2σ	40(p)/39(k) ± 2σ	Age ± 2σ (Ma)	39Ar(k) (%.n)	K/Ca ± 2σ
<b>Age Plateau</b>	152.60532 ± 0.65%	± 0.89786	73.58 ± 0.68%	1.07	0.073 ± 0.008
		Minimal External Error ± 0.55		38%	
		Analytical Error ± 0.47		1.85	2σ Confidence Limit
<b>Total Fusion Age</b>	159.69552 ± 0.52%	± 0.83223	76.93 ± 0.43	19	0.137 ± 0.001
		Minimal External Error ± 0.49			
		Analytical Error ± 0.39			
<b>Normal Isochron</b>	331.24 ± 20.32%	± 5.27251	72.23 ± 2.50	1.16	30.80
<b>No Convergence</b>		± 3.52%		31%	12
		Minimal External Error ± 2.51		1.89	2σ Confidence Limit
		Analytical Error ± 2.49		1.0776	Error Magnification
<b>Inverse Isochron</b>	326.31 ± 19.73%	± 5.07944	72.48 ± 2.41	100	Number of Iterations
		± 3.38%		0.0017154590	Convergence
		Minimal External Error ± 2.42		1.05	30.80
		Analytical Error ± 2.40		39%	12
		3		1.89	2σ Confidence Limit
				1.0304	Error Magnification
				0.0000079160	Number of Iterations
				13%	Spreading Factor

\* Alteration Index values in italics indicate analyses from fresh material, normal font is from altered material (Baksi, 2007)

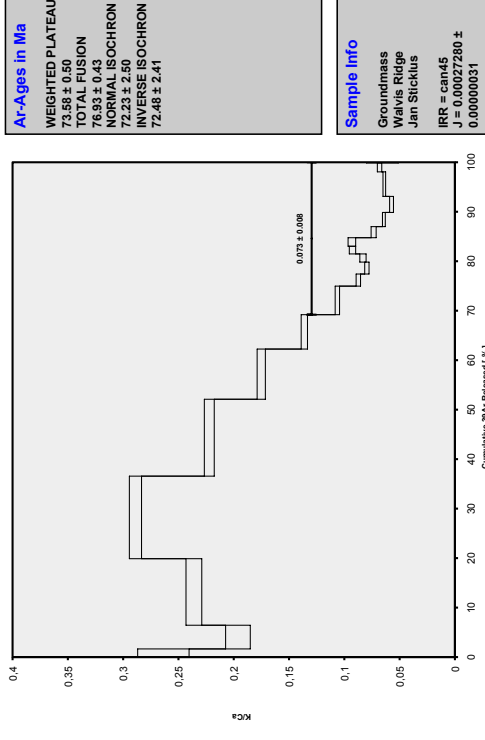
Procedure Blanks		36Ar [V]	1 $\sigma$	37Ar [V]	1 $\sigma$	38Ar [V]	1 $\sigma$	39Ar [V]	1 $\sigma$	40Ar [V]	1 $\sigma$
C45BA111	0,13 W	0,0001207	0,0000089	0,0002079	0,0000083	0,0000522	0,0000078	0,0001118	0,0000163	0,0024363	0,0009251
C45BA112	0,20 W	0,0001249	0,0000089	0,0002169	0,0000083	0,0000615	0,0000078	0,0001365	0,0000163	0,0029238	0,0009251
C45BA113	0,30 W	0,0001284	0,0000089	0,0002239	0,0000083	0,0000687	0,0000078	0,0001554	0,0000163	0,0033185	0,0009251
C45BA114	0,40 W	0,0001312	0,0000089	0,0002289	0,0000083	0,0000740	0,0000078	0,0001689	0,0000163	0,0036270	0,0009251
C45BA115	0,50 W	0,0001332	0,0000089	0,0002322	0,0000083	0,0000775	0,0000078	0,0001774	0,0000163	0,0038493	0,0009251
C45BA116	0,60 W	0,0001356	0,0000089	0,0002345	0,0000083	0,0000803	0,0000078	0,0001829	0,0000163	0,0040750	0,0009251
C45BA117	0,70 W	0,0001364	0,0000089	0,0002343	0,0000083	0,0000803	0,0000078	0,0001815	0,0000163	0,0041269	0,0009251
C45BA118	0,80 W	0,0001368	0,0000089	0,0002330	0,0000083	0,0000793	0,0000078	0,0001771	0,0000163	0,0041233	0,0009251
C45BA119	0,90 W	0,0001368	0,0000089	0,0002309	0,0000083	0,0000775	0,0000078	0,0001702	0,0000163	0,0040708	0,0009251
C45BA120	1,00 W	0,0001365	0,0000089	0,0002281	0,0000083	0,0000752	0,0000078	0,0001614	0,0000163	0,0039760	0,0009251
C45BA121	1,10 W	0,0001354	0,0000089	0,0002226	0,0000083	0,0000704	0,0000078	0,0001438	0,0000163	0,0037439	0,0009251
C45BA122	1,20 W	0,0001345	0,0000089	0,0002191	0,0000083	0,0000673	0,0000078	0,0001323	0,0000163	0,0035691	0,0009251
C45BA123	1,35 W	0,0001335	0,0000089	0,0002156	0,0000083	0,0000644	0,0000078	0,0001207	0,0000163	0,0033762	0,0009251
C45BA124	1,50 W	0,0001314	0,0000089	0,0002124	0,0000083	0,0000618	0,0000078	0,0001098	0,0000163	0,0031791	0,0009251
C45BA125	2,00 W	0,0001298	0,0000089	0,0002096	0,0000083	0,0000597	0,0000078	0,0000995	0,0000163	0,0029701	0,0009251
C45BA126	3,00 W	0,0001290	0,0000089	0,0002063	0,0000083	0,0000577	0,0000078	0,0000857	0,0000163	0,0026311	0,0009251
C45BA127	5,00 W	0,0001290	0,0000089	0,0002055	0,0000083	0,0000577	0,0000078	0,0000802	0,0000163	0,0024411	0,0009251
C45BA128	8,00 W	0,0001283	0,0000089	0,0002058	0,0000083	0,0000590	0,0000078	0,0000774	0,0000163	0,0022703	0,0009251
C45BA129	10,00 W	0,0001279	0,0000089	0,0002074	0,0000083	0,0000617	0,0000078	0,0000780	0,0000163	0,0021255	0,0009251

Sample Parameters	Sample	Material	Location	Analyst	Temp	Standard (in Ma)	%1σ	J	%1σ	MDF	%1σ	Volume Ratio	Sensitivity (mol/vol)	Day	Month	Year	Hour	Min	Res	Irradiation	Project	Experiment	Nmb	Standard Name	
C45BA111	0.13 W	SO233 DR89-2 (892m)	Groundmass	Valve Ridge	Jan Sticklus	0.13	27.87	0.14	0.0002728	0.115	1.0098	0.21	1.211E-14	9	FEB	2018	23	15	1	can45	Examples	c45st10p8_892m	01	TCS2	
C45BA112	0.20 W	SO233 DR89-2 (892m)	Groundmass	Valve Ridge	Jan Sticklus	0.2	27.87	0.14	0.0002728	0.115	1.0098	0.21	1.211E-14	9	FEB	2018	23	44	1	can45	Examples	c45st10p8_892m	01	TCS2	
C45BA113	0.30 W	SO233 DR89-2 (892m)	Groundmass	Valve Ridge	Jan Sticklus	0.3	27.87	0.14	0.0002728	0.115	1.0098	0.21	1.211E-14	10	FEB	2018	0	13	1	can45	Examples	c45st10p8_892m	01	TCS2	
C45BA114	0.40 W	SO233 DR89-2 (892m)	Groundmass	Valve Ridge	Jan Sticklus	0.4	27.87	0.14	0.0002728	0.115	1.0098	0.21	1.211E-14	10	FEB	2018	0	42	1	can45	Examples	c45st10p8_892m	01	TCS2	
C45BA115	0.50 W	SO233 DR89-2 (892m)	Groundmass	Valve Ridge	Jan Sticklus	0.5	27.87	0.14	0.0002728	0.115	1.0098	0.21	1.211E-14	10	FEB	2018	1	10	1	can45	Examples	c45st10p8_892m	01	TCS2	
C45BA116	0.60 W	SO233 DR89-2 (892m)	Groundmass	Valve Ridge	Jan Sticklus	0.6	27.87	0.14	0.0002728	0.115	1.0098	0.21	1.211E-14	10	FEB	2018	1	58	1	can45	Examples	c45st10p8_892m	01	TCS2	
C45BA117	0.70 W	SO233 DR89-2 (892m)	Groundmass	Valve Ridge	Jan Sticklus	0.7	27.87	0.14	0.0002728	0.115	1.0098	0.21	1.211E-14	10	FEB	2018	2	27	1	can45	Examples	c45st10p8_892m	01	TCS2	
C45BA118	0.80 W	SO233 DR89-2 (892m)	Groundmass	Valve Ridge	Jan Sticklus	0.8	27.87	0.14	0.0002728	0.115	1.0098	0.21	1.211E-14	10	FEB	2018	2	56	1	can45	Examples	c45st10p8_892m	01	TCS2	
C45BA119	0.90 W	SO233 DR89-2 (892m)	Groundmass	Valve Ridge	Jan Sticklus	0.9	27.87	0.14	0.0002728	0.115	1.0098	0.21	1.211E-14	10	FEB	2018	3	25	1	can45	Examples	c45st10p8_892m	01	TCS2	
C45BA120	1.00 W	SO233 DR89-2 (892m)	Groundmass	Valve Ridge	Jan Sticklus	1	27.87	0.14	0.0002728	0.115	1.0098	0.21	1.211E-14	10	FEB	2018	3	54	1	can45	Examples	c45st10p8_892m	01	TCS2	
C45BA121	1.10 W	SO233 DR89-2 (892m)	Groundmass	Valve Ridge	Jan Sticklus	1.1	27.87	0.14	0.0002728	0.115	1.0098	0.21	1.211E-14	10	FEB	2018	4	42	1	can45	Examples	c45st10p8_892m	01	TCS2	
C45BA122	1.20 W	SO233 DR89-2 (892m)	Groundmass	Valve Ridge	Jan Sticklus	1.2	27.87	0.14	0.0002728	0.115	1.0098	0.21	1.211E-14	10	FEB	2018	5	11	1	can45	Examples	c45st10p8_892m	01	TCS2	
C45BA123	1.35 W	SO233 DR89-2 (892m)	Groundmass	Valve Ridge	Jan Sticklus	1.35	27.87	0.14	0.0002728	0.115	1.0098	0.21	1.211E-14	10	FEB	2018	5	40	1	can45	Examples	c45st10p8_892m	01	TCS2	
C45BA124	1.50 W	SO233 DR89-2 (892m)	Groundmass	Valve Ridge	Jan Sticklus	1.5	27.87	0.14	0.0002728	0.115	1.0098	0.21	1.211E-14	10	FEB	2018	6	8	1	can45	Examples	c45st10p8_892m	01	TCS2	
C45BA125	2.00 W	SO233 DR89-2 (892m)	Groundmass	Valve Ridge	Jan Sticklus	2	27.87	0.14	0.0002728	0.115	1.0098	0.21	1.211E-14	10	FEB	2018	6	37	1	can45	Examples	c45st10p8_892m	01	TCS2	
C45BA126	3.00 W	SO233 DR89-2 (892m)	Groundmass	Valve Ridge	Jan Sticklus	3	27.87	0.14	0.0002728	0.115	1.0098	0.21	1.211E-14	10	FEB	2018	7	25	1	can45	Examples	c45st10p8_892m	01	TCS2	
C45BA127	5.00 W	SO233 DR89-2 (892m)	Groundmass	Valve Ridge	Jan Sticklus	5	27.87	0.14	0.0002728	0.115	1.0098	0.21	1.211E-14	10	FEB	2018	7	54	1	can45	Examples	c45st10p8_892m	01	TCS2	
C45BA128	8.00 W	SO233 DR89-2 (892m)	Groundmass	Valve Ridge	Jan Sticklus	8	27.87	0.14	0.0002728	0.115	1.0098	0.21	1.211E-14	10	FEB	2018	8	23	1	can45	Examples	c45st10p8_892m	01	TCS2	
C45BA129	10.00 W	SO233 DR89-2 (892m)	Groundmass	Valve Ridge	Jan Sticklus	10	27.87	0.14	0.0002728	0.115	1.0098	0.21	1.211E-14	10	FEB	2018	8	52	1	can45	Examples	c45st10p8_892m	01	TCS2	
C45BA111	0.13 W	295.5	0.178	0.018	35	0.1869	0.107	1.493	3	0.00702	1.71	0.000196	4.08	0.0002702	0.15	0.00073	12.33	0.01215	0.27	262.8	0.65	0.51	0	0	0
C45BA112	0.20 W	295.5	0.178	0.018	35	0.1869	0.107	1.493	3	0.00702	1.71	0.000196	4.08	0.0002702	0.15	0.00073	12.33	0.01215	0.27	262.8	0.65	0.51	0	0	0
C45BA113	0.30 W	295.5	0.178	0.018	35	0.1869	0.107	1.493	3	0.00702	1.71	0.000196	4.08	0.0002702	0.15	0.00073	12.33	0.01215	0.27	262.8	0.65	0.51	0	0	0
C45BA114	0.40 W	295.5	0.178	0.018	35	0.1869	0.107	1.493	3	0.00702	1.71	0.000196	4.08	0.0002702	0.15	0.00073	12.33	0.01215	0.27	262.8	0.65	0.51	0	0	0
C45BA115	0.50 W	295.5	0.178	0.018	35	0.1869	0.107	1.493	3	0.00702	1.71	0.000196	4.08	0.0002702	0.15	0.00073	12.33	0.01215	0.27	262.8	0.65	0.51	0	0	0
C45BA116	0.60 W	295.5	0.178	0.018	35	0.1869	0.107	1.493	3	0.00702	1.71	0.000196	4.08	0.0002702	0.15	0.00073	12.33	0.01215	0.27	262.8	0.65	0.51	0	0	0
C45BA117	0.70 W	295.5	0.178	0.018	35	0.1869	0.107	1.493	3	0.00702	1.71	0.000196	4.08	0.0002702	0.15	0.00073	12.33	0.01215	0.27	262.8	0.65	0.51	0	0	0
C45BA118	0.80 W	295.5	0.178	0.018	35	0.1869	0.107	1.493	3	0.00702	1.71	0.000196	4.08	0.0002702	0.15	0.00073	12.33	0.01215	0.27	262.8	0.65	0.51	0	0	0
C45BA119	0.90 W	295.5	0.178	0.018	35	0.1869	0.107	1.493	3	0.00702	1.71	0.000196	4.08	0.0002702	0.15	0.00073	12.33	0.01215	0.27	262.8	0.65	0.51	0	0	0
C45BA120	1.00 W	295.5	0.178	0.018	35	0.1869	0.107	1.493	3	0.00702	1.71	0.000196	4.08	0.0002702	0.15	0.00073	12.33	0.01215	0.27	262.8	0.65	0.51	0	0	0
C45BA121	1.10 W	295.5	0.178	0.018	35	0.1869	0.107	1.493	3	0.00702	1.71	0.000196	4.08	0.0002702	0.15	0.00073	12.33	0.01215	0.27	262.8	0.65	0.51	0	0	0
C45BA122	1.20 W	295.5	0.178	0.018	35	0.1869	0.107	1.493	3	0.00702	1.71	0.000196	4.08	0.0002702	0.15	0.00073	12.33	0.01215	0.27	262.8	0.65	0.51	0	0	0
C45BA123	1.35 W	295.5	0.178	0.018	35	0.1869	0.107	1.493	3	0.00702	1.71	0.000196	4.08	0.0002702	0.15	0.00073	12.33	0.01215	0.27	262.8	0.65	0.51	0	0	0
C45BA124	1.50 W	295.5	0.178	0.018	35	0.1869	0.107	1.493	3	0.00702	1.71	0.000196	4.08	0.0002702	0.15	0.00073	12.33	0.01215	0.27	262.8	0.65	0.51	0	0	0
C45BA125	2.00 W	295.5	0.178	0.018	35	0.1869	0.107	1.493	3	0.00702	1.71	0.000196	4.08	0.0002702	0.15	0.00073	12.33	0.01215	0.27	262.8	0.65	0.51	0	0	0
C45BA126	3.00 W	295.5	0.178	0.018	35	0.1869	0.107	1.493	3	0.00702	1.71	0.000196	4.08	0.0002702	0.15	0.00073	12.33	0.01215	0.27	262.8	0.65	0.51	0	0	0
C45BA127	5.00 W	295.5	0.178	0.018	35	0.1869	0.107	1.493	3	0.00702	1.71	0.000196	4.08	0.0002702	0.15	0.00073	12.33	0.01215	0.27	262.8	0.65	0.51	0	0	0
C45BA128	8.00 W	295.5	0.178	0.018	35	0.1869	0.107	1.493	3	0.00702	1.71	0.000196	4.08	0.0002702	0.15	0.00073	12.33	0.01215	0.27	262.8	0.65	0.51	0	0	0
C45BA129	10.00 W	295.5	0.178	0.018	35	0.1869	0.107	1.493	3	0.00702	1.71	0.000196	4.08	0.0002702	0.15	0.00073	12.33	0.01215	0.27	262.8	0.65	0.51	0	0	0

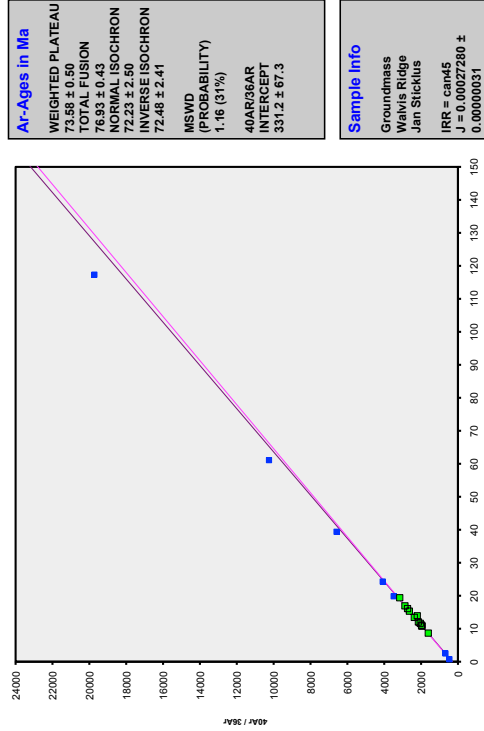
C45T10IP8\_892M.AGE >>> SO233 DR89-2 (892M) >>> EXAMPLES PROJECT



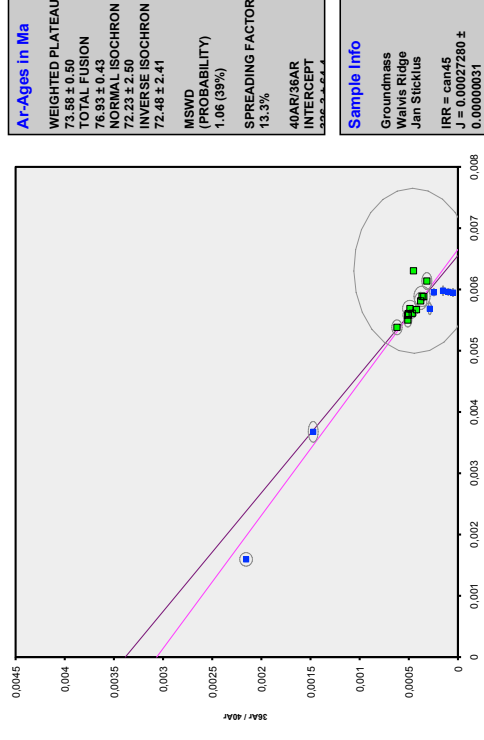
C45T10IP8\_892M.AGE >>> SO233 DR89-2 (892M) >>> EXAMPLES PROJECT



C45T10IP8\_892M.AGE >>> SO233 DR89-2 (892M) >>> EXAMPLES PROJECT



C45T10IP8\_892M.AGE >>> SO233 DR89-2 (892M) >>> EXAMPLES PROJECT



## **Appendices A-C: Comparison of New Age and Geochemical Data from the Walvis Ridge with other South Atlantic Hotspots: Mapping the base of the lower mantle beneath the South Atlantic**

---

---

### **Appendix A: Analytical Methods and Supplementary Figures**

#### ***Sample preparation***

The sample sites of cruises S0233 and S0234 and a detailed description of the recovered rocks are reported by Hoernle et al. (2014) and Werner and Wagner (2014). To ensure the best possible quality material for our analytical methods, only the freshest parts of the rocks were used and altered regions and encrustation were cut-off on-board the R/V Sonne. The freshest parts (usually the cores) of the lavas were used to prepare rock chips, powders and mineral separates for the analytical methods. The lava blocks were cleaned with water and then dried at 50°C before they were crushed in a steel jaw crusher. Afterwards, the crushed rocks were dry sieved and cleaned with distilled water in an ultrasonic bath to remove dust. To obtain the freshest possible material for the geochemical analyses, we carefully handpicked the 0.5-1 mm size fraction under a binocular microscope. Several grams of the picked rock chips were milled to fine powder using an agate mortar grinder and an agate planetary ball mill. This powder was used for major and trace element analysis, and hot-acid leached powders were used for Hf isotopes and Sr isotopes. The remaining half of the rock chips were used for Sr-Nd-Pb isotopic analysis.

Two recovered submarine samples (S0233 DR62-2 and S0234 DR6-1) contained a glassy margin, which was cut-off, crushed, handpicked under a binocular microscope and cleaned with deionized water in an ultrasonic bath. The glass shards were used for

major and trace element analysis, as well as for Sr-Nd-Pb-Hf analysis, and sample S0234 DR6-1 was used for  $^{40}\text{Ar}/^{39}\text{Ar}$  analyses.

Feldspars for the  $^{40}\text{Ar}/^{39}\text{Ar}$  age dating determinations were hand-picked under a binocular microscope, using the 0.25-0.5 mm size fraction. Feldspar separates were treated with 5% hydrofluoric acid for 10 minutes, rinsed with distilled water, cleaned with distilled water for 4 minutes using an ultrasonic stick, and then dried overnight at 50°C in an oven. We prepared approximately 20 mg of each mineral separate (or glass shards) and loaded them into individual holes within 20 mm diameter 99.999% aluminium disks. These disks were stacked and bolted together, and then placed in a 99.9% Al canister to make up the irradiation package, which was irradiated with fast neutrons in the Cadmium-Lined In-Core Irradiation Tube (CLICIT) reactor core position for 4 hours at the Oregon State University nuclear reactor, Corvallis, USA. Grains of Taylor Creek sanidine (TCR-2) age standard ( $27.87 \pm 0.04$  Ma,  $1\sigma$  error; M.A. Lanphere, pers. comm., calibrated to SB-3 biotite ;Lanphere and Dalrymple, 2000) were regularly interspersed in the aluminium disks with our samples to monitor the fast neutron gradient.



### ***<sup>40</sup>Ar/<sup>39</sup>Ar dating methods***

The <sup>40</sup>Ar/<sup>39</sup>Ar analysis was carried out at the GEOMAR Argon Geochronology in Oceanography (ARGO) Laboratory using an 25 W Coherent Sabre 25TSM argon ion laser ( $\lambda = 455\text{-}515\text{ nm}$ ), with a computer-controlled isel X-Y stage and a Mass Analyser Products (MAP) 216 series noble gas mass spectrometer. The sample separates were loaded into variously sized aluminium laser palettes and loaded into an ultra-high vacuum 4.5" laser chamber fitted with a Kovar viewport. To remove adsorbed atmospheric argon from the samples and chamber walls, the laser chamber was baked at 230°C, and the whole extraction line was baked in an oven at 195°C for 8 hours, and then pumped for 2 days. The laser system was fitted with a binocular microscope and light source for sample illumination and X-Y stage calibration, and a camera for video recording of the laser heating of each sample. The incremental heating steps were performed with a 0.25-1.0 mm diameter laser beam for 45 seconds.

The gases released by laser heating were cleaned for 3 minutes using an automatically-refilling liquid nitrogen Dewar attached to a glass finger, and two SAES AP10 getter pumps (one at 400°C and one at room temperature) to remove all active gases. The remaining noble gases were equilibrated into a high sensitivity MAP 216 mass spectrometer, containing a Bauer-Signer-type source, operated at a 240  $\mu\text{A}$  emission current, with a Becton Dickinson MM-1 Mesh electron multiplier, and a mass spectrometer sensitivity of  $2.70 \times 10^{-10}\text{ cm}^3/\text{V}$  ( $1.203 \times 10^{-14}\text{ moles}/\text{V}$ ), for the standard operating gain value.

The five Ar isotopes (<sup>36</sup>Ar to <sup>40</sup>Ar) and baselines (masses 35.5 to 40.5) for the system blanks, age standards and samples were measured via peak-hopping using a single electron multiplier with two variable gain settings. The fully automated laser

heating, X-Y stage movement, automated valves operation, and data acquisition were computer controlled using a Turbo Pascal program.

The average extraction system blank Ar isotope measurements obtained during our sample analyses were  $1.42 \times 10^{-13}$ ,  $1.79 \times 10^{-13}$ ,  $7.94 \times 10^{-14}$ ,  $1.50 \times 10^{-13}$ , and  $2.29 \times 10^{-12}$  cm<sup>3</sup> STP (standard temperature and pressure) for <sup>36</sup>Ar, <sup>37</sup>Ar, <sup>38</sup>Ar, <sup>39</sup>Ar, and <sup>40</sup>Ar, respectively (Appendix C). The sample analyses were corrected for mass spectrometer discrimination using a <sup>40</sup>Ar/<sup>36</sup>Ar ratio of 285.9 and nuclear interference reaction correction factors of  $^{40}\text{Ar}/^{39}\text{Ar}_{\text{K}} = 7.30 \times 10^{-4}$ ,  $^{36}\text{Ar}/^{37}\text{Ar}_{\text{Ca}} = 2.65 \times 10^{-4}$ , and  $^{39}\text{Ar}/^{37}\text{Ar}_{\text{Ca}} = 7.02 \times 10^{-4}$  (Renne et al., 2013; Renne et al., 2015). Errors are quoted at 1σ and 2σ levels, and the <sup>40</sup>Ar/<sup>39</sup>Ar ages were calculated using the decay constants and atmospheric <sup>40</sup>Ar/<sup>36</sup>Ar ratio of Steiger and Jäger (1977). The J values and errors are noted in the sample <sup>40</sup>Ar/<sup>39</sup>Ar data tables (Appendix C).

All the plots and plateau and inverse isochron age determinations were made using the Excel Isoplot macro v. 4.15 (Ludwig, 2011). The <sup>40</sup>Ar/<sup>39</sup>Ar ages reported here were determined by the following criteria (e.g., Lanphere and Dalrymple, 1978): 1) a valid <sup>40</sup>Ar/<sup>39</sup>Ar plateau age contains least three consecutive laser heating steps, comprising >50% of the <sup>39</sup>Ar released, with ages overlapping within 2σ errors, 2) the plateau and inverse isochron ages should be concordant at the 95% confidence level, 3) the statistical validity of plateau, inverse isochron and mean <sup>40</sup>Ar/<sup>39</sup>Ar ages was tested by calculating Mean Squared Weighted Deviation values (MSWD) and probability fraction values (P; > 0.05), and 4) the degree of sample alteration was monitored via <sup>36</sup>Ar/<sup>37</sup>Ar (plagioclase) or <sup>36</sup>Ar/<sup>39</sup>Ar (K-feldspar) alteration indices (AI), following the method and cut-off values of Baksi (2007) and van den Bogaard (2013). In addition, the % atmospheric <sup>40</sup>Ar (<sup>40</sup>Ar<sub>atm</sub>) and Ca/K ratios (obtained from measured <sup>37</sup>Ar<sub>Ca</sub>/<sup>39</sup>Ar<sub>K</sub>

ratios) were used to check for the presence of alteration or mixed phases in the samples, respectively.

#### ***<sup>40</sup>Ar/<sup>39</sup>Ar age spectra descriptions***

The <sup>40</sup>Ar/<sup>39</sup>Ar step-heating tables and plots are presented in Appendix C and the results are described below. K-feldspar sample SO233 DR4-1 from the Guyot Province yielded a statistically valid plateau age of  $59.17 \pm 0.20$  Ma ( $2\sigma$ ; MSWD=0.51; Probability fraction value (P)= 0.90; 91.8% <sup>39</sup>Ar). The high-temperature steps (8-13) give <sup>36</sup>Ar/<sup>39</sup>Ar alteration index (AI) values below the K-feldspar cut-off value of  $< 0.00006$  (van den Bogaard, 2013) with low <sup>40</sup>Ar atmospheric (<sup>40</sup>Ar<sub>atm</sub>) values of  $< 5\%$ , indicating the presence of fresh material. The low-temperature steps (2-7) contain altered material (the <sup>36</sup>Ar/<sup>39</sup>Ar AI values are above the cut-off value and the steps also give high % <sup>40</sup>Ar<sub>Atm</sub> values), however, the low-temperature step ages lie within  $2\sigma$  errors of the higher-temperature fresh material steps. The plateau age is backed-up by a statistically robust inverse isochron age of  $59.14 \pm 0.23$  Ma (95% conf.; MSWD = 0.37; P = 0.96; initial <sup>40</sup>Ar/<sup>36</sup>Ar =  $296.0 \pm 1.4$ ).

Plagioclase step-heating of sample SO233 DR19-1A yields a slightly disturbed statistically valid pseudo-plateau age of  $70.84 \pm 0.28$  Ma ( $2\sigma$ ; MSWD = 0.83; P = 0.48; 41.9% <sup>39</sup>Ar). All the pseudo-plateau steps yield <sup>36</sup>Ar/<sup>37</sup>Ar AI values below the plagioclase <sup>36</sup>Ar/<sup>37</sup>Ar cut-off value of  $<0.00006$  (Baksi, 2007) indicating the degassing of Ar from fresh plagioclase. The statistically valid inverse isochron age of  $71.20 \pm 0.47$  Ma (95% conf.; MSWD = 1.3; P = 0.26; initial <sup>40</sup>Ar/<sup>36</sup>Ar =  $249 \pm 50$ ) confirms the plateau age.

Plagioclase sample SO233 DR35-12 yields a statistically valid plateau age of  $75.4 \pm 1.2$  Ma ( $2\sigma$ ; MSWD = 1.6; P = 0.15; 55.4% <sup>39</sup>Ar). Four of the six plateau steps have <sup>36</sup>Ar/<sup>37</sup>Ar AI values below the plagioclase cut-off value (Baksi, 2007) and yield relatively

low %  $^{40}\text{Ar}_{\text{Atm}}$  values, indicating the presence of fresh plagioclase. The plateau age is confirmed by the statistically valid inverse isochron age of  $76.30 \pm 2.6$  Ma (95% conf.; MSWD = 1.04; P = 0.38; initial  $^{40}\text{Ar}/^{36}\text{Ar} = 289 \pm 13$ ).

One plagioclase separate (S0233 DR37-1A) with an estimated  $\text{K}_2\text{O}$  content of 0.15 wt. % (calculated from the total  $^{39}\text{Ar}$  concentration and the step-heated sample weight) does not yield a plateau age. The  $^{36}\text{Ar}/^{37}\text{Ar}$  AI values indicate the presence of fresh plagioclase from steps 7-15. The age spectrum is slightly disturbed, but analyses with < 10 %  $^{40}\text{Ar}_{\text{Atm}}$  contents (i.e., steps 8-10 and 12-14) yield a statistically valid weighted mean age of  $79.59 \pm 0.72$  ( $2\sigma$ ; MSWD = 2.0; P = 0.069) and represents the best age estimate of this sample. An inverse isochron plot, calculated from steps 8-10 and 12-14, yields an invalid age of  $80.4 \pm 2.1$  Ma (95% conf.; MSWD = 2.7; P = 0.029; initial  $^{40}\text{Ar}/^{36}\text{Ar} = 200 \pm 110$ ).

Plagioclase step heating analysis of sample S0233 DR41-2 yielded a statistically valid plateau age of  $81.31 \pm 0.21$  Ma ( $2\sigma$ ; MSWD = 0.82; P = 0.62; 94.7 %  $^{39}\text{Ar}$ ). The degassing of fresh plagioclase material is indicated by the low  $^{36}\text{Ar}/^{37}\text{Ar}$  AI values for the plateau steps (8-16). The medium-temperature plateau steps (5-7) have higher  $^{36}\text{Ar}/^{37}\text{Ar}$  AI values (0.000118-0.001627), indicating the presence of altered material, but these step ages agree within  $2\sigma$  errors with the fresh material high-temperature steps. The plateau age is confirmed by a statistically valid inverse isochron age of  $81.27 \pm 0.27$  Ma (95% conf.; MSWD = 0.44; P = 0.93; initial  $^{40}\text{Ar}/^{36}\text{Ar} = 296.4 \pm 8.2$ ).

From sample site S0233 DR43 we analyzed two relatively fresh pillow basalt fragments that yield statistically valid plagioclase plateau ages of  $78.84 \pm 0.50$  Ma (S0233 DR43-3;  $2\sigma$ ; MSWD = 2.0; P = 0.06; 51.9%  $^{39}\text{Ar}$ ), and  $80.00 \pm 0.52$  Ma (S0233 DR43-6;  $2\sigma$ ; MSWD = 0.96; P = 0.49, 89.5%  $^{39}\text{Ar}$ ). The plateau age of sample DR43-3 is statistically valid, but an inverse isochron of the plateau steps resulted in a invalid age of

83.56 ± 0.10 Ma (95% conf.; MSWD = 2.4; P = 0.034; initial  $^{40}\text{Ar}/^{36}\text{Ar} = 233 \pm 150$ ) that clustered near the radiogenic  $^{39}\text{Ar}/^{40}\text{Ar}$  axis. The majority of the plateau steps yielded low  $^{36}\text{Ar}/^{37}\text{Ar}$  plagioclase AI values indicating the presence of fresh material. Low  $^{36}\text{Ar}/^{37}\text{Ar}$  plagioclase AI values for the majority of plateau steps from sample DR43-6, coupled with low %  $^{40}\text{Ar}_{\text{atm}}$  values, yield a statistically valid plateau age, which is backed up by a statistically valid inverse isochron age of 79.86 ± 0.71 Ma (95% conf.; MSWD = 0.64; P = 0.81; initial  $^{40}\text{Ar}/^{36}\text{Ar} = 296.9 \pm 5.0$ ; Table 1).

Plagioclase sample SO233 DR62-2 has a low wt. % K<sub>2</sub>O value of 0.13 resulting in some large errors on individual steps (2-30% 2σ errors). Apart from one plateau step (step 12), all the other plateau steps show elevated  $^{36}\text{Ar}/^{37}\text{Ar}$  AI values (0.000098-0.00027), higher than the plagioclase  $^{36}\text{Ar}/^{37}\text{Ar}$  AI cut of value of < 0.00006 (Baksi, 2007), and thus indicating the presence of altered material. Despite this, sample DR62-2 yields a statistically valid plateau age of 84.2 ± 1.2 Ma (2σ; MSWD = 1.3; P = 0.24; 57.1%  $^{39}\text{Ar}$ ). However, an inverse isochron plot of the plateau steps yields a statistically invalid inverse isochron age of 84.2 ± 2.0 Ma (95% conf.; MSWD = 5.7; P = 0.00; initial  $^{40}\text{Ar}/^{36}\text{Ar} = 295.5 \pm 1.6$ ). This ~84 Ma age is confirmed by another plagioclase sample from the same dredging site (SO233 DR62), which yields a statistically valid plateau age of 83.85 ± 0.48 Ma (sample DR62-1; 2σ; MSWD = 1.4; P = 0.21; 52.1% of  $^{39}\text{Ar}$ ). We assume that both samples are derived from the same rock unit and thus calculated a combined weighted mean of the two plateau ages of 83.90 ± 0.45 Ma (2σ; MSWD = 0.29, P = 0.59).

Plagioclase/K-feldspar mixed sample SO233 DR84-2 yields a disturbed age spectrum, but yields a statistically invalid pseudo-plateau age of 109.0 ± 1.0 Ma (95% conf.; MSWD = 3.8; P = 0.000; 48%  $^{39}\text{Ar}$ ), and a statistically invalid inverse isochron age of 109.1 ± 2.5 Ma (95% conf.; MSWD 3.3; P = 0.001; initial  $^{40}\text{Ar}/^{36}\text{Ar} = 294 \pm 20$ ). The

statistically invalid pseudo-plateau age of sample DR84-2 should be treated with some caution.

$^{40}\text{Ar}/^{39}\text{Ar}$  step-heating analyses on a plagioclase separate from dredge location SO234 DR-4 (sample DR4-1) yields a statistically invalid plateau age of  $91.34 \pm 0.34$  Ma ( $2\sigma$ ; MSWD = 2.2;  $P = 0.032$ ; 66.6 %  $^{39}\text{Ar}$ ), and a statistically invalid inverse isochron age of  $91.24 \pm 0.57$  Ma (95% conf.; MSWD = 8.4;  $P = 0.00$ ; initial  $^{40}\text{Ar}/^{36}\text{Ar} = 297.1 \pm 3.1$ ). The  $^{40}\text{Ar}/^{39}\text{Ar}$  plateau age of sample SO234 DR4-1 of  $91.34 \pm 0.4$  Ma ( $2\sigma$ ) should be treated with some caution.

However, the basaltic glass step-heating analysis of site SO234 DR6 (sample DR6-1), is located ~30 km east of site SO234 DR4, yields a similar age to sample SO234 DR4-1, with a statistically valid plateau age of  $89.33 \pm 0.20$  Ma (MSWD = 0.79;  $P = 0.69$ ; 87.4 %  $^{39}\text{Ar}$ ). Low  $^{36}\text{Ar}/^{39}\text{Ar}$  AI values indicate the degassing of fresh basaltic material for all the plateau steps. The plateau age is confirmed by a statistically valid inverse isochron age of  $89.01 \pm 0.27$  (95% conf.; MSWD = 0.61;  $P = 0.86$ ; initial  $^{40}\text{Ar}/^{36}\text{Ar} = 491 \pm 310$ ).

## ***Geochemistry***

### *Major elements*

Whole rock major element analysis of sample powders were carried out on fused pellets at the Institute of Mineralogy and Petrography at the University of Hamburg by X-ray Fluorescence Analysis (XRF, Magix Pro PW 2540). Reference materials JGB-1, JB-3, JB-2, JA-3, JG3 and JG-2 were determined along with the samples and the accuracy of the standards lies within 3% of the reference values from Govindaraju (1994) for most elements. At element concentrations significantly below 1 wt. % larger deviations from the suggested values are observed (see Appendix D).

The mounted glass shards were analyzed with a JEOL JXA 8200 wavelength dispersive microprobe at GEOMAR (Kiel, Germany) using a defocused 5 µm electron beam, 15 kV acceleration voltage and 6 nA beam current. The instrument was calibrated using basaltic reference glasses USNM 111240/52 VG-2. The reported data in Appendix B represent average compositions obtained from 10 analyses.

### *Trace elements*

Trace element concentrations were measured by inductively coupled plasma mass spectrometry (ICP-MS) at the Institute of Geosciences, Christian-Albrechts-University of Kiel, using an AGILENT 7500cs ICP-MS. 100 mg of powder for each sample was dissolved by pressure digestion and analyzed following the method of Garbe-Schönberg (1993). International rock standards BHVO-2 and BIR-1 were run along with the samples and for most elements agree within 5% of the GeoReM reference values (<http://georem.mpch-mainz.gwdg.de/>). Reproducibility of replicates by means of separate digests are typically better than 2% for standards and samples (Appendix E.).

The trace element concentrations of the glass shards were determined by LA-ICP-MS using an Agilent 7500s quadrupole instrument coupled with a GeoLas Pro 193nm excimer laser system at the Institute of Geosciences, Kiel University. Glass shards were analysed with 60–80  $\mu\text{m}$  laser pits, using a laser energy of 10 J  $\text{cm}^{-2}$  laser energy and a laser frequency of 10 Hz. Sample mounts were mounted in a two-volume ablation cell (Fricker et al., 2011). The ablated sample aerosol was transported using helium as the carrier gas and mixed with argon prior to introduction into the quadrupole mass spectrometer. Each analysis started with 20 s of background analyses and 60 s of sample analyses counting time during laser ablation. The measured intensities were converted to concentrations in the Glitter software by using  $^{43}\text{Ca}$  as an internal standard with Ca concentrations obtained from microprobe analysis. The SRM NIST612 standard was used for initial calibration (Jochum et al., 2011). Matrix correction was applied by using data from KL2-G reference glass (Jochum et al., 2006).

#### *Sr-Nd-Pb-Hf isotope analyses*

Radiogenic isotope analyses were carried out at GEOMAR Helmholtz Centre for Ocean Research Kiel using a Thermo Scientific TRITON+ thermal ionization mass spectrometer (TIMS) for Sr-Nd-Pb and a Nu-Plasma Multi-Collector-ICPMS for Hf analyses, with both instruments operating in static multi-collection mode. Sr, Nd and Pb chemistry was conducted on 100-250 mg whole-rock chips. Prior to dissolution in a 5:1 mixture of concentrated HF and  $\text{HNO}_3$  the samples were leached in 2N HCl at 70°C for one hour and then triple rinsed in 18.2 M $\Omega$  water thereafter. Additional Sr isotope analyses were carried out on 100 mg of leached sample powders (6N HCl at 150 °C for 3 days) to remove possible seawater alteration effects more thoroughly than the mild leaching of chips. Note that fresh glass chips of sample S0233 DR62-2 underwent mild



2N HCl leaching similar to the rock chips. Twenty-three out of 32 samples produced lower  $^{87}\text{Sr}/^{87}\text{Sr}_{\text{Measured}}$  ratios for the leached powders than the chips, while nine samples gave slightly higher values. These observations suggest that leaching of powders in hot 6N HCl does not always remove the seawater-derived imprint. Therefore the lowest  $^{87}\text{Sr}/^{86}\text{Sr}$  obtained in pairs of powder and chips is presumed to be closest to the prime magmatic value and were used for petrogenetic interpretations.

The ion chromatography analyses followed established standard procedures (Hoernle et al., 2008). Nd and Sr ratios were normalized within run to  $^{146}\text{Nd}/^{144}\text{Nd}=0.7219$  and  $^{86}\text{Sr}/^{88}\text{Sr}=0.1194$ , respectively. NBS 987 and LaJolla reference materials were measured 4-6 times for each sample turret. The numerical average obtained for the standards is subtracted from the preferred standard values and the offset value is applied to the sample data. This procedure compensates for long-term machine drift and thereby ensures maximum comparability and quality of data generated at different times. Sample data are reported relative to  $^{87}\text{Sr}/^{86}\text{Sr} = 0.710250 \pm 0.000007$  (n=37; 2SD) for NBS987 and  $^{143}\text{Nd}/^{144}\text{Nd}=0.511850 \pm 0.000005$  (n=23; 2SD external reproducibility) for La Jolla. The Pb double spike (DS) technique of Hoernle et al. (2011) was used to mass bias correct the Pb isotope ratios. DS corrected NBS981 values are  $^{206}\text{Pb}/^{204}\text{Pb} = 16.9413 \pm 0.0020$ ,  $^{207}\text{Pb}/^{204}\text{Pb} = 15.4984 \pm 0.0027$ ,  $^{208}\text{Pb}/^{204}\text{Pb} = 36.7220 \pm 0.0068$ ,  $^{207}\text{Pb}/^{206}\text{Pb} = 0.91483 \pm 0.00006$  and  $^{208}\text{Pb}/^{206}\text{Pb} = 2.16760 \pm 0.00015$  (n=7; 2SD). The total Pb chemistry blanks were below 20 pg and thus considered negligible.

Hf chemistry analyses used 200-300 mg of unleached rock powder and chemical separation followed the procedure of Blichert-Toft et al. (1997). The in-house standard SPEX Hf ICP solution (lot #9), has been calibrated from a  $^{176}\text{Hf}/^{177}\text{Hf}$  ratio of 0.282170 to a JMC457  $^{176}\text{Hf}/^{177}\text{Hf}$  ratio of 0.282163, and was measured every 4<sup>th</sup> sample. The

resulting standard bracketing normalized 2SD external reproducibility of Hf SPEX is  $^{176}\text{Hf}/^{177}\text{Hf}=0.282170 \pm 0.000006$  (n=386; 2SD, 2011-2016) on the NU MCICPMS at GEOMAR.

Two samples were replicated for Sr-Nd-Pb analyses and a single sample was replicated for Hf analyses. The sample analyses have  $^{143}\text{Nd}/^{144}\text{Nd}_{\text{Measured}}$ ,  $^{208}\text{Pb}/^{204}\text{Pb}_{\text{Measured}}$  and,  $^{207}\text{Pb}/^{204}\text{Pb}_{\text{Measured}}$  ratios within 2SD errors of the standards. As expected, the sample  $^{87}\text{Sr}/^{86}\text{Sr}$  ratios displays slightly higher deviations from standard reproducibility in one replicate and the applied leaching techniques. Finally  $^{206}\text{Pb}/^{204}\text{Pb}$  was reproduced slightly outside 2SD of NBS981 in a single sample. Both observations reflect inhomogeneous distribution of seawater alteration, namely exchange with seawater derived Sr and uptake of seawater-derived U but they do not affect the overall scientific interpretations. (see Appendix B for details).

**Table 1: Composition of the components used in the mixing models**

Mixing Component	Elan Bank	FOZO Comoros	90%FOZO-10%Elan Bank	Low- $\mu$ Gough-type	High- $\mu$ Gough-type
Sr	159	799	735	428	767
Nd	80.0	55.1	57.6	32.1	45.5
Hf	16.70	7.47	8.39	5.29	6.79
Pb	25.8	3.1	5.3	3.1	4.4
$^{206}\text{Pb}/^{204}\text{Pb}_{60\text{Ma}}$	18.46	20.18	19.35	17.37	18.18
$^{207}\text{Pb}/^{204}\text{Pb}_{60\text{Ma}}$	<i>15.81</i>	15.67	15.74	15.42	15.58
$^{208}\text{Pb}/^{204}\text{Pb}_{60\text{Ma}}$	39.78	39.89	39.84	37.88	38.78
$^{87}\text{Sr}/^{86}\text{Sr}_{60\text{Ma}}$	0.73159	0.70310	0.70372	0.70563	
$^{143}\text{Nd}/^{144}\text{Nd}_{60\text{Ma}}$	<i>0.51213</i>	0.51280	0.51271	0.51227	
$^{176}\text{Hf}/^{177}\text{Hf}_{60\text{Ma}}$	0.28223	0.28300	0.28285	0.28268	

The composition of the Elan Bank samples is an average value from gneisses, sandstones and granitoids found at the Elan Bank site, reported by Ingle et al. (2002) (shown in italics) and Nobre Silva et al. (2013) (shown as normal text). Trace element concentrations and Hf-isotope ratios from FOZO-component is the average composition from FOZO-type lavas defined by Stracke et al. (2005) and Pb isotope ratios (PN12F; Pelleter et al., 2014) and Sr-Nd isotope ratios (G18A; Class and Goldstein, 1997) are from the Comoros island. The trace element concentrations of the Gough-type components are the average composition of Gough-type lavas from the Walvis Ridge (low- $\mu$ ) and from the Guyot Province (high- $\mu$ ). The isotope ratios of the low- $\mu$  components represent the most unradiogenic composition from samples S0233 DR84-2 and CH19 DR4-1 (Hoernle et al., 2015), and the low- $\mu$  component is represented by sample S0233 DR3-1 (Hoernle et al., 2015).

## Figures

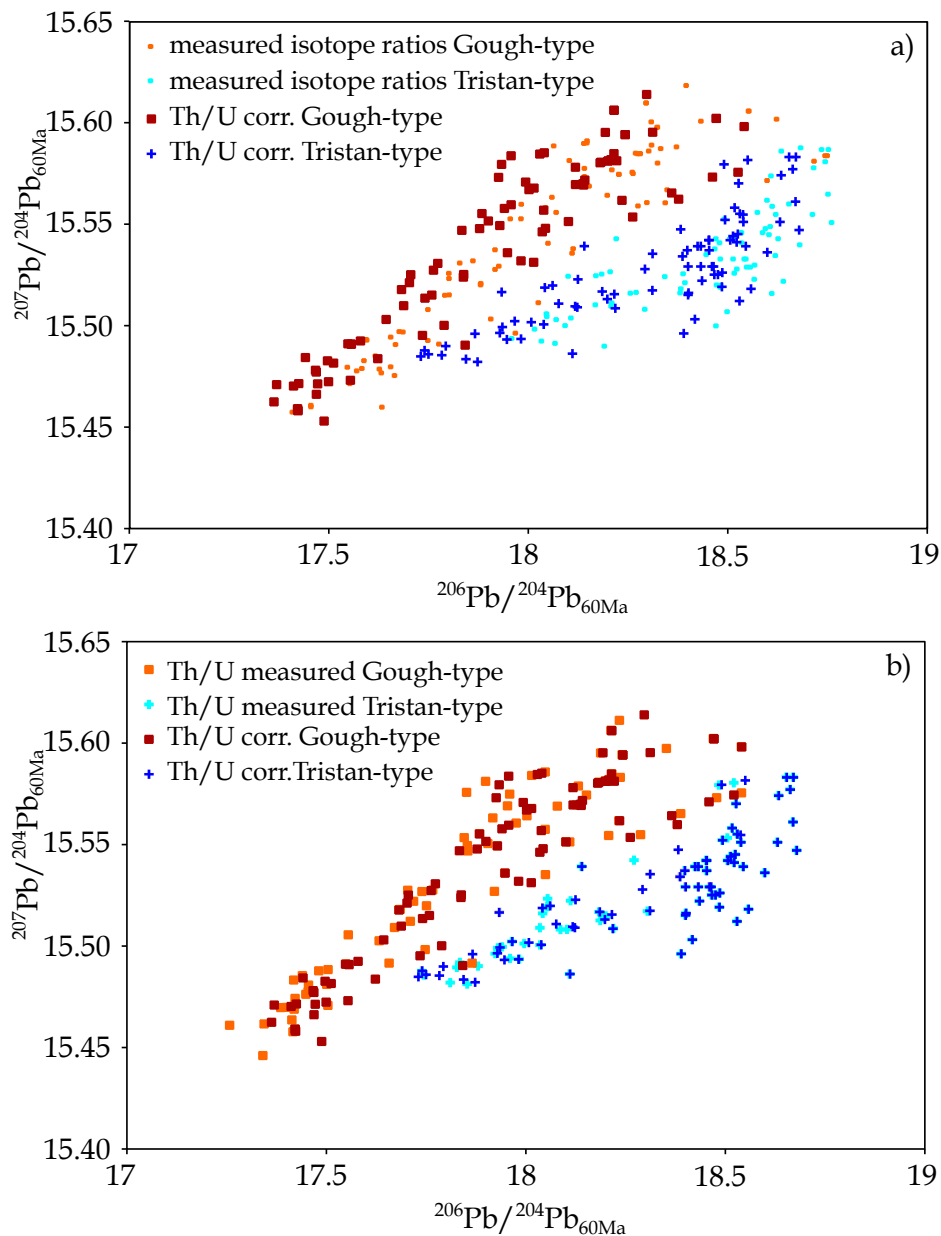


**Figure 1:** Illustration of the different methods used for the age correction of the sample data. In a) the measured isotope ratios are compared to the initial isotope ratios calculated with normalized Th/U (4.7) ratios, following age projection to 60 Ma using proposed source parent/daughter ratios for EM I (Willbold and Stracke, 2006). b) This plot shows the measured and normalized Th/U ratios, which are used for the calculation of the initial isotopes and age projection to 60 Ma.

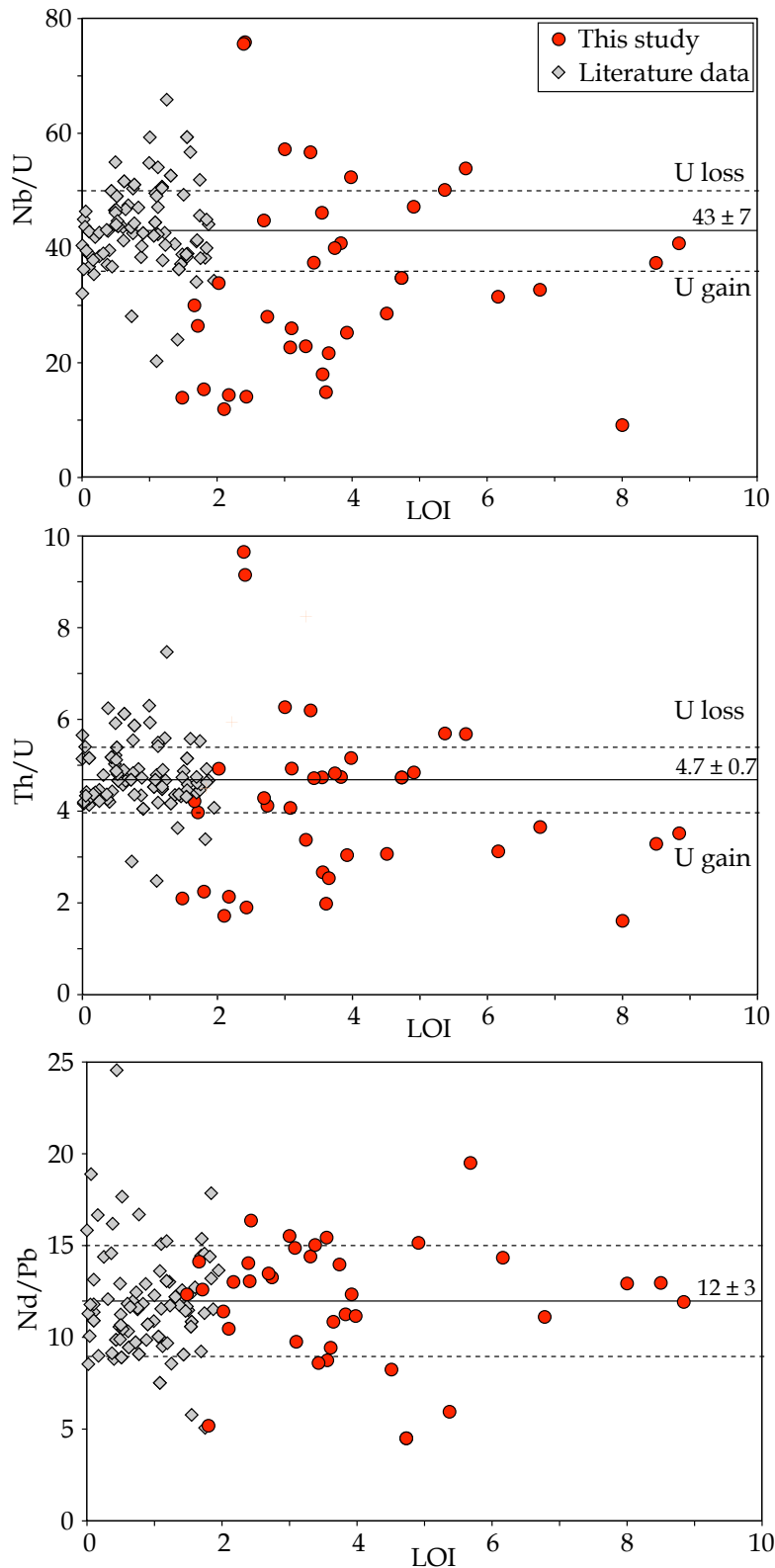


**Figure 2:** Comparison of Nb/U, Th/U and Nd/Pb ratios of the fresh lavas of the Tristan-Gough hotspot track (LOI < 2 wt. %) and our sample collection. The error on the average ratios of the fresh Tristan-Gough lavas along the entire track is 1SD.

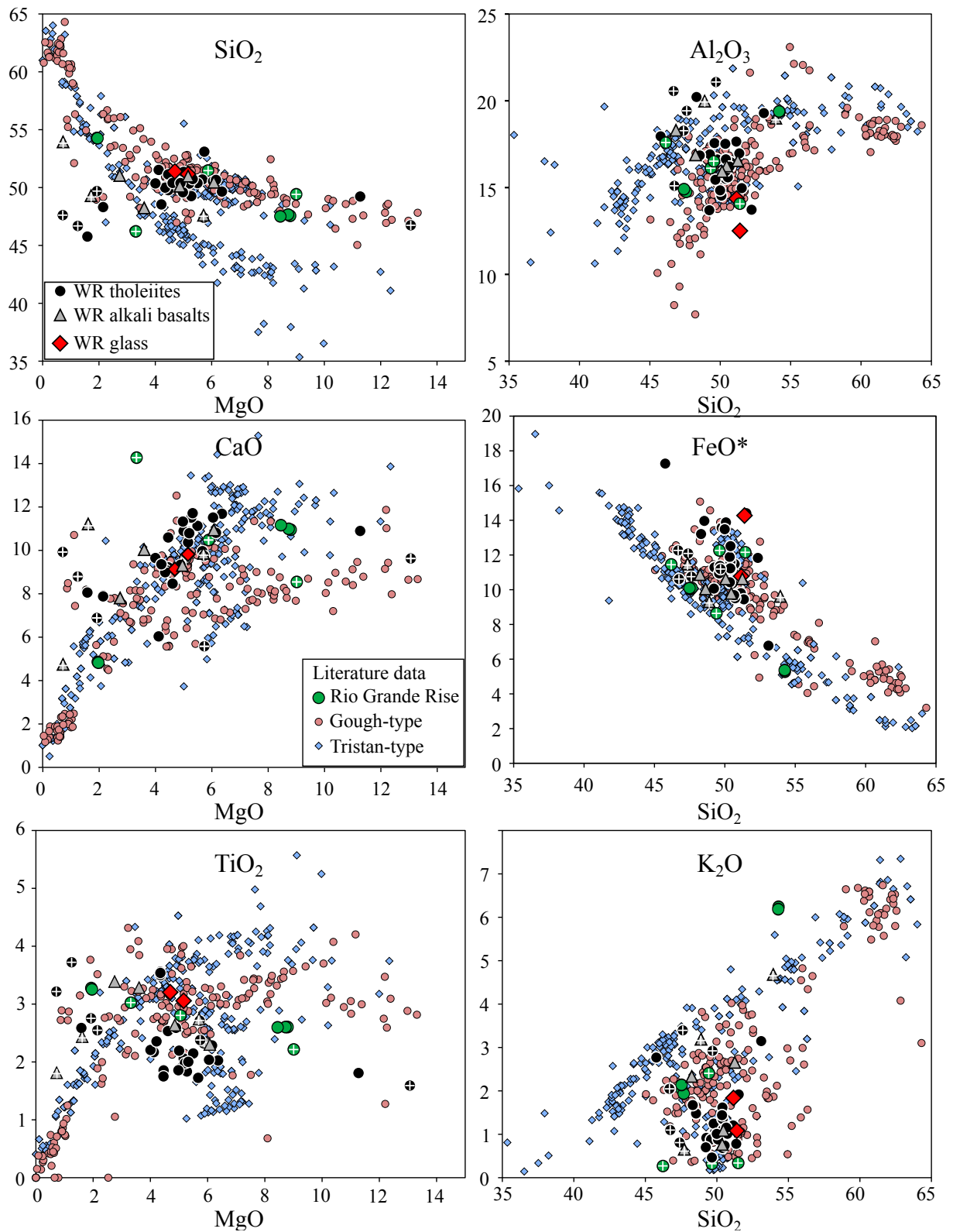


**Figure 3:** Major element plots of our samples compared to lavas from the Rio Grande Rise and from the entire Tristan-Gough hotspot track divided in Gough-type and Tristan-type compositions. Note that samples with LOI values of > 3.96 are marked with a white cross through the existing sample symbols. WR = whole rock.

## References

- Baksi, A. K., 2007, A quantitative tool for detecting alteration in undisturbed rocks and minerals—I: Water, chemical weathering, and atmospheric argon: *Geological Society of America Special Papers*, v. 430, p. 285-303.
- Blichert-Toft, J., Chauvel, C., and Albarède, F., 1997, Separation of Hf and Lu for high-precision isotope analysis of rock samples by magnetic sector-multiple collector ICP-MS: *Contributions to Mineralogy and Petrology*, v. 127, no. 3, p. 248-260.
- Class, C., and Goldstein, S. L., 1997, Plume-lithosphere interactions in the ocean basins: constraints from the source mineralogy: *Earth and Planetary Science Letters*, v. 150, no. 3, p. 245-260.
- Fricke, M. B., Kutscher, D., Aeschlimann, B., Frommer, J., Dietiker, R., Bettmer, J., and Günther, D., 2011, High spatial resolution trace element analysis by LA-ICP-MS using a novel ablation cell for multiple or large samples: *International Journal of Mass Spectrometry*, v. 307, no. 1, p. 39-45.
- Garbe-Schönberg, C.-D., 1993, Simultaneous Determination of 37 Trace-Elements in 28 International Rock Standards by ICP-MS: *Geostandards Newsletter*, v. 17, no. 1, p. 81-97.
- Govindaraju, K., 1994, Compilation of Working Values and Sample Description for 383 Geostandards: *Geostandards Newsletter*, v. 18, no. 2, p. 331-331.
- Hoernle, K., Abt, D. L., Fischer, K. M., Nichols, H., Hauff, F., Abers, G. A., van den Bogaard, P., Heydolph, K., Alvarado, G., Protti, M., and Strauch, W., 2008, Arc-parallel flow in the mantle wedge beneath Costa Rica and Nicaragua: *Nature*, v. 451, no. 7182, p. 1094-1097.
- Hoernle, K., Rohde, J., Hauff, F., Garbe-Schönberg, D., Homrighausen, S., Werner, R., and Morgan, J. P., 2015, How and when plume zonation appeared during the 132 Myr evolution of the Tristan Hotspot: *Nature Communication*, v. 6, p. 10.1038/ncomms8799.
- Hoernle, K., Werner, R., and Lüter, C., 2014, RV SONNE Fahrtbericht/Cruise Report SO233 WALVIS II, 14.05-21.06. 2014, Cape Town, South Africa-Walvis Bay, Namibia: GEOMAR Report v. no. 23 (N. Ser.), p. 53 pp + Appendices.
- Ingle, S., Weis, D., and Frey, F. A., 2002, Indian Continental Crust Recovered from Elan Bank, Kerguelen Plateau (ODP Leg 183, Site 1137): *Journal of Petrology*, v. 43, no. 7, p. 1241-1257.
- Jochum, K. P., Stoll, B., Herwig, K., Willbold, M., Hofmann, A. W., Amini, M., Aarburg, S., Abouchami, W., Hellebrand, E., Mocek, B., Raczek, I., Stracke, A., Alard, O., Bouman, C., Becker, S., Dostal, M., Bräse, H., Klemm, R., de Bruin, D., Canil, D., Cornell, D., de Hoog, C.-J., Dalpé, C., Danyushevsky, L., Eisenhauer, A., Gao, Y., Snow, J. E., Groschopf, N., Günther, D., Latkoczy, C., Guillong, M., Hauri, E. H., Hvalby, H. E., Lahaye, Y., Horz, K., Jacob, D. E., Kasemann, S. A., Kent, A. J. R., Ludwig, T., Zack, T., Mason, P. R. D., Meixner, A., Rosner, M., Misawa, K., Nash, B. P., Pfänder, J. R., Premo, W. R., Sun, W. D., Tiepolo, M., Vannucci, R., Vennemann, T., Wayne, D., and Woodhead, J. D., 2006, MPI-DING reference glasses for in situ microanalysis: New reference values for element concentrations and isotope ratios: *Geochemistry, Geophysics, Geosystems*, v. 7, no. 2.
- Jochum, K. P., Weis, U., Stoll, B., Kuzmin, D., Yang, Q., Raczek, I., Jacob, D. E., Stracke, A., Birbaum, K., Frick, D. A., Günther, D., and Enzweiler, J., 2011, Determination of Reference Values for NIST SRM 610–617 Glasses Following ISO Guidelines: *Geostandards and Geoanalytical Research*, v. 35, no. 4, p. 397-429.
- Lanphere, M. A., and Dalrymple, G. B., 1978, The use of  $^{40}\text{Ar}/^{39}\text{Ar}$  data in evaluation of disturbed K-Ar systems: *Geological Survey Open-File Report 78-701*, p. 141-148.
- Lanphere, M. A., and Dalrymple, G. B., 2000, First-principles calibration of  $^{38}\text{Ar}$  tracers: Implications for the ages of  $^{40}\text{Ar}/^{38}\text{Ar}$  fluence monitors: *US Geological Survey Professional Paper*, no. 1621, p. 1-10.
- Ludwig, K. R., 2011, Users manual for Isoplot 4.15: A geochronological toolkit for Microsoft Excel: *Special Publication 4*, Berkeley, p. 77.
- Nobre Silva, I. G., Weis, D., Scoates, J. S., and Barling, J., 2013, The Ninetyeast Ridge and its Relation to the Kerguelen, Amsterdam and St. Paul Hotspots in the Indian Ocean: *Journal of Petrology*, v. 54, no. 6, p. 1177-1210.
- Pelleter, A.-A., Caroff, M., Cordier, C., Bachelery, P., Nehlig, P., Debeuf, D., and Arnaud, N., 2014, Melilite-bearing lavas in Mayotte (France): An insight into the mantle source below the Comores: *Lithos*, v. 208-209, no. Supplement C, p. 281-297.
- Renne, P. R., Deino, A. L., Hilgen, F. J., Kuiper, K. F., Mark, D. F., Mitchell, W. S., Morgan, L. E., Mundil, R., and Smit, J., 2013, Time Scales of Critical Events Around the Cretaceous-Paleogene Boundary: *Science*, v. 339, no. 6120, p. 684-687.
- Renne, P. R., Sprain, C. J., Richards, M. A., Self, S., Vanderkluysen, L. Ø., and Pande, K., 2015, State shift in Deccan volcanism at the Cretaceous-Paleogene boundary, possibly induced by impact: *Science*, v. 350, no. 6256, p. 76-78.

- Steiger, R. H., and Jäger, E., 1977, Subcommittee on geochronology: Convention on the use of decay constants in geo- and cosmochronology: *Earth and Planetary Science Letters*, v. 36, no. 3, p. 359-362.
- Stracke, A., Hofmann, A. W., and Hart, S. R., 2005, FOZO, HIMU, and the rest of the mantle zoo: *Geochemistry, Geophysics, Geosystems*, v. 6, no. 5, p. Q05007.
- van den Bogaard, P., 2013, The origin of the Canary Island Seamount Province - New ages of old seamounts: *Scientific Reports*, v. 3, p. 2107.
- Werner, R., and Wagner, H.-J., 2014, RV SONNE Fahrtbericht/Cruise Report SO234/1 "SPACES": Science or the Assessment of Complex Earth System Processes, 22.06.-06.07. 2014, Walvis Bay/Namibia-Durban/South Africa: GEOMAR Report v. no. 17 (N. Ser.), p. 29 pp + Appendices.
- Willbold, M., and Stracke, A., 2006, Trace element composition of mantle end-members: Implications for recycling of oceanic and upper and lower continental crust: *Geochemistry, Geophysics, Geosystems*, v. 7, no. 4, p. Q04004.



Appendix B: <sup>40</sup>Ar/<sup>39</sup>Ar age, major element, trace element and isotope data

Sample	Rock type	Ar/ <sup>39</sup> Ar Age (Ma)	Lat. (°)	Long. (°)	Location	Method	SiO <sub>2</sub> <sup>a</sup> (wt.%)	TiO <sub>2</sub> <sup>a</sup> (wt.%)	Al <sub>2</sub> O <sub>3</sub> <sup>a</sup> (wt.%)	FeO <sup>a</sup> (wt.%)	MnO <sup>a</sup> (wt.%)	MgO <sup>a</sup> (wt.%)	CaO <sup>a</sup> (wt.%)	Na <sub>2</sub> O <sup>a</sup> (wt.%)	K <sub>2</sub> O <sup>a</sup> (wt.%)	P <sub>2</sub> O <sub>5</sub> <sup>a</sup> (wt.%)	SO <sub>4</sub> <sup>a</sup> (wt.%)	L.O.I. (wt.%)	Sum (wt.%)	
<b>Western Margin</b>																				
SO233 DR28-1	Basalt	77.2	-26.31	3.05	Westward rifted seamount, lower slope	XRF <sup>1</sup>	50.72	2.14	14.73	15.76	4.05	4.40	9.04	4.29	1.89	0.29	na	3.08	100.02	
SO233 DR28-3	Basalt	77.2	-26.31	3.05	Westward rifted seamount, lower slope	XRF <sup>2</sup>	49.04	1.83	16.38	14.86	0.15	5.40	2.80	1.23	0.25	0.25	na	0.01	3.31	100.23
SO233 DR29-1	Basalt	77.2	-26.28	3.04	inslope of DR28	XRF <sup>1</sup>	50.06	1.70	16.02	12.60	0.12	5.60	9.84	2.66	1.12	0.26	na	0.13	3.56	99.83
SO233 DR29-6	Basalt	77.2	-26.28	3.04	inslope of DR28	XRF <sup>2</sup>	44.90	2.54	17.61	18.83	0.06	1.56	7.90	2.77	2.72	1.11	na	0.00	99.70	
SO233 DR32-1	Basalt	76.9	-26.49	3.15	counterpart at the margin of the ridge of the rifted seamount, upper slope	XRF <sup>1</sup>	49.79	2.03	16.44	12.25	0.11	5.10	10.24	2.68	1.08	0.27	na	0.13	3.61	100.46
SO233 DR32-2	Basalt	76.9	-26.49	3.15	counterpart at the margin of the ridge of the rifted seamount, upper slope	XRF <sup>2</sup>	50.59	1.73	17.46	10.78	0.09	4.41	10.48	3.08	1.19	0.20	na	0.00	1.80	99.99
SO233 DR35-1	Basalt	75.4	-26.22	3.32	inslope of DR32	XRF <sup>1</sup>	50.82	2.12	16.79	10.39	0.12	4.95	10.28	2.92	0.77	0.28	na	0.00	2.17	99.30
SO233 DR35-3	Basalt	75.4	-26.22	3.32	inslope of DR32	XRF <sup>2</sup>	49.74	2.12	15.31	12.72	0.16	5.43	10.99	2.62	0.68	0.24	na	0.00	1.71	99.37
SO233 DR35-4	Basalt	75.4	-26.22	3.32	inslope of DR32	XRF <sup>3</sup>	48.65	1.95	16.70	12.39	0.15	5.21	11.37	2.45	0.91	0.31	na	0.00	2.24	99.84
SO233 DR35-5	Basalt	75.4	-26.22	3.32	inslope of DR32	XRF <sup>4</sup>	49.69	1.95	15.53	13.04	0.16	5.14	10.65	2.74	0.79	0.25	na	0.00	1.66	99.87
SO233 DR35-10	Basalt	75.4	-26.22	3.32	inslope of DR32	XRF <sup>5</sup>	50.20	1.98	16.29	10.46	0.13	5.27	11.59	2.84	1.00	0.23	na	0.00	2.10	100.02
SO233 DR35-12	Basalt	75.4	-26.22	3.32	inslope of DR32	XRF <sup>6</sup>	49.03	2.00	15.26	12.48	0.18	6.29	11.54	2.53	0.46	0.23	na	0.00	2.02	100.02
SO233 DR35-14	Basalt	75.4	-26.22	3.32	inslope of DR32	XRF <sup>7</sup>	49.96	2.01	15.41	11.38	0.16	5.98	11.38	2.23	0.73	0.24	na	0.00	1.48	99.79
SO233 DR84-1	Basalt	109.0	-20.35	7.64	lower part of the western margin	XRF <sup>1</sup>	52.70	2.36	19.14	7.48	0.34	5.70	5.54	3.28	3.12	0.34	na	0.00	4.73	99.17
SO233 DR84-1_Rep	Basalt	109.0	-20.35	7.64	lower part of the western margin	XRF <sup>2</sup>	51.72	1.91	18.60	10.41	0.09	5.23	5.06	3.91	2.85	0.23	na	0.00	4.30	99.78
<b>Eastern Margin</b>																				
SO233 DR15-1	Basalt	70.8	-28.60	3.14	trough-like structure	XRF <sup>1</sup>	49.00	1.83	12.35	12.01	0.11	4.92	11.19	2.47	0.87	0.25	0.01	2.43	100.02	
SO233 DR16-1	Alkali basalt	72.4	-28.43	3.68	lower part of a cove	XRF <sup>2</sup>	46.76	2.68	18.03	13.26	0.15	5.65	9.63	4.63	0.80	0.58	0.12	5.37	99.56	
SO233 DR16-1B	Basalt	71.0	-28.44	3.66	inslope of DR16	XRF <sup>3</sup>	46.06	3.67	20.28	13.45	0.07	1.23	8.68	3.44	2.02	1.11	0.25	4.51	98.95	
SO233 DR16-1A	Trachandite	70.8	-28.44	3.66	inslope of DR16	XRF <sup>4</sup>	46.19	1.57	14.92	11.66	0.17	12.91	9.51	1.67	1.08	0.30	0.18	6.78	99.14	
SO233 DR36-1A	Basalt	70.6	-26.85	4.94	Middle of the bank of the Walvis Ridge	XRF <sup>1</sup>	47.05	3.18	19.19	11.81	0.12	0.71	9.91	3.67	3.35	1.10	0.04	6.16	100.21	
SO233 DR36-1B	Basalt	70.6	-26.85	4.94	Middle of the bank of the Walvis Ridge	XRF <sup>2</sup>	47.61	2.51	19.92	14.47	0.10	2.12	7.77	2.98	1.65	0.88	na	0.00	2.41	100.43
SO233 DR36-3	Basalt	80.0	-26.51	5.19	Southeastern wall of the NW-SE trending Graben southwest of the Walvis Ridge	XRF <sup>1</sup>	49.32	3.45	14.31	15.19	0.19	4.38	8.98	2.94	0.87	0.47	na	0.00	2.39	99.93
SO233 DR36-20	Basalt	80.0	-26.51	5.19	Southeastern wall of the NW-SE trending Graben southwest of the Walvis Ridge	XRF <sup>2</sup>	49.25	3.49	14.62	14.76	0.19	4.39	8.96	3.04	0.89	0.50	na	0.00	3.83	99.87
SO233 DR36-21	Basalt	80.0	-26.51	5.19	Southeastern wall of the NW-SE trending Graben southwest of the Walvis Ridge	XRF <sup>3</sup>	49.71	2.50	16.40	13.21	0.08	4.55	8.35	3.01	1.33	0.35	0.02	3.74	99.55	
SO233 DR40-1	Trachandite	91.7	-26.82	5.61	Seamount west to the eastern margin of the Walvis Bank	XRF <sup>1</sup>	49.77	2.55	15.75	12.23	0.10	4.83	9.22	2.92	1.60	0.92	0.02	3.99	99.70	
SO233 DR41-1	Alkali basalt	82.7	-26.84	5.67	inslope of DR40	XRF <sup>2</sup>	53.27	1.79	18.79	10.57	0.14	0.72	4.70	4.21	4.63	1.06	0.02	8.84	100.10	
SO233 DR42-1	Alkali basalt	91.3	-26.84	5.67	inslope of DR40	XRF <sup>3</sup>	48.20	2.41	19.77	10.24	0.05	1.40	11.10	2.47	3.16	0.81	0.06	8.50	99.19	
SO233 DR42-2	Basalt	76.8	-26.77	4.95	Southeastern wall of the NW-SE trending Graben southwest of the Walvis Ridge	XRF <sup>1</sup>	49.02	2.73	20.92	12.48	0.04	1.80	15.00	2.26	2.69	0.69	0.11	5.69	99.60	
SO233 DR42-3	Basalt	76.8	-26.77	4.95	Southeastern wall of the NW-SE trending Graben southwest of the Walvis Ridge	XRF <sup>2</sup>	49.65	1.76	13.52	11.06	0.13	11.15	10.28	2.93	2.89	0.26	0.44	0.01	2.65	99.92
SO233 DR62-1	Alkali basalt	82.9	-25.85	6.73	Southeastern wall of the NW-SE trending Graben southwest of the Walvis Ridge	XRF <sup>1</sup>	49.78	2.18	17.22	11.02	0.09	3.48	9.74	3.21	1.92	0.49	0.00	2.69	100.23	
SO233 DR62-2	Basalt	82.9	-25.85	6.73	Southeastern wall of the NW-SE trending Graben southwest of the Walvis Ridge	XRF <sup>2</sup>	51.55	2.73	13.03	13.03	0.21	5.09	2.60	0.97	0.36	0.01	1.49	100.22		
SO233 DR62-2_LA	Basalt	82.9	-25.85	6.73	Eastern margin of the Walvis Bank	XRF <sup>3</sup>	49.59	3.10	12.93	15.03	0.23	4.02	9.09	3.00	1.07	0.39	0.01	1.92	99.62	
SO233 DR64-1	Basalt	87.3	-25.87	7.57	Eastern margin of the Walvis Bank	XRF <sup>1</sup>	47.80	2.32	16.53	15.28	0.12	4.13	9.22	2.63	1.46	0.43	na	0.00	3.92	100.93
SO233 DR66-2	Basalt	96.7	-22.72	7.57	Rift arm at the eastern margin of the Walvis Ridge	XRF <sup>2</sup>	47.40	2.40	16.53	15.28	0.12	4.13	9.22	2.63	1.46	0.43	na	0.00	3.58	99.72
SO233 DR66-3	Basalt	96.7	-22.72	7.57	Rift arm at the eastern margin of the Walvis Ridge	XRF <sup>3</sup>	50.12	2.40	16.94	10.95	0.12	6.09	10.69	2.56	1.14	0.34	na	0.00	3.00	99.63
SO234 DR4-1	Alkali basalt	89.3	-22.08	8.38	Seamount east of DR66	XRF <sup>1</sup>	49.91	2.48	16.97	10.76	0.12	6.01	10.82	2.62	1.08	0.33	0.01	3.10	100.09	
SO234 DR6-1	Alkali basalt	89.3	-22.10	8.10	Cove between DR66 and SO233 DR84	XRF <sup>2</sup>	50.55	3.02	14.20	11.84	0.18	5.10	9.70	3.03	1.82	0.36	0.00	1.00	100.09	
SO234 DR6-1	Alkali basalt	89.3	-22.10	8.10	Cove between DR66 and SO233 DR84	XRF <sup>3</sup>	47.66	2.68	16.03	13.26	0.15	5.63	9.63	2.48	0.80	0.00	4.91	100.13		
<b>Guyot Province</b>																				
SO233 DR4-1	Alkali basalt	59.2	-32.93	1.40	Guyot	XRF <sup>1</sup>	47.66	3.24	16.68	11.93	0.33	3.36	9.91	3.32	2.30	1.06	0.08	3.43	99.24	
SO233 DR6-1	Alkali basalt	50.7	-33.27	-0.32	Guyot	XRF <sup>2</sup>	50.65	3.53	16.35	11.67	0.20	2.72	7.71	3.67	2.62	1.05	0.04	3.53	99.65	

<sup>1</sup> recalculated to 100% on a volatile free basis.  
<sup>2</sup> Major elements by electron microprobe from GEOMAR Kiel and trace elements by LA-ICP-MS by university Kiel  
<sup>3</sup> Mineralogisch-Petrographisches Institut, Universität, Hamburg  
<sup>4</sup> Trace element analysis by ICP-MS from the Institute of Oceanography, Christian-Albrechts University of Kiel  
<sup>5</sup> Trace element analysis by ICP-MS from the Institute of Oceanography, Christian-Albrechts University of Kiel  
<sup>6</sup> leached powder in 6N HCl at 150°C for 72 hours and thereafter reprecipitated at 18000 H<sub>2</sub>O  
<sup>7</sup> leached chips; 2h at 70°C for 1 hour and thereafter triple rinsed in 18MΩ H<sub>2</sub>O  
<sup>8</sup> major trace and Sr-Nd-Pb-Hf data published in Heimann et al. (2015)  
<sup>9</sup> age calculated for the last significant diatom.  
 Age in italic from this study  
 Age in normal fonts calculated after age progression  
 Hf ratios measure on a VG Atom MG-CPMS  
 BDJ = Below detection limit  
 na = not analyzed  
 Lit. = geochemical data from Heimann et al. (2015); How and when plume zonation appeared during the 132 Myr evolution of the Tristan Hotspot; Nature Communication  
 Calculated age = 0.033 \* Distance (km) + 0.37  
 Derivation = Ar/<sup>39</sup>Ar Age - Calculated Age

Sample	Method	Li	Sr	V	Sr	Rb	Sr	V	Zr	Nh	Ba	La	Ce	Pr	Nd	Sm	Eu	Gd	Tb	Dy	Ho	Er	Tm	Yb	Lu	Hf	Ta	Ph	Th	U		
		ppm	ppm	ppm	ppm	ppm	ppm	ppm	ppm	ppm	ppm	ppm	ppm	ppm	ppm	ppm	ppm	ppm	ppm	ppm	ppm	ppm	ppm	ppm	ppm	ppm	ppm	ppm	ppm	ppm		
Western Margin																																
S0233DR28-2	ICP-MS	31.2	40.6	37.4	12	41.6	28.9	70	146	21.8	32.9	27.6	33.5	27.6	33.5	27.6	33.5	27.6	33.5	27.6	33.5	27.6	33.5	27.6	33.5	27.6	33.5	27.6	33.5	27.6	33.5	
S0233DR28-3	ICP-MS	39.6	51.6	41.7	38	37.9	48.6	71	152	22.8	40.7	21.8	27.1	33.3	23.6	6.03	1.68	4.82	1.83	7.55	1.55	4.29	6.61	4.11	0.617	4.33	0.878	1.59	2.54	0.624		
S0233DR29-1	ICP-MS	27.7	44.1	33.5	114	37.9	48.6	61	129	22.8	40.7	21.8	27.1	33.3	23.6	6.03	1.68	4.82	1.83	7.55	1.55	4.29	6.61	4.11	0.617	4.33	0.878	1.59	2.54	0.624		
S0233DR29-6	ICP-MS	18.2	51.4	41.7	68	34.1	44.1	134	175	19.1	33.6	27.6	33.5	27.6	33.5	27.6	33.5	27.6	33.5	27.6	33.5	27.6	33.5	27.6	33.5	27.6	33.5	27.6	33.5	27.6	33.5	
S0233DR32-1	ICP-MS	25.7	43.7	28.0	175	28.9	51.9	127	105	20.3	18.5	29.3	28.5	31.9	12.7	13.8	10.8	13.7	10.8	13.7	10.8	13.7	10.8	13.7	10.8	13.7	10.8	13.7	10.8	13.7	10.8	
S0233DR32-2	ICP-MS	15.6	41.2	30.0	163	30.3	33.3	42	85	22.2	23.5	26.3	21.2	33.5	26.3	21.2	33.5	26.3	21.2	33.5	26.3	21.2	33.5	26.3	21.2	33.5	26.3	21.2	33.5	26.3	21.2	
S0233DR35-1	ICP-MS	21.3	40.3	28.9	221	34.0	56.6	132	108	21.1	11.9	29.5	36.8	16.6	10.5	13.0	16.9	33.9	4.31	20.2	5.42	18.5	6.02	10.06	6.26	12.5	3.33	4.82	3.13	0.463	4.22	
S0233DR35-4	ICP-MS	14.5	46.1	33.8	129	34.0	51.8	118	102	21.0	14.1	23.7	31.0	17.0	10.8	10.6	12.6	33.5	4.31	20.2	5.42	18.5	6.02	10.06	6.26	12.5	3.33	4.82	3.13	0.463		
S0233DR35-5	ICP-MS	29.8	45.3	34.1	275	35.9	55.4	101	118	21.3	18.3	25.9	31.0	18.1	19.1	5.00	1.73	5.68	0.937	5.96	1.19	3.21	4.70	3.03	0.458	3.46	0.547	1.44	1.33	0.322		
S0233DR35-5	ICP-MS	5.7	46.3	34.0	176	33.5	44.9	140	104	20.5	13.9	27.1	31.4	14.1	8.3	11.6	12.6	28.4	4.03	19.2	5.13	1.77	5.74	0.954	5.96	1.19	3.21	4.70	3.03	0.458		
S0233DR35-10	ICP-MS	19.8	43.5	31.1	252	45.6	61.6	81	103	20.6	20.4	27.9	30.6	15.1	9.6	16.9	14.0	31.6	4.31	20.2	5.42	18.5	6.02	10.06	6.26	12.5	3.33	4.82	3.13	0.463		
S0233DR35-12	ICP-MS	24.8	46.6	35.7	260	54.6	76.0	106	111	20.2	7.8	27.1	31.6	14.9	9.6	10.1	14.4	31.9	4.50	20.9	5.43	1.87	6.06	0.983	6.11	1.22	3.24	0.468	2.97	0.442		
S0233DR35-14	ICP-MS	18.2	47.4	32.2	252	43.4	69.0	103	105	20.2	9.8	27.1	33.0	14.7	9.6	15.1	15.0	32.2	4.49	21.1	5.46	1.89	6.14	1.007	6.28	1.26	3.29	0.400	3.15	0.473		
S0233DR44-1	ICP-MS	27.1	26.9	24.8	54	21.2	40.2	112	229.7	21.1	58.5	39.4	28.3	22.4	20.1	45.5	23.2	51.8	6.62	28.6	6.41	2.21	6.29	0.968	5.60	1.07	2.81	0.388	2.42	0.355		
S0233DR44-1	ICP-MS	27.1	26.9	24.8	54	21.2	40.2	112	229.7	21.1	58.5	39.4	28.3	22.4	20.1	45.5	23.2	51.8	6.62	28.6	6.41	2.21	6.29	0.968	5.60	1.07	2.81	0.388	2.42	0.355		
S0233DR44-2	ICP-MS	40.7	25.4	19.9	162	25.1	68.6	56	21.3	19.9	45.9	31.8	20.2	31.8	38.6	5.00	2.20	5.12	1.90	5.04	0.773	4.33	0.729	2.00	2.24	1.75	0.255	3.94	0.881	8.96	2.01	
Eastern Margin																																
S0233DR15-1	ICP-MS	11.7	34.2	30.0	1120	23.0	207.0	104	99	21.3	7.4	33.5	24.7	130	7.9	80	12.0	24.6	4.04	18.8	4.79	1.71	5.07	0.817	4.82	0.93	2.42	0.329	2.06	0.306		
S0233DR16-1	ICP-MS	27.4	29.5	23.3	588	52.1	250.4	53	74	15.8	27.7	38.7	20.6	99	29.2	51.4	27.1	49.3	54.5	21.0	41.6	14.3	4.20	0.658	3.90	0.76	2.06	0.291	1.86	0.280	3.13	1.565
S0233DR16-1B	ICP-MS	5.4	17.1	26.9	93	15.8	42.9	74	140	24.0	38.7	60.3	142.6	33.6	46.1	81.1	143.0	108.7	22.78	93.6	16.97	5.03	18.60	2.652	16.02	3.44	9.44	1.200	2.91	1.227	7.24	2.759
S0233DR16-1A	ICP-MS	41.2	25.6	28.5	96	10.5	34.6	64	227	24.0	23.0	28.88	52.6	41.2	51.3	85.8	59.9	121.8	14.66	60.1	12.09	3.89	11.33	1.657	9.44	1.80	4.70	0.556	2.80	0.410	4.58	0.897
S0233DR32-1A	ICP-MS	28.6	34.4	23.8	66	27.4	45.7	73	155	25.4	31.6	50.4	34.2	19.4	23.4	21.8	27.5	57.7	7.70	33.8	7.67	2.65	7.79	1.194	6.90	1.31	3.33	0.456	2.80	0.410	4.58	
S0233DR36-1A	ICP-MS	15.52	38.1	44.6	34	44.3	25.7	64	182	24.5	16.3	37.0	41.5	25.4	20.7	23.2	24.4	59.5	8.10	37.0	9.14	3.04	9.25	1.455	8.45	1.60	4.09	0.552	3.44	0.406		
S0233DR36-3	ICP-MS	119.6	41.7	47.4	35	47.8	29.3	67	222	24.2	17.9	36.1	41.5	25.4	20.7	23.2	24.4	59.5	8.10	37.0	9.14	3.04	9.25	1.455	8.45	1.60	4.09	0.552	3.44	0.406		
S0233DR36-20	ICP-MS	30.2	34.6	27.0	192	37.8	56.0	92	144	21.3	32.5	32.7	29.7	17.7	14.4	15.1	18.1	39.5	54.7	25.1	6.22	2.12	6.53	1.013	8.96	1.14	2.94	0.405	2.46	0.362		
S0233DR36-21	ICP-MS	27.7	42.0	31.9	153	26.5	54.8	119	187	21.3	32.5	32.7	29.7	17.7	14.4	15.1	18.1	39.5	54.7	25.1	6.22	2.12	6.53	1.013	8.96	1.14	2.94	0.405	2.46	0.362		
S0233DR40-1	ICP-MS	19.7	12.4	12.0	45	4.5	25.4	78	151	25.5	21.0	59.7	59.4	50.5	91.7	156.8	89.8	170.5	201.6	76.9	13.77	4.36	12.27	4.36	12.27	4.36	12.27	4.36	12.27	4.36	12.27	
S0233DR41-1	ICP-MS	1.69	32.4	14.9	236	11.3	46.6	95	117	18.0	55.6	59.7	59.4	50.5	91.7	156.8	89.8	170.5	201.6	76.9	13.77	4.36	12.27	4.36	12.27	4.36	12.27	4.36	12.27	4.36	12.27	
S0233DR41-2	ICP-MS	3.59	36.7	19.5	442	15.2	66.4	95	117	18.0	55.6	59.7	59.4	50.5	91.7	156.8	89.8	170.5	201.6	76.9	13.77	4.36	12.27	4.36	12.27	4.36	12.27	4.36	12.27	4.36	12.27	
S0233DR42-1	ICP-MS	7.23	36.2	24.2	1043	44.5	118.0	81	136	15.9	9.0	24.7	23.8	20.0	11.7	11.4	14.5	30.6	41.7	19.7	4.27	1.53	4.46	0.773	4.33	0.84	2.17	0.247	1.65	0.267		
S0233DR42-2	ICP-MS	26.6	32.5	22.4	182	29.2	49.2	139	189	21.7	14.0	42.1	39.0	20.1	19.1	21.7	39.3	50.0	70.1	30.2	6.75	2.23	6.98	0.973	6.39	1.25	3.17	0.452	2.93	0.267		
S0233DR42-3	ICP-MS	3.9	32.0	29.4	115	27.2	70.3	51	127	27.2	30.0	46.9	38.3	21.1	27.0	30.2	39.2	63.7	70.1	30.2	6.75	2.23	6.98	0.973	6.39	1.25	3.17	0.452	2.93	0.267		
S0233DR62-1	ICP-MS	9.3	37.0	44.1	57	42.7	69.7	210	162	23.6	22.5	32.9	40.3	24.6	24.1	33.5	38.2	63.6	60.5	33.9	8.11	2.46	8.46	1.890	7.63	1.49	3.03	0.453	3.79	0.517		
S0233DR62-2	ICP-MS	8.1	37.2	44.1	57	42.7	69.7	210	162	23.6	22.5	32.9	40.3	24.6	24.1	33.5	38.2	63.6	60.5	33.9	8.11	2.46	8.46	1.890	7.63	1.49	3.03	0.453	3.79	0.517		
S0233DR62-2	ICP-MS	8.1	37.2	44.1	57	42.7	69.7	210	162	23.6	22.5	32.9	40.3	24.6	24.1	33.5	38.2	63.6	60.5	33.9	8.11	2.46	8.46	1.890	7.63	1.49	3.03	0.453	3.79	0.517		
S0233DR64-1	ICP-MS	19.0	47.5	39.5	92	35.6	69.3	211	116	23.2	27.1	37.5	39.3	15.5	14.4	18.3	60.5	54.3	24.5	5.94	2.06	6.25	0.897	5.91	1.15	3.01	0.429	3.72	0.445			
S0233DR66-2	ICP-MS	37.0	37.7	27.1	326	33.8	97.9	61	123	19.3	17.4	34.6																				



Appendix C:  $^{40}\text{Ar}/^{39}\text{Ar}$  analytical data

Sample	Material		J value	2 $\sigma$ % error	Mass (mg)																								
S0233 DR4-1	K-feldspar		0,001041	0,138	6,65	Step #	power (W)	$^{40}\text{Ar}/^{39}\text{Ar}$	$^{37}\text{Ar}/^{39}\text{Ar}$	$^{36}\text{Ar}/^{39}\text{Ar}$	$^{39}\text{Ar}/^{39}\text{Ar}$	$^{39}\text{Ar}_k$ (moles)	Ca/K	% $^{40}\text{Ar}_{\text{cum}}$	Cumulative Fraction of $^{39}\text{Ar}$	Age (Ma)	$\pm 2\sigma$ (Ma)	$^{36}\text{Ar}/^{39}\text{Ar}$ AI	P	MSWD	Initial $^{40}\text{Ar}/^{36}\text{Ar}$ (95% conf.)	Inverse isochron age (Ma; 95% conf.)	Steps	P	MSWD	P			
						1	0,8	1970,88	17,10	6,52	1,00E-16	33,92	97,62	0,01	87,10	21,88	0,028106												
						2	1,0	656,52	13,50	2,12	1,67E-16	26,71	95,15	0,03	59,42	8,60	0,009125												
						3	1,2	287,78	12,39	0,87	1,86E-16	24,49	88,85	0,05	59,81	5,08	0,003735												
						4	1,5	176,20	11,50	0,49	2,77E-16	22,73	81,71	0,08	60,02	2,46	0,002103												
						5	2,0	82,63	12,34	0,17	4,18E-16	24,39	61,03	0,13	60,00	1,81	0,000736												
						6	2,5	67,03	12,17	0,12	3,10E-16	24,07	52,41	0,16	59,44	1,62	0,000513												
						7	3,0	36,68	10,45	0,02	9,34E-16	20,64	13,56	0,27	59,02	0,49	0,000072												
						8	4,0	33,18	11,90	0,01	2,11E-15	23,52	4,58	0,50	58,99	0,31	0,000022												
						9	5,0	32,04	11,91	0,00	1,31E-15	23,54	0,86	0,65	59,18	0,43	0,000004												
						10	6,0	32,83	11,19	0,01	6,60E-16	22,11	2,87	0,72	59,38	0,62	0,000014												
						11	8,0	32,04	11,76	0,00	5,85E-16	23,24	0,68	0,79	59,28	0,64	0,000003												
						12	10,0	31,88	11,02	0,00	6,58E-16	21,78	0,10	0,86	59,30	0,52	0,000000												
						13	12,0	32,26	11,35	0,00	6,28E-16	22,42	0,72	0,93	59,63	0,75	0,000003												
						14	15,0	32,89	11,41	0,01	4,82E-16	22,54	1,85	0,98	60,10	0,72	0,000009												
						15	20,0	35,94	11,94	0,02	1,54E-16	23,60	10,51	1,00	59,91	1,97	0,000055												
S0233	DR4-1	K-feld.							0,50	59,17	$\pm 0,20$	91,8	0,51	0,90	2-13	Plateau steps = 59.14 $\pm$ 0.23	296,0 $\pm$ 1.4	0,37	0,96										

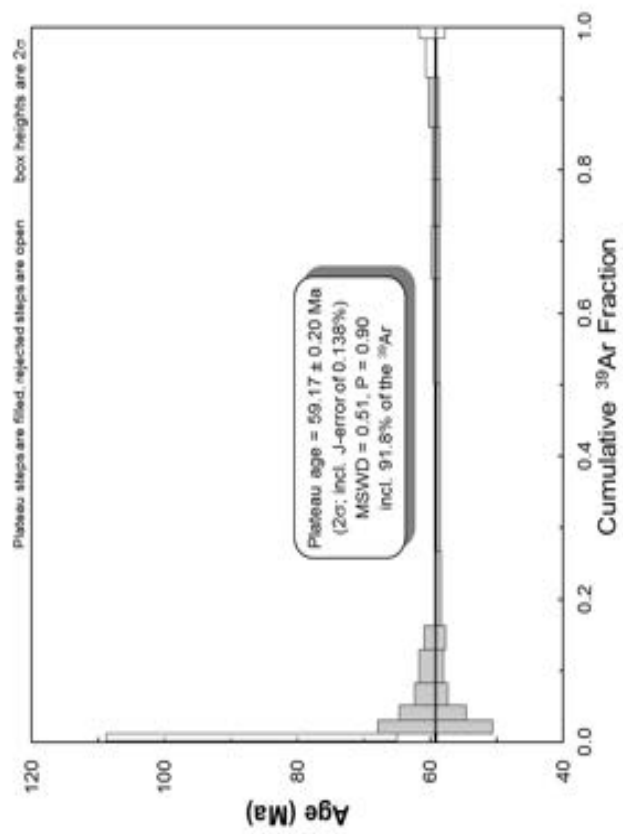
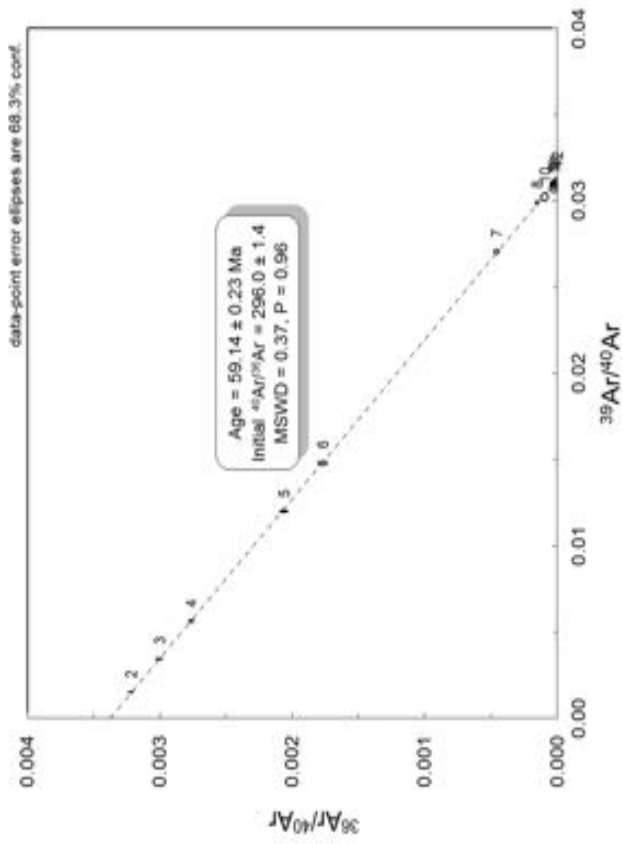


Figure 1: Laser setp-heating results S0233 DR4-1

<b>Sample S0233 DR19-1A</b>														
Material Plagioclase														
J value		2σ % error		Mass (mg)										
0,001041		0,138		7,886										
Laser														
Step #	power (W)	<sup>40</sup> Ar/ <sup>39</sup> Ar	<sup>37</sup> Ar/ <sup>39</sup> Ar	<sup>36</sup> Ar/ <sup>39</sup> Ar	<sup>39</sup> Ar <sub>K</sub> (moles)	Ca/K	% <sup>40</sup> Ar <sub>atm</sub>	Cumulative fraction of <sup>39</sup> Ar	Age (Ma)	± 2σ (Ma)	<sup>36</sup> Ar/ <sup>37</sup> Ar AI			
1	0,8	6133,45	32,01	20,53	6,70E-17	64,18	98,89	0,01	126,70	33,03	0,066752			
2	1,0	882,47	16,63	2,84	1,94E-16	32,99	95,01	0,03	81,74	9,67	0,017759			
3	1,2	367,73	14,92	1,12	2,48E-16	29,55	89,61	0,06	71,08	3,52	0,007782			
4	1,5	188,84	14,18	0,51	3,05E-16	28,07	79,43	0,10	72,22	3,39	0,003726			
5	2,0	129,19	12,43	0,32	4,48E-16	24,58	71,38	0,15	68,73	1,93	0,002613			
6	2,5	52,75	13,73	0,05	9,18E-16	27,16	28,45	0,26	70,18	0,58	0,000385			
7	3,0	41,61	14,97	0,02	7,68E-16	29,66	10,45	0,35	69,37	0,62	0,000102			
8	4,0	38,54	14,63	0,01	1,18E-15	28,97	3,83	0,48	69,00	0,53	0,000035			
9	5,0	39,75	14,58	0,01	1,57E-15	28,86	4,36	0,67	70,73	0,38	0,000041			
10	6,0	38,83	15,24	0,01	5,15E-16	30,19	1,54	0,73	71,16	0,70	0,000013			
11	8,0	39,14	14,72	0,01	1,27E-15	29,16	2,84	0,88	70,76	0,45	0,000026			
12	10,0	38,77	16,01	0,01	2,20E-16	31,74	1,04	0,90	71,44	1,09	0,000008			
13	12,0	38,80	15,35	0,00	4,53E-16	30,42	0,50	0,96	71,85	0,80	0,000004			
14	15,0	42,48	15,51	0,02	2,93E-16	30,74	8,68	0,99	72,20	1,34	0,000083			
15	20,0	48,56	15,20	0,04	7,37E-17	30,10	24,82	1,00	68,00	4,83	0,000279			
Cruise	Sample	Phase	wt. % K <sub>2</sub> O	Pseudo-plateau age (Ma)	± 2σ (Ma)	% <sup>39</sup> Ar fraction	MSWD	P	Steps	Inverse isochron age (Ma; 95% conf.)	Initial <sup>40</sup> Ar/ <sup>36</sup> Ar (95% conf)	MSWD	P	
S0233	DR 19-1A	Plag.	0,40	70,84*	± 0,28	41,9	0,83	0,48	9-12	Plateau steps = 71.2 ± 0.47	249 ± 50	1,3	0,26	

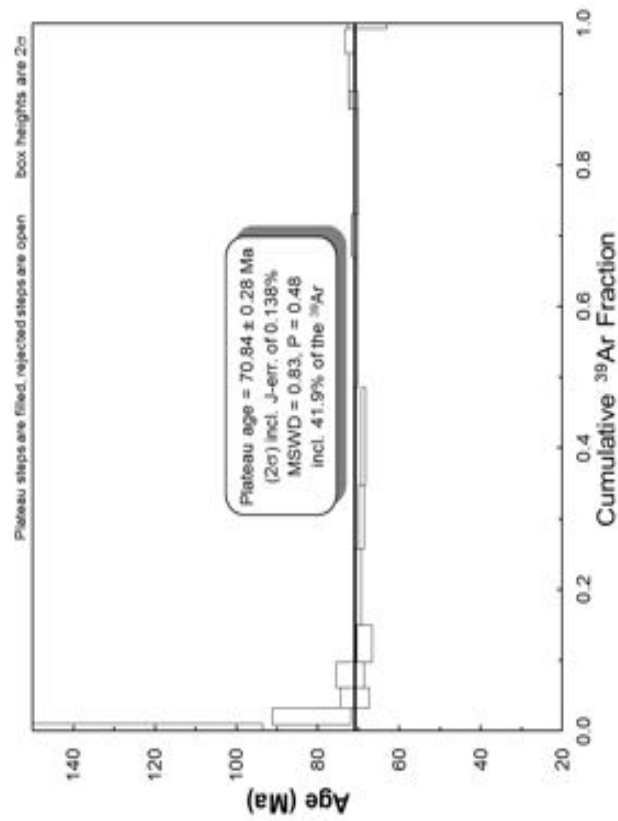
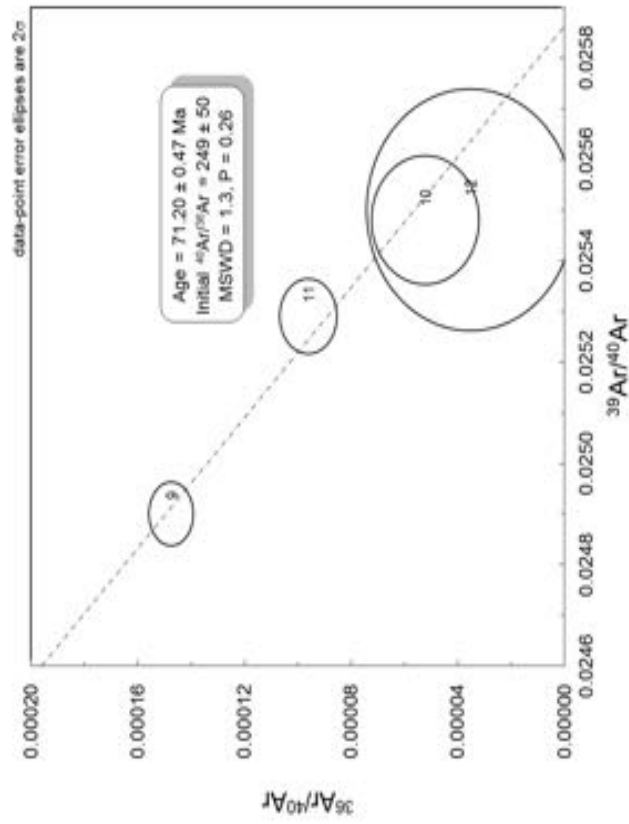


Figure 2: Laser setp-heating results S0233 DR19-1A

<b>Sample S0233 DR35-12</b>														
Material Plagioclase														
J value		2σ % error		Mass (mg)										
0,001042		0,123		7,622										
Laser														
Step #	power (W)	<sup>40</sup> Ar/ <sup>39</sup> Ar	<sup>37</sup> Ar/ <sup>39</sup> Ar	<sup>36</sup> Ar/ <sup>39</sup> Ar	<sup>39</sup> Ar <sub>K</sub> (moles)	Ca/K	% <sup>40</sup> Ar <sub>atm</sub>	Cumulative fraction of <sup>39</sup> Ar	Age (Ma)	± 2σ (Ma)	<sup>36</sup> Ar/ <sup>37</sup> Ar AI			
1	0,8	2012,95	65,12	6,68	1,03E-16	133,76	97,84	0,07	83,62	26,68	0,010663			
2	1,0	591,09	67,06	1,92	9,94E-17	137,93	94,87	0,13	58,85	9,03	0,002948			
3	1,2	625,02	68,60	2,05	8,64E-17	141,26	96,15	0,19	46,89	14,58	0,003089			
4	1,5	580,58	76,93	1,85	1,18E-16	159,39	92,87	0,26	80,45	7,85	0,002471			
5	2,0	225,02	79,59	0,66	1,66E-16	165,24	84,49	0,37	68,18	5,30	0,000842			
6	2,5	81,78	91,73	0,18	2,30E-16	192,16	54,61	0,51	73,08	2,98	0,000171			
7	3,0	73,45	101,73	0,15	2,05E-16	214,73	47,78	0,65	76,03	2,45	0,000121			
8	4,0	45,49	103,18	0,05	1,73E-16	218,03	15,61	0,76	76,18	2,90	0,000024			
9	5,0	43,99	107,92	0,05	1,03E-16	228,87	16,82	0,82	72,93	3,26	0,000024			
10	6,0	46,16	113,08	0,05	5,44E-17	240,75	15,04	0,86	78,35	5,25	0,000021			
11	8,0	42,95	111,58	0,04	9,95E-17	237,29	9,86	0,92	77,28	2,92	0,000013			
12	10,0	60,14	112,02	0,10	5,18E-17	238,29	32,16	0,95	81,37	5,75	0,000060			
13	12,0	56,15	125,46	0,09	3,47E-17	269,65	29,48	0,98	79,83	9,97	0,000046			
14	13,5	58,13	117,88	0,10	2,52E-17	251,89	33,53	0,99	77,49	14,04	0,000058			
15	15,0	99,48	96,66	0,27	9,73E-18	203,24	74,06	1,00	51,31	38,19	0,000268			
Cruise	Sample	Phase	wt. % K <sub>2</sub> O	Plateau age (Ma)	± 2σ (Ma)	% <sup>39</sup> Ar fraction	MSWD	P	Steps	Inverse isochron age (Ma; 95% conf.)	Initial <sup>40</sup> Ar/ <sup>36</sup> Ar (95% conf.)	MSWD	P	
S0233	DR 35-12	Plag.	0,08	75.4	± 1.2	55.4	1,6	0,15	6-11	Plateau steps = 76.3 ± 2.6	289 ± 13	1,04	0,38	



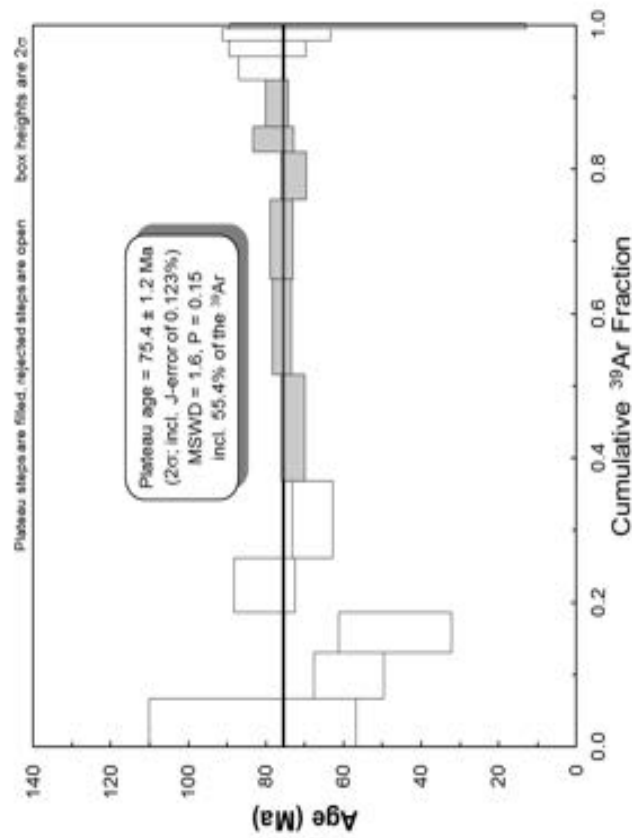
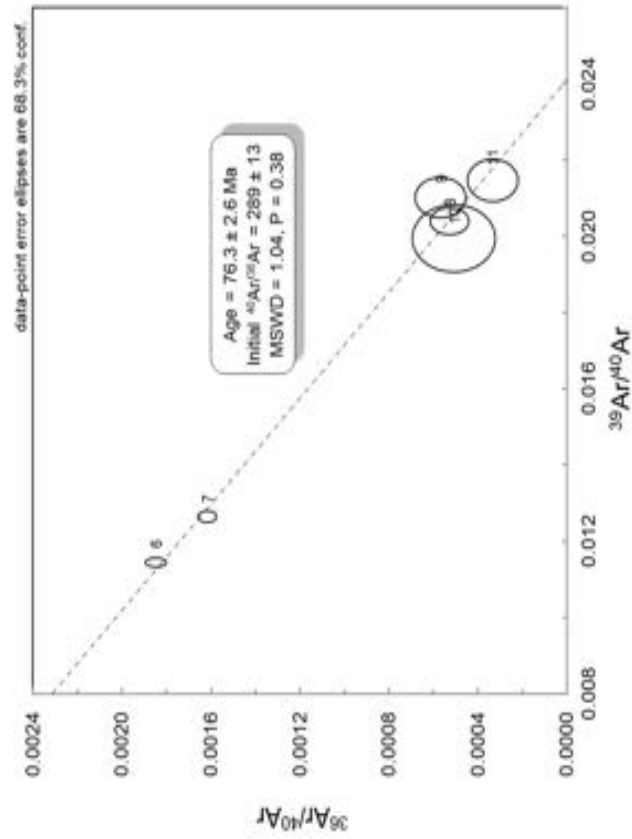


Figure 3: Laser setp-heating results S0233 DR35-12

Sample		S0233 DR37-1A															
Material		Plagioclase															
J value		0,001042															
2σ % error		0,123															
Mass (mg)		6,226															
Laser																	
Step #	power (W)	<sup>40</sup> Ar/ <sup>39</sup> Ar	<sup>37</sup> Ar/ <sup>39</sup> Ar	<sup>36</sup> Ar/ <sup>39</sup> Ar	<sup>39</sup> Ar <sub>K</sub> (moles)	Ca/K	% <sup>40</sup> Ar <sub>am</sub>	Cumulative fraction of <sup>39</sup> Ar	Age (Ma)	± 2σ (Ma)	<sup>36</sup> Ar/ <sup>37</sup> Ar AI						
1	0.8	18489,70	195,64	62,22	1,06E-17	444,51	99,36	0,00	239,63	130,88	0,033112						
2	1.0	2222,75	46,61	7,36	4,77E-17	94,44	97,74	0,02	94,95	20,41	0,016437						
3	1.2	647,07	43,06	2,06	5,57E-17	87,03	93,67	0,05	77,67	14,30	0,004963						
4	1.5	449,14	43,46	1,39	8,71E-17	87,86	90,88	0,08	77,72	8,49	0,003311						
5	2.0	210,33	63,73	0,60	1,31E-16	130,77	81,23	0,13	76,07	4,56	0,000945						
6	2.5	95,24	42,47	0,20	3,26E-16	85,79	58,08	0,27	75,75	1,66	0,000459						
7	3.0	47,50	47,49	0,03	4,43E-16	96,28	11,99	0,44	79,52	0,98	0,000042						
8	4.0	42,79	49,03	0,02	2,45E-16	99,52	2,60	0,54	79,36	1,44	0,000007						
9	5.0	44,78	49,73	0,03	2,24E-16	100,99	8,32	0,63	78,25	1,44	0,000026						
10	6.0	42,78	49,64	0,01	1,85E-16	100,81	0,06	0,71	81,40	1,57	0,000000						
11	8.0	41,87	52,16	0,02	1,10E-16	106,12	6,48	0,75	74,84	3,97	0,000018						
12	10.0	42,42	45,13	0,01	1,94E-16	91,34	2,11	0,83	78,86	2,01	0,000006						
13	12.0	42,83	51,01	0,02	1,71E-16	103,68	1,95	0,90	80,07	2,37	0,000005						
14	13.5	43,26	44,71	0,01	1,65E-16	90,47	1,62	0,97	80,76	2,99	0,000005						
15	15.0	49,22	46,18	0,04	1,35E-17	93,55	14,02	0,97	80,40	20,88	0,000052						
16	20.0	57,29	44,19	0,06	6,56E-17	89,38	24,77	1,00	81,74	5,48	0,000113						
Cruise	Sample	Phase	wt. % K <sub>2</sub> O	WMA	± 2σ (Ma)	MSWD	P	Steps	Inverse isochron age (Ma; 95% conf.)	Initial <sup>40</sup> Ar/ <sup>36</sup> Ar (95% conf.)	MSWD	P					
S0233	DR 37-1A	Plag.	0,15	79,59	± 0,72	2,0	0,069	8-10 & 12-14	8-10 & 12-14 = 80.4 ± 2.1	200 ± 110	2,7	0,029					

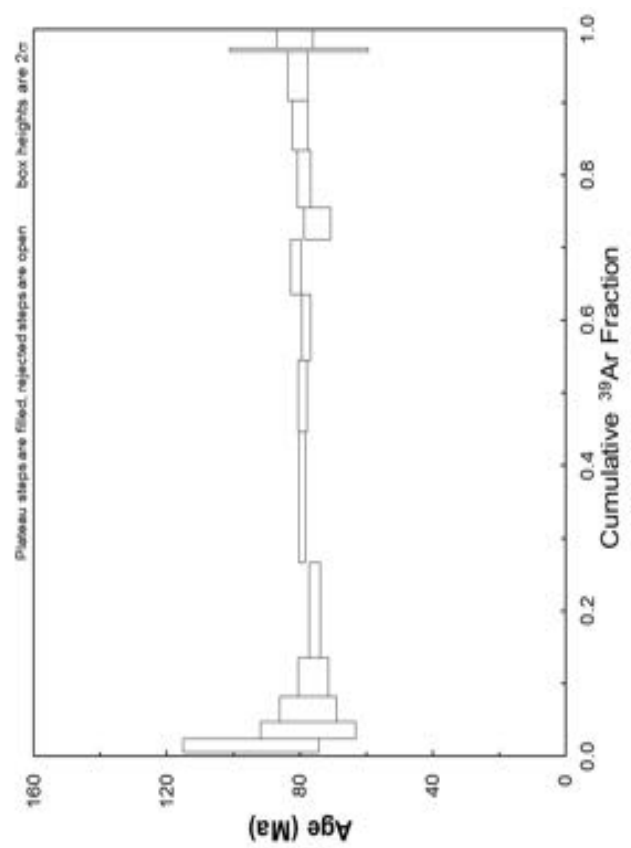
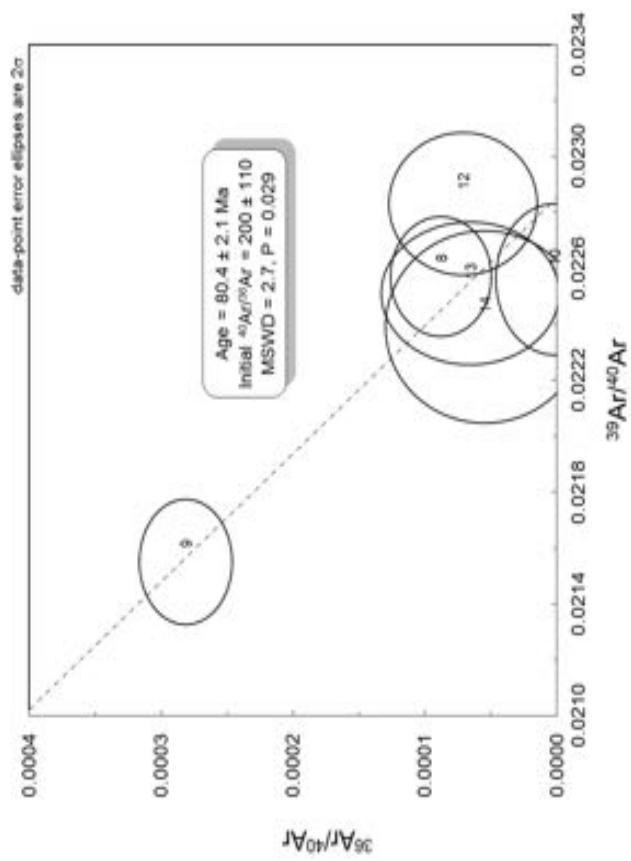


Figure 4: Laser step-heating results S0233 DR37-1A

<b>Sample S0233 DR41-2</b>															
Material Plagioclase															
J value		2σ % error		Mass (mg)											
0,001042		0,123		6,793											
Laser															
Step #	power (W)	<sup>40</sup> Ar/ <sup>39</sup> Ar	<sup>37</sup> Ar/ <sup>39</sup> Ar	<sup>36</sup> Ar/ <sup>39</sup> Ar	<sup>39</sup> Ar <sub>K</sub> (moles)	Ca/K	% <sup>40</sup> Ar <sub>atm</sub>	Cumulative fraction of <sup>39</sup> Ar	Age (Ma)	± 2σ (Ma)	<sup>36</sup> Ar/ <sup>37</sup> Ar AI				
1	1,0	2307,54	17,77	7,61	2,95E-17	35,27	97,46	0,00	108,46	25,35	0,044623				
2	1,2	793,34	12,59	2,51	6,85E-17	24,91	93,34	0,01	97,50	13,91	0,020732				
3	1,5	307,87	11,87	0,89	1,35E-16	23,46	84,84	0,03	86,38	3,63	0,007758				
4	2,0	140,76	11,57	0,33	2,41E-16	22,86	67,82	0,05	83,86	3,62	0,002909				
5	2,5	97,98	11,71	0,19	2,21E-16	23,13	55,14	0,08	81,44	2,76	0,001627				
6	3,0	49,48	13,02	0,02	5,55E-16	25,75	10,65	0,14	81,97	0,80	0,000142				
7	4,0	47,78	11,84	0,02	1,73E-15	23,41	8,35	0,33	81,15	0,45	0,000118				
8	5,0	43,95	11,73	0,00	1,56E-15	23,18	0,22	0,51	81,25	0,40	0,000002				
9	6,0	44,26	10,69	0,00	9,07E-16	21,11	0,79	0,61	81,30	0,53	0,000011				
10	8,0	44,08	10,62	0,00	1,01E-15	20,98	0,44	0,72	81,26	0,44	0,000006				
11	10,0	43,70	11,26	0,00	6,46E-16	22,25	-0,72	0,79	81,52	0,73	-				
12	12,0	43,68	11,34	0,00	8,77E-16	22,40	-0,02	0,89	80,93	0,65	-				
13	13,5	43,96	11,03	0,00	4,85E-16	21,79	-0,01	0,94	81,43	0,83	-				
14	15,0	44,01	11,54	0,00	3,03E-16	22,80	-0,24	0,98	81,73	1,44	-				
15	20,0	44,61	11,48	0,00	1,81E-16	22,68	-0,71	1,00	83,19	2,09	-				
16	22,5	46,70	11,35	0,00	1,65E-17	22,43	-2,00	1,00	88,08	24,93	-				
Cruise	Sample	Phase	% K <sub>2</sub> O	Plateau age (Ma)	± 2σ (Ma)	% <sup>39</sup> Ar fraction	MSWD	P	Steps	Inverse isochron age (Ma; 95% conf.)	Initial <sup>40</sup> Ar/ <sup>36</sup> Ar (95% conf.)	MSWD	P		
S0233	DR 41-2	Plag.	0,49	81,31	± 0,21	94,7	0,82	0,62	5-16	Plateau steps = 81.27 ± 0.27	296,4 ± 8.2	0,44	0,93		

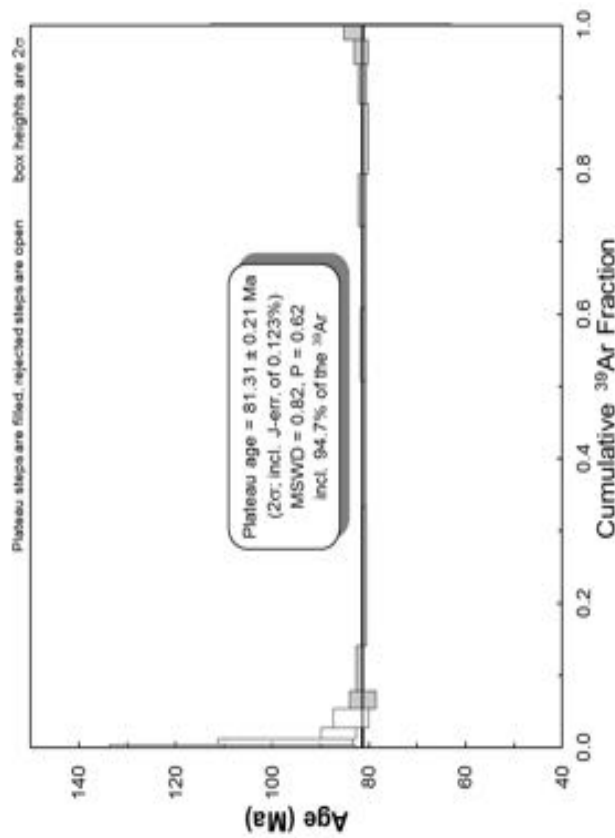
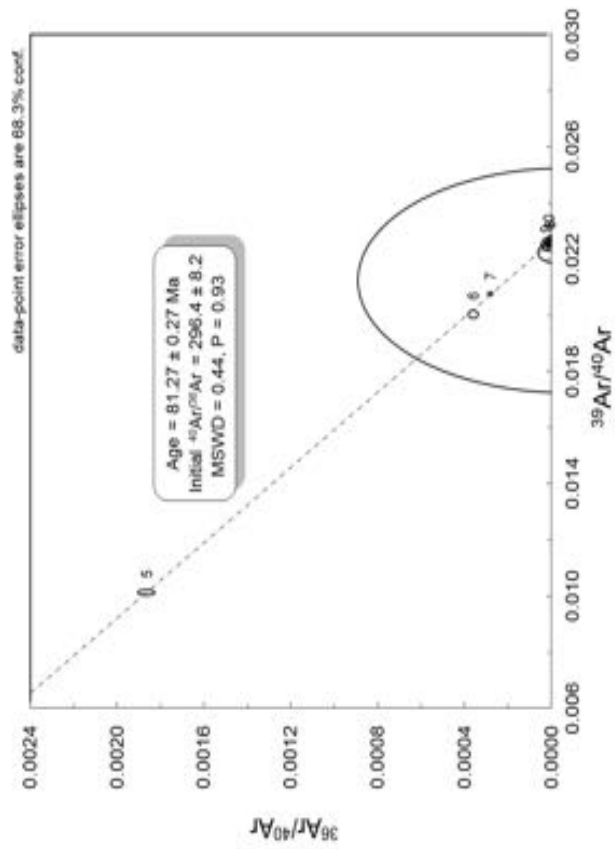


Figure 5: Laser setp-heating results S0233 DR41-2

<b>Sample S0233 DR43-3</b>														
Material Plagioclase														
J value		2σ % error		Mass (mg)										
0,001042		0,123		4,942										
		Laser												
Step #	power (W)	<sup>40</sup> Ar/ <sup>39</sup> Ar	<sup>37</sup> Ar/ <sup>39</sup> Ar	<sup>36</sup> Ar/ <sup>39</sup> Ar	<sup>39</sup> Ar <sub>K</sub> (moles)	Ca/K	% <sup>40</sup> Ar <sub>atm</sub>	Cumulative fraction of <sup>39</sup> Ar	Age (Ma)	± 2σ (Ma)	<sup>36</sup> Ar/ <sup>37</sup> Ar AI			
1	0,6	16684,90	72,43	55,95	3,73E-17	149,57	99,05	0,01	289,13	90,09	0,080457			
2	0,8	1417,19	24,61	4,62	1,36E-16	49,08	96,17	0,06	100,96	13,54	0,019528			
3	1,0	376,28	23,51	1,15	1,37E-16	46,85	89,90	0,12	71,21	8,35	0,005073			
4	1,2	183,70	21,55	0,51	1,30E-16	42,89	80,85	0,16	65,91	4,62	0,002430			
5	1,5	233,35	27,86	0,68	1,26E-16	55,70	84,92	0,21	66,22	4,86	0,002507			
6	2,0	202,68	36,99	0,56	1,91E-16	74,44	80,94	0,28	73,05	2,61	0,001563			
7	2,5	60,15	32,37	0,08	1,26E-16	64,93	33,72	0,33	75,11	2,11	0,000220			
8	3,0	44,82	30,12	0,02	4,13E-16	60,31	9,14	0,48	76,56	0,73	0,000047			
9	4,0	45,19	33,66	0,02	3,70E-16	67,56	8,06	0,62	78,27	0,81	0,000038			
10	5,0	43,15	44,19	0,02	2,56E-16	89,38	2,97	0,71	79,44	0,85	0,000010			
11	6,0	43,13	37,59	0,02	2,69E-16	75,67	4,92	0,81	77,49	1,35	0,000019			
12	8,0	43,89	34,15	0,01	1,98E-16	68,57	3,78	0,89	79,56	2,16	0,000017			
13	10,0	46,15	45,91	0,03	1,20E-16	92,98	8,28	0,93	80,40	2,72	0,000029			
14	12,0	45,91	29,86	0,02	1,64E-16	59,78	7,31	0,99	79,92	1,54	0,000039			
15	13,5	52,93	44,04	0,06	1,46E-17	89,07	28,77	1,00	71,68	22,86	0,000121			
Cruise	Sample	Phase	% K <sub>2</sub> O	Plateau age (Ma)	± 2σ (Ma)	% <sup>39</sup> Ar fraction	MSWD	P	Steps	Inverse isochron age (Ma; 95% conf.)	Initial <sup>40</sup> Ar/ <sup>36</sup> Ar (95% conf.)	MSWD	P	
S0233	DR 43-3	Plag.	0,20	78,84	± 0,50	51,9	2	0,06	9-15	Plateau steps = 83.56 ± 0.10	233 ± 150	2,4	0,034	

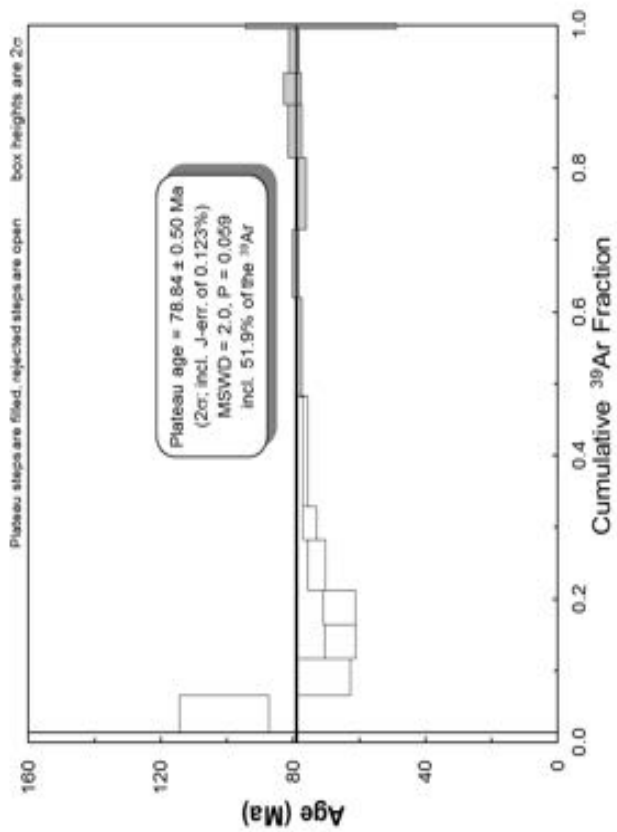
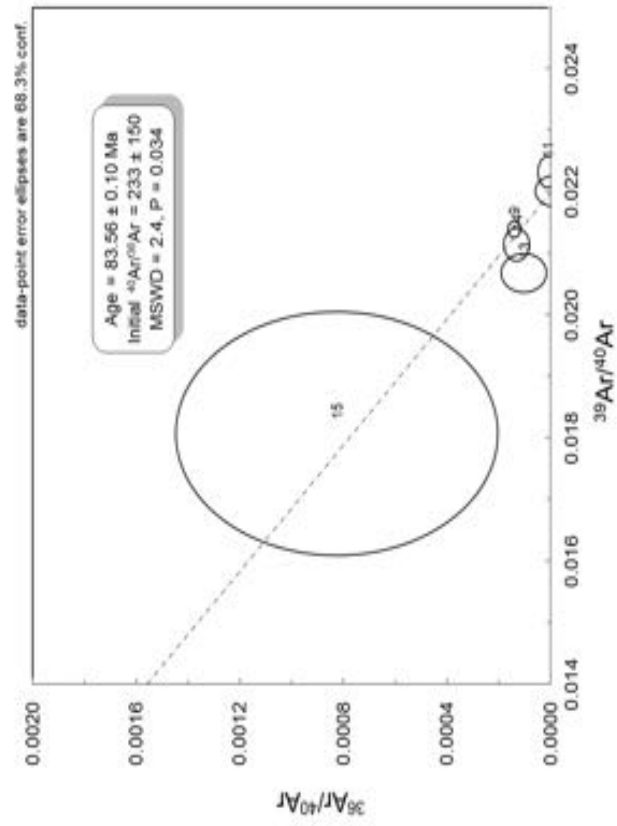


Figure 6: Laser step-heating results S0233 DR43-3

<b>Sample S0233 DR43-6</b>													
Material Plagioclase													
J value	2σ % error	Mass (mg)											
0,001042	0,123	6,142											
<b>Laser</b>													
Step #	power (W)	<sup>40</sup> Ar/ <sup>39</sup> Ar	<sup>37</sup> Ar/ <sup>39</sup> Ar	<sup>36</sup> Ar/ <sup>39</sup> Ar	<sup>39</sup> Ar <sub>K</sub> (moles)	Ca/K	% <sup>40</sup> Ar <sub>atm</sub>	Cumulative fraction of <sup>39</sup> Ar	Age (Ma)	± 2σ (Ma)	<sup>36</sup> Ar/ <sup>37</sup> Ar AI		
1	0,6	61502,50	695,43	204,87	3,23E-18	2663,17	98,35	0,00	2023,43	1350,61	0,030669		
2	0,8	922,65	50,89	2,98	9,06E-17	103,43	95,16	0,03	85,11	14,33	0,006083		
3	1,0	394,05	46,72	1,19	1,01E-16	94,69	88,13	0,07	88,72	6,21	0,002620		
4	1,2	195,75	45,38	0,51	8,99E-17	91,87	75,29	0,11	91,56	6,17	0,001145		
5	1,5	120,31	43,30	0,27	1,19E-16	87,52	64,41	0,15	81,15	4,46	0,000631		
6	2,0	111,51	40,57	0,24	2,03E-16	81,85	62,05	0,22	80,08	2,20	0,000601		
7	2,5	47,35	40,08	0,03	5,70E-16	80,83	11,18	0,44	79,56	0,95	0,000046		
8	3,0	44,74	46,77	0,02	3,71E-16	94,79	6,42	0,57	79,60	1,22	0,000021		
9	4,0	44,26	42,30	0,02	2,56E-16	85,44	4,30	0,67	80,25	1,31	0,000015		
10	5,0	44,59	41,34	0,02	2,66E-16	83,44	5,85	0,77	79,50	1,37	0,000022		
11	6,0	46,27	43,17	0,03	1,18E-16	87,25	9,28	0,81	79,59	2,51	0,000035		
12	8,0	49,36	43,39	0,03	1,90E-16	87,72	12,78	0,88	81,60	2,16	0,000051		
13	10,0	48,20	47,52	0,03	6,58E-17	96,35	8,29	0,90	83,97	4,02	0,000029		
14	12,0	47,13	41,05	0,02	1,28E-16	82,85	7,98	0,95	82,04	2,84	0,000032		
15	13,5	44,31	37,91	0,02	7,71E-17	76,34	3,88	0,98	80,42	4,48	0,000015		
16	15,0	54,84	40,00	0,05	3,91E-17	80,66	23,33	0,99	79,54	8,71	0,000112		
17	20,0	363,99	46,14	1,00	4,64E-18	93,46	79,82	1,00	137,32	82,15	0,002220		
18	22,5	82,61	52,50	0,16	1,15E-17	106,84	51,24	1,00	76,95	37,54	0,000284		
Cruise	Sample	Phase	% K <sub>2</sub> O	Plateau age (Ma)	± 2σ (Ma)	% <sup>39</sup> Ar fraction	MSWD	P	Steps	Inverse isochron age (Ma; 95% conf.)	Initial <sup>40</sup> Ar/ <sup>36</sup> Ar (95% conf.)	MSWD	P
S0233	DR 43-6	Plag.	0,16	80,00	± 0,52	89,5	0,96	0,49	5-18	Plateau steps = 79,86 ± 0,71	296,9 ± 5,0	0,64	0,81



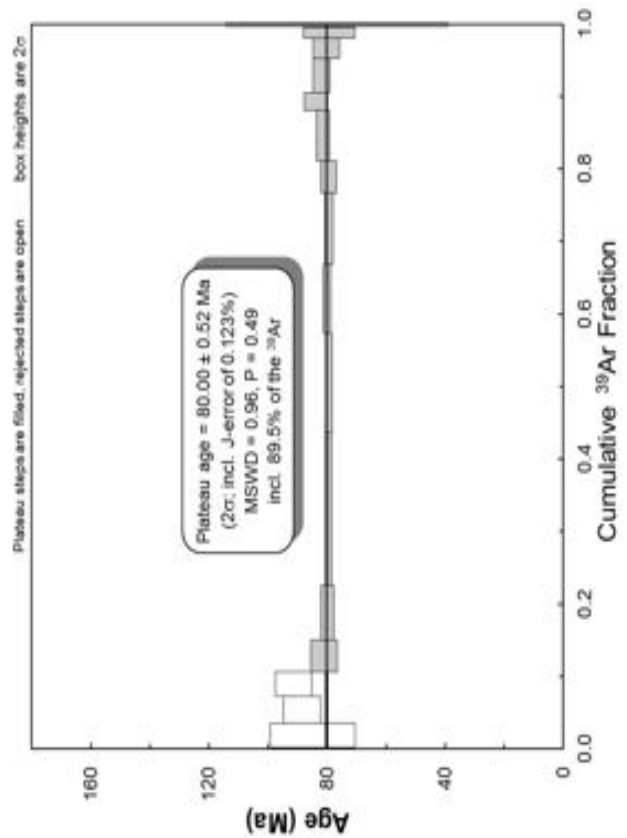
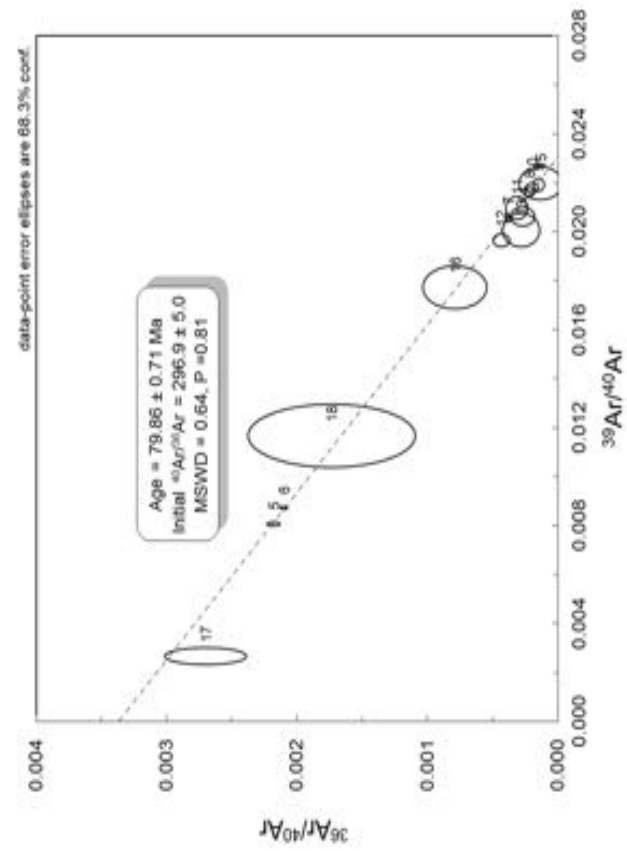


Figure 7: Laser setp-heating results S0233 DR43-6

<b>Sample S0233 DR62-1</b>															
Material Plagioclase															
J value		2σ % error		Mass (mg)											
0,001042		0,123		6,371											
Laser															
Step #	power (W)	<sup>40</sup> Ar/ <sup>39</sup> Ar	<sup>37</sup> Ar/ <sup>39</sup> Ar	<sup>36</sup> Ar/ <sup>39</sup> Ar	<sup>39</sup> Ar <sub>K</sub> (moles)	Ca/K	% <sup>40</sup> Ar <sub>atm</sub>	Cumulative fraction of <sup>39</sup> Ar	Age (Ma)	± 2σ (Ma)	<sup>36</sup> Ar/ <sup>37</sup> Ar AI				
1	0,6	5467,14	52,25	18,26	8,74E-17	106,30	98,60	0,03	143,10	102,20	0,036384				
2	0,8	1531,39	36,57	4,99	1,19E-16	73,57	96,10	0,06	111,72	21,04	0,014189				
3	1,0	738,81	32,46	2,35	1,05E-16	65,11	93,82	0,09	85,76	14,31	0,007528				
4	1,2	307,03	33,14	0,89	1,06E-16	66,50	85,11	0,13	85,92	9,31	0,002780				
5	1,5	185,59	32,08	0,49	2,06E-16	64,32	77,15	0,19	79,78	3,55	0,001573				
6	2,0	116,69	32,98	0,26	4,59E-16	66,17	62,94	0,33	81,36	1,43	0,000785				
7	2,5	97,61	33,06	0,19	4,87E-16	66,34	55,49	0,48	81,74	1,00	0,000577				
8	3,0	54,19	34,41	0,04	3,80E-16	69,10	17,32	0,59	84,31	0,77	0,000096				
9	4,0	46,87	34,56	0,02	3,56E-16	69,43	5,82	0,70	83,10	1,08	0,000027				
10	5,0	50,90	33,48	0,03	1,52E-16	67,21	12,57	0,75	83,70	2,22	0,000067				
11	6,0	45,79	34,71	0,01	1,44E-16	69,74	2,32	0,79	84,19	1,80	0,000010				
12	8,0	47,38	34,42	0,02	1,67E-16	69,13	6,06	0,84	83,77	1,57	0,000029				
13	10,0	50,69	34,18	0,03	1,74E-16	68,64	12,24	0,90	83,70	1,88	0,000063				
14	12,0	53,51	33,96	0,04	1,33E-16	68,18	15,51	0,94	85,04	1,86	0,000086				
15	15,0	46,02	34,08	0,02	1,53E-16	68,43	4,65	0,98	82,59	1,43	0,000022				
16	20,0	53,78	34,89	0,03	4,99E-17	70,11	13,00	1,00	87,97	5,09	0,000070				
Cruise	Sample	Phase	% K <sub>2</sub> O	Plateau age (Ma)	± 2σ (Ma)	% <sup>39</sup> Ar fraction	MSWD	P	Steps	Inverse isochron age (Ma; 95% conf.)	Initial <sup>40</sup> Ar/ <sup>36</sup> Ar (95% conf.)	MSWD	P		
S0233	DR 62-1	Plag.	0,19	83,85	± 0,48	52,1	1,4	0,21	8-16	Plateau steps = 87.4 ± 1.0	322 ± 31	0,44	0,88		

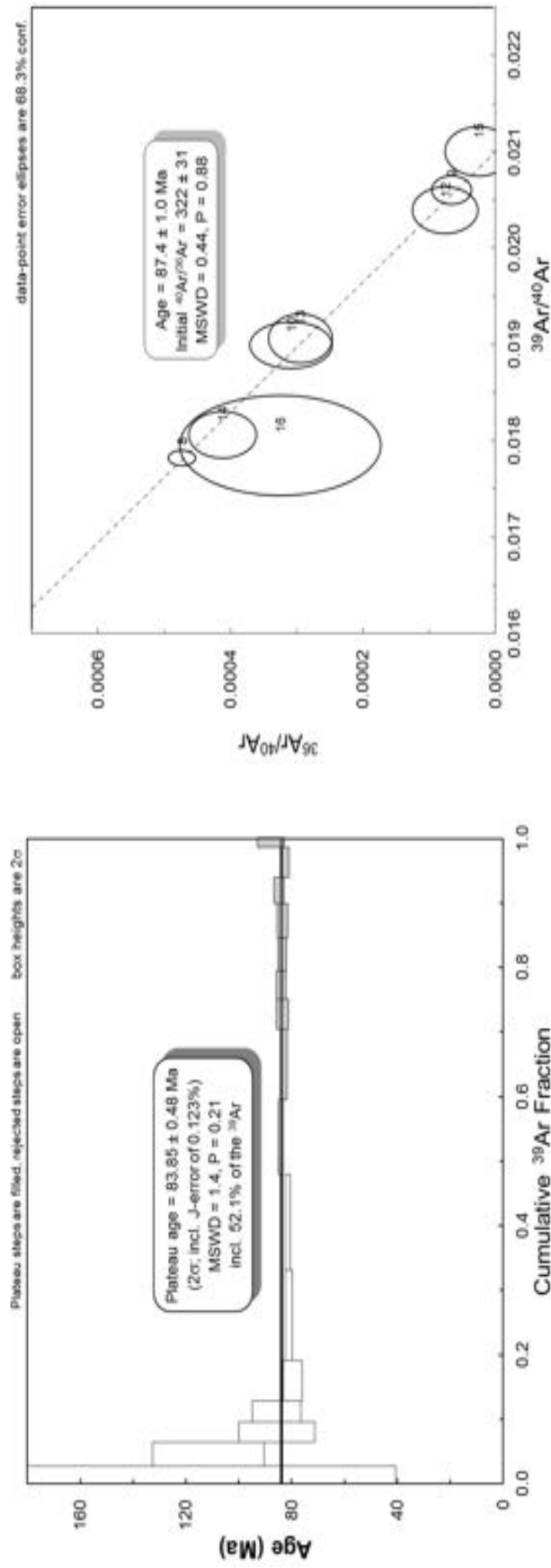


Figure 8: Laser step-heating results S0233 DR62-1

<b>Sample S0233 DR62-2</b>													
Material Plagioclase													
J value		2σ % error		Mass (mg)									
0,001042		0,123		4,99									
Laser													
Step #	power (W)	<sup>40</sup> Ar/ <sup>39</sup> Ar	<sup>37</sup> Ar/ <sup>39</sup> Ar	<sup>36</sup> Ar/ <sup>39</sup> Ar	<sup>39</sup> Ar <sub>K</sub> (moles)	Ca/K	% <sup>40</sup> Ar <sub>atm</sub>	Cumulative fraction of <sup>39</sup> Ar	Age (Ma)	± 2σ (Ma)	<sup>36</sup> Ar/ <sup>37</sup> Ar AI		
1	0,6	5674,39	294,56	18,90	2,69E-17	727,83	98,02	0,02	247,93	55,75	0,006658		
2	0,8	2265,33	337,05	7,60	4,15E-17	865,36	97,97	0,04	109,59	32,56	0,002321		
3	1,0	1115,22	366,70	3,77	2,77E-17	967,89	97,27	0,06	75,40	20,27	0,001043		
4	1,2	699,67	238,46	2,31	4,01E-17	561,36	94,79	0,08	80,51	7,85	0,000980		
5	1,5	155,68	115,92	0,41	9,72E-17	247,33	71,92	0,14	87,31	4,83	0,000340		
6	2,0	87,79	58,10	0,16	2,64E-16	118,73	50,34	0,29	83,49	2,13	0,000268		
7	2,5	76,73	42,74	0,12	2,11E-16	86,37	42,82	0,41	83,08	2,34	0,000271		
8	3,0	135,83	42,01	0,32	1,44E-16	84,84	67,43	0,50	83,71	4,05	0,000768		
9	4,0	86,89	45,03	0,15	1,57E-16	91,13	47,88	0,59	85,83	2,30	0,000325		
10	5,0	116,80	44,75	0,25	1,51E-16	90,56	60,40	0,67	87,61	3,16	0,000555		
11	6,0	117,25	51,67	0,26	1,63E-16	105,09	63,15	0,77	82,38	1,82	0,000505		
12	8,0	48,77	43,19	0,03	2,82E-16	87,30	11,40	0,93	81,88	1,41	0,000045		
13	10,0	93,75	53,87	0,18	6,97E-17	109,74	51,39	0,97	86,90	6,44	0,000315		
14	12,0	61,72	55,33	0,07	4,10E-17	112,82	25,01	1,00	88,32	7,26	0,000098		
Cruise	Sample	Phase	% K <sub>2</sub> O	Plateau age (Ma)	± 2σ (Ma)	% <sup>39</sup> Ar fraction	MSWD	P	Steps	Inverse isochron age (Ma; 95% conf.)	Initial <sup>40</sup> Ar/ <sup>36</sup> Ar (95% conf.)	MSWD	P
S0233	DR 62-2	Plag.	0,13	84,2	± 1,2	57,1	1,3	0,24	2-9	Plateau steps = 84.2 ± 2.0	295.5 ± 1.6	5,7	0,000

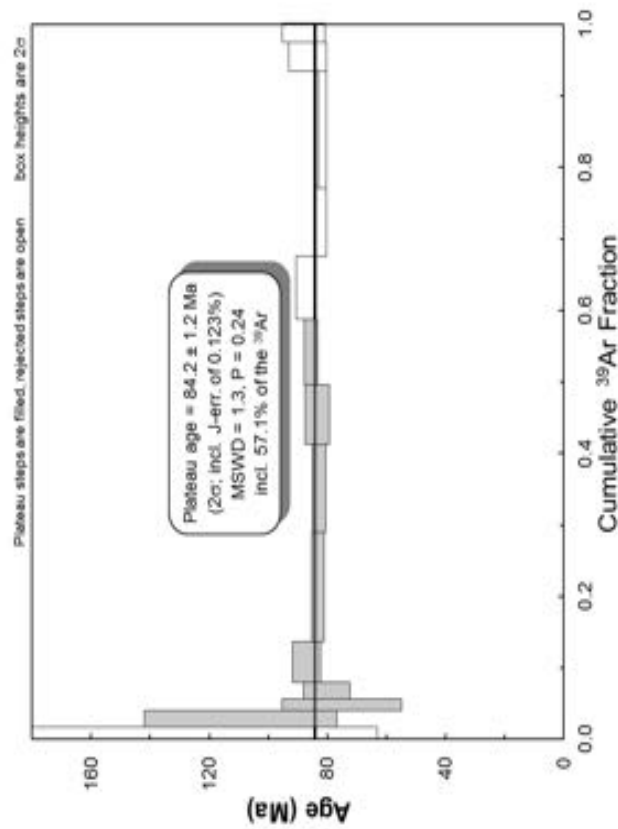
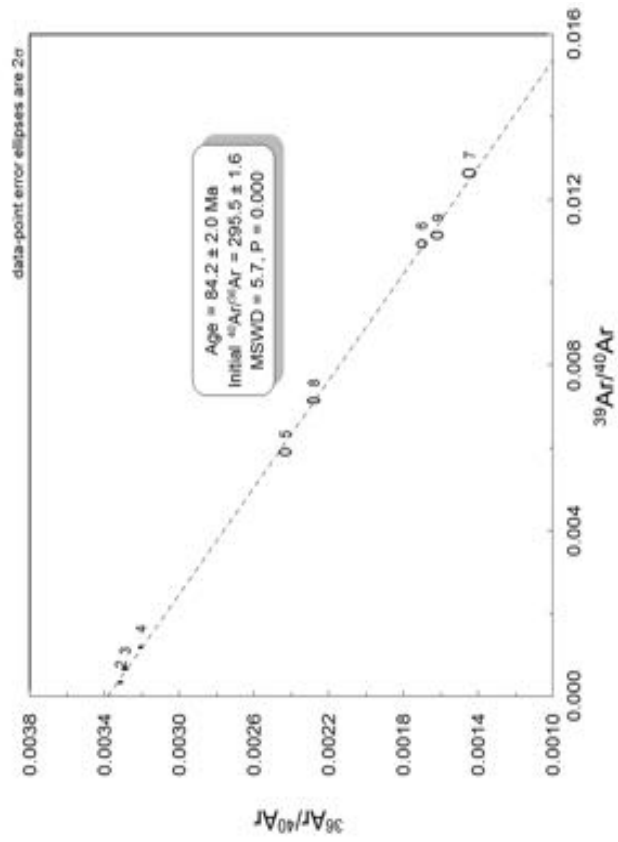


Figure 9: Laser setp-heating results S0233 DR62-2



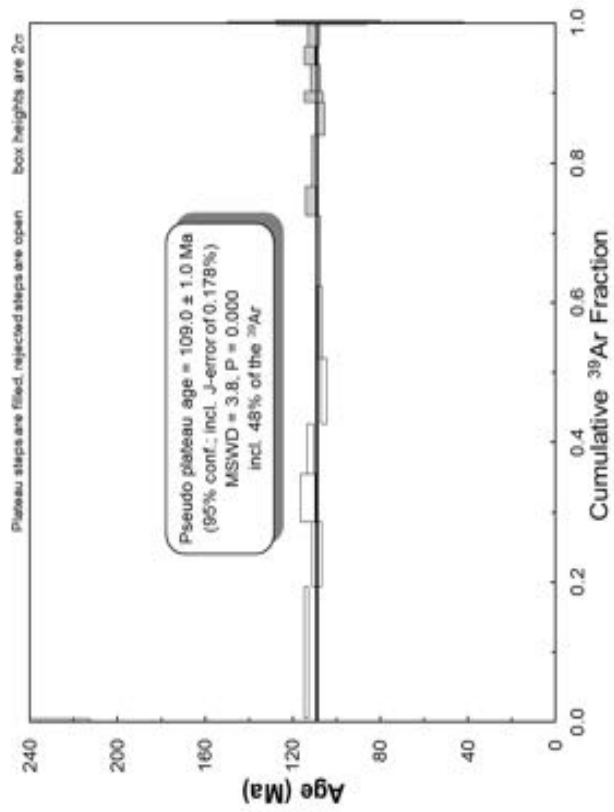
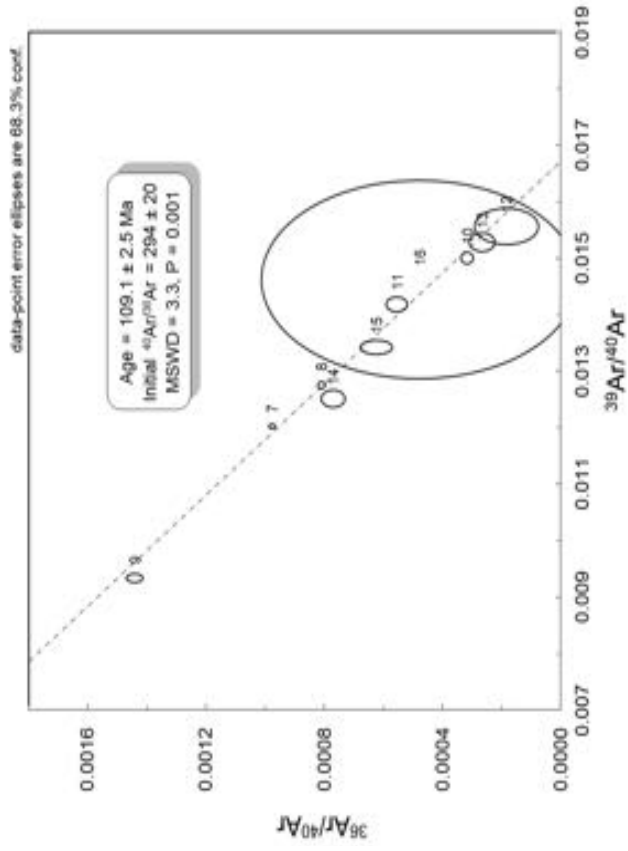


Figure 10: Laser step-heating results S0233 DR84-2

Sample		S0234 DR4-1																		
Material				Plagioclase/K-feldspar																
J value		2σ % error		Mass (mg)																
0,001042		0,178		7,875																
Laser																				
Step #	power (W)	<sup>40</sup> Ar/ <sup>39</sup> Ar	<sup>37</sup> Ar/ <sup>39</sup> Ar	<sup>36</sup> Ar/ <sup>39</sup> Ar	<sup>39</sup> Ar/ <sup>39</sup> Ar	<sup>39</sup> Ar <sub>K</sub> (moles)	Ca/K	% <sup>40</sup> Ar <sub>atm</sub>	Cumulative fraction of <sup>39</sup> Ar	Age (Ma)	± 2σ (Ma)									
1	0,6	14491,60	52,25	47,91	3,36E-17	106,30	97,66	0,00	564,16	446,19										
2	0,8	1509,36	17,10	4,81	1,18E-16	33,93	94,12	0,02	161,33	25,77										
3	1,0	509,54	12,93	1,54	1,73E-16	25,58	89,06	0,03	102,76	8,34										
4	1,2	348,29	13,43	1,01	1,60E-16	26,56	85,81	0,05	91,47	4,10										
5	1,5	218,95	12,80	0,57	2,79E-16	25,32	76,37	0,07	95,59	3,39										
6	2,0	105,64	12,87	0,19	5,22E-16	25,46	52,98	0,13	91,86	1,20										
7	2,5	58,43	12,52	0,03	1,02E-15	24,75	15,50	0,23	91,30	0,57										
8	3,0	53,31	12,98	0,02	1,43E-15	25,68	6,94	0,37	91,76	0,56										
9	4,0	50,86	12,17	0,01	1,82E-15	24,06	3,84	0,54	90,43	0,83										
10	5,0	51,81	13,01	0,01	1,07E-15	25,74	5,15	0,65	90,91	0,76										
11	6,0	50,14	12,29	0,01	5,17E-16	24,30	1,34	0,70	91,46	1,00										
12	8,0	51,83	12,37	0,01	7,03E-16	24,46	4,06	0,77	91,93	0,56										
13	10,0	51,18	12,81	0,01	1,14E-15	25,33	2,77	0,88	92,01	0,48										
14	12,0	50,35	12,95	0,01	3,68E-16	25,61	1,50	0,91	91,74	0,92										
15	13,5	50,28	12,98	0,00	3,94E-16	25,68	0,86	0,95	92,19	0,79										
16	15,0	50,86	11,90	0,01	2,03E-16	23,52	3,01	0,97	91,18	0,99										
17	20,0	53,12	12,81	0,02	2,20E-16	25,33	7,48	0,99	90,91	1,28										
18	22,5	140,64	13,33	0,32	7,21E-17	26,38	65,65	1,00	89,44	4,55										
Cruise	Sample	Phase	% K <sub>2</sub> O	Plateau age (Ma)	± 2σ (Ma)	% <sup>39</sup> Ar fraction	MSWD	P	Steps	Inverse isochron age (Ma; 95% conf.)	Initial <sup>40</sup> Ar/ <sup>36</sup> Ar (95% conf.)	MSWD	P							
S0234	DR 4-1	Plag./K-feld.	0,48	91,34	± 0,34	66,6	2,2	0,03	4-11	Plateau steps = 91,24 ± 0,57	297,1 ± 3,1	8,4	0,00							



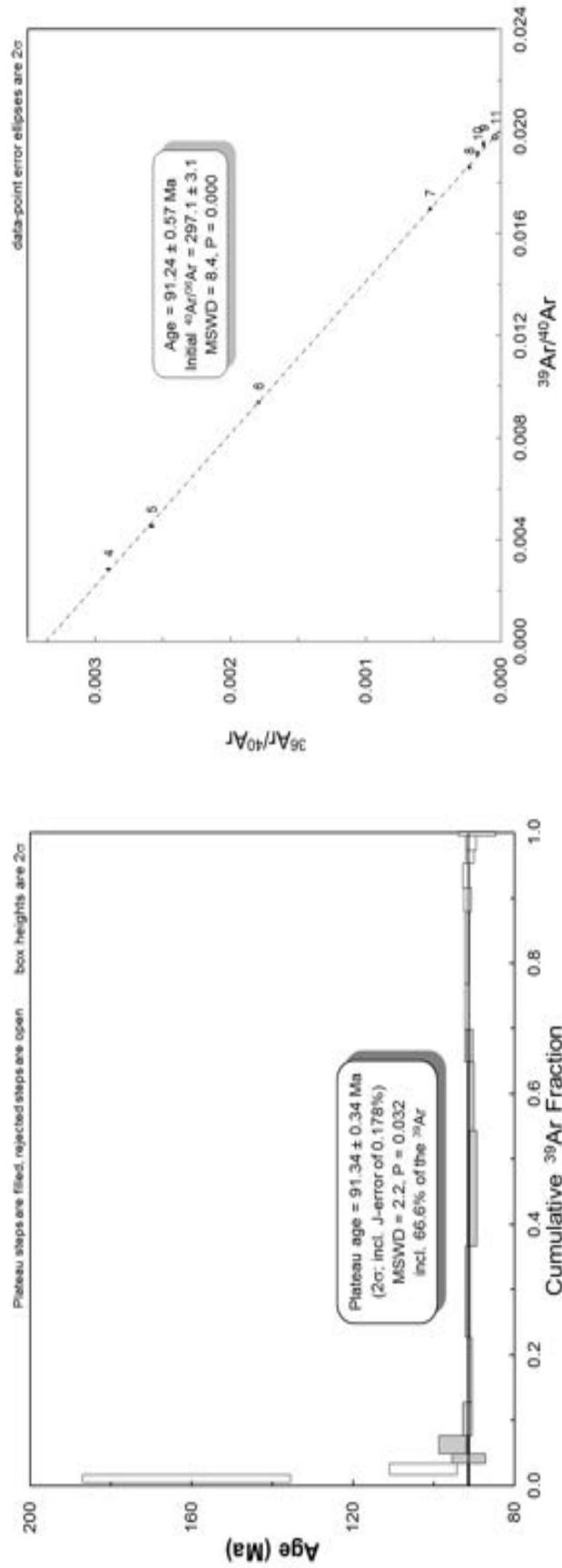


Figure 11: Laser step-heating results S0234 DR4-1

Sample		S0234 DR6-1		Material		Glass							
J value	2σ % error	Mass (mg)											
0,001042	0,178	3,586											
Step #	power (W)	<sup>40</sup> Ar/ <sup>39</sup> Ar	<sup>37</sup> Ar/ <sup>39</sup> Ar	<sup>36</sup> Ar/ <sup>39</sup> Ar	<sup>39</sup> Ar <sub>K</sub> (moles)	Ca/K	% <sup>40</sup> Ar <sub>atm</sub>	Cumulative fraction of <sup>39</sup> Ar	Age (Ma)	± 2σ (Ma)	<sup>36</sup> Ar/ <sup>39</sup> Ar AI		
1	0,1	72,74	1,79	0,07	1,87E-16	3,52	26,88	0,01	97,44	2,09	0,016808		
2	0,2	53,43	2,10	0,01	7,53E-16	4,11	5,69	0,05	92,47	0,44	0,002610		
3	0,3	50,36	2,24	0,00	1,39E-15	4,39	2,15	0,13	90,48	0,40	0,000929		
4	0,4	49,14	2,33	0,00	1,49E-15	4,57	0,93	0,21	89,42	0,40	0,000390		
5	0,5	48,87	2,37	0,00	1,66E-15	4,64	0,34	0,30	89,47	0,28	0,000138		
6	0,6	48,91	2,39	0,00	1,81E-15	4,68	0,55	0,39	89,36	0,40	0,000228		
7	0,7	48,77	2,41	0,00	2,05E-15	4,73	0,50	0,50	89,16	0,35	0,000205		
8	0,8	48,63	2,46	0,00	1,49E-15	4,84	0,46	0,58	88,95	0,36	0,000187		
9	0,9	48,91	2,49	0,00	1,35E-15	4,89	0,67	0,66	89,25	0,38	0,000279		
10	1,0	48,93	2,50	0,00	9,83E-16	4,90	0,59	0,71	89,37	0,48	0,000245		
11	1,1	49,09	2,69	0,00	7,43E-16	5,29	0,81	0,75	89,47	0,76	0,000338		
12	1,2	48,90	2,68	0,00	5,73E-16	5,26	0,42	0,78	89,47	0,83	0,000174		
13	1,4	48,65	2,69	0,00	6,49E-16	5,29	0,31	0,82	89,13	0,72	0,000125		
14	1,5	48,99	2,77	0,00	6,73E-16	5,43	0,21	0,85	89,83	0,62	0,000083		
15	2,0	48,89	2,85	0,00	8,67E-16	5,59	0,34	0,90	89,54	0,71	0,000139		
16	3,0	48,88	3,14	0,00	7,96E-16	6,17	0,72	0,94	89,20	0,49	0,000298		
17	5,0	49,01	3,76	0,00	8,25E-16	7,39	0,66	0,99	89,52	0,55	0,000271		
18	10,0	49,25	5,10	0,00	2,08E-16	10,02	1,22	1,00	89,53	1,71	0,000511		
19	15,0	50,43	7,48	0,00	3,31E-17	14,74	-0,39	1,00	93,23	9,31	-		
Cruise	Sample	Phase	% K <sub>2</sub> O	Plateau age (Ma)	± 2σ (Ma)	% <sup>39</sup> Ar fraction	MSWD	P	Steps	Inverse isochron age (Ma; 95% conf.)	Initial <sup>40</sup> Ar/ <sup>36</sup> Ar (95% conf.)	MSWD	P
S0234	DR 6-1	Glass	1,91	89,33	± 0,20	87,4	0,79	0,69	4-19	Plateau steps = 89,01 ± 0,27	491 ± 310	0,61	0,86

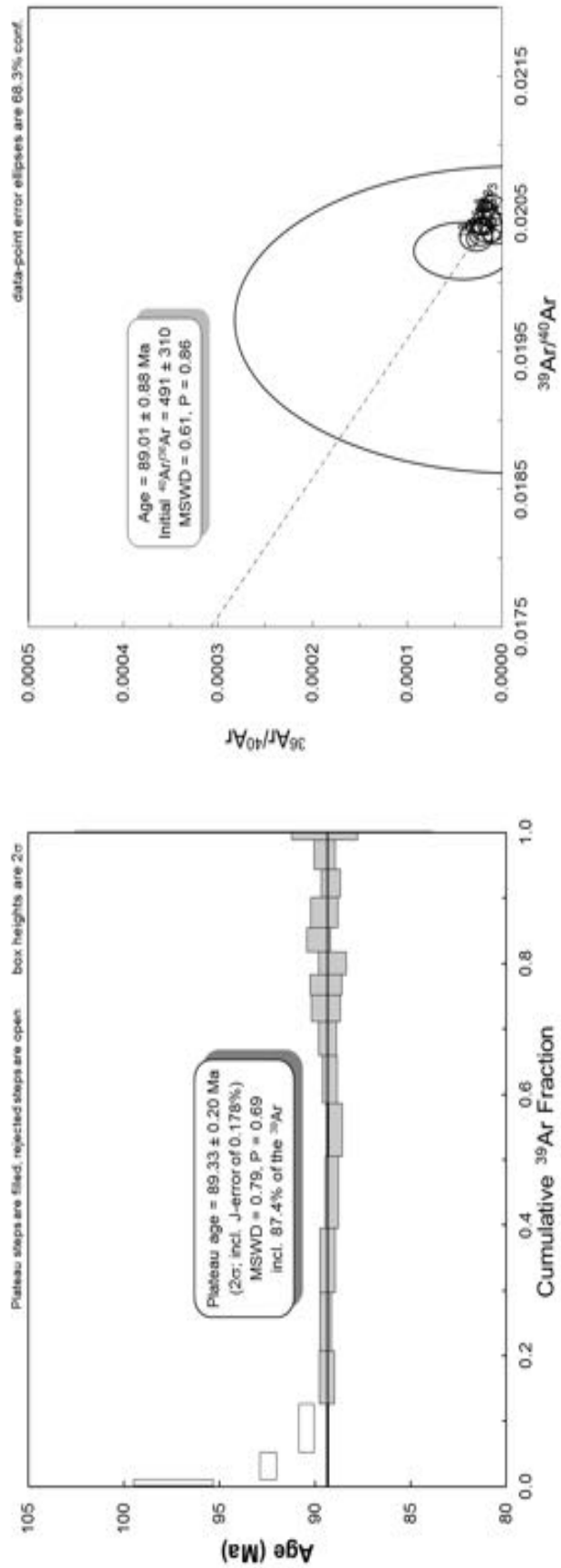


Figure 12: Laser step-heating results S0234 DR6-1

**Appendix D: Accuracy of major element data**

Accuracy of XRF major element data for several international reference materials (Institute of Mineralogy and Petrography at the University of Hamburg)						
Element	JGB-1	JGB-1	JGB-1*	Mean	Std. dev. ( $\pm 1\sigma$ abs)	Std. dev. ( $\pm 1\sigma$ %)
SiO <sub>2</sub>	44,1	43,73	43,44	43,92	0,26	0,60
TiO <sub>2</sub>	1,62	1,62	1,62	1,62	0,00	0,00
Al <sub>2</sub> O <sub>3</sub>	17,8	17,71	17,66	17,76	0,06	0,36
Fe <sub>2</sub> O <sub>3</sub>	15,41	15,33	15,16	15,37	0,06	0,37
MnO	0,19	0,19	0,17	0,19	0,00	0,00
MgO	7,78	7,91	7,83	7,85	0,09	1,17
CaO	11,84	11,87	11,98	11,86	0,02	0,18
Na <sub>2</sub> O	1,26	1,29	1,23	1,28	0,02	1,66
K <sub>2</sub> O	0,23	0,23	0,24	0,23	0,00	0,00
P <sub>2</sub> O <sub>5</sub>	0,05	0,06	0,05	0,06	0,01	12,86
<b>SUM</b>	100,28	99,94	99,38	100,11		

Accuracy of XRF major element data for several international reference materials (Institute of Mineralogy and Petrography at the University of Hamburg)						
Element	JB-3	JB-3	JB-3*	Mean	Std. dev. ( $\pm 1\sigma$ abs)	Std. dev. ( $\pm 1\sigma$ %)
SiO <sub>2</sub>	50,79	50,28	51,04	50,54	0,36	0,71
TiO <sub>2</sub>	1,43	1,42	1,45	1,43	0,01	0,50
Al <sub>2</sub> O <sub>3</sub>	17,25	17,2	16,89	17,23	0,04	0,21
Fe <sub>2</sub> O <sub>3</sub>	11,84	11,8	11,88	11,82	0,03	0,24
MnO	0,18	0,18	0,16	0,18	0,00	0,00
MgO	5,05	5,14	5,2	5,10	0,06	1,25
CaO	9,7	9,71	9,86	9,71	0,01	0,07
Na <sub>2</sub> O	2,69	2,81	2,82	2,75	0,08	3,09
K <sub>2</sub> O	0,75	0,75	0,78	0,75	0,00	0,00
P <sub>2</sub> O <sub>5</sub>	0,29	0,29	0,29	0,29	0,00	0,00
<b>SUM</b>	99,97	99,58	100,37	99,775		

Accuracy of XRF major element data for several international reference materials (Institute of Mineralogy and Petrography at the University of Hamburg)						
Element	JB-2	JB-2	JB-2*	Mean	Std. dev. ( $\pm 1\sigma$ abs)	Std. dev. ( $\pm 1\sigma$ %)
SiO <sub>2</sub>	54,08	53,48	53,2	53,78	0,42	0,79
TiO <sub>2</sub>	1,18	1,18	1,19	1,18	0,00	0,00
Al <sub>2</sub> O <sub>3</sub>	14,83	14,77	14,67	14,80	0,04	0,29
Fe <sub>2</sub> O <sub>3</sub>	14,51	14,41	14,34	14,46	0,07	0,49
MnO	0,22	0,22	0,2	0,22	0,00	0,00
MgO	4,57	4,66	4,66	4,62	0,06	1,38
CaO	9,87	9,86	9,89	9,87	0,01	0,07
Na <sub>2</sub> O	2,06	2,11	2,03	2,09	0,04	1,70
K <sub>2</sub> O	0,42	0,41	0,42	0,42	0,01	1,70
P <sub>2</sub> O <sub>5</sub>	0,1	0,1	0,1	0,10	0,00	0,00
<b>SUM</b>	101,84	101,2	100,7	101,52		

Accuracy of XRF major element data for several international reference materials (Institute of Mineralogy and Petrography at the University of Hamburg)						
Element	JA-3	JA-3	JA-3*	Mean	Std. dev. ( $\pm 1\sigma$ abs)	Std. dev. ( $\pm 1\sigma$ %)
SiO <sub>2</sub>	60,82	61,7	62,26	61,26	0,62	1,02
TiO <sub>2</sub>	0,68	0,68	0,68	0,68	0,00	0,00
Al <sub>2</sub> O <sub>3</sub>	15,37	15,37	15,57	15,37	0,00	0,00
Fe <sub>2</sub> O <sub>3</sub>	6,43	6,44	6,59	6,44	0,01	0,11
MnO	0,1	0,11	0,106	0,11	0,01	6,73
MgO	3,65	3,59	3,65	3,62	0,04	1,17
CaO	6,14	6,16	6,28	6,15	0,01	0,23
Na <sub>2</sub> O	3,18	3,1	3,17	3,14	0,06	1,80
K <sub>2</sub> O	1,38	1,37	1,41	1,38	0,01	0,51
P <sub>2</sub> O <sub>5</sub>	0,11	0,11	0,11	0,11	0,00	0,00
<b>SUM</b>	97,86	98,63	99,826	98,245		

Accuracy of XRF major element data for several international reference materials (Institute of Mineralogy and Petrography at the University of Hamburg)						
Element	JG-3	JG-3	JG-3*	Mean	Std. dev. ( $\pm 1\sigma$ abs)	Std. dev. ( $\pm 1\sigma$ %)
SiO <sub>2</sub>	67,66	66,6	67,1	67,13	0,75	1,12
Al <sub>2</sub> O <sub>3</sub>	15,5	15,5	15,52	15,50	0,00	0,00
Fe <sub>2</sub> O <sub>3</sub>	3,72	3,69	3,73	3,71	0,02	0,57
MnO	0,07	0,07	0,072	0,07	0,00	0,00
MgO	1,78	1,83	1,79	1,81	0,04	1,96
CaO	3,77	3,73	3,76	3,75	0,03	0,75
Na <sub>2</sub> O	4,04	4,18	4,03	4,11	0,10	2,41
K <sub>2</sub> O	2,62	2,62	2,63	2,62	0,00	0,00
TiO <sub>2</sub>	0,48	0,48	0,48	0,48	0,00	0,00
P <sub>2</sub> O <sub>5</sub>	0,13	0,12	0,12	0,13	0,01	5,66
<b>SUM</b>	99,77	98,82	99,232	99,295		

Accuracy of XRF major element data for several international reference materials (Institute of Mineralogy and Petrography at the University of Hamburg)						
Element	JG-2	JG-2	JG-2*	Mean	Std. dev. ( $\pm 1\sigma$ abs)	Std. dev. ( $\pm 1\sigma$ %)
SiO <sub>2</sub>	76,47	78	76,95	77,24	1,08	1,40
TiO <sub>2</sub>	0,04	0,04	0,04	0,04	0,00	0,00
Al <sub>2</sub> O <sub>3</sub>	12,38	12,41	12,41	12,40	0,02	0,17
Fe <sub>2</sub> O <sub>3</sub>	0,91	0,93	0,92	0,92	0,01	1,54
MnO	0,02	0,02	0,015	0,02	0,00	0,00
MgO	0,05	0,04	0,04	0,05	0,01	15,71
CaO	0,7	0,72	0,8	0,71	0,01	1,99
Na <sub>2</sub> O	3,68	3,58	3,55	3,63	0,07	1,95
K <sub>2</sub> O	4,71	4,71	4,72	4,71	0,00	0,00
P <sub>2</sub> O <sub>5</sub>	0,01	0,01	0,002	0,01	0,00	0,00
<b>SUM</b>	98,97	100,46	99,447	99,715		

EMP	VG-2	VG-2	VG-2	VG-2	VG-2	VG-2
SiO <sub>2</sub>	50,85	51,14	51,31	50,40	51,21	49,75
TiO <sub>2</sub>	1,91	1,91	1,84	1,87	1,84	1,86
Al <sub>2</sub> O <sub>3</sub>	13,90	13,98	13,80	13,66	13,60	13,45
FeO	11,61	11,38	11,92	11,90	11,88	11,27
MnO	0,23	0,23	0,25	0,27	0,24	0,19
MgO	6,96	7,08	6,99	7,12	7,06	7,02
CaO	11,32	11,35	11,30	11,25	11,24	11,15
Na <sub>2</sub> O	2,58	2,72	2,94	2,63	2,81	2,85
K <sub>2</sub> O	0,20	0,19	0,20	0,20	0,18	0,20
P <sub>2</sub> O <sub>5</sub>	0,21	0,14	0,19	0,16	0,14	0,22
F	0,06	0,00	0,03	0,03	0,00	0,00
SO <sub>3</sub>	0,41	0,37	0,41	0,41	0,36	0,38
Cl	0,02	0,03	0,03	0,02	0,03	0,03
<b>Total</b>	100,28	100,53	101,19	99,91	100,60	98,38

EMP	VG-2	VG-2	Mean	Std. dev. (±1σ abs)	Std. dev. (±1σ %)	VG-2*
SiO <sub>2</sub>	50,74	50,63	50,76	0,51	1,00	50,81
TiO <sub>2</sub>	1,90	1,85	1,87	0,03	1,61	1,85
Al <sub>2</sub> O <sub>3</sub>	13,97	13,81	13,77	0,19	1,35	14,06
FeO	11,80	11,73	11,69	0,24	2,07	11,84
MnO	0,18	0,11	0,21	0,05	23,53	0,22
MgO	7,05	7,00	7,04	0,05	0,74	6,71
CaO	11,10	11,28	11,25	0,09	0,77	11,12
Na <sub>2</sub> O	3,01	2,73	2,78	0,15	5,30	2,62
K <sub>2</sub> O	0,20	0,20	0,20	0,01	3,29	0,19
P <sub>2</sub> O <sub>5</sub>	0,16	0,19	0,18	0,03	16,82	0,20
F	0,08	0,08	0,03	0,03	99,31	0,03
SO <sub>3</sub>	0,36	0,46	0,39	0,03	8,61	0,35
Cl	0,04	0,04	0,03	0,01	25,24	0,03
<b>Total</b>	100,58	100,10				

\* Working values are from Govindaraju, K., 1994, Compilation of Working Values and Sample Description for 383 Geostandards: Geostandards Newsletter, v. 18, no. 2, p. 331-331.

Std. dev.= Standard deviation

abs=absolute

## Appendix E: Accuracy of trace element data

Sample:	BIR-1	BIR-1	BIR-1	BIR-1	Mean	Std. dev. ( $\pm 1\sigma$ abs)	Std. dev. ( $\pm 1\sigma$ %)	GEOREM
Li (ppm)	3,36	3,39	3,38	3,41	3,39	0,02	0,62	3,2
Sc (ppm)	44,4	44,0	42,3	43,2	43,5	0,91	2,10	43
V (ppm)	316	319	309	316	315	4,25	1,35	319
Cr (ppm)	378	377	367	372	373	5,09	1,36	391
Co (ppm)	50,5	51,1	50,4	50,8	50,7	0,33	0,66	52
Ni (ppm)	160	162	161	164	162	1,30	0,81	166
Cu (ppm)	116	119	112	113	115	3,13	2,73	119
Zn (ppm)	70,6	70,3	68,2	68,3	69,4	1,28	1,84	72
Ga (ppm)	16,0	15,9	15,6	15,7	15,8	0,19	1,23	15,3
Rb (ppm)	0,205	0,208	0,211	0,210	0,209	0,00	1,35	0,2
Sr (ppm)	106	106	108	107	107	0,70	0,65	109
Y (ppm)	15,2	15,4	15,7	15,8	15,5	0,29	1,86	15,6
Zr (ppm)	14,5	14,6	14,9	14,9	14,7	0,22	1,49	14
Nb (ppm)	0,520	0,526	0,533	0,539	0,529	0,01	1,57	0,55
Cs (ppm)	0,008	0,008	0,007	0,006	0,007	0,00	13,65	0,007
Ba (ppm)	6,55	6,61	6,85	6,97	6,75	0,20	2,93	7,14
La (ppm)	0,601	0,608	0,616	0,626	0,613	0,01	1,76	0,615
Ce (ppm)	1,86	1,88	1,93	1,96	1,91	0,05	2,51	1,92
Pr (ppm)	0,365	0,367	0,383	0,384	0,375	0,01	2,69	0,37
Nd (ppm)	2,41	2,39	2,48	2,49	2,44	0,05	2,12	2,38
Sm (ppm)	1,11	1,12	1,16	1,16	1,14	0,03	2,42	1,12
Eu (ppm)	0,528	0,525	0,554	0,556	0,541	0,02	3,08	0,53
Gd (ppm)	1,79	1,82	1,83	1,86	1,82	0,03	1,53	1,87
Tb (ppm)	0,355	0,356	0,370	0,372	0,363	0,01	2,55	0,36
Dy (ppm)	2,58	2,57	2,66	2,68	2,62	0,05	2,04	2,51
Ho (ppm)	0,566	0,567	0,586	0,594	0,578	0,01	2,38	0,56
Er (ppm)	1,61	1,63	1,69	1,70	1,66	0,04	2,68	1,66
Tm (ppm)	0,245	0,246	0,254	0,255	0,250	0,01	2,10	0,25
Yb (ppm)	1,63	1,65	1,66	1,68	1,66	0,02	1,14	1,65
Lu (ppm)	0,254	0,257	0,259	0,261	0,258	0,00	1,14	0,25
Hf (ppm)	0,565	0,570	0,569	0,575	0,570	0,00	0,74	0,582
Ta (ppm)	0,038	0,040	0,040	0,041	0,040	0,00	2,52	0,036
Pb (ppm)	2,88	3,01	3,18	3,25	3,08	0,17	5,42	3,1
Th (ppm)	0,033	0,034	0,031	0,030	0,032	0,00	5,53	0,032
U (ppm)	0,014	0,015	0,011	0,012	0,013	0,00	13,73	0,01

Sample:	BHVO-2	BHVO-2	BHVO-2	BHVO-2	BHVO-2	Mean	Std. dev. ( $\pm 1\sigma$ abs)	Std. dev. ( $\pm 1\sigma$ %)	GEOREM
Li (ppm)	4,71	4,60	4,66	4,73	4,53	4,65	0,08	1,77	4,8
Sc (ppm)	32,6	31,7	32,1	33,3	32,4	32,4	0,61	1,87	32
V (ppm)	319	315	317	327	320	320	4,65	1,45	317
Cr (ppm)	296	290	288	300	292	293	4,64	1,58	280
Co (ppm)	45,3	44,2	44,9	46,1	44,9	45,1	0,72	1,60	45
Ni (ppm)	122	118	120	121	119	120	1,88	1,57	119
Cu (ppm)	133	128	133	130	127	130	2,70	2,08	127
Zn (ppm)	110	106	107	109	107	108	1,56	1,45	103
Ga (ppm)	22,7	22,1	22,7	22,6	22,0	22,4	0,34	1,51	22
Rb (ppm)	9,49	9,31	9,37	9,42	9,20	9,36	0,11	1,16	9,11
Sr (ppm)	385	377	384	395	384	385	6,37	1,65	396
Y (ppm)	25,7	25,4	25,6	26,6	26,0	25,9	0,46	1,79	26
Zr (ppm)	168	166	166	171	170	168	2,16	1,28	172
Nb (ppm)	17,9	17,4	17,8	18,5	18,1	17,9	0,38	2,10	18,1
Cs (ppm)	0,110	0,106	0,108	0,109	0,108	0,108	0,00	1,22	0,1
Ba (ppm)	133	127	128	134	131	131	2,97	2,27	131
La (ppm)	15,5	15,1	15,3	15,6	15,3	15,4	0,18	1,15	15,2
Ce (ppm)	37,7	37,0	37,1	38,6	37,6	37,6	0,63	1,67	37,5
Pr (ppm)	5,32	5,18	5,25	5,45	5,32	5,31	0,10	1,88	5,35
Nd (ppm)	25,0	24,5	24,6	25,5	25,0	24,9	0,42	1,68	24,5
Sm (ppm)	6,21	6,12	6,13	6,38	6,18	6,20	0,11	1,71	6,07
Eu (ppm)	2,10	2,07	2,08	2,17	2,12	2,11	0,04	1,86	2,07
Gd (ppm)	6,23	6,13	6,16	6,31	6,20	6,21	0,07	1,15	6,24
Tb (ppm)	0,936	0,929	0,934	0,977	0,949	0,945	0,02	2,04	0,92
Dy (ppm)	5,38	5,27	5,35	5,50	5,37	5,37	0,08	1,56	5,31
Ho (ppm)	0,979	0,967	0,986	1,009	0,981	0,984	0,02	1,54	0,98
Er (ppm)	2,45	2,41	2,42	2,52	2,48	2,46	0,05	1,89	2,54
Tm (ppm)	0,330	0,326	0,325	0,333	0,327	0,328	0,00	0,95	0,33
Yb (ppm)	2,01	1,98	1,97	2,03	1,98	2,00	0,03	1,34	2
Lu (ppm)	0,285	0,282	0,284	0,292	0,285	0,285	0,00	1,38	0,274
Hf (ppm)	4,31	4,25	4,26	4,31	4,19	4,26	0,05	1,15	4,36
Ta (ppm)	1,11	1,08	1,10	1,16	1,13	1,12	0,03	2,60	1,14
Pb (ppm)	1,65	1,47	1,54	1,79	1,58	1,61	0,12	7,44	1,6
Th (ppm)	1,25	1,19	1,20	1,20	1,18	1,20	0,03	2,26	1,22
U (ppm)	0,412	0,404	0,410	0,422	0,412	0,412	0,01	1,58	0,403

Sample	DR-90-1		Diff. (%)	DR90-6		Diff. (%)	DR62-1		Diff. (%)
	Dup 1	Dup 2		Dup1	Dup2		Dup1	Dup2	
Li (ppm)	28,5	28,8	<b>1,1</b>	28,2	28,2	<b>0,2</b>	9,30	9,25	<b>0,56</b>
Sc (ppm)	24,0	23,6	<b>1,3</b>	24,8	24,9	<b>0,3</b>	37,0	36,9	<b>0,41</b>
V (ppm)	257	254	<b>1,3</b>	249	250	<b>0,2</b>	407	401	<b>1,27</b>
Cr (ppm)	162	159	<b>1,7</b>	379	380	<b>0,3</b>	57,4	57,1	<b>0,45</b>
Co (ppm)	38,9	38,9	<b>0,0</b>	47,5	47,4	<b>0,3</b>	40,4	40,0	<b>1,19</b>
Ni (ppm)	86,5	86,5	<b>0,1</b>	184	185	<b>0,5</b>	47,7	47,3	<b>0,85</b>
Cu (ppm)	68,6	68,5	<b>0,1</b>	85,6	86,0	<b>0,5</b>	220	216	<b>1,84</b>
Zn (ppm)	112	112	<b>0,8</b>	111	112	<b>0,8</b>	115	115	<b>0,82</b>
Ga (ppm)	24,3	24,2	<b>0,6</b>	21,9	22,0	<b>0,7</b>	22,9	22,6	<b>1,07</b>
Rb (ppm)	29,9	30,0	<b>0,0</b>	14,7	14,8	<b>0,8</b>	18,9	18,7	<b>1,18</b>
Sr (ppm)	702	698	<b>0,7</b>	552	551	<b>0,0</b>	371	366	<b>1,42</b>
Y (ppm)	29,0	28,9	<b>0,3</b>	25,0	25,2	<b>0,7</b>	36,23	35,93	<b>0,84</b>
Zr (ppm)	299	297	<b>0,8</b>	225	227	<b>1,0</b>	228	226	<b>0,90</b>
Nb (ppm)	68,6	68,1	<b>0,7</b>	46,2	46,6	<b>0,8</b>	21,0	20,6	<b>1,71</b>
Cs (ppm)	0,887	0,886	<b>0,1</b>	1,58	1,61	<b>1,6</b>	0,27	0,27	<b>0,83</b>
Ba (ppm)	392	393	<b>0,5</b>	260	261	<b>0,5</b>	306	306	<b>0,21</b>
La (ppm)	48,6	48,4	<b>0,2</b>	32,9	33,1	<b>0,5</b>	26,6	26,3	<b>1,18</b>
Ce (ppm)	99,7	99,7	<b>0,0</b>	68,9	69,4	<b>0,7</b>	58,6	57,7	<b>1,51</b>
Pr (ppm)	11,7	11,7	<b>0,1</b>	8,50	8,54	<b>0,4</b>	7,50	7,42	<b>1,12</b>
Nd (ppm)	47,6	47,4	<b>0,4</b>	35,8	35,9	<b>0,3</b>	32,9	32,4	<b>1,59</b>
Sm (ppm)	9,34	9,35	<b>0,1</b>	7,56	7,62	<b>0,8</b>	7,57	7,48	<b>1,18</b>
Eu (ppm)	2,96	2,96	<b>0,0</b>	2,47	2,48	<b>0,5</b>	2,46	2,43	<b>1,34</b>
Gd (ppm)	8,26	8,27	<b>0,1</b>	6,94	7,02	<b>1,2</b>	7,57	7,56	<b>0,18</b>
Tb (ppm)	1,16	1,16	<b>0,3</b>	1,01	1,01	<b>0,5</b>	1,19	1,18	<b>0,74</b>
Dy (ppm)	6,19	6,24	<b>0,9</b>	5,39	5,43	<b>0,9</b>	6,99	6,95	<b>0,65</b>
Ho (ppm)	1,11	1,11	<b>0,1</b>	0,961	0,967	<b>0,6</b>	1,36	1,34	<b>1,03</b>
Er (ppm)	2,77	2,78	<b>0,1</b>	2,35	2,37	<b>0,9</b>	3,57	3,52	<b>1,44</b>
Tm (ppm)	0,370	0,374	<b>1,1</b>	0,309	0,310	<b>0,5</b>	0,497	0,493	<b>0,87</b>
Yb (ppm)	2,29	2,29	<b>0,2</b>	1,83	1,84	<b>0,9</b>	3,13	3,12	<b>0,22</b>
Lu (ppm)	0,332	0,332	<b>0,1</b>	0,264	0,262	<b>0,7</b>	0,465	0,464	<b>0,25</b>
Hf (ppm)	6,52	6,54	<b>0,3</b>	5,03	5,09	<b>1,2</b>	5,36	5,29	<b>1,42</b>
Ta (ppm)	4,00	4,01	<b>0,4</b>	2,89	2,92	<b>1,0</b>	1,27	1,24	<b>2,20</b>
Pb (ppm)	2,76	2,81	<b>1,8</b>	1,87	1,90	<b>1,7</b>	2,88	2,83	<b>1,78</b>
Th (ppm)	5,16	5,21	<b>0,9</b>	3,39	3,39	<b>0,1</b>	2,44	2,41	<b>1,12</b>
U (ppm)	1,47	1,47	<b>0,3</b>	1,05	1,07	<b>1,8</b>	0,568	0,551	<b>2,95</b>

Sample	DR84-1		Diff. (%)	DR-35-1		Diff. (%)
	Dup1	Dup2		Dup 1	Dup 2	
Li (ppm)	27,1	27,2	<b>0,45</b>	21,4	21,2	<b>0,69</b>
Sc (ppm)	26,6	27,2	<b>2,14</b>	49,2	49,4	<b>0,35</b>
V (ppm)	245	252	<b>2,87</b>	287	290	<b>0,80</b>
Cr (ppm)	53,2	54,7	<b>2,84</b>	222	221	<b>0,33</b>
Co (ppm)	20,9	21,4	<b>2,49</b>	27,8	28,1	<b>1,22</b>
Ni (ppm)	39,7	40,7	<b>2,55</b>	55,3	55,9	<b>0,97</b>
Cu (ppm)	111	114	<b>3,02</b>	131	132	<b>0,72</b>
Zn (ppm)	2260	2335	<b>3,32</b>	110	105	<b>4,38</b>
Ga (ppm)	20,9	21,2	<b>1,34</b>	21,8	22,0	<b>0,85</b>
Rb (ppm)	58,0	59,0	<b>1,80</b>	11,9	11,9	<b>0,18</b>
Sr (ppm)	391	398	<b>1,68</b>	297	293	<b>1,39</b>
Y (ppm)	28,1	28,5	<b>1,50</b>	36,8	36,8	<b>0,11</b>
Zr (ppm)	221	227	<b>3,05</b>	166	166	<b>0,01</b>
Nb (ppm)	20,0	20,2	<b>1,45</b>	10,5	10,5	<b>0,03</b>
Cs (ppm)	0,28	0,29	<b>1,40</b>	0,45	0,45	<b>0,71</b>
Ba (ppm)	452	459	<b>1,45</b>	130	131	<b>0,83</b>
La (ppm)	23,0	23,3	<b>1,52</b>	16,9	16,9	<b>0,36</b>
Ce (ppm)	51,5	52,1	<b>1,26</b>	35,8	35,7	<b>0,26</b>
Pr (ppm)	6,59	6,65	<b>0,79</b>	4,96	4,96	<b>0,20</b>
Nd (ppm)	28,5	28,8	<b>1,06</b>	23,1	23,0	<b>0,75</b>
Sm (ppm)	6,37	6,44	<b>1,20</b>	5,97	5,95	<b>0,43</b>
Eu (ppm)	2,20	2,22	<b>1,03</b>	2,03	2,03	<b>0,36</b>
Gd (ppm)	6,24	6,33	<b>1,55</b>	6,69	6,65	<b>0,51</b>
Tb (ppm)	0,963	0,974	<b>1,08</b>	1,09	1,10	<b>0,41</b>
Dy (ppm)	5,58	5,62	<b>0,77</b>	6,86	6,83	<b>0,39</b>
Ho (ppm)	1,06	1,08	<b>1,50</b>	1,38	1,37	<b>1,31</b>
Er (ppm)	2,78	2,83	<b>1,61</b>	3,71	3,70	<b>0,38</b>
Tm (ppm)	0,384	0,391	<b>1,72</b>	0,540	0,541	<b>0,08</b>
Yb (ppm)	2,40	2,43	<b>1,46</b>	3,47	3,45	<b>0,43</b>
Lu (ppm)	0,353	0,356	<b>1,05</b>	0,521	0,518	<b>0,51</b>
Hf (ppm)	5,21	5,27	<b>1,23</b>	4,15	4,15	<b>0,22</b>
Ta (ppm)	1,32	1,33	<b>0,96</b>	0,646	0,647	<b>0,12</b>
Pb (ppm)	6,33	6,40	<b>1,06</b>	1,86	1,68	<b>9,46</b>
Th (ppm)	2,72	2,75	<b>1,05</b>	1,56	1,56	<b>0,27</b>
U (ppm)	0,574	0,581	<b>1,13</b>	0,732	0,730	<b>0,23</b>

Diff. = Difference

Std. dev.= Standard deviation

abs=absolute

Rel. Dev.=relative deviation

GEOREM values from: Jochum et al. (2016), Reference Values Following ISO Guidelines for Frequently

Requested Rock Reference Materials. Geostand Geoanal Res, 40: 333-350. doi:10.1111/j.1751-



## Appendix F: Literature data

### South Atlantic

---

---

#### Ascension

- Cohen, R. S., and O'Nions, R. K., 1982, Identification of recycled continental material in the mantle from Sr, Nd and Pb isotope investigations: *Earth and Planetary Science Letters*, v. 61, no. 1, p. 73-84.
- Halliday, A. N., Davies, G. R., Lee, D.-C., Tommasini, S., Paslick, C. R., Fitton, J. G., and James, D. E., 1992, Lead isotope evidence for young trace element enrichment in the oceanic upper mantle: *Nature*, v. 359, p. 623.
- Harris, C., Bell, J. D., and Atkins, F. B., 1982, Isotopic composition of lead and strontium in lavas and coarse-grained blocks from Ascension Island, South Atlantic: *Earth and Planetary Science Letters*, v. 60, no. 1, p. 79-85.
- Kar, A., Weaver, B., Davidson, J., and Colucci, M., 1998, Origin of Differentiated Volcanic and Plutonic Rocks from Ascension Island, South Atlantic Ocean: *Journal of Petrology*, v. 39, no. 5, p. 1009-1024.
- Salters, V. J. M., and White, W. M., 1998, Hf isotope constraints on mantle evolution: *Chemical Geology*, v. 145, no. 3-4, p. 447-460.
- Weaver, B., Kar, A., Davidson, J., and Colucci, M., 1996, Geochemical characteristics of volcanic rocks from ascension island, South Atlantic Ocean: *Geothermics*, v. 25, no. 4, p. 449-470.
- Weis, D., 1983, Pb isotopes in Ascension Island rocks: oceanic origin for the gabbroic to granitic plutonic xenoliths: *Earth and Planetary Science Letters*, v. 62, no. 2, p. 273-282.

#### Bouvet

- Sun, S.-S., 1980, Lead isotopic study of young volcanic rocks from mid-ocean ridges, ocean islands and island arcs: *Philosophical Transactions of the Royal Society of London. Series A, Mathematical and Physical Sciences*, v. 297, no. 1431, p. 409-445.

#### Discovery

- Schwindrofska, A., Hoernle, K., Hauff, F., van den Bogaard, P., Werner, R., and Garbe-Schönberg, D., 2016, Origin of enriched components in the South Atlantic: Evidence from 40 Ma geochemical zonation of the Discovery Seamounts: *Earth and Planetary Science Letters*, v. 441, p. 167-177.

## **Mid-Atlantic Ridge**

Class, Conny; Lehnert, Kerstin (2012): PetDB Expert MORB (Mid-Ocean Ridge Basalt)

Compilation. EarthChem Library. <http://dx.doi.org/10.1594/IEDA/100060>

## **Shona**

Hoernle, K., Schwindrofska, A., Werner, R., van den Bogaard, P., Hauff, F., Uenzelmann-Neben, G., and Garbe-Schönberg, D., 2016, Tectonic dissection and displacement of parts of Shona hotspot volcano 3500 km along the Agulhas-Falkland Fracture Zone: *Geology*, v. 44, no. 4, p. 263-266.

## **St. Helena**

Baker, I., 1969, Petrology of the Volcanic Rocks of Saint Helena Island, South Atlantic: *Geological Society of America Bulletin*, v. 80, no. 7, p. 1283-1310.

Chaffey, D. J., Cliff, R. A., and Wilson, B. M., 1989, Characterization of the St. Helena magma source: *Magmatism in the Ocean Basins*, v. 42, p. 19.

Grant, N. K., Powell, J. L., Burkholder, F. R., Walther, J. V., and Coleman, M. L., 1976, The isotopic composition of strontium and oxygen in lavas from St. Helena, South Atlantic: *Earth and Planetary Science Letters*, v. 31, no. 2, p. 209-223.

Hanyu, T., Kawabata, H., Tatsumi, Y., Kimura, J.-I., Hyodo, H., Sato, K., Miyazaki, T., Chang, Q., Hirahara, Y., Takahashi, T., Senda, R., and Nakai, S. i., 2014, Isotope evolution in the HIMU reservoir beneath St. Helena: Implications for the mantle recycling of U and Th: *Geochimica et Cosmochimica Acta*, v. 143, p. 232-252.

Kawabata, H., Hanyu, T., Chang, Q., Kimura, J.-I., Nichols, A. R. L., and Tatsumi, Y., 2011, The Petrology and Geochemistry of St. Helena Alkali Basalts: Evaluation of the Oceanic Crust-recycling Model for HIMU OIB: *Journal of Petrology*, v. 52, no. 4, p. 791-838.

Salters, V. J. M., Mallick, S., Hart, S. R., Langmuir, C. E., and Stracke, A., 2011, Domains of depleted mantle: New evidence from hafnium and neodymium isotopes: *Geochemistry, Geophysics, Geosystems*, v. 12, no. 8, p. n/a-n/a.

Weaver, B. L., Wood, D. A., Tarney, J., and Joron, J. L., 1987, Geochemistry of ocean island basalts from the South Atlantic: Ascension, Bouvet, St. Helena, Gough and Tristan da Cunha: *Geological Society, London, Special Publications*, v. 30, no. 1, p. 253-267.

Willbold, M., and Stracke, A., 2006, Trace element composition of mantle end-members: Implications for recycling of oceanic and upper and lower continental crust: *Geochemistry, Geophysics, Geosystems*, v. 7, no. 4, p. Q04004.

-, 2010, Formation of enriched mantle components by recycling of upper and lower continental crust: *Chemical Geology*, v. 276, no. 3-4, p. 188-197.

## **Walvis Ridge – Tristan-Gough hotspot track (EM I)**

- Class, C., and le Roex, A. P., 2008, Ce anomalies in Gough Island lavas — Trace element characteristics of a recycled sediment component: *Earth and Planetary Science Letters*, v. 265, no. 3–4, p. 475-486.
- Cliff, R. A., Baker, P. E., and Mateer, N. J., 1991, Geochemistry of inaccessible island volcanics: *Chemical Geology*, v. 92, no. 4, p. 251-260.
- Hoernle, K., Rohde, J., Hauff, F., Garbe-Schonberg, D., Homrighausen, S., Werner, R., and Morgan, J. P., 2015, How and when plume zonation appeared during the 132 Myr evolution of the Tristan Hotspot: *Nature Communication*, v. 6, p. 10.1038/ncomms8799.
- Le Maitre, R. W., 1962, Petrology of Volcanic Rocks, Gough Island, South Atlantic: *Geological Society of America Bulletin*, v. 73, no. 11, p. 1309-1340.
- Le Roex, A. P., 1985, Geochemistry, Mineralogy and Magmatic Evolution of the Basaltic and Trachytic Lavas from Gough Island, South Atlantic: *Journal of Petrology*, v. 26, no. 1, p. 149-186.
- Le Roex, A. P., Cliff, R. A., and Adair, B. J. I., 1990, Tristan da Cunha, South Atlantic: Geochemistry and Petrogenesis of a Basanite-Phonolite Lava Series: *Journal of Petrology*, v. 31, no. 4, p. 779-812.
- O'Connor, J. M., and Jokat, W., 2015a, Tracking the Tristan-Gough mantle plume using discrete chains of intraplate volcanic centers buried in the Walvis Ridge: *Geology*, v. 43, no. 8, p. 715-718.
- , 2015b, Age distribution of Ocean Drill sites across the Central Walvis Ridge indicates plate boundary control of plume volcanism in the South Atlantic: *Earth and Planetary Science Letters*, v. 424, p. 179-190.
- Richardson, S. H., Erlank, A. J., Reid, D. L., and Duncan, A. R., 1984, Major and Trace-Elements and Nd and Sr Isotope Geochemistry of Basalts from the Deep-Sea Drilling Project Leg-74 Walvis Ridge Transect: Initial Reports of the Deep Sea Drilling Project, v. 74, no. Mar, p. 739-754.
- Rohde, J., Hoernle, K., Hauff, F., Werner, R., O'Connor, J., Class, C., Garbe-Schönberg, D., and Jokat, W., 2013a, 70 Ma chemical zonation of the Tristan-Gough hotspot track: *Geology*, v. 43, no. 3, p. 335-338.
- Rohde, J. K., van den Bogaard, P., Hoernle, K., Hauff, F., and Werner, R., 2013b, Evidence for an age progression along the Tristan-Gough volcanic track from new  $^{40}\text{Ar}/^{39}\text{Ar}$  ages on phenocryst phases: *Tectonophysics*, v. 604, p. 60-71.
- Salters, V. J. M., and Sachi-Kocher, A., 2010, An ancient metasomatic source for the Walvis Ridge basalts: *Chemical Geology*, v. 273, no. 3–4, p. 151-167.
- Thompson, G., and Humphris, S., 1984, Petrology and Geochemistry of rocks from the Walvis Ridge-Deep-Sea Drilling Project Leg-74, Site525, Site527 and Site528 Initial Reports of the Deep Sea Drilling Project, v. 74, no. MAR, p. 755-764.
- Weaver, B. L., Wood, D. A., Tarney, J., and Joron, J. L., 1987, Geochemistry of ocean island basalts from the South Atlantic: Ascension, Bouvet, St. Helena, Gough and Tristan da Cunha: Geological Society, London, Special Publications, v. 30, no. 1, p. 253-267.
- Willbold, M., and Stracke, A., 2006, Trace element composition of mantle end-members: Implications for recycling of oceanic and upper and lower continental crust: *Geochemistry, Geophysics, Geosystems*, v. 7, no. 4, p. Q04004.
- , 2010, Formation of enriched mantle components by recycling of upper and lower continental crust: *Chemical Geology*, v. 276, no. 3–4, p. 188-197.

## **Indian OIBs**

---

### **Comoros**

- Class, C., Goldstein, S. L., Altherr, R., and Bachèlery, P., 1998, The Process of Plume–Lithosphere Interactions in the Ocean Basins—the Case of Grande Comore: *Journal of Petrology*, v. 39, no. 5, p. 881-903.
- Deniel, C., 1998, Geochemical and isotopic (Sr, Nd, Pb) evidence for plume–lithosphere interactions in the genesis of Grande Comore magmas (Indian Ocean): *Chemical Geology*, v. 144, no. 3, p. 281-303.
- Pelleter, A.-A., Caroff, M., Cordier, C., Bachelery, P., Nehlig, P., Debeuf, D., and Arnaud, N., 2014, Melilite-bearing lavas in Mayotte (France): An insight into the mantle source below the Comores: *Lithos*, v. 208-209, no. Supplement C, p. 281-297.
- Späth, A., Roex, A. P. L., and Duncan, R. A., 1996, The Geochemistry of Lavas from the Gomores Archipelago, Western Indian Ocean: Petrogenesis and Mantle Source Region Characteristics: *Journal of Petrology*, v. 37, no. 4, p. 961-991.

### **Crozet**

- Breton, T., Nauret, F., Pichat, S., Moine, B., Moreira, M., Rose-Koga, E. F., Auclair, D., Bosq, C., and Wavrant, L.-M., 2013, Geochemical heterogeneities within the Crozet hotspot: *Earth and Planetary Science Letters*, v. 376, p. 126-136.

### **Reunion**

- Albarède, F., Luais, B., Fitton, G., Semet, M., Kaminski, E., Upton, B. G. J., Bachèlery, P., and Cheminée, J. L., 1997, The Geochemical Regimes of Piton de la Fournaise Volcano (Réunion) During the Last 530 000 Years: *Journal of Petrology*, v. 38, no. 2, p. 171-201.
- Boivin, P., and Bachèlery, P., 2009, Petrology of 1977 to 1998 eruptions of Piton de la Fournaise, La Réunion Island: *Journal of Volcanology and Geothermal Research*, v. 184, no. 1, p. 109-125.
- Luais, B., 2004, Temporal changes in Nd isotopic composition of Piton de la Fournaise magmatism (Réunion Island, Indian Ocean): *Geochemistry, Geophysics, Geosystems*, v. 5, no. 1, p. n/a-n/a.
- Moore, J., White, W. M., Paul, D., Duncan, R. A., Abouchami, W., and Galer, S. J. G., 2011, Evolution of shield-building and rejuvenescent volcanism of Mauritius: *Journal of Volcanology and Geothermal Research*, v. 207, no. 1, p. 47-66.
- Oversby, V. M., 1972, Genetic relations among the volcanic rocks of Réunion: chemical and lead isotopic evidence: *Geochimica et Cosmochimica Acta*, v. 36, no. 10, p. 1167-1179.
- Paul, D., White, W. M., and Blichert-Toft, J., 2005, Geochemistry of Mauritius and the origin of rejuvenescent volcanism on oceanic island volcanoes: *Geochemistry, Geophysics, Geosystems*, v. 6, no. 6, p. n/a-n/a.
- Vlastélic, I., Deniel, C., Bosq, C., Télouk, P., Boivin, P., Bachèlery, P., Famin, V., and Staudacher, T., 2009, Pb isotope geochemistry of Piton de la Fournaise historical lavas: *Journal of Volcanology and Geothermal Research*, v. 184, no. 1, p. 63-78.
- Vlastélic, I., Peltier, A., and Staudacher, T., 2007, Short-term (1998–2006) fluctuations of Pb isotopes at Piton de la Fournaise volcano (Reunion Island): Origins and constraints on the size and shape of the magma reservoir: *Chemical Geology*, v. 244, no. 1, p. 202-220.
- Vlastelic, I., Staudacher, T., and Semet, M., 2005, Rapid Change of Lava Composition from 1998 to 2002 at Piton de la Fournaise (Réunion) Inferred from Pb Isotopes and Trace Elements: Evidence for Variable Crustal Contamination: *Journal of Petrology*, v. 46, no. 1, p. 79-107.

## **Prince Edward**

Le Roex, A. P., Chevallier, L., Verwoerd, W. J., and Barends, R., 2012, Petrology and geochemistry of Marion and Prince Edward Islands, Southern Ocean: Magma chamber processes and source region characteristics: *Journal of Volcanology and Geothermal Research*, v. 223-224, p. 11-28.

## **Elan Bank sediments**

Ingle, S., Weis, D., and Frey, F. A., 2002, Indian Continental Crust Recovered from Elan Bank, Kerguelen Plateau (ODP Leg 183, Site 1137): *Journal of Petrology*, v. 43, no. 7, p. 1241-1257.

Nobre Silva, I. G., Weis, D., Scoates, J. S., and Barling, J., 2013, The Ninetyeast Ridge and its Relation to the Kerguelen, Amsterdam and St. Paul Hotspots in the Indian Ocean: *Journal of Petrology*, v. 54, no. 6, p. 1177-1210.

## **Pacific Ocean**

---

### **Chatham Island and Eastern Chatham Rise**

Panter, K. S., Blusztajn, J., Hart, S. R., Kyle, P. R., Esser, R., and McIntosh, W. C., 2006, The origin of HIMU in the SW Pacific: Evidence from intraplate volcanism in southern New Zealand and subantarctic islands: *Journal of Petrology*, v. 47, no. 9, p. 1673-1704.

Timm, C., Hoernle, K., Werner, R., Hauff, F., den Bogaard, P. v., White, J., Mortimer, N., and Garbe-Schönberg, D., 2010, Temporal and geochemical evolution of the Cenozoic intraplate volcanism of Zealandia: *Earth-Science Reviews*, v. 98, no. 1-2, p. 38-64.

### **Cook Austral islands (Mangaia, Tubuai and Old Rurutu)**

Chauvel, C., Hofmann, A. W., and Vidal, P., 1992, HIMU-EM : The French-Polynesian Connection: *Earth and Planetary Science Letters*, v. 110, no. 1-4, p. 99-119.

Dupuy, C., Barszczus, H. G., Dostal, J., Vidal, P., and Liotard, J. M., 1989, Subducted and recycled lithosphere as the mantle source of ocean island basalts from southern Polynesia, central Pacific: *Chemical Geology*, v. 77, no. 1, p. 1-18.

Hanyu, T., Dosso, L., Ishizuka, O., Tani, K., Hanan, B. B., Adam, C., Nakai, S. i., Senda, R., Chang, Q., and Tatsumi, Y., 2013, Geochemical diversity in submarine HIMU basalts from Austral Islands, French Polynesia: *Contributions to Mineralogy and Petrology*, v. 166, no. 5, p. 1285-1304.

Hanyu, T., Tatsumi, Y., Senda, R., Miyazaki, T., Chang, Q., Hirahara, Y., Takahashi, T., Kawabata, H., Suzuki, K., Kimura, J. I., and Nakai, S., 2011, Geochemical characteristics and origin of the HIMU reservoir: A possible mantle plume source in the lower mantle: *Geochemistry Geophysics Geosystems*, v. 12.

Kogiso, T., Tatsumi, Y., Shimoda, G., and Barszczus, H. G., 1997, High  $\mu$  (HIMU) ocean island basalts in southern Polynesia: New evidence for whole mantle scale recycling of subducted oceanic crust: *Journal of Geophysical Research: Solid Earth*, v. 102, no. B4, p. 8085-8103.

Lassiter, J. C., Blichert-Toft, J., Hauri, E. H., and Barszczus, H. G., 2003, Isotope and trace element variations in lavas from Raivavae and Rapa, Cook-Austral islands: constraints on the nature of HIMU- and EM-mantle and the origin of mid-plate volcanism in French Polynesia: *Chemical Geology*, v. 202, no. 1-2, p. 115-138.

Maury, R. C., Guille, G., Guillou, H., Chauvel, C., Rossi, P., Pallares, C., and Legendre, C., 2013, Temporal evolution of a Polynesian hotspot: New evidence from Raivavae (Austral islands, South Pacific ocean): *Bulletin de la Societe Geologique de France*, v. 184, p. 557-567.

Salters, V. J. M., Mallick, S., Hart, S. R., Langmuir, C. E., and Stracke, A., 2011, Domains of depleted mantle: New evidence from hafnium and neodymium isotopes: *Geochemistry, Geophysics, Geosystems*, v. 12, no. 8, p. n/a-n/a.

Woodhead, J. D., 1996, Extreme HIMU in an oceanic setting: the geochemistry of Mangaia Island (Polynesia), and temporal evolution of the Cook—Austral hotspot: *Journal of Volcanology and Geothermal Research*, v. 72, no. 1, p. 1-19.

### **FOZO (Raivavae, Mauke and young Rurutu)**

Chauvel, C., McDonough, W., Guille, G., Maury, R., and Duncan, R., 1997, Contrasting old and young volcanism in Rurutu Island, Austral chain: *Chemical Geology*, v. 139, no. 1-4, p. 125-143.

Lassiter, J. C., Blichert-Toft, J., Hauri, E. H., and Barszczus, H. G., 2003, Isotope and trace element variations in lavas from Raivavae and Rapa, Cook–Austral islands: constraints on the nature of HIMU- and EM-mantle and the origin of mid-plate volcanism in French Polynesia: *Chemical Geology*, v. 202, no. 1-2, p. 115-138.

### **Hikurangi**

Hoernle, K., Hauff, F., van den Bogaard, P., Werner, R., Mortimer, N., Geldmacher, J., Garbe-Schönberg, D., and Davy, B., 2010, Age and geochemistry of volcanic rocks from the Hikurangi and Manihiki oceanic Plateaus: *Geochimica et Cosmochimica Acta*, v. 74, no. 24, p. 7196-7219.

### **Manihiki-Baseament**

Hoernle, K., Hauff, F., van den Bogaard, P., Werner, R., Mortimer, N., Geldmacher, J., Garbe-Schönberg, D., and Davy, B., 2010, Age and geochemistry of volcanic rocks from the Hikurangi and Manihiki oceanic Plateaus: *Geochimica et Cosmochimica Acta*, v. 74, no. 24, p. 7196-7219.

Ingle, S., Mahoney, J. J., Sato, H., Coffin, M. F., Kimura, J.-I., Hirano, N., and Nakanishi, M., 2007, Depleted mantle wedge and sediment fingerprint in unusual basalts from the Manihiki Plateau, central Pacific Ocean: *Geology*, v. 35, no. 7, p. 595-598.

Timm, C., Hoernle, K., Werner, R., Hauff, F., den Bogaard, P. v., Michael, P., Coffin, M. F., and Koppers, A., 2011, Age and geochemistry of the oceanic Manihiki Plateau, SW Pacific: New evidence for a plume origin: *Earth and Planetary Science Letters*, v. 304, no. 1-2, p. 135-146.

### **Continental Rocks**

---

### **East African Rift volcanics**

Furman, T., Kaleta, K. M., Bryce, J. G., and Hanan, B. B., 2006, Tertiary Mafic Lavas of Turkana, Kenya: Constraints on East African Plume Structure and the Occurrence of High- $\mu$  Volcanism in Africa: *Journal of Petrology*, v. 47, no. 6, p. 1221-1244.

Keller, J., Zaitsev, A. N., and Wiedenmann, D., 2006, Primary magmas at Oldoinyo Lengai: The role of olivine melilitites: *Lithos*, v. 91, no. 1-4, p. 150-172.

Mana, S., Furman, T., Carr, M. J., Mollet, G. F., Mortlock, R. A., Feigenson, M. D., Turrin, B. D., and Swisher Iii, C. C., 2012, Geochronology and geochemistry of the Essimigor volcano: Melting of metasomatized lithospheric mantle beneath the North Tanzanian Divergence zone (East African Rift): *Lithos*, v. 155, p. 310-325.

Paslick, C., Halliday, A., James, D., and Dawson, J. B., 1995, Enrichment of the continental lithosphere by OIB melts: Isotopic evidence from the volcanic province of northern Tanzania: *Earth and Planetary Science Letters*, v. 130, no. 1, p. 109-126.

- Roex, A. P., Späth, A., and Zartman, R. E., 2001, Lithospheric thickness beneath the southern Kenya Rift: implications from basalt geochemistry: *Contributions to Mineralogy and Petrology*, v. 142, no. 1, p. 89-106.
- Rogers, N., Macdonald, R., Fitton, J. G., George, R., Smith, M., and Barreiro, B., 2000, Two mantle plumes beneath the East African rift system: Sr, Nd and Pb isotope evidence from Kenya Rift basalts: *Earth and Planetary Science Letters*, v. 176, no. 3-4, p. 387-400.
- Simonetti, A., and Bell, K., 1995, Nd, Pb and Sr Isotopic Data from the Mount-Elgon Volcano, Eastern Uganda Western Kenya - Implications for the Origin and Evolution of Nephelinite Lavas: *Lithos*, v. 36, no. 2, p. 141-153.
- Stewart, K., and Rogers, N., 1996, Mantle plume and lithosphere contributions to basalts from southern Ethiopia: *Earth and Planetary Science Letters*, v. 139, no. 1-2, p. 195-211.
- Vollmer, R., and Norry, M. J., 1983, Unusual isotopic variations in Nyiragongo nephelinites: *Nature*, v. 301, no. 5896, p. 141-143.

### **Gaussberg and Western Australien lamproites**

- Fraser, K. J., Hawkesworth, C. J., Erlank, A. J., Mitchell, R. H., and Scott-Smith, B. H., 1985, Sr, Nd and Pb isotope and minor element geochemistry of lamproites and kimberlites: *Earth and Planetary Science Letters*, v. 76, no. 1, p. 57-70.
- Murphy, D. T., Collerson, K. D., and Kamber, B. S., 2002, Lamproites from Gaussberg, Antarctica: Possible Transition Zone Melts of Archaean Subducted Sediments: *Journal of Petrology*, v. 43, no. 6, p. 981-1001.

### **Marie Byrd Land and Seamounts**

- Hart, S. R., Blusztajn, J., LeMasurier, W. E., and Rex, D. C., 1997, Hobbs Coast Cenozoic volcanism: Implications for the West Antarctic rift system: *Chemical Geology*, v. 139, no. 1-4, p. 223-248.
- Kipf, A., Hauff, F., Werner, R., Gohl, K., van den Bogaard, P., Hoernle, K., Maicher, D., and Klügel, A., 2014, Seamounts off the West Antarctic margin: A case for non-hotspot driven intraplate volcanism: *Gondwana Research*, v. 25, no. 4, p. 1660-1679.
- Panter, K. S., Hart, S. R., Kyle, P., Blusztajn, J., and Wilch, T., 2000, Geochemistry of Late Cenozoic basalts from the Crary Mountains: characterization of mantle sources in Marie Byrd Land, Antarctica: *Chemical Geology*, v. 165, no. 3-4, p. 215-241.

### **Northeast Africa; Sudan and Egypt**

- Lucassen, F., Franz, G., Romer, R. L., Pudlo, D., and Dulski, P., 2008, Nd, Pb, and Sr isotope composition of Late Mesozoic to Quaternary intra-plate magmatism in NE-Africa (Sudan, Egypt): high- $\mu$  signatures from the mantle lithosphere: *Contributions to Mineralogy and Petrology*, v. 156, no. 6, p. 765-784.

### **Olivine Mellilite Province –Alphard Bank**

- Janney, P. E., Le Roex, A. P., Carlson, R. W., and Viljoen, K. S., 2002, A Chemical and Multi-Isotope Study of the Western Cape Olivine Melilitite Province, South Africa: Implications for the Sources of Kimberlites and the Origin of the HIMU Signature in Africa: *Journal of Petrology*, v. 43, no. 12, p. 2339-2370.

## **Kimberlites**

---

Collerson, K. D., Williams, Q., Ewart, A. E., and Murphy, D. T., 2010, Origin of HIMU and EM-1 domains sampled by ocean island basalts, kimberlites and carbonatites: The role of CO<sub>2</sub>-fluxed lower mantle melting in thermochemical upwellings: *Physics of the Earth and Planetary Interiors*, v. 181, no. 3-4, p. 112-131.

Kramers, J. D., 1977, Lead and strontium isotopes in Cretaceous kimberlites and mantle-derived xenoliths from Southern Africa: *Earth and Planetary Science Letters*, v. 34, no. 3, p. 419-431.

## **Kimberlites**

### **(Figure 1: Unexpected HIMU-type Late-Stage Volcanism on the Walvis Ridge)**

Faure, S., 2010, World kimberlites CONSOREM database, Version.

## **Carbonatites**

---

### **Namaqua Natal Belt -Namibia**

Cooper, A. F., and Reid, D. L., 1998, Nepheline Sövites as Parental Magmas in Carbonatite Complexes: Evidence from Dicker Willem, Southwest Namibia: *Journal of Petrology*, v. 39, no. 11-12, p. 2123-2136.

Cooper, A. F., and Reid, D. L., 2000, The association of potassic trachytes and carbonatites at the Dicker Willem Complex, southwest Namibia: coexisting, immiscible, but not cogenetic magmas: *Contributions to Mineralogy and Petrology*, v. 139, no. 5, p. 570-583.

### **East African Rift**

Bell, K., and Tilton, G. R., 2001, Nd, Pb and Sr Isotopic Compositions of East African Carbonatites: Evidence for Mantle Mixing and Plume Inhomogeneity: *Journal of Petrology*, v. 42, no. 10, p. 1927-1945.

Kalt, A., Hegner, E., and Satir, M., 1997, Nd, Sr, and Pb isotopic evidence for diverse lithospheric mantle sources of East African Rift carbonatites: *Tectonophysics*, v. 278, no. 1, p. 31-45.

Nelson, D. R., Chivas, A. R., Chappell, B. W., and McCulloch, M. T., 1988, Geochemical and isotopic systematics in carbonatites and implications for the evolution of ocean-island sources: *Geochimica et Cosmochimica Acta*, v. 52, no. 1, p. 1-17.

## **Carbonatites**

### **(Figure 1: Unexpected HIMU-type Late-Stage Volcanism on the Walvis Ridge )**

Woolley, A. R., and Kjarsgaard, B. A., 2008, Carbonatite occurrences of the world: map and database, Geological Survey of Canada.



## **DANKSAGUNG**

Die vorliegende Arbeit entstand durch das vom Bundesministerium für Bildung und Forschung geförderte Projekt SO233 WALVIS II „Zeitliche und geochemische Entwicklung des Walvisrückens im Südatlantik“ (03G0233A). Für die Ausarbeitung der Projektanträge möchte ich mich zunächst bei Prof. Dr. Kaj Hoernle, Dr. Folkmar Hauff, Dr. Reinhard Werner, Dr. Maxim Portnyagin und Dr. Jörg Geldmacher bedanken, die damit den Grundstein für meine Promotion gelegt haben.

Mein besonderer Dank gilt Prof. Dr. Kaj Hoernle für die Möglichkeit zur Promotion, für seine Unterstützung in den letzten Jahren und die kritische Durchsicht meiner Manuskripte. Besonders möchte ich ihm für seine Ideen danken, die mir in unzähligen Bereichen einen neuen Blickwinkel auf meine Daten ermöglicht haben und die schier unzählbaren Stunden, die er in mich und meine Promotion investiert hat.

Prof. Dr. Colin Devey möchte ich für das Zweitgutachten zu dieser Arbeit danken. Prof. Dr. Martin Frank und Dr. Jörg Geldmacher danke ich für die Teilnahme an meiner Prüfungskommission und ihrem Interesse an meiner Arbeit.

Ganz besonders möchte ich mich bei Dr. Folkmar Hauff für die Einarbeitung in die Isotopenanalyse, seine Unterstützung bei der Auswertung und Interpretation der Daten, sowie für die Überarbeitung der Manuskripte und Hilfe bei Fragen jeglicher Art bedanken.

In diesem Zuge möchte ich mich auch ganz herzlich bei Dr. Reinhard Werner und Dr. Maxim Portnyagin bedanken, die mich in die Kunst des Dredgens eingearbeitet haben und mich in den nachfolgenden Jahren immer bei der Erstellung meiner Manuskripte unterstützt haben.

Des Weiteren möchte ich mich bei Dr. Jörg Geldmacher bedanken, der zum einen ausschlaggebend an der Bergung der Proben beteiligt war und zum anderen mit zahlreichen Ideen, Vorschlägen und der kritischen Überarbeitung der Manuskripte zu meiner Promotion beigetragen hat.

Bei Dr. Paul van den Bogaard und Dr. Jo-Anne Wartho möchte ich mich für die Unterstützung und Durchführung der  $^{40}\text{Ar}/^{39}\text{Ar}$ -Datierung bedanken. Besonderer Dank gilt Dr. Jo-Anne Wartho, die entscheidend an der Erstellung, Auswertung und Interpretation der Altersdaten in dieser Arbeit beteiligt war. In diesem Zuge möchte ich mich auch bei Jan Sticklus für die Laborarbeiten und Messung bedanken.

Weiterhin möchte ich allen danken, die mich bei der Promotion unterstützt haben. Angefangen bei den Fahrteilnehmern von SO233 und SO234 ohne die dieses Projekt nicht möglich gewesen wäre, bei Kapitän Meyer und der Crew der Sonne mit denen ich ein wunderbares halbes Jahr auf verschiedenen Ozeanen und Häfen verbracht habe.

Im Weiteren möchte ich mich bei Marie Anders für die Hilfe bei der Probenbearbeitung bedanken, bei Prof. Dr. Stefan Jung für die RFA-Analytik, sowie Dr. Dieter Garbe-Schönberg und Dipl.-Ing. Ulrike Westernströer für die Unterstützung bei der Vorbereitung der Proben zur ICP-MS Analytik und Spurenelementanalysen. Des Weiteren danke ich Karin Jung und Silke Hauff, die mich Labor eingearbeitet und unterstützt haben und mir bei unzähligen Situationen geholfen haben. Besonders möchte ich mich bei Antje Dürkefälden bedanken, die mich in die Probenaufbereitung eingearbeitet hat und mir bei vielen grundlegenden Aspekten der Promotion geholfen hat.

Abschließend bedanke ich mich bei meinen Freunden und meiner Familie, die für diverse Ablenkungen an den Wochenenden gesorgt haben und durch ihre unendliche Unterstützung immer für mich da waren, besonders in den schwierigen Zeiten. Ob im Norden, Sauerland, Mainz oder sonst wo auf der Welt, bei euch fühl ich mich immer zu Hause und mögen noch zahlreiche Anlässe gefeiert werden.

Mein größter Dank geht an Rebecca, die während der gesamten Promotion mein Leben bereichert hat, mich täglich unterstützt und mich besonders in der schwierigen Phasen der letzten Jahre gestützt und getragen hat. Danke für deine Geduld und für die schöne Zeit, die hoffentlich noch lange anwährt.

## CURRICULUM VITAE

**Name:** Stephan Homrighausen  
**Date of birth:** 01.12.1985  
**Place of birth:** Winterberg  
**Nationality:** German  
**Sex:** Male  
**Marital status:** Single

### PROFESSIONAL EXPERIENCE

---

since 12/2017: Research assistant at GEOMAR Helmholtz Centre for Ocean Research Kiel within the BMBF project SO258 INGON Leg 1: "The Indian – Antarctic Break-up Enigma"  
Research Division: Dynamics of the Ocean Floor  
Research Unit: Magmatic and Hydrothermal Systems

05/2014-7/2017: Research assistant at GEOMAR Helmholtz Centre for Ocean Research Kiel within the BMBF project SO233 Walvis I: " Insights into the temporal and geochemical evolution of the Walvis Ridge"  
Research Division: Dynamics of the Ocean Floor  
Research Unit: Magmatic and Hydrothermal Systems

04/2013-11/2013: Scholarship student at the Darmstadt Graduate School of Excellence Energy Science and Engineering of the technical university of Darmstadt

02/2013-04/2013: Student assistant at Technical University of Darmstadt  
Research Division: Institute for Geotechnics

05/2011–04/2012: Student assistant at Johannes Gutenberg-University of Mainz  
Research Division: Institute for Geosciences; Petrology

09/2008: Student assistant at Johannes Gutenberg-University of Mainz

#### **ACADEMIC EDUCATION**

---

- since 05/2014: Doctoral Studies at the Christian-Albrechts University of Kiel
- 10/2006-03/2013: Diploma study of Geology and Paleontology at the Johannes Gutenberg-University of Mainz  
Diploma thesis: Geochemistry and Origin of Ultrapotassic Lavas from Karadirek, Central West Anatolia, Turkey  
Major subjects: Magmatic Petrology, Tectonophysics, Isotopegeochemistry and Historical Geology

#### **FIELDWORK AND EXPEDITIONS**

---

- 06/2017-07/2017: Shift leader at the research cruise SO258 Leg 1, INGON: "The Indian – Antarctic Break-up Enigma" with the R/V Sonne
- 02/2016-03/2016: Shift leader at the research cruise SO246, Chatham Rise: "Compressional, extensional and breakup mechanism of a submarine continental plateau" with the R/V Sonne
- 06/2014-07/2014: Shift leader at the research cruise SO234 Leg 1, Spaces: "Science or the Assessment of Complex Earth System Processes" with the R/V Sonne
- 05/2014-06/2014: Participation at the research cruise SO233, WALVIS II: "Insights into the temporal and geochemical evolution of the Walvis Ridge" with the R/V Sonne
- 07/2011: Diploma mapping at Karadirek, Central West Anatolia, Turkey
- 10/2006-03/2013: Many field trips (~100 days) in Germany, Turkey, Austria, Switzerland and Spain within the university program

## PUBLICATIONS AND CONFERENCE CONTRIBUTIONS

---

### PUBLICATIONS

**Homrighausen, S.**, Hoernle, K., Geldmacher, J., Wartho, J.-A., Hauff, F., Potnyagin, M., Werner, R., van den Bogaard, P. and Garbe-Schönberg, C.D. (in press), Unexpected HIMU-type Late-Stage Volcanism on the Walvis Ridge. *Earth Planet Sc Lett.*

Hoernle, K., Rohde, J., Hauff, F., Garbe-Schonberg, D., **Homrighausen, S.**, Werner, R., and Morgan, J. P., 2015, How and when plume zonation appeared during the 132 Myr evolution of the Tristan Hotspot: *Nature Communication*, v. 6, p. 10.1038/ncomms8799.

### CONFERENCE CONTRIBUTIONS

Werner, R., Hoernle, K., **Homrighausen, S.**, Gohl, K. and Davy, B. (2017) Hintergrund und erste Ergebnisse der vulkanologisch-petrologischen Untersuchungen von SO-246 (CHATHAM RISE): Kompressions-, Extensions- und Abbruchmechanismen eines submarinen Kontinentalplateaus. [Talk] In: Statusseminar Meeresforschung mit FS SONNE 2017., 14.-15.02.2017, Oldenburg

**Homrighausen, S.**, Hoernle, K., Hauff, F., Portnyagin, M., Werner, R., Geldmacher, J. and Garbe-Schönberg, C. D. (2015) Late-Stage HIMU-Type Volcanism on the Walvis Ridge: Not just Part of an Age-Progressive Tristan-Gough Hotspot Track [Poster] In: AGU Fall Meeting 2015, 14.-18.12.2015, San Francisco, USA

**Homrighausen, S.**, Hoernle, K., Werner, R., Portnyagin, M., Geldmacher, J. and Hauff, F. and SO233 Fahrtteilnehmer (2015) Walvis II: Hintergrund und erste Ergebnisse, Zeitliche und geochemische Entwicklung des Walvisrückens [Talk] In: Statusseminar Meeresforschung mit FS SONNE 2015, 12.-13.02.2015, Bremen . Tagungsband Statusseminar Meeresforschung mit FS SONNE 2015 ; pp. 162-165 .

Werner, R., Wagner, H. J., Mattheus, U., Geldmacher, J. and **Homrighausen, S.** and SO-234/1 Fahrtteilnehmer (2015) Verlauf und erste Ergebnisse der Ausbildungsfahrt SO-234/1 SPACES (Walvis Bay - Durban) [Talk] In: Statusseminar Meeresforschung mit FS SONNE 2015, 12.-13.02.2015, Bremen . Tagungsband Statusseminar Meeresforschung mit FS SONNE 2015 ; pp. 171-174